Advances in
QUANTUM CHEMISTRY

UNSTABLE STATES IN THE CONTINUOUS SPECTRA, PART II: INTERPRETATION, THEORY AND APPLICATIONS

VOLUME **63**

Special Editors

CLEANTHES A. NICOLAIDES
Theoretical and Physical Chemistry Institute
National Hellenic Research Foundation
Athens, Greece

ERKKI BRÄNDAS
Department of Quantum Chemistry
Uppsala University
Uppsala, Sweden

Editors

JOHN R. SABIN
Quantum Theory Project
University of Florida
Gainesville, Florida

ERKKI BRÄNDAS
Department of Quantum Chemistry
Uppsala University
Uppsala, Sweden

ELSEVIER

Amsterdam • Boston • Heidelberg • London • New York • Oxford
Paris • San Diego • San Francisco • Singapore • Sydney • Tokyo

Academic Press is an imprint of Elsevier

Academic Press is an imprint of Elsevier
525 B Street, Suite 1900, San Diego, CA 92101-4495, USA
225 Wyman Street, Waltham, MA 02451, USA
32 Jamestown Road, London NW1 7BY, UK
Linacre House, Jordan Hill, Oxford OX2 8DP, UK

First edition 2012

ISBN: 978-0-12-397009-1
ISSN: 0065-3276

For information on all Academic Press publications visit our web site at *www.elsevierdirect.com*

Printed and bounded in USA
12 13 14 15 10 9 8 7 6 5 4 3 2 1

PREFACE

Since the late 1920s, most of the many thousands of publications contributing to quantum chemistry have dealt with issues and problems that essentially concern, or are applicable to, the ground or the low-lying discrete states of atoms and molecules and of electronic matter in general. In this context, samples of topics that have been examined are many-faceted formalisms, analysis and computation of various features of the many-electron problem, computational methodologies and techniques, results of computation of properties and of low-energy chemical reactions, computation of spectroscopic data involving mainly discrete states, etc.

On the other hand, significant advances have also been made in the broader domain of quantum chemistry, a prime example being areas of research that involve the continuous spectrum and, as such, are more complex, conceptually, formally, and computationally. When the continuous spectrum of a quantum system acquires physical significance, a plethora of special and challenging physical and mathematical features and questions emerge that are absent in problems involving just the discrete spectrum.

In the variety of excitation or de-excitation processes that allow the preparation and/or observation of the system via the participation of the continuous spectrum, the dominant and most interesting characteristics are generated by the transient formation of *nonstationary* or *unstable states*. For example, the excitation may be caused by the absorption of one or of many photons during the interaction of an initial atomic or molecular state with pulses of long or of short duration. Or, the transient formation and influence on the observable quantity may occur during the course of electron–atom scattering or of chemical reactions.

In principle, the physics involving unstable states ought to engage descriptions that are time dependent. Yet, in the formulation and practical solution of related problems, both time-dependent and time-independent treatments are pertinent and necessary. Furthermore, in certain theoretical approaches, the phenomenologies as well as the computational methodology are based on constructions that are non-Hermitian. We add that the Hamiltonians may

or may not include the coupling of atomic or molecular states to external electromagnetic fields.

The two volumes of *Unstable States in the Continuous Spectra*, which we have edited (Part I is AQC volume 60 and Part II is the present volume, 63), contain a total of 15 review articles on topics covered by the general theme. The invitation of the contributing experts had as one of its purposes to create a book on the above theme where the spectrum of the information contained in it is wide, authoritative, and relevant to quantum chemistry. The invited authors were free to choose their topic(s) and style of presentation. Before final acceptance, their manuscripts were subjected to "friendly yet critical" review by referees suggested by the authors, aiming at improving the contents as much as possible.

The first volume contained nine state-of-the-art chapters on fundamental aspects, on formalism, and on a variety of applications. The various discussions employ both stationary and time-dependent frameworks, with Hermitian and non-Hermitian Hamiltonian constructions. A variety of formal and computational results address themes from quantum and statistical mechanics to the detailed analysis of time evolution of material or photon wave packets, from the difficult problem of combining advanced many-electron methods with properties of field-free and field-induced resonances to the dynamics of molecular processes and coherence effects in strong electromagnetic fields and strong laser pulses, from portrayals of novel phase space approaches of quantum reactive scattering to aspects of recent developments related to quantum information processing.

The present volume of the *Advances in Quantum Chemistry* is the sequel of the first volume, mentioned above, i.e., *Unstable States in the Continuous Spectra, Part II: Interpretation, Theory and Applications.* It contains six chapters with contents varying from a pedagogical introduction to the notion of unstable states to the presence and role of resonances in chemical reactions, from discussions on the foundations of the theory to its relevance and precise limitations in various fields, from electronic and positronic quasi-bound states and their role in certain types of reactions to applications in the field of electronic decay in multiply charged molecules and clusters, as well.

Given the plurality of the aforementioned discussions in both volumes, we hope that both senior and young quantum chemists and physicists with an interest in the specific theme of "unstable states in the continuous spectra" and in quantum theory, in general, will find the present set of two volumes resourceful, innovative, and helpful.

Cleanthes A. Nicolaides
Athens, Greece

Erkki J. Brändas
Uppsala, Sweden

CONTRIBUTORS

Erkki J. Brändas, Quantum Chemistry, Department of Physical and Analytical Chemistry, Uppsala University, Uppsala, Sweden.

Eva Lindroth, Department of Physics, Stockholm University, AlbaNova University Center, 106 91 Stockholm, Sweden.

Ido Gilary, Schulich Faculty of Chemistry, Technion-Israel Institute of Technology, Haifa 32000, Israel.

Isao Shimamura, Atomic Physics Laboratory, RIKEN, Wako, Saitama 351-0198, Japan.

Luca Argenti, Dept. Química, Módulo 13, Universidad Autónoma de Madrid, 28049 Madrid, Spain.

Přemysl Kolorenč, Institute of Theoretical Physics, Faculty of Mathematics and Physics, Charles University in Prague, V Holešovičkách 2, 180 00 Prague, Czech Republic.

Rex T. Skodje, Department of Chemistry and Biochemistry, University of Colorado, Boulder, CO 80309, USA.

Shachar Klaiman, Schulich Faculty of Chemistry, Technion-Israel Institute of Technology, Haifa 32000, Israel.

Vitali Averbukh, Department of Physics, Imperial College London, Prince Consort Road, SW7 2AZ London, UK.

CHAPTER 1

On Resonance: A First Glance into the Behavior of Unstable States

Shachar Klaiman[a] and **Ido Gilary**[a]

Contents

Abstract Dynamical processes in nature often involve unstable states. Analyzing systems with a finite lifetime can be challenging for a practitioner of quantum mechanics. To study such processes in a quantum system, one must venture

[a] Schulich Faculty of Chemistry, Technion-Israel Institute of Technology, Haifa 32000, Israel
E-mail address: shachark@technion.ac.il

Advances in Quantum Chemistry, Volume 63
ISSN 0065-3276, DOI: 10.1016/B978-0-12-397009-1.00001-1

into the continuum where the use of a continuous superposition of states, i.e., a wave packet, is required. Most of our quantum education focuses on quantized bound states rather than on the behavior of wave packets. Here, we aim to give a pedagogic introduction to the behavior and analysis of unstable states. To achieve this, we introduce two complementary viewpoints by which such states can be analyzed. We further discuss the physical mechanisms through which quantum unstable states are formed.

1. INTRODUCTION

The word *resonance* is a very widespread term in the scientific world. Common uses range from being *in a* or *on* resonance to resonance poles and peaks. As with many such ubiquitous terms, they evolve with time and tend to take a life of their own acquiring new meaning and connotations as time goes by. This can lead to some confusion and ambiguity when different definitions are evoked. Here, we wish to explore the meaning of this term attributed to unstable states in quantum mechanics.

Given a quantum mechanical system, i.e., a Hamiltonian, one can generally separate the spectrum into two types of solutions: bound states and continuum states. Regularly, introductory courses and texts in quantum mechanics focus on bound states. These are found by searching for solutions of the time-independent Schrödinger equation (TISE) with the appropriate boundary conditions (BCs), which for bound states are such that the wavefunction vanishes at all the boundaries. The imposed BCs lead to the quantization of the bound spectrum. This quantization facilitates the understanding of quantum phenomena related to bound states since one can often relate the desired phenomenon with the occupation of only a few well-defined states. Unfortunately, the continuum part of the spectrum is not as gratifying. In the continuum, we are forced to use wave packets rather than a single eigenstate to describe quantum particles. Single eigenstates in the continuum are not amenable to the usual probabilistic interpretation, which requires the normalization of the particle wavefunction. Wave packets are built by integrating over a continuous range of energy eigenstates to create localized wavefunctions. Therefore, when describing phenomena that require the continuous part of the spectrum, it becomes increasingly difficult to correlate an observed effect with a single eigenstate of the TISE.

The necessity of working with wave packets presents an intrinsic difficulty in the treatment of the system. One can no longer be content with the solutions of the time-independent Schrödinger equation, and a solution to the time-dependent Schrödinger equation (TDSE) is required. Although analysis based on the TDSE is certainly possible, one is often not well accustomed to it. This is mainly because most of quantum mechanical textbooks build our intuition and understanding with examples of solution of the TISE, and the TDSE is mostly disregarded. We should mention here a recent textbook by Tannor [1], which recognized this void and aims to fill it.

Notwithstanding the above mentioned difficulties in treating processes in the continuum, many physical situations allow for a simpler approach based on resonance states. Resonance states are solutions of the TISE, which correspond to unstable quantum states, i.e., states with a *finite* lifetime. Although, by definition, these processes occur solely in the continuum, i.e., bound states have an *infinite* lifetime, resonance states are quantized solutions of the TISE. Therefore, describing a continuum wave packet using such resonance states would circumvent one of the biggest difficulties in the continuum – the inability to associate the physical phenomenon with a finite number of physical states. An extensive account of the theoretical framework of resonance phenomena as well as the various methods used to treat it can be found in Refs. [2, 3]. Quite generally, one can classify processes in the continuum into two types: a full-collision process and a half-collision process, according to the initial preparation of the system. In a full-collision process, particles are scattered from a potential and are then measured in the asymptotic region, i.e., the particles start and finish in the asymptotes. In a half collision, however, the system is prepared in an excited state and one measures the breakup into products of this excited state, i.e., particles that are initially located in the interaction region are measured at the asymptotic region. In this chapter, we focus on half-collision processes demonstrating the connection between a wave packet solution of the TDSE and a resonance solution of the TISE. This connection between the solutions of the TDSE and the TISE puts one on solid ground even when the continuum is involved.

Since we hope to give here an introductory account of resonances, we shall focus on systems where the dynamics is controlled by a single metastable state, i.e., an unstable state with an appreciable lifetime. This might seem at first rather limiting, but in fact it accounts for many physical situations. The conditions for single resonance dynamics will be expanded on further in the following. In addition in order to maintain a simple picture we will illustrate everything for a single particle in one dimension although most of the arguments that will be made in this chapter could be readily generalized to many-body problems in higher dimensions. One of the most famous examples as well as one of the first applications of resonance theory in quantum mechanics was given by Gamow in 1928 [4] in his study of α decay. Since this phenomenon is extremely robust, many other examples can be found in various fields of physics [5]. Just to name a few disciplines, these include, for example: particle [6–8], atomic [9–13], molecular [14–16], and mesoscopic [17–20] physics, as well as the interaction of such systems with electromagnetic radiation [21, 22] or their implementation in electronic applications [23–25].

The simplest way to construct a system that supports a metastable state is to first consider a system with at least a single bound state. If we wish to probe a particle in this bound state, we must couple it to the "outside" world where our measurement devices are. There are, in general, many ways by which such a coupling can occur. One common possibility is to scatter

particles of the bound target and measure the resulting cross section, i.e., a full-collision experiment. This is the situation, for example, in experiments probing quantum dots via a conductance measurement [17, 26]. Yet another possibility is to manipulate the bounding potential using external forces such that the bound state is pushed into the continuum, i.e., a half-collision experiment. A well-known example are Stark resonances, which are the result of placing atoms inside a dc electric field [27].

For pedagogic as well as illustrative reasons, we begin our discussion by presenting a solution of the TDSE for a model problem. On this model problem, we demonstrate in Section 2 that a wave packet solution of the TDSE can be of a dual nature and possess both the characteristics of a bound and a continuum state. Most importantly we show a *stationary* nature of the time-dependent dynamics. This *oxymoron* is at the heart of resonance theory. Following the time-dependent analysis, we proceed to discuss a stationary analysis using resonances. This is done in Section 3. Ensuing from the complementary pictures of both the stationary and the time-dependent strategies, Section 4 aims to clarify and unite the two approaches, settling the seemingly disturbing dissonance. In Section 5, we present the possible quantum mechanical sources for the formation of metastable states. We then present our conclusions along with possible other features that could be the subject of further study.

2. A QUANTUM MECHANICAL RESONANCE STATE FROM A TIME-DEPENDENT PERSPECTIVE

At first glance, one can not hope to find general features that are common to different solutions of the TDSE. There are simply to many variables, one might rightfully assume that the solution depends greatly on the initial condition and that every potential displays completely different features. Unlike a solution of the TISE, where we can define a state by its energy and write its time dependence explicitly, a general wave packet solution of the TDSE cannot be so characterized in a similar manner. In this section, however, we will show that under certain conditions even a wave packet, a dynamic time-dependent entity by definition, has many of the common attributes of a stationary state.

2.1. From bound state to metastable state

Consider, as an example, the following variation of the often-used one-dimensional potential [28]:

$$V(x) = \left(1 - \frac{V_0}{\cosh^2 \beta x}\right) e^{-\alpha x^2}. \tag{1}$$

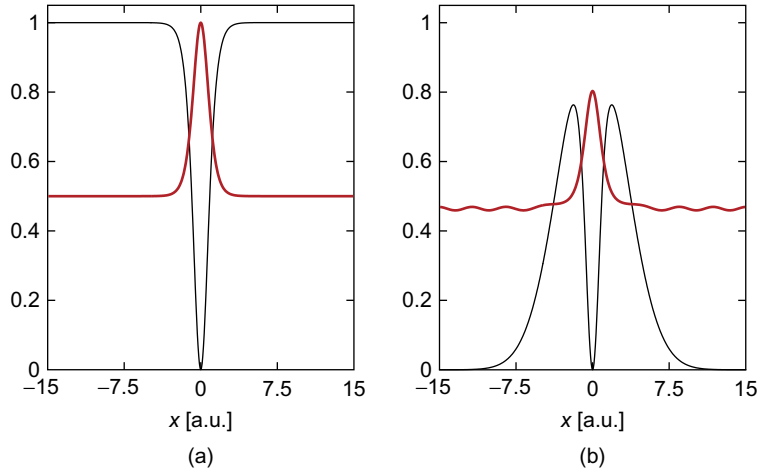

Figure 1.1 The one-dimensional potential given in Eq. (1) is depicted for two different choices of α: (a) $\alpha = 0$ and (b) $\alpha = 0.05$. The following parameters are the same for both potentials: $V_0 = 1$, $\beta = 1$. The potential in (a) supports a single bound state at the energy $E_0 = 0.5$[a.u.], and the corresponding probability density is drawn, where the energy of the state serves as a baseline. The potential in (b) supports no bound states but only continuum states. Still we draw the probability density of the continuum eigenfunction close in energy to $E_0 = 0.5$[a.u.].

We shall use the values $V_0 = 1$ and $\beta = 1$ throughout. If we take α to be zero, the potential in Figure 1.1a supports a single bound state at the energy $E_0 = 0.5$[a.u.]. Here and in the following, all quantities are given in atomic units for which $\hbar = 1$ and $m = 1$. Figure 1.1a also displays the corresponding bound state wavefunction, $\psi_0(x)$. The bound state wavefunction, as expected, decays exponentially in the classically forbidden region and is highly localized within the potential well. Consider now a particle in the bound state of the above potential with $\alpha = 0$ at time $t = 0$. The solution of the TDSE reads

$$\psi(x,t) = e^{-iE_0 t}\psi_0(x), \tag{2}$$

where E_0 and $\psi_0(x)$ are defined above. Clearly, the probability density is time independent, i.e., a stationary state. If we write a general time-dependent solution as

$$\psi(x,t) = \Lambda(x,t)e^{iS(x,t)}, \tag{3}$$

where $\Lambda(x,t)$ and $S(x,t)$ are real functions, which give the amplitude and phase of the wavefunction, respectively, then a stationary state also has

the unique property that $S(x,t) = f(t)$, i.e., the phase of the time-dependent wavefunction, is position independent. We should remark here that the above "definition" of a stationary state assumes that the solution of the TISE is real. For a Hamiltonian with time-reversal symmetry one can always satisfy this condition. We shall see the importance of this property in the following. The particle itself will always remain in the bound state, a property which can be quantified as an infinite lifetime of the state.

We now perturb the bound system described above such that the potential is changed and now $\alpha = 0.05$. The new potential is depicted in Figure 1.1b. Basically, we left the bottom of the potential well, where the bound state was situated intact and etched away the potential everywhere else. The new potential does not support any bound states, and the entire spectrum is continuous. A scattering continuum state at an energy close to that of the bound state in Figure 1.1a is also shown in Figure 1.1b. Evidently, a large amplitude of the probability density of the continuum state in Figure 1.1b is still localized in between the barriers. Note, however, that outside the barriers, the small amplitude of the wavefunction oscillates all the way to infinity; thus, this state is not square integrable. This means that it cannot by itself describe a single particle trapped between the barriers.

Following the perturbation, the particle previously inhabiting the bound state wavefunction $\psi_0(x)$ is no longer in a stationary state. The previous eigenstate is now a wave packet, i.e., a superposition of the eigenstates of the perturbed Hamiltonian. Since the perturbed potential supports no bound states (see. Figure 1.1b), this superposition will include only continuum states $\phi_E(x)$, which can be energy normalized according to $\langle \phi_E | \phi_{E'} \rangle = \delta(E - E')$. Thus, the wave packet will have the form

$$\psi(x,0) = \int_0^\infty C(E)\phi_E(x)\mathrm{d}E, \tag{4}$$

where

$$C(E) = \int_{-\infty}^{\infty} \phi_E^*(x)\psi(x,0)\mathrm{d}x. \tag{5}$$

As discussed above, the continuum eigenfunctions $\phi_E(x)$ are not square integrable. Nevertheless, since we begin with a square integrable function $\psi(x,0)$, the integrals for the expansion coefficients $C(E)$ will converge and the wave packet will remain square integrable at all times. The time-reversal symmetry of the Hamiltonian also implies the conservation of the total momentum; hence, if we have an initially bound system where $< p(0) >= 0$, this average value will remain constant even when the wave packet evolves and leaks out of the interaction region.

If we wish to follow the time-dependent, dynamical properties of the wave packet, we must solve the TDSE with the ground state $\psi_0(x)$ of the unperturbed system as an initial condition:

$$\psi(x,0) = \psi_0(x) = \frac{1}{\sqrt{2}\cosh x}. \tag{6}$$

2.2. Evolution of the resonance wavefunction

We begin our analysis by discussing the probability density of our wave packet and its evolution in time. In the absence of a potential, a free wave packet would simply diffract, spreading through all space up to a uniform distribution at infinite times. A common textbook example [29] is to show that at sufficiently long times, regardless of the initial wave packet, the probability density at each point falls as t^{-1}. In the presence of the potential, however, the behavior of the wave packet changes dramatically. Figure 1.2 displays the probability density $\rho(x,t) = |\psi(x,t)|^2$ as a function of time inside the interaction region, i.e., between the barriers. Clearly, the probability density decays inside the interaction region pointing out the finite lifetime of the previously bound particle, i.e., the formation of a metastable state. Evidently, the decay is much slower than the diffraction limit of t^{-1}. We shall see in the following that for times larger $t_0 \approx 5$[a.u.], the decay actually takes an exponential form.

We turn now to study the properties of the metastable state in more detail. We, therefore, concentrate on the long-time behavior, i.e., $t > t_0$, and defer the discussion of the short-time dynamics to a later section. Figure 1.3 shows snapshots of the probability density of the evolving wave packet at different

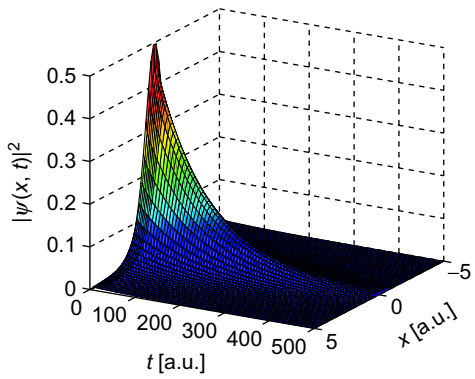

Figure 1.2 The probability density as a function of time in atomic units. The probability at time zero is given by $\rho(x,0) = \frac{1}{2\cosh^2 x}$. The decay in the interaction region can be well approximated as exponential.

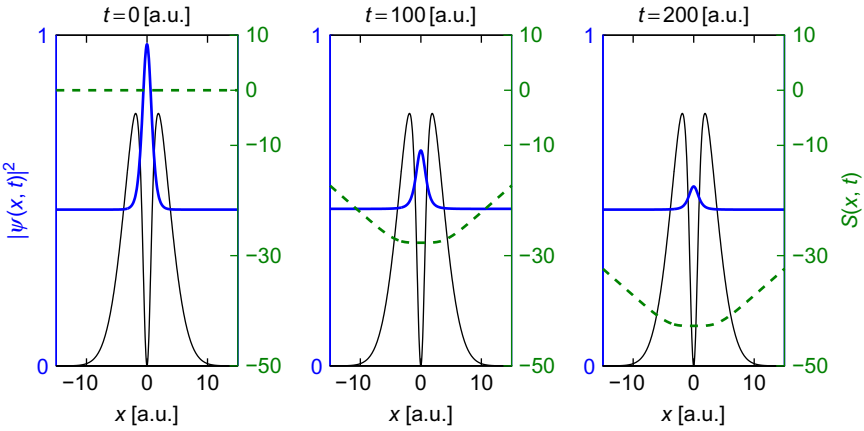

Figure 1.3 Snapshots of the probability density (solid line, left *y*-axis) at different times. The phase $S(x,t)$, see Eq. (3), of the wave packet is also displayed (dashed line, right *y*-axis). Note that at times different than zero, the phase is *x* dependent, meaning that we are not in a stationary state. Furthermore, note that in the interaction region, i.e., between the barriers, the phase is approximately constant.

times. At time $t = 0$, the wave packet is completely localized between the two barriers. As time progresses, one can see that the probability density between the barriers falls, i.e., the particle is tunneling out of the potential well and is moving to the asymptotes. Thus, the original bound state with an infinite lifetime now decays and has a finite lifetime. This metastable state has been produced by coupling the bound state with the continuum outside of the potential well, or in other words, we have perturbed the potential such that the particles in the bound state can escape – in this case via tunneling. We should emphasize here that there is no violation of the conservation of matter. The decay is only evident since we are restricting our view of the world to the interaction region. If we were to integrate the probability density of the wave packet over the whole space, no loss of matter would be evident. Figure 1.3 also displays the phase $S(x,t)$ (see Eq. [3]) of the wave packet at different times. Initially (at $t = 0$), the phase was zero. As the wave packet evolves in time, however, the phase starts to modulate and becomes spatially dependent. This is to be expected from a nonstationary state. Still, as one can see in Figure 1.3, the phase in the interaction region, i.e., between the barriers, is almost constant, reminiscent of the constant phase one would get for a bound state of the system. Outside the interaction region, the phase becomes linear with the position.

To better understand both the position and the time dependence of $S(x, t > t_0)$, we plot the phase as a function of these variables in Figure 1.4. Evidently, the phase drops linearly with time. In accordance with Figure 1.3, Figure 1.4 also shows the phase growing linearly with the position outside the interaction region and remaining constant within it. The above evidence

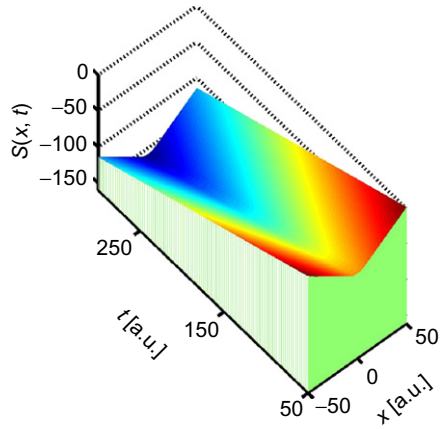

Figure 1.4 The phase $S(x,t)$ of the wave packet as defined in Eq. (3). The initial state is the bound state of the unperturbed potential given in Eq. (6).

suggests the following general form for $S(x,t)$:

$$S(|x|, t > t_0) = \begin{cases} -\epsilon t + \varphi & |x| < L \\ k_r|x| - \epsilon t + \varphi & |x| > L \end{cases}, \tag{7}$$

where we have defined the interaction region in the range $x \in [-L, L]$. In our example, the rate of change of the local phase obtained from a linear regression on the outer part is $\frac{\partial S}{\partial x} = k_r = 0.965$[a.u.] while the rate of change of the phase in time is $\frac{\partial S}{\partial t} = -\varepsilon = -0.465$[a.u.], and φ is an arbitrary phase factor. The behavior outside the interaction region is reminiscent of a free-propagating wave that behaves as $e^{ik_r x}$. The particles leave the interaction region with momentum k_r moving toward the asymptotes. In other words, outside the interaction region, all we have are free particles escaping. To summarize, inside the interaction region, we have the phase behavior of a bound state, whereas outside we have the behavior of a continuum state.

2.3. Dynamics inside the interaction region

Let us now turn to the kinetics of the particles escaping the interaction region and analyze the decay rate of the wave packet. Figure 1.2 shows the probability density in the interaction region as a function of time. From the figure, it seems that the probability density in the interaction region decays exponentially. This can be verified by calculating the norm inside the interaction region, which is given by

$$N_L(t) = \int_{-L}^{L} |\psi(x,t)|^2 \mathrm{d}x, \tag{8}$$

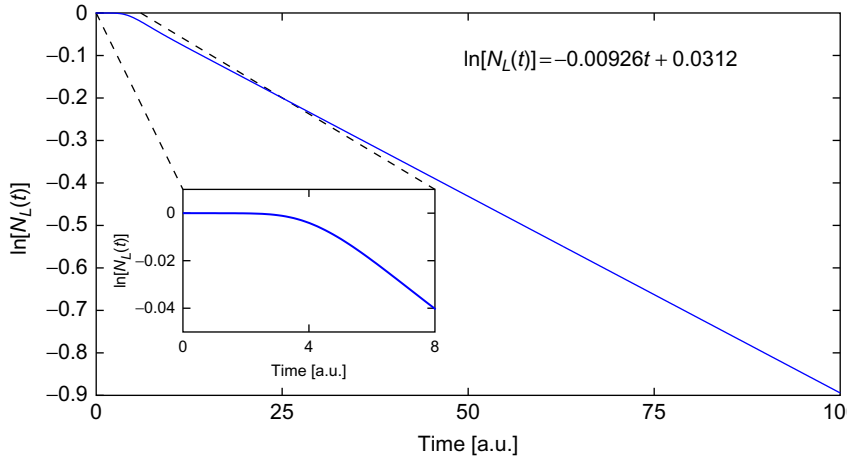

Figure 1.5 The natural logarithm of the local norm, see Eq. (8), as a function of time. The straight line at long times confirms our conjecture of exponential decay, see Figure 1.2. The formula for the straight line found from a linear regression is also presented in the figure.

where as before we have defined an interaction region for $x \in [-L, L]$. Clearly the value of L is not uniquely defined, but as a rule of thumb, one can choose L such that it is larger than the last classical turning point at the average energy of the wave packet. For the potential used in our example, see Figure 1.1b, we choose $L = 5$. Figure 1.5 depicts $\ln(N_L(t))$ as a function of time. The resulting equation of a linear regression is also presented. This indicates that from a certain time t_0, the decay of $N_L(t)$ is exponential and we can write

$$N_L(t > t_0) = e^{-t/\tau} N_L(t_0), \tag{9}$$

where we define τ to be the lifetime of the metastable state. In our example, $\tau = 108$[a.u.] and it appears from the inset of Figure 1.5 that $t_0 \approx 5$.

In the spirit of the above discussion, let us consider a local expectation value of the Hamiltonian where we confine the integration to the interaction region. By doing so, we are considering only the part of the wave packet that remains in the interaction region. In order for this expectation to have meaningful physical context, we must normalize it by the total probability to remain in this region given by $N_L(t)$. Thus, we are evaluating the average energy of the particles that are yet to escape. Explicitly, the local expectation value reads

$$\langle \hat{H} \rangle_L = \frac{\int_{-L}^{L} \psi^*(x,t) \hat{H} \psi(x,t) \mathrm{d}x}{\int_{-L}^{L} |\psi(x,t)|^2 \mathrm{d}x}. \tag{10}$$

Figure 1.6 portrays the real and imaginary parts of the local average energy for the example given above. Note that the local expectation value is not real since we are not integrating over the entire space, i.e., the Hamiltonian operator in the restricted space is non-Hermitian. The first thing evident from the behavior of the local expectation value is its saturation to a constant value at large times. This is one more property the wave packet at large times has in common with a stationary state, which would have a constant average energy at all times. The actual physical meaning of the real and imaginary parts of the local average energy still needs to be examined. Consider $\psi(x,t)$, a solution of the TDSE satisfying

$$\hat{H}\psi(x,t) = i\frac{\partial}{\partial t}\psi(x,t). \tag{11}$$

Multiplying Eq. (11) by $\psi^*(x,t)$ from the left and then subtracting from the result its complex conjugate, we are left with

$$\psi^*(x,t)\hat{H}\psi(x,t) - \psi(x,t)\hat{H}\psi^*(x,t) = i\frac{\partial}{\partial t}|\psi(x,t)|^2. \tag{12}$$

Integrating from $-L$ to $+L$, we find that

$$\frac{\partial}{\partial t}N_L(t) = 2\,\mathrm{Im}\left[\int_{-L}^{L}\psi^*(x,t)\hat{H}\psi(x,t)\right]. \tag{13}$$

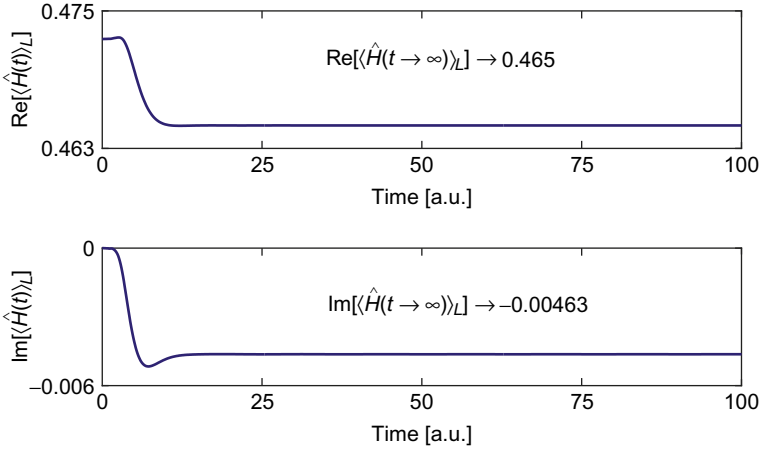

Figure 1.6 The real (top) and imaginary (bottom) parts of the local average energy defined in Eq. (10) as a function of time. At large time, the values of both the real and imaginary parts converge and become approximately constant.

Comparing Eqs. (9) and (13), we can conclude that for sufficiently long times such that Eq. (9) is satisfied, we get that

$$\mathrm{Im}\left[\langle\hat{H}\rangle_L\right] = -\frac{1}{2\tau}. \tag{14}$$

Similar manoeuvering, i.e., multiplying Eq. (11) by $\psi^*(x,t)$ from the left and then adding to the result its complex conjugate and integrating over the interaction region, one finds

$$\mathrm{Re}\left[\int_{-L}^{L}\psi^*(x,t)\hat{H}\psi(x,t)\right] = -\mathrm{Im}\left[\int_{-L}^{L}\psi^*(x,t)\frac{\partial\psi(x,t)}{\partial t}\right]. \tag{15}$$

Using Eq. (3) and the fact that for sufficiently long times the behavior of the phase $S(x,t)$ is portrayed in Eq. (7), we get that the real part of the local expectation value of the Hamiltonian reads

$$\mathrm{Re}\left[\langle\hat{H}\rangle_L\right] = -\frac{\partial S(x,t)}{\partial t} = \varepsilon. \tag{16}$$

Therefore, the local expectation value of the Hamiltonian reads

$$\langle\hat{H}\rangle_L = \mathrm{Re}\left[\langle\hat{H}\rangle_L\right] + i\,\mathrm{Im}\left[\langle\hat{H}\rangle_L\right] = \varepsilon - \frac{i}{2}\frac{1}{\tau}. \tag{17}$$

Taking into consideration the observed analogy between the behavior of a wave packet at large times and a stationary state in the interaction region, we are prompt to make the following ansatz for the wavefunction $\psi_R(x,t)$ in the interaction region:

$$\psi_R(x,t) = \psi(|x| < L, t > t_0) = e^{-i\left(\varepsilon - \frac{i}{2}\Gamma\right)t}\psi(|x| < L, t_0). \tag{18}$$

We are essentially postulating, in light of the evidence given above, that from a certain time t_0 the wave packet inside the interaction region evolves like a stationary state with a *complex energy* $E = \varepsilon - \frac{i}{2}\Gamma$.

We should now examine how this ansatz agrees with the "experimental" evidence given above. First, we look on the probability density as a function of time, which reads

$$\rho(x,t) = |\psi_R(x,t)|^2 = e^{-\Gamma t}\rho(x,t_0), \tag{19}$$

when

$$|x| < L; \quad t > t_0. \tag{20}$$

This is indeed the behavior observed in Figure 1.2 in which the probability density decays exponentially with time. In view of Eqs. (9) and (17), one can identify the relation between the imaginary part of the complex energy in Eq. (18) and the lifetime of the state, i.e., $\tau = \frac{1}{\Gamma}$. We remind the reader that we are working in atomic units where $\hbar = 1$; thus, the energy is inversely proportional to time. Next, we turn to examine the local energy expectation value given the ansatz in Eq. (18). The wavefunction in Eq. (18) is postulated to be a solution of the TDSE in the interaction region and for times larger than $t > t_0$. We can, therefore, write

$$\hat{H}\psi_R(x,t) = i\dot{\psi}_R(x,t) = \left(\varepsilon - \frac{i}{2}\Gamma\right)\psi_R(x,t). \tag{21}$$

Integrating Eq. (21) in the interaction region and dividing by $N_L(t)$ immediately yields that the local energy expectation value reads

$$\langle \hat{H} \rangle_L = \varepsilon - \frac{i}{2}\Gamma. \tag{22}$$

This is precisely what we found earlier using the TDSE and the asymptotic behavior of the norm and phase in Eq. (17). If we return now to examine the asymptotic limit of $\langle \hat{H} \rangle_L$, see Figure 1.6, we can indeed verify that the asymptotic value of the imaginary part of the local average coincides with half of the value of Γ that was extracted from Figure 1.5. As with an ordinary stationary state, the real part of the local expectation value tells as something about the position in energy of the state. Note that the value of ε is close to the original value of the bound state energy (see Figure 1.1), suggesting that the coupling to the continuum outside the well is rather weak.

2.4. Dynamics outside the interaction region

So far we have concentrated on the dynamics inside the interaction region and have shown that in this region the wave packet at long times behaves much like a stationary state with a *complex energy*. We now turn to discuss what happens outside the interaction region. Looking on the amplitude of the evolving wave packet just outside the interaction region, we observe a "wave front." This wave front has an exponential form as can be observed in Figure 1.7, where we show the density $|\psi(x,t)|^2$ of the wave packet at some time $t = 200$[a.u.] on a logarithmic scale. That is outside the barriers we can more or less write $\Lambda(x,t)$ of Eq. (3) as

$$\Lambda(|x| > L, t) \simeq \eta(t)e^{k_i|x|}. \tag{23}$$

The rate of exponential increase in this example, which was obtained from a linear regression on the outer region, is $\frac{\partial \ln \Lambda}{\partial x} = k_i = 0.0048$[a.u.].

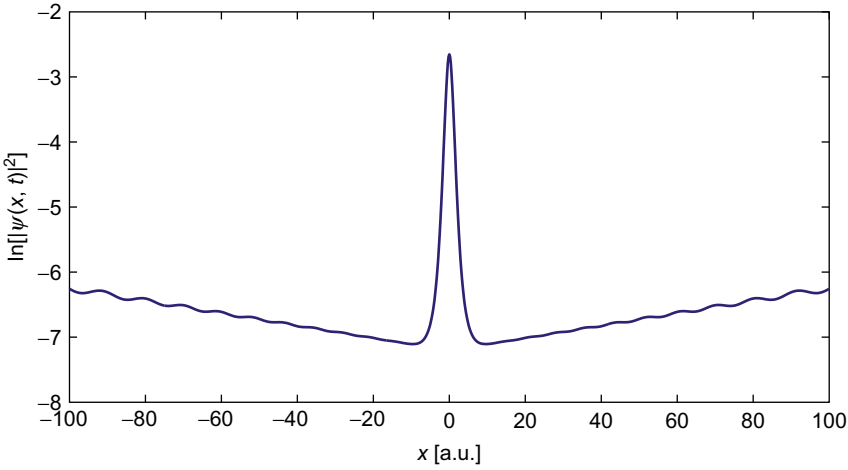

Figure 1.7 The probability density of the wave packet at time $t = 200$ on a logarithmic scale. Note that outside the interaction region, we have an exponentially diverging function.

It is important to stress that the behavior of the wave packet outside the interaction region portrayed in Figures 1.4, 1.7 and correspondingly Eqs. (7, 23) does not extend over the whole space and the wavefunction eventually decays (in space). This is to be expected because we are dealing with a well-behaved square integrable function. This important point will be addressed in Section 4.

Let us recapitulate our findings from the above example. By exposing a bound state to a continuum, a metastable state is formed. Inside the interaction region at sufficiently long times, we can approximate the dynamics very well by using the resonance wavefunction $\psi_R(x,t)$, see Eq. (18). This resonance state resembles a stationary state albeit with a *complex energy*. The properties of the resonance state can be extracted via local expectation values where the integration is performed over the interaction region only. Hopefully, we are now comfortable to state that *a quantum mechanical resonance state is an exponentially decaying metastable state of the system localized in the interaction region with a finite lifetime τ and positioned at an energy ε.*

3. A STATIONARY ANALYSIS OF RESONANCE STATES

In the previous section, we have shown that resonance states can be described using the solution of the TDSE by analyzing the evolution of a wave packet. This kind of analysis is, however, usually difficult and time consuming as the wave packet needs to be propagated to large times, which is often challenging numerically. We have also observed that the long-time behavior of the wave packet in the interaction region resembles that of a

stationary state with a *complex energy*. It would thus be extremely beneficial if one could calculate this stationary state without the need to solve the TDSE, i.e., propagate a wave packet in time. This is the goal of the forthcoming section.

3.1. Expansion of localized functions in terms of scattering states

Consider the stationary solutions of the TISE for the perturbed potential, see Figure 1.1b. Explicitly the solution of the following eigenvalue equation:

$$\left[-\frac{1}{2}\frac{\partial^2}{\partial x^2} + V(x)\right]\phi(x) = E\phi(x). \tag{24}$$

The bound state of the unperturbed system ($\alpha = 0$), see Figure 1.1a, becomes a superposition of the eigenstates of the perturbed system ($\alpha = 0.05$) when we etch the potential at the asymptotes. We may attempt an analysis of the evolving wave packet based on the the eigenstates of the new problem. Since the potential is now unbound, it supports only a continuum of scattering states ϕ_E. Figure 1.8 portrays several continuum eigenstates of the Hamiltonian. As can be seen, the vast majority of the continuum eigenstates have a very small amplitude inside the potential well. We can label these as ϕ_E^{out}. In a sharp contrast, some of the continuum eigenstates are highly localized inside the potential, as can be seen in the solid line in Figure 1.8, and in fact

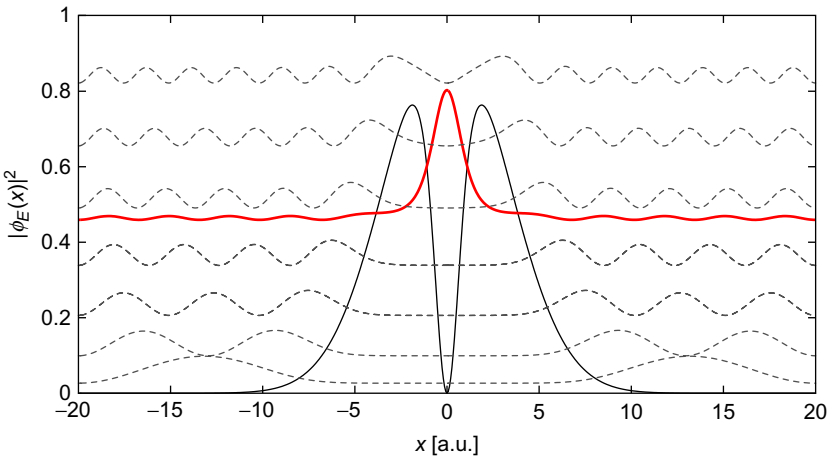

Figure 1.8 The probability density of several continuum eigenstates of the Hamiltonian in Eq. (24) plotted on the baseline of their corresponding energy. The potential is also plotted for convenience. Note that most continuum states (dashed lines) are delocalized and have a very small amplitude inside the potential well between the two barriers, whereas there are continuum functions that are localized inside the well. The localized eigenstate (solid line) is the same as shown in Figure 1.1.

appear to behave much like bound states. Thus, we attach the label ϕ_E^{in} to these states. A closer inspection reveals that even though the ϕ_E^{in} states seem at first identical to the wavefunctions of bound states, they differ greatly in their behavior outside the potential well. The continuum states oscillate outside the potential barriers and thus cannot describe a localized particle. Obviously, the distinction between "localized" states – ϕ_E^{in} and "delocalized" states ϕ_E^{out} is rather arbitrary, and the behavior of the continuum states will change continuously from one type of states to the other, but around the energy of a localized continuum state, one will find a highly dense energy range with similar localized continuum states.

Looking now at the expansion in Eq. (4), the wave packet $\psi(x,t)$ will contain contributions from these two "groups" of continuum eigenstates, which will depend on the expansion coefficients $C(E)$ given in Eq. (5) and can now be separated to

$$\begin{aligned} C_{\text{in}}(E) &= \int_{-\infty}^{\infty} [\phi_E^{\text{in}}(x)]^* \psi(x,0) \mathrm{d}x, \\ C_{\text{out}}(E) &= \int_{-\infty}^{\infty} [\phi_E^{\text{out}}(x)]^* \psi(x,0) \mathrm{d}x. \end{aligned} \tag{25}$$

With this somewhat artificial separation, we can recast Eq. (4) as

$$\begin{aligned} \psi(x,0) = &\int_0^{\infty} C_{\text{in}}(E) \phi_E^{\text{in}}(x) W(E) \mathrm{d}E \\ &+ \int_0^{\infty} C_{\text{out}}(E) \phi_E^{\text{out}}(x) [1 - W(E)] \mathrm{d}E, \end{aligned} \tag{26}$$

where $W(E)$ is a window function that is equal to 1 in the energy range of $\phi_E^{\text{in}}(x)$ and 0 elsewhere. Bearing in mind that our initial wave packet is a localized function in the potential well, it is straightforward to conclude that ϕ_E^{in} will be highly occupied as opposed to ϕ_E^{out}. Accordingly, we can expect that $C_{\text{in}}(E)$ will peak at the energy where ϕ_E^{in} has the largest amplitude inside the well and will drop sharply with the variation of E while the character of the continuum wavefunction changes from ϕ_E^{in} to ϕ_E^{out}. The energy range over which this occurs can be very narrow and is comparable with Γ. Nevertheless, we must still use a continuous superposition of eigenstates, albeit over a short range of energy, in order to correctly describe the evolution of the wave packet.

Even though we have a continuous superposition of states in Section 2, we observed in the interaction region the behavior of a stationary state, which

can be characterized in a very similar manner to a bound state. Consequently, we want now to employ a mechanism by which all of the information gathered from the time propagation of the wave packet would be extracted from a time-independent formulation. For simplicity, we restrict the discussion to one dimension although it can readily be applied to multidimensional systems as well.

Given a one-dimensional potential, in all but the rarest situations, one can quite easily define an interaction region. Let us define the interaction region as the region in space where $x \in [-L, L]$. Considering the example described in the previous section, we wish to treat the case where a particle is placed initially at the interaction region but due to the occupation of continuum states begins to leak from the interaction region and moves toward the asymptotes. If the particle does not occupy any bound states, then at infinite time there will be a zero probability of finding it inside the interaction region. Therefore, if we situate ourselves in the interaction region, it appears that particles are vanishing. This fictitious loss of particles is the physical origin of the non-Hermiticity to be introduced shortly.

3.2. Stationary solutions with outgoing waves

Consider the one dimensional TISE in Eq. (24), where we allow x to vary between $-L$ and L, i.e., in the interaction region only. In order to solve this equation, we must supplement it with some boundary conditions. Although motivated from different quantum phenomena, Siegert [30] was the first to introduce the idea of solving the TISE with outgoing BCs, also known as Siegert boundary conditions or radiation boundary conditions. In one dimension, these outgoing BCs read

$$\left[\frac{\partial}{\partial x} - ik\right]\phi(x) = 0 \quad \text{at} \quad x = L, \tag{27}$$

$$\left[\frac{\partial}{\partial x} + ik\right]\phi(x) = 0 \quad \text{at} \quad x = -L, \tag{28}$$

where $k = \sqrt{2E}$. These BCs imply that we are seeking solutions that have only outgoing flux at the boundaries, i.e., $\phi(|x| \geq L) = e^{ik|x|}$. This is precisely the behavior of the states we wish to describe where a particle reaching the boundary of the interaction region moves past it and never returns. This was the situation illustrated in Section 2, where as depicted in Figure 1.3 only outgoing flux was observed. The BCs in Eqs. (27) and (28) render the Hamiltonian in Eq. (24) non-Hermitian unless k is purely imaginary. We also note that in principle the boundary conditions in Eqs. (27) and (28) accommodate for purely incoming solutions if the real part of the wave vector k is allowed to be negative. The solution of the TISE with the Siegert boundary conditions yields an infinite, discrete set of eigenstates and eigenvalues.

In general, the eigenvalues and eigenstates are complex. It is common to divide the spectrum of the Hamiltonian with Siegert boundary conditions into four parts:

1. If k is purely imaginary and positive, then these states correspond to bound states with asymptotic behavior $\phi(|x| \geq L) \propto e^{-|k||x|}$. The bound state solutions are the only solutions with positive imaginary values of the wave vector [31].
2. The second type of solutions are those for which k is purely imaginary and negative. These states are called antibound states and have the asymptotic behavior of $\phi(|x| \geq L) \propto e^{+|k||x|}$.
3. The next type of states and those that will interest us the most are the resonance states for which $k = k_r - ik_i$, where k_r and k_i are real positive numbers. These are outgoing states because the real part of k is positive. As will be shown below, these states diverge asymptotically.
4. Due to time-reversal symmetry, every resonance solution has an antiresonance solution, also known as antiresonance states, that occurs at $k = -k_r - ik_i$. These antiresonance states are incoming states that also diverge at the asymptotes.

In addition to looking at the position of the eigenvalues in the **k**-plane, we can also analyze their appearance on the complex energy plane due to the direct connection between the energy of the particle and its momentum at the asymptotes: $E = \frac{k^2}{2}$. Figure 1.9 shows the distribution of the Siegert solutions on both the Energy and the wave vector (**k**) planes.

3.3. Properties of the stationary resonance state

The Siegert states that have to do with metastable decaying states are the resonance solutions for which $k_{\text{res}} = k_r - ik_i$. These are the only states with a negative imaginary part of the energy, the signature of a decaying state. We can define the resonance complex energy as $E_{\text{res}} = \frac{k_{\text{res}}^2}{2} = \varepsilon - \frac{i}{2}\Gamma$, where ε is called the resonance position and Γ is called the width of the resonance and is related to the lifetime of the metastable state by $\tau = \frac{1}{\Gamma}$. Accordingly, the time dependence of such stationary solution reads

$$\psi_{\text{res}}(x,t) = e^{-iE_{\text{res}}t}\phi_{\text{res}}(x) = e^{-\Gamma t/2}e^{-i\varepsilon t}\phi_{\text{res}}(x), \tag{29}$$

which decays exponentially with time. The problem with such a solution is the asymptotic behavior in the spatial domain, which is

$$\phi_{\text{res}}(x \to \pm\infty) = A_{\pm}e^{\pm ik_{\text{res}}x} = A_{\pm}e^{\pm ik_r x}e^{k_i|x|}. \tag{30}$$

From this equation, we see that the particles in such a stationary state will be escaping the interaction region with momentum k_r as can be verified by

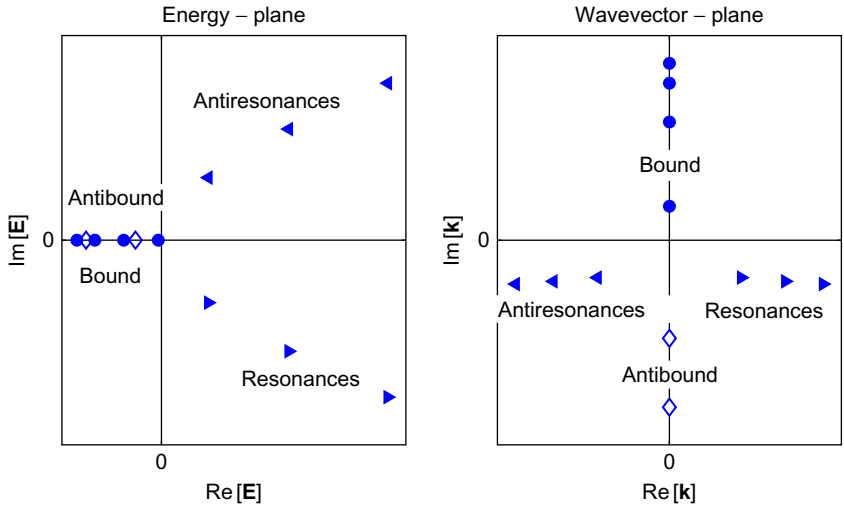

Figure 1.9 Distribution of the Siegert solutions in the complex energy plane (left) and the complex wavevector (**k**) plane (right). The resonance solutions (▶) resulting from outgoing wave boundary conditions are situated in the fourth quadrant of both the energy and wave vector planes. For every resonance, there corresponds an antiresonance (◀) with a complex conjugate energy that results from incoming wave boundary conditions. On the real axis of the energy plane and on the imaginary axis of the wave vector plane, one finds the bound states (●) with asymptotically vanishing solutions and antibound states (◇) with asymptotically diverging solutions.

evaluating the flux $J(x,t)$ of the wavefunction at the asymptotes:

$$J(|x| \to \infty, t) = \mathrm{Im}\left[\psi^*_{\mathrm{res}} \frac{\partial}{\partial x} \psi_{\mathrm{res}}\right] = k_r \rho(x,t). \tag{31}$$

Equations (29) and (30) show us that whenever we have a solution with temporal decay, it will be accompanied by spatial divergence. This means we cannot use these solutions for any quantum mechanical evaluation since they cannot be normalized. This, however, does not mean these solutions should be rendered useless for the interpretation of the physical situation. First, knowing the complex resonance energy tells us the rate of decay. Second, in many scattering experiments, sharp features in the cross section appear because of the existence of resonances. In fact, the resonance solutions can be correlated with the poles of the scattering matrix. The nomenclature *width* attached to the imaginary part of the complex energy relates between the width of a peak in the cross section and the corresponding resonance energy [32, 33].

The Siegert resonance state provides a method of calculating the lifetime and position of the decaying state without the need to solve the TDSE. Aside from the practical advantage, they also greatly facilitate the understanding

of such metastable states since we can now describe them using a single state and not by using a wave packet, see Section 2. The information that can be extracted from the resonance state is not limited to its complex energy, i.e., to its position and lifetime. If one extends the basic framework of quantum mechanics to include non-Hermitian operators, many physical observable can be calculated using only a single resonance state, which would otherwise require the solution of the TDSE with a wave packet. For more details and examples, see the review article [34].

Except for very few cases, e.g., [35], one cannot solve the TISE explicitly; therefore, one cannot find the Siegert states directly. Still one would like to be able to calculate the resonances of the system. Most of the methods developed over the years, which allow the solution of the TISE for different potentials, are based on the variational principle. These in turn are based on square integrable functions. In the 1970s, Balslev and Combes [36] and Simon [37] presented a complex scaled Hamiltonian with the same bound spectrum as the original Hamiltonian along with complex energies, which corresponded to the resonance solutions. This complex scaling was done by continuing the coordinates of the Hamiltonian into the complex plane, i.e., $x \to xe^{i\theta}$. The main advantage of this continuation is that the resonance wavefunctions become square integrable and can be calculated using the ordinary methods by which the Schrödinger equation is solved. For an introductory presentation on complex scaled Hamiltonian, see [38]. Several variations as well as alternatives of the original complex scaling method have been suggested over the years. We refer the interested reader to the reviews in Ref. [34, 39, 40] and references therein. Over the past decade methods that do not rely on transforming the Siegert solutions into square integrable states have emerged, e.g., [41].

We can use any of the above mentioned techniques to find the resonance solutions of the TISE for the model potential presented in the previous section. Doing so, we find that there is a resonance solution at the complex energy (in atomic units):

$$E_{\text{res}} = 0.465 - \frac{i}{2} \cdot 0.00926. \tag{32}$$

This is the resonance solution with the smallest position, i.e., smallest real part of the complex energy. Comparing this result with the measurements from the time-dependent simulation in Section 2, the agreement is truly remarkable. The corresponding momentum k_{res},

$$k_{\text{res}} = \sqrt{2E_{\text{res}}} = 0.964 - i \cdot 0.00480, \tag{33}$$

is also in absolute agreement with the analysis of the wave packet outside the interaction region in Section 2. This is the great advantage of the stationary

method. While the time-dependent perspective discussed in the previous section required the propagation of the wave packet to long times in order to recover the resonance parameters, the time-independent method requires finding just a single eigenstate and eigenvalue of the system at hand.

4. UNIFIED PICTURE OF RESONANCE STATES

In the previous sections, we have seen that a resonance can be described through both a time-dependent approach and a time-independent approach. The goal of this section is to create a unified picture that joins both methodologies and explain how general wave packets evolve into pseudostationary decaying states.

Let us recap the properties of a wave packet populating a resonant state we observed in Section 2:

1. After some initial rearrangement time, a bound-like wavefunction is obtained in the interaction region.
2. Outside the interaction region, one observes escaping particles with constant velocity.
3. The probability to remain inside the interaction region decays exponentially with time.
4. The local expectation of the energy inside the interaction region is complex. This complex value saturates to a constant value as time evolves. The real part of the local average energy dictates the phase modulation in time, whereas the imaginary part of the local average energy is one-half the rate of decay from the interaction region.
5. Outside the interaction region, the probability density seems to increase exponentially in space.

If the stationary analysis of Section 3 is to replace the time-dependent one, the above properties must be in some way related to the stationary resonance solutions. Recalling that in the stationary analysis we enforced certain boundary condition that led to the following unique properties of resonance eigenstates:

1. The asymptotic behavior of a resonance state is of outgoing waves, i.e., $\phi_{\text{res}}(|x| > L) \propto e^{\pm ik_r x} e^{k_i |x|}$.
2. The energy of a resonance state is complex. This is the result of the BCs that render the Hamiltonian non-Hermitian.
3. The time-dependent resonance wavefunction $\psi_{\text{res}}(x, t)$ decays in time because of the negative imaginary part of the complex energy.
4. The momentum (wave vector) is also complex. The real part of the complex momentum k_r defines the velocity of the escaping particles while the imaginary part of the complex wavevector causes the wavefunction to exponentially diverge in space.

The joint properties of the two approaches above stem from the fact that the time-dependent resonance ansatz of Section 2, see Eq. (18), is completely reproduced by the stationary resonance solution of the TISE of Section 3, see Eq. (29). This is the great advantage of the Siegert BCs – to produce solutions to the Schrödinger equation that satisfy the aforementioned ansatz.

4.1. Expansion of the stationary resonance state in time

What is most upsetting about resonance solutions of the TISE is that they are exponentially diverging in space and thus cannot describe our metastable wave packet, which is square integrable by its own. As we saw in the previous section, this is a direct consequence of the temporal decaying property of the resonance state. We have also observed some local exponential divergence in the time-dependent solution in Figure 1.7, but how does it all come together? If we assume that the wave packet behaves like the stationary state in some restricted part of space and write $\Lambda(x,t)$ of Eq. (3) in the outer region, we get

$$\Lambda(|x| > L) = |A_{\pm}|e^{-\Gamma t/2}e^{\pm k_i x}. \tag{34}$$

This is the manner at which the wave packet in Section 2 evolves just outside the interaction region as portrayed in Figure 1.7 and Eq. (23), where $\eta(t) = e^{-\Gamma t/2}|A_{\pm}|$. There we got that the exponential increase of the amplitude goes exactly as the imaginary part of the complex momentum of the stationary state $k_i = \mathrm{Im}[k_{\mathrm{res}}] = 0.0048$[a.u.]. This shows that even outside the barriers, there is a region where the evolution is similar to that of the stationary resonance state.

An important question emerges from this analysis regarding the choice of the boundary of the interaction region, which from the above argument can now extend well into the asymptotic region. In order to address this issue, we can study the behavior of our wave packet over a wider extent in the spatial domain. This is portrayed in Figure 1.10, where we show the evolution of the probability density on a logarithmic scale. What is seen in the evolution can be characterized as a "resonance front" that expands in time. Evidently, as time goes by, the resonance nature of the wave packet occupies a larger part of space. In other words, the boundary of the resonance state is expanding in time. This idea was eloquently presented in Ref. [42], where it was used to demonstrate that when one considers a moving boundary, there is a conservation of the particles in the stationary resonance state. A crude approximation that yields a similar result was previously given in Ref. [33].

At this point, we have a comprehensive picture of quantum resonance states. The discussion above shows that the non-Hermitian stationary resonance solutions of Section 3 are real *flesh and blood* beings even in the Hermitian world dictated by the TDSE. As a wave packet evolves with time,

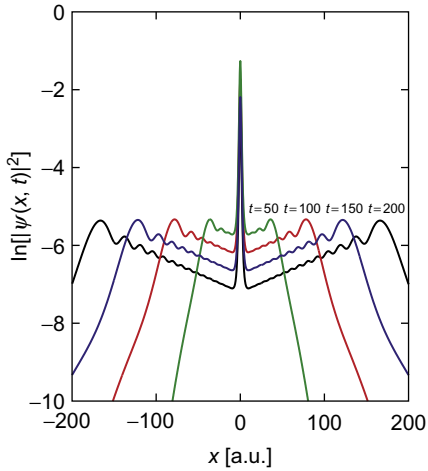

Figure 1.10 The probability density of the wave packet at different times on a logarithmic scale. Note that the region of exponential increase in the spatial domain is expanding with time.

the larger the region in space exhibiting the properties of the resonance is. In order for the wave packet to "fully occupy" the resonance, it had to have started decaying infinitely long time ago, which would be the source for the particles accumulated at the asymptotes. Since this is not possible when we are starting with an initially localized wavefunction, this means that we can never solely populate exactly a single resonance state. This is the reason we still have oscillations superimposed over the asymptotic exponential behavior of the wavefunction.

4.2. The "death" of a resonance state

This brings us to one final important point. The fact that we cannot populate just a resonance state implies that just like other mortal beings, the resonance is born at some instance in the dynamics and dies at some later time in the evolution of the wave packet. There will always be contributions to the wave packet from either faster or slower continuum states. The fast-moving states dominate the dynamics before we observe the properties of the resonance state in the interaction region. This can be seen in the inset of Figure 1.5, where we see the probability density of the wave packet in the interaction region before we arrive at the exponential decay on the long timescale of Figure 1.5. When we propagate the wave packet to very long times with respect to the lifetime of the resonance, we eventually will reach a point where the decay of the probability density inside the interaction region will change to a power law of t^{-3}, which is much slower than the exponential decay [43–45]. This behavior is evident in Figure 1.11, where we see a

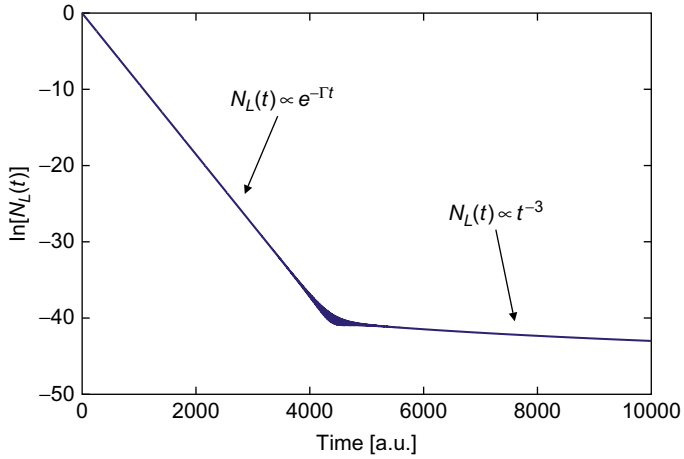

Figure 1.11 The probability density of the wave packet inside the interaction region ($N_L(t)$) at extremely long times on a logarithmic scale. Note that the decay from the interaction region changes its behavior from exponential to a power law of t^{-3}.

transition from the exponential decay law after $t = 4000$[a.u.], which means that a period of more than 38 times of the resonance lifetime has passed by. We can study the physical properties of the system using the stationary resonance solution in the intermediate times, which are usually more relevant since the probability to remain in the interaction region is still significant.

5. THE ORIGIN OF RESONANCES

In the previous sections, we introduced resonance states and discussed situations in which resonances can be observed. In this section, we address the question of the origin for the appearance of resonances, or in other words, the basic question is what can bring about the formation of metastable states. In a very general manner, it is common to classify resonances into two main groups: shape-type resonances and Feshbach-type resonances. Although the classification is not unique and may depend on the chosen representation of the Hamiltonian [46, 47], it can be extremely helpful in understanding the physical mechanism that leads to the formation of the metastable state.

5.1. Shape-type resonances

As the name suggests, shape-type resonances result from the shape of the potential at hand. But, what attributes must a potential have in order to trap the particle for a finite time and thus form a metastable state? The wave nature of particles in quantum mechanics provides two typical ways for a

potential to form a metastable state. If the potential has a local minimum above the threshold, e.g., see Figure 1.1b, one can consider a reference Hamiltonian where we modify the potential such that the previous local minimum becomes a global one, e.g., see Figure 1.1a. Thus, we have moved the local potential well below the threshold. If the reference Hamiltonian supports any bound states, then it is likely to observe metastable states around the bound states' energies in the original potential. The decay of the metastable state in this case can be associated with the tunneling through the potential barriers that form the local minimum.

In order to elucidate this concept, let us consider perhaps the simplest molecular system, the hydrogen molecular ion H_2^+. Within the Born–Oppenheimer approximation, the potential in the ground electronic state of this molecular ion is very well represented by the following Morse potential [48]:

$$V_g(R) = D_0(e^{-2\alpha(R-R_0)} - 2e^{-\alpha(R-R_0)}), \tag{35}$$

where $D_0 = 0.1025$ [a.u.], $\alpha = 0.72$ [a.u.], and $R_0 = 2$ [a.u.]. When the system has no rotational energy (i.e., $j = 0$), the system supports several vibrational bound states. When the system is rotationally excited, the above potential energy curve is perturbed by the centrifugal term:

$$V_{\text{rot}}(R) = \frac{j(j+1)}{2\mu R^2}. \tag{36}$$

As the rotational number j is increased, the bottom of the potential well in Eq. (35), which is holding the nuclei together, is pushed up and a centrifugal barrier is formed between the potential well and the asymptote. Eventually the molecular ground state is pushed above the threshold and into the continuum. This is evident in Figure 1.12, where we display the effective potential for the vibration in several rotational levels. We can see that for $j = 40$ the molecular ion is no longer bound and will eventually dissociate by tunneling through the centrifugal barrier.

Such high rotationally excited states in diatomic systems play a significant role in understanding molecular processes occurring in interstellar space [49]. For the specific system of H_2^+, these rotationally hot states can be produced for instance by the dissociation of CH_4^{2+} dications [50].

The situation depicted above is an example for the most common and vivid manner for the appearance of a resonance due to the shape of the potential. However, such metastable states can form even when the energy of the resonance state does not reside within some effective local well in the potential under study. A second way by which shape-type metastable states can form has much in common with optical resonators. In order to form a

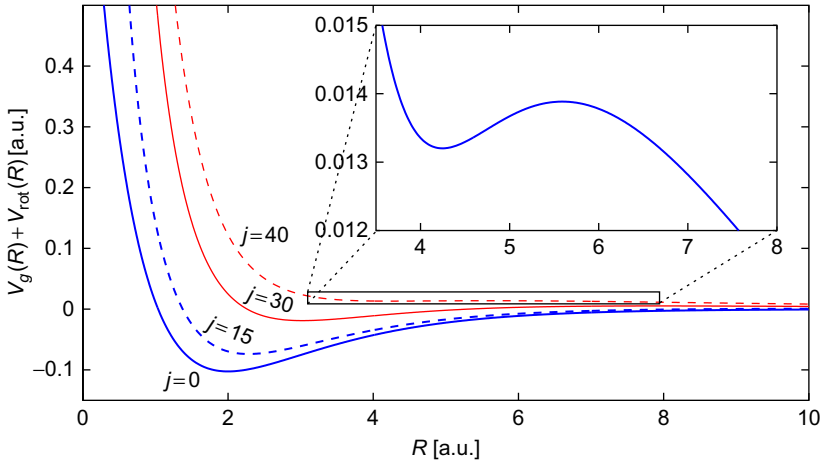

Figure 1.12 The potential energy curves for the vibrational motion of H_2^+ in the ground electronic state in various rotational states. The various plots are a sum of the potential energy in the ground electronic state given in Eq. (35) and the rotational energy given in Eq. (36). The plotted curves correspond to rotational numbers $j = 0$ (solid dark line), $j = 15$ (dashed dark line), $j = 30$ (solid light line), and $j = 40$ (dashed light line). The inset shows the region in the potential formed for $j = 40$ where the well holding the rovibrational ground state of the molecular ion is pushed above the dissociation threshold. This will eventually lead to the dissociation of the molecule.

resonator, we need the wave to scatter back and forth between two scatterers. A scatterer for this purpose can be any sharp variation of the potential. If the potential provides such a situation, then at a certain energy a resonance state may form. Furthermore, metastable states, albeit short-lived resonances, exist even above the potential maxima, so there is not necessarily a straightforward connection with some bound state of a reference Hamiltonian.

5.2. Feshbach-type resonances

Feshbach-type resonances [51], also known as Fano resonances [52] and Floquet resonances [22] depending on the system studied, are formed in a different manner. We encounter this type of metastable states whenever a bound system is coupled to an external continuum. In the same spirit as before, one can define a reference Hamiltonian in which the closed channel containing the bound states is uncoupled from the open channel through which the asymptote can be reached. When the coupling is introduced, the previously bound state decays into the continuum of the open channel. The distinction from shape-type resonances, described above, is that the resonance state decays into a different channel of the reference Hamiltonian.

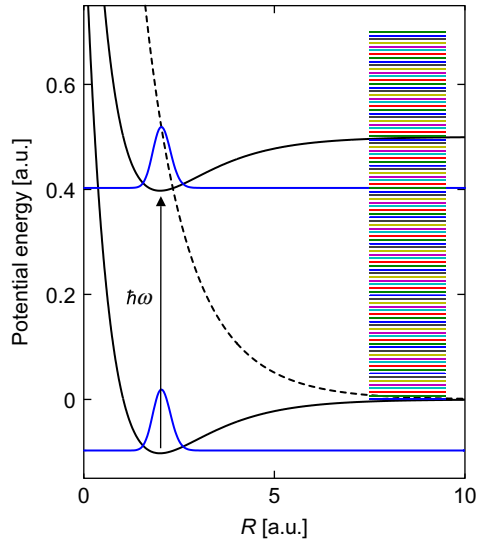

Figure 1.13 The ground (lower solid line) and excited (dashed line) potential energy curves of the molecular ion H_2^+. The upper potential curve represents the ground electronic potential curve shifted by the energy $\hbar\omega$ of one photon of the electromagnetic radiation. The ground vibrational wavefunction in the ground electronic state is coupled to the continuum of scattering states of the excited electronic potential depicted here by dense set of energy levels.

To illustrate this phenomenon, we return to the molecular hydrogen ion H_2^+. The ground vibrational state of the system is bound in the potential depicted in Figure 1.13. Suppose now that we expose the system to a monochromatic electromagnetic radiation with a frequency ω. The radiation field now couples between the ground electronic state and the excited electronic state of the system. The excited electronic state of the hydrogen molecular ion is a dissociative potential curve, which is well approximated by [48]:

$$V_e(R) = D_0(e^{-2\alpha(R-R_0)} + 2.22e^{-\alpha(R-R_0)}), \tag{37}$$

where α, D_0, and R_0 are identical to those of Eq. (35). For simplicity, we will assume that the whole effect of the radiation field is twofold: (i) To add the photon's energy of $\hbar\omega$ to the electron in the ground state. (ii) To couple between the ground and electronic states via the dipole $d(R)$. The above physical situation is visualized in Figure 1.13, where we draw the potential energy curves of the ground electronic state $V_g(R)$, the shifted ground electronic state $V_g(R) + \hbar\omega$, and the excited electronic state $V_e(R)$.

To capture the essence of the Feshbach resonance phenomenon, we will need to understand what happens to the ground vibrational state $\phi_0(R)$ of the ground electronic state, also depicted in Figure 1.13, because of the interaction with the continuum of states $\varphi_E(R)$ of the excited electronic state. The physical process described above can be formulated as a two coupled channels problem where the solution $\psi_g(R)$ in the closed channel (the ground state) depends on the solution $\psi_e(R)$ in the open channel (the excited state) and vice-versa. The coupled Schrödinger equations read

$$\begin{pmatrix} \hat{T}_R + V_g(R) + \hbar\omega & d(R) \\ d^*(R) & \hat{T}_R + V_e(R) \end{pmatrix} \begin{pmatrix} \psi_g(R) \\ \psi_e(R) \end{pmatrix} = E \begin{pmatrix} \psi_g(R) \\ \psi_e(R) \end{pmatrix}. \tag{38}$$

It is obvious that the total solution of this problem,

$$\psi(R) = \begin{pmatrix} \psi_g(R) \\ \psi_e(R) \end{pmatrix}, \tag{39}$$

will be a mixture of the system in the ground state $\psi_g(R)$ and the system in the excited state $\psi_e(R)$. Thus, the previously bound vibrational state ϕ_0 on the ground electronic potential will now decay because of the coupling to the continuum of scattering states on the excited electronic potential induced by the radiation. The interaction with the continuum comes through the transition dipole elements $d = \langle \phi_0 | d(R) | \varphi_E \rangle$ and will couple ϕ_0 to the states φ_E in the continuum in the vicinity of $E_b = E_0 + \hbar\omega$. The strength of the coupling with the continuum is controlled by intensity of the radiation and will determine how long it takes the molecular ion to dissociate. So, the situation we describe here is of a state that is initially bound in a closed channel but will decay after a characteristic time to the open channel. In other words, we have a Feshbach-type resonance state.

6. CONCLUSIONS

The analysis of a wave packet constructed from continuum states can be a formidable task. The ability to fully grasp an observed phenomenon lies to a great extent in our ability to associate it with a well-defined origin. Whenever a bound state is exposed to a continuum, e.g., when one wishes to probe it, a metastable state is very likely to be formed. Any exceptions are mostly constructed examples rather than physical realities. If the system supports a metastable state, any wave packet that at time zero is located inside the interaction region would adhere to the following general behavior. At short times, any components whose lifetime is shorter than that of the longest lived metastable state leave the interaction region to the asymptote. The extent of

this short timescale depends on the initial wave packet. Following this departure of fast components from the interaction region, the regime of resonance dynamics commences. This regime was the focus of this manuscript. During this time, the dynamics in the interaction region can be well described by a pseudostationary resonance state, a solution of the TISE with outgoing BCs, which has a *complex energy*. In many cases, this is the most important physical regime because it does not depend on the initial wave packet and can be used to extract physical information about the system. The final stage of the dynamics occurs when the density inside the interaction region is almost depleted and the slowest components of the wave packet start to be noticeable. This is manifested in the transition of the decay from exponential to a power law behavior as discussed in the text.

The chapter is intended to be only a first glance on resonances, hopefully providing compelling evidence for the physical importance of the stationary solutions of the non-Hermitian TISE with Siegert BCs. If the physical system supports a long-lived metastable state, most of the physics in the interaction region of interest can be extracted from the stationary solution and there would be no need to solve the TDSE at all. This is a truly remarkable advantage of non-Hermitian quantum mechanics. Although we have demonstrated this only on a single state, one could imagine situations where two metastable states are occupied, thus introducing interesting dynamical effects into the interaction region. One would then be inclined to calculate other local expectation values such as the position and momentum of the wave packet. This can be done very successfully using the stationary resonance states [53] but is beyond the current scope. Yet another aspect that we can be discussed is the connection of resonance states and resonance peaks appearing in the cross section of full-collision processes. We refer the interested reader elsewhere [31, 33, 54].

ACKNOWLEDGMENT

The authors are indebted to Prof. Nimrod Moiseyev for many helpful discussions.

REFERENCES

[1] D.J. Tannor, Introduction to Quantum Mechanics: A Time-Dependent Prespective, University Science Books, Sausalito, 2007.
[2] E. Brändas, N. Elander (Eds.), Resonances: The Unifying Route towards the Formulation of Dynamical Processes. Foundations and Applications in Nuclear, Atomic and Molecular Physics. Proceedings of a Symposium Held at Lertorpet, Värmland, Sweden, August 1926, 1987, Lecture Notes in Physics Vol. 325, Springer Verlag, Berlin, 1989.
[3] C.A. Nicolaides, E. Brändas (Eds.), Unstable states in the sontinuous spectra, part I: Analysis, concepts, methods and results, Adv. Quant. Chem. 60 (2010) 1.

[4] G. Gamow, The quantum theory of the atom nucleus, Z. Phys. 51 (1928) 204.
[5] N. Elander, Resonances in nuclear, atomic, and molecular Physics – An introduction with some examples, Int. J. Quant. Chem. 31 (1987) 707.
[6] E. Eichten, Υ family of resonances above threshold, Phys. Rev. D 22 (1980) 1819.
[7] N. Yabusaki, M. Hirano, K. Kato, M. Sakai, Y. Matsuda, Masses and OZI-allowed decay widths of Υ states in a coupled channel model, Prog. Theo. Phys. 106 (2001) 389.
[8] T. Myo, K. Kato, S. Aoyama, K. Ikeda, Analysis of ^6He Coulomb breakup in the complex scaling method, Phys. Rev. C 63 (2001) 054313/1.
[9] C.A. Nicolaides, Theoretical approach to the calculation of energies and widths of resonant (Autoionizing) states in many-electron atoms, Phys Rev. A 6 (1972) 2078.
[10] N. Moiseyev, P.R. Certain, F. Weinhold, Complex-coordinate studies of helium autoionizing resonances, Int. J. Quant. Chem. 14 (1978) 727.
[11] J.F. McNutt, C.W. McCurdy, Complex self-consistent-field and configuration-interaction studies of the lowest 2P resonance state of Be^-, Phys. Rev. A 27 (1983) 132.
[12] W.P. Reinhardt, Complex coordinates in the theory of atomic and molecular structure and dynamics, Ann. Rev. Phys. Chem. 33 (1982) 223.
[13] G.J. Schulz, Resonances in electron impact on atoms, Rev. Mod. Phys. 45 (1973) 378.
[14] D.J. Haxton, C.W. McCurdy, T.N. Rescigno, Dissociative electron attachment to the H_2O molecule I. Complex-valued potential-energy surfaces for the $^2B_1$, $^2A_1$, and $^2B2$ metastable states of the water anion, Phys. Rev. A 75 (2007) 012710/1.
[15] R. Santra, L.S. Cederbaum, An efficient combination of computational techniques for investigating electronic resonance states in molecules, J. Chem. Phys. 115 (2001) 6853.
[16] M. Berman, H. Estrada, L.S. Cederbaum, W. Domcke, Nuclear dynamics in resonant electron-molecule scattering beyond the local approximation: The 2.3-eV shape resonance in N_2, Phys. Rev. A 28 (1983) 1363.
[17] J. Göres, D. Goldhaber-Gordon, S. Heemeyer, M.A. Kastner, H. Shtrikman, D. Mahalu, U. Meirav, Fano resonances in electronic transport through a single-electron transistor, Phys. Rev. B 62 (2000) 2188.
[18] M. Heiblum, M.V. Fischetti, W.P. Dumke, D.J. Frank, I.M. Anderson, C.M. Knoedler, L. Osterling, Electron interference effects in quantum wells: Observation of bound and resonant states, Phys. Rev. Lett. 58 (1987) 816.
[19] A.C. Johnson, C.M. Marcus, M.P. Hanson, A.C. Gossard, Coulomb-modified Fano resonance in a one-lead quantum dot, Phys. Rev. Lett. 93 (2004) 106803/1.
[20] G. Garcia-Calderon, Tunneling in semiconductor resonant structures. Phys. Low-Dimens. Semicond. Struct. 6 (1993) 267.
[21] O. Latinne, N.J. Kylstra, M. Dörr, J. Purvis, M. Terao-Dunseath, C.J. Joachain, P.G. Burke, C.J. Noble, Laser-induced degeneracies involving autoionizing states in complex atoms, Phys. Rev. Lett. 74 (1995) 46.
[22] S.-I. Chu, D.A. Telnov, Beyond the Floquet theorem: Generalized Floquet formalisms and quasienergy methods for atomic and molecular multiphoton processes in intense laser fields, Phys. Rep. 390 (2004) 1.
[23] M. Galperin, A. Nitzan, M.A. Ratner, Resonant inelastic tunneling in molecular junctions, Phys. Rev. B 73 (2006) 045314/1.
[24] N. Sergueev, A.A. Demkov, H. Guo, Inelastic resonant tunneling in C_{60} molecular junctions, Phys. Rev. B 75 (2007) 233418/1.
[25] M. Caspary-Toroker, U. Peskin, On the relation between steady-state currents and resonance states in molecular junctions, J. Phys. B 42 (2009) 044013/1.
[26] K. Kobayashi, H. Aikawa, S. Katsumoto, Y. Iye, Tuning of the Fano effect through a quantum dot in an Aharonov-Bohm interferometer, Phys. Rev. Lett. 88 (2002) 256806/1.
[27] P.S. Epstein, The Stark effect from the point of view of Schroedinger's quantum theory, Phys. Rev. 28 (1926) 695.
[28] N. Rosen, P.M. Morse, On the vibrations of polyatomic molecules, Phys. Rev. 42 (1932) 210.
[29] C. Cohen-Tannoudji, B. Diu, F. Laloë, Quantum Mechanics, John Wiley & Sons, New York, NY, 1977, pp. 63 & 342.

[30] A.J.F. Siegert, On the derivation of the dispersion formula for nuclear reactions, Phys. Rev. 56 (1939) 750.
[31] R.G. Newton, Scattering Theory of Waves and Particles, McGraw-Hill, New York, NY, 1966.
[32] G. Breit, E. Wigner, Capture of slow neutrons, Phys. Rev. 49 (1936) 519.
[33] J.R. Taylor, Scattering Theory: The Quantum Theory of Nonrelativistic Collision, John Wiley & Sons, New York, NY, 1972, p. 238.
[34] N. Moiseyev, Quantum theory of resonances: calculating energies, widths and cross-sections by complex scaling, Phys. Rep. 302 (1998) 211.
[35] G. Doolen, Complex scaling: An analytic model and some new results for e+ hydrogen atom resonances, Int. J. Quant. Chem. 14 (1978) 523.
[36] E. Balslev, J. Combes, Spectral properties of many-body Schrödinger operators with dilation-analytic interactions, Commun. Math. Phys. 22 (1971) 280.
[37] B. Simon, Quadratic form techniques and the Balslev-Combes theorem, Commun. Math. Phys. 27 (1972) 1.
[38] J. Simons, The complex coordinate rotation method and exterior scaling: A simple example, Int. J. Quant. Chem. 14 (1980) 113.
[39] R. Santra L.S. Cederbaum, Non-Hermitian electronic theory and applications to clusters, Phys. Rep. 368 (2002) 1.
[40] J.G. Muga, J.P. Palao, B. Navarro, I.L. Egusquiza, Complex absorbing potentials, Phys. Rep. 395 (2004) 357.
[41] O.I. Tolstikhin, V.N. Ostrovsky, H. Nakamura, Siegert pseudo-states as a universal tool: Resonances, S matrix, Green function, Phys. Rev. Lett. 79 (1997) 2026.
[42] N. Hatano, K. Sasada, H. Nakamura, T. Petrosky, Some properties of the resonant state in quantum mechanics and its computation, Prog. Theo. Phys. 119 (2008) 187.
[43] T. Mercouris, C.A. Nicolaides, Time dependence and properties of nonstationary states in the continuous spectrum of atoms, J. Phys. B 30 (1997) 811.
[44] G. Garcí-Calderón, J.L. Mateos, M. Moshinsky, Resonant spectra and the time evolution of the survival and nonescape probabilities. Phys. Rev. Lett. 74 (1995) 337.
[45] R. Santra, J.M. Shainline, Chris H. Greene, Siegert pseudostates: Completeness and time evolution, Phys. Rev. A 71 (2005) 032703/1.
[46] C.A. Nicolaides, Theory and state-specific methods for the analysis and computation of field-free and field-induced unstable states in atoms and molecules, Adv. Quant. Chem. 60 (2010) 163.
[47] P.R. Certain, N. Moiseyev, New molecular bound and resonance states, in: B. Pullman (Ed.), The Fourteenth Jerusalem Symposium: Intermolecular Forces, Dordrecht Reidel Publishing Co., Dordrecht, Holland, 1981.
[48] F.V. Bunkin, I.I. Tugov, Multiphoton processes in homopolar diatomic molecules, Phys. Rev. A 8 (1973) 601.
[49] H. Helm, P.C. Cosby, M.M. Graff, J.T. Moseley, Photofragment spectroscopy of CH^+: Laser excitation of shape resonances in the A^Π state, Phys. Rev. A 25 (1973) 304.
[50] V. Krishnamurthi, D. Mathur, G.T. Evans, On the formation of rotationally hot $H_2{}^{+\cdot}$ by dissociation of $CH_4{}^{2+}$ dications, Rap. Comm. Mass Spec. 5 (1991) 557.
[51] H. Feshbach, Unified theory of nuclear reactions. I, Ann. Phys. 5 (1958) 357; H. Feshbach, Unified theory of nuclear reactions. II, Ann. Phys. 19 (1962) 287.
[52] U. Fano, Effects of configuration interaction on intensities and phase shifts, Phys. Rev. 124 (1961) 1866.
[53] I. Gilary, A. Fleischer, N. Moiseyev, Calculations of time-dependent observables in non-Hermitian quantum mechanics: The problem and a possible solution, Phys. Rev. A 72 (2005) 012117/1.
[54] S. Klaiman, N. Moiseyev, The absolute position of a resonance peak, J. Phys. B 43 (2010) 185205/1.

CHAPTER 2

Examining the Limits of Physical Theory: Analytical Principles and Logical Implications

Erkki J. Brändas[a]

Contents

[a] Quantum Chemistry, Department of Physical and Analytical Chemistry, Uppsala University, Uppsala, Sweden

Advances in Quantum Chemistry, Volume 63
ISSN 0065-3276, DOI: 10.1016/B978-0-12-397009-1.00002-3

Abstract Owing to the remarkable agreement between precise quantum chemical predictions and the most accurate experiments including sophisticated advanced instrumentation, it is usually concluded that the many-body Schrödinger equation in particular and also quantum mechanics in general describe reality to an unsurpassed exactitude. However, the correlation between the micro- and the macroscopic (classical) levels leads to well-known paradoxes in our fundamental scientific understanding. Hence, our aim is to examine the characteristics and the rationale for developing an analytic foundation for rigorous extensions of quantum mechanics beyond its long-established domain in physics, chemistry, and biology. In this discourse, we will see the fundamental importance of the notion of so-called unstable states, their definition, determination, and characterization. Within this vein, paradoxical and inconsistent issues related to the various attempts to apply microscopic organization to derive scientific laws in the macroworld are considered. The theoretical framework is augmented with quantum logical principles via a reformulation of Gödel's theorems. We arrange the assemblage of the mathematical ideas as follows. First, we give a detailed examination of the second-order differential equation with respect to specific boundary conditions and associated spectral expansions, followed by a general formulation via precise complex symmetric representations exemplified and derived from dilation analytic transformations. Associated dynamical timescales are represented and investigated via the corresponding Dunford formula. Relevant applications, where the above-mentioned unstable or metastable states emerge, are reviewed and compared with conventional bound-state and scattering theories with an analysis of their directive performance and stability. The manifestation and generation of triangular Jordan block entities as extended versions of nonstationary states are derived and further investigated and generalized to thermally excited scattering environments of open dissipative systems. Illustrative applications to condensed- and soft condensed matter are provided, and a surprising treatment is given to the Einstein laws of relativity. As a conclusion, we emphasize the computational and model building advantages of a conceptual continuation of quantum mechanics to rigorously incorporate universal complex resonance structures, their life times, and associated localization properties. We also prove the appearance of nonconventional time evolution including the emergence of Jordan blocks in the propagator, which leads to the origin of so-called coherent dissipative structures (CDSs) derived via uniquely defined spatiotemporal neumatic (from the Greek pneuma) units. This self-referential organization yields specific information bearing transformations, cf. the Gödel encoding system, which might connect developmental and building matters with functional and mental issues within a biological framework at the same time providing background-dependent features of both special and general relativity theory. With these theoretical ideas as background, we advocate a new clarification of the dilemma facing micro–macro correlates including an original characterization of *unus mundus*, i.e., the underlying holistic reality.

1. INTRODUCTION

A general query facing every scientifically oriented mind is whether the unity of the language of science (physicalism) in the strict sense, i.e., if all scientific laws can be derived from the laws of physics, will reduce the different branches of science to physical theory. The ongoing debate between intellectuals and scholars honoring monistic or dualistic doctrines are comprehensive and intensive [1]. The novel understanding of causation in terms of Schrödinger's equation [2], the nondeterministic and a-causal flavor of Heisenberg's uncertainty principle [3], and finally the nonstationary nature of Dirac's quantum theory of emission and absorption of radiation [4] has far from resolved the issues with ferocious disputations still going on, from general mind-body issues to detailed concerns regarding the possibility to simulate a living brain with a machine, e.g., artificial intelligence. With this ambient portrayal, it is therefore a valid question to ask whether the limits of physical theory in general and quantum mechanics in particular have been achieved and if not: what remains to be improved and further developed, and if new domains of exploration and research become successful, what are the ensuing consequences?

In the above assessment, there lie paradoxical and contradictory issues, *viz.* the incongruous understanding of certain deep-seated properties of micro–macro correlates. On the macroscopic level it is natural to characterize the law of causality as a fundamental rule, while cause and effect appear to come to an end and hence nonexistent in the microscopic arena. Similarly, time reversible laws appear legitimate in the latter domain while temporal irreversibility directs the macroworld. An analogous inconsistency emerges when one attempts to derive thermodynamic laws from the position of statistical mechanics. Other difficulties emanate from problems to unify quantum mechanics with general relativity and to incorporate the functionalistic aspects of biology, see more below, into a unitary science based on physics. Obviously, the thesis of physicalism, see above, is far from complete, but notwithstanding this uneasiness, there appears an agreed adherence to monistic doctrines among many various scientific specialists. This is underscored despite the logical conundrums, which seem to follow from Gödel's incompleteness theorem(s) [5].

However, the split between monistic and dualistic systems of belief often borders along the concept of supervenience (characterization of a relation that emergent properties bear to their base properties), see also Ref. [6] for a modern appraisal. To use philosophical relationship terminology: if one states that biology (naturally) supervenes on physics, i.e., when physical (spatiotemporal) facts about the world determine biological facts, it is nevertheless called into question whether biology logically supervenes

on physics [6]. Although this review will examine the present limits of physics in general and quantum physics in particular we will also attempt to import imperative analytical implications via the use of fundamental logical principles. In this endeavor, we will continue our research toward the resolution of persistent micro–macro paradoxes comprising stronger statements of reductive explanation and the possibility of logical supervenience (logical relationship to the base facts) on physics.

In previous reviews of the present author [7–9], the extension of quantum mechanical laws to open, so-called dissipative, systems has been propounded. The area of applications has involved atomic and molecular target computations, scattering theoretical arrangements, structure and classification, large complex multipart structures in condensed and soft condensed matter including complex biological organizations and ultimately the integration of small microscopic systems, all things considered, capable of depicting cosmological dimensions. From the theoretical viewpoint, the generality of the development concerns the original formulation of boundary conditions in Schrödinger-like, second-order differential equations using rigorously defined spectral categorizations via general scaling transformations to the subsequent incorporation of these modifications to general master equations within the domain of thermodynamics and statistical mechanics all the way up to biological, complex enough, systems. Accordingly, the generalized notion of unstable resonance states has been utilized as conceptual representations for the scientific picture. In particular, the author has belabored nonstatistical interpretations of open dissipative systems and associated dynamical consequences. The self-referential character of the description, here made obvious by its classical canonical form, with a Segrè characteristic larger than one separates directive teleonomic statements from nonteleological language. For definitions and references, see the brief statement before the end of the section below. To get a flavor of the type of problems that one might discuss and analyze within this edifice, we mention the following issues:

what distinguishes living matter from inanimate systems?
what is the proper framework for a bona fide science of biology? (Mayr [10])
are we as living subjects subjected to Gödel's incompleteness theorem? (Seel and Ladik [11])
do we have a law of microscopic self-organization?
could self-referentiability be turned into a (biological) natural law?
are there sentient computers? (Dyson [12])
can physical teleomatic laws be transformed into teleonomic rules?
are there any similarities between the analogies mind-body and structure-matter?
is there a global principle under which classical and quantum mechanics can coexist?
what is the role of temperature in biological systems?

how can we merge quantum and thermal correlations?
what is the role of gravity in biology?
what are the consequences regarding the positions on AI? (Penrose [13])
what are the cosmological teleological consequences? (Hawking [14])
can decoherence be prohibited and what does this mean?

The use above of the somewhat controversial terms of teleology goes back to Mayr's essay collection [10], where, slightly simplified, teleomatic processes are governed by natural laws and teleonomic ones are goal-directed due to the influence of an evolved program.

Before we proceed to discuss and further examine the feasibility of such wide-ranging proposals along the lines developed in the introduction above, we will prepare the potential reader with the appropriate mathematical background for the necessary analytic extension and its associated logical principles.

2. GENERAL MATHEMATICAL DETAILS

Since teleological–functional explanations, i.e., normally those prescribing a macroscopic goal-directed organization, seem to "evaporate" as soon as one acquires a microscopic perspective based on fundamental time-reversible physical laws, we have yet another realization of an inconsistent micro–macro correlates. Hence, our first task will be to review and analyze the appropriate mathematical aspects regarding the fundamental formulation of microscopic fundamental physical laws. Since we will attempt to build a bridge between quantum theory and a nonquantal vernacular, we will focus on the descriptions in terms of original operator expression in a complex symmetric setting. Rather than expounding on modern developments including exotic dimensions at unconventional scales and interpretations, we will find that the former exhibits self-referential gauges, see more in subsequent sections, so far not integrated in the latter. We will not make this exposition all-inclusive since we have discussed and re-examined these issues recurrently. In Ref. [7], we gave an initial motivation regarding how to find realistic time developments going beyond the traditional view based on unitary time evolution.

The goal is to find unique analytic structures, of basic importance for advanced physical theories, which are concerned with particular complex structures on the so-called unphysical Riemann sheet and to determine the associated build-up of the corresponding resolvents or Green's functions. This includes the analysis of related autocorrelation functions, their Fourier–Laplace transforms, and in general examining the signal determining the extended spectrum (and vice versa) giving new insights into the properties

of chemical and physical systems. It is also appropriate in this development to mention and refer to Schrödinger's famous treatise, posing quantization as an eigenvalue problem, and the relation between this requisite and the technical problems of square integrability appropriately defining the well-known Hilbert space.

Note that there are precise relations between the time-independent and the time-dependent formulations. A detailed account was recently given in Ref. [8], pertaining to research carried out while the author spent extended visits at the Florida Quantum Theory Project. For the most part Hamiltonian operators exhibiting absolutely continuous spectra, i.e., in most atomic and molecular applications, time-dependent investigations have been significant; see a recent edition of Advances in Quantum Chemistry [15]. In particular, variance and width variational calculations [16–18], normalization studies via contour integration and scaling transformations [17, 18], and derivation of novel types of uncertainty principles [19] showed promise for further studies beyond pure formalism. For instance, successful and accurate computations on so-called state-specific methods for field-free and field-induced unstable states in atoms and molecules have been examined and studied thoroughly over the years by Nicolaides and collaborators [15, 18, 20].

For more about basic formulations of general time-dependent and time-independent partitioning techniques, see Appendices A and B as well as Refs. [21–31]. Note that our rationale is to give a mathematical platform, based on unstable or metastable resonance states, for a rigorous appraisal of physical theories and related applications in general and to a discussion of the above-mentioned issues in particular. It is, therefore, necessary to give a precise and consistent account of the standard theoretical regime in terms of relevant mathematical formulations to establish a nontrivial but nevertheless much needed generalization. As our recent reviews have not included a more detailed exposition of the boundary condition problem, we will first turn toward this task below.

2.1. Boundary conditions—the differential equation

As mentioned in Appendix A, we are interested in problems where the differential operator exhibits an absolutely continuous spectrum, σ_{AC}, and to consider its consequences and operational importance. In particular, we are interested in the relationship between the implementation of singular boundary conditions, the spectral properties, and the topological consequences. Normally these problems are adequately handled by conventional scattering theory. However, there are many physical situations, e.g., the standard example of the hydrogen atom perturbed by an electric field, where standard scattering theory does not apply. The Stark effect in the hydrogen atom, nevertheless, concerns potentials that belong to Weyl's limit point case [32–35]

(separated in conventional parabolic coordinates). In addition to yielding alternative formulations and numerical treatments of problems involving σ_{AC}, the Weyl–Titchmarsh theory [32, 33] provides a rigorous platform for analytic continuation of the whole differential equation onto the complex plane. We will examine the generalization of the spectral theory as well as the attendant consequences for the Fourier–Laplace transform and the precise microscopic time evolution. The formulation, below, conforms to previous applications [35, 36], yet we will make the portrayal a bit different.

2.1.1. Weyl's theory

Although we will use analogous notations of previous references, we will make a simple generalization by discussing the partial differential equation (V is real with the mass of the particle left out in the kinetic part)

$$L[u] = (-\Delta + V)u = \lambda u; \quad \lambda = E + i\varepsilon; \quad \varepsilon \neq 0 \tag{1}$$

where Δ is the Laplacian and V is a real potential to be defined appropriately below. Since our aim with this review concerns the limits of physical theories, we will make some general comments and exemplify some relevant trends, see Figures 2.1, 2.2 and Refs. [37–39]. Note that there are 11 sets of orthogonal coordinate systems [37] in which the Helmholtz equation, Eq. (1) with V constant, separates, see Figure 2.1 above for the coordinate surfaces of the most general orthogonal curvilinear system, the so-called

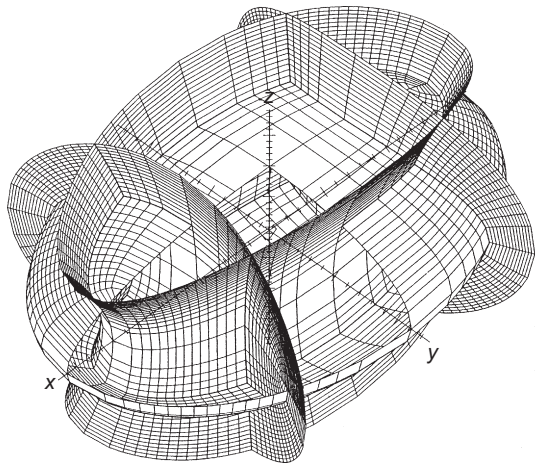

Figure 2.1 Examples of ellipsoidal coordinate surfaces. The grid is formed by the intersection of the coordinate surfaces. From Ref. [38] with permission of IJQC.

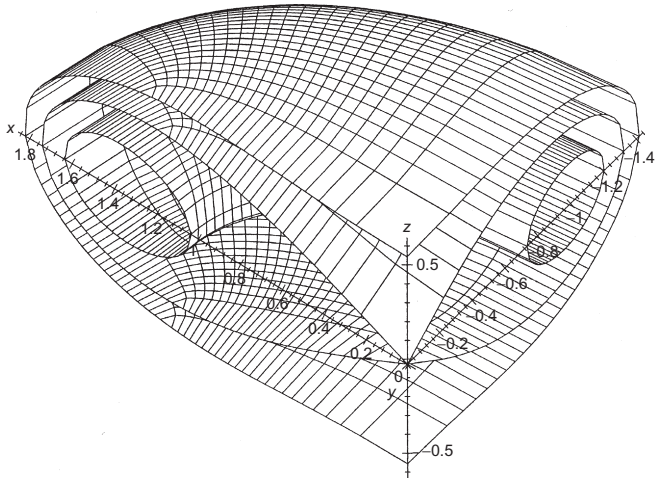

Figure 2.2 Display of the equipotential surfaces of a general potential, separable in ellipsoidal coordinates. Taken from Ref. [38] with permission of IJQC. For more details see Refs. [38, 39].

ellipsoidal coordinate system [37–39], see also references therein. The solution sought for is denoted by u, satisfying prescribed boundary conditions with λ a complex parameter. More details will be discussed below. In passing, we observe that the classical Sturm–Liouville theory for second-order ordinary differential equations consists of finding the eigensolution u_k and eigenvalues E_k to Eq. (1) on a finite interval of their variables (and with no singularities of the potential inside). Note that we will formulate Eq. (1) generally as a partial differential equation, nevertheless, the equation may be separable provided the potential has a suitable symmetry. For example, we may mention the problem of scattering off the most general type of potential, separable in ellipsoidal coordinates, Figure 2.2, and the analysis of associated cross section expansions in terms of perturbed Lamé wavefunctions [39].

To determine the interplay between the spectral properties, both σ_P and σ_{AC}, of the operator L and the prescribed boundary conditions, we return to Weyl's theory [32]. The key quantity in Weyl's extension of the Sturm–Liouville problem to the singular case is the m-function or m-matrix [32–36]. To define this quantity, we need the so-called Green's formula that essentially relates the volume integral over the product of two general solutions of Eq. (1), u and υ with eigenvalue λ and the Wronskian between the two solutions; for more details, see Appendix C. The formulas are derived so that it immediately conforms to appropriate coordinate separation into the

ordinary case depending on the properties of the potential V. Hence, we obtain

$$(\lambda - \lambda^*) = \int_{V_b - V_0} u v^* \mathrm{d}V = \int_{S_b - S_0} [uv]\,\mathrm{d}S \tag{2}$$

where

$$[uv] = u\frac{\partial v^*}{\partial n} - \frac{\partial u}{\partial n}v^* \tag{3}$$

and $\frac{\partial}{\partial n}$ means the derivative along the normal to the surface S, and V_b and V_0 are volumes defined by the surfaces S_b and S_0, with $V_b > V_0$. Subsequently, we introduce two linearly independent initial value solutions φ and ψ (not to confuse with the notation in Appendices A and B), where ψ is chosen to be the regular solution, i.e., with an initial value on S_0, such that $\psi = 0$ in the limit $V_0 \to 0$ (if V is nonsingular at the origin we impose the condition $\psi = 0$, while in the singular case the boundary condition is obtained from an appropriate limiting procedure, more on this is discussed later). The m-coefficient, $m(\lambda)$, is defined by the requirement that χ, defined by (with φ canonically chosen, see below and Appendix C)

$$\chi(\lambda) = \varphi(\lambda) + m(\lambda)\psi(\lambda) \tag{4}$$

remains square integrable as $V_b \to \infty$. In fact if the potential is singular at the origin a similar analysis should be carried for $V_0 \to 0$. For simplicity, we will only discuss the singular point associated with one of the limits, i.e., infinity, but the extra complication of two singular end points are easily handled by an appropriate m-matrix for the left-hand and the right-hand problem, respectively, with the trace of the so-called Coddington–Levinson m-matrix identified with the presently derived formula, see below, for the m-function [36, 40].

For λ, nonreal, i.e., $\varepsilon \neq 0$, solutions of Eq. (4) exist for most potentials of physical interest. In particular, in Weyl's terminology, the limit point case guarantees that the limit $V_b \to \infty$ exists uniquely [32]; see Ref. [35] for some simple limit point conditions, including not only most potentials of conventional scattering theory but also background effects related to dilated short-range potentials, including the Coulomb case and the previously mentioned Stark effect in the hydrogen atom [35, 41, 42]. Note the complications at the origin of the radial part of the Coulomb differential equation (spherical coordinates $(r, \vartheta, \phi) = (r, \Omega)$), see [36, 42] for more details. In this particular case, the boundary condition, $\psi = 0\,; r = 0$, assures the self-adjointness of the three-dimensional (3D) Laplacian.

With this background, we can choose φ and ψ canonically without restriction at S_0, see Appendix C for more details, i.e.,

$$[\varphi\psi] = 1 \tag{5}$$

It is now a trivial matter to determine m such that $\chi(\lambda)$, in Eq. (4), is square integrable at infinity, i.e.,

$$\begin{aligned} m^{\pm}(E \pm i0) &= -\lim_{V_0\to\infty} \frac{\varphi(E \pm i0)}{\psi(E \pm i0)} = -\lim_{V_0\to\infty} \frac{W(\varphi(E \pm i0), \chi(E \pm i0))}{W(\psi(E \pm i0), \chi(E \pm i0))} \\ &= -\lim_{V_0\to\infty} \frac{[\varphi(E \pm i0), \chi^*(E \pm i0)]}{[\psi(E \pm i0), \chi^*(E \pm i0)]} \end{aligned} \tag{6}$$

where the Wronskian is simply defined as $W(u, \upsilon) = [u\upsilon*]$.

Since we will, see further below, introduce the Mellin transformation to analyze scale invariance in connection with the micro–macro problems, it will be natural to rewrite some of our formulas in a spherical coordinate system, i.e., in terms of $(r, \vartheta, \phi) = (r, \Omega)$ with $(u \to ru)$

$$L[u] = \left(-\frac{\partial^2}{\partial r^2} + \mathcal{L}^2(r, \Omega) + V(r, \Omega)\right) u(r, \Omega) = \lambda u(r, \Omega) \tag{7}$$

and with the angular term given by

$$\mathcal{L}^2(r, \Omega) = (r^2 \sin^2\vartheta)^{-1} \frac{\partial^2}{\partial\phi^2} + (r^2 \sin\vartheta)^{-1} \frac{\partial}{\partial\vartheta}\left(\sin\vartheta \frac{\partial}{\partial\vartheta}\right) \tag{8}$$

It is customary to introduce the auxiliary quantity or the logarithmic derivative (since we have taken $\frac{\hbar}{2\pi} = 1$, the coupling constant $g = 1$)

$$igz(r, \Omega) = \frac{\frac{\partial u(r,\Omega)}{\partial r}}{u(r, \Omega)} \tag{9}$$

to obtain the well-known Riccati equation, which is stable for the appropriate exponential type solution, compare for instance the celebrated Jost function in scattering theory, see Ref. [36]

$$-igz'(r, \Omega) = (\lambda - V) - z^2(r, \Omega) - \frac{\mathcal{L}^2(r, \Omega)u(r, \Omega)}{u(r, \Omega)} \tag{10}$$

Although Eq. (10) contains a "difficult non-local term," we can obviously handle this by analyzing each case in terms of eigenfunctions to $\mathcal{L}^2$. Projecting out the odd and even parts of z, see Ref. [43] for more details, $z = z_e + z_o$, where $z_e(z_o)$ is even (odd) in g (or real and imaginary if V is real and $\varepsilon = 0$),

one obtains

$$\begin{aligned} iz_{\mathrm{e}}' &= 2g z_{\mathrm{e}} z_{\mathrm{o}} \\ iz_{\mathrm{o}}' &= g\left\{ z_{\mathrm{e}}^2 + z_{\mathrm{o}}^2 - (\lambda - V) + \frac{\mathcal{L}^2(r,\Omega)u(r,\Omega)}{u(r,\Omega)} \right\} \end{aligned} \tag{11}$$

which can easily be formally solved (r_0 is the radius of the sphere V_0)

$$\left\{ \frac{z_{\mathrm{e}}(r,\Omega)}{z_{\mathrm{e}}(r_0,\Omega)} \right\}^{\frac{1}{2}} = \exp\left\{ -ig \int_{r_0}^{r} z_{\mathrm{o}}(s,\Omega)\,\mathrm{d}s \right\} \tag{12}$$

yielding the formal expression for $u(r,\Omega)$, λ suppressed and $g = 1$. Note also that z_{e} has two branches, i.e., if $z_{\mathrm{e}}(r)$ satisfies Eq. (11), so does $-z_{\mathrm{e}}(r)$ (depending on the limiting procedure $\varepsilon \to \pm 0$) and hence we obtain

$$u^{\pm}(r,\Omega) = u^{\pm}(r_0,\Omega)\left\{ \left\{ \frac{z_{\mathrm{e}}(r,\Omega)}{z_{\mathrm{o}}(r,\Omega)} \right\}^{\frac{1}{2}} \right\} \exp\left\{ \pm i \int_{r_0}^{r} z_{\mathrm{e}}(s,\Omega)\,\mathrm{d}s \right\} \tag{13}$$

Realizing that Eq. (13) gives an explicit solution of (1) with an appropriate V, in terms of logarithmic derivatives, it is possible to identify u with the well-known Jost solution denoted as $f(r,\Omega)$, see more below and Ref. [44], which here must be proportional to the Weyl's solution $\chi(r,\Omega)$. With this identification, we obtain the generalized Titchmarsh formula (generalized since it applies to all asymptotically convergent exponential-type solutions commensurate with Weyl's limit point classification)

$$m(\lambda,\Omega) = -\frac{[\phi\,\chi^{\pm}]}{[\psi\,\chi^{\pm}]} = -\frac{[\phi f^{\pm}]}{[\psi f^{\pm}]} \tag{14}$$

or in terms of logarithmic derivatives, the formula is

$$m^{\pm}(\lambda,\Omega) = -\frac{\phi(iz^{\pm}) - \phi'}{\psi(iz^{\pm}) - \psi'} \tag{15}$$

Before leaving this subsection, we confirm that no subjective features and/or approximations have been incorporated in the description.

2.1.2. Scattering theory

As already mentioned, there are precise conditions that tell whether a potential belongs to Weyl's limit point, see Ref. [32–36, 40]. These conditions guarantee that there exists a unique square integrable solution at the singular

point at infinity (remember $\varepsilon \neq 0$). The limit $\varepsilon \to \pm 0$ gives the unique square integrable eigenfunction for an eigenvalue in the point spectrum σ_{P} and the $\pm$ exponential-type solutions corresponding to σ_{AC}. For the Stark effect in the hydrogen atom these are the so-called Airy functions, whereas for a limit point potential

$$V(r,\Omega) \underset{r\to\infty}{\to} 0 \text{ as } \frac{\text{const}\,(\Omega)}{r^{1+\delta}}; \quad \delta > 0 \tag{16}$$

they are the well-known Jost functions $f^{\pm}(k,r)$, see Ref. [44]. In the asymptotic limit, they become (Ω is suppressed)

$$f^{\pm}(k,r) \propto \exp(\pm ikr); \quad k = \sqrt{\lambda} \tag{17}$$

For $\delta = 0$ (limit point at infinity), one obtains the corresponding Coulomb modifications, see Refs. [36, 42] for the complications at origin. Note also the strong dependence on the incident directions for "ellipsoidal" potentials yet the optical theorem holds, see Ref. [39].

To complete the relation with standard scattering theory (using commensurate potentials), we conclude that Weyl's and Jost's solutions relate as

$$\chi^{\pm}(r,\lambda) = c^{\pm}(\lambda) f^{\pm}(k,r) \tag{18}$$

Incidentally we can limit ourselves to real energies, identifying, in the limit to the real axis and the unique bound state solution alternatively the two branches in the continuum, while if the energy is complex we must keep in mind that $f^{+}(k,r)$ correspond to a unique square integrable solutions if $\mathcal{I}(k) > 0$ and $f^{-}(k,r)$ if $\mathcal{I}(k) < 0$, where $\mathcal{I}(k)$ denotes the imaginary part of k. In the case of σ_{AC}, the logarithmic derivative obtains two branches corresponding to the limits $\varepsilon \to \pm 0$

$$z^{\pm}(r,\Omega,\lambda) \underset{r\to\infty}{\to} \pm ik \tag{19}$$

and for $E \in \sigma_{\mathrm{P}}$

$$z^{+}(r,\Omega,\lambda) \underset{r\to\infty}{\to} -\kappa; \quad \kappa = ik \tag{20}$$

(and similarly for $z^{-}(r,\Omega,\lambda)$). The coefficient $c^{\pm}$ in Eq. (18) is now easily expressed in bracket notation

$$c^{\pm} = -\frac{1}{[\psi, f^{\mp}(k)]} = \frac{1}{W(f^{\pm},\psi)} \tag{21}$$

which leads the definition of the "generalized" Jost function

$$f_J^{\pm}(k) = -[\psi, f^{\mp}] = W(f^{\pm}, \psi) = \left|f_J^{\pm}(k)\right| \exp\{\mp i\delta_k\} \tag{22}$$

and

$$\chi^{\pm}(r,\lambda) = \frac{\exp\{\pm i\delta_k\}}{\left|f_J^{\pm}(k)\right|} f^{\pm}(r,k) \tag{23}$$

To complete the reformulation of scattering theoretical concepts, we can also write down the S-matrix, the flux J (Weyl normalized)

$$S = \frac{f_J^-(k)}{f_J^+(k)}; \quad J(k) = iW(k, \chi^+, \chi^-) = i[\chi, {}^+\, \chi^-] \tag{24}$$

From Eqs. (14) and (15), one obtains with $m^{\pm}(E) = \mathcal{R}m(E) \pm i\,\mathcal{I}m(E) = m_R(E) \pm i\, m_I(E)$, where $\mathcal{R}m$, $\mathcal{I}m$ are the real and imaginary parts of m^+), i.e., when ($k = \sqrt{E}$)

$$m_I(E) = i\frac{W(E, f^+, f^-)}{2\left|f_J(\sqrt{E})\right|^2} = \frac{k}{\left|f_J(k)\right|^2} \tag{25}$$

Equation (25) is known as Kodaira's theorem [45], see also Refs. [36, 46], and it expresses the spectral density for ordinary second-order singular differential equations in terms of the known scattering quantity, the Jost function. The formula can be easily extended to more general asymptotic behaviors using the general bracket/Wronskian expression. It is quite easy to simulate the behavior of the m-function by introducing a small imaginary component of λ for bound states. Figure 2.3, for instance see Ref. [47], displays the imaginary part of m for the hydrogen atom.

2.1.3. Spectral concentration

However, rather than continuing to extract differential and total cross sections, see Ref. [36], we will return to the precise meaning of m_I defined in Eq. (25), remembering that our original task, defined above, is to give a uniform formulation of both bound and so-called quasibound states. In Appendix C, we have explicitly demonstrated the relation between $m_I(E)$ and the spectral function $\lim_{b\to\infty} \rho_b(E) = \rho(E)$ that gives

$$m_I(E) = \lim_{\varepsilon\to 0+0} \{\mathcal{I}m_\infty(E + i\varepsilon)\} = \pi \left(\frac{\mathrm{d}\rho}{\mathrm{d}\omega}\right)_{\omega=E} \tag{26}$$

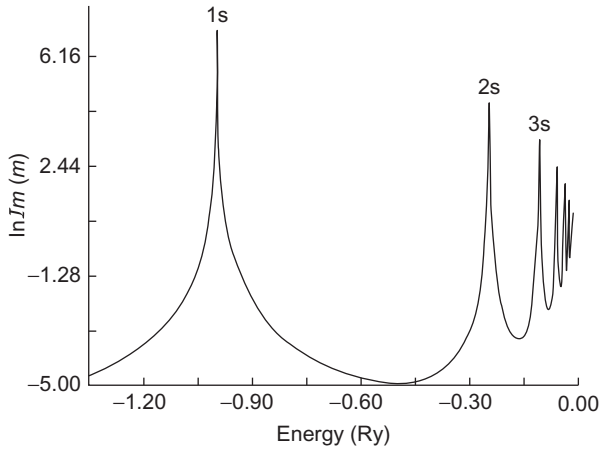

Figure 2.3 Display of the imaginary part Weyl's *m*-function for the radial equation of the hydrogen atom. The imaginary part of the energy is 0.001 Ry. Taken from Ref. [47] with permission of IJQC.

see Refs. [36, 47] for more details. Combining these relations for the spherically symmetric case and for all *l*-values of the angular momentum we obtain, cf. Ref. [48],

$$\begin{aligned}
\left(\frac{\mathrm{d}\rho_l}{\mathrm{d}\omega}\right)_{\omega=E} &= \begin{cases} \frac{1}{\pi}\frac{E^{l+1/2}}{|f_l(E^{1/2})|}; & E \geq 0 \\ \sum_j \left|a_j^{(l)}\right|^2 \delta(E - E_j^{(l)}) \end{cases} \\
f_l(k) &= (-k)^l W(f_l(k,r), \psi_l(E,r)) = \left|f_l(k)\right| \exp(-i\delta_l) \\
\lim_{r\to\infty}&(i^l \exp(ikr) - f_l(k,r)) = 0 \\
\delta(r - r') &= \sum_l \int_{-\infty}^{+\infty} \psi_l(\omega, r)\mathrm{d}\rho_l(\omega)\psi(\omega, r')
\end{aligned} \tag{27}$$

With these quantities we have all the information we need regarding the properties of the differential equation, e.g., the spectrum, the resolution of the identity (from which Green's functions, propagators, and resolvents can be obtained), and various scattering quantities like Jost functions, phase shifts, cross sections, S- and K- matrices, etc. The interesting question arises, namely whether this formulation provides enough information for analytic extension into the complex plane and furthermore if the structures that appears are not only rigorously defined mathematically as well as providing interesting results and understanding regarding our initial question of the examination of the limits of physical theory. For instance what can be

obtained and known from the Kodaira form of $m_I(\lambda)$? The full representation of m can, in principle, be made from Eqs. (14) and (15) although some technical problems appear if one wants to give the appropriate analytic (Nevanlinna) form not to mention the general case of two singular end points. In the first case, the imaginary part of m grows too fast ($l \neq 0$) to provide analytic information for an appropriate analytic function, and in the second case, there is the energy dependence of the left boundary a ($l \neq 0$) occurring in the m-function through the limiting procedure associated with the left boundary. In the first case, we will obtain the relevant information, without approximations, via proper analytic continuation of the associated Green's function, as will be seen below, and in the second case, we could always revert to the appropriate m-matrix if needed. We will end this section by noting that the simple case of a free particle, with $l = 0$, $V(r) \equiv 0$, and the left boundary given by $a = 0$ yields a very simple result, i.e.,

$$m = i\sqrt{\lambda} \tag{28}$$

which, as can easily be shown, gives rise to two branches, depending on whether the real axis is approached from below or above.

In summary, we have derived formulas for the Weyl–Titchmarsh m-function, where the imaginary part serves as a spectral function of the differential equation in question. Before we look at the full m-function, we will see how it works in connection with the spectral resolution of the associated Green's function

$$G^+(\lambda, r, r') = \psi(\lambda, r_<)\chi^+(\lambda, r_>)/W(\psi(\lambda)\chi^+(\lambda)) \tag{29}$$

satisfying

$$(\lambda - L)G^+(\lambda, r, r') = \delta(r - r') \tag{30}$$

Here, $r_<$ and $r_>$ are the smaller and the larger of r and $r\prime$, respectively. From the general formulas derived above we obtain

$$G^+(E + i0) = \lim_{\varepsilon \to 0} \int_{-\infty}^{+\infty} \frac{\mathrm{d}\rho(\omega)}{E + i\varepsilon - \omega} = \int_{-\infty}^{+\infty} \frac{\mathrm{d}\rho(\omega)}{E + i0 - \omega} \tag{31}$$

or in terms of the coordinate representation, we get

$$G^+(\lambda, r, r') = \sum_j \frac{\psi(\lambda_j, r)\psi(\lambda_j, r')/\langle\psi(\lambda_j)|\psi(\lambda_j)\rangle}{\lambda + i0 - \lambda_j} + \int_0^\infty \frac{\psi(\omega, r)\psi(\omega, r')\left(\frac{1}{\pi}m_I^+(\omega)\right)\mathrm{d}\omega}{\lambda + i0 - \omega} \tag{32}$$

In Eq. (32), we have included the full spectrum of a second-order ordinary differential equation with negative bound state eigenvalues and the continuum being the positive real axis. The free-particle background is $m_{\text{free}} = i\sqrt{\lambda}$. In this case, the full m-function becomes [in the equation below we have introduced a natural generalization of $\mathcal{I}_g$, the "jump" or imaginary part, see Eq. (36) for the general case]

$$m(\lambda) - i\sqrt{\lambda} = \sum_j \frac{-\text{Res}(m(\lambda))}{\lambda - \lambda_j} + \int_0^\infty \frac{\frac{1}{\pi}(\mathcal{I}_g(m^+(\omega) - \sqrt{\omega})\mathrm{d}\omega}{\omega - \lambda} \tag{33}$$

which in the Coulomb case modifies to

$$m(\lambda) - iC_0^2(\lambda)\sqrt{\lambda} = -R(\lambda) + \sum_j \frac{-\text{Res}(m(\lambda))}{\lambda - \lambda_j} + \int_{R^+} \frac{\frac{1}{\pi}(\mathcal{I}_g(m^+(\omega) - \sqrt{\omega})\mathrm{d}\omega}{\omega - \lambda} \tag{34}$$

with the general Coulomb background given by $V_C(r) = -Q/r$ (here $Q = 1$) is

$$C_0^2 = \frac{2\pi\xi}{\exp(2\pi\xi) - 1}; \quad \xi = -Q/\sqrt{\omega}; \quad R(\lambda) = \sum_{n=1}^{\infty} \frac{2Q^3/n^3}{-Q^2/n^2 - \lambda} \tag{35}$$

A popular case studied is $V(r) = 7.5r^2\exp(-r)$, which does not contain any bound states (only resonances, see more below) and modifies the Coulomb spectrum accordingly. As we will see later these formulas are easily generalized to the complex plane by contour integration. In Figure 2.4, we show the integration contour for the so-called Cauchy representation of m, in the simple case of two bound states, and the cut along the positive real axis.

A function $f(z)$ is said to be of Nevanlinna type if it maps the upper (lower) complex half-plane onto itself and is Cauchy analytic in each half-plane with possible singularities on the real axis. The theory of Nevanlinna functions leads to the existence of a uniquely defined function $\rho(\omega)$, called the spectral function of $f(z)$; for more details see Ref. [49]. As we will see below, there exist rigorous techniques of analytic continuation that not only lends itself to complex path integration but also generalizes to a whole set of dilation analytic operators, which, suitably modified, can be used alongside standard many-body approaches used in chemical and physical applications. To forebode this development, we demonstrate some of the interesting results that are begotten by this more general view. In Figure 2.5, we show a deformed contour, where the cut has been tilted at an angle down in the complex plane. The analytic continuation behind this transformation can

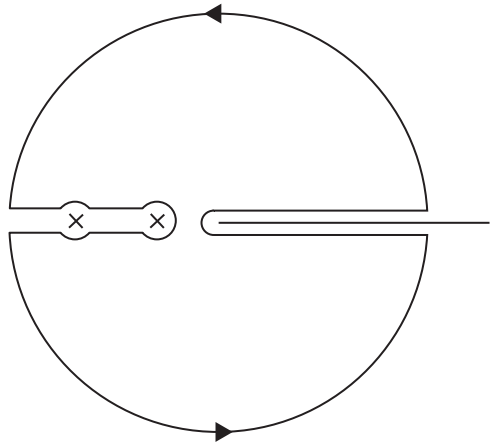

Figure 2.4 Integration contour for the Cauchy representation in the complex plane of a function of Nevanlinna type showing the deformation around the bound states and the cut along the real axis.

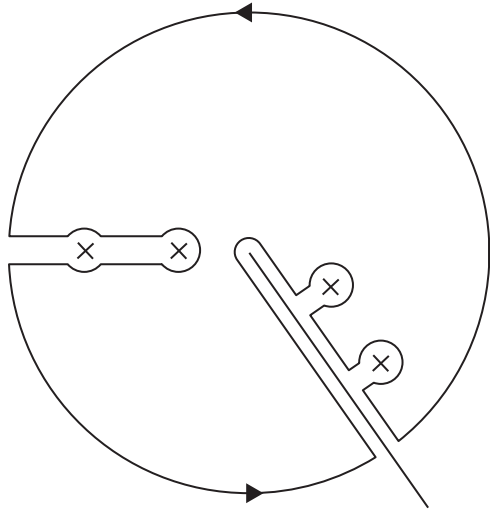

Figure 2.5 Integration contour for the analytically continued Nevanlinna function, $f(z)$, displaying the "new cut" and deformations around bound states and resonance poles.

be rigorously defined both theoretically and practically. Also the generalized spectral function, which displays a cut, or a "jump," along the "new continuum" can be easily calculated and analyzed.

There are two simple observations that immediately come to mind when confronted with the results of the popular potential mentioned below

Eq. (35). With a free-particle background, there are no bound states and the resonances fall nicely along a string in the complex energy plane, see Figure 2.6. Here we have shown seven resonances, but only six of them appear above the cut, indicated by the line in the picture drawn between resonance numbers six and seven. The "new cut" contains three regions marked out by a weakly drawn and the thickly drawn line intertwined by a broken line. The reason is as follows: the thick line implies that the spectral function asymptotically approaches the free-particle background, whereas the thin line is essentially zero inside the string with a transition interval in between, see further Figures 2.6 and 2.7.

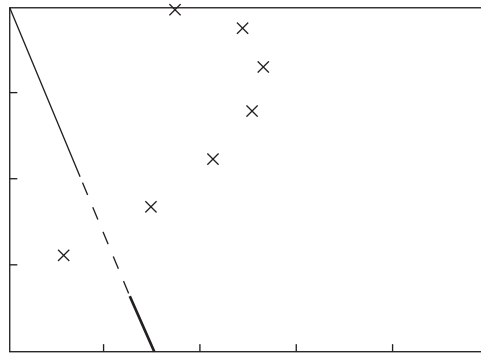

Figure 2.6 Pole string for $m^{+}(\lambda)$ of the potential $V(r) = 7.5\, r^2 \exp(-r)$ with a free-particle background, see Ref. [41], Figure 2.3 for details. Published with permission from American Institute of Physics.

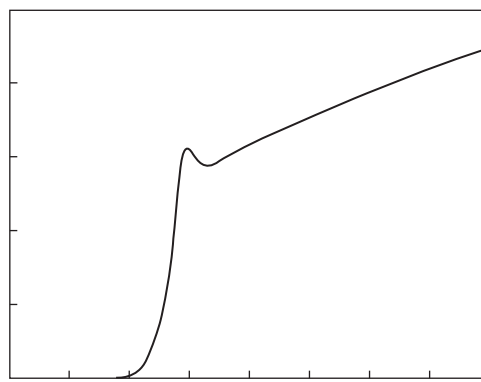

Figure 2.7 Display of the absolute value of $\mathcal{I}_g(m^{+}(\lambda))$ along the ray displayed in Figure 2.6, see Ref. [41], Figure 2.14 for details. Published with permission from American Institute of Physics.

The jump in the m-function at the "tilted cut" is complex; therefore, we will display the absolute value of the generalized imaginary part of m^+ given by

$$\mathcal{I}_g(m^+(\lambda)) = (m^+(\lambda) - m^-(\lambda))/2i \tag{36}$$

where $\mathcal{I}_g(m^+(\lambda))$ is the analytic continuation of $\mathcal{I}(m^+(\lambda)) = (m^+(\lambda) - m^-(\lambda))/2i$ for λ complex along the cut. Figure 2.7 displays a surprising deflation effect, namely "inside" the pole string, the generalized density is effectively zero approaching the free-particle background "outside." The appearing drop in spectral density close to the intersection between the "new cut" and the pole string leads to simple approximation of m. With the assumption of a sharp transition point Λ between a negligible and the free-particle density, we obtain the general approximation and analogously for the Coulomb case [42]

$$m(\lambda) - i\sqrt{\lambda} = \sum_j \frac{-\mathrm{Res}(m(\lambda))}{\lambda_j - \lambda} - \frac{2}{\pi}\sqrt{\Lambda} + \frac{\sqrt{\lambda}}{\pi} \ln\left(\frac{\sqrt{\lambda} + \sqrt{\Lambda}}{\sqrt{\lambda} - \sqrt{\Lambda}}\right) \tag{37}$$

Although the present section has emphasized the fundamental theory of Weyl as a basis for a reformulation and generalization of conventional scattering theory, our illustrations have focused on the possibility to analytically continue the full differential equation with its spectral function and associated Green's functions and resolvents, the S-matrix etc., into the complex plane. This calls attention to appropriate methods for both rigorous and practical techniques to accomplish this operation.

2.2. Non-selfadjoint formulations

To advance fundamental knowledge of the differential equation to the complex plane, we need to rigorously examine the topological features of various definitions of the Hilbert space with respect to problems of convergence, completeness, and how to define the binary product in connection with appropriate extension to nonself adjoint formulations. In other words, we want to analytically continue the general many-body Schrödinger equation (and similarly the associated Liouville equation) to the so-called unphysical Riemann sheet of the energy plane or k-plane. This leads to the second path of our development, *viz.* the theory of dilation analytic potentials [50]. As we will see, this will not only lead to a precise formulation of Weyl's theory, referred to above, but also to a rigorous and a practical extension to the general time-dependent and time-independent partitioning description alluded to above and presented in the appendices. In addition to giving accurate methods for numerical integration of the differential equation along appropriate complex contours in the so-called second Riemann sheet, "picking up"

resonance eigenvalues (including residues), and eigenfunctions (Gamow waves) [42, 51], it will moreover mimic traditional approaches for ordinary bound states with only minor but nevertheless important differences [52], see also appendices and further below.

To carry out the program referred to in the section above, compare also the difference between Figures 2.4 and 2.5, we will impart the aforementioned mathematical theorem due to Balslev and Combes [50]; see also part IV [53] of the four-volume treatise on "Methods of Modern Mathematical Physics" by Reed and Simon, which includes the Balslev–Simon "no eigenvalue theorem," i.e., the absence of eigenvalues on $(0,\infty)$ for potentials of form $\bar{\mathcal{F}}_{\pi/2}$. For definitions we refer to Appendix D and references therein, see also [9, 54] for details regarding the steps involved to obtain the dilated analogue of the Schrödinger equation, Eqs. (D.7), using the Nelson subset of analytic vectors [54]. Although there are many other successful methods, e.g., the use of non-Hermitean constructions [55] or the very popular method of complex absorbing potentials [56], we will not discuss this point any further since it will not alter the conclusions regarding our general query formulated in the introduction.

The theory of dilation analyticity or simply the complex scaling method represents simultaneously both a powerful and a practical approach for applications to atomic and molecular systems. In passing we also note that analytic continuation in practice also works for the Stark effect case, see Nicolaides [55] regarding how to bypass the conundrum of the linear potential by proper regularization of the resonance eigenfunction. In addition to being a valid potential comprising Weyl's limit point, the addition of an external electric field, meromorphic continuations are subject to the translation analytic group [57]. In more general settings complex scaling rotates the essential spectrum about a certain set of thresholds when subject to a particular gauge [57]. For a more recent overview of experimental mathematics, acquiring information from otherwise "impossible computations," see Reinhardt's contribution to Barry Simon's Festschrift [58].

2.2.1. Bounds to resonances

To expand on the background provided in Appendix D, we will briefly discuss the spectral consequences of the introduction of the dilation analytic family of operators and the option to "move" or rotate the absolutely continuous spectrum, σ_{AC}. Considering again the Hamiltonian of Eq. (D.3), i.e., $H = T + V$, where V is dilation analytic, r is continued to Ω, where

$$\Omega = \left\{ re^{i\vartheta} : r \geq 0,\, 0 \leq \vartheta < \vartheta_0 \right\} \tag{38}$$

for some $\vartheta_0 > 0$. The first question that comes to mind naturally is whether there exists spectrum, i.e., a resonance eigenvalue $\varepsilon_{\mathrm{res}}$, in the ensuing sector

given by

$$\left\{-2\vartheta_0 < -2\arg\eta < \arg\varepsilon_{\text{res}} \leq 0\right\} \tag{39}$$

where $\eta = e^{i\vartheta}$ (or in general $\eta = |\eta|\, e^{i\vartheta}$) is the complex scaling of r. We follow the portrayal of this problem discussed in Ref. [59], see also Appendix D and Eqs. (D.10)–(D.12), introducing the projection operator $O(C)$ and the condition for a nonempty spectrum

$$O(C) = \frac{1}{2\pi i}\oint_C \frac{\mathrm{d}z}{(z-H)} \tag{40}$$

$$\|O(C)\tilde{\varphi}\| > 0 \tag{41}$$

for a trial function $\tilde{\varphi}$. It is straightforward to prove that condition, i.e., Eq. (41), holds if

$$K(C,\varepsilon)M(C)\lambda(\varepsilon) < 1 \tag{42}$$

where the bounding parameters will be defined in detail below.

To define K, M, and λ, see inequality Eq. (42), we need to define the following procedure. First the plot, Figure 2.8 below, displays the dashed test circle C with the center $\varepsilon_{\text{test}}$ marked with a cross. In addition we have so-called probe circles $C_{\text{p}}(\varepsilon, \lambda(\varepsilon))$ defined by the eigenvalue relation

$$(H-\varepsilon)^{\dagger}(H-\varepsilon)\varphi(\varepsilon) = \lambda^2(\varepsilon)\varphi(\varepsilon) \tag{43}$$

with the center at ε and radius $\lambda(\varepsilon)$. For $\varphi = \psi_{\text{res}}$, where

$$H\psi_{\text{res}} = \varepsilon_{\text{res}}\psi_{\text{res}} \tag{44}$$

and ε_{res} is the closest (resonance) eigenvalue to ε, one obtains for the lowest eigenvalue

$$\lambda^2(\varepsilon) \leq \sigma^2(\varepsilon, \tilde{\varphi}) \tag{45}$$

where the expectation value $\sigma^2(\varepsilon, \tilde{\varphi}) = \langle (H-\varepsilon)\tilde{\varphi} | (H-\varepsilon)\tilde{\varphi}\rangle$ is evaluated for a trial $\tilde{\varphi}$ of unit norm for simplicity. Furthermore, Moiseyev [60, 61], using matrix elements of the type investigated in [55], observed that

$$\lambda^2(\varepsilon) \equiv \sigma^2(\varepsilon, \varphi) \leq \sigma^2(\varepsilon, \psi_{\text{res}}) = |\varepsilon - \varepsilon_{\text{res}}|^2 \tag{46}$$

leading up to the formulation of the so-called exclusion theorem; i.e., inside the probe circle $C_{\text{p}}(\varepsilon, \lambda(\varepsilon))$ there are no (resonance) eigenvalues and hence the region defined by C_{p} is a spectrally excluded region.

These conclusions call for the following ichthyoidal construction. Using relation (46), we can probe every point on the test circle C, taking the envelope of all these excluded region circles centered on the test curve. This defines an inner and outer boundary. The inner boundary $I(C)$, due to the form of the enveloping curve – the boundary looks like a fish (ichthys in Greek) – see Ref. [59] and Figure 2.8, are termed ichthyoids. The smallest radius of all probe circles centered on C gives the bound $M(C)$, i.e.,

$$M(C) = \sup_{z\in C}\left\{\left\|(z-H)^{-1}\right\|\right\} = \left\{\inf_{z\in C}[\lambda(z)]\right\}^{-1} \tag{47}$$

If we select $\varepsilon = \varepsilon_{\text{test}}$, then the bound, (42), is given by the product $M(C)\lambda(\varepsilon)$ since $K(C,\varepsilon)$ is 1. In general one might select a probe circle centered at a different point, i.e., with $|\Delta\varepsilon| = |\varepsilon - \varepsilon_{\text{test}}|$, which amounts to determining the average value of the reciprocal distance from a point inside the test circle to

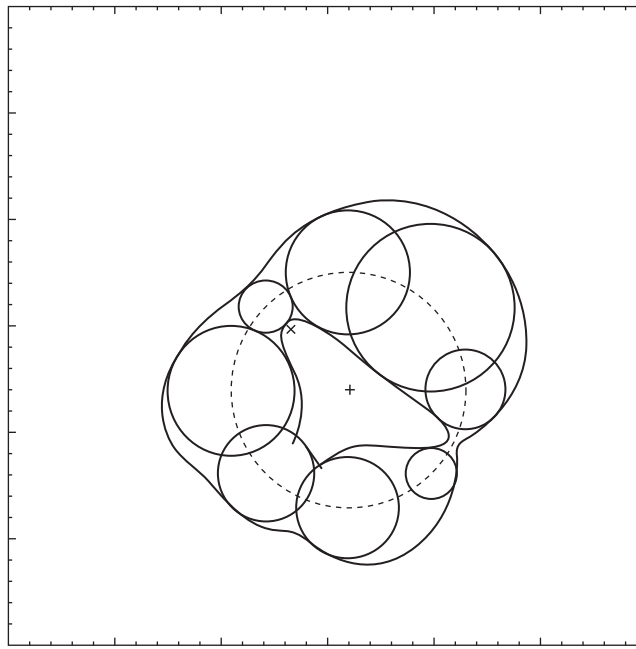

Figure 2.8 Plot showing the ichthyoidal construction for a dashed test circle centered at the cross, $\varepsilon_{\text{test}}$, with the radius r_{test}, see Ref. [59] for details. Published with permission from Phys. Rev. A.

its circumference

$$K(C,\varepsilon) = F\left(\frac{\Delta\varepsilon}{r_{\text{test}}}\right) = F(\gamma) = \frac{1}{\pi}\int_0^{2\pi} \frac{\mathrm{d}\theta}{\sqrt{1-2\gamma+\gamma^2}} = {}_2F_1\left(\frac{1}{2},\frac{1}{2};1;\gamma^2\right) \quad (48)$$

Thus F is monotonically increasing, e.g., $F(0) = 1$ and $F(0.99) \approx 2.136$. Utilizing the information from the ichthyoid, Figure 2.8, we conclude from condition Eq. (42) that there is at least an eigenvalue inside the test curve C if there exists a probe circle (inside C) smaller than every excluded region circle centered on C. If the probe inside the test curve is not centered at $\varepsilon_{\text{test}}$, one needs to multiply the latter with $F(\gamma)$ before the estimation. In fact the evaluation of the resonance region can be narrowed to the curve $I(C)$, the inner ichthyoid, see Figures 2.8 and 2.9. In principle, one may look for higher order eigenvalues (Jordan blocks) by carrying through a similar procedure in the orthogonal complement to ψ_{res}.

Note that this method is not only restricted to dilation analytic situations, see Ref. [59]. Also the numerical examples, referred to, are considered as

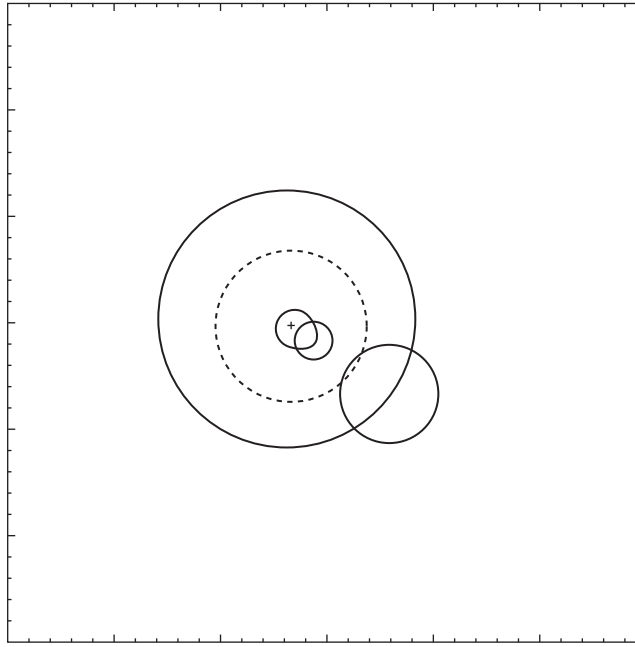

Figure 2.9 Display of the ichthyoidal construction for a dashed test circle C centered at $\varepsilon = \varepsilon_{\text{res}}$. For the point on C with the smallest excluded region circle, the corresponding probe circles on the inner and outer ichthyoid are shown. Published with permission from Phys. Rev. A.

exact due to their simplicity; the generality of the present technique needs to be accompanied by rigorous methods obtaining lower bounds to $\lambda(\varepsilon)$ in order to yield strict boundaries for resonances. This is in principle possible by representing H by lower operator bounds [22]. Furthermore related criticisms have been voiced by Siedentop [62] and also in connection with proofs depending on the classical Lévy–Hadamard–Gerschgorin theorem [63]. A similar consideration affects the work described in Refs. [60, 61]. A final deliberation concerns the domain characteristics of the operators occurring in Eq. (43) and in the definition of $\sigma^2(\varepsilon, \tilde{\varphi}) = \langle (H-\varepsilon)\tilde{\varphi} | (H-\varepsilon)\tilde{\varphi}\rangle$. Obviously, the latter exhibits no difficulties when we work consistently within the domain of H (or T). However, the definition of the operator $H^{\dagger}H$ in Eq. (43) implies domain and range issues, which, however, are easily taken care of provided the application of the "turn-over-rule" is carried out with caution, see the appendix of Ref. [64].

2.2.2. Virial theorems

It is well known that the satisfaction of the quantum mechanical virial theorem is closely related to the optimum property of the trial wavefunction [65]. Löwdin showed that the theorem in its conventional form follows from the variation principle by taking the first derivative of expectation value of the Hamiltonian with respect the scale factor η. The proof demonstrates the necessity but not the sufficiency. Thus, the exact solution to the Schrödinger equation and the optimal scaling solution from the Ritz variation principle exhibit the fulfilment of the virial theorem, including a generalization of the Hellman–Feynman theorem. From this insight it follows that a complex rotation analysis must be intimately connected with generalized versions of these theorems for the resonance eigenvalues defined in the previous section and appendices.

Using the complex symmetric representation introduced above, observing the complex conjugate of η inserted in the wavefunction of the bra-position (see Ref. [17] and Appendix D), we write in analogy with the real scaling case the Ritz quotient and associated variational expressions as

$$\tilde{E}(\eta) = \frac{\left\langle \tilde{\psi}(\eta^*) \middle| H(\eta) \middle| \tilde{\psi}(\eta) \right\rangle}{\left\langle \tilde{\psi}(\eta^*) \middle| \tilde{\psi}(\eta) \right\rangle} \tag{49}$$

The generalized expectation value in Eq. (49) is stationary for arbitrary variations around the exact solutions $\psi(\eta)$ of $H(\eta)$ with the eigenvalue $E(\eta)$, or from

$$\tilde{\psi}(\eta) = \psi(\eta) + \delta\psi(\eta); \quad \eta \in \Omega \tag{50}$$

$$\tilde{E}(\eta) - E(\eta) = \langle \delta\psi(\eta^*) | H(\eta) - E(\eta) | \delta\psi(\eta)\rangle \tag{51}$$

with $\delta\psi(\eta)$ biorthogonal to $\psi(\eta)$, and it follows that the error is second order in $\delta\psi$. Note that the expression above and below implies stationarity, but it is not an extremum as in the self-adjoint case. For more details regarding appropriate definitions, see Appendix D and references therein.

Before continuing we note incidentally that pioneering applications [66, 67] found resonance trajectories (as a function of rotation angle) pause near a true resonance. The "pausing" behavior near the converged result gives a good reason for the generalization of the virial theorem to resonance or metastable states [17]. Several workers in the field did independently point out the inference of this possibility and gave the subsequent proof more or less simultaneously [17, 68, 69]. Reinhardt [67] has nicely portrayed the "pausing phenomenon," see Figure 2.10. Note that, assuming the energy to be analytic in η, a stationary phase angle ϑ requires stationarity in the variations of $\eta = \alpha e^{i\vartheta}$ since

$$\frac{\partial}{\partial\vartheta} = \frac{\partial\eta}{\partial\vartheta}\frac{\mathrm{d}}{\mathrm{d}\eta} = i\alpha\frac{\partial}{\partial\alpha} \tag{52}$$

It follows that $\eta \neq 0$, $\frac{\partial}{\partial\vartheta} = 0$ implies $\frac{\partial}{\partial\alpha} = 0$ and consequently $\frac{\partial}{\partial\eta} = 0$, and hence the "pausing" improves with the accuracy of the basis set.

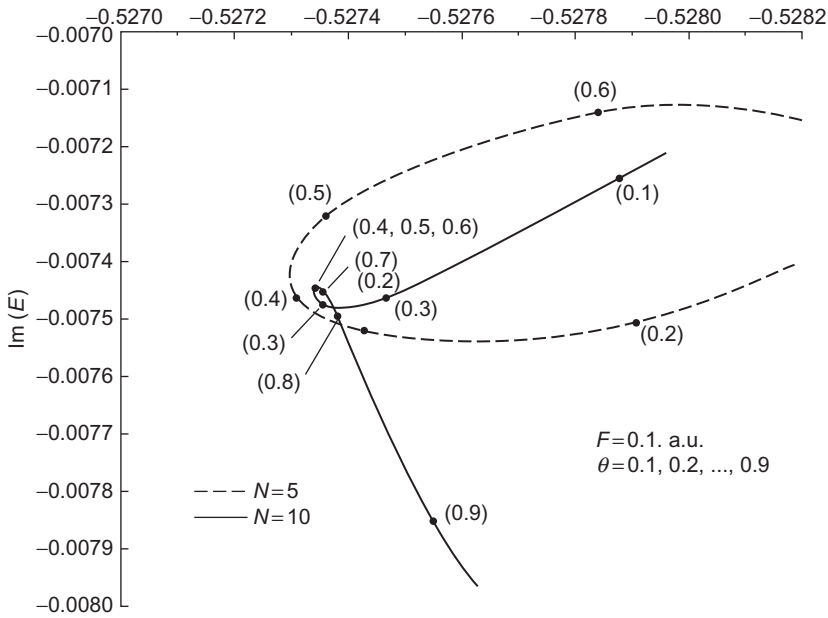

Figure 2.10 ϑ-trajectories for the resonance energy (Stark effect in the hydrogen atom), where *N* is the number of basis functions per *l*-value, for more details see Ref. [67]. Taken from Reinhardt [67] with permission of IJQC.

In analogy with the exact eigenfunction, $\psi(\eta)$, of the dilation analytic Hamiltonian, $H(\eta)$, satisfying the equation

$$(T(\eta) + V(\eta))\psi(\eta) = \varepsilon_{\text{res}}\psi(\eta) \tag{53}$$

or using the properties of scaling transformation

$$(\eta^{-2}T(1) + V(\eta))\psi(\eta) = \varepsilon_{\text{res}}\psi(\eta) \tag{54}$$

we will consider an approximate stationary solution of Eq. (49), optimal for the scaling factor $\eta_0 \in \Omega$. Generalizing the scaling procedure of Löwdin [65], Eqs. (49)–(51) yields for N particles and optimal trial function $\tilde{\psi}(\eta_0)$

$$2\left\langle \tilde{\psi}(\eta_0^*)\right| T(\eta_0) \left|\tilde{\psi}(\eta_0)\right\rangle = \sum_{i=1}^{N} \left\langle \tilde{\psi}(\eta_0^*)\right| \eta_0 \vec{r}_i \cdot \vec{\nabla}_{\eta_0 \vec{r}_i} V(\eta_0) \left|\tilde{\psi}(\eta_0)\right\rangle \tag{55}$$

where we have introduced the virial in terms of the nabla operator ∇. From Eq. (55), we obtain in addition to the standard expression for the Coulomb operator V_{C}

$$2\langle\tilde{\psi}(\eta_0^*)|T(\eta_0)|\tilde{\psi}(\eta_0)\rangle = -\langle\tilde{\psi}(\eta_0^*)|V_{\text{C}}(\eta_0)|\tilde{\psi}(\eta_0)\rangle \tag{56}$$

new forms for metastable or unstable states. For an electric field $V_{\text{F}} = F\sum_{i=1}^{N} z_i$, one gets

$$2\langle\tilde{\psi}(\eta_0^*)|T(\eta_0)|\tilde{\psi}(\eta_0)\rangle + \langle\tilde{\psi}(\eta_0^*)|V_{\text{C}}(\eta_0)|\tilde{\psi}(\eta_0)\rangle - \langle\tilde{\psi}(\eta_0^*)|V_{\text{F}}(\eta_0)|\tilde{\psi}(\eta_0)\rangle = \Delta_{\text{F}} = 0 \tag{57}$$

which demonstrates a necessary (but not sufficient) condition to hold for a resonance eigenvalue and eigenfunction of Eq. (53). To give additional information regarding the precision of an approximate determination of resonance data, one might evaluate Δ_{F} recurrently, not only for the accuracy provided but also for the possibility to rescale the calculation via the procedure of successive scaling [70]. Numerical data for the Stark effect in the hydrogen atom [17] is displayed in Ref. [71], see also Table 2.1, published with permission from IJQC.

In conclusion, we note that the "pausing" of the ϑ-trajectory indicating an optimum scale factor prompts the statement of a generalized virial theorem. Since general techniques to ascertain resonances in the non-selfadjoint case are so much more difficult in comparison to the usual (Hermitean) case it is obvious that every bit of complementary information counts. This statement becomes no less important when realizing that the complex part of a resonance eigenvalue in many situations is order of magnitudes smaller in size compared to the real part.

Table 2.1 Various energy contributions to the resonance energy $\varepsilon = E - i\varepsilon$ for $F = 0.25$ a.u. and $\eta_{\text{opt}} = (0.90149 - i0.52339)$

	Real part	Imaginary part
$\langle T \rangle$	0.44697	−0.2548
$\langle V_{\text{C}} \rangle$	−0.96333	0.3355
$\langle V_{\text{F}} \rangle$	−0.06939	−0.1739
ε	−0.58575	−0.0932
Δ	-6.0×10^{-5}	-1.0×10^{-4}

$\Delta = \langle 2T \rangle + \langle V_{\text{C}} \rangle - \langle V_{\text{F}} \rangle$.

2.2.3. Time evolution

Keeping in mind the problems stated in the introduction, we have up to this point not made use of any procedures that would risk a physical formulation that would incorporate any loss of information and/or memory. It is true that the definition of an unstable state proceeds via the redefinition of appropriate domains and ranges. However, this is recoverable information within the realm of the time-independent formulation. What about the state of affairs in the time-dependent situation? Formally it looks straightforward to write the causal evolution operator as

$$G(t) = e^{-iH(\eta)t} \tag{58}$$

as the formal solution of

$$H(\eta)\psi(\eta, t) = i\frac{\partial}{\partial t}\psi(\eta, t) \tag{59}$$

Setting

$$\psi(\eta, t) = e^{-iH(\eta)t}\psi(\eta) = \psi(\eta)e^{-iE(\eta)t} \tag{60}$$

we note that

$$\psi^*(\eta, t) = \psi(\eta*, -t)) \tag{61}$$

from which we could proceed to derive the virial theorem via the Heisenberg's equation. The possibility to use the formal equations above in connection with a rigorous time evolution was considered by Kumicák and the author [72, 73]. Without being too detailed, a proper formulation of the dilated dynamics relies on the answer to the question whether the scaled Hamiltonian is the generator of a so-called contractive semigroup [74], which

is strongly continuous and $\|G(t)\| \leq 1; t \geq 0$. This question prompts the introduction of the concept of a Lyapunov converter; see also the work of Braunss [75].

Following Ref. [73] we describe first the steps before we comment on the mathematical results. Let us start with an isometric semigroup, $G(t); t \geq 0$, appropriately defined in the Hilbert space $\acute{h}$. If there exists a contractive semigroup $S_G; t \geq 0$ (defined on $\acute{h}$) and an invertible linear operator Λ, with its domain and range both dense in $\acute{h}$, such that

$$S_G = \Lambda G(t)\Lambda^{-1}; \quad t \geq 0 \tag{62}$$

on a dense linear subset of $\acute{h}$, then Λ is called a Lyapunov converter. A necessary condition for the existence of Λ is that the generator of the isometric semigroup G (recall that the isometry can always be extended to a unitary group) has a nonvoid absolutely continuous spectral part, σ_{AC}. Returning to the Balslev–Combes theorem for dilation analytic Hamiltonians, we will examine the choice $\Lambda = U(\vartheta) = \exp(iA\theta)$, see Appendix D how to define the scaling transformation, e.g. Eqs. (D.5) and (D.6), by asking the question whether $H(\eta)$ generates a contractive semigroup or writing

$$S_G^+(t,\eta) = U(\eta)G(t)U(\eta)^{-1} = \mathrm{e}^{-iH(\eta)t}; \quad t \geq 0 \tag{63}$$

We observe that this is true for many types of potentials and one might be tempted to conclude that this can be proven for general dilation analytic potentials, particularly since the (modified) spectrum lies on the real axis (bound states) and in a subset of the closed lower complex half-plane. However, this turns out to be a false statement since the attractive Coulomb potential, being dilation analytic, will not fulfill the Hille–Yosida theorem [74]. The latter (necessary and sufficient) states that in addition to the requirement of a nonempty σ_{AC} and that $i\varepsilon$ belongs to the resolvent set, for all $\varepsilon > 0$, a further stipulation is that the numerical range (expectation values of the generator over the all functions belonging to its domain) must be contained in the lower part of the complex energy plane. The features displayed in Figures 2.6 and 2.7 are not very much distorted when going from a conventional scattering to Coulomb background, see Refs. [41, 42] for details, hence one may think that the analogous deflation effect, see Figures 2.6 and 2.7, would have "saved" the long-range Coulomb tail for time-contracted evolution. Anyway to circumvent this problem, one must further restrict the operator domains suitably or alternatively to introduce a generalized notion of quasi-isometry [73]. Accepting such generalizations, one might state that $U(\eta)$ as a Lyapunov converter converts isometric (quasi-isometric) evolution of unscaled functions to contractive (including strictly contractive) evolution of scaled functions. Here, we confront for the first time in this presentation a rule of informity, (inadequate in form), i.e., a generic

loss of information imposed by changing the definition of the original isometric operator by first restricting its domain and then extending its range during contractive evolution. The loss is enforced via rigorous mathematical operations and excludes any subjective gradation.

It goes without saying that the generalized Fourier–Laplace transform implied by a combination of results in Appendices B and D in their scaled versions depends critically on the specific properties of the contractive semigroup, Eq. (63). Although not yet explicitly mentioned we must also consider explicitly the possibility of emerging higher order degeneracies, i.e., so-called Jordan blocks. To conform to our dilation analytic formulation, we need to find a complex symmetric representation. The general form of such a Jordan block with a finite Segrè characteristic (>1) is derived in Appendix E, see also Refs. [76, 77]. This complication adds to the general query that what type of information is lost in connection with the contraction phenomenon.

To belabor this point, let us consider in more detail a simple case, Refs. [78, 79], where the bound states of the Coulomb potential, through successive switching of a short-range barrier potential, becomes associated with resonances in the continuum. The simplicity of the problem demonstrates that resonances have decisively bound state properties, yields insights into the curve-crossing problem, and displays the tolerance of Jordan blocks. The potential has the form

$$V(r) = -\frac{z}{r} + V_{\max}\left(\frac{r}{r_0}\right)^2 e^{2\left(1-\frac{r}{r_0}\right)} \tag{64}$$

i.e., a Coulomb potential perturbed by a short-range exponential barrier with maximum at $r_0 = 2$ and with $V_{\max}$ a varying parameter that measures the height of the perturbation.

To better understand Figure 2.11, we will display in Figure 2.12 the first four bound states of the perturbation as a function of barrier height for the potential in Eq. (64) with the charge $z = 1$. Above the continuum threshold the eigenvalue turns complex and we show the real part, i.e., the resonance with the smallest imaginary part. The most striking conclusion is that the barrier alters only one state at the time, with the principal variation being handed over from one state to the other immediately above at particular values of the barrier strength. Even if the rapidly varying state mimics a localized ground state, the ordering of the states is intact since the perturbation does not alter the number of nodes. After the escaping state has "passed" the bound states, cf. the metaphor of a relay race, the "bound state" is expelled as a resonance into the continuum, see Figure 2.12. For all practical purposes, the resonance state exhibits the attributes of a bound state as can be easily confirmed, see Refs. [78, 79] for more details, from the calculation of various properties like $\langle r\rangle$, $\left\langle \frac{1}{r}\right\rangle$, $\sqrt{(\langle r - \langle r\rangle\rangle)^2}$.

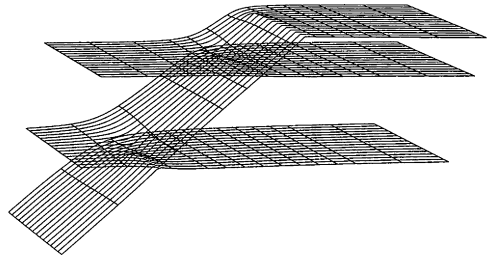

Figure 2.11 3D plot of the Riemann sheet structure of the perturbed Coulomb potential as displayed in Eq (64) with a varying barrier height parameter. The imaginary part of V_{max} grows toward the viewer.

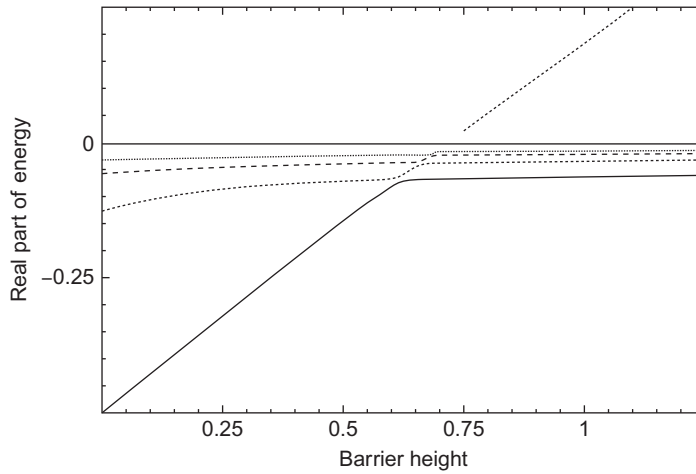

Figure 2.12 Display of the first four bound states of the perturbed Coulomb potential, defined in Eq. (64) as a function of varying barrier heights. Note the dotted line above the continuum threshold at zero energy. Taken from Ref. [78] with permission of IJQC.

To compute the averages above for the resonance states, one must use the prescription defined in Appendix D, Eq. (D.7), that is implementing the proper bilinear construction.

It is easy to see that the occurrence of the imaginary part in the energy $E_{res} = E_0 - i\varepsilon$ provides loss of "evolution information" in that the contribution from the resonance eigenvalue disappears asymptotically as $t \to \infty$, cf. Figures 2.5–2.7. Although records can in principle be retrieved within a given time interval, the contraction property of the scaled, contractive evolution via the aforementioned inadequateness or informity rule [80] asymptotically discard the contribution from the pertinent part of the spectrum – note that we

are using norm convergence. For the present case of a Coulomb potential perturbed by sufficiently large barrier, crucial information about the hydrogen ground state "disappears" during evolution. We further learn that crossings of energy surfaces occur in the complex plane. The illustrious non-crossing rule or the curve-veering phenomenon as clearly revealed in Figure 2.12, see also the innermost curve of the 3D plot of Figure 2.11, is abruptly spoiled in the complex energy plane, Figure 2.11. The simple lesson learned is that complex scaling employed in molecular problems might provide additional information through complex crossings of energy surfaces off the real axis. Being generic properties of the model they bring about additional information regarding electron transfer phenomena, etc. related for example to so-called conical intersections. For more on the emergence of Jordan blocks, see Appendix E and Refs. [76, 77].

It is interesting to observe that the Fourier–Laplace transforms exercised in Appendix B, cf. the contours $C^{\pm}$ and the generalizations in Figures 2.4 and 2.5, relating the retarded-advanced propagators $G^{\pm}(t)$ and the resolvents $G(z)$, prompt the pronouncement that time-less formulations are possible. In addition, since the cosmological Wheeler–DeWitt equation, is of the form $H\psi = 0$, Barbour in his elegant and thought-provoking volume "The End of Time The Next Revolution in Physics" [81] makes strong arguments for a fundamental nontemporal description of the Universe. His evaluation is based both on general aspects of the theory of general relativity and on the current understanding of contemporary quantum mechanics. There are basically two perspectives to be incorporated here. The first concerns the issue of contractive evolution that (even if we assume asymptotic completeness, which is still an open problem [48, 53, 74]) invokes objective loss of information during evolution. The second relates to the unidirected form of time as induced by relativity theory to be briefly considered below – a more general remark including the general theory of gravity will be given in a later section.

The present account has been published before, see Refs. [7, 82, 83], and references therein. Using our preference for complex symmetric forms we will proceed directly to derive a Klein–Gordon-like equation as follows. Consider the nonpositive square root, cf. the Dirac equation, from the simple ansatz of the Hamiltonian H

$$\begin{aligned} \boldsymbol{H}^2 &= m_0^2 \begin{pmatrix} 1 & 0 \\ 0 & 1 \end{pmatrix}; \quad \boldsymbol{H}^{\pm} = \begin{pmatrix} m_0 & 0 \\ 0 & \pm m_0 \end{pmatrix} \\ \boldsymbol{H}^{-} &= \boldsymbol{H} = \begin{pmatrix} m_0 & 0 \\ 0 & -m_0 \end{pmatrix} = \begin{pmatrix} m & -i\nu \\ -i\nu & -m \end{pmatrix} \end{aligned} \tag{65}$$

where Eq. (65) demands $m_0^2 = m^2 - \nu^2$ with the obvious identifications $\nu = p/c$; p is the momentum of a particle of mass m, relative to an inertial system,

where m_0 is the (nonzero) rest mass and finally with c the velocity of light. The "negative" square root in the complex symmetric form above is enforced so as to provide a suitable platform for a nonstationary description and to conform to a nonpositive definite metric, cf. the Minkowski space-time. In general, velocities and momenta should be represented as vectors, but scalar operators are enough for the present discussion.

From the secular equation, based on the matrix $\boldsymbol{H}$, we define the eigenvalues $\lambda_{\pm} = \pm m_0$ via

$$\lambda^2 = m_0^2 = m^2 - v^2 = m^2 - p^2 c^{-2} \tag{66}$$

In analogy with the classical case in terms with the familiar parameter $\beta = p/mc = (\text{classical particles}) = \upsilon/c$, with υ the velocity of the particle, we obtain the well-known result

$$m = \frac{m_0}{\sqrt{1 - \upsilon^2/c^2}} = \frac{m_0}{\sqrt{1 - \beta^2}} \tag{67}$$

In addition to the possibility to interpret the result from a classical and/or a quantum mechanical viewpoint, we have also at hand a more general biorthogonal construction. Introducing general ket-vectors $|m\rangle; |\bar{m}\rangle$ and $|m_0\rangle; |\bar{m}_0\rangle$ corresponding to the states of a particle with mass m and its antiparticle (with negative energy $-mc^2$), respectively, and m_0 similarly for the rest mass in the interaction free case, we find the general superpositions

$$\begin{aligned}
|m_0\rangle &= c_1|m\rangle + c_2|\bar{m}\rangle; \quad \lambda_+ = m_0 \\
|\bar{m}_0\rangle &= -c_2|m\rangle + c_1|\bar{m}\rangle; \quad \lambda_- = -m_0 \\
|m\rangle &= c_1|m_0\rangle - c_2|\bar{m}_0\rangle \\
|\bar{m}\rangle &= c_2|m_0\rangle + c_1|\bar{m}_0\rangle \\
c_1 &= \sqrt{\frac{1+X}{2X}}; \quad c_2 = -i\sqrt{\frac{1-X}{2X}}; \quad X = \sqrt{1-\beta^2}; \quad c_1^2 + c_2^2 = 1
\end{aligned} \tag{68}$$

As already mentioned the derivation above leaves the interpretation, classical or quantum to the eye of the beholder. The second remark concerns biorthogonality, which implies that the coefficients c_i will not be associated with a probability interpretation since we have the rule $c_1^2 + c_2^2 = 1$. The operators, in Eqs. (65)–(68), are in general non-selfadjoint and nonnormal (do not commute with its own adjoint), hence the order between them must be respected. We finally note that the general kets in Eq. (68) depend on energy and momenta, whereas in the conjugate problem, to be introduced below, they rely on time and position. Introducing well-known operator identifications, ($h = 2\pi\hbar$ is Planck's constant and $\vec{\nabla}$ the gradient operator)

$$E_{\text{op}} = i\hbar\frac{\partial}{\partial t}; \quad \vec{p} = -i\hbar\vec{\nabla} \tag{69}$$

we recognize, from the eigenvalue relation, Eq. (66), explicit relations between the Klein–Gordon-like equation and Maxwell's equations for vacuum, i.e., by setting the determinant of $\boldsymbol{H}$ in Eq. (65) equal to zero

$$\begin{vmatrix} i\hbar\dfrac{\partial}{\partial t} & -i\vec{p}c \\ -i\vec{p}c & -i\hbar\dfrac{\partial}{\partial t} \end{vmatrix} = \hbar^2\frac{\partial^2}{\partial t^2} - \hbar^2c^2\nabla^2 \tag{70}$$

It is then easy to formally introduce the conjugate operators (possible in an extended sense)

$$\tau = T_{\text{op}} = -i\hbar\frac{\partial}{\partial E}; \quad \vec{x} = i\hbar\vec{\nabla}_p \tag{71}$$

and (note the invariance under strong parity and $E \to -E$, $\vec{p} \to -\vec{p}$, which also holds in the general case, cf. also the CPT theorem)

$$\mathcal{H}_{\text{conj}} = \begin{pmatrix} c\tau & -i\vec{x} \\ -i\vec{x} & -c\tau \end{pmatrix} \tag{72}$$

from which the eigenvalues τ_0 or $x_0 = \sqrt{\vec{x}_0 \cdot \vec{x}_0}$ analogous to Eqs. (65)–(67), using $\vec{x} = \vec{v}\tau$ in Eq. (72), obtains

$$\tau = \frac{\tau_0}{\sqrt{1 - v^2/c^2}} = \frac{\tau_0}{\sqrt{1-\beta^2}}; \quad x = \frac{x_0}{\sqrt{1-\beta^2}} \tag{73}$$

Incidentally we point out that, notwithstanding the reference to general complex symmetric forms and biorthogonality, we recover equations commensurate with classical Lorentz invariance, see Eq. (73). At the same time, there seems to be a universal superposition principle at work irrespective of whether we are representing classical wave propagation, quantum mechanical matter waves, or classical point particles. The conjugate arrangement also indicates, like the energy–momentum problem, that time and position can be represented formally in a general non-selfadjoint context and that the former is unidirectional as "positive time" by definition must relate to "positive mass." The kets and the bras from the conjugate operator representations are related in the traditional sense as

$$\langle \boldsymbol{r}, -ict | \boldsymbol{p}, iE/c \rangle = (2\pi\hbar)^{-2}\, e^{\frac{i}{\hbar}(\vec{r}\cdot\boldsymbol{p} - Et)} \tag{74}$$

Note that the underlying scale transformation generates non-selfadjoint timescale and length scale, see Ref. [7] and references therein, whereas the ket (bra) notation refers to abstract indicators identifying appropriate quantum/classical (conjugate) states in configuration space. This convention will be made more specific in the general case as it will provide the necessary background dependence for general relativity including covariance.

3. GENERAL APPLICATIONS

As pointed out, the present extension of quantum mechanics to incorporate a rigorous non-Hermitean scaling transformation embedding traditional self-adjoint formulations has been particularly convenient in atomic and molecular applications. Implementing analyticity requirements as prescribed above, allowing broken symmetry solutions, if appropriate, could easily bequeath attacks on general problems connected with bound and quasibound states. Matrix elements of the analytically continued secular equation provide complex resonance eigenvalues and eigenfunctions as mathematically rigorous and computationally valid solutions. Proper extensions of scattering theory quantities could, e.g., be examined by direct integration of the actual differential equation along appropriate complex paths; using Weyl's theory, see the numerical examinations on the superimposed Coulomb potential as well as the criteria for resonance region estimates discussed previously. It is interesting that dilation group extensions of Titchmarsh–Weyl theory have attracted acquiescent interest in the mathematical community [84–86] with Ref. [36] being the lead reference.

Reviving accounts on the level of complex deformations of the many-body problem, we will call attention to some simple applications as feasible and viable demonstrations, leaving abundant and worthy documentations in this field to another occasion. For instance, optimal scaling in actual situations can be resolved via extended versions of the virial theorem including specific relationships between various energy contributions, cf. applications to the Stark effect in the hydrogen atom [35] and the $^1\Pi$ near degeneracy in SiO [87, 88]. Applications within a generalized scattering view concern predissociation by rotation [46, 89], continuum electron exchange in electron atom scattering [90–92], resonance structures in charge transfer cross sections [93], and various applications to time-resolved molecular spectroscopy, see Ref. [94].

A completely different avenue is considered in the treatment of amorphous condensed matter [7, 52, 95] like proton transfer in aqueous solutions [96], molten alkali chlorides [97], general features of high-T_C cuprates [98, 99], quantum Hall effect [100], and the effects of spin dynamics in ferromagnetic systems [101]. For details on the definition and employment of the so-called Coherent-Dissipative Structure, CDS, we refer to Appendix F and Refs. [52, 102–104] and [76, 77] in particular the role of symmetric representations of Jordan blocks [105] their emergence from associated reduced density matrices [106, 107] properly thermalized [7, 52]. The introduced new concepts impart surprising aspects on complex enough systems in biology as well as on background-dependent portrayals of general relativity [82, 83].

3.1. Atoms and molecules

We will initially consider applications of dilated analogues of traditional approaches to quantum mechanics and in particular look at molecular studies based on the decay properties of excited levels including rovibrational spectroscopy, see Refs. [94, 108] and references therein for details. As mentioned above, the analytic theory allows examination of barrier penetration problems, curve crossings, coupling between adiabatic curves, etc. with the studies of several diatomic systems like HgH [46, 89], SiO [87], CH [109], and CH^+ [110]. For convenience we show the scaling operation for a simple case, where the complex eigenvalues are uncovered after complex dilation, see Figure 2.13. Since many realistic physical potentials are numerically known in the short- and medium-range regions with analytic tails on hand only for the long-range part, a simple trick around this obstacle is given by employing exterior scaling [18, 108, 111]. Note that similar techniques had already been developed within the domain of nuclear physics [112]. We also refer to [113] for a prerunner to complex scaling already 10 years before the rigorous mathematical theorem of Balslev and Combes [50], see also [20] for additional information. Hence, considering

$$x \to \begin{cases} x,\ x \le R_0 \\ R_0 + \eta(x - R_0),\ x > R_0 \\ \eta = e^{i\vartheta};\quad \vartheta > 0 \end{cases} \tag{75}$$

one can use numerical data for coordinate values less than R_0. Although earlier verifications and outlines had been established, see [18, 110], a mathematically rigorous proof was not provided until 1989, see Helffer's contribution to the Lertorpet symposium [114].

A simple case is the portrayal of the ground state of the OH radical, see Figure 2.14. For simplicity, we show a part of the Morse potential energy curve with the highest bound and quasibound vibrational levels indicated by solid lines and dashed line, respectively, Figure 2.14a. The spectral density is

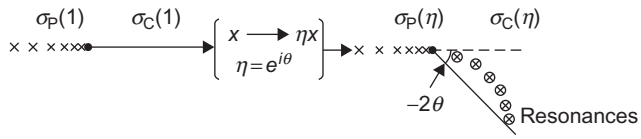

Figure 2.13 Display of the nondilated (left) and dilated differential operator (right) consisting of discrete spectrum σ_P and the absolutely continuous part σ_C. Taken from Ref. [108] with permission of IJQC.

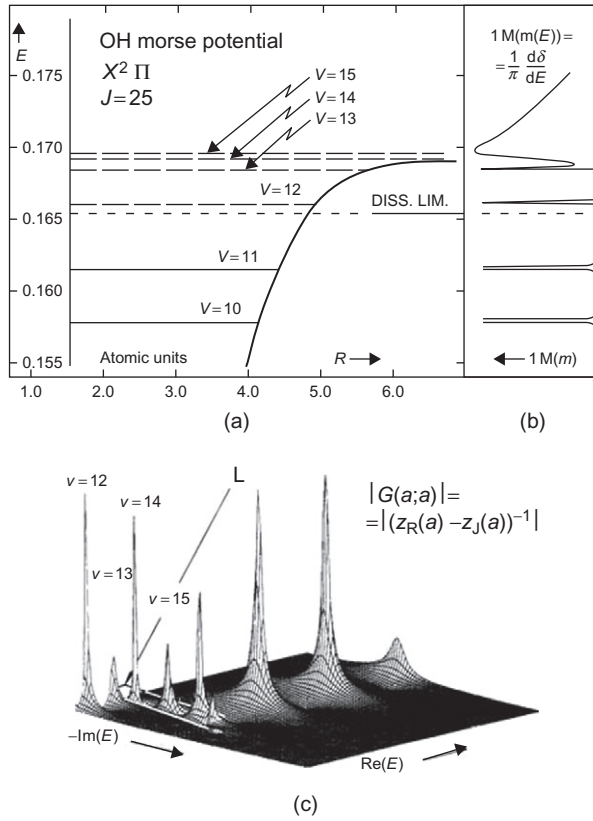

Figure 2.14 Display of the continuous spectrum describing the ground state of the OH radical with the rotational quantum number chosen to $J = 25$. For more details see the text. The area corresponding to nonresolved part of the spectrum is denoted by *L*. Taken from Ref. [108] with permission of IJQC.

displayed in Figure 2.14b and the associated Green's function in Figure 2.14c. From previous Weyl's theory formulas, one obtain in a simple way (easily generalized to the case of a systems of coupled equations Ref. [115]) the Green's function from the Riccati equation, see Refs. [36, 116]

$$G(x;x') = (H-\lambda I)^{-1} = \psi(x_<)\left[W(f,\psi)\right]^{-1} f(x_>) \tag{76}$$

with the diagonal element G($a;a$) given by

$$G(a;a) = \left[\psi'(a)\psi^{-1}(a) - f'(a)f^{-1}(a)\right]^{-1} = \left[z_R(a) - z_J(a)\right]^{-1} \tag{77}$$

In Eq. (77), z_R and z_J are the logarithmic derivatives (matrices) of the regular solution and the asymptotic (Jost) solution, respectively.

As can be seen from Figure 2.14, the method gives a very stable procedure to determine and examine the structure of the continuous spectrum as well as provides means for peak identification and comparisons with time-resolved spectroscopy including systematic studies of molecular dynamics. Using the multichannel technique, rich resonance structures were found in the computed cross section for the charge transfer from atomic hydrogen to the excited 3s level of the doubly charged nitrogen, triply charged nitrogen, and atomic hydrogen at very low relative collision energies [93].

Although a rigorous treatment of molecular problems should go beyond the Born–Oppenheimer (BO) approximation, the full scaling problem should also include scaling of the nuclear coordinates [65], see also related discussions regarding complex scaling in Ref. [20]. In current applications this is not done and as a result the internuclear distances are "sharp" notwithstanding complex branch points existing in the complex energy surface. The latter, if close to the real axis, are indeed an indication of the breakdown of the BO separation. A candidate for this violation is the case of silicon monoxide, SiO. This calls for a more general treatment where multidimensional partitioning technique is necessary. A visual graph displaying a sequence of avoided crossings with spectral information inserted from experiments is shown in Figure 2.15.

A study of this situation using the complex virial theorem, see details in Ref. [87], shows that the bound state level is always situated above the diffuse one; the width of the diffuse level increases with energy and that the

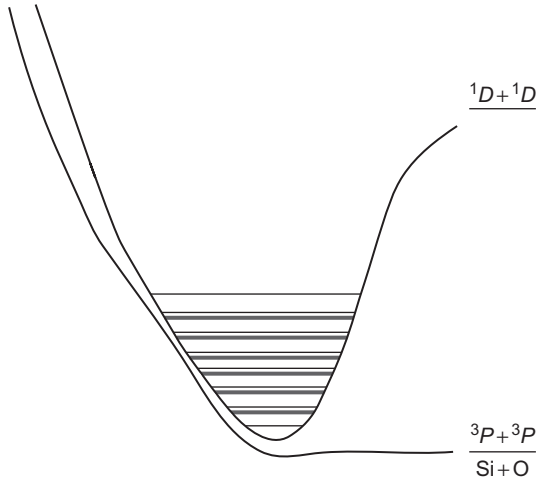

Figure 2.15 Display of the nearly degenerate $^1\Pi$ potential curves in SiO as obtained from Ref. [117]. The vibrational levels are symbolically included as they would be interpreted conventionally. Modified from Ref. [87].

splittings between levels increase with the vibrational quantum number. One also infers that term energies are lower and the splittings are larger in SiO^{18} than in SiO^{16}.

The exterior complex scaling model may suitably be used in electron–atom scattering in connection with local density models based on static exchange plus polarization approximations, where one could formally include the continuum electron exchange with just the uppermost bound orbital or alternatively with all the target electrons. Although this works well in many cases [90–92], one would need to improve the formulation so that it obeys the proper boundary conditions for large radial distances as well as for very low energy of the incoming electron. A complex dilated study within such and asymptotic complete form of exchange improves the reliability and rigor of the model. In Figure 2.16, we show the trajectory of the partial wave S-matrix pole for the ^2P case of the Be^- ion in two different continuum exchange approximations, for details see Ref. [90]. In addition to testing the method for the ^2P shape resonances in the Be^- and the Mg^- metastable ions and the ^2D shape resonances in the $e-$Mg scattering system, the asymptotically complete form of the local-density-based approximation provided evidence for a possibly bound $(4s^24p)\ ^2P$ state in Ca^-. Although the resolution of this result depends critically on the state-specific electronic structure and correlation, one might argue that invoking a one-electron complex scaling method as input in a local density approach may not be reliable. For instance in the past incorrect predictions of bound negative ions of noble gases made news in the 1990s. Nevertheless, the present modeling is notably rigorous in that it incorporates exchange between the continuum electron and all bound state electrons (not just the valence electron). What's more the result presented in Ref. [92] was independently confirmed by rigorous ab-initio calculations of Froese Fischer et al. [118] in support of experiments [119].

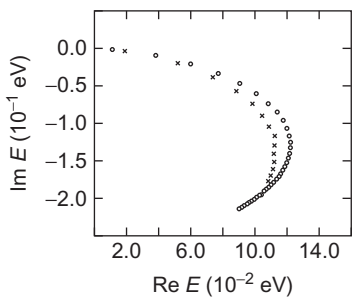

Figure 2.16 Display of the ^2P shape resonance in the $e-$Be collisional system. The crosses represent the first partial wave of the p-wave S-matrix resonance pole as a function of the cut off parameter. Taken from Ref. [90] with permission of IJQC.

In closing the section on non-Hermitean approaches to continuum processes in atomic and molecular physics, we will also mention accurate examinations on resonance parameters in molecular predissociation displaying unexpected resonance overlapping [46, 89]. The phenomenon of predissociation by rotation in HgH was analyzed via an isotopically combined potential due to Stwalley [120]. The potential, i.e., a relatively shallow energy curve with a nonzero J-value giving rise to a rotational barrier, supported novel metastable states above the dissociation limit. The Weyl's method was able to resolve the closely lying vibrational states $v = 3$ and $v = 4$ for the rotational quantum number $K = 9$.

Although both experimental and theoretical advances have been great since some of the quoted applications took place, the methodological understanding, accuracy, and insight are clearly confirmed. Novel improved theoretical and computational advances are continually upgraded, see the work of Elander et al. [121].

As a précis to the work presented in this section, we emphasize that Weyl's theory and conventional scattering theory compliment each other for instance in the proven rigor of a large class of physically and mathematically relevant potentials. The combined use of (uniform) complex scaling with the theoretical approach of Weyl and Titchmarsh yields rigorous numerical results and provides a fundamental basis for the concept of unstable or metastable states. In more general cases, i.e., using exterior scaling and/or other regularization procedures to obtain resonance states and eigenfunctions of complex many-body-systems and/or wide-ranging reaction coordinate representations, it is imperative to be familiar with the broad spectral features of universal analytic structures and their all-embracing strength in scientific modeling. The advance of the latter will be the topic of the next section.

3.2. Condensed matter

As already brought up above, we will extend the discussion to incorporate hierarchies of complexity levels. In particular, we will show that flexible and robust treatments of so-called dissipative systems are viable within our analytic approach, but first some definitions.

With an open or dissipative system we identify: *a system in which there exists a flow of entropy due to exchange of energy or matter with the environment*. Additionally, we will consider a specific order or organization that will be of particular relevance for both condensed matter and complex enough biological systems, see also next section. Hence, we append the conditions for a *Coherent-Dissipative Structure, CDS*, by stipulating that *(1) they are created or destroyed by integrated quantum and thermal correlations, (2) they exchange energy with an (partially) entangled environment, and (3) they cannot have a size smaller than a critical one*.

Detailed accounts of applications to condensed matter topics have been communicated elsewhere over the years, see [95–100], see also [7, 82, 83] and references therein. We will nevertheless summarize the basics, which are significant for the present review. In short, the theoretical formulation concerns appropriate system operators, represented as reduced density matrices, leading to dynamical evolution expressing nonexponential decay and bearing signs of microscopic self-organization. This understanding matches explicit thermal conditions and inclusive timescales. Thermalization of the system operator produces temperature-regulated correlations and the materialization of canonical Jordan forms with sizeable Segrè characteristics, n, i.e., the dimension of the largest Jordan block in the degenerate representation.

To establish timescales, one needs to study the generator of the dynamics, providing the foundation for Hamiltonian and Liouvillian isometric and contractive evolution, see Appendix F and Refs. [28, 102, 122] for technical discussions involving ensuing organization of appropriate levels of description. As will be seen, the dimension n is controlled by the physicochemical conditions of the dissipative system. As has been shown in Appendix E, the theoretical formulation is founded on the transformation $\mathbf{B}$

$$\boldsymbol{B} = \frac{1}{\sqrt{n}} \begin{pmatrix} 1 & \omega & \omega^2 & . & \omega^{n-1} \\ 1 & \omega^3 & \omega^6 & . & \omega^{3(n-1)} \\ . & . & . & . & . \\ . & . & . & . & . \\ 1 & \omega^{2n-1} & \omega^{2(2n-1)} & . & \omega^{(n-1)(2n-1)} \end{pmatrix}; \quad \omega = \mathrm{e}^{\frac{i\pi}{n}} \tag{78}$$

connecting a preferred orthonormal basis $\boldsymbol{h} = h_1, h_2, \ldots h_n$, on local sites representing pairs of light carriers in a nuclear skeleton, like superconductivity, base pairs (or a group) of DNA, elements of protein structures or neural sites in cybernetic mechanisms related to functions of the brain in biological systems, etc., to a canonical basis $\boldsymbol{f} = f_1, f_2, \ldots f_n$, with special properties and unique dynamics, and at the same time also to a coherent basis, $\boldsymbol{g} = g_1, g_2, \ldots g_n$, containing for example encoding information for ontogenetic evolution, see next section.

$$|\boldsymbol{h}\rangle\mathbf{B} = |\mathbf{g}\rangle; \quad |\boldsymbol{h}\rangle\mathbf{B}^{-1} = |\boldsymbol{f}\rangle \tag{79}$$

In passing we note, see again Appendix E, that the unitary transformation $\mathbf{B}$ connects the complex symmetric expression $\mathbf{Q}$ and the canonical form $\mathbf{J}_n(0)$, i.e.,

$$\mathbf{Q} = \mathbf{B}^{-1}\mathbf{J}_n(0)\mathbf{B}; \quad Q_{kl} = \exp\left\{\frac{i\pi}{n}(k+l-2)\right\}\left(\delta_{kl} - \frac{1}{n}\right) \tag{80}$$

where

$$\mathbf{J}_n(0) = \begin{pmatrix} 0 & 1 & 0 & \cdot & \cdot & 0 \\ 0 & 0 & 1 & \cdot & \cdot & 0 \\ 0 & 0 & 0 & 1 & \cdot & 0 \\ \cdot & \cdot & \cdot & \cdot & \cdot & \cdot \\ 0 & 0 & \cdot & \cdot & 0 & 1 \\ 0 & 0 & \cdot & \cdot & 0 & 0 \end{pmatrix} \tag{81}$$

In Appendix F, we have derived a simplified version of Coleman's extreme state [107] as well as indicated the onset of ODLRO [106]. Our first examples of applications within disordered condensed matter concern the discovery of high-temperature superconductivity. From appendix, Eqs. (F.4)–(F.7), we will use the relation below [note the quadratic expression in the occupation number p in the large eigenvalue λ_L to be used in Eq. (82), for more details see Refs. [7, 103] and references therein]

$$\mathcal{E} = \mathrm{Tr}\,\{H_2\rho\}; \quad \rho \approx \lambda_L \left|g_1\right\rangle\left\langle g_1\right|$$

There are many anomalies associated with this problem, which is still not satisfactorily resolved. Rather than giving a complete set of references we direct the reader to previous work within the present formulation [7, 95, 98, 124] and references therein. We mention a few problems that have been analyzed and explained: anomalous gaps, universal linear relation, Uemura et al. [123], saturation effects, short coherence lengths, transition temperature dependence, unusual heat capacities, Knight shift temperature dependence [125], spin gaps, etc. Many of these have been examined separately in the light of various mechanisms. It is nevertheless striking that the present description gives sufficient clarifications and noncontradictory justification from the general overall behavior without initially elucidating the exact nature of the pairing mechanism, cf. Figure 2.17, where both Uemura's universal linear relation as well as the saturation effect obtains from the negative quadratic deviation predicted by λ_L in Eq. (E.6). Note the sudden breakdown of the superconducting state at higher carrier concentration. Although the microscopic mechanism is needed for quantitative data, optimizing the energy Eq. (F.7) for a given interaction yields, see Ref. [103] for details, the relation, see Refs. [103, 126]

$$T_C = T_{C,\max} \cdot 4(x - x^2) \tag{82}$$

where $x = N/2 = n_c^*/n_r^*$; $n_c^* = N/Vm^*$; $n_r = 2n/Vm^*$, m^* is the effective mass, and V is the volume. Also, n_c^* and n_r^* are the carrier concentration per effective mass and the available concentration (per effective mass; large N and n) of

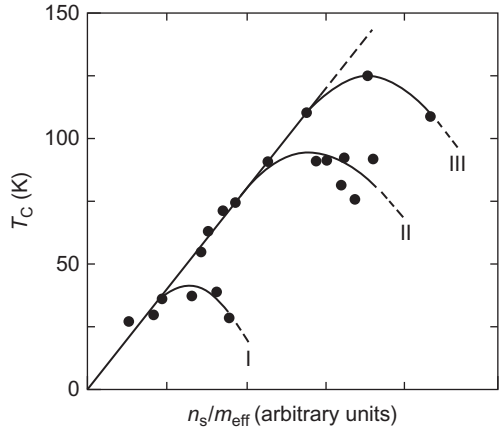

Figure 2.17 Schematic representation of the superconducting transition temperature T_C plotted versus carrier concentration n_s divided by the effective mass m. For details see Uemura et al. [123]. Taken from Ref. [95] with permission of IJQC.

fermion states (virtual particle concentration), respectively. Assuming that n_c^* varies while n_r^* and m^* are assumed constant for each class of superconductor, one obtains the various curves in Figure 2.17; for a list of compiled data for various classes, see reference to Burns in [103]. In addition, the formula for λ_L gives consistent fractional statistics in the Quantum Hall effect, see Refs. [100, 103].

A rather different case, studied within the present framework [101], obtains from measurements of the magnetic excitation spectra of Gadolinium, Gd, by inelastic neutron scattering above the Curie temperature T_{cu}. For instance, experimental results of scattering along the (110) direction demonstrate a crossover from spin diffusion at small scattering wave vector q to damped spin-wave behavior at large q. It is a surprising result that spin correlations exist even at $T = 850\,\mathrm{K}$, which is far above the Curie point $T_{cu} = 293\,\mathrm{K}$. It was concluded that the destruction of spin waves above T_{cu} is not due to thermal breakup [127]. Although we will not discuss previous applications to proton transfer in water [96], conductivity of molten alkalichlorides [97], see also the review in Ref. [7], we will draw on analogous results, see also the Appendix F. The quantization condition, Eq. (F.10), implies maximum relaxation time τ_{rel} for the minimal size $n = s_{min}$ commensurate with the temperature T through the relation

$$s_{min} = \frac{4\pi k_B T}{\tau_{rel}} \tag{83}$$

where k_B being the Boltzmann constant. In the applications mentioned above, the spatial dimension of the CDS have been shown to obey the linear relation

$$d_{\min} = F(H_{\text{rel}}) W_i^{\text{dB}} \cdot s_{\min} \tag{84}$$

i.e., showing a linear dependence on the thermal de Broglie wavelength

$$W_i^{\text{dB}} = \hbar \sqrt{2\pi / k_B T m_i} \tag{85}$$

In Eqs. (84) and (85), F relies on the proper Hamiltonian (depending on some relevant thermodynamic variables and/or external parameters) and m_i is the effective mass of "particle i" corresponding to the inertial mass associated with the motion of a magnetic cluster in the presence of other clusters. This mass depends on factors describing domain wall motion, magnetic exchange, and anisotropy energy. For more details regarding the underlying analysis and assumptions that go into the derivation of Eq. (84), see Refs. [96, 97]. One obtains from Eqs. (84) and (85) the relation

$$d_{\min} = \text{const.} \times F(H_{\text{rel}}) \sqrt{T} \cdot \tau_{\text{rel}} \tag{86}$$

The experimental data shown in Figure 2.18 show that the size $d_{\min}$ of magnetically ordered regions above T_{cu} is nearly independent of the temperature.

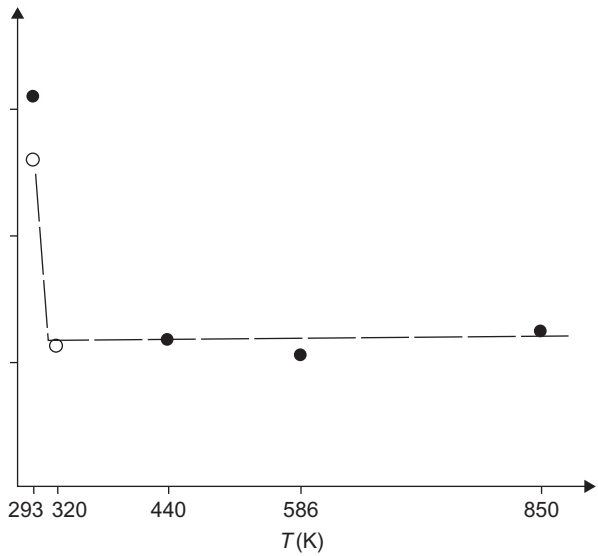

Figure 2.18 Temperature dependence of the spatial size $d_{\min} \propto \sqrt{T} \cdot \tau_{\text{rel}}$ (arbitrary units $K^{1/2}\,THz^{-1}$). The constancy of this quantity above T_{cu} is clearly demonstrated in Ref. [101]. Solid (open) circles correspond to Table I (II) in Ref. [127]. Published with permission of Phys. Rev. B.

In more detail we see that the value of the spatial size at $T_{cu} = 293\,\mathrm{K}$ is clearly larger than at other temperatures, which is anticipated since this regime is dominated by the critical phenomenon of the spin system. There are several assumptions and identifications that go into the interpretation of present data, for instance the crossover wave vector ς_c represents a rough measure of the size of the magnetically ordered regions D_{magn} considered. The theoretical analysis of the experimental results in [127] is established via the concept of a CDS and therefore assumes the validity of $D_{magn} \propto d_{min}$. Hence, the present analysis suggests the surprising result that the actual size D_{magn} remains constant between 320 and 850 K.

Although we have not made use of the full quantization condition Eq. (F.10), only the matching between the temperature, size, and relaxation time, it is clear that the spatiotemporal structure (coherent dissipative system) integrating quantum–thermal correlations allows more general mappings of open systems beyond self-adjoint formulations. One might further predict, through relation (83), that thermal correlations are able to maintain constructive effects. This will be even more important in connection with applications to complex enough systems within a biological framework.

3.3. Correlations in biology

This section is devoted to biological order, organization, and evolution. We have already seen in Appendix F that constructive integration of quantum and thermal correlations under appropriate conditions lead to a so-called CDS, i.e., an optimal spatiotemporal structure formed by the precise relations between time, size, and temperature scales. CDS suggests microscopic self-organization including Gödel-like self-referential traits.

The analytic theory underscores the structure–matter dilemma with profound implications for teleological thinking; see Ernst Mayr's last survey of quote "controversial concepts in biology" [10]. As discussed in Appendices F and G, the outcome is the emergence of a dissipative degenerate organization, which corresponds to a distinctive form of matter. The latter should be distinguished from the habitual range of long-established traditions of understanding and predicting properties of matter from quantum theoretical first principles. In the latter we might correlate general teleomatic processes as ruled by natural laws and in the former, goal-directed teleonomic progression as controlled by the regulation of an evolved program.

As already expressed in e.g. in [11], and extended in [83, 128], the *living state* should require the following necessary conditions: (1) the coupling to an environment for *metabolic processes*, (2) the *genetic function*, and (3) a spatiotemporal regulation for optimal function or *homeostasis*. A fourth condition was added in [128], i.e., (4) the possible evolution of higher level *meta-codes* for relating diverse levels of organization, e.g., between genotypic

and phenotypic processes. Hence as will be shown below, the spatiotemporal rhythm-like configuration, CDS, proposes new promising connections within a condensed matter biological outline. It challenges traditional views on the structure–matter dilemma concerning the natural world, perception, and consciousness also adding a polymorphic quality to the picture.

Returning to the formulations of mainly Appendices E and F, we will proceed to analyze in some detail the time-irreversible self-organized structure denoted as CDS. A key concept in the formulation is given by the transformation **B**, Eq. (E.11), which links the canonical basis $\boldsymbol{f}$, with the physically preferred local basis $\boldsymbol{h}$, and the latter with the coherent order defined by $\boldsymbol{g}$. As can easily be seen by inspection **B** exhibits an interesting factorization property, i.e., the columns display a certain repetitive structure involving certain correlated groups of sites and, depending on the value of n, all possible factors develop as closed cyclic structures. To demonstrate the cyclic order, we will display $\sqrt{12}$ **B**, i.e., the array for $n = 12$ in Eq. (87) below. The dimension of the cyclic vectors is given in parenthesis and for simplicity we have removed the first vector of one-dimensional units (1) leaving the diagram with only 11 columns.

$$\begin{array}{ccccccccccc} & & & & (2) & & & & & & \\ & & & (3) & (2) & & (3) & & & & \\ & & (4) & (3) & (2) & & (3) & (4) & & & \\ & (6) & (4) & (3) & (2) & & (3) & (4) & (6) & & \\ (12) & (6) & (4) & (3) & (2) & (12) & (3) & (4) & (6) & (12) \\ & & (4) & (3) & (2) & & (3) & (4) & & & \\ & & & (3) & (2) & & (3) & & & & \\ & & & & (2) & & & & & & \end{array} \tag{87}$$

While noting the obvious symmetry of the diagram, we observe for $n = 15$ the occurrence of many nonpartitioned columns as well as the omission of the middle column, when n is odd.

$$\begin{array}{ccccccccccccccc} & & & & (3) & & & & & (3) & & & & & \\ & & (5) & & (3) & & & & & (3) & & (5) & & & \\ (15) & (15) & (5) & (15) & (3) & (15) & (15) & (15) & (15) & (3) & (15) & (5) & (15) & (15) \\ & & (5) & & (3) & & & & & (3) & & (5) & & & \\ & & & & (3) & & & & & (3) & & & & & \end{array} \tag{88}$$

The essential idea is that the map of biological order on a CDS conveys information stored in the transformation B, suggesting numerous ways of encoding depending on the levels of organization under study. For instance describing a quantum chemical representation of the constituents of our genes or of folded protein–DNA coils, e.g., intrinsic genome-wide organization of nucleosomes [129], the present CDS with its precise transformation properties prompts the creation of program instructions via subsequent factorizations, signifying certain functions, positioning, and or traits. One

might, e.g., consider the sequence $s_1 s_2 s_3 \ldots s_k$ of positive integers with the Gödel numbering, i.e., being the product of the first primes raised to the corresponding values in the sequence

$$n(s_1 s_2 s_3 \ldots s_k) = 2^{s_1} \cdot 3^{s_2} \cdot 5^{s_3} \cdots p_k^{s_k} \tag{89}$$

The cyclic diagram corresponding to this Gödel numeral becomes ($n_k = n/k$)

$$\begin{array}{ccccccccccccccccccc}
 & & & & & & & & (n_{\frac{n}{2}}) & & & & & & & & & & \\
 & & & & (n_{p_k}) & & & & \cdot & & & & (n_{p_k}) & & & & & & \\
 & & & & \cdot & & & & (\cdot) & & & & \cdot & & & & & & \\
 & & (n_3) & & \cdot & & & & \cdot & & & & \cdot & & (n_3) & & & & \\
 & (n_2) & \cdot & & (n_{p_k}) & & & & (n_{\frac{n}{2}}) & & & & (n_{p_k}) & & \cdot & & (n_2) & & \\
(n) & \cdot & (n_3) & \cdot & (n_{p_k}) & \cdot & (n) & \cdot & (n_{\frac{n}{2}}) & \cdot & (n) & \cdot & (n_{p_k}) & \cdot & (n_3) & \cdot & (n) & & \\
 & (n_2) & \cdot & & (n_{p_k}) & & & & (n_{\frac{n}{2}}) & & & & (n_{p_k}) & & \cdot & & (n_2) & & \\
 & & (n_3) & & \cdot & & & & \cdot & & & & \cdot & & (n_3) & & & & \\
 & & & & (\cdot) & & & & (\cdot) & & & & (\cdot) & & & & & & \\
 & & & & \cdot & & & & \cdot & & & & \cdot & & & & & & \\
 & & & & (n_{p_k}) & & & & (n_{\frac{n}{2}}) & & & & (n_{p_k}) & & & & & &
\end{array} \tag{90}$$

where the columns are partitioned according to the factors that are divisors of n [with nonpartitioned columns (n) properly interspersed]. Other numeral systems are of course possible; see Ref. [83] for more details. In passing we observe that various values of n will generate an increasing number of unpartitioned columns above. They appear to carry no obvious information, cf. the existence of long sequences of noncoding DNA, introns, interrupting the relatively short segments of protein coding DNA, exons. Nevertheless they need to be there to give an appropriate background to the encoding functions of the exons. For some further related topics, see Ref. [83] and the concluding section.

Before ending this section, we conclude that the present model couples the physical unidirection of time with perceived time through the CDS neumatic structure including up-down cognition but not left-right mirroring, see also the next section.

3.4. Einstein's laws and cosmology

As already discussed at the end of Section 2.2.3, we derived a universal superposition principle from a complex symmetric ansatz arriving at a Klein–Gordon-like equation relevant for the theory of special relativity. This approach, which posits a secular-like operator equation in terms of energy and momenta, was adjoined with a conjugate formal operator representation in terms of time and position. As it will be seen, this provides a viable extension to the general theory [7, 82]. We will hence recover Einstein's laws of relativity as construed from the overall global superposition, demonstrating in addition the independent choice of a classical and/or a quantum representation. In this way, decoherence to classical reality seems always possible provided that appropriate operator realizations are made.

As hinted in the *Introduction*, the present viewpoint combines the microscopic and the macroscopic domain. Hence, we need to incorporate a satisfactory treatment also of the theory of general relativity. Simultaneously the problem associated with micro–macro correlates, discussed initially, and the universality of the superposition principle, briefly mentioned above and to be discussed in more detail below, aims at the idea of decoherence in regard to classical reality. Since the issues brought up are interrelated, we will illustrate the problem of decoherence by examples drawn from general relativity, i.e., the law of light deflection, the gravitational redshift, and the time delay.

The extension of a Klein–Gordon-like equation, see Eqs. (65)–(73), to include gravitational interactions is quite straightforward in our present theory. Since general relativity associates gravity with tensor fields, we need to incorporate the operator and their conjugate counterparts simultaneously. To accomplish the first part of the conjugate pair formulation, we will attach to our previous model in the basis $|m, \bar{m}\rangle$, the interaction

$$m\kappa(r) = m\mu/r; \quad \mu = \frac{G \cdot M}{c^2} \tag{91}$$

generating the modified Hamiltonian (operator) matrix for the case $m_0 \neq 0$

$$\mathcal{H} = \begin{pmatrix} m(1-\kappa(r)) & -iv \\ -iv & -m(1-\kappa(r)) \end{pmatrix} \tag{92}$$

with μ the gravitational radius, G the gravitational constant, M a spherically symmetric nonrotating mass distribution (which does not change sign when $m \to -m$) and $v = p/c$ as in (65–73). For more details on the fundamental nature of M and on the emergence of black-hole-like objects, see Refs. [7, 9]. The tensorial issue relates to consistency relations between Eq. (92) and its conjugate analogue together with a surprising link to the associated problem of decoherence as will be discussed in more detail below.

Incidentally we find that the positive operator $\kappa(r) \geq 0$ depends formally on the coordinate r of the particle m, with origin at the center of mass of M. Since the dimensions or scales $\vec{x}$ and τ are subject to the description of the conjugate problem, we will on balance recover a geometry of curved space-time scales reminiscent of the classical theories, see more below.

We obtain in analogy with for the matrix $\mathcal{H}$, in analogy, with Eqs. (65)–(68)

$$\begin{aligned} \lambda^2 &= m^2(1-\kappa(r))^2 - p^2/c^2 \\ \lambda_\pm &= \pm m_0(1-\kappa(r)); \quad v = p/c \end{aligned} \tag{93}$$

with the eigenvalues $\lambda_\pm$ scaled so that m_0 is consistent with the special theory, i.e.,

$$\begin{aligned} m_0^2 &= m^2 - p^2/((1-\kappa(r))^2c^2) \\ \lambda_\pm/(1-\kappa(r)) &= \pm m_0 = \pm\sqrt{m^2 - p^2/((1-\kappa(r))^2c^2)} \\ m &= m_0/\sqrt{1-\beta'^2};\ \beta' \leq 1; 1 > \kappa(r) \\ \beta' &= p/(mc(1-\kappa(r))) = \upsilon/(c(1-\kappa(r))). \end{aligned} \tag{94}$$

As mentioned, Eqs. (93) and (94) mimic the formulas of special relativity by rewriting the operator matrix (note that $\kappa(r) < 1/2$ rather than $\kappa(r) < 1$, see below)

$$\boldsymbol{H}_{\text{sp}} = \begin{pmatrix} m & -ip'/c \\ -ip'/c & -m \end{pmatrix}; \quad p' = p/(1-\kappa(r)) \tag{95}$$

Since we have modeled that the gravitational source is a spherical black-hole-like object, see details in [7, 9], it follows that angular momentum is a constant of motion and postulating the limit velocity c at the limiting distance given by the gravitational radius μ, one obtains

$$m\upsilon r = m\mu c \tag{96}$$

or

$$\upsilon = \kappa(r)c = \mu c/r \tag{97}$$

Equation (97) serves as a boundary condition for the operator matrix model, which in the complex symmetric representation, making the replacement $\upsilon/c = \kappa(r)$, reads (note that $\kappa(r) < \frac{1}{2}$, see below)

$$\mathcal{H} = m\begin{pmatrix} (1-\kappa(r)) & -i\kappa(r) \\ -i\kappa(r) & -(1-\kappa(r)) \end{pmatrix} \rightarrow m\begin{pmatrix} \sqrt{(1-2\kappa(r))} & 0 \\ 0 & -\sqrt{(1-2\kappa(r))} \end{pmatrix} \tag{98}$$

Although m is not determined by Eq. (98), cf. also the conjugate problem below, the quotient m/m_0 (nonzero restmass) follows uniquely from Eqs. (93) and (94) and the eigenvalues of Eq. (98), i.e.,

$$\frac{m}{m_0} = \frac{1-\kappa(r)}{\sqrt{1-2\kappa(r)}} \tag{99}$$

We note the singularity at $r = 2\mu$ and that Eqs. (65)–(68), (95), and (98) invoke the scalings $m\sqrt{1-\beta^2}$ and $m\sqrt{1-\beta'^2}$, while Eq. (98) require $m\sqrt{1-2\kappa(r)}$.

Returning briefly to the decoherence theme we observe a fundamental property of the formulation. The matrix $\mathcal{H}$ exhibits a singularity, consistent with Eq. (99), at the degenerate point $\kappa(r) = \frac{1}{2}$, i.e.,

$$\mathcal{H}_{\text{deg}} = m \begin{pmatrix} \frac{1}{2} & -i\frac{1}{2} \\ -i\frac{1}{2} & -\frac{1}{2} \end{pmatrix} \rightarrow \begin{pmatrix} 0 & m \\ 0 & 0 \end{pmatrix} \tag{100}$$

under the unitary transformation

$$\begin{aligned} |m_0\rangle \rightarrow |0\rangle &= \frac{1}{\sqrt{2}} |m\rangle - i\frac{1}{\sqrt{2}} |\overline{m}\rangle ; \\ |\overline{m}_0\rangle \rightarrow |\overline{0}\rangle &= \frac{1}{\sqrt{2}} |m\rangle + i\frac{1}{\sqrt{2}} |\overline{m}\rangle . \end{aligned} \tag{101}$$

It is interesting that our present global superposition principle unequivocally leads to the famous Laplace–Schwarzschild radius $r = 2\mu = R_{\text{LS}}$ (we assume that M is totally confined inside R_{LS}). There is a difference, however. Although the classical "Schwartzschild singularity" depends on the choice of the coordinate system, the present result is a generic property that exhibits the autonomic nature of the universal linear principle. Hence, decoherence to classical reality may occur for $0 < \kappa(r) < \frac{1}{2}$, while potential quantum-like structures arise inside R_{LS} for $\frac{1}{2} \leq \kappa(r) < 1$.

The present formulation yields additional meaning to the point $\kappa(r) = \frac{1}{2}$, see the recent discussion of Gödel's theorem, Appendix G. Making the substitutions

$$q = (1 - \kappa(r)); \quad (1 - q) = \kappa(r) \tag{102}$$

the self-referential character of the situation is revealed. The difference between the nonsymmetric formulation in Appendix G and the complex symmetric form given here is only a technicality and not essential. Although decoherence, cf. a classical measurement, would correspond to the result either $q = 1$ or $q = 0$, the famous Gödel proposition, provable neither right nor wrong within the given set of arithmetical axioms, can consistently be formulated as the special point singularity, see Eqs. (100) and (101). Obviously, decoherence to a "classical" result (or measurement) is not possible and in this context self-referentiability serves as an automatic protection against decoherence.

We will now proceed to the conjugate problem and discuss the case of zero mass, i.e., $m_0 = 0$. To prepare the background for this development, we will apply the present theory to particles of zero rest mass, e.g., the particles of light or photons. As can be expected from previous equations, for $m_0 \neq 0$, inconsistencies are due to appear in the operator–conjugate operator structure for these particles. To maintain consistency, we require that a distinct gravitational law for zero rest mass particles must exist, which we indicate by the notation $\kappa_0(r) = G_0 \cdot M/(c^2 r)$ in Eqs. (92) and (93).

The first anomaly is exposed by rewriting Eqs. (92)–(94) for particles with $m_0 = 0$, i.e., when $\mathcal{H}$ is singular since

$$m(1 - \kappa_0(r)) = p/c \tag{103}$$

where $\kappa_0(r)$ is to be uniquely decided below. Furthermore

$$\mathcal{H} = \begin{pmatrix} p/c & -ip/c \\ -ip/c & -p/c \end{pmatrix} \rightarrow \begin{pmatrix} 0 & 2p/c \\ 0 & 0 \end{pmatrix} \tag{104}$$

transforms under the same unitary transformation as in the previous section, see Eq. (101). We note that Eqs. (103) and (104) do not show singular behavior, except describing for all r a Jordan block, i.e., an eigenvalue degeneracy with a Segrè characteristic equal to 2. A consistent formulation requires Eq. (103) to be compatible with the boundary condition Eq. (97) and with the eigenvalue relations of Eqs. (98) and (99). A necessary condition is zero average momentum, Eq. (103), at the Schwarzschild radius $r = 2\mu = R_{\mathrm{LS}}$. The condition is that $\bar{p} = 0$ at $\kappa(r) = 1/2$ and hence that $G_0 = 2G$ or

$$\kappa_0(r) = 2\kappa(r) \tag{105}$$

Equation (105) follows Einstein's law of light deflection, i.e., photons are deflected twice than that of Newtonian gravity.

It is obvious that the behavior at the Schwartzschild radius is different for the cases $m_0 \neq 0$ and $m_0 = 0$, see Eqs. (95), (103), and (104). Hence, we need to find consistent relations that link the two, independent of the specific eigenvalue of the mass operator examining the conjugate operator formulation based on the representations, i.e., Eqs. (98) and (104), where the energies scale as $E_{\mathrm{op}}\sqrt{1 - 2\kappa(r)}$. By a straightforward generalization of Eq. (72), we obtain

$$\mathrm{d}\mathcal{H}_{\mathrm{conj}} = \begin{pmatrix} c\mathrm{d}s & 0 \\ 0 & -c\mathrm{d}s \end{pmatrix} = \begin{pmatrix} cA\mathrm{d}\tau & -iB\mathrm{d}\vec{x} \\ -iB\mathrm{d}\vec{x} & -\mathrm{c}A\mathrm{d}\tau \end{pmatrix} \tag{106}$$

where the conjugate operator, see Eqs. (69) and (71) for general definitions, is given by

$$\begin{aligned} E_{\mathrm{op}}\sqrt{1 - 2\kappa(r)} = E_s &= i\hbar\frac{\partial}{\partial s} \\ s &= -i\hbar\frac{\partial}{\partial E_s} \end{aligned} \tag{107}$$

and with the operators $A(r)$ and $B(r)$ to be defined consistently below. Note that E_{s} and s, are independent of r. For $r > R_{\mathrm{LS}}$, we obtain directly from Eq. (107)

$$h\nu\sqrt{1 - 2\kappa(r)} = h\nu_0 = hc\lambda^{-1}\sqrt{1 - 2\kappa(r)} = hc\lambda_0^{-1} \tag{108}$$

from which one gets

$$\nu\sqrt{1-2\kappa(r)}=\nu_0;\quad \lambda_0\sqrt{1-2\kappa(r)}=\lambda \tag{109}$$

i.e., the law of the gravitational redshift. λ (ν) is the wavelength (frequency) of the emitted photon measured at coordinate r, defined above, and λ_0 (ν_0) is the wavelength (frequency) of the photon measured by the observer at "infinite" distance from M.

Returning to Eq. (103), we find in the classical picture since $r > R_{\mathrm{LS}}$

$$c\mathrm{d}\tau(1-2\kappa(r))=\mathrm{d}r \tag{110}$$

which in combination with Eq. (106) (note that ds is zero for photons) yield

$$(1-2\kappa(r))=AB^{-1} \tag{111}$$

which together with Eq. (109) gives

$$\mathrm{d}r_0=\mathrm{d}r(1-2\kappa(r))^{-1/2} \tag{112}$$

and the choice $\mathrm{d}\tau=0$ giving

$$-c^2\mathrm{d}s^2=\mathrm{d}r_0^2=B^2\mathrm{d}r^2=(1-2\kappa(r))^{-1}\mathrm{d}r^2 \tag{113}$$

from which we conclude that

$$A=B^{-1}=(1-2\kappa(r))^{1/2} \tag{114}$$

Hence one obtains the result

$$\mathrm{d}\mathcal{H}_{\mathrm{conj}}=\begin{pmatrix} c\mathrm{d}t(1-2\kappa(r))^{1/2} & -i\mathrm{d}r(1-2\kappa(r))^{-1/2} \\ -i\mathrm{d}r(1-2\kappa(r))^{-1/2} & -c\mathrm{d}t(1-2\kappa(r))^{1/2}\end{pmatrix} \tag{115}$$

Although Eq. (110) is a classical result, Eq. (115) is decoherence protected for zero rest mass particles since $\mathrm{d}\mathcal{H}_{\mathrm{conj}}$ is nondiagonal with a zero determinant (for all values of r). For a particle with $m_0 \neq 0$, the only singular point is at $r = R_{\mathrm{LS}}$. This occurs when Newton's law of gravity is appended with an appropriate boundary condition, see Eqs. (98)–(101). Nevertheless, the introduction of the operator E_{s} replacing the conventional notion of a rest mass implies the construction of an invariant $\left|\mathrm{d}\mathcal{H}_{\mathrm{conj}}\right| = -c^2\mathrm{d}s^2$, which by definition must be zero for photons. The result is the well-known line element expression (in the spherical case)

$$-c^2\mathrm{d}s^2=-c^2\mathrm{d}t^2(1-2\kappa(r))+\mathrm{d}r^2(1-2\kappa(r))^{-1} \tag{116}$$

Note that Eq. (116) is compatible with the gravitational redshift and the gravitational time delay

$$\tau_0 = \tau\sqrt{1 - 2\kappa(r)} \tag{117}$$

where τ_0 is the proper time for an observer in a gravitational field at r, and τ is the time at large distance from M. Note also the up-down, but not the left-right, coupling to time.

We conclude that the present (global) complex symmetric ansatz has generated a covariant transformation compatible with the classical Schwartzschild gauge. In this picture, there is obviously no gravitational waves, but only electromagnetic and matter waves. Using the results of Appendices D–G, one can further devise a cosmological scenario based on an extreme configuration quantum mechanical model of a black hole, characterized by a massive rotational quantum number J, which in its excited CDS state exhibits transient shifts between all the rotational z-components, M_J, where the z-axis is arbitrary. This model supports the additional limitation that the cosmological horizon replicates the event horizon. Obviously no cosmological constant is needed. For more details regarding cosmological setup including the absolute fulfilment of the second law, see Ref. [9].

4. CONCLUSIONS

To put the finishing touch to the present review, we need to return to the general questions and statements launched in the introduction. First, we will attempt an answer to the question whether the analytic theoretical framework outlined here contributes to the paradoxical issues introduced earlier, i.e., to those related with the general contradictions found in connection with micro–macro correlates, including the problem of causality, temporal irreversibility, the unidirection of time, the derivation of thermodynamics from statistical mechanics, and whether biology supervenes logically on physics. This resolution also embeds the importance, both computationally and theoretically, of concepts like unstable states including degeneracies with nonconventional unidirectional time evolution and spatiotemporal Gödelian structures with self-referential characteristics.

As a second undertaking, one should consider, if possible, if the listed topics, at the end of the introduction, could be apprehended and successfully challenged. Although the proposed issues are forbidding in their generality and interdisciplinary characteristics, future generations of scientists must be able to play the role of being a factor in this general area, otherwise physics in particular and natural science in general will decline. In my commentaries below, I will not explicitly refer to precise sections and/or equations; this will be the task of the reader. Appropriate references, however, will be made when the conclusions reached falls outside the present portrayal.

To add some final comments along chartered territory, it is first of all clear that the universal superposition principle combined with the conjugate operator formulation provide unidirectional time through the coupling to proper energy–mass realizations. Furthermore, the loss of information, or the so-called informity (inadequacy) rule, guarantees that the second law holds absolutely commensurate with temporal irreversibility. Note that the present analytic approach embodies nonprobabilistic features and suggests a retarded–advanced contractive evolution [9, 28, 73]. The self-referential nature of gravity and biological order produce interesting inferences and conjectures. In the former case, space and time cease to exist inside the Schwarzschild–Kerr domain, which is consistent with decoherence protection, whereas in the latter case, the living state is code protected against decoherence (death) via CDS and its self-organizational character. The biological order associates in this picture goal-directed teleonomic processes influenced by the regulation of an evolved program, thereby providing higher order meta-codes for the possible link between genotypic and phenotypic processes and the existence of wide-ranging appropriate biological timescales. The self-referential aspects as exemplified by Gödelian structures and self-organization first of all makes the theory independent on the concept of an observer as well as shapes the identification of the free will (prohairesis, volition, choice, intention) and finally adds a logical dimension to physics (*unus mundus*), which might prove the conjecture that biology should logically supervene on physics.

It is customary to delineate evolution, including the question of free will, as a two-step process, i.e., via random variation plus selection. The present proposal derives from a spatiotemporal dissipative structure through concomitant nonprobabilistic teleonomic processes. Although the DNA digital code includes material self-organization, the presently derived meta-code (analog or digital) makes higher level structures possible. The latter leads to semiotic evolution in a causal setting, including language and mathematics. Hence, free will and the principle of self-reference are one-step commensurate, while on the other hand it is not correct to conclude, as the popular saying goes, that the medium is the message!

Finally some comments referring to the order on the issues listed in the introduction are:

the requirements for a living state have been given in this review
the physical base of biology supports teleonomic processes regulated by an evolved program
the self-referential question first framed by Seel and Ladik is an unequivocal yes
the law of microscopic self-organization is demonstrated in this review
the programmed evolution is incorporated in CDS
the sentient computers developed are we; see more on AI in Ref. [83]
the teleological question was further discussed in [82, 128],

the similarities mind–body/structure–matter have also been detailed in Ref. [83]
the universal superposition principle and decoherence are discussed in [82]
the important role of temperature for biological systems is precisely tuned in CDS
the answer to how the two types of correlations merge is included in this review
the concurring features of gravity and biology are self-referential, see [9, 82, 83]
the position on AI is consistent with Penrose's point C, see Refs. [13, 83]
the cosmological consequences are of quantum origin, see Ref. [9]
the Jordan block is protected against decoherence via Gödel's theorem(s), Appendix G

Although the present approach appears to open new avenues in the theoretical regimes combining biology, chemistry, and physics, it is obvious that much work remains to consolidate the results and to provide a proper platform for the future steps.

APPENDICES

A. TIME-INDEPENDENT PARTITIONING TECHNIQUE

Partitioning technique refers to the division of data into isolated sections and it was put into successful practice in connection with matrix operations. Löwdin, in his pioneering studies, [21, 22] developed standard finite dimensional formulas into general operator transformations, including treatments appropriate for both the bound state and the continuous part of the spectrum, see also details in later appendices. Complementary generalizations to resonance-type problems were initiated in Ref. [23], and simple variational formulations were demonstrated in Refs. [24, 25]. Note that analogous forms were derived for the Liouville equation [26, 27] and further developed in connection with a retarded–advanced subdynamics formulation [28].

For the present illustration, we will focus directly on the operator formulation by a brief introduction of the Löwdin bracketing function

$$f(z) = \langle\phi|H + HT(z)H\,|\phi\rangle \tag{A.1}$$

where H is the Hamiltonian, ϕ the normalized reference function (not orthogonal to the exact wavefunction) belonging to Hilbert space, $\phi \in \hat{h}$, with $T(z)$ the reduced resolvent, and z in general a complex variable (important for the continuous spectrum, see next section)

$$T(z) = P(z - PHP)^{-1}P; \quad P = I - O; \quad O = |\phi\rangle\langle\phi| \tag{A.2}$$

We are interested in the solution of the time-independent Schrödinger equation (ψ is an eigenfunction and E a nondegenerate eigenvalue)

$$H\Psi = E\Psi \tag{A.3}$$

Defining a general complex variable z, Eqs. (A.1)–(A.3) yields the inhomogeneous equation

$$\begin{aligned}(z-H)\Psi(z) &= (z-f(z))\phi \\ \Psi(z) &= \phi + T(z)H\phi\end{aligned} \tag{A.4}$$

with the trial function $\psi(z)$ intermediately normalized, i.e., $\langle\phi|\psi(z)\rangle = 1$. An eigenvalue of H is given by

$$z = f(z) = E; \quad \Psi = \Psi(E) \tag{A.5}$$

i.e., Eqs. (A.4) and (A.5) reduce to Eq. (A.3). Obviously, since ψ is not normalized, we obtain

$$\langle\Psi(z^*)|\Psi(z)\rangle = 1 + \Delta = 1 - f'(z) \tag{A.6}$$

Note that z^* should be inserted in the bra position if z is complex. Explicit relations to perturbation theory obtains from $H = H_0 + V$ with $\phi = \varphi_0$ and $H_0\varphi_0 = E_0\varphi_0$, where the wave and reaction operators, W and t, are defined below through the relations

$$\begin{aligned}\Psi(z) &= (1 + T(z)V)\varphi_0 = W\varphi_0 \\ f(z) &= \langle\varphi_0|H_0 + V + VT(z)V|\varphi_0\rangle = \langle\varphi_0|H_0 + t(z)|\varphi_0\rangle\end{aligned} \tag{A.7}$$

with the Brillouin–Wigner series given via repeated iterations of

$$T(E) = P(E - H_0 - PVP)^{-1}P = T_0 + T_0VT; \quad T_0 = P(E - H_0)^{-1}$$

and alternatively the Rayleigh–Schrödinger expansion carried out in terms of the resolvent

$$R(E_0) = P(E_0 - H_0)^{-1}$$

If the zero-order problem is degenerate, one may generalize the formulation with minor modifications to the multidimensional case with the p-dimensional manifold $f = \phi_1, \phi_2, \ldots \phi_p$ (orthonormal for simplicity) and $\Psi(z) = \Psi_1(z), \Psi_2(z), \ldots \Psi_p(z)$, i.e.,

$$O = \left|\phi_1, \phi_2, \ldots, \phi_p\right\rangle\left\langle\phi_1, \phi_2, \ldots, \phi_p\right| = |\boldsymbol{\phi}\rangle\langle\boldsymbol{\phi}| \tag{A.8}$$

Through well-known operator relations from partitioning technique [22, 26–28], one finds

$$\begin{aligned}O(z-H)^{-1} &= O(z - O\mathcal{H}(z)O)^{-1}(I + HT(z)) \\ \mathcal{H}(z) &= H + HT(z)H\end{aligned} \tag{A.9}$$

arriving straightforwardly at the multidimensional version of (A.4), i.e.,

$$(z - H)\Psi(z) = O(z - \mathcal{H}(z))O\boldsymbol{\phi} \tag{A.10}$$

The precise connection with finite dimensional matrix formulas obtains simply from Löwdin's inner and outer projections [21, 22], see more below, or equivalently from the corresponding Hylleraas–Lippmann–Schwinger-type variational principles [24, 25]. For instance, if we restrict our operator representations to an n-dimensional linear manifold (orthonormal for simplicity) defined by

$$\boldsymbol{h} = h_1, h_2, \ldots h_n \tag{A.11}$$

and the so-called outer projection

$$|\boldsymbol{h}\rangle\langle\boldsymbol{h}|H|\boldsymbol{h}\rangle\langle\boldsymbol{h}| \tag{A.12}$$

one may easily find that the exact resolvent corresponding to Eq. (A.12) writes, [22, 24], for more details we also refer to Ref. [15].

$$|\boldsymbol{h}\rangle\langle\boldsymbol{h}|z - H|\boldsymbol{h}\rangle^{-1}\langle\boldsymbol{h}| \tag{A.13}$$

In addition to formulate convenient approximations for operator representations, rigorous operator bounds [22, 24], and fast and efficient nonlinear perturbation series summations [24, 29–31], partitioning technique also provides a platform for an extended quantum formulation and associated time evolution.

B. TIME-DEPENDENT PARTITIONING TECHNIQUE

The formulas of Appendix A are easily transformed to time-dependent forms via the Fourier–Laplace transform. For the purpose of upcoming extensions to the nonself adjoint case, we introduce the self-adjoint Hamiltonian $H = H^{\dagger} = H^{\dagger\dagger}$. Furthermore the function ϕ considered above is said to belong to the domain of the operator H, i.e., $\phi \in D(H)$. For self-adjoint problems $D(H^{\dagger}) = D(H)$ and for bounded operators, the range $R(H)$ and the domain $D(H)$ are identical with the full Hilbert space; however, in general applications they will differ as we will see later.

We also need to say a few words regarding the spectrum, σ, of a general unbounded (closable) operator H, defined on a complete separable Hilbert space. We will make use of the Lebesque decomposition theorem that divides the spectrum into three parts (with respect to the spectral measure on σ): the pure point part σ_{P}, the absolutely continuous part σ_{AC}, and the singularly

continuous part σ_{SC}. Since most of our applications do not contain the singularly continuous spectrum, we will not discuss this option here, rather we will study the importance of the existence σ_{AC}.

Starting with the causal formulation ($h = 2\pi$ for simplicity) of the time-independent and time-dependent Schrödinger equation ($E \in \sigma_{AC}$)

$$(E - H)\psi(E) = 0; \quad \left(i\frac{\partial}{\partial t} - H\right)\psi(t) = 0; \quad \psi(t) = e^{-iHt}\psi(0) \tag{B.1}$$

To connect the equations in (B.1) through the Fourier–Laplace transform, we need to define suitable complex contours to make the transforms convergent. Specifically we identify the contours $C^{\pm}$ by the lines in upper and lower complex planes defined by $C^{\pm}$: $(\pm id - \infty \to \pm id + \infty)$, where $d > 0$ may be arbitrary. Using the Heaviside function, $\theta(t)$, and the Dirac delta function, $\delta(t)$, we can characterize positive and negative times (with respect to $t = 0$) as linked with appropriate contours $C^{\pm}$ as

$$G^{\pm}(t) = \pm(-i)\theta(\pm t)e^{-iHt}; \quad G(z) = (z - H)^{-1} \tag{B.2}$$

defining retarded–advanced propagators $G^{\pm}(t)$ and their resolvents $G(z^{\pm})$; $z^{\pm} = \mathcal{R}z \pm i\mathcal{I}z$ connected through ($\mathcal{R}z$, $\mathcal{I}z$ are the real and imaginary parts of $z = E + i\varepsilon\,;\ \varepsilon > 0$)

$$\begin{aligned} G^{\pm}(t) &= \frac{1}{2\pi}\int_{C^{\pm}} G(z)e^{-izt}\mathrm{d}z; \quad G(z) = \int_{-\infty}^{+\infty} G^{\pm}(t)\, e^{izt}\mathrm{d}t \\ &\{t > 0;\ \mathcal{I}z > 0\} \\ &\{t < 0;\ \mathcal{I}z < 0\} \end{aligned} \tag{B.3}$$

The integrals, Eqs. (B.3), exist quite generally by closing the contours $C^{\pm}$ in the lower and upper complex planes, respectively, for extensions to the nonself adjoint case, see Figures 2.4, 2.5 and Appendix D. The retarded–advanced formulation including memory terms becomes

$$\begin{aligned} &\left(i\frac{\partial}{\partial t} - H\right)G^{\pm}(t) = \delta(t); \quad \psi^{\pm}(t) = \pm iG^{\pm}(t)\psi^{\pm}(0) \\ &\left(i\frac{\partial}{\partial t} - H\right)\psi^{\pm}(t) = \pm i\delta(t)\psi^{\pm}(0) \end{aligned} \tag{B.4}$$

and

$$\begin{aligned} &(z - H)G(z) = I; \quad \psi^{\pm}(z) = \pm iG(z)\psi^{\pm}(0) \\ &(z - H)\psi^{\pm}(z) = \pm i\psi^{\pm}(0) \end{aligned} \tag{B.5}$$

At this junction, the importance of the absolutely continuous spectrum, σ_{AC}, appears explicitly as can be seen by taking the limits $\mathcal{I}(z) \to \pm 0$, i.e.,

$$G(E + i\varepsilon) = \lim_{\varepsilon \to \pm 0} (E + i\varepsilon - H)^{-1} = \mathcal{P}(E - H)^{-1} \pm (-i)\pi\delta(E - H) \tag{B.6}$$

where $\mathcal{P}$ is the well-known principal value of the integral. From Eqs. (A.1)–(A.5) and Eqs. (B.1)–(B.5), the formulas of time-dependent partitioning technique are easily derived. Note that the retarded–advanced wavefunctions $\Psi^{\pm}$ are unit normalized, whereas the time-independent functions $\Psi(z)$ of the previous section are not.

The full-time dependence, from an incompletely known wavefunction φ at time $t = 0$, can now be determined from the boundary conditions

$$\psi(0) = \psi^{+}(0) = \psi^{-}(0); \quad O\psi(0) = \varphi(0); \quad P\psi(0) = \kappa(0); \; O + P = I \tag{B.7}$$

We can still assume that the limits $t \to \pm 0$ are the same, although it is not necessary in general. From above, the projection operator O may be both one- or p-dimensional, see Eqs. (A.9) and (A.10). Using Eq. (A.9), we obtain

$$\varphi^{\pm}(t) = \pm\frac{i}{2\pi}\int_{C^{\pm}} O(z - H)^{-1}\psi(0)e^{-izt}\mathrm{d}z = \pm\frac{i}{2\pi}\int_{C^{\pm}} \varphi(z)e^{-izt}\mathrm{d}z \tag{B.8}$$

with

$$\begin{gathered}\varphi(z) = O(z - H)^{-1}\psi(0) = O(z - O\mathcal{H}(z)O)^{-1}(\varphi(0) + HT(z)\kappa(0)) \\ \mathcal{H}(z) = H + HT(z)H\end{gathered} \tag{B.9}$$

The exact time evolution within subspace O follows from the convolution theorem of the Fourier–Laplace transform, i.e.,

$$\begin{aligned}\left(i\frac{\partial}{\partial t} - OHO\right)\varphi^{\pm}(t) &= \pm i\delta(t)\varphi(0) \\ &+ OHP\left\{\int_0^t (G_P(t - \tau)PH\varphi(\tau))^{\pm}d\tau \pm iG_P^{\pm}(t)\kappa(0)\right\}\end{aligned} \tag{B.10}$$

with

$$G_P^{\pm}(t) = \pm(-i)\,\theta(\pm t)e^{-iPHPt} = \frac{1}{2\pi}\int_{C^{\pm}} T(z)e^{-izt}\mathrm{d}z \tag{B.11}$$

and

$$\int_0^t (G_P(t - \tau)PH\varphi(\tau))^{\pm}\mathrm{d}\tau = \pm\frac{i}{2\pi}\int_{C^{\pm}} T(z)H\varphi(z)e^{-izt}\mathrm{d}z \tag{B.12}$$

Since we are interested in the contradictions between micro–macro correlates, it is important to point out that so far no approximations have been conceded; the first term of Eq. (B.10) gives the description of the partially known amplitude, φ, as it would evolve in time according to the Hamiltonian *OHO*. The subsequent term depends on all times between 0 and t, whereas the last term evolves the unknown part κ at $t = 0$ completing the memory of initial time.

It is natural to define the causal representation, e.g., the stationary wave $\psi_c(E)$, given by the causal propagator $G_c(t)$ as follows

$$\psi_c(t) = G_c(t)\psi(0) = \psi^+(t) + \psi^-(t); \quad G_c(t) = e^{-iHt} \tag{B.13}$$

and formally

$$\psi_c(E) = \lim_{\varepsilon \to +0} \int_{-\infty}^{+\infty} \psi^+(t) e^{i(E+i\varepsilon)t} \mathrm{d}t + \lim_{\varepsilon \to -0} \int_{-\infty}^{+\infty} \psi^-(t) e^{i(E+i\varepsilon)t} \mathrm{d}t = \int_{-\infty}^{+\infty} \psi_c(t) e^{iEt} \mathrm{d}t \tag{B.14}$$

With symmetric boundary conditions at the chosen time $t = 0$, the microscopic formulation conforms to time reversible laws as expected. The same conclusion follows from an analogous examination of the Liouville equation. In this setting, the initial data at time, $t = 0$, is a statistical density distribution or density matrix. Although there are celebrated discussions on the problem of the approach to equilibrium, we nevertheless observe that without course graining or any other simplifying approximations the exact subdynamics would submit to the same physical laws as above, i.e., time reversibility and therefore constant entropy.

C. WEYL'S THEORY AND THE SPECTRUM

In this addendum, we will derive the spectral function from Weyl's theory and in particular demonstrate the relationship between the imaginary part of the Weyl–Titchmarsh m-function, m_I, and the concept of spectral concentration. For simplicity we will restrict the discussion to the spherical symmetric case with the radial coordinate defined on the real half-line. Remember that m could be defined via the Sturm–Liouville problem on the radial interval $[0,b]$ (if zero is a singular point, the interval $[a,b]$, $b > a > 0$), and the boundary condition at the left boundary is given by [commensurate with Eq. (5)]

$$\begin{pmatrix} \phi(\lambda,a) & \psi(\lambda,a) \\ \phi'(\lambda,a) & \psi'(\lambda;a) \end{pmatrix} = \begin{pmatrix} \sin\alpha & \cos\alpha \\ -\cos\alpha & \sin\alpha \end{pmatrix} \tag{C.1}$$

where α could be chosen so that ψ is regular at origin (see Ref. [46] for details regarding this determination in practical applications) and the requirement that χ defined by

$$\chi(\lambda) = \varphi(\lambda) + m(\lambda)\psi(\lambda) \tag{C.2}$$

satisfies a real boundary condition at b, i.e.,

$$\chi(\lambda, b)\cos\beta + \chi'(\lambda, b)\sin\beta = 0 \tag{C.3}$$

The connection with Weyl's theory comes from the condition that χ should remain square integrable as the right boundary b "moves to infinity" with the parameter $\lambda = E + i\varepsilon$ kept nonreal until the end, see more below, before the approach to the real axis is made. Equation (C.3) describes m as a meromorphic function of λ which, when $\cot\beta$ varies on the real line, lies on a circle C_b defined by (remember imposing the real boundary condition (C.3) at b)

$$[\chi\chi](b) = 0 \tag{C.4}$$

with the center m_b and the radius r_b given by

$$m_b = -\frac{[\phi\psi](b)}{[\psi\psi](b)}; \quad r_b = \frac{1}{[\psi\psi](b)} \tag{C.5}$$

Using the standard Green's formula

$$\int_{r_1}^{r_2} (\phi(r)^* L\psi(r) - \psi(r)\{L\phi(r)\}^*)\mathrm{d}r = [\psi\phi](r_2) - [\psi\phi](r_1) \tag{C.6}$$

it is straightforward to see that points m are on C_b if and only if

$$\int_a^b |\chi(r)|^2 \mathrm{d}r = \frac{m_I}{\varepsilon}; \quad \varepsilon \neq 0 \tag{C.7}$$

As $b \to \infty$, Weyl proved, see Ref. [32], that C_b converges to either a limit circle C_∞ or to a limit point m_∞. In the first situation, all solutions are square integrable and in the latter case the only unique square integrable solution (at the singular point here being ∞) is

$$\chi = \varphi + m_\infty(\lambda)\psi \tag{C.8}$$

If $\mathcal{R}(\lambda) = E$ equals a Sturm–Liouville eigenvalue E_k then the normalized eigenfunction $u_k(r)$ must be proportional to $\psi_k(E_k, r)$ (note that the dependence on the right-hand boundary is not explicitly indicated in u_k and E_k), i.e.,

$$u_k(r) = d_{bk}\psi_k(E_k, r) \tag{C.9}$$

From Eq. (C.2) we conclude that the square integrable solution χ contains the independent solution ϕ, hence $m(\lambda)$ exhibits a (simple) pole at the eigenvalue E_k. The fundamental importance of the coefficients d_{bk} is obvious since they define the spectral function $\rho(E)$ to be used in the completeness relation and the eigenfunction expansion. The former gives

$$\begin{aligned}
\int_a^b |\chi|^2 \,\mathrm{d}r &= \int_{-\infty}^{\infty} \left|g(\omega)\right|^2 \mathrm{d}\rho_b(\omega) \\
g(\omega) &= \int_a^b \chi^*(r)\psi(\omega, r)\mathrm{d}r \\
\rho_b(\omega) &= \sum_{E_n \le \omega} \left|d_{bn}\right|^2 \\
\left|d_{bn}\right|^2 &= \left(\int_a^b \left|\psi(E_n, r)\right|^2 \mathrm{d}r\right)^{-1}
\end{aligned} \tag{C.10}$$

Green's formula Eqs. (C.6) and (C.10) yields

$$\varepsilon \int_a^b |\chi(r)|^2 \mathrm{d}r = \int_{-\infty}^{\infty} \frac{\varepsilon \,\mathrm{d}\rho_b(\omega)}{(\omega - E)^2 + \varepsilon^2} \tag{C.11}$$

Summarizing, $\psi_k(E_k, r)$ (proportional to u_k) is the Sturm–Liouville solution of the differential equation

$$L[u_k] = \left(-\frac{\partial^2}{\partial r^2} + \mathcal{L}^2 + V(r)\right) u_k(r) = E_k u_k(r) \tag{C.12}$$

on the interval $[a, b]$ fulfilling boundary conditions at a and b, see Eqs. (C.1) and (C.3). The coefficients d_{bk} are the proportionality factors that relates ψ_k with u_k. Note that χ is a solution of Eq. (1), defines through Eqs. (C.1)–(C.4) and most importantly with $\lambda = E + i\varepsilon;\ \varepsilon \neq 0$. As the next step, we take the

limit $b \to \infty$, assuming the limit point case obtaining uniquely m_∞ and ρ_∞ (the limits exist also in the limit circle case, but not uniquely).

For the case of a point spectrum, σ_P, the spectral function,ρ_∞, is a constant function of E, with discrete steps $\left|d_{\infty k}\right|^2$ at each point eigenvalue E_k. For the continuous spectrum, σ_{AC}, one obtains

$$\lim_{\varepsilon\to 0+0}\left\{\varepsilon\int_a^\infty |\chi(r)|^2 \mathrm{d}r\right\} = \lim_{\varepsilon\to 0+0}\int_{-\infty}^{\infty}\frac{\varepsilon\,\mathrm{d}\rho_\infty(\omega)}{(\omega-E)^2+\varepsilon^2} = \pi\left(\frac{\mathrm{d}\rho_\infty}{\mathrm{d}\omega}\right)_{\omega=E} = m_I(E) \tag{C.13}$$

with the definition ($\mathcal{I}z$, the imaginary part of z)

$$m_I(E) = \lim_{\varepsilon\to 0+0}\{\mathcal{I}m_\infty(E+i\varepsilon)\} \tag{C.14}$$

displaying the explicit connection between m and the spectral function. Finally, the resolution of the identity writes with the unit operator I_{op}, i.e.,

$$\int_{-\infty}^{\infty}|\psi\omega\rangle \mathrm{d}\rho(\omega)\langle\psi(\omega)| = I_{\mathrm{op}} \tag{C.15}$$

For more details, we refer to Ref. [47].

D. COMPLEX DILATIONS

In this appendix, we will briefly consider the theorem due to Balslev and Combes [50]. In their groundbreaking article they derived general spectral theorems for a so-called self-adjoint dilation analytic family of operators. The name originates from the consideration of many-body Schrödinger operators that, if the potential consists of a sum of dilation analytic two-body potentials, permit the definition of the family through a set of proper scaling transformations appropriately extending the operators to the nonself adjoint regime. By exploiting rigorous mathematical properties of the so-defined dilation analytic operator, including the existence of the absolutely continuous spectrum, σ_{AC}, and notably the absence of the singularly continuous spectrum, σ_{SC}, rigorous spectral theorems were proven and analytically extended to the non-Hermitean domain. We use the interchanging nomenclature non-selfadjoint or non-Hermitean a bit carelessly, but the meaning should be clear once the results are stated.

The opportunity to modify the absolutely continuous spectrum, shown in more detail below, was immediately taken to advantage in quantum theoretical applications in a variety of quantum theoretical applications in both

quantum chemistry and nuclear physics [52]. The fundamental idea develops from a trivial but nevertheless elaborated scaling argument. For instance consider an apt change, or common scaling, of all the space coordinates in the partial (dilation analytic) differential equation. If the scale factor is nonreal, it is easy to convince oneself that the modified (non-selfadjoint) equation allows the posit of outgoing exponential (square integrable) solutions (for σ_{AC}) adequate for the treatment of long-established stable numerical techniques relevant within the conventions of the traditional Hilbert space. The price, as already mentioned, is the appearance of non-selfadjoint operators [50] and the corresponding generation of the time evolution.

To recognize the advantage the scaling transformation, we will briefly look at a typical matrix element of a standard quantum mechanical calculation. Consider for example the general operator $W(r)$, where we write $r = r_1, r_2, \ldots r_N$ assuming $3N$ fermionic degrees of freedom. By making the scaling (radial coordinates for simplicity) $r' = \eta^{3N} r$; $\eta = e^{i\vartheta}$ (or $\eta = |\eta|\, e^{i\vartheta}$), with the phase $\vartheta < \vartheta_0$ for some ϑ_0 conditional in general on the potential, one gets

$$\int \varphi^*(r) W(r) \phi(r) \mathrm{d}r = \int \varphi^*(r'^*) W(r') \phi(r') \mathrm{d}r' \tag{D.1}$$

or expressed in bra–kets (with $\varphi^*(\eta^*) = \varphi(\eta)$)

$$\langle \varphi | W | \phi \rangle = \langle \varphi(\eta^*) | W(\eta) | \phi(\eta) \rangle \tag{D.2}$$

For our example we assume, for more relevant details see further below, that the operator $W(r)$ and the functions $\varphi(r)$, $\phi(r)$ are aptly defined for the scaling to be meaningful. Such a family of potentials will be denoted by $\mathcal{F}_{\vartheta_0}$ [53]. If the family has an extension, see more details below, to $\arg \eta \leq \vartheta_0$ analytic in the interior and up to the boundary, the class is denoted by $\bar{\mathcal{F}}_{\vartheta_0}$. At this point, it is trivial to deduce from Eq. (D.1) that the matrix element is analytic in the parameter η provided that the complex conjugate of η is inserted on the "bra" side of Eq. (D.2). Hence, many complex scaling treatments in quantum chemistry are operationally derived from complex symmetric representations.

The dilation analytic concept is founded on an unbounded scaling operation that transforms σ_{AC}, the absolutely continuous spectrum, without shifting the bound states, opening up domains in the complex energy plane, the so-called un-physical Riemann sheet, allowing usage of standard Hilbert space methods with minor modifications. Following Balslev and Combes [50], see also part IV [53] of the four-volume treatise on "Methods of Modern Mathematical Physics" by Reed and Simon, which includes the Balslev–Simon "no eigenvalue theorem," i.e., the absence of eigenvalues on $(0,\infty)$ for potentials of form $\bar{\mathcal{F}}_{\frac{\pi}{2}}$, we introduce the N-body (molecular) Hamiltonian as

(not writing out the mass of the particles for simplicity)

$$H = T + V = \sum_i \Delta_i + \sum_{i<j} V_{ij} \tag{D.3}$$

In Eq. (D.3), T is the kinetic energy operator and V is the (dilation analytic) interaction potential, characterized as a sum of two-body potentials V_{ij}, where each V_{ij} is bounded relative Δ_{ij}, where Δ_{ij} is the Laplace operator corresponding to the coordinate $\boldsymbol{r}_i - \boldsymbol{r}_j$ with i and j referring to particles i and j, respectively. Noting that the scaling or dilation operator is unbounded in the general case of a general (complex) scaling calls for domain restrictions.

Before we discuss this problem we notice that the Hamiltonian, Eq. (D.3), is bounded from below in contrast to the Stark Hamiltonian treated earlier, which however is a valid potential for Weyl's theory to hold. Without giving the full details, we first define $\mathcal{D}(H)$, the domain of H, as

$$\mathcal{D}(H) = \{\Phi \in h,\, H\Phi \in h\} \tag{D.4}$$

where h is the well-known Hilbert space.

We will make use of the crucial property of the dilation analytic operator, defined above, i.e., $\mathcal{D}(H) = \mathcal{D}(T)$. Moving on to the dilation transformation, we recognize as the first step that the scaling operator $U(\vartheta) = \exp(iA\theta)$ is unitary for real ϑ and is generated by

$$A = \frac{1}{2}\sum_{k=1}^{k=N} [\boldsymbol{p}_k \boldsymbol{x}_k + \boldsymbol{x}_k \boldsymbol{p}_k] \tag{D.5}$$

where $\boldsymbol{x}_k$ and $\boldsymbol{p}_k$ are the coordinate and momentum vectors of the particle k. One finds

$$U(\vartheta)\Phi(r) = \exp(iA\theta)\Phi(r) = e^{\frac{3N\vartheta}{2}}\Phi(e^{\vartheta} r) \tag{D.6}$$

The proof follows by direct differentiation of both sides of Eq. (D.6) with respect to the parameter ϑ. Alternatively one can work with the Mellin transformation (here restricted to $N = 1$ for simplicity) between ν and $\tilde{\nu}$

$$\nu(\lambda) = (2\pi)^{-\frac{3}{2}} \frac{1}{2} \int_{\mathbf{R}^3} \tilde{\nu}(\mathbf{r}) \mathbf{r}^{-i\lambda - \frac{3}{2}} d^3\mathbf{r}$$

with its eigenfunction $|\mathbf{r}|^{i\lambda - \frac{3}{2}}$ satisfying

$$A|\mathbf{r}|^{i\lambda - \frac{3}{2}} = \lambda |\mathbf{r}|^{i\lambda - \frac{3}{2}}$$

Analytic continuation, i.e., letting $\vartheta \to i\vartheta$, $U(i\vartheta)$ (or using the notation $U(|\eta|\, e^{i\vartheta})$ is converted into an unbounded similitude impinging on operator domains and ranges. Above all σ_{AC}, the positive real axis $(0,\infty)$ will be "rotated down" in the complex plane with a rotation angle of 2ϑ.

To summarize, we have considered a quantum mechanical N-body system with dilation analytic potentials, V_{ij}, and its dependence on the scaling parameter $\eta = |\eta|\, e^{i\vartheta}$ (for some $0 \le \vartheta < \vartheta_0$, depending on V). To be more detailed, we need to restrict Hilbert space to a dense subspace [54], the so-called Nelson class $\mathcal{N}$, which provides the domain over which the unbounded complex scaling is well-defined. Closing the subset $\mathcal{N} \to \mathcal{D}(T)$ in $\mathcal{H}$, see [9] and references therein for a more detailed expose, one obtains the scaled version of the original partial differential equation

$$\begin{gathered} H(\eta)\Psi(\eta) = E(\eta)\Psi(\eta);\ \Psi(\eta) = U(\eta)\Psi(1) \\ H(\eta) = U(\eta)H(1)U^{-1}(\eta) = \eta^{-2}T(1) + V(\eta) \end{gathered} \tag{D.7}$$

The theorem due to Balslev–Combes states that the spectrum $[\lambda_e, \infty)$ of T, where λ_e is the lowest many-body threshold of the system, owing to the factor η^{-2} in front of T in Eq. (D.7), will be rotated "down" (along with the system of half-lines $[\lambda_b, \infty)$, where the threshold λ_b in principle could be complex) in the complex energy plane with an angle $-2\arg(\eta)$, while the discrete spectrum, the complement of the set of thresholds, remains independent of η. On the so-called Riemann sheet of the energy plane, i.e., the sector bounded by the half-lines mentioned above, "exposed" by the rotation, there emerges a set of nonreal finite-dimensional eigenvalues (independent of η) accumulating at most at the thresholds λ_b. The analytic structure implemented in Eq. (D.1) inherently aims toward complex symmetric representations, however, with the self-adjoint formulation logically embedded.

Returning to the partitioning technique formulation, see Appendices A and B, we recover the following modifications of the projection operator formulations

$$\begin{gathered} T(\eta; z) = P(\eta)(z - P(\eta)U(\eta)H(1)U^{-1}(\eta)P(\eta))^{-1}P(\eta) \\ O(\eta) = |\phi(\eta)\rangle\langle\phi(\eta^*)|\,;\ \ P(\eta) = I - O(\eta) \\ \langle\phi(\eta^*)|\phi(\eta)\rangle = \langle\phi(1)|\phi(1)\rangle = 1 \end{gathered} \tag{D.8}$$

Note that these are far from "only" formal extensions. First there are two fundamental points to consider: one that the projectors are oblique, i.e., idempotent

$$O^2(\eta) = O(\eta)$$

but not self-adjoint

$$O^{\dagger}(\eta) = O(\eta^{*}) \neq O(\eta)$$

and further that the biorthogonal construction, Eq. (D.8), contains zero norms, cf. Eq. (A.6)

$$\langle \Psi(\eta^{*}; z^{*}) | \Psi(\eta; z) \rangle = 1 + \Delta(\eta; z) = 1 - f'(z) = 0 \tag{D.9}$$

The second point relates with emerging degeneracies of so-called Jordan block type, a nightmare in matrix theory but in our case, at the same time a "blessing in disguise."

In closing this appendix, we note that the present development allows the general use of the Cauchy representation formula for a projection operator associated with resonance and bound state eigenvalues situated inside the contour C, i.e.,

$$O(C) = \frac{1}{2\pi i} \oint_{C} \frac{\mathrm{d}z}{(z - H)} \tag{D.10}$$

To establish the spectrum inside C, one needs to check whether the condition

$$\| O(C)\varphi \| > 0 \tag{D.11}$$

or if the result of the nonzero projection yields a unique eigenvector ψ_{res}, i.e.,

$$O(C)\varphi = c\psi_{\mathrm{res}} \tag{D.12}$$

for some $c \neq 0$ corresponding to a (resonance) eigenvalue $\varepsilon_{\mathrm{res}}$. If the contour C (usually a test circle) contains several eigenvalues, the projection will pick up the corresponding linear manifold, for more details, see Ref. [59].

E. SYMMETRIC JORDAN BLOCK REPRESENTATIONS

In this appendix, we will derive a complex symmetric form for the Jordan block, see Eq. (E.1). We will also learn how such a degenerate representation may emerge in a realistic situation where the map reflects the property of an open (dissipative) structure. A general proof of the theorem, see below, was given already by Gantmacher [105] in 1959, but the theorem seems to be seldom mentioned. Here we will give an alternative proof, which also provides an explicit result that is also suggestive in connection with physical applications.

Theorem: Any matrix can be brought to complex symmetric form by a similarity transformation.

First we observe that any matrix is similar to a block diagonal matrix, where the sub-matrices along the main diagonal are Jordan blocks. It is thus sufficient to prove that any Jordan block can be transformed to a complex symmetric matrix. In passing we note that any matrix with distinct eigenvalues can be brought to diagonal form by a similarity transformation. The key study therefore relates to $\lambda\mathbf{1} + \mathbf{J}_n(0)$, where $\mathbf{1}$ is the n-dimensional unit matrix and

$$\mathbf{J}_n(0) = \begin{pmatrix} 0 & 1 & 0 & \cdot & \cdot & 0 \\ 0 & 0 & 1 & \cdot & \cdot & 0 \\ 0 & 0 & 0 & 1 & \cdot & 0 \\ \cdot & \cdot & \cdot & \cdot & \cdot & \cdot \\ 0 & 0 & \cdot & \cdot & 0 & 1 \\ 0 & 0 & \cdot & \cdot & 0 & 0 \end{pmatrix} \tag{E.1}$$

If we can show that there exists a matrix $\mathbf{B}$ such that $\mathbf{B}^{-1}\mathbf{J}_n\mathbf{B}$ is a symmetric matrix the proof follows trivially. This requirement implies the transpose relations

$$\mathbf{B}^{-1}\mathbf{J}_n\mathbf{B} = (\mathbf{B}^{-1}\mathbf{J}_n\mathbf{B})^{\mathrm{T}} = \mathbf{B}^{\mathrm{T}}\mathbf{J}_n^{\mathrm{T}}(\mathbf{B}^{-1})^{\mathrm{T}} = \mathbf{B}^{\mathrm{T}}\mathbf{J}_n^{\mathrm{T}}(\mathbf{B}^{\mathrm{T}})^{-1} \tag{E.2}$$

that yields $\mathbf{J}_n\mathbf{B}\mathbf{B}^{\mathrm{T}} = \mathbf{B}\mathbf{B}^{\mathrm{T}}\mathbf{J}_n^{\mathrm{T}} = (\mathbf{J}_n\mathbf{B}\mathbf{B}^{\mathrm{T}})^{\mathrm{T}}$, i.e., when $(\mathbf{J}_n\mathbf{B}\mathbf{B}^{\mathrm{T}})^{\mathrm{T}}$ is symmetric. Expressed in another way, if we can find a factorizable symmetric matrix $\mathbf{S} = \mathbf{B}\mathbf{B}^{\mathrm{T}}$ such that also $\mathbf{J}_n\mathbf{S}$ is symmetric then Eq. (E.2) holds. It follows that

$$(\mathbf{J}_n\mathbf{S})_{ij} = \sum_{k=1}^{n} \delta_{i+1,j} s_{kj} = \begin{cases} s_{i+1,j} & i < n \\ 0 & i = n \end{cases} \tag{E.3}$$

and since both $\mathbf{J}_n\mathbf{S}$ and $\mathbf{S}$ are symmetric that

$$\begin{gathered} s_{i+1,j} = s_{j+1,i} = s_{i,j+1} \; (i \neq n \neq j) \\ s_{i+1,n} = 0 \end{gathered} \tag{E.4}$$

Parenthetically, we notice that $\mathbf{S}$ is per-symmetric, i.e., its elements depend only on the sum of indices. From Eq. (E.4), we deduce that the only nonzero element in the last column of $\mathbf{S}$ is s_{1n} while all elements below and to the right of the secondary diagonal are zero (those on the second diagonal cannot vanish if $\mathbf{S}$ is nonsingular). The remaining elements, above and to the left are arbitrary except for the condition of per-symmetry. How to find a construction that satisfies these requirements?

To discuss this issue we interrupt for a little intermezzo. The hint obtains from the following particulars. The first come out from the author's work [52, 76] connecting Yang's celebrated notion of Off-Diagonal Long-Range Order, ODLRO [106], and Coleman's concept of extreme type wavefunctions [107]. To be brief, for more details see Appendix F, see also Refs. [7, 102, 103], the (two fermion) geminal representation of the second order reduced density matrix, $\Gamma^{(2)}$, save the so-called tail part, writes in Coleman's extreme case for N fermions as

$$\Gamma^{(2)} = \Gamma_L^{(2)} + \Gamma_S^{(2)} = \lambda_L \left|g_1\right\rangle\left\langle g_1\right| + \lambda_s \sum_{k,l=1}^{n} \left|h_k\right\rangle \left(\delta_{kl} - \frac{1}{n}\right) \left\langle h_l\right| \tag{E.5}$$

where $|\boldsymbol{h}\rangle$ is the original n-dimensional geminal basis and

$$\begin{aligned} |g_1\rangle &= \frac{1}{\sqrt{n}} \sum_{k=1}^{n} h_k \\ \lambda_L &= \frac{N}{2} - (n-1)\lambda_S; \quad \lambda_S = \frac{N(N-2)}{4n(n-1)} \end{aligned} \tag{E.6}$$

Rather than to focus on the eigenvalues, λ_L, λ_S, (a simple derivation will follow in the Appendix F and exploited in the section devoted to biological applications) we will bear in mind the form of the spectral decomposition of $\Gamma_L^{(2)}$ and $\Gamma_S^{(2)}$. The second hint originates from the theory of cyclic matrices. It is a well-known that the cyclic matrix

$$\mathbf{C}_n(0) = \begin{pmatrix} 0 & 1 & 0 & \cdot & \cdot & 0 \\ 0 & 0 & 1 & \cdot & \cdot & 0 \\ 0 & 0 & 0 & 1 & \cdot & 0 \\ \cdot & \cdot & \cdot & \cdot & \cdot & \cdot \\ 0 & 0 & \cdot & \cdot & 0 & 1 \\ 1 & 0 & \cdot & \cdot & 0 & 0 \end{pmatrix} \tag{E.7}$$

is diagonalized by the unitary matrix $U_{kl} = (1/\sqrt{n})\,\omega^{2k(l-1)}$; $k, l = 1, 2, \ldots n$; $\omega = \exp(i\pi/n)$. Observing that $\mathbf{U}\mathbf{U}^{\mathrm{T}}$ is persymmetric (depends only on $r+s$) and that

$$(\mathbf{U}\mathbf{U}^{\mathrm{T}})_{rs} = \sum_{l=1}^{n} \omega^{2(r+s)(l-1)} = \frac{1-\omega^{2n(r+s)}}{1-\omega^{2(r+s)}} \tag{E.8}$$

one finds that the only nonzero contributions in (E.8) occur for $r+s = n, 2n$ and therefore Eq. (E.4) will not be satisfied. Keeping in mind that we need to account for the fundamental difference between (E.1) and (E.7), implicit

in Eq. (E.4), we conclude that the latter relation, i.e., $r+s=n+1$, leads to slight modification of Eq. (E.8), i.e.,

$$(\mathbf{U}\mathbf{U}^{\mathrm{T}})_{rs}=\sum_{l=1}^{n}\omega^{2(r+s-1)(l-1)}=\frac{1-\omega^{2n(r+s-1)}}{1-\omega^{2(r+s-1)}} \tag{E.9}$$

suggestive of the ansatz with $\mathbf{U}\rightarrow\mathbf{B}$

$$B_{kl}=(1/\sqrt{n})\omega^{(2k-1)(2l-1)} \tag{E.10}$$

To sum up we have attained the following construction. We have proved that the transformation matrix

$$\mathbf{B}=\frac{1}{\sqrt{n}}\begin{pmatrix}1 & \omega & \omega^{2} & . & \omega^{n-1}\\ 1 & \omega^{3} & \omega^{6} & . & \omega^{3(n-1)}\\ . & . & . & . & .\\ . & . & . & . & .\\ 1 & \omega^{2n-1} & \omega^{2(2n-1)} & . & \omega^{(n-1)(2n-1)}\end{pmatrix};\quad \omega=\mathrm{e}^{\frac{i\pi}{n}} \tag{E.11}$$

satisfies the conditions Eqs. (E.1)–(E.4) with the factorizable persymmetric matrix $\mathbf{S}$ becoming

$$\mathbf{S}=\mathbf{B}\mathbf{B}^{\mathrm{T}}=\mathbf{B}^{\mathrm{T}}\mathbf{B}=\begin{pmatrix}0 & 0 & 0 & \cdot & \cdot & n\\ 0 & 0 & 0 & \cdot & n & 0\\ 0 & 0 & 0 & n & \cdot & 0\\ \cdot & \cdot & \cdot & \cdot & \cdot & \cdot\\ 0 & n & \cdot & \cdot & 0 & 0\\ n & 0 & \cdot & \cdot & 0 & 0\end{pmatrix} \tag{E.12}$$

This explicit construction proves the theorem. What remains is to work out the actual form the Jordan block $\mathbf{Q}$

$$\mathbf{Q}=\mathbf{B}^{-1}\mathbf{J}_{n}\mathbf{B} \tag{E.13}$$

As already stated, the transformation $\mathbf{B}$ is not unique. Nonetheless it is interesting, with the aforementioned intermezzo as background, to note that the result (E.13), to be demonstrated below, i.e., $e^{i\pi(k+l-2)/n}(\delta_{kl}-\frac{1}{n})$ carries a crucial semblance with $\Gamma_{S}^{(2)}$ in Eq. (E.5). In fact $\Gamma^{(2)}$, see more below, relates the complex symmetric representation of the Jordan block through thermalization, and furthermore the matrix $\mathbf{B}$ can also be used to diagonalize the latter. Employing the transformation $|\boldsymbol{H}\rangle\mathbf{B}=|\mathbf{g}\rangle=|g_1,g_2,\ldots g_n\rangle$ Eq. (E.5) writes

$$\Gamma^{(2)}=\lambda_{L}|g_1\rangle\langle g_1|+\lambda_{s}\sum_{k=2}^{n}|g_k\rangle\langle g_k| \tag{E.14}$$

A final "accident" appears from the related Dunford formula given by transformation $\mathbf{B}^{-1}$. A closer examination will be given below (Appendix F).

In Ref. [76], an elegant proof was instigated through the theory of Vandermonde determinants. Here, we will offer an alternative route, i.e., by directly computing ($n > 1$)

$$\mathbf{Q}_n = \mathbf{B}_n^{-1}\mathbf{J}_n\mathbf{B}_n \tag{E.15}$$

recalling the definitions [note a slight difference between $\boldsymbol{B}_n$ and the unitary transformation matrix in Eq. (E.11)]

$$[\mathbf{J}_n]_{ik} = \delta_{i+1,k};\ [B_n]_{ik} = \omega^{(2i-1)(k-1)}$$

and noting that the indices i and k should run from 1 to n (if an index becomes larger than n, the corresponding matrix element is zero). The particular form of the Jordan block, i.e., when $\mathbf{J}_n^n = 0;\ \mathbf{J}_n^{n-1} \neq 0$ defines its Segrè characteristic to be n. Since $\det(\mathbf{B}_n) \neq 0$, we define the inverse as

$$\alpha = \mathbf{B}_n^{-1} = \frac{1}{n}\mathbf{B}_n^{\dagger} \tag{E.16}$$

Straightforward evaluation of the right-hand side of (E.15) yields

$$[\mathbf{Q}_n]_{ik} = \sum_{j=1}^{n-1}\sum_{l=1}^{n}\alpha_{ij}\,[\mathbf{J}_n]_{jk}\,\omega^{(2l-1)(k-1)} = \sum_{j=1}^{n-1}\alpha_{ij}\omega^{(2j+1)(k-1)} = \left\{\sum_{j=1}^{n-1}\alpha_{ij}\omega^{(2j-1)(k-1)}\right\}\omega^{2(k-1)}$$

Using Eq. (E.16) for subtracting the "missing term," and matching $j = n$, the result becomes

$$[\mathbf{Q}_n]_{ik} = \omega^{2(k-1)}\left\{\delta_{ik} - \alpha_{in}\omega^{(2n-1)(k-1)}\right\} = \omega^{2(k-1)}\left\{\delta_{ik} - \frac{1}{n}\omega^{(i-k)}\right\} \tag{E.17}$$

Making use of the fact that $\omega^{2n} = 1$ and $\delta_{ik} = \delta_{ik}\omega^{(i-k)}$, the result becomes

$$[\mathbf{Q}_n]_{ik} = \omega^{2(k-1)}\left\{\delta_{ik}\omega^{(i-k)} - \frac{1}{n}\omega^{(i-k)}\right\} = \omega^{(k+i-2)}\left\{\delta_{ik} - \frac{1}{n}\right\}$$

or explicitly

$$[\mathbf{Q}_n]_{ik} = e^{i\frac{\pi}{n}(k+i-2)}\left\{\delta_{ik} - \frac{1}{n}\right\} \tag{E.18}$$

Similarly, one obtains the general formula for the powers of J_n

$$(\mathbf{Q}_n)^s = (\mathbf{B}_n^{-1}\mathbf{J}_n\mathbf{B}_n)^s = \mathbf{B}_n^{-1}\mathbf{J}_n^s\mathbf{B}_n \tag{E.19}$$

cf. the results above for $s = 1$

$$\begin{aligned}\left[\mathbf{Q}_n^s\right]_{ik} &= \omega^{2s(k-1)}\left\{\delta_{ik} - \frac{1}{n}\sum_{j=n-s+1}^{n}\omega^{(2j-1)(k-i)}\right\} \\ &= \omega^{s(i+k-2)}\left\{\delta_{ik} - \frac{1}{n}\omega^{-(s-1)(i-k)}\sum_{j=0}^{s-1}\omega^{-2j(k-i)}\right\}\end{aligned} \tag{E.20}$$

Summing the geometric series in (E.20) yields

$$\left[\mathbf{Q}_n^s\right]_{ik} = \omega^{s(i+k-2)}[\delta_{ik} - \left[\mathbf{R}_n^s\right]_{ik}]; \quad i,k = 1,2,\ldots n \tag{E.21}$$

$$\left[\mathbf{R}_n^s\right]_{ik} = \begin{cases} \frac{1}{n}\frac{\sin(\frac{\pi s\,(k-i)}{n})}{\sin(\frac{\pi(k-i)}{n})} & i \neq k \\ \frac{s}{n} & i = k \end{cases} \tag{E.22}$$

F. COHERENT DISSIPATIVE ENSEMBLES

As we have frequently pointed out that the present analytic formulation carries over straightforwardly to the Liouville formulation. For some technical discussions see Refs. [28, 102, 122]. In principle we need to replace the Schrödinger equation with the Liouville equation, i.e.,

$$i\frac{\partial\rho}{\partial t} = \hat{L}\rho;\ \hat{L}|\cdot\rangle\langle\cdot| = H|\cdot\rangle\langle\cdot| - |\cdot\rangle\langle\cdot|H \tag{F.1}$$

where ρ is the density matrix (an analogous equation holds for the classical case with the commutator above being substituted with the Poisson bracket). It is sometimes convenient to combine time evolution and temperature dependence through the analogous Bloch equation

$$\frac{\partial\rho}{\partial\beta} = \hat{L}_{\mathrm{B}}\rho;\ \hat{L}_{\mathrm{B}}|\cdot\rangle\langle\cdot| = \frac{1}{2}\{H|\cdot\rangle\langle\cdot| + |\cdot\rangle\langle\cdot|H\} \tag{F.2}$$

with the temperature parameter $\beta = (k_{\mathrm{B}}T)^{-1}$ and T the absolute temperature. The difference between the properties of the energy superoperator $\hat{L}_{\mathrm{B}}$ and the Liouvillian $\hat{L}$ generate nontrivial analytic extensions, a somewhat technical yet straightforward procedure [28, 122]. In principle, one needs to impose

a suitable complex conjugate in the bra position so as to conform with the given analytic structure.

Rather than deriving the general formulas related to Coleman's extreme configuration [107], we will derive the statistical coherent dissipative ensemble in a much more simple way, see also Ref. [95] for more details. To exemplify the generality of our formulation, we will thus consider $M = N/2$ bosons (or N fermions) described by set of $n \geq N/2$ localized pair functions or geminals $\boldsymbol{h} = h_1, h_2 \ldots h_n$ obtained from appropriate pairing of one-particle basis spin functions. With this somewhat imprecise model, we will demonstrate how it will depict many of the essential properties of the open system through various interesting phenomena inherently described via the density operator

$$\Gamma = \rho = \sum_{k,l}^{n} |h_k\rangle \rho_{kl} \langle h_l|; \quad \mathrm{Tr}\{\rho\} = \frac{N}{2} \tag{F.3}$$

For more details see also Ref. [7]. A simple quantum statistical argument goes as follows, illustrating the model and its quantum content. The density matrix elements ρ_{kl} define probabilities, p, for finding particles at site or state k and $(1-p)$ for particles to make the transition from state k to l. Hence, the matrix ρ has the following elements:

$$\rho_{kk} = p; \quad \rho_{kl} = p(1-p); \quad p = \frac{N}{2n} \tag{F.4}$$

It is interesting to note that the density operator Γ has a structure that essentially captures the extreme configuration, i.e., the associated secular equation reveals a nondegenerate large eigenvalue $\lambda_{\mathrm{L}} p - (n-1)p^2$ and a small $(n-1)$ degenerate $\lambda_{\mathrm{S}} = p^2$. Hence the density operator becomes

$$\Gamma = \rho = \lambda_{\mathrm{L}} |g_1\rangle \langle g_1| + \lambda_{\mathrm{S}} \sum_{k,l}^{n} |h_k\rangle \left(\delta_{kl} - \frac{1}{n}\right) \langle h_l| \tag{F.5}$$

or using the transformation from Appendix E, i.e., $|\boldsymbol{h}\rangle\, \mathbf{B} = |\boldsymbol{g}\rangle = |g_1, g_2 \ldots g_n\rangle$, one obtains a compact diagonal representation for the degenerate part (note the small difference between λ_{L} and λ_{S} in Eqs. (E.5) and (F.5), cf. derivations in Ref. [95])

$$\Gamma = \rho = \lambda_{\mathrm{L}} |g_1\rangle \langle g_1| + \lambda_{\mathrm{S}} \sum_{k=2}^{n} |g_k\rangle\langle g_k| \tag{F.6}$$

As presented, the model exhibits a quantum probabilistic origin. Nevertheless, in view of the similarity between Eqs. (E.5) and (E.14) and (F.5) and

(F.6), there appears the possibility to consider the latter to be the reduction of a many-body fermionic pure state to an N-representable two-matrix. Since the density matrix above, if adapted appropriately, consequently is essentially N-representable through its relation to Coleman's extreme case [107], one might, via appropriate projections, completely recover the proper information, cf. corresponding partitioning procedures depicted in Appendix A. The structure described here is also of fundamental importance in connection with the phenomena of superconductivity and superfluidity through its intimate connections with Yang's concept of ODLRO [106], see more under Section 3.2.

To find the key to efficiently incorporate the temperature in our analytic structure and to learn the effects of the outcome, we will return to the Bloch equation, opting for the unambiguous integration of thermal and quantum fluctuations. This is obviously a highly complex problem since we are not only looking at nonequilibrium systems but we must also contend with constructive interaction from the environment. We have already defined our dissipative system as a system exchanging entropy and/or energy with the environment; see the introduction to Section 3.2. There we also mentioned the specifications for a so-called *CDS* to be explicitly defined below.Incidentally we emphasize that we do not assume the thermodynamic limit, unless explicitly stated, and that no subjective loss of knowledge has so far been conceded.

Representing the complex scaling operation as our selected Lyapunov converter, remembering that we have a biorthogonal complex symmetric form signified, as emphasized earlier, by complex conjugation in the bra-position, we start by assigning to our model a complex energy $\mathcal{E}_k = E_k - i\varepsilon$ to every site described by the basis function h_k from which the total energy expression obtains as

$$\mathcal{E} = \mathrm{Tr}\,\{H_2\Gamma\}; \quad H_2 = \frac{1}{N-1}(\bar{h}_1 + \bar{h}_2) + \bar{h}_{12} \tag{F.7}$$

where the reduced Hamiltonian H_2 only depends on the one and to particle operators in Eq. (F.7) (denoted by a bar so as not be confused with the basis set h_k). Without restriction, we put the total energy $\mathcal{E} = 0$. The formal solution of Eq. (F.2) is given by

$$\Gamma_{\mathrm{T}} = e^{-\beta \hat{L}_{\mathrm{B}}}\Gamma$$

or by using the standard factorization property of the exponential superoperator (note that there should be a complex conjugate sign in the bra position

below, but choosing the basis set $\boldsymbol{h}$ real "solves" the problem)

$$\Gamma_{\mathrm{T}} = \lambda_{\mathrm{L}} \sum_{k,l}^{n} |h_k\rangle e^{i\beta\frac{1}{2}(\varepsilon_k+\varepsilon_l)}\rangle \left\langle h_l| + \lambda_{\mathrm{s}} \sum_{kl}^{n} |h_k \right\rangle e^{i\beta\frac{1}{2}(\varepsilon_k+\varepsilon_l)} \left(\partial_{kl} - \frac{1}{n}\right) \langle h_l| \tag{F.8}$$

The assumption that the real part of the energies $\mathcal{E}_k$ for each site can be set equal to zero is matching to $\mathcal{E} = 0$. Introducing the well-known relation between the imaginary part of the energy and the timescale

$$\varepsilon_k = \frac{\hbar}{2\tau_k} \tag{F.9}$$

one can derive the following "quantization condition" from the assumption of harmonicity introducing the relaxation time τ_{rel} and the correlation time from the uncertainty relation $\tau_{\mathrm{lim}} = \tau_{\mathrm{corr}}$, see Refs. [7, 122]

$$\begin{aligned} \beta\varepsilon_l &= 2\pi\frac{l-1}{n}; \quad l = 1, 2, \ldots n \\ \tau_{\mathrm{rel}} &= (l-1)\tau_l = \tau_2 = \frac{\hbar n}{4\pi k_{\mathrm{B}} T} = n\tau_{\mathrm{corr}}; \quad l = 2, 3, \ldots n \end{aligned} \tag{F.10}$$

From the quantization condition Eq. (F.10), see also Ref. [7], we recognize that the thermalized matrix, Eq. (F.8) admits the Jordan form

$$\Gamma_{\mathrm{T}} = \lambda_{\mathrm{L}} \sum_{k,l}^{n} |h_k\rangle e^{i\frac{\pi}{n}(k+l-2)} \left\langle h_l| + \lambda_s \sum_{k,l}^{n} |h_k \right\rangle e^{i\frac{\pi}{n}(k+l-2)} \left(\partial_{kl} - \frac{1}{n}\right) \langle h_l| \tag{F.11}$$

Introducing the basis $|\boldsymbol{h}\rangle\mathbf{B}^{-1} = |\boldsymbol{f}\rangle = |f_1, f_2, \ldots f_n\rangle$, we obtain Dunford's form in the degenerate case, i.e.,

$$\Gamma_{\mathrm{T}} = \lambda_{\mathrm{L}} J^{(n-1)} + \lambda_{\mathrm{S}} J; \quad J = \sum_{t=1}^{n-1} |f_k\rangle\langle f_{k+1}|; \quad J^{(n-1)} = |f_1\rangle\langle f_n| = |f_1\rangle\langle f_1^*| \tag{F.12}$$

Note that the standard decay law given by

$$\mathrm{d}N = -\frac{1}{\tau} N(t)\mathrm{d}t; \quad N(t) = \left|\langle\psi(0)|\psi(t)\rangle^2\right| \tag{F.13}$$

modifies to, see Ref. [7] for details,

$$\mathrm{d}N = t^{n-2}\left(n - 1 - \frac{1}{\tau}\right) N(t)\mathrm{d}t \tag{F.14}$$

Since $dN(t) > 0; t < (n-1)\tau$, one may establish a microscopic law of self-organization. The relations above are consistent if we identify τ with τ_{lim} and $(n-1)\tau$ with τ_{rel}.

From the condition Eq. (F.10), we deduce the existence of an exceptional spatiotemporal structure that acquires prolonged survival times or timescales as well as optimum spatial properties. This defines in more detail the so-called *coherent dissipative system, CDS*, by appending additionally that *(1) they are created or destroyed by integrated quantum and thermal correlations ($T \neq 0$), (2) they exchange energy and information with an entangled environment, and (3) they cannot have a size smaller than a critical one*. Precise dynamical (contractive) evolution of such systems imparts nonexponential decay including the universal law of microscopic self-organization Eq. (F.14). In Section 3, we will consider situations in condensed matter and in biological systems, where matching configurations subsist and where we have examined and discovered unpredicted organizations and emerging order.

G. GÖDELIAN STRUCTURES AND SELF-REFERENCES

In this appendix, we will provide links between the results of our analysis of general degeneracy conditions discussed above and the infamous theorem due to Gödel. Hence we will set the stage for a multivalued quantum logical description, considering some simple points on propositional logics. We will follow closely the account given in Ref. [83]. There is no need here to go into technical questions or concepts such as ω-logic or ω-consistency. Hence we will only consider a formal system, fulfilling necessary premises, corresponding to propositions consistent with syntactic expressions, so-called well-formed formulas (wffs). The strategy will be to transform the interpretation of a truth functional propositional calculus. In other words we will assign truth-values to each propositional symbol, i.e., using their usual truth functional meanings true and false. We will study two simple propositions P and $Q = \neg P$ to be expressed via the following table, cf. the operation of logical negation

$$\mathcal{Truth\ Table} = \begin{array}{c} \\ \text{true} \\ \text{false} \end{array} \begin{array}{c} \begin{array}{cc} \text{true} & \text{false} \end{array} \\ \begin{pmatrix} \mathcal{P}(x) & \mathcal{Q}(x) \\ \neg\mathcal{Q}(x) & \neg\mathcal{P}(x) \end{pmatrix} \end{array} \tag{G.1}$$

The table simply reads "the first row" is true when P is true and Q is false, the second row reads false if Q is true and P is false. The translation connotes the conversion of (G.1) into a truth matrix P in terms of the probability operators/functions p and $(1-p)$ in the basis (Dirac notation) $|\text{true}\rangle$ and $|\text{false}\rangle$

and assigning a negative signature to the negation row

$$\mathcal{P} = \begin{array}{c} \\ |\text{true}\rangle \\ |\text{false}\rangle \end{array} \begin{array}{c} \begin{array}{cc} |\text{true}\rangle & |\text{false}\rangle \end{array} \\ \begin{pmatrix} p & (1-p) \\ -(1-p) & -p \end{pmatrix} \end{array} \tag{G.2}$$

This is a nonsymmetric construction, which could be derived from a traditional Hermitean version via a nonpositive definite metric Δ; $\Delta_{11} = -\Delta_{22} = 1$, $\Delta_{12} = \Delta_{21} = 0$. As we will see analogous constructions also follow from our complex symmetric realizations, cf. previous developments above. We emphasize that these realizations are required with the intention to mimic our dissipative system, the "environment" here being made up of the other wffs of the formal system. The probability operator p is represented in an abstract space spanned by the vectors $|\text{true}\rangle$ and $|\text{false}\rangle$. Diagonalising $\mathcal{P}$ ($p > \frac{1}{2}$), i.e.,

$$\begin{gathered} \mathcal{P} = \begin{pmatrix} p & (1-p) \\ -(1-p) & -p \end{pmatrix} \rightarrow \begin{pmatrix} \lambda_+ & 0 \\ 0 & \lambda_- \end{pmatrix} \\ \lambda^2 = p^2 - (1-p)^2 \\ \lambda_\pm = \pm\sqrt{2p-1} \end{gathered} \tag{G.3}$$

with the new transformed eigenvectors $|\overline{\text{true}}\rangle$ and $|\overline{\text{false}}\rangle$ given by

$$\begin{aligned} |\overline{\text{true}}\rangle &= c_1|\text{true}\rangle + c_2|\text{false}\rangle; \quad \lambda_+ = \lambda = \sqrt{2p-1} \\ |\overline{\text{false}}\rangle &= c_2|\text{true}\rangle + c_1|\text{false}\rangle; \quad \lambda_- = -\lambda = -\sqrt{2p-1} \end{aligned} \tag{G.4}$$

where the components of the eigenvectors are given by

$$\begin{aligned} c_1 &= \sqrt{\frac{(p+\lambda)}{2p}} \\ c_2 &= \frac{-(1-p)}{\sqrt{2p(p+\lambda)}} \end{aligned} \qquad c_1^2 + c_2^2 = 1. \tag{G.5}$$

We find, cf. the complex symmetric case, that the eigenvectors are biorthogonal via the specification $c^+ \Delta d$ for general vectors c and d. Furthermore, the requirement $p > \frac{1}{2}$ is simple to implement since if not, i.e., $p < \frac{1}{2}$, one can let $p \rightarrow (1-p)$. Also Eqs. (G.2)–(G.5) hold for $p < \frac{1}{2}$ with the condition that $\lambda_\pm$ becomes purely imaginary. However, the crucial point is $p = \frac{1}{2}$.

Before we examine the degeneracy, $p = \frac{1}{2}$, we need to interpret the operator $\mathcal{P}$. The first observation is that the quantum mechanical operators/functions,

e.g. p and $(1-p)$, decohere to a definite (classical) value as soon as a measurement has been made. This entails no specific consequences if $p \neq \frac{1}{2}$ since we have the simple matrix identifications (I is the unit matrix)

$$\frac{1}{2}(I + \mathcal{P}^2) = p\, I; \quad \frac{1}{2}(I - \mathcal{P}^2) = (1-p)\, I \tag{G.6}$$

with the superoperator $\hat{\mathcal{P}}$, diagonally represented as

$$\hat{\mathcal{P}} = \left(|\overline{\text{true}}\rangle, |\overline{\text{false}}\rangle\right)\begin{pmatrix} \sqrt{2p-1} & 0 \\ 0 & -\sqrt{2p-1} \end{pmatrix}\begin{pmatrix} \langle\overline{\text{true}}| \\ \langle\overline{\text{false}}| \end{pmatrix}. \tag{G.7}$$

From Eq. (G.6) we obtain appropriate probability information via the system operators $\Gamma_{\pm} = \frac{1}{2}(I \pm \mathcal{P}^2)$, while the transformation formulas (G.4) correspond to proper truth-values consistent with Eq. (G.7). The new eigenvectors here are obtained as a superposition of vectors corresponding to legitimate input values for $p = 1$. For $\hat{\mathcal{P}}^2 = 0$, Eq. (G.6) gives the classical result $p = \frac{1}{2}$, i.e., no information at all. Consequently $\hat{\mathcal{P}}^2$ yields a bias to the no information platform. Note that the operator $\hat{\mathcal{P}}$, or the truth matrix $\mathcal{P}$, is a nonclassical quantity (operator), which will play a crucial role below serving as the square root of the relevant "bias" part of the system operator transforming the input information accordingly.

To examine the degeneracy in more detail, we will introduce the following definitions. If $\mathcal{P}$ can be brought to diagonal form, Eq. (G.7), we will say that the formulation is *nonsingular*; if not it is by definition *singular*. From the limiting procedure, it follows that the diagonal elements $\lambda_{\pm} = \pm\sqrt{2p-1} \to 0$ as $p \to \frac{1}{2}$. However at $p = \frac{1}{2}$, one obtains

$$\hat{\mathcal{P}} = (|\text{true}\rangle, |\text{false}\rangle)\begin{pmatrix} \frac{1}{2} & \frac{1}{2} \\ -\frac{1}{2} & -\frac{1}{2} \end{pmatrix}\begin{pmatrix} \langle\text{true}| \\ \langle\text{false}| \end{pmatrix} = |\overline{\text{true}}\rangle\langle\overline{\text{false}}| \tag{G.8}$$

or explicitly transformed to the canonical Jordan form

$$\hat{\mathcal{P}} = (|\overline{\text{true}}\rangle, |\overline{\text{false}}\rangle)\begin{pmatrix} 0 & 1 \\ 0 & 0 \end{pmatrix}\begin{pmatrix} \langle\overline{\text{true}}| \\ \langle\overline{\text{false}}| \end{pmatrix} \tag{G.9}$$

where for $p = \frac{1}{2}$ we find

$$\begin{aligned} |\overline{\text{true}}\rangle &= \frac{1}{\sqrt{2}}\{|\text{true}\rangle - |\text{false}\rangle\} \\ |\overline{\text{false}}\rangle &= \frac{1}{\sqrt{2}}\{|\text{true}\rangle + |\text{false}\rangle\} \end{aligned} \tag{G.10}$$

Accordingly, the propositions P and $Q = \neg P$ from

$$\begin{array}{c} \\ \text{true} \\ \text{false} \end{array} \begin{array}{c} \begin{array}{cc} \text{true} & \text{false} \end{array} \\ \begin{pmatrix} P(x) & Q(x) \\ \neg Q(x) & \neg P(x) \end{pmatrix} \end{array}$$

are neither true nor false, or according to the truth matrix P,

$$\mathcal{P} = \begin{array}{c} \\ |\text{true}\rangle \\ |\text{false}\rangle \end{array} \begin{array}{c} \begin{array}{cc} |\text{true}\rangle & |\text{false}\rangle \end{array} \\ \begin{pmatrix} \frac{1}{2} & \frac{1}{2} \\ -\frac{1}{2} & -\frac{1}{2} \end{pmatrix} \end{array} = \begin{array}{c} \\ |\overline{\text{true}}\rangle \\ |\overline{\text{false}}\rangle \end{array} \begin{array}{c} \begin{array}{cc} |\text{true}\rangle & |\text{false}\rangle \end{array} \\ \begin{pmatrix} 0 & 1 \\ 0 & 0 \end{pmatrix} \end{array} \tag{G.11}$$

We note that classical information is not distorted since the system operators $\Gamma_{\pm}$ depend entirely on $\mathcal{P}^2$. However, from the consistency relations, Eqs. (G.6) and (G.7), we have established that $\mathcal{P} \to 0$ as $p \to \frac{1}{2}$, but also that Eqs. (G.5) and (G.7) break down at $p = \frac{1}{2}$ proving that $\mathcal{P}$ is a Jordan matrix with Segrè characteristic $n = 2$. Hence, we have proven that there is a *singularity* at the precise value $p = \frac{1}{2}$, as well as the following theorem:

Theorem: At the degenerate point $p = \frac{1}{2}$, the truth matrix $\mathcal{P}$ is singular, i.e., it is dissimilar to the zero matrix 0 since

$$\mathcal{P} \neq 0; \quad \mathcal{P}^2 = 0 \tag{G.12}$$

The present theorem imparts a special interpretation of the *singularity* since it represents self-referential statements as Jordan blocks (Segrè characteristics larger than one) in our quantum logical framework. For example choosing $P = G$, where G is the famous Gödel arithmetical proposition constructed so that neither G nor $\neg G$ are provable within the given set of axioms of elementary arithmetic [5]. The present formulation displays a *singularity*, given that $\mathcal{P}$ is nondiagonal, while the truth table tells that simultaneously G is not true and $\neg G$ is not false or both G and $\neg G$ are false. The fundamental implication is that decoherence into classical truth-values (collapse of wavefunction) is not possible at the special point $p = \frac{1}{2}$. Note that classical truth-values, being here undecidable, will not reveal any singularity in Eq. (G.6) since $P^2 = 0$. Note that the canonical vectors in (G.10) nevertheless replicates inclusive uncertainty with respect to input information.

Summarizing we find that the classical contradiction or paradox related with the Gödel proposition G has been represented by a matrix degeneracy with a Segrè characteristic equal to two. In this formulation, we have reproduced a truth functional propositional calculus by "quantum-like" states determined by probability operators/functions. This allows the case $p = \frac{1}{2}$ to

be expressed as a quantum transition between truth and falsity (cf. Cantor's diagonal slash argument). Hence, we have succeeded to give a well-defined, yet singular, formulation, of a classical inconsistency. Regardless of the fact that the situation seems contraintuitive, we will see in Section 3 that our result offers new perspectives and opportunities to consider, characterize, study, and program the emergent Jordan block structures in the evolution of coherent dissipative systems and comparable biological organization. Most surprisingly we will establish simple connections with the self-referential aspects of gravitational interactions.

ACKNOWLEDGMENTS

I gratefully acknowledge financial support over the years from the Swedish Natural Science Research Council, the Swedish Research Council for Engineering Sciences, the Foundation for Strategic Research and the Royal Swedish Academy of Sciences. The author is indebted to Alejandro Engelmann for making the picture, Figure 2.11, in relation to Ref. [78].

REFERENCES

[1] H. Feigl, M. Brodbeck, Readings in the Philosophy of Science, Appleton-Century-Crofts, Inc., New York, 1953.
[2] E. Schrödinger, Quantisierung als Eigenwertproblem, Annal. d. Physik. 79 (1926) 361.
[3] W. Heisenberg, Über den anschaulichen Inhalt der quantentheoretischen Kinematik und Mechanik, Zeitschrift. für. Physik. 43 (1927) 172.
[4] P.A.M. Dirac, Principles of Quantum Mechanics, Oxford University Press, London, 1930.
[5] K. Gödel, Über Formal Unentscheidbare Sätze der Principia Matematica und Verwandter Systeme I, Monatshefte für Mathematik und Physik. 38 (1931) 173.
[6] D.J. Chalmers, The Conscious Mind: In Search of a Fundamental Theory, Oxford University Press, Oxford, 1996.
[7] E. Brändas, Complex Symmetry, Jordan Blocks and Microscopic Selforganization: An Examination of the Limits of Quantum Theory Based on Nonself-adjoint Extensions with Illustrations from Chemistry and Physics, in: N. Russo, V. Ya. Antonchenko, E. Kryachko (Eds.), *Self-Organization of Molecular Systems: From Molecules and Clusters to Nanotubes and Proteins*, NATO Science for Peace and Security Series A: Chemistry and Biology, Springer Science+Business Media B.V., Dordrecht, 2009, p. 49.
[8] E.J. Brändas, Partitioning Technique for Open Systems, Mol. Phys. 108 (2010) 3259.
[9] E.J. Brändas, Time Asymmetry and the Evolution of Physical Laws, in Frontiers in Quantum Systems in Chemistry and Physics, in: P. Hoggan, E. Brändas, J. Maruani, P. Piecuch, G. Delgado Barrio, Springer Verlag, Dordrecht, Vol. XXI, 2011, p. 3.
[10] E. Mayr, What Makes Biology Unique? Cambridge University Press, Cambridge, 2004, pp. 1–232.
[11] M. Seel, J. Ladik, The Tragicomedy of Modern Theoretical Biology, in: P. Weingartner, G. Dorn (Eds.), Foundations of Biology, Verlag Hölder-Pichler-Tempsky, Vienna, 1986, p. 145.
[12] F. Dyson, Time Without End: Physics and Biology in an Open Universe, Rev. Mod. Phys. 51 (1979) 447.

[13] S. Penrose, Shadows of the Mind: A Search for the Missing Science of Consciousness, Oxford University Press, Oxford, 1994.
[14] S. Hawking, The Objections of an Unshamed Reductionist, in: M. Longair (Ed.), The Large, the Small and the Human Mind, Cambridge University Press, 1997, p. 169.
[15] C.A. Nicolaides, E.J. Brändas (Eds.), Unstable States in the Continuous Spectra, Part I: Analysis, Concepts, Methods, and Results, Adv. Quant. Chem. 60 (2010).
[16] P. Froelich, E. Brändas, Variational Principle for Quasibound States, Phys. Rev. A12 (1975) 1; P. Froelich, E. Brändas, Calculation of Resonance Widths via $\mathcal{L}^2$ Expansion Techniques, Int. J. Quant. Chem. Symp. 10 (1976) 353.
[17] E. Brändas, P. Froelich, Continuum Orbitals, Complex Scaling, and the Extended Virial Theorem, Phys. Rev. A16 (1977) 2207.
[18] C.A. Nicolaides, D.R. Beck, A Variational Method for Calculating the Energies and Widths of Resonances, Phys. Lett. 60A (1977) 92; C.A. Nicolaides, D.R. Beck, The Variational Calculation of Energies and Widths of Resonances, Phys. Lett. 65A (1978) 11.
[19] E.A. Gislason, N.H. Sabelli, New Form of the Time-Energy Uncertainty Relation, Phys. Rev. 31 (1985) 2078.
[20] C.A. Nicolaides, Theory and State-Specific Methods for the Analysis and Computation of Field-Free and Field-Induced Unstable States in Atoms And Molecules, Adv. Quant. Chem. 60 (2010) 163; C.A. Nicolaides, Time-Dependence, Complex Scaling and the Calculation of Resonances in Many-Electron Systems, Int. J. Quant. Chem. 14 (1978) 457.
[21] P.O. Löwdin, A Note on the Quantum-Mechanical Perturbation Theory, J. Chem. Phys. 19 (1951) 1396.
[22] P.O. Löwdin, Studies in Perturbation Theory, I-XIII; PT X, Phys. Rev. 139 (1965) A357; PT XIII, Int. J. Quant. Chem. 2 (1968) 867; P.O. Löwdin, O. Goscinski, PT XIV, Int. J. Quant. Chem. 5 (1971) 685–705.
[23] D.A. Micha, E. Brändas, Variational Methods in the Wave Operator Formalism. A Unified Treatment for Bound and Quasi-Bound Electronic and Molecular States, J. Chem. Phys. 55 (1971) 4792.
[24] E. Brändas, O. Goscinski, Variation-Perturbation Expansions and Padé Approximants to the Energy, Phys. Rev. A1 (1970) 552.
[25] E. Brändas, D.A. Micha, Variational Methods in the Wave Operator Formalism. Applications in Variation Perturbation Theory and the Theory of Energy Bounds, J. Math. Phys. 13 (1972) 155.
[26] S. Nakajima, On Quantum Theory of Transport Phenomena – Steady Diffusion, Prog. Theor. Phys. 20 (1958) 948.
[27] R. Zwanzig, Ensemble Method in the Theory of Irreversibility, J. Chem. Phys. 33 (1960) 1338.
[28] C.H. Obcemea, E. Brändas, Analysis of Prigogine's Theory of Subdynamics, Ann. Phys. 151 (1983) 383.
[29] E. Brändas, R.J. Bartlett, Reduced Partitioning Technique for Configuration Interaction Calculations Using Padé Approximants and Inner Projections, Chem. Phys. Lett. 8 (1971) 153.
[30] E.J. Brändas, The Reduced Partitioning Technique Revisited, Mol. Phys. 103 (2005) 2073.
[31] Dz. Belkic, Quantum-Mechanical Signal Processing and Spectral Analysis, Institute of Physics Publishing, Series in Atomic and Molecular Physics, Bristol, 2005.
[32] H. Weyl, Über gewöhnliche Differentialgleichungen mit Singularitäten und die zugehörigen Entwicklungen willkürlicher Funktionen, Math. Ann. 68 (1910) 220.
[33] E.C. Titchmarsh, Eigenfunction Expansions Associated with Second-Order Differential Equations, Claredon, Oxford, Vol. 1, 1946, 1962; Vol. 2, 1958.
[34] J. Chaudhuri, W.N. Everitt, On the Spectrum of Ordinary Second-Order Differential Equations, Proc. Roy. Soc. Edinburgh A 68 (1969) 95.

[35] M. Hehenberger, H.V. McIntosh, E. Brändas, Weyl's Theory Applied to the Stark Effect in the Hydrogen Atom, Phys. Rev. A10 (1974) 1494.
[36] E. Brändas, M. Rittby, N. Elander, Titchmarsh-Weyl Theory and Its Relations to Scattering Theory: Spectral Densities and Cross Sections; Theory and Applications, J. Math. Phys. 26 (1985) 2648.
[37] L.P. Eisenhart, Separable Systems in Euclidean 3-Space, Phys. Rev. 45 (1934) 427.
[38] T. Levitina, E.J. Brändas, Scattering by a Potential Separable in Ellipsoidal Coordinates, Int. J. Quant. Chem. 65 (1997) 601.
[39] T. Levitina, E.J. Brändas, On the Schrödinger Equation in Ellipsoidal Coordinates, Comput. Phys. Commun. 126 (2000) 107.
[40] E.A. Coddington, N. Levinson, Theory of Ordinary Differential Equations, McGraw Hill, New York, 1955.
[41] E. Engdahl, E. Brändas, Generalized Green's Functions and Spectral Densities in the Complex Plane, J. Math. Phys. 27 (1986) 2629.
[42] E. Engdahl, E. Brändas, M. Rittby, N. Elander, Resonances and Background: A Decomposition of Scattering Information, Phys. Rev. A37 (1988) 3777.
[43] E. Brändas, Time Evolution and Spectral Concentration in Quantum Systems, Physica 82A (1976) 97; E. Brändas, P. Froelich, A. Remark on Time Evolution and Spectral Concentration, Int. J. Quant. Chem. S9 (1975) 457.
[44] R. Jost, A. Pais, On the Scattering of a Particle by a Static Potential, Phys. Rev. 82 (1951) 840.
[45] K. Kodaira, The Eigenvalue Problem for Ordinary Differential Equations of the Second Order and Heisenberg's Theory of S-Matrices, Am. J. Math. 71 (1949) 921.
[46] M. Hehenberger, B. Laskowski, E. Brändas, Weyl's Theory Applied to Predissociation by Rotation. I. Mercury Hydride, J. Chem. Phys. 65 (1976) 4559.
[47] E Brändas, M. Hehenberger, H.V. McIntosh, Dispersion Relations and Spectral Densities, Int. J. Quant. Chem. 9 (1975) 103.
[48] R.G. Newton, Scattering Theory of Waves and Particles, Springer Verlag, New York, 1966, 1983.
[49] N.I. Akhiezer, The Classical Moment Problem, First English Edition, Oliver & Boyd Ltd, Edinburgh and London, 1965.
[50] E. Balslev, J.M. Combes, Spectral Properties of Many-Body Schrödinger Operators with Dilatation-Analytic Interactions, Commun. Math. Phys. 22 (1971) 280.
[51] G. Gamow, Zur Quantentheorie des Atomkernes, Z. Phys. 51 (1928) 204.
[52] E. Brändas, N. Elander (Eds.), Resonances the Unifying Route Towards the Formulation of Dynamical Processes Foundations and Applications in Nuclear, Atomic and Molecular Physics, Vol. 325, Springer Verlag, Berlin, Lecture Notes in Physics, 1989.
[53] M. Reed, B Simon, Methods of Modern Mathematical Physics IV: Analysis of Operators, Academic Press, New York, 1978.
[54] E. Nelson, Analytic Vectors, Ann. Math. 70 (1959) 572.
[55] C.A. Nicolaides, H.J. Gotsis, On the Calculation of the Complex Energies of Resonances, J. Phys. B. 25 (1992) L171; C.A. Nicolaides, S.I. Themelis, Theory of the Resonances of the LoSurdo-Stark Effect, Phys. Rev. A45 (1992) 349.
[56] U.V. Riss, H.-D. Meyer, Calculation of Resonance Energies an Widths Using the Complex Absorbing Potential Method, J. Phys. B: Atom. Mol. Opt. Phys. 26 (23) (1993) 4503.
[57] I.W. Herbst, J.S. Howland, The Stark Ladder and Other One-Dimensional External Field Problems, Commun. Math. Phys. **80** (1981) 23; J.S. Howland, Complex Scaling of ac Stark Hamiltonians, J. Math. Phys. **24** (1982) 1240.
[58] W. P. Reinhardt, Complex Scaling in Atomic Physics: A Staging Ground for Experimental Mathematics and for Extracting Physics from Otherwise Impossible Computations, In Spectral Theory and Mathematical Physics: A Fest Schrift in Honor of Barry Simon's 60th

Birthday, in: F. Gesztesy, P. Deift, C. Galvez, P. Perry, W. Schlag (Eds.), Proceedings in Pure Mathematics, American Mathematical Society, Providence, Rhode Island, Vol. 76, Part I, 2007, p. 357.
[59] E. Engdahl, E. Brändas, Resonance Regions Determined by a Projection-Operator Formulation, Phys. Rev. A37 (1988) 4145.
[60] N. Moiseyev, Resonance by the Complex Coordinate Method with Hermitean Hamiltonian, Chem. Phys. Lett. 99 (1983) 364.
[61] N. Moiseyev, Non-Hermitean Quantum Mechanics, Cambridge University Press, Cambridge, 2011.
[62] H.K.H. Siedentop, Bound on Resonance Eigenvalues of Schrödinger Operators, Phys. Lett. 99A (1983) 65.
[63] P. Froelich, E.R. Davidson, E. Brändas, Error Estimates for Complex Eigenvalues of Dilated Schrödinger Operators, Phys. Rev. A28 (1983) 2641.
[64] E. Brändas, O. Goscinski, Symmetry-Adapted Second-Order Energy. Some Comments and Results for H^{2+}, J. Chem. Phys. 51 (1969) 975.
[65] P.O. Löwdin, Scaling Problem, Virial Theorem, and Connected Relations in Quantum Mechanics, J. Mol. Spectros. 3 (1959) 46.
[66] G. Doolen, A Procedure for Calculating Resonance Eigenvalues, J. Phys. B: At. Mol. Phys. 8 (1975) 525.
[67] W.P. Reinhardt, Method of Complex Coordinates: Application to the Stark Effect in Hydrogen, Int. J. Quant. Chem. Symp. 10 (1976) 359
[68] N. Moiseyev, P.R. Certain, F. Weinhold, Resonance Properties of Complex-Rotated Hamiltonians, Mol. Phys. 36 (1978) 1613.
[69] R. Yaris, P. Winkler, Electron Scattering Resonances Using Dilatation Transformations. I. Conditions for Dilatational Stability, J. Phys. B: At. Mol. Phys. 11 (1978) 1475.
[70] J.O. Nordling, J.S. Faulkner, Approximate Linear Dependence, Scaling and Operator Convergence in the Harmonic Oscillator Problem, J. Mol. Spectros. 12 (1964) 171.
[71] P. Froelich, M. Hehenberger, E. Brändas, A Note on the Complex Transformation Method and the Extended Virial Theorem for Treating Resonances in the Continuous Spectrum, Int. J. Quant. Chem. S11 (1977) 295.
[72] J. Kumicák, E. Brändas, Some Aspects of Approach to Equilibrium in Classical and Quantum Systems, Int. J. Quant. Chem. 32 (1987) 669.
[73] J. Kumicák, E. Brändas, Complex Scaling and Lyapunov Converters, Int. J. Quant. Chem. 46 (1993) 391.
[74] M. Reed, B Simon, Methods of Modern Mathematical Physics II: Fourier Analysis, Self-Adjointness, Academic Press, New York, 1975.
[75] G. Braunss, Intrinsic Stochasticity of Dynamical Systems, Acta Appl. Math. 3 (1985) 1.
[76] C.E. Reid, E. Brändas, On a Theorem for Complex Symmetric Matrices and Its Relevance in the Study of Decay Phenomena, Lect. Notes. Phys. 325 (1989) 476.
[77] E. Brändas, A Theorem for Complex Symmetric Matrices Revisited, Int. J. Quant. Chem. 109 (2009) 2860.
[78] A.R. Engelmann, M.A. Natiello, M. Höghede, E. Engdahl, E. Brändas, Association of Bound States of the Coulomb Potential with Resonances of the Coulomb Potential Perturbed by a Barrier, Int. J. Quant. Chem. 31 (1987) 841.
[79] M.A. Natiello, E.J. Brändas, A.R. Engelmann, Some Comments on the Alteration of the Coulomb Bound States by a Barrier Perturbation, Int. J. Quant. Chem. Symposium. 21 (1987) 555.
[80] E. Brändas, Resonances and Microscopic Irreversibility: An introduction, Int. J. Quant. Chem. (1993) 339.
[81] J. Barbour, The End of Time the Next Revolution of Physics, Oxford University Press, Oxford, 1999.

[82] E. Brändas, Some Comments on the Problem of Decoherence, Int. J. Quant. Chem. 111 (2011) 215.
[83] E. Brändas, Gödelian Structures and Self-Organization in Biological Systems, Int. J. Quant. Chem. 111 (2011) 1321.
[84] M.S.P. Eastham, On the Location of Spectral Concentration for Sturm-Liouville Problems with Rapidly Decaying Potential, Mathematika 45 (1998) 25.
[85] D.J. Gilbert, B.J. Harris, Bounds for the Points of Spectral Concentration of Sturm-Liouville Problems, Mathematika 47 (2000) 327.
[86] B.M. Brown, M.S.P. Eastham D.K.R. McCormack, Resonances and Analytic Continuation for Exponentially Decaying Sturm-Liouville Potentials, J. Comp. Appl. Math. 116 (2000) 181.
[87] E. Brändas, N. Elander, P. Froelich, Extended Virial Theorem Applied to Predissociation Phenomena. Interpretation of the Nearly Degenerate $G^1\Pi \sim I^1\Pi$ Energy Spectra in SiO, Int. J. Quant. Chem. XIV (1978) 443.
[88] E. Brändas, P. Froelich, M. Hehenberger, Theory of Resonances in Many-Body Systems: Spectral Theory of Unbounded Schrödinger Operators, Complex Scaling, and Extended Virial Theorem, Int. J. Quant. Chem. XIV (1978) 419.
[89] M. Hehenberger, P. Froelich, E. Brändas, Weyl's Theory Applied to Predissociation by Rotation. II. Determination of Resonances and Complex Eigenvalues: Application to HgH, J. Chem. Phys. 65 (1976) 4571.
[90] P. Krylstedt, N. Elander, E. Brändas, Complex Scaled Local Density Calculations: A Review of Recent Developments, Int. J. Quant. Chem. Symp. 20 (1986) 253.
[91] P. Krylstedt, M. Rittby, N. Elander, E. Brändas, A Complex Rotated Approach to Resonant Electron Scattering on Atoms in a Static Exchange Plus Polarization Formulation, J. Phys. B: At. Mol. Phys. 20 (1987) 1295.
[92] P. Krylstedt, N. Elander, E. Brändas, A Complex Dilated Study of Shape Resonances and Negative Ions in Electron-Atom Scattering, within an Asymptotic Complete Form of Continuum Exchange, J. Phys. B: At. Mol. Opt. Phys. 22 (1989) 1623.
[93] M. Rittby, N. Elander, E. Brändas, A. Bárány, Resonance Structure in Charge Transfer Cross Sections: An Application to the $N^{3+} + H \rightarrow N^{2+} + H^+$ Reaction, J. Phys. B: At. Mol. Phys. 17 (1984) L677.
[94] E. Brändas, N. Elander, Energy Scrambling Out in the Continuum: Weyl's Theory and Predissociation, in: J. Hinze (Ed.), Proceedings Bielefeld Symposium on Energy Storage and Redistribution in Molecules, Plenum Press, New York, 1983, p. 543.
[95] E. Brändas, C.A. Chatzidimitriou-Dreismann, On the Connection Between Certain Properties of the Second-Order Reduced Density Matrix and the Occurrence of Coherent-Dissipative Structures in Disordered Condensed Matter, Int. J. Quant. Chem. 40 (1991) 649.
[96] C.A. Chatzidimitriou-Dreismann, E.J. Brändas, Proton Delocalization and Thermally Activated Quantum Correlations in Water: Complex Scaling and New Experimental Results, Ber. Bunsenges. Phys. Chem. 95 (1991) 263.
[97] C.A. Chatzidimitriou-Dreismann, E.J. Brändas, Coherence in Disordered Condensed Matter. IV: Conductivities of Molten Alkali Chlorides – A Novel Relation, Ber. Bunsenges. Phys. Chem. 93 (1989) 1065.
[98] E.J. Brändas, C.A. Chatzidimitriou-Dreismann, Coherence in Disordered Condensed Matter. V: Thermally Activated Quantum Correlations in High-T_C Superconductivity, Ber. Bunsenges. Phys. Chem. 95 (1991) 462.
[99] L.J. Dunne, E.J. Brändas, D-Wave Bipolaronic Condensate with Short Range Repulsive Electronic Correlations in an Extended Hubbard Model of High-T_C Cuprate Superconductors, Adv. Quant. Chem. 40 (2001) 225.
[100] E.J. Brändas, Quantum Correlations and Topological Quantum Numbers in the Fractional Quantum Hall Effect, Ber. Bunsenges. Phys. Chem. 96 (1992) 49.

[101] C.A. Chatzidimitriou-Dreismann, E.J. Brändas, E. Karlsson, Quantum Correlation Effects in the Spin Dynamics of Gd at High Temperatures in the Light of Complex Dilation Theory, Phys. Rev. Rapid. Commun. B 42 (1990) 2704.
[102] E.J. Brändas, Relaxation Processes and Coherent Dissipative Structures, in: E. Lippert, J.D. Macomber (Eds.), Dynamics during Spectroscopic Transitions, Springer Verlag, Berlin, 1995, p. 148.
[103] E.J. Brändas, Applications of CSM Theory, in: E. Lippert, J.D. Macomber (Eds.), Dynamics during Spectroscopic Transitions, Springer Verlag, Berlin, 1995, p. 194.
[104] E.J. Brändas, Resonances and Dilation Analyticity in Liouville Space, Adv. Chem. Phys. 99 (1997) 211.
[105] F.R. Gantmacher, The Theory of Matrices, Vols. I and II, Chelsea Publishing, New York, 1959.
[106] C.N. Yang, Concept of Off-Diagonal Long-Range Order and the Quantum Phases of Liquid He and of Superconductors, Rev. Mod. Phys. 34 (1962) 694.
[107] A.J. Coleman, Structure of Fermion Density Matrices, Rev. Mod. Phys. 35 (1963) 668.
[108] M. Rittby, N. Elander, E. Brändas, Scattering in View of the Titchmarsh-Weyl Theory, Int. J. Quant. Chem. XXIII (1983) 865.
[109] N. Elander, M. Hehenberger, P.R. Buenker, Theoretical Studies Related to Time Resolved Spectroscopy: The Iterative Rydberg-Klein-Dunham Method and Weyl Theory Applied to the Predissociations in the $B^2\Sigma^-$ State of CH, Phys. Scr. 20 (1979) 631.
[110] M. Rittby, N. Elander, E.J. Brändas, Complex Rotated Titchmarsh-Weyl Theory: A Review and Some Recent Results, Int. J. Quant. Chem. S17 (1983) 117.
[111] B. Simon, The Definition of Molecular Resonance Curves by the Method of Exterior Complex Scaling, Phys. Lett. A71 (1979) 211.
[112] B. Gyarmati, R.T. Vertse, On the Normalization of Gamow Functions, Nucl. Phys. A160 (3) (1971) 523.
[113] A.M. Dykhne, A.V. Chaplik, Normalization of the Wave Functions of Quasi Stationary States, Sov. Phys. JETP 13 (1961) 1002.
[114] B. Helffer, Comparison Between Different Notions of Resonances, Lect. Notes Phys. 325 (1989) 11.
[115] E. Brändas, M. Rittby, N. Elander, Multichannel Complex Scaled Titchmarsh Weyl Theory a Model for Diatomic Fragmentation, Lect. Notes Phys. 325 (1989) 345.
[116] E. Brändas, M. Hehenberger, Determination of Weyl's m-Coefficient for a Continuous Spectrum, Lect. Notes Math. 415, (1974) 316.
[117] J. Oddershede, N. Elander, Spectroscopic Constants and Radiative Lifetimes for Valence-Excited Bound States, J. Chem. Phys. 56 (1972) 3495.
[118] C. Froese Fischer, J.B. Lagowski, S.H. Vosko, Ground States of Ca^- and Sc^- from Two Theoretical Points of View, Phys. Rev. Lett. 59 (1987) 2263.
[119] D.J. Pegg, J.S. Thompson, R.N. Compton, G. Alton, Evidence for a Stable Negative Ion of Calcium, Phys. Rev. Lett. 59 (1987) 2267.
[120] W.C. Stwalley, Mass-Reduced Quantum Numbers: Application to the Isotopic Mercury Hydrides, J. Chem. Phys. 63 (1975) 3062.
[121] S.L. Yakolev, M.V. Volkov, E. Yarevsky, N. Elander, The Impact of Sharp Screening on the Coulomb Scattering Problem in Three Dimensions, J. Phys. A: Math. Theor. 43 (2010) 245302.
[122] E. Brändas, C.A. Chatzidimitriou-Dreismann, Creation of Long Range Order in Amorphous Condensed Systems, Lect. Notes Phys. 325 (1989) 485.
[123] Y.J. Uemura, G.M. Luke, B.J. Sternlieb, J.H. Brewer, J.F. Carolan, W.N. Hardy, R. Kadono, J.R. Kempton, R.F. Kiefl, S.R. Kreitzman, P. Mulhern, T.M. Riseman, D.L. Williams, B.X. Yang, S. Uchida, H. Takagi, J. Gopalakrishnan, A.W. Sleight, M.A. Subramanian, C.L. Chien, M.Z. Cieplak, G. Xiao, V.Y. Lee, B.W. Statt, C.E. Stronach, W.J. Kossler, X.H. Yu,

Universal Correlations between T_C and n_s/m^* (Carrier Density over Effective Mass) in High-T_C Cuprate Superconductors, Phys. Rev. Lett. (1989) 2317.
[124] L.J. Dunne, E.J. Brändas, J.N. Murrell, V. Coropceanu, Group Theoretical Identification of Active High-TC-Cuprate Superconductors, Solid State Commun. 108 (1998) 619.
[125] E.J. Brändas, L.J. Dunne, J.N. Murrell, Phenomenological Description of d-Wave Condensates of High-T_C Superconducting Cuprates, in: J. Maruani et al. (Eds.), New Trends in Quantum Systems in Chemistry and Physics, Kluwer Academic Publishers, Vol. 2, 2000, p. 289.
[126] H. Zhang, H. Sato, Universal Relationship Between T_C and the Hole Content in *p*-Type Cuprate Superconductors, Phys. Rev. Lett. 70 (1993) 1697.
[127] J.W. Cable, R.M. Nicklow, Spin Dynamics of Gd at High Temperatures, Phys. Rev. B39 (1989) 11732.
[128] E.J. Brändas, Microscopic Self-Organization and Self-Referential Systems. A Progress Report. Int. J. Quant. Chem. 109 (2009) 3500.
[129] E. Segal, Y. Fondufe-Mittendorf, L. Chen, A Thåström, Y. Field, I. K. More, J-P. Z. Wang, J. Widom, A Genomic Code for Nucleosome Positioning, Nature 442 (2006) 772.

CHAPTER 3

Resonances in Bimolecular Chemical Reactions

Rex T. Skodje[a]

Contents

Abstract

The existence of reactive resonances has long been predicted based on theoretical quantum reaction dynamics. Although many aspects of the theoretical modeling of such resonances are understood, it has remained an open question as to how resonance phenomena may be observed in a molecular beam experiment. Many of the simple ideas for resonance signatures are based on the idealization of the isolated narrow resonance, which generally does not

[a] Department of Chemistry and Biochemistry, University of Colorado, Boulder, CO 80309, USA
E-mail address: Rex.Skodje@Colorado.EDU

Advances in Quantum Chemistry, Volume 63
ISSN 0065-3276, DOI: 10.1016/B978-0-12-397009-1.00003-5

apply to reactive resonances. Due to the occurrence of impact parameter averaging, the resonant scattering becomes smeared over broad ranges of collision energy making it difficult to distinguish between direct and complex scattering mechanisms. In this article, recent advances in the study of short-lived reactive resonances are reviewed. The imprint of resonances upon dynamical observables is discussed. Three case studies are presented for simple triatomic systems that are believed to exhibit resonance phenomena: $F+HD \rightarrow D+HF$, $H+HD \rightarrow D+H_2$, and $F+HCl \rightarrow Cl+HF$. It is seen that reactive resonances do strongly influence collision observables, but in a different way for each case. At this stage, there does not appear to be a unique resonance signature that can be applied to all reactions.

1. INTRODUCTION

Gas phase bimolecular chemical reactions are collision processes in which reagent molecular species scatter from one another and produce product species where the pattern of bonding has changed. Reactive scattering is thus an example of rearrangement scattering similar to problems frequently encountered in nuclear and atomic physics. As with many other scattering problems, chemically reactive scattering can exhibit resonance phenomena associated with trapping in the interaction region. Chemically reactive resonances (or just reactive resonances) are interesting because of the great diversity of resonant mechanisms that have been found, and perhaps the unique union of experiment and theory that is required to confirm their existence in particular problems.

It is useful to distinguish chemical reactions that proceed directly over a potential barrier from those that form intermediate complexes. In terms of kinetic modeling, complex forming reactions in the limit of long lifetimes can be viewed as a two-step process involving the formation and decay of the intermediate complex. In some problems, the occurrence of reactive complexes is totally predictable based on the existence of deep potential energy wells along the reaction coordinate. Well-known examples include ion–molecule reactions and insertion-type reactions. For cases where deep-well trapping occurs, the mean lifetime for the intermediates will typically be quite long, i.e., at least hundreds of internal vibrational periods. In principle, this permits the "complex molecules" to be studied as a distinct chemical species from either the reactants or products. Such an approach is commonly used in traditional chemical modeling. On the other hand, complexes have also recently been observed for systems where the potential energy surface (PES) is purely (or dominantly) repulsive. In these cases, the intermediates tend to be extremely short-lived and are often viewed inseparably from the collision process itself [1–10]. For reactions that fall into this category, which include a number of hydrogen abstraction reactions like $F+HD \rightarrow HF+D$, the trapping occurs due to dynamical effects

near the transition state and is not obvious from the landscape of the PES. The theoretically predicted lifetimes of these intermediates are often just a few, or merely one, internal vibrational period. Despite their transitory existence, these "reactive resonances" can strongly influence the rate of reaction, the rovibrational product state distribution, and the angular distribution of product molecules. However, it is on more fundamental grounds that reactive resonances have proven to be of most interest. Since resonance energies and lifetimes are extremely sensitive functions of the PES and dynamics near the transition state, these elusive states can be viewed as probes of the transition state regions [11]. The spectroscopy of resonance states can provide critical information about bond forming and bond breaking at the most basic level.

The possibility of the existence of short-lived reactive resonances has been discussed often over the years. The early advances in this field were largely theoretical and based on the analysis of quantum reaction dynamics using approximate PESs [12–20]. These studies provided much insight into the dynamical origin of complex formation. However, they were speculative in that the PES and dynamics calculations were too approximate to permit quantitative comparisons with experiment. The extreme sensitivity of resonance properties to the PES and dynamical approximations greatly reduced the usefulness of these calculations in studying real systems. With the dramatically increased computational power now available, theory has evolved to the point where very accurate potential surfaces and essentially converged quantum scattering calculations can be used to predict the existence of reactive resonances a priori for sufficiently simple systems [21–27]. Furthermore, techniques of analysis have been developed that allow the resonance wavefunction to be extracted, and hence, the full assignment of quantum numbers and other physical characteristics [28–31].

Although theoretical techniques for the characterization of resonance states advanced, the experimental search for reactive resonances has proven to be a much more difficult task [32–34]. The extremely short lifetime of reactive resonances makes the direct observation of these species very challenging. In some reactions, transition state spectroscopy can be employed to study resonances through "half-collision experiments," where even very short-lived resonances may be detected as peaks in a Franck–Condon spectrum [35–38]. Neumark and coworkers [39] were able to assign peaks in the $[IHI]^-$ photodetachment spectrum to resonance states for the neutral $I+HI$ reaction. Unfortunately, transition state spectroscopy is not always feasible due to the absence of an appropriate Franck–Condon transition or due to practical limitations in the required level of energetic resolution. The direct study of reactive resonances in a full collision experiment, such as with a molecular beam apparatus, is the traditional and more usual environment to work. Unfortunately, observing resonance behavior in such experiments has proven to be exceedingly difficult. The heart of the problem is not a

technical issue in experiment, but rather it is a lack of knowledge about how the existence of a resonance will affect the collision observables in a uniquely identifiable way. As of this point, there is no known general and unique resonance signature that can be sought, even given perfectly resolved scattering cross-sectional data.

In this article, we shall review recent advances that have been made in detecting and understanding short-lived reactive resonances. Theory and experiment have matured to the point where state- and angle-resolved reactive cross sections can be measured accurately in the laboratory and brought into quantitative agreement with the results of converged scattering calculations on an accurate PES. We shall attempt to illustrate how theory and experiment can work in tandem to identify resonance signatures in reactive collisions. In Section 2, a practical discussion of the theory of reactive resonances is presented, with special emphasis given to how collision observables are affected by the existence of a resonance. In Sections 3–5, we shall present three case studies of systems where reactive resonances are believed to exist: *F+HD*, *H+HD*, and *F+HCl*. Although these three hydrogen abstraction reactions are seemingly quite similar, we shall see that, in fact, the resonance signatures are very different in each case. We are thus led to the conclusion that the search for resonance signatures in collision experiments must still be pursued on a case-by-case basis with close interplay between theory and experiment. Finally, in Section 6 we present a brief conclusion.

2. THEORETICAL METHODS FOR REACTIVE RESONANCES

The theory of resonance phenomena in scattering has been an enduring topic of study in physics and chemistry since the advent of quantum mechanics. As a problem in mathematical physics, the study of resonance can be an extremely elegant formal pursuit. Indeed, there have been countless theoretical studies of resonance scattering that have reformulated the subject in new and interesting ways. We shall not attempt to review that massive literature, and instead we shall simply refer the interested reader to the previous volumes in the present series. Here, we shall focus on those methods that have some practical bearing on the analysis of chemical resonances. Furthermore, we shall restrict ourselves to those methods that have proven to be actually useful in understanding or modeling real reactive resonances. We shall emphasize a few of the main themes that underlie computational methods that have proven useful for computing resonance properties. The most interesting cases are resonances described by a single Born–Oppenheimer PES that exhibits no deep trapping wells. Of course, this excludes interesting behavior associated with nonadiabatic coupling, as well as issues arising from dense manifolds of overlapping resonances. This is consistent with our

goal to investigate how resonances affect scattering observables for simple barrier-type potential, rather than providing an exhaustive review.

2.1. Vibrationally adiabatic model: an ultra simple model

We begin with a simple physical picture of chemical resonance that goes back to the earliest treatments of the reactive resonance problem. Resonance phenomenon can generically be associated with some form of dynamical trapping in the interaction region. The trapping involved in the formation of reactive resonances occurs near the transition state barrier. Sometimes, the trapping can be at relatively long range associated with shallow van der Waal wells that lie in the entrance or exit channels. In such cases, the reagent (or product) species are more-or-less intact in their bonding structure. Other times, the resonance state is localized near the saddle point of the PES and the chemical bonds of the complex are partially broken (or formed). In such cases, the nature of the trapping is dynamical in origin and cannot be easily inferred directly from the PES.

The conventional interpretation of reactive resonances makes use of one-dimensional dynamical potentials constructed using decoupling approximations such as the vibrationally adiabatic theory of reaction [40]. In this way, the multidimensional reaction dynamics is modeled using a set of effective potential barriers constructed along a reaction coordinate; each of these curves represents different internal excitations of the collision complex. In natural collision coordinates, the reaction coordinate "$\boldsymbol{s}$" represents distance along the minimum energy path, whereas the orthogonal vibrational modes are described by the normal mode coordinate "$\boldsymbol{u}$." Although natural collision coordinates are difficult to use since they are curvilinear and numerically defined from the PES, they nevertheless conform to chemists' intuition about how the reaction occurs. The vibrationally adiabatic theory is constructed assuming that the quantum number $\boldsymbol{n}$, corresponding to the modes described by the coordinate $\boldsymbol{u}$, is conserved during the collision [41, 42]. Thus, one obtains vibrationally adiabatic potential curves of the form

$$V_{\mathrm{ad}}(\boldsymbol{s};\boldsymbol{n}) = V_0(\boldsymbol{s}) + \varepsilon_{\boldsymbol{n}}(\boldsymbol{s}), \tag{1}$$

where $V_0(\boldsymbol{s})$ is the potential along reaction path and $\varepsilon_{\boldsymbol{n}}(\boldsymbol{s})$ are the quantized state energies of the orthogonal motion. Since the vibrational frequencies tend to change dramatically near the transition state, $V_{\mathrm{ad}}(\boldsymbol{s};\boldsymbol{n})$ can be quite different from the Born–Oppenheimer surface and can even exhibit wells although the PES is purely repulsive. Indeed, near the saddle point where the bonding is weakened, it is common for some of the normal mode frequencies, ω_{i}, to be significantly lower than in the asymptotic region. Thus, the barrier in $V_0(\boldsymbol{s})$ can be overcome by a well in $\varepsilon_{\boldsymbol{n}}(\boldsymbol{s})$ leading to the formation of a well in $V_{\mathrm{ad}}(\boldsymbol{s};\boldsymbol{n})$. Although the dynamical conditions for high-level accuracy of the vibrationally adiabatic model are virtually never satisfied,

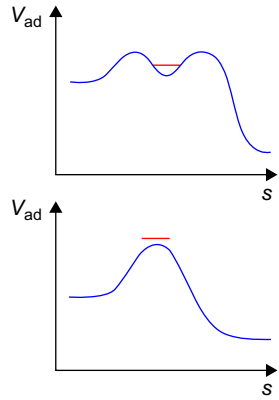

Figure 3.1 A schematic diagram showing the relationship of reactive resonances to the vibrationally adiabatic potential curve. The upper panel illustrates a Feshbach resonance trapped in a well; the lower panel shows a barrier resonance or QBS.

this simple model often captures the essence of reaction dynamics near the transition state.

The resonance trapping can be pictured in a simple one-dimensional representation when expressed in terms of the vibrationally adiabatic curves. There are two common scenarios for resonance formation. First, Feshbach-type resonance states can exist as intermediates trapped in wells on the adiabatic potential curves, as shown in the upper panel of Figure 3.1. This requires the adiabatic wells to be deep enough to support one or more quantum states. Usually, this demands that the collision complex be internally excited (i.e., $\boldsymbol{n} \neq 0$) so that the $\boldsymbol{u}$-direction(s) widening of the PES near the saddle is accentuated in $\varepsilon_n(\boldsymbol{s})$. The resonance state may decay to products by tunneling through the barrier or by energy transfer from $\boldsymbol{u} \rightarrow \boldsymbol{s}$ resulting in a transition to a lower adiabatic curve. The lifetime of the resonance depends strongly on the strength of the vibrationally nonadiabatic coupling. The accuracy of the adiabatic approximation relies on a separation of timescales between the "essential" vibrational motions (described by a few of the most important $\boldsymbol{u}$ coordinates) and the reaction coordinate $\boldsymbol{s}$. When the reaction coordinate is slow compared to the orthogonal vibrational motion, the adiabatic approximation becomes more accurate and the nonadiabatic coupling is smaller.

A second scenario is provided by barrier-type resonances (sometimes referred to as quantum bottleneck states [QBS]), which do not rely on the internal excitation of the collision complex for their existence. In fact, barrier resonances are observed even when there is no well in $V_{\mathrm{ad}}(\boldsymbol{s};\boldsymbol{n})$. Collisional time delay occurs near the barrier maximum simply because the motion along the $\boldsymbol{s}$-coordinate slows down passing over the barrier, as in the lower

panel of Figure 3.1 [1, 29, 43, 44]. This sort of kinematic trapping occurs even in classical mechanics and is related to the existence of a periodic orbit perched on top of the dynamical barrier [45–47]. Although there are some important differences between "barrier-states" and more conventional Feshbach resonances, it can be shown [1, 9, 43, 44, 48–52] that barrier-states behave much like resonances with energy $E_R = V_{\rm ad}(\boldsymbol{s} = \text{barrier}; \boldsymbol{n})$ and width $\Gamma = \hbar\omega$, where ω being the barrier frequency of $V_{\rm ad}(\boldsymbol{s}; \boldsymbol{n})$. The lifetimes of barrier-states are typically about one period of vibration for the most essential $\boldsymbol{u}$-coordinate.

The division of the total Hamiltonian into an adiabatic component, $\boldsymbol{H}_{\rm ad}$, and a nonadiabatic component, $\boldsymbol{H}_{\rm na}$, permits the use of several familiar computational methods to determine the resonance properties. In the limit of weak nonadiabatic coupling, the resonance energies are obtained from the eigenvalues of $\boldsymbol{H}_{\rm ad}$ while the widths and partial widths can be estimated using simple golden rule formulae. For stronger coupling, the full Feshbach projection operator formalism can be employed. Although it is possible to get reasonable approximations to the true resonance widths in this way, this technique is seldom used in practice. The numerical instability of the derivative coupling terms in $\boldsymbol{H}_{\rm na}$, especially when using natural collision coordinates, makes the direct use of the vibrationally adiabatic model undesirable compared to other existing methods. Since chemical reactions usually show significant nonadiabaticity, there are naturally quantitative errors in the predictions of the vibrationally adiabatic model. Furthermore, there are ambiguities about how to apply the theory, such as the optimal choice of coordinate system. It should be pointed out, however, that the vibrationally adiabatic model can be more stable when implemented in other coordinate systems such as hyperspherical coordinates. In particular, for the heavy–light–heavy mass combination it is found that adiabatic model is much more accurate in the hyperspherical coordinate system [53]. Besides the issue of the coordinate system, there is also the matter of which degrees of freedom are identified as "fast" and which as "slow." There can be significant differences in performance of the adiabatic model depending on these choices.

2.2. Barrier resonances

Although barrier resonances have only recently been fully appreciated, they are expected to be quite common in real problems [1, 9, 44, 54]. Since chemical reactions generically exhibit energetic barriers, they will generically possess barrier-type resonances. Barrier resonances are distinguished most clearly from the more conventional Feshbach resonances by the nature of the trapping mechanism. When the energy of the colliding pair of reagent molecules equals the energy of an adiabatic barrier, the classical motion along the reaction coordinate comes to a stop leading to collision time delay. One is tempted to conclude that the distinction between barrier and

Feshbach resonances is purely model dependent since trapping well may exist on one type of adiabatic potential, say in hyperspherical coordinates, while only a barrier may exist on another type, say in natural collision coordinates. However, this is not correct since there are fundamental differences between QBS and Feshbach states. First, the pole structure of the S-matrix is intrinsically different in the two cases. A Feshbach resonance corresponds to a single isolated pole of the scattering matrix (S-matrix) below the real axis of the complex energy plane, see the discussion below. On the other hand, the barrier resonance corresponds to an infinite sequence of poles extending into the lower half plane. For a parabolic barrier, it is easy to show that the pole positions are given by

$$E_n = V_0 - i\hbar\omega(n + 1/2) \quad n = 0, 1, 2, \ldots, \tag{2}$$

where V_0 is the (real) barrier height and ω is the barrier frequency. In a previous work on transition state spectroscopy of barrier resonances, we have demonstrated that this pole structure gives rise to a lineshape formula completely different from the usual Lorentzian form corresponding to conventional Breit–Wigner resonances [29, 50]. Another distinction between Feshbach and barrier-type resonances concerns their behavior in the semiclassical limit. Although Feshbach states correspond to trapped volumes of phase space, barrier-states arise from single-trapped orbits that obviously have zero volume in phase space. Indeed, Sadeghi and Skodje [50] have shown that the lowest-order term in an $\hbar$-expansion of the Wigner phase space distribution for a decaying barrier state is localized on the unstable manifolds of the periodic orbit, i.e.,

$$W(p, q, t) \underset{t\to\infty}{\to} e^{-t/\tau} \sum \delta(p - p_{\mathrm{i}}(q)), \tag{3}$$

where τ is the classical lifetime (the inverse barrier frequency) and $p_{\mathrm{i}}(q)$ are the unstable branches of the reactive separatrix. Finally, we note that the shape of the reaction probability for a barrier resonance shows a threshold structure while a Feshbach state is expected to lead to a generalized Lorentzian peak. From model problems, we can conclude that the step-like threshold behavior of the reaction probability is due to the collective influence of the infinite sequence of poles. For example, an Eckart barrier, $V = V_0/\cos h^2(\alpha x)$, is shown to have a reaction probability, $P_{\mathrm{R}}(E)$, that can be written as [9]

$$P_{\mathrm{R}}(E) = 1 - \left| \prod_{n=0}^{\infty} \frac{k_n}{k - k_n} \right|^2, \tag{4}$$

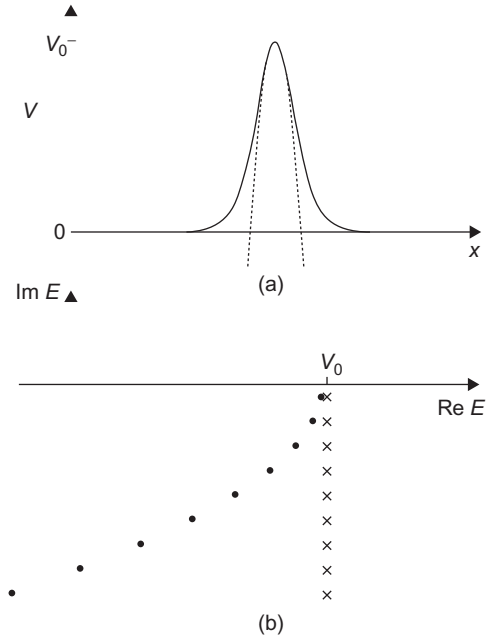

Figure 3.2 The pole structure of the *S*-matrix for a parabola (×) and an Eckart barrier (•).

where $k = \sqrt{2\mu E/\hbar^2}$, k_n are the pole positions

$$k_n = \frac{\hbar\alpha}{2}\left[\sqrt{\frac{8\mu V_0}{\hbar^2\alpha^2} - 1} - i(1+2n)\right], \tag{5}$$

and μ is the mass. In Figure 3.2, we compare the pole structure of a parabolic barrier to that of the Eckart barrier.

One expects to observe a barrier resonance associated with each vibrationally adiabatic barrier for a given chemical reaction. Since the adiabatic theory of reactions is closely related to the rate of reaction, it is perhaps not surprising that Truhlar and coworkers [44, 55] have demonstrated that the cumulative reaction probability, $N_R(E)$, shows the influence barrier resonances. Specifically, dN_R/dE shows peaks at each resonance energy and $N_R(E)$ itself shows a staircase structure with a unit step at each QBS energy. It is a more unexpected result that the properties of the QBS seem to also imprint on other reaction observables such as the state-to-state cross sections [1, 56] and even can even influence the helicity states of the products [57–59]. This more general influence of the QBS on scattering observables makes possible the direct verification of the existence of barrier-states based on molecular beam experiments.

2.3. Computational methods to extract resonance properties

Although simple models for resonance dynamics can prove useful to gain physical insight, the accurate determination of resonance energies, widths, and partial widths is best accomplished using fully quantum mechanical treatment based on the exact Hamiltonian. There have been a wide variety of practical methods proposed to compute the resonance parameters of a system given its Hamiltonian. Some methods attempt to directly obtain the resonance state within an L^2 basis set. These include real and complex stabilization methods and also basis set diagonalization, where $\boldsymbol{H}$ is modified to incorporate a complex absorbing potential. The resonance properties can also be extracted from time-dependent quantum wave packets where the resonance state is filtered from the wave packet using a Fourier transform

$$\varphi_{\text{res}} \sim \int_{-\infty}^{\infty} \phi(t) e^{iE_{\text{res}}t} \mathrm{d}t \tag{6}$$

The spectral quantization (SQ) method, based on Eq. (6), has been found to yield good results for a number of simple chemical reactions.

If it is possible to numerically compute the S-matrix as an accurate function of energy, then a robust method to extract the resonance parameters is to simply fit the S-matrix elements to standard resonance formulae [60, 61]. The usual picture of resonance phenomena is based on the concept of the isolated narrow resonance (INR) proposed by Breit and Wigner [62]. The INR is pictured as a "nearly bound" state of the system lying at energies above the threshold for complex breakup, i.e., in the continuum region of the energy spectrum. In the Breit–Wigner treatment, the fundamental characteristic of the INR is the existence of complex energy pole in the S-matrix, i.e.,

$$\boldsymbol{S}(E) = \boldsymbol{S}_{\text{d}}(E)\left[1\frac{i\boldsymbol{A}}{E - E_{\text{R}} + i\Gamma/2}\right], \tag{7}$$

where E_{R} is the (real) resonance energy and Γ is the total width [63]. The energy regime over which the fitting should be done may be established by monitoring the eigenphase sum, which undergoes a jump of π in the vicinity of a resonance. In Eq. (7), $\boldsymbol{S}_{\text{d}}(E)$ is the direct or background contribution, which is assumed to be a slowly varying function of the total system energy E. In this form, both $\boldsymbol{S}(E)$ and $\boldsymbol{S}_{\text{d}}(E)$ are assumed to be unitary. This requires the matrix $\boldsymbol{A}$ to be Hermitian and of the form

$$\boldsymbol{A}_{i,j} = \gamma_i^* \gamma_j. \tag{8}$$

The quantities γ_i are related to the partial widths of the resonance according to

$$\Gamma_i = |\gamma_i|^2, \tag{9}$$

which, in turn, satisfy

$$\Gamma = \sum_i \Gamma_i. \tag{10}$$

The amplitudes γ_i are generally complex, and the relative phase between the resonant term and the background term determines the precise lineshape that will be observed. An alternative to Eq. (7) makes use of the sum form

$$\boldsymbol{S}(E) = \boldsymbol{S}'_{\mathrm{d}}(E) - \frac{i\boldsymbol{A}'}{E - E_{\mathrm{R}} + i\Gamma/2}. \tag{11}$$

This expression, which is the more common expression used in numerical fitting, has a matrix $\boldsymbol{A}'$ which is not as simply related to the partial widths. For an INR, we assume that the complex energy

$$z = E_{\mathrm{R}} - i\Gamma/2 \tag{12}$$

lie very close to the real axis, i.e., Γ is small so that the background contribution to $\boldsymbol{S}(E)$ may be readily separated from the resonance pole. Furthermore, it is assumed that no other poles of the S-matrix lies nearby in energy as defined on the scale set by Γ. When these conditions are met, the existence of a resonance is heralded by the occurrence of set of well-defined effects that are amenable to observation or computation.

The INR approximation can be extended to cases of two overlapping resonances. When two resonance states lie close to one another, the rapid variation of the S-matrix against energy must be modeled with a unitary two-pole formula

$$\boldsymbol{S}(E) = \boldsymbol{S}_{\mathrm{d}}(E)\left[1 - \frac{i\boldsymbol{A}_1}{E - E_{1,\mathrm{R}} + \frac{i\Gamma_1}{2}}\right]\left[1 - \frac{i\boldsymbol{A}_2}{E - E_{2,\mathrm{R}} + \frac{i\Gamma_2}{2}}\right]. \tag{13}$$

The resonance parameters are then extracted by numerically fitting the formula to the results of the scattering calculation. Numerical instabilities that sometimes arise in fitting the pole structure, either using Eq. (7) for one resonance or Eq. (13) for two resonances, may be assuaged using more sophisticated approaches such as the Pade' approximation [64].

The simple INR concept has succeeded beautifully for many problems in atomic and nuclear physics. Unfortunately, the INR picture is seldom valid for reactive resonances, which, on the contrary, tend to be broad and overlapping. The breakdown of the INR idealization for reactive resonances was appreciated long ago in terms of the impact parameter averaging implicit in reactive collisions [65]. If we imagine that an "isolated" reactive resonance

corresponds to a vibrational state of an intermediate molecule, then the rotational energy levels built on that state have energies given by

$$E_R(J) = E_0 + B_0 \cdot J(J+1), \tag{14}$$

where E_0 is the ground rotational energy and B_0 is the rotation constant of the complex. (For simplicity, we have specialized to the case of a collinear collision complex.) Hence, each resonance state is part of a rotational progression with spacing $2JB_0$. The typical B-constant for a reactive resonance can be inferred from the geometry of the saddle point on the PES and is usually on the order of several wave numbers. On the other hand, the resonance lifetimes tend to be less than 100 fs, corresponding to widths greater than $50\,\mathrm{cm}^{-1}$, thus implying that the rotational states are overlapping, i.e., their spacings are smaller than their widths. Stated in dynamical terms, the rotational period of the complex is significantly greater than the lifetime of the resonance. The rotational quantum number of the resonance is expected to correlate to the total angular momentum, J, which labels the partial waves in an expansion of the cross sections. Since dozens of partial waves generally contribute to the cross section at typical collision energies, this congestion of resonance states is expected to occur generically in a collision experiment. Thus, the sharp structure (on the scale set by Γ) in the cross sections versus energy that one might expect to observe for an INR will generally be smeared out over a much larger energy range. Since the background scattering has some energy dependence as well, it becomes very difficult to identify the resonant signature in the cross section.

One important class of exceptions to the preceding discussion is provided by prereactive or postreactive van der Waals (vdW) complexes. The lifetimes for such resonances can be much longer than that for conventional transition state resonance trapped near the saddle point. In the discussion of the $F+HCl$ reaction below, we shall see that resonances of this sort can have lifetimes much longer than the rotational period of the complex and thus may show INR signatures.

It is clear that the unmistakable resonance fingerprint provided by a narrow Lorentzian peak in the integral cross section (ICS) will be rare for reactive resonances in a collision experiment. However, a fully resolved scattering experiment provides a wealth of data concerning the reaction dynamics. We expect that the state-to-state differential cross sections (DCS) as functions of energy can be analyzed, using various methods, to reveal the presence of reactive resonances. In the following subsections, we discuss how various collision observables are influenced by existence of a complex intermediate. Many of the resonance detection schemes that have been proposed, such as the use of collision time delay, are purely theoretical in that the observations required are not currently feasible in the laboratory. Nevertheless, these ideas are also discussed since it is useful to have method available

to determine whether a given PES supports resonances for comparison and interpretation of experiment.

2.4. Integral cross sections

An ideal INR is dramatically revealed by the appearance of narrow feature in the ICS, $\sigma(E)$ at total energy $E = E_R$ of width Γ. Obviously, the resonance peak is closely related to the existence of the resonance pole in the S-matrix. Using the normal body-fixed representation for an $A+BC(v,j) \rightarrow AB(v',j')+C$ reaction, the ICS is related to the S-matrix by

$$\sigma_R(v,j \rightarrow v',j';E_C) = \frac{\pi}{k^2} \sum_J (2J+1) \cdot P_R(v,j \rightarrow v',j';E_C,J) \tag{15}$$

with k being the incident wave number and

$$P_{R(\,)v,j \rightarrow v',j';E_C,J} = \frac{1}{2j+1} \sum_{k,k'} [|S_J(v,j,k \rightarrow v',j',k';E_C)|^2 \tag{16}$$

where the (presumably) unobserved helicity quantum numbers k and k' are averaged over. It is clear from Eq. (7) that, for a given partial wave, the resonance peak should occur at the same total energy for all state-to-state ICSs with the relative heights set by the partial widths. When the resonance exists for only a single partial wave, such as in many nuclear physics problems, a resonance feature of width Γ should survive in the ICS even if other partial waves contribute a smooth background. When many partial waves support resonance states, as with reactive resonances, the individual peaks that may be quite apparent in $P_R(v,j \rightarrow v',j';E_C,J)$ merge together in the ICS over a broad energy range and are difficult to distinguish from background scattering. A special case, of relevance to the $F+HD$ reaction considered below, is when the background scattering happens to be nearly zero around the resonance energy. In this case, the reaction is purely resonance mediated and we can approximately construct the behavior of the ICS from a combination of Lorentzian profiles. Using J-shifting approximation, the reaction probability for the Jth-partial wave is given by

$$P_R(v,j \rightarrow v',j';E_C,J) \approx \frac{C\sqrt{E_C}\sqrt{E_C'}}{(E - E_R(J))^2 + \Gamma^2/4}, \tag{17}$$

where E_C and E_C' are the initial and final translational energies, E is the total energy, C is a constant and

$$E_R(J) = E_0 + B_0 J(J+1) \tag{18}$$

is the J-shifted resonance energy with B-constant B_0. The square root factors are inserted to improve the threshold behavior of the expression. When the partial cross sections are combined according to Eq. (15), a step-like feature occurs in the ICS that can be analytically modeled using the formula

$$\sigma_R \approx \frac{C}{\sqrt{E_C}} Im\left[\theta(E_C)\ln\left(\frac{\theta(E_C)+1}{\theta(E_C)-1}\right)\right], \tag{19}$$

where

$$\theta(E_C) = \sqrt{\frac{E_0 - i\Gamma/2}{E_C}}. \tag{20}$$

The inclusion of J-dependence into the resonance width generally produces only a small change in the shape of the resonance step. Schatz et al. [66] have noted that such a step feature may occur for the *Cl+HCl* reaction.

2.5. Time delay

Scattering cross sections for chemical reactions may exhibit structure due to resonance or due to other dynamical effects such as interference or threshold phenomena. It is useful to have techniques that can identify resonance behavior in theoretical simulations and distinguish it from other sorts of dynamics [67]. Since resonance is associated with dynamical trapping, the concept of the collision time delay proves quite useful in this regard. Of course since collision time delay for chemical reactions is typically in the subpicosecond domain, this approach is, at present, only useful in analyzing theoretical scattering results. Nevertheless, time delay is a valuable tool for the theoretical identification of reactive resonances.

There are two common definitions of collision time delay: one proposed by Wigner and Eisenbud [68] and another suggested by Smith [69]. Although identical for single channel scattering, these two definitions can yield very different results in multichannel scattering such as chemically reactive collisions. Both definitions were formulated for the scattering of a single partial wave (single J-values), but an extension of the Wigner–Eisenbud model is possible for full scattering (see below). The Wigner–Eisenbud approach is based on the shift in the center of a spatially localized wave packet relative to dynamics in the absence of an interaction potential. At early times, long before the collision, a wave packet started in the $\boldsymbol{n}$-th internal channel of the J-th partial wave is represented as

$$\Psi = \phi(R - v_n t)\chi_n, \tag{21}$$

where ϕ is broadly peaked at $R - v_n t = 0$ in position space but is narrowly peaked in translational momentum space at μv_n, R is the collision coordinate,

v_n is the channel velocity, and χ_n is the initial internal state wavefunction. Then, long after the collision, the n'-th component of the wave packet takes the form

$$\Psi = C\phi(R - v_{n'}t + v_{n'}\tau_{n.n'})\chi_{n'}, \tag{22}$$

where the quantity $\tau_{n,n'}$ is the state-to-state collision time delay defined by

$$\tau_{n,n'} = \mathrm{Re}\left[\frac{-i\hbar}{S_{n.n'}(E)}\frac{\mathrm{d}S_{n.n'}(E)}{\mathrm{d}E}\right]. \tag{23}$$

The Wigner–Eisenbud definition is physically equivalent to the idea of a signal time delay. Clearly, each channel will display a different value for this quantity, although for an INR each approaches $2\hbar/\Gamma$ at $E = E_{\mathrm{R}}$. Smith's definition of the time delay is based on a different concept, namely the residence time within the interaction region of the collision, referred to as the collision lifetime. It can be shown that for a multidimensional scattering problem, the residence time (relative to free-particle motion) within a large sphere enclosing the interaction is given in terms of a Hermitian lifetime matrix,

$$Q_{n,n'} = -i\hbar\sum_{\mathrm{j}}\frac{\mathrm{d}S_{n,\mathrm{j}}(E)}{\mathrm{d}E}S^{*}_{n',j}(E). \tag{24}$$

The average time delay for a particle injected into the n-th channel but emerging in any final channel is given by the diagonal element $Q_{n,n}$. The resonance contribution to the time delay is expected to emerge more distinctly from the background when $\boldsymbol{Q}$ is diagonalized. In this case, the largest eigenvalue should show a peak against energy near a resonance energy.

Either the Wigner–Eisenbud or Smith definitions of time delay require as the input the values of $\boldsymbol{S}$ computed on a sufficiently fine grid of energies to compute $\mathrm{d}\boldsymbol{S}/\mathrm{d}E$. However, the Smith version generally requires a much larger calculation since the determination of the eigenvalues of $\boldsymbol{Q}$ requires the full S-matrix between all open channels at energy E while the Wigner–Eisenbud theory requires only a single element.

We expect that every resonance will yield extra time delay at energies near E_{R}. However, it is extremely dangerous to interpret all sharp structure in the function $\tau_{n,n'}(E)$ as due to resonance [67]. For example, it is easy to see that if $S_{n,n'}(E)$ should accidentally pass near zero at an energy E_0, then the τ will show a positive or negative spike at $E = E_0$ that is not necessarily related to any resonance state. If a peak of the time delay occurs near the minimum of the reaction probability, great caution should be exercised before concluding that the peak is due to resonance. Furthermore, near energetic thresholds it is known that the elastic phase shift for $J = 0$ has a singularity of the form

$\delta \sim \sqrt{E_C}$. This leads to (elastic) time delays that diverge at threshold. Since thresholds are quite dense in energy for a typical chemical reaction, this can yield very erratic behavior of the Smith lifetime matrix, and hence the eigenvalues.

Since the time delay as defined above applies directly only to scattering of a single partial wave, it cannot be used to compute the scattering angle-resolved time delay, $\tau_{n,n'}(E,\theta)$. This quantity, which is a theoretical observable in a wave packet calculation [70], measures the delay of a plane wave signal as a function of the final center-of-mass scattering angle. To this end, Goldberger and Watson [71] have generalized the Wigner–Eisenbud time delay using the scattering amplitude, $F_{n,n'}(E,\theta)$, in place of the S-matrix. It was found that quantity

$$\tau_{n,n'}(E,\theta) = \hbar \frac{\mathrm{d}}{\mathrm{d}E} Arg\left(F_{n,n'}(E,\theta)\right) \tag{25}$$

provided a sensible extension of the signal time delay concept to angle-resolved scattering. Kuppermann and Wu [72] have used a somewhat different definition based on the same approach for the $H+D_2$ reaction. We note that the angle-resolved time delay may prove quite useful for reactive resonances since resonant scattering may occur much more strongly into certain scattering angles such as the forward direction.

2.6. Exponential decay

Associated with the pole of the S-matrix is a Siegert state, Ψ_{res}, which has purely outgoing boundary conditions and satisfies (with some caveats) the equation, $\boldsymbol{H}\Psi_{\mathrm{res}} = z\Psi_{\mathrm{res}}$, $\boldsymbol{H}$ being the system Hamiltonian [73]. If a square integrable approximation to Ψ_{res} is constructed, then its time evolution, $\Psi_{\mathrm{res}}(t)$, will exhibit pure exponential decay after a transient induction period. Of course, any L^2 state will show quadratic, and hence nonexponential, decay at short times since

$$|\langle \Psi(0)\Psi(\Delta t)\rangle|^2 \approx 1 - \Delta t^2 \langle \Psi(0)|\widehat{\boldsymbol{H}}^2|\Psi(0)\rangle/\hbar^2. \tag{26}$$

However, at long times a sample of prepared "complex" molecules will deplete according to the law, $N(t) = N(0)e^{-t/\tau}$, where the lifetime τ is related to the resonance width according to $\tau = \hbar/\Gamma$. Furthermore, the decay flux into each outgoing channel is locked in fixed proportion at all times.

Although it is not feasible to measure exponential decay of resonance states in the environment of a molecular beam experiment, in theoretical work the exponential decay law provides a necessary condition that a proposed state, generated by some method, is in fact a resonance state. Furthermore, the rate of exponential decay provides probably the most accurate method for the numerical determination of the lifetime.

One can use various techniques to generate Siegert states from numerically accurate quantum dynamics. The most straightforward approach involves the use of a real stabilization calculation [74, 75]. Unfortunately, real stabilization tends to become rather inconclusive for broad resonances especially at high state densities required to treat three-dimensional reaction dynamics. The performance of stabilization calculations can be greatly improved by including an absorbing optical potential outside the interaction region to enforce outgoing boundary conditions [30, 76]. Direct calculation of a state corresponding to complex energy eigenvalue is possible within the framework of the complex coordinate rotation method [77]. In our work, we have generally preferred the use of the SQ method since it is ideally suited for the study of broad transition state resonances [23, 28, 29, 78–80]. The SQ method is a straightforward application of conventional techniques available for the study of time-dependent quantum wave packet dynamics. In the first stage of the method, energy spectra are obtained for various initial wave packets launched in the transition state region, i.e.,

$$I(E) \sim \int_{-\infty}^{\infty} \langle \varphi(0) | \varphi(t) \rangle e^{iEt/\hbar} \mathrm{d}t \tag{27}$$

Peaks in the spectrum, $I(E)$, identify the location of possible resonance states. Then, the initial state $\varphi(0)$ is optimized to reduce direct background scattering and the resonance state is extracted using the standard relation

$$\Psi \mathrm{res} \sim \int_{-\infty}^{\infty} \varphi(t) e^{iE_{\mathrm{P}}t/\hbar} \mathrm{d}t \tag{28}$$

where E_{p} is a peak energy.

2.7. Angular product distributions

A pole of the S-matrix close to the real axis can lead to a clear peak in the ICS if the resonance occurs for just one partial wave or if the resonances for each J are well separated in energy. It is not surprising that similar conclusions can be drawn for the DCS. The DCS is defined from the usual [27] body fixed S-matrix for $A+BC(v,j) \rightarrow AB(v',j')+C$

$$\frac{\mathrm{d}\sigma_{\mathrm{R}}(v,j,k \rightarrow v',j',k')}{\mathrm{d}\Omega} = \frac{1}{4k_{vj}^2} \left| \sum_J (2J+1) \cdot d^J_{k,k'}(\pi - \theta) \cdot S_{\mathrm{R}}(v,j,k \rightarrow v',j',k') \right|^2, \tag{29}$$

where k_{vj} are the initial channel translational wave numbers and $d^J_{k,k'}$ are the Wigner functions in terms of the helicity indices k and k'. If the S-matrix is

slowly varying against E except near a pole for some value of J, then it is obvious that the DCS will show rapid variation around $E = E_R$ at all scattering angles where $d^J_{k,k'}$ is significant. As we have noted already, however, this behavior is not to be expected for reactive resonances because of impact parameter averaging. A progression of poles of the form Eq. (7) with energies given by Eq. (14) must be combined coherently (with phases) to obtain the resonance signature in the DCS. Making this difficult is the variation of the background phase as a function of J. Unlike the ICS, which depends only on $|S^2|$, the relative phase of the partial wave contributions is crucial in determining the angular product distributions. This issue has been understood for quite a long time, and the question of how the existence of an intermediate complex might affect the DCS has received considerable discussion. For an intermediate with a lifetime long compared to the rotational period, Herschbach [81] noted that the DCS should become forward–backward symmetric in the center of mass frame. Unfortunately, reactive resonances are often short lived compared to the rotation period making subtler the angular signature of resonance.

Miller and Zhang suggested searching for a ridge structure in the DCS as a function of E_C and θ. The ridge is an $E_C - \theta$ correlation resulting from the J-shifting of the dominant resonance decay angle, which appears in the DCS. Miller and Zhang [82] observed clear ridge features in the $H+H_2$ and $D+H_2$ systems. However, it is unclear whether ridge structures uniquely correlate to quantum resonances since Aoiz and coworkers [83] have noted similar ridges occur in QCT simulations. In another discussion of angular correlation, Connor and Sokolovski have recently proposed that decomposing the scattering amplitude into nearside/farside contributions may elucidate resonance behavior [84, 85].

In a very important work, Lee and coworkers [86, 87] surmised that forward peaks in the state-resolved DCS might indicate the existence of resonances. The physical picture behind this idea is somewhat subtle and involves resonant time delay. As the impact parameter (or J) of the collision increases, the total reactive product distribution generally shifts from backward to more sideways scattering, reflecting the orientation of the complex. One expects that the resonant contribution to the product distribution will show greater angular deflection (toward forward) since the complex will rotate further due to the time delay. Thus, in the most forward direction the dynamics will be filtered to enhance the resonant contribution to the reaction. Forward peaks have in fact been observed experimentally in the $F+H_2$ [86], $H+D_2$ [88–90], and $H+HD$ [91–93] reactions. To determine the range of J (and hence the impact parameter) that gives rise to a feature in the DCS, it is useful to compute the angle-resolved integrated opacity function,

$$\frac{\mathrm{d}\sigma_{\mathrm{R}}^{J_{\max}}(\theta)}{\mathrm{d}\Omega} = \frac{1}{4k_{vj}^2}\left|\sum_{J=0}^{J_{\max}}(2J+1)\cdot d^J_{k,k'}(\pi-\theta)\cdot \boldsymbol{S}_{\mathrm{R}}(v,j,k\to v',j',k')\right|^2. \qquad (30)$$

This quantity gives the truncated contribution to the DCS of partial wave up to J_{max}. Thus, holding E and θ fixed, the most important J values for a process can be determined by plotting Eq. (30) against J_{max}.

2.8. Product rovibrational branching ratios

The dynamics of a reaction that proceeds directly over the transition state is expected to be qualitatively different from that of a resonance-mediated reaction. In particular, one expects that the branching ratios into the product rovibrational states will be very different between the direct and the resonant mechanisms. For example, if a given Feshbach resonance corresponds to trapping on the $v=1$ vibrationally adiabatic curve, then one might expect that the population of the $v'=1$ vibrational state of the product molecule may be greatly enhanced by the resonant mechanism. Similarly, the rotational product distribution resulting from the fragmentation of a resonance molecule may show a quite distinct pattern from that of a direct reaction. Indeed, Liu and coworkers [94], and Nesbitt and coworkers [95] have noted distinct rotational patterns in the *F+HD* resonant reaction.

The phenomenon of impact parameter averaging will lead to a smearing of the resonance decay products over large energy range. Nevertheless, under certain circumstances the influence of resonance may still be discerned. For example, if the resonance energy of lowest partial wave is $E_R(J=0)$, then any reaction occurring at $E<E_R(0)$ (by more than the resonance width) must necessarily take place through the direct mechanism. If the product branching ratios are monitored against E, one might expect to see a sudden change in the branching ratios which begins at $E=E_R(0)$ and persists continuously to higher energy. Conversely, if $E_R(0)$ is below the threshold for direct reaction, as in a resonance-tunneling-mediated reaction, then there will be a range of energies $E_R(0)<E<E_{thr}$ in which the reaction proceeds solely through the resonance mechanism. In this case, product branching ratios for $E<E_{thr}$ are then completely determined by the partial widths of the resonance. Since the partial widths are generally rather weak functions of J, the branching ratios should be relatively constant up to $E=E_{thr}$. At higher energies, the direct mechanism begins to contribute and the branching ratios will begin to show much more rapid variation against E.

3. FESHBACH RESONANCE: *F+HD*

It is clear that reactive resonance can potentially affect many scattering observables. It is not obvious a priori, however, which particular quantities may prove the most effective in identifying the existence of a resonance state. To assess the utility of various ideas for resonance signatures in this and in the following two sections, we shall consider three reactions believed to support reactive resonances. These are the hydrogen exchange reactions: $F+HD\rightarrow HF+D$, $H+HD\rightarrow D+H_2$, and $F+HCl\rightarrow HF+Cl$. For the first two of

these reactions, state of the art molecular beam experiments have recently been performed. Furthermore, very accurate PESs have also been computed for these reactions, which have been used to carry out accurate quantum scattering calculations. Given the general similarity of these reactions, one might expect that their resonance fingerprints would be closely related. Indeed, each of these systems is a triatomic hydrogen abstraction reaction dominated by the lowest PES that exhibits no potential well near the transition state. However, we shall see that presence of resonances is manifested in different observables for each case. The chameleon-like nature of the resonance emphasizes the need for combined theoretical and experimental work to firmly establish the resonance on a case-by-case basis.

The first unambiguous observation of a reactive resonance in a collision experiment was recently made for the $F+HD \rightarrow HF+D$ reaction [96–98]. This reaction was one isotopomer of the $F+H_2$ system studied in the landmark molecular beam experiments of Lee and coworkers in 1985 [86, 87]. Unlike the $F+H_2$ case, no anomalous forward peaking of the product states was reported, and the results for $F+HD$ were described as the most classical-like of the isotopes considered. Furthermore, a detailed quantum mechanical study [99] of $F+HD \rightarrow HF+D$ reaction on the accurate Stark–Werner potential energy surface (SW-PES) [100] failed to locate resonance states. Therefore, it was surprising that the unmistakable resonance fingerprints emerged so clearly upon re-examination of this reaction.

The molecular beam experiments of Liu and coworkers [94, 96, 97] employed the Doppler profile time-of-flight technique that allowed the ready observation of the excitation function (i.e., the total reactive ICS summed over final product state) at many collision energies for an HD reagent molecule 90% populated in its ground rovibrational state. The excitation function for both possible product channels, $HF+D$ and $DF+H$, over the range of collision energies 0.2–3 kcal/mol is shown in Figure 3.3. A pronounced step-like feature occurs in $\sigma_R(E)$ for the $HF+D$ channel near $E_C = 0.5$ kcal/mol that is clearly absent for the $DF+H$ channel. A converged quantum scattering calculation [65, 66, 101] on the SW-PES is found to yield similar results, as seen in the figure. The QCT results of Aoiz and coworkers [102] showed reasonable agreement with experiment for the $H+FD$ channel but completely failed to predict the step-feature for the $D+HF$ product. Since the step occurs below the adiabatic barrier, one led to the conclusion that the reaction step is due to quantum effects. With close interaction between theory and experiment, the interpretation that emerged [96, 97] for this result was that the reactive step was due to the existence of a reactive resonance with an $F–H–D$ collinear geometry. The step was not seen in the $DF+H$ channel since the decay probability of an $F–H–D$ configured resonance was very small into that unfavorable product channel. The difference in the step height predicted by quantum scattering and that observed in the experiment is likely

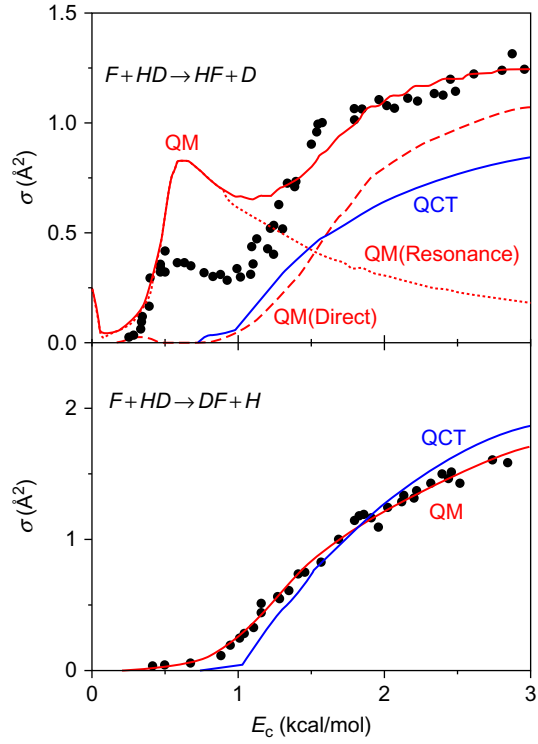

Figure 3.3 The normalized excitation functions in Å^2 versus collision energy for the two isotopic channels for the *F+HD* reaction. The solid line is the result of quantum scattering theory using the SW-PES. The QCT simulations from Aoiz et al. are plotted for comparison. The experiment, shown with points, is normalized to theory by a single scaling factor for both channels. Also shown in the upper panel is the theoretical decomposition of the excitation function into direct and resonant contributions using the *J*-shifting procedure.

due to small errors in the SW-PES affecting the rate of resonant tunneling [103, 104].

In light of the discussion above, it is very surprising that a clear resonant feature should survive in $\sigma_R(E)$, which, after all, involves averaging over impact parameter, scattering angle, and final states. Some insight into this result is obtained by considering the partial cross sections computed for the individual partial waves that are shown in Figure 3.4. As a function of E_C, each of the partial cross sections shows a clear Lorentzian-like peak at low E_C followed by the normal threshold-type behavior at higher E_C. The individual peaks fit well to a Lorentzian shape function with peak positions at

$$E_{res}(J) = E_0 + B_0 \cdot J\,(J+1) \tag{31}$$

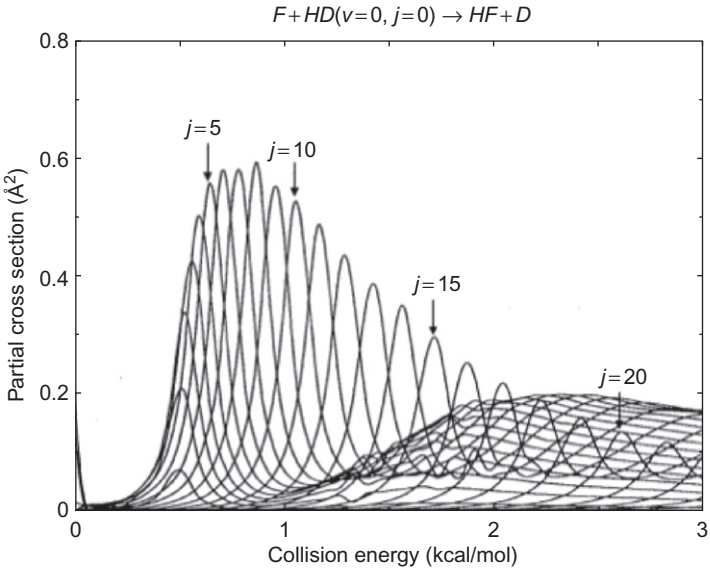

Figure 3.4 Computed partial cross sections in Å^2 for the $F+HD(v=0, j=0) \rightarrow HF+D$ reaction as a function of the total angular momentum quantum number, J, up to collision energies of 3 kcal/mol.

with $E_0 = 0.52$ kcal/mol and $B_0 = 0.0051$ kcal/mol, and widths given by fitted form

$$\Gamma(J) = \Gamma_0 + a(\exp(bJ) - 1) \tag{32}$$

with $\Gamma_0 = 0.15$ kcal/mol, $a = 0.00127$ kcal/mol, and $b = 0.2635$. Since the threshold energy for the "direct" $F+HD \rightarrow HF+D$ reaction obtained from the lowest vibrationally adiabatic barrier is about 1.1 kcal/mol, the reactive step in $\sigma_R(E)$ is due almost entirely to the superposition of the Lorentzian peaks. Indeed, by numerically decomposing the partial cross sections into separate resonant and direct contributions, and then summing over J to obtain $\sigma_R(E)$, we see in Figure 3.3 that the step is essentially the sum of J-shifted Lorentzian peaks. The reaction occurs almost exclusively through resonance-mediated tunneling at energies below 1 kcal/mol.

The quantum product state distributions from the reaction show a similar dichotomy for $E_C < 1$ kcal/mol and $E_C > 1$ kcal/mol. Focusing on the rotational state distribution for the dominant $HF(v' = 2)$ product, in Figure 3.5 we show the ICS for $F+HD \rightarrow HF(v' = 2, j')$ as a function of j' and E_C. The scattering calculations show a clear change in the rotational product distribution between low- and high-energy scatterings. The rotational distribution at low

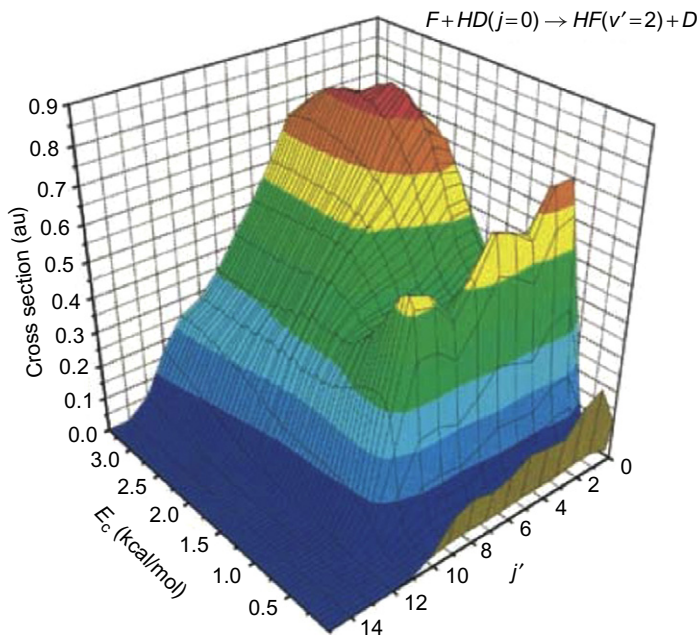

Figure 3.5 The ICS for $F+HD(v=0, j=0) \rightarrow HF(v'=2, j') + D$ versus E_C and j' computed from quantum scattering theory using the SW-PES.

E_C is rather flat, yet hot, extending up to about $j'=10$. By contrast, the higher E_C results show the more usual envelop peaking at much lower values of j'. Nesbitt and coworkers [95] measured the product distribution in a "crossed jet" experiment, and obtained results are consistent with Figure 3.5. Again, the result is consistent with a resonance state picture in that the low E_C distribution is entirely due to a resonance decay mechanism that is expected to be quite different from the direct reaction mechanism that dominates at higher E_C.

The DCS for the $F+HD \rightarrow HF+D$ reaction is also imprinted with resonance signatures. In Figure 3.6, we show the DCS versus E_C and θ, for the $HF(v'=2)+D$ product, summed over j'-states, obtained experimentally and theoretically. At low collision energies, a resonance ridge of the sort proposed by Miller and Zhang [82] is clearly apparent. The product distribution is backward peaked at the lowest energy and then shifts progressively toward the sideways direction. At high E_C, the DCS develops strong forward/backward peaking. A decomposition of the DCS into resonant and direct components, by fitting each S-matrix element to a Breit–Wigner pole plus a background, verifies that this peaking is in fact due primarily to the resonant contribution.

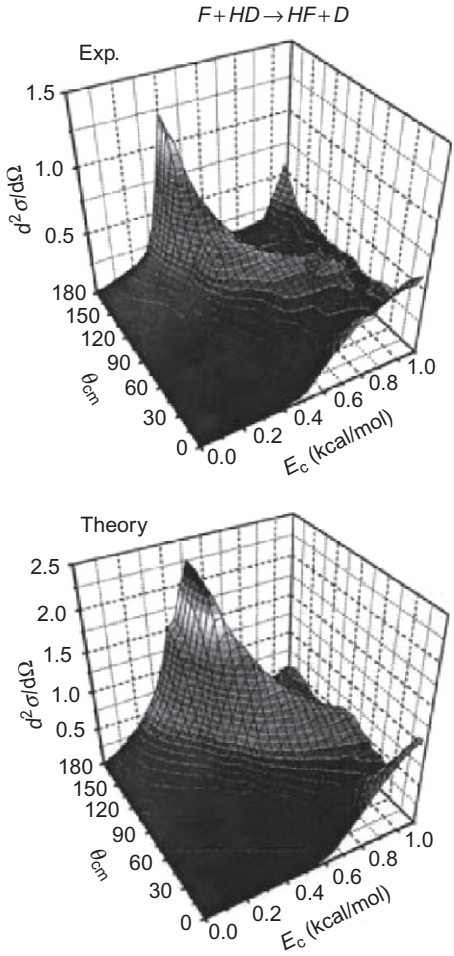

Figure 3.6 The total differential cross section (DCS) in $Å^2/sr$ for the *HF+D* reactive channel. Panel (a) shows the experimental results, whereas panel (b) presents the result of the scattering calculation. Note the ridge running from large θ (backward) at low energies to small θ (sideways) at higher energies.

To uniquely associate the unusual behavior of the collision observables with the existence of a reactive resonance, it is necessary to theoretically characterize the quantum state that gives rise to the Lorentzian profile in the partial cross sections. Using the method of SQ, it is possible to extract a Siegert state wavefunction from time-dependent quantum wave packets using the Fourier relation Eq. (28). The state obtained in this way for $J=0$ is shown in Figure 3.7; this state is localized in the collinear *F–H–D* arrangement with three quanta of excitations in the asymmetric stretch

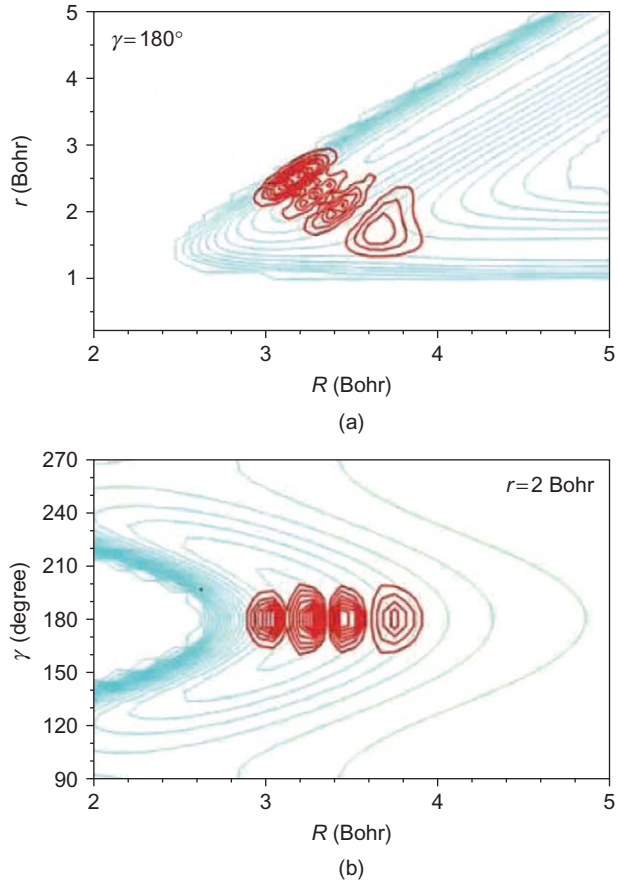

Figure 3.7 The probability density of the reactive resonance at $E_C = 0.52$ kcal/mol. In the top panel, the *F–H–D* collinear subspace is shown using the Jacobi coordinates (R, r). In the bottom panel, the probability density is sliced $r = 2$ Bohr and is shown in the (R, γ) coordinates. The plot clearly shows a state with three nodes along the asymmetric stretch and zero nodes in the symmetric stretch and bend.

mode and no quantum of excitation in the bend and symmetric stretch modes. If the state pictured in Figure 3.7 is used as an initial (prepared) state in a wave packet calculation, one observes pure exponential decay with a lifetime of 109 fs, consistent with the width of the Lorentzian peak in the partial cross section. Furthermore, the product state distribution of the decaying resonance is consistent with the results of the scattering calculations for $E_C < 1$ kcal/mol. Takayanagi and Wada [105] have performed a stabilization calculation that confirmed the existence of the resonance state on the SW-PES.

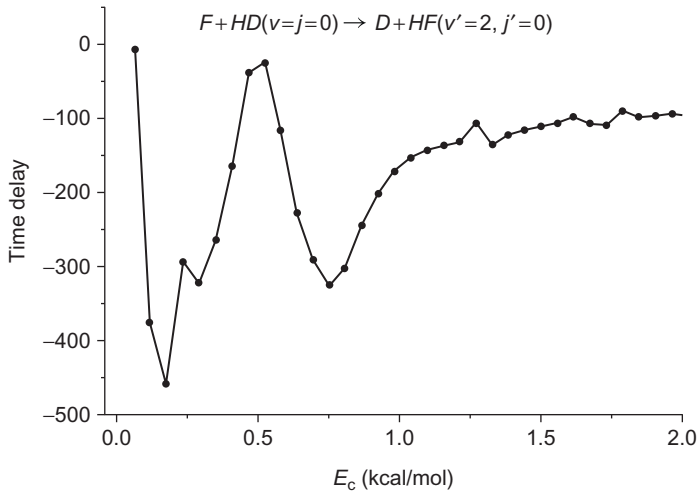

Figure 3.8 The Wigner–Eisenbud time delay versus E_C for the reaction $F+HD(v=0, j=0) \rightarrow D+HF(v'=2, j'=0)$ with $J=0$.

Quantum mechanical trapping at the resonance energy can also be verified using a time delay analysis on the quantum S-matrix. In Figure 3.8, the average time delay for the $J=0$ partial wave of the $F+HD \rightarrow HF+D$ reaction, defined using Eq. (23), is plotted against collision energy. A clear peak in the time delay is observed near the resonance energy. Higher partial waves exhibit similar behavior with the peak of the time delay J-shifting according to Eq. (31).

In summary, the reactive resonance for the $F+HD \rightarrow HF+D$ reaction is found to leave clear signatures on a variety of collision observables. The resonance state itself is readily extracted from the quantum dynamics on the SW-PES, and the scattering observables are found to correlate well with the predictions of theory.

We should point out that the $F+H_2 \rightarrow HF+H$ reaction actually shows some significant differences from its isotopic partner $F+HD$ [94, 104, 106, 107]. The $F+H_2$ reaction is mediated through two closely spaced resonances. One state is the analog of the [FHD] Feshbach resonance that is isotopically shifted to a slightly lower collision energy. The other state is slightly higher in energy and is spatially localized further into the exit channel. The quantum interference of the scattering amplitude between these two states produces interesting patterns in the observable cross sections [56, 108–110].

4. BARRIER RESONANCE: $H+HD$

The search for reactive resonances in the $H+H_2$ reaction (and its isotopomers) has a long history [1–5, 111, 112]. The existence of resonances was first

conjectured based on theoretical collinear quantum dynamics simulations using approximate PES [12–15]. Subsequent improvements in theory, such as the use of a very accurate PES and the implementation of full three-dimensional dynamics, strongly implied that the resonances should actually exist in the "real" system [21–23]. Despite the simplicity of this reaction, it has only been rather recently that ab initio theoretical reaction dynamics has been brought into agreement with state-resolved experimental results [113, 114]. Nevertheless, clear signatures of resonant behavior have proven to be very difficult to identify in experiment, and there have been several false sightings reported. By any measure, experimental conditions required for the measurements are quite rigorous. The resonances are predicted to exist at high E_C, requiring hot-atom beam sources such as *HI* photolysis products for which it is difficult to obtain a well-calibrated energy tunable beam. Furthermore, the resonances will likely have very short lifetimes (~20 fs) and thus will display very large widths as a function of collision energy, ~0.5 kcal/mol. Therefore, it becomes a subtle matter to distinguish between the direct and resonance contributions to the scattering cross sections. Further complicating the analysis is the possible influence of the geometrical phase [115] that might have significant effects on the resonance properties as stressed by Kuppermann and coworkers [116]. Weak undulations in certain state-resolved ICSs versus E_C for $H+D_2$ have been predicted by Chao and Skodje [117] but are likely to be at or below the detection threshold. These undulations, seen most strongly for the ICS's $\sigma_R(00 \rightarrow 00)$ and $\sigma_R(00 \rightarrow 02)$, are problematic as resonance fingerprints since they are not uniquely correlated to the barrier-states of the reaction. Zare and coworkers [88] have observed a forward peak in the $H+D_2$ DCS, which is consistent with a resonance picture. Theoretical simulations have in fact demonstrated that the forward peak does exhibit extra time delay in line with the physical picture outlined above [88, 118].

Here, we consider the $H+HD \rightarrow D+H_2$ reaction, which has recently been studied experimentally and theoretically by Harich et al. [93]. The reaction was investigated experimentally in a cross-molecular beam apparatus employing the *D*-atom Rydberg tagging detection scheme originally proposed by Welge and coworkers [113]. The hot *H*-atom beam source was provided by *HI* photolysis that produced two well-separated collision energies, $E_C = 0.499$ and 1.200 eV. The initial *HD* beam was cooled to the point that only the ground state, $HD(0, 0)$, was represented in the beam. The state-resolved DCSs were obtained for all the important rovibrational product channels. The theoretical analysis involved QCT, quantum scattering, and wave packet calculation on the accurate BKMP2-PES [119], but without the geometrical phase.

In Figure 3.9, the ICSs for several channels are plotted against total energy, $E = E_C + 0.235$ eV. The experiment (plotted with symbols) and theory are in good agreement, but show no clear sign of resonance behavior over the energy range considered. Although the underlying reaction probabilities

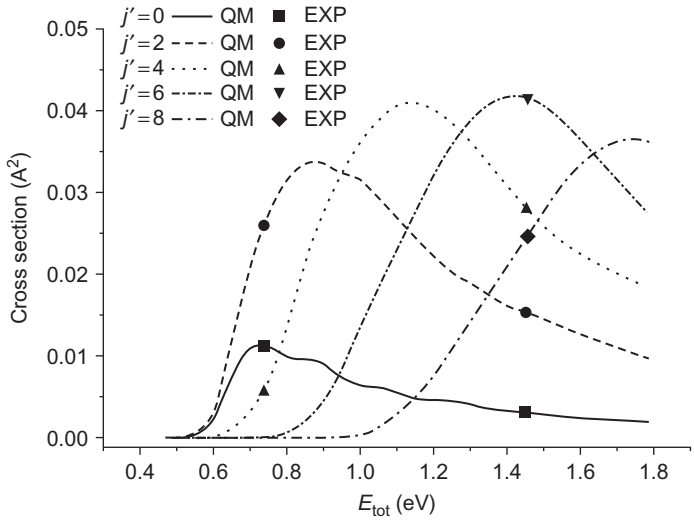

Figure 3.9 The ICS for $H+HD(v=0,j=0)\rightarrow D+H_2(v'=0,j')$ versus total energy for several final rotational channels. The curves are obtained from quantum scattering theory while the symbols are experimental results.

$P_R(v,j\rightarrow v',j';E_C,J)$ exhibit modest oscillation against E_C, the impact parameter averaging effectively washes out this structure in the cross sections. Similarly, the j'-dependence of the $D+H_2(v'=0,j')$ products, Figure 3.10, shows no unusual energy dependence of the sort seen previously for $F+HD$. We note parenthetically, however, there is a dramatic effect of spin–statistics that causes the distributions to exhibit a saw-toothed dependence on j'. The state resolved DCS's for several states is shown in Figure 3.11. Several of the DCSs do show weak vestiges of the resonance ridge, such as the $d\sigma_R(0,0\rightarrow 0,0)/d\Omega$. The ridge in these cases is clearly associated with the maximum of the ground adiabatic potential (i.e., the lowest barrier state) and not with any higher lying Feshbach-type resonances. The most dramatic effect in the angular distributions is the presence of a strong and very narrow forward scattering peak in the DCS for low rotational product states. This forward peak was observed in both the theoretical and experimental results. As seen in Figure 3.11, the forward peak for the $(0,0\rightarrow 0,0)$ case begins at about $E_C=1$ eV and persists to the highest energies considered. Other final rotational states likewise show a forward peak, but at progressively higher energies.

The results indicate that the strongest case for reactive resonances in the $H+HD$ reaction is to be found in the forward peaking of the DCS. To establish the link between the forward peak and resonance behavior, it is necessary to analyze the underlying reaction dynamics that gives rise to

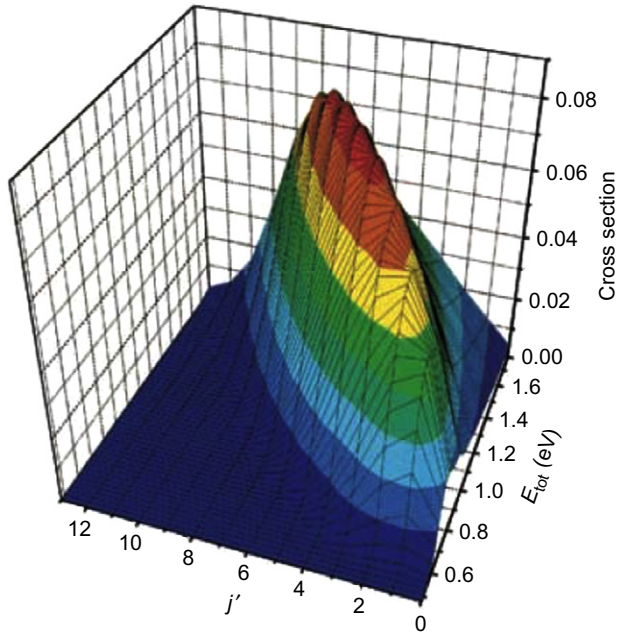

Figure 3.10 The ICS for $H+HD(v=0,j=0)\rightarrow D+H_2(v'=0,j')$ versus E_C and j' computed from quantum scattering theory using the BKMP2-PES.

the forward peaking. First, as noted in other reactions, the forward peak is the by-product of high impact parameter (i.e., high J) reactive scattering. As an illustration, in Figure 3.12 we plot forward scattering integrated opacity function, Eq. (30), $d\sigma_R(0,0\rightarrow 0,0;\theta=0,E_C,J_{max})/d\Omega$ versus J_{max} at the experimental collision energy of $E_C=1.200\,\text{eV}$. As seen in the figure, the forward peak comes from just a small number of partial waves near the value $J_{max}=25$; at this value of J, the vibrationally adiabatic barriers are centrifugally shifted upward about 0.5 eV relative to the nonrotating barriers. Next, we note that the forward scattering peak is rotationally cold and vibrationally hot compared to scattering in other directions. By averaging the DCS over the narrow interval $\theta=[0^\circ-5^\circ]$, it is found that $<j'>_{\theta=0}=1.3$ and $<E'_{vib}-E_{H_2}(v'=0,j'=0)>_{\theta=0}=1155\,\text{cm}^{-1}$. These numbers can be contrasted with the ICS's results that are averaged over all scattering angles: $<j'>_{all}=5.3$ and $<E'_{vib}-E_{H_2}(v'=0,j'=0)>_{all}=574\,\text{cm}^{-1}$. In Figure 3.13, we plot the mean product vibrational energy against scattering angle for $H+HD(0,0)\rightarrow D+H_2(v',j')$ at $E_C=1.200\,\text{eV}$, which clearly reveals the special product distribution in the forward direction. Finally, to connect the forward scattering to dynamical trapping phenomena, we consider the behavior of the angle-dependent time delay. In Figure 3.14, we plot the j'-averaged

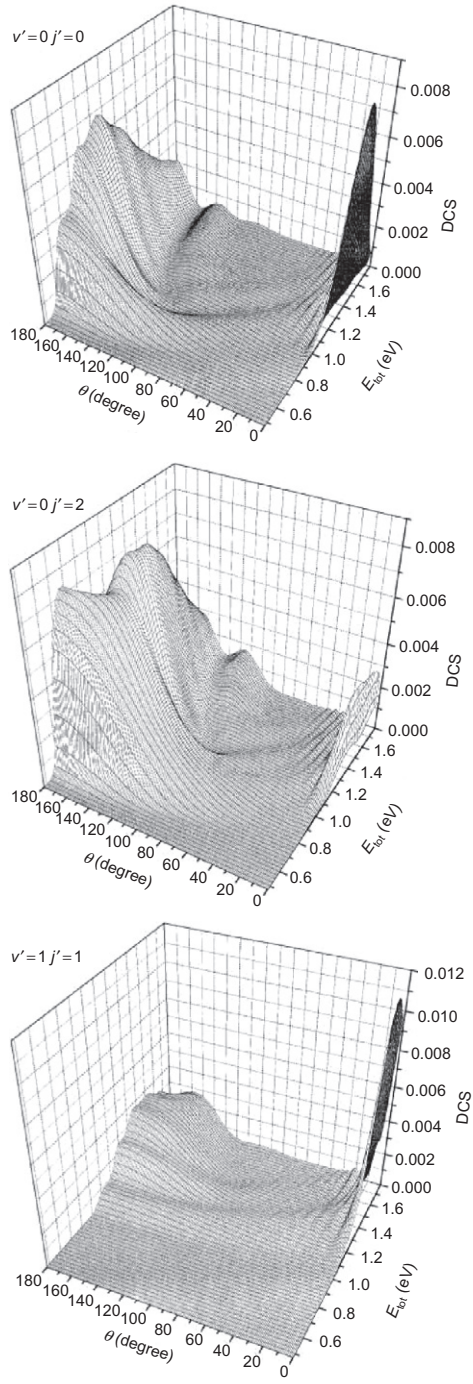

Figure 3.11 The DCS in Å^2/sr for the several final states of the $H+HD(v=0, j=0) \rightarrow D+H_2(v', j')$ reaction. The results were computed from quantum scattering theory using the BKMP2-PES.

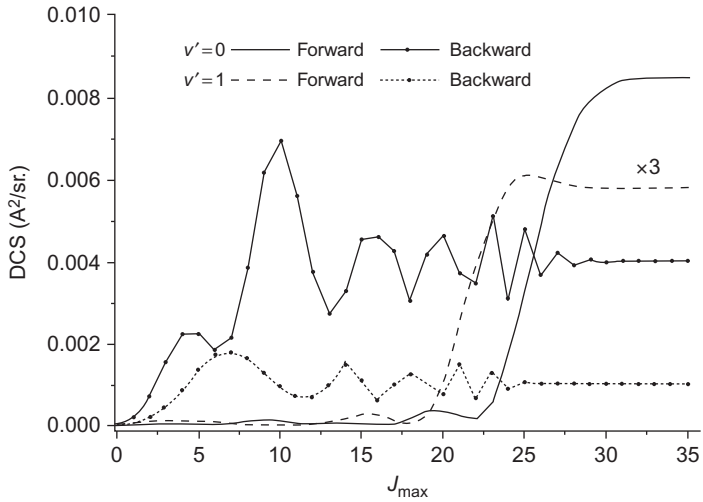

Figure 3.12 The angle-dependent integrated opacity function $d\sigma_R(00 \rightarrow v' = 0, 1, j' = 0; \theta, E_C, J_{max})$ versus J_{max} computed for the experimental energy $E_C = 1.200$ eV. This quantity is computed by restricting the partial wave sum in the DCS to the terms $J \leq J_{max}$. The result is shown for forward and backward scattering to illustrate the J-contributions to scattering at different θ.

time delay for $H+HD(0,0) \rightarrow D+H_2(v' = 0, j' = \text{all})$ against scattering angle at $E_C = 1.200$ eV. The forward direction is seen to exhibit a time delay about 20 fs longer than the other scattering directions.

The state assignment of resonance which gives rise to the forward peaking is a delicate issue. It is clear from Figure 3.12 that state involved is highly rotationally excited; thus, the resonance states are distorted from their $J = 0$ counterparts. However, it is possible to demonstrate on energetic grounds that the $J = 25$ resonance corresponds to the adiabatic barrier maximum of two internal states of the H–H–D complex, viz. the $(v_{ss}, v_{bend}) = (1, 0)$ and (0,2). Since neither adiabatic potential curve, $V_{ad}(\boldsymbol{s}; 1, 0)$ nor $V_{ad}(\boldsymbol{s}; 0, 2)$, exhibit sufficiently deep wells to trap a Feshbach resonance at $J = 25$, the resonance state is a barrier state. Because of the near degeneracy of the two barrier heights, the trapping will involve a combination of symmetric stretch and bend excitations at the transition state.

The SQ method was used to extract resonance states for the $J = 25$ dynamics by using the centrifugally shifted Hamiltonian. In Figure 3.15, the SQ wavefunction for a trapped state at $E_C = 1.2$ eV is shown. The wavefunction has been sliced perpendicular to the minimum energy path and is plotted in the symmetric stretch and bend normal mode coordinates. As anticipated, the wavefunction shows a combination of one quantum of symmetric stretch excitation and two quanta of bend excitations.

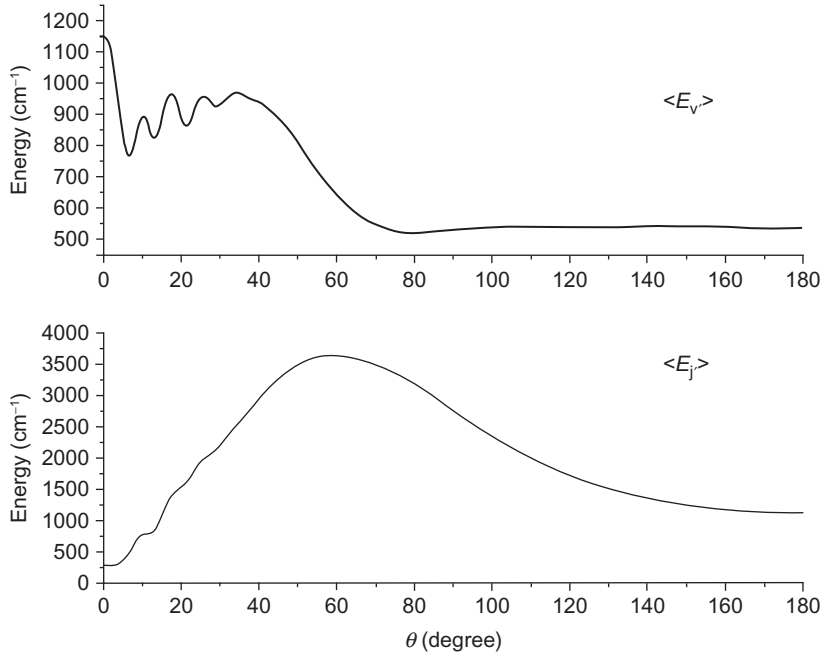

Figure 3.13 The average product rotational and vibrational excitations (above zero point) versus scattering angle for $H+HD(v=0, j=0) \rightarrow D+H_2$ at $E_C = 1.200$ eV computed by quantum scattering theory.

In summary, the $H+HD$ reaction shows little sign of resonance scattering in the ICS. Furthermore, the product distributions without angle resolution show no unusual behavior as functions of energy that might indicate resonance behavior. On the other hand, the forward peaking in the angular product distribution does appear to reveal resonance structure. Since time delay analysis is at present not possible in a molecular beam experiment, it is the combination of a sharp forward peak with the unusual angular product distribution, which most clearly indicates the presence of a resonance.

5. PREREACTIVE/POSTREACTIVE RESONANCES: *F+HCL*

For both the Feshbach resonance in $F+HD$ and the barrier resonance in $H+HD$, the trapped resonance state was localized close to the saddle point. Thus, the complexes correspond to the intermediates with partially formed (or broken) bonds. The $F+HCl \rightarrow HF+Cl$ reaction illustrates a third category of resonance, the prereactive (and postreactive) resonance. In this case, the bonding of the reagent (or product) is only weakly perturbed by the colliding

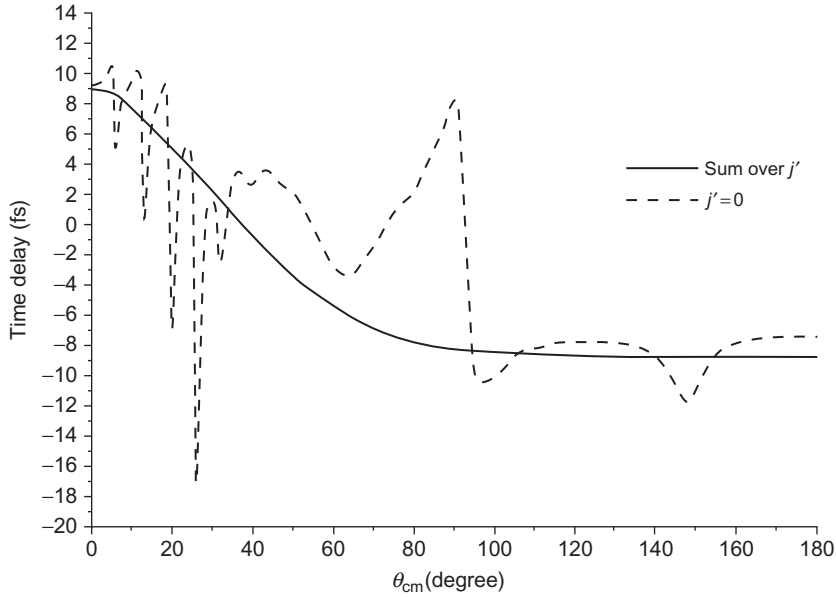

Figure 3.14 The scattering time delay versus θ for $H+HD(v=0,j=0)\rightarrow D+H_2$ at $E_C=1.200$ eV. The dashed curve is obtained using the formula of Goldberger for the final state $H_2(v'=0,j'=0)$, whereas the solid line is the result of averaging over the final rotational states, j' for the dominant $v'=0$ product. Both curves show roughly an extra 20 fs of time delay in the forward direction but the averaging eliminates the spurious structure that are related to minima in the DCS versus θ.

radical [120]. As we shall see, this category of resonance can have dramatically longer lifetimes than those seen for conventional Feshbach or barrier resonances [121].

The $F+HCl$ ($\Delta H_{rxn}=-33$ kcal/mol) reaction was studied experimentally by Houston and coworkers [122] as a problem in thermal kinetics. The observed rate coefficient exhibited a strong non-Arrhenius behavior that was attributed to the possible formation of a reactive complex. Later Nesbitt and coworkers [123] studied the rovibrational product distribution in a single collision environment. The observed unusual product distribution seemed also to suggest complex formation. Several theoretical studies were carried out to model the dynamics of the reaction [124, 125]; however, the results were qualified because of the lack of a high-quality PES. Deskevich et al. [126] have recently produced a fitted PES using the multireference configuration interaction (MRCI) method with a large basis. The classical barrier to reaction was found to be 3.8 kcal/mol. When corrections due to zero point energy were included, the barrier fell to 3.5 kcal/mol. Although this barrier is slightly too high to fully account for the results of Houston and coworkers,

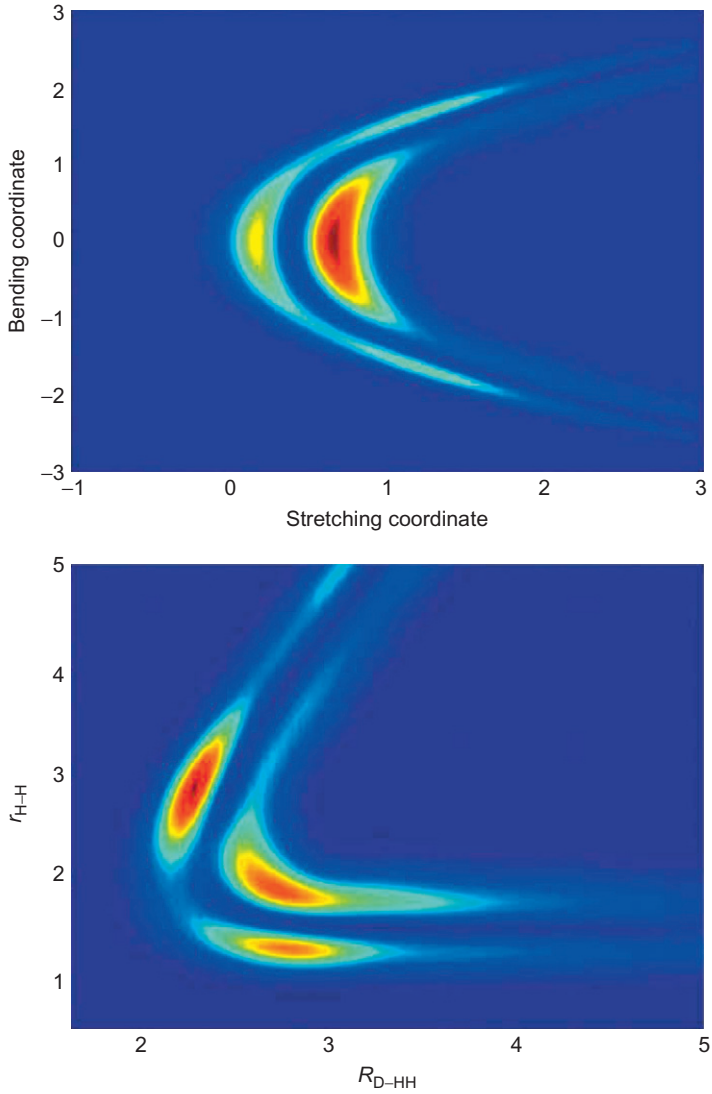

Figure 3.15 A resonance state for the $H+HD$ system at $E_C = 1.2$ eV at a total angular momentum of $J = 25$. In the upper panel, the wavefunction is shown in the $H+HD$ Jacobi coordinates for the collinear subspace. In the lower panel, the wavefunction has been sliced perpendicular to the minimum energy path and is plotted in symmetric stretch and bend normal mode coordinates.

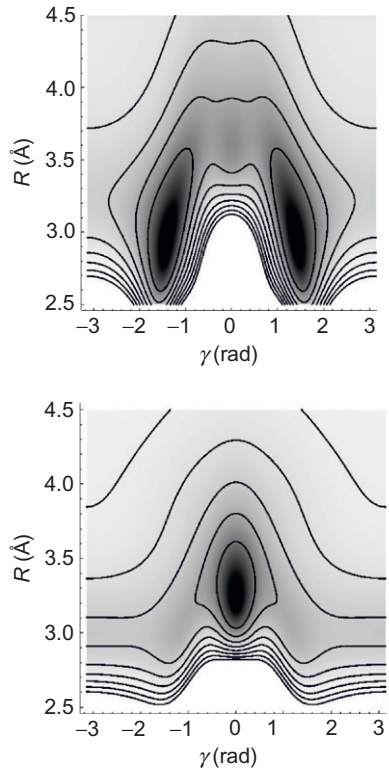

Figure 3.16 The PES for the *F+HCl* reaction in the entrance and exit channels as a function of the Jacobi coordinates (R, γ).

the PES is believed to be reasonably realistic. The most interesting aspect of the nonresonant dynamics observed from simulations on this surface is an extremely strong rotational enhancement of the reaction [127]. Indeed, the reaction of $F+HCl(j = 10)$ proceeds about 100 times faster than $F+HCl(j = 0)$ at the same total energy.

In Figure 3.16, we show the potential contours in the entrance and exit channels. In these plots, the diatomic distance is held fixed at the equilibrium bond length and the PES is plotted against Jacobi distance and angle (R, θ). A vdW well of depth 2.5 kcal/mol is observed in the entrance channel with a bent configuration. In the exit channel, a collinear vdW well of depth 2.0 kcal/mol is found. Variational calculations of the vibrational states reveal that several bound states exist in these wells [128]. More pertinent to the present discussion, the vdW wells can also lead to the existence of resonance states in both the entrance and exit channels.

The quantum dynamics for the $J = 0$ partial wave of the *F+HCl* reaction was simulated on a very fine grid of energies using the method of

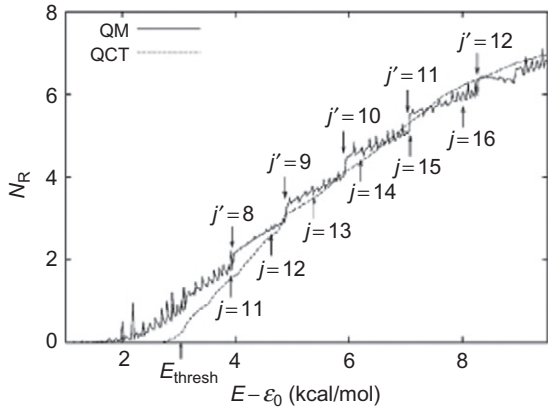

Figure 3.17 The cumulative reaction probability for $J = 0$ $F+HCl$ versus collision energy. The location of the $HCl(v = 0, j)$ energetic threshold is indicated. For comparison, the QCT result is also shown.

Manolopoulos and coworkers [101]. In Figure 3.17, we show the resulting cumulative reaction probability, $N_R(E)$, versus energy [127]. A dense set of extremely narrow peaks are apparent. In Figure 3.18, a blowup of $N_R(E)$ for a narrow range of energies near threshold is shown. (To aid in the assignment process, we also plot $N_R(E)$ for the $J = 2$ partial wave. The additional peaks observed for this higher angular momentum state relate to the rotational progressions in the complex.) The relationship between the peaks in $N_R(E)$ and resonance phenomena is clearly revealed by the lifetime matrix. In Figure 3.19, we show the dominant eigenvalue of $\boldsymbol{Q}$ [defined by Eq. (24)] versus energy [128]. For each peak in $N_R(E)$, we observe a corresponding peak in the time delay which typically lies in the range of 1–20 ps. These lifetimes are one to two orders of magnitude larger than those observed for Feshbach or barrier resonances.

The model that has emerged for the resonance structure in $F+HCl$ is based on progressions of vdW states in the entrance and exit channels and is pictured in the schematic of Figure 3.20. In the entrance channel, we view the $HCl(v, j)$ rovibrational state as weakly perturbed by the distant F-atom. Thus, for most of the resonance states, the motion of the HCl diatom more closely resembles that of a hindered rotor than small vibration around the geometry of the vdW minimum. For $J = 0$, the observed resonance states can be labeled by the quantum numbers (ν_R, j). All entrance channel resonance states lie in the $HCl(v = 0)$ vibrational state while the rotational levels are observed for the range $j \geq 5$ [128]. The quantum number ν_R represents the vibrational level in the vdW stretching coordinate R_{F-HCl}. The vibrational frequency of this weak bond is only about 50 cm^{-1}, and vdW well supports roughly 10 ν_R states

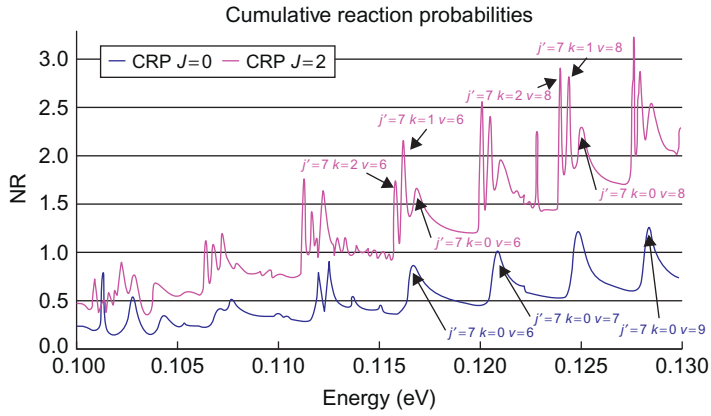

Figure 3.18 A high-resolution view of the cumulative reaction probability (CRP) for $J = 0$ and $J = 2$. The resonance peaks in this range are assigned to the *Cl-HF*($v' = 3, j', k'$) postreactive states, where v is the quantum number for the low frequency vdW stretching mode.

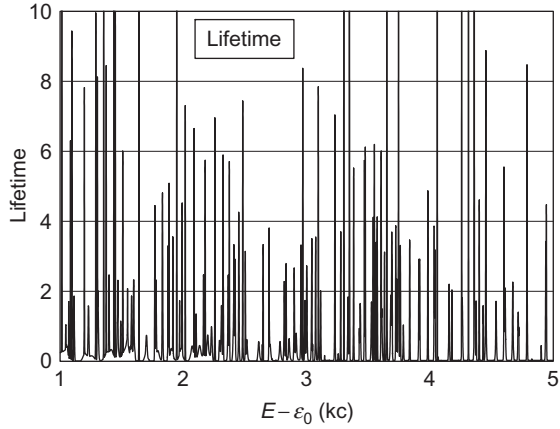

Figure 3.19 Collision lifetime in picoseconds from the time delay matrix versus collision energy in kcal/mol. The resonance states are seen to be long lived.

for each j. A separable first-order representation of the resonance state is

$$\psi^{\text{res}}_{j,n_R}(r, R, \theta) = \varphi_{v=0}(r; R, \theta) Y^0_j(\theta) \xi_{n_R}(R) \tag{33}$$

The vibrationally adiabatic approximation should be made for the fast *HCl* vibrational coordinate r. Solving the one-dimensional Schrodinger equation with (R, θ) fixed leads to the parameterized form $\varphi_{v=0}(r; R, \theta)$. The rotationally averaged potential is then used to compute the one-dimensional potential

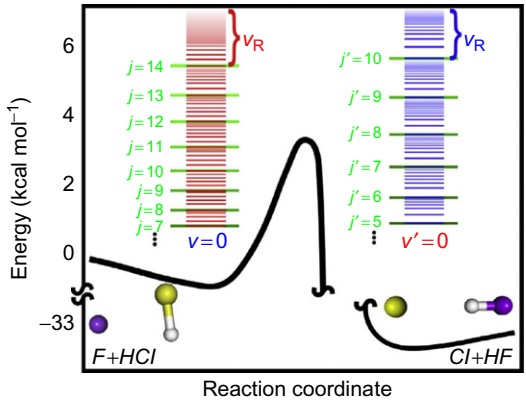

Figure 3.20 A schematic diagram representing the resonance structure of the *F+HCl* reaction. The prereactive resonances (for $J = 0$) are labeled by the HCl rotational quantum number j and the vdW stretching quantum number ν_R. The postreactive resonances are labeled by the *HF* rotational quantum number and the vdW stretching quantum number.

well in the *R*-coordinate. Approximate expressions similar to Eq. (33) have been used to represent vdW states of closed shell systems such as rare gas atoms + diatoms [129, 130].

Completely analogous expressions can be used to represent resonance states in the product channel, *Cl+HF*. Because of the 33 kcal/mol exothermicity of the reaction, all the resonance states we have observed correspond to the excited final vibrational channels $HF(v' = 2)$ and $HF(v' = 3)$.

Chemical reaction in the *F+HCl* system can be resonance mediated in two ways. First, a reagent channel resonance can form through rotationally inelastic scattering which then decays by tunneling into the product channel. Second, the product channel resonance can be formed directly by tunneling, which then inelastically decays by product molecules. The probabilities for these reactive decay events can be directly extracted by fitting the partial widths to the *S*-matrix using Eq. (7). A more elegant approach employs the eigenvector of the time delay matrix corresponding to the largest eigenvalue. This eigenvector can be directly analyzed to give the flux into each open channel for resonance decay.

Although most resonances in the *F+HCl* system are clearly of the reagent type or product type, there are some "mixed" cases. Because the resonance manifold is dense, degeneracies can occur between zero-order reagent-type or product-type states. Thus, the resonance wavefunctions for these states are linear combinations of entrance and exit channel expressions.

Even though the *F+HCl* reaction does not possess the deep trapping wells that are apparent for insertion or ion–molecule reactions, the sheer number of resonance states that exist for this system make it a complex-forming

reaction. Thus, a substantial fraction of the reaction proceeds through the complex intermediate. This implies that the complex can be inferred from the non-Arrhenius behavior of the rate constant without the necessity of a cross beam experiment.

6. CONCLUSIONS

The influence of reactive resonances on the outcome of a collision experiment can be subtle. Unlike the dramatic resonance phenomena observed in nuclear and atomic collision processes, reactive resonances are often only revealed after a careful analysis of scattering observables. Nevertheless, reactive resonances play an essential role in the detailed dynamical analysis of many systems. As we have seen, resonances can have a large influence on physical observables such as excitation functions, state-to-state branching ratios, and angular product distributions. Even highly averaged quantities, like the low temperature reaction rate constant for $F+HD \rightarrow D+HF$, can be strongly affected by processes like resonance tunneling. In addition to large quantitative effects on the reaction attributes, we should also emphasize that these effects are also very sensitive to details of the PES and to dynamical approximation. Agreement between theory and experiment for resonant observables provides, for both, a very stringent test of accuracy.

Undoubtedly, many reactions investigated in the future will possess reactive resonances. It would be desirable to have in place unambiguous diagnostic tests that would reveal whether or not a new system supported resonance states. The case studies considered above should make it clear, however, that such diagnostics are not easily identified. Perhaps as more systems are investigated, a more or less complete set of possible resonance signatures may be determined. At this point, however, each new system shows some novel resonance features. Given an accurate PES, theoretical analysis can, in principle, provide a more definitive determination of whether or not a reactive resonance exists for a system. Since scattering can be investigated for single partial waves, resonance signatures are identified using techniques such as time delay analysis or SQ without the complication of impact parameter averaging. Given that theory shows the existence of a reactive resonance on a reliable PES, it then becomes a somewhat empirical undertaking to determine which dynamical observables are the most strongly affected.

ACKNOWLEDGMENTS

I am extremely grateful to my group members without whom none of this work would have been possible. They include Raymond Sadeghi, Sheng

der Chao, Magnus Gustafsson, Michael Hayes, Kaito Takahashi, and Zeb Kramer. I also own a deep debt to my senior collaborators K. Liu, David Manolopoulos, Donghui Zhang, David Nesbitt, and Xueming Yang on the resonance studies. This work was supported by the National Science Foundation and through a Distinguished Foreign Professorship from the Chinese Academy of Science.

REFERENCES

[1] R.T. Skodje, X.M. Yang, The observation of quantized bottleneck states in chemical reactions. Int. Rev. Phys. Chem. 23 (2004) 253.
[2] A. Kuppermann, in: D.G. Truhlar, (Ed.), Reactive scattering resonances and their physical interpretation, Potential Energy Surfaces and Dynamics Calculations, Plenum Press, New York, 1981, p. 375.
[3] B.C. Garrett, D.W. Schwenke, R.T. Skodje, D. Thirumalai, T.C. Thompson, D.G. Truhlar, Adiabatic and Nonadiabatic Methods for Energies, Lifetimes, and Branching Ratios of Reactive Resonances in Bimolecular Collisions, ACS Symposium Series 263, American Chemical Society, Washington DC, 1984, 375.
[4] K. Liu, Crossed-beam studies of neutral reactions: State-specific differential cross sections, Annu. Rev. Phys. Chem. 52 (2001) 139.
[5] F. Fernandez-Alonso, R.N. Zare, Scattering resonances in the simplest chemical reaction, Annu. Rev. Phys. Chem. 53 (2002) 67.
[6] X.M. Yang, D.H. Zhang, Dynamical resonances in the fluorine atom reaction with the hydrogen molecule, Acct. Chem. Res. 41 (2008) 981.
[7] J.C. Polanyi, A.H. Zewail, Direct observation of the transition state, Acct. Chem. Res. 28 (1995) 119.
[8] G.C. Schatz, Detecting resonances, Science 288 (2000) 1599.
[9] S.D. Chao, R.T. Skodje, Signature of reactive resonance: Three case studies, Theor. Chem. Acc. 108 (2002) 273.
[10] K. Liu, R.T. Skodje, D.E. Manolopoulos, Perspective: Resonances in bimolecular chemical reactions, Phys. Chem. Comm. 5 (2002) 27.
[11] J.M. Bowman, Resonances: Bridge between spectroscopy and dynamics, J. Phys. Chem. A 102 (1998) 3006.
[12] D.G. Truhlar, A. Kuppermann, Quantum mechanics of the $H+H_2$ reaction: Exact scattering probabilities for collinear collisions, J. Chem. Phys. 52 (1970) 3841.
[13] D.G. Truhlar, A. Kuppermann, Exact and approximate quantum mechanical reaction probabilities and rate constants for the collinear $H+H_2$ reaction, J. Chem. Phys. 56 (1972) 2232.
[14] R.D. Levine, S-F. Wu, Resonances in reactive collisions: Computational study of the $H+H_2$ collision, Chem. Phys. Lett. 11 (1971) 557.
[15] S.–F. Wu, R.D. Levine, Quantum mechanical computational studies of chemical reactions: 1. Close-coupling method for collinear $H+H_2$ reaction, Mol. Phys. 22 (1971) 881.
[16] G.C. Schatz, A. Kuppermann, Role of direct and resonant (compound state) processes and of the interferences in the quantum dynamics of the collinear $H+H_2$ exchange reaction, J. Chem. Phys. 59 (1973) 964.
[17] G.C. Schatz, A. Kuppermann, Dynamical resonances in collinear, coplanar, and three-dimensional quantum mechanical reactive scattering, Phys. Rev. Lett. 35 (1975) 1266.
[18] G.C. Schatz, J.M. Bowman, A. Kuppermann, Exact quantum, quasiclassical, and semiclassical reaction probabilities for the collinear $F+H_2 \rightarrow HF+F$ reaction, J. Chem. Phys. 63 (1975) 674.

[19] S.L. Latham, J.F. McNutt, R.E. Wyatt, M.J. Redmon, Quantum dynamics of the F+H_2 reaction: Resonance models, and energy and flux distributions in the transition state, J. Chem. Phys. 69 (1978) 3746.
[20] R.H. Bisseling, R. Kosloff, J. Manz, Dynamics of hyperspherical and local mode resonance decay studied by time dependent wave packet propagation, J. Chem. Phys. 83 (1985) 993.
[21] M.S. Zhao, M. Mladenovic, D.G. Truhlar, D.W. Schwenke, O. Sharafeddin, Y. Yan, D.J. Kouri, Spectroscopic analysis of transition state energy levels: Bending-rotational spectrum and lifetime analysis of H_3 quasibound states, J. Chem. Phys. 91 (1989) 5302.
[22] S.A. Cuccaro, P.G. Hipes, A. Kuppermann, Symmetry analysis of accurate H+H_2 resonances for low partial waves, Chem. Phys. Lett. 157 (1989) 440.
[23] R.T. Skodje, R. Sadeghi, H. Koppel, J.L. Krause, Spectral quantization of transition state dynamics for the three-dimensional H+H_2 reaction, J. Chem. Phys. 101 (1994) 1725.
[24] S.K. Gray, Wave packet dynamics of resonance decay: An iterative equation approach with application to HCO→H+CO, J. Chem. Phys. 96 (1992) 6543.
[25] V. Aquilanti, S. Cavalli, D. De Fazio, A. Volpi, A. Aguilar, J.M. Lucas, Benchmark rate constants by the hyperquantization algorithm. The F+H_2 reaction for various potential energy surfaces: Features of the entrance channel and of the transition state, and low temperature reactivity, Chem. Phys. 308 (2005) 237.
[26] Z.G. Sun, S.Y. Lee, H. Guo, D.H. Zhang, Comparison of second-order split operator and Chebyshev propagator in wave packet based state-to-state reactive scattering calculations, J. Chem. Phys. 130 (2009) 174102.
[27] S.C. Althorpe, D.C. Clary, Quantum scattering calculations on chemical reactions, Annu. Rev. Phys. Chem. 54 (2003) 493.
[28] R. Sadeghi, R.T. Skodje, High energy transition state resonances in the H+H_2 reaction, J. Chem. Phys. 98 (1993) 9208; R. Sadeghi and R.T. Skodje, Spectral quantization of high energy transition state resonances in the H+H_2 reaction, J. Chem. Phys. 99, 5126 (1993).
[29] R. Sadeghi, R.T. Skodje, J. Barriers, Thresholds, and resonances: Spectral quantization of the transition state for the collinear D+H_2 reaction, Chem. Phys. 102 (1995) 193.
[30] G. Jolicard, C. Leforestier, E.J. Austin, Resonance states using the optical potential model. Study of Feshbach resonances and broad shape resonances, J. Chem. Phys. 88 (1988) 1026.
[31] V. Mandelstam, H.S. Taylor, A simple recursion polynomial expansion of the Greens function with absorbing boundary conditions—Application to the reactive scattering, J. Chem. Phys. 103 (1995) 2903.
[32] N. Balucani, G. Capozza, F. Leonori, E. Segoloni, P. Casavecchia, Crossed molecular beam reactive scattering: From simple triatomic to multichannel polyatomic reactions, Int. Rev. Phys. Chem. 25 (2006) 109.
[33] X.M. Yang, State-to-state dynamics of elementary chemical reactions using Rydberg translational spectroscopy, Int. Rev. Phys. Chem. 24, 37 (2005).
[34] K. Liu, Recent advances in crossed-beam studies of bimolecular reactions, J. Chem. Phys. 125, 132307 (2006).
[35] D.M. Neumark, Transition state spectroscopy of bimolecular chemical reactions, Annu. Rev. Phys. Chem. (1992) 43153.
[36] D.M. Neumark, Probing chemical dynamics with negative ions, J. Chem. Phys. 125 (2006) 132303.
[37] S. Mahapatra, Quantum non-adiabatic dynamics through conical intersections: Spectroscopy to reactive scattering, Int. Rev. Phys. Chem. 23 (2006) 483.
[38] D.E. Manolopoulos, K. Stark, H-J. Werner, D.A. Arnold, S.E. Bradforth, D.M. Neumark, The transition state of the F+H_2 reaction, Science 262 (1993) 1852.
[39] A. Weaver, R.B. Metz, S.E. Bradforth, D.M. Neumark, Spectroscopy of the I+HI transition-state region by photodetachment of IHI^-, J. Phys. Chem. 92 (1988) 5558.
[40] J.O. Hirschfelder, Some quantum mechanical considerations in the theory of reactions involving an activation energy, J. Chem. Phys. 7 (1939) 616.
[41] W.H. Miller, N.C. Handy, J.E. Adams, Reaction path Hamiltonian for polyatomic molecules, J. Chem. Phys. 72 (1980) 99.

[42] A.D. Isaacson, D.G. Truhlar, Polyatomic canonical variational theory for chemical reaction rates. Separable-mode formalism with application to $OH+H_2 \rightarrow H_2O+H$, J. Chem. Phys. 76 (1982) 1380.
[43] R.S. Friedman, D.G. Truhlar, Chemical reaction thresholds are resonances, Chem. Phys. Lett. 183 (1991) 539.
[44] D.C. Chatfield, R.S. Friedman, S.L. Mielke, G.C. Lynch, D.G. Truhlar, and D.W. Schwenke, Computational spectroscopy of the transition state, in: R.E. Wyatt, J.Z.H. Zhang, (Eds.), Dynamics of Molecules and Chemical Reactions, Marcel Dekker, New York, 1996, p. 323.
[45] E. Pollak, P. Pechukas, Transition states, trapped trajectories, and classical bound states embedded in the continuum, J. Chem. Phys. 69 (1978) 1218.
[46] O. Zobay, G. Alber, Periodic orbits and molecular photoabsorption, J. Phys. B 26 (1993) L539.
[47] I. Burhardt, P. Gaspard, Molecular transition state, resonances, and periodic orbit theory, J. Chem. Phys. 100 (1994) 6395.
[48] T. Seideman, W.H. Miller, Transition state theory, Siegert eigenstates, and quantum mechanical reaction rates, J. Chem. Phys. 95 (1991) 1768.
[49] V. Ryaboy, N. Moiseyev, Cumulative reaction probability from Siegert eigenvalues: Model studies, J. Chem. Phys. 98 (1993) 9618.
[50] R. Sadeghi, R.T. Skodje, The spectroscopy of potential barriers: An analytic line shape formula for broad resonances, Phys. Rev. A 52 (1995) 1996.
[51] R.S. Freidman, D.G. Truhlar, Barrier resonances and chemical reactivity, in: D.G. Truhlar, B. Simon, (Eds.), Multiparticle Quantum Scattering with Applications to Nuclear, Atomic, and Molecular Physics, Springer-Verlag, New York, 1997, p. 243.
[52] H-D. Meyer, Analytically continued S-matrix potentials defined as a sum of exponentials. 1. The single channel problem, J. Phys. B 16 (1983) 2265.
[53] R.T. Skodje, The adiabatic theory of heavy-light-heavy chemical reactions, Annu. Rev. Phys. Chem. 44 (1993) 145.
[54] X.G. Wang, W.R. Dong, M.H. Qiu, R.F. Ren, L. Che, D.X. Dai, X.Y. Wang, X.M. Yang, Z.G. Sun, B.N. Fu, S.Y. Lee, X. Xu, and D.H. Zhang, $HF(v' = 3)$ forward scattering in the $F+H_2$ reaction: Shape resonance and slow-down mechanism, Proc. Natl. Acad. Sci. 105 (2008) 6227.
[55] D.C. Chatfield, S.L. Mielke, T.C. Allison, D.G. Truhlar, Quantum dynamical bottlenecks and transition state control of the reaction of D with H_2: Effect of varying the total angular momentum, J. Chem. Phys. 112 (2000) 8387.
[56] D.X. Dai, C.C. Wang, S.A. Harich, X.Y. Wang, X.M. Yang, S.D. Chao, R.T. Skodje, Interference of quantized transition state pathways in the $H+D_2 \rightarrow D+HD$ chemical reaction, Science 300 (2003) 1730.
[57] J.Y. Zhang, D.X. Dai, C.C. Wang, S.A. Harich, X.Y. Wang, X.M. Yang, M. Gustafsson, R.T. Skodje, The state-to-state-to-state dynamics of the $D+H_2 \rightarrow HD+D$ reaction: Control of transition state pathways via reagent orientation, Phys. Rev. Lett. 96 (2006) 093201.
[58] F.J. Aoiz, V.J. Herrero, M.P. de Miranda, V.S. Ranbanos, Constraints at the transition state of the $D+H_2$ reaction: Quantum bottlenecks vs. stereodynamics, Phys. Chem. Chem. Phys. 9 (2007) 5367.
[59] M. Gustafsson, R.T. Skodje, Probing the stereodynamics of chemical reactions using helicity filtering, Chem. Phys. Lett. 434 (2007) 20.
[60] S.A. Rakityansky, N. Elander, Analyzing the contribution of individual resonance poles of the S-matrix to two-channel scattering, Int. J. Quantum Chem. 106 (2006) 1105.
[61] M.L. Goldberger, K.M. Watson, Collision Theory, Wiley, New York, 1964.
[62] G. Breit, E.P. Wigner, Capture of slow neutrons, Phys. Rev. 49 (1936) 519.
[63] J.R. Taylor, Scattering Theory, Wiley, New York, 1972.
[64] D. Sokolovski, E. Akhmatskaya, and S. K. Sen, Extracting S-matrix poles for resonances from numerical data: Type-II Pade' reconstruction, Comput. Phys. Commun. 182, 448 (2011).

[65] M.J. Redmon, R.E. Wyatt, Quantum resonance structure in the three-dimensional F+H2 reaction, Chem. Phys. Lett. 63 (1979) 209.
[66] G.C. Schatz, D. Sokolovski, J.N.L. Connor, Influence of transition state resonances on integral cross sections and product rovibrational distributions for the Cl+HCl→ClH+Cl reaction, J. Chem. Phys. 94 (1991) 4311.
[67] S.D. Chao, R.T. Skodje, Time delay as a tool to identify the signatures of reactive resonance: F+HD and F+H_2, J. Chem. Phys. 119 (2003) 1462.
[68] E.P. Wigner, Lower limit for the energy derivative of the scattering phase shift, Phys. Rev. 98 (1955) 145; L. Eisenbud, PhD thesis; Princeton University, Princeton, NJ.
[69] F.T. Smith, Lifetime matrix in collision theory, Phys. Rev. 118 (1960) 349.
[70] S.C. Althorpe, A plane wave packet approach to quantum scattering theory, Int. Rev. Phys. Chem. 23 (2004) 219.
[71] Ref. [61], p. 494; also see, M.L. Goldberger, K.M. Watson, Concerning the notion of "time interval" in S-matrix theory, Phys. Rev. 127 (1962) 2284; M. Froissart, M.L. Goldberger, K.M. Watson, Spatial separation of events in S-matrix theory, Phys. Rev. 131, 2820 (1963).
[72] A. Kuppermann, Y-S.M. Wu, The quantitative prediction and lifetime of a pronounced reactive scattering resonance, Chem. Phys. Lett. 241 (1995) 229; ibid 243, 586 (1995) (Erratum).
[73] A.J. Seigert, On the derivation of the dispersion formula for nuclear reactions, Phys. Rev. 56 (1939) 750.
[74] A.U. Hazi, H.S. Taylor, Stabilization method of calculating resonance energies: Model problem, Phys. Rev. A 1 (1970) 1109.
[75] T.C. Thompson, D.G. Truhlar, Stabilization calculations and probability density for the well-studied collision resonances in collinear F+H_2, F+HD, and F+D_2, J. Phys. Chem. 88 (1984) 210.
[76] S. Skokov, J.M. Bowman, Complex L2 calculation of the variation of the resonance widths of HOCl with total angular momentum, J. Chem. Phys. 111 (1999) 4933.
[77] W.P. Reinhardt, Complex coordinates in the theory of atomic and molecular structure and dynamics, Annu. Rev. Phys. Chem. 33 (1982) 223.
[78] R.T. Skodje, R. Sadeghi, J.L. Krause, Control of transition state spectra: A variational algorithm, Chem. Phys. 240 (1999) 129.
[79] B. Maiti, S. Mahapatra, N. Sathyamurthy, A time-dependent quantum mechanical investigation of dynamical resonances in three-dimensional HeH_2^+ and $HeHD^+$ systems, J. Chem. Phys. 113 (2000) 59.
[80] A.J.C. Varandas, H.G. Yu, Spectral quantization of transition state resonances in collinear Mu+H_2 and Mu+D_2 collisions, Chem. Phys. 209 (1996) 31.
[81] W.B. Miller, S.A. Safron, D.R. Herschbach, Exchange reactions of alkali atoms with alkali halides—A collision complex mechanism, Discuss. Faraday Soc. 44 (1967) 108.
[82] W.H. Miller, J.Z.H. Zhang, How to observe the elusive resonances in H or D+H_2→H_2 or HD+H reactive scattering, J. Phys. Chem. 95 (1991) 12.
[83] F.J. Aoiz, V.J. Herrero, V.S. Rabanos, Classical collision complexes in the D+H_2 (v = 0, j = 0)→HD(v′, j′)+H reaction, J. Chem. Phys. 95 (1991) 7767; ibid 97 (1994) 7423.
[84] D. Sokolovski, J.N.L. Connor, Semiclassical nearside-farside theory for inelastic and reactive atom-diatom collisions, Chem. Phys. Lett. 305 (1999) 238.
[85] D. Sokolovski, J.F. Castillo, C. Tully, Semiclassical angular scattering in the F+H2 → HF+H reaction: Regge pole analysis using the Pade' approximation, Chem. Phys. Lett. 313 (1999) 225.
[86] D.M. Neumark, A.M. Wodke, G.N. Robinson, C.C. Hayden, R. Shobatake, Y.T. Lee, Molecular beam studies of the F+H_2 reaction, J. Chem. Phys. 82 (1985) 3045.
[87] D.M. Neumark, A.M. Wodke, G.N. Robinson, C.C. Hayden, R. Shobatake, R.K. Sparks, T.P. Schafer, and Y.T. Lee, Molecular beam studies of the F+D_2 and F+HD reactions, J. Chem. Phys. 82 (1985) 3067.

[88] F. Fernandez-Alonso, B.D. Bean, J.D. Ayers, A.E. Pomerantz, R.N. Zare, L. Banares, and F.J. Aoiz, Evidence for scattering resonances in the H+D_2 reaction, Angew. Chem. Int. Ed. 39 (2000) 2748.
[89] F. Fernandez-Alonso, B.D. Bean, R.N. Zare, Measurement of the HD(v'=2,j'=3) product differential cross section for the H+D_2 exchange reaction at 1.55 eV using the photoloc technique, J. Chem. Phys. 111 (1999) 1022.
[90] F. Fernandez-Alonso, B.D. Bean, R.N. Zare, F.J. Aoiz, L. Banares, J.F. Castillo, Forward scattering in the H+D_2→HD+D reaction: Comparison between experiment and theoretical predictions, J. Chem. Phys. 114 (2001) 4534.
[91] S.A. Harich, D.X. Dai, C.C. Wang, X. Yang, S.D. Chao, R.T. Skodje, Experimental and theoretical study of the H+HD→D+H_2 reaction at collision energy E=0.5 eV, J. Chem. Phys. 116 (2002) 4769.
[92] S.D. Chao, S.A. Harich, D.X. Dai, C.C. Wang, X.M. Yang, R.T. Skodje, A fully state and angle resolved study of the H+HD→D+H_2 reaction: Comparison of a molecular beam experiment to *ab initio* quantum reaction dynamics, J. Chem. Phys. 117 (2002) 8341.
[93] S.A. Harich, D.X. Dai, C.C. Wang, X. Yang, S.D. Chao, R.T. Skodje, Forward scattering due to slow-down of the intermediate in the H+HD→D+H_2 reaction, Nature 419 (2002) 6904.
[94] F. Dong, S.H. Lee, K. Liu, Reactive excitation functions for F+p-H_2/n-H_2/D_2 and the vibrational branching for F+HD, J. Chem. Phys. 113 (2000) 3633.
[95] W.W. Harper, S.A. Nizkorodov, D.J. Nesbitt, Reactive scattering of F+HD→HF(v,J)+H: HF(v,j) nascent product state distributions and evidence for quantum transition state resonances, J. Chem. Phys. 116 (2002) 5622.
[96] R.T. Skodje, D. Skouteris, D.E. Manolopoulos, S-H. Lee, F. Dong, K. Liu, Observation of a transition state resonance in the integral cross-section of the F+HD reaction, J. Chem. Phys. 112 (2000) 4536.
[97] R.T. Skodje, D. Skouteris, D.E. Manolopoulos, S-H. Lee, F. Dong, K. Liu, F+HD→HF+D: A resonance mediated reaction, Phys. Rev. Lett. 85 (2000) 1206.
[98] K. Liu, R.T. Skodje, D.E. Manolopoulos, Perspective: Resonances in bimolecular chemical reactions, Phys. Chem. Comm. 4 (2002).
[99] J.F. Castillo, D.E. Manolopoulos, Quantum mechanical angular distributions for the F+HD reaction, Faraday Discuss. 110 (1998) 119; ibid pp. 213.
[100] K. Stark, H-J. Werner, An accurate multireference configuration interaction calculation of the potential energy surface for the F+H_2→HF+H reaction, J. Chem. Phys. 104 (1996) 6515.
[101] D. Skouteris, J.F. Castillo, D.E. Manolopoulos, ABC: A quantum reactive scattering program, Computer Phys. Comm. 133 (2000) 128.
[102] F.J. Aoiz, L. Banares, V.J. Herrero, V.S. Rabanos, K. Stark, H-J. Werner, The F+HD→ DF(HF)+H(D) reaction revisited: Quasiclassical trajectory study on an ab initio potential energy surface and comparison with molecular beam experiments, J. Chem. Phys. 102 (1995) 9248.
[103] M. Hayes, M. Gustafsson, A.M. Mebel, R.T. Skodje, An improved potential energy surface for the F+H_2 reaction, Chem. Phys. 308 (2005) 259.
[104] M.H. Qiu, Z.F. Ren, L. Che, D.X. Dai, S.A. Harrich, X.Y. Wang, X.M. Yang, C.X. Xu, D.Q. Xie, M. Gustafsson, R.T. Skodje, Z.G. Sun, D.H. Zhang, Observation of Feshbach resonances in the F+H_2→HF+H reaction, Science 311 (2006) 1440.
[105] T. Takayanagi, A. Wada, Quantum reactive scattering calculations of photodetachment spectra of the FHD− anion, Chem. Phys. Lett. 348 (2001) 514.
[106] J.F. Castillo, D.E. Manolopoulos, K. Stark, H.J. Werner, Quantum mechanical angular distributions for the F+H_2 reaction, J. Chem. Phys. 104 (1996) 6531.
[107] S.D. Chao, R.T. Skodje, The case for a reactive resonance in the F+H_2 reaction, J. Chem. Phys. 113 (2000) 3487.
[108] T. Takayanagi, Y. Kurosaki, Van der Waals resonances in cumulative reaction probabilities for the F+H_2, D_2, and HD reactions, J. Chem. Phys. 109 (1998) 8929.

[109] L. Tao, M.H. Alexander, Role of van der Waals resonances in the vibrational relaxation of HF by collision with H atoms, J. Chem. Phys. 127 (2007) 114301.
[110] D. Sokolovski, S.K. Sen, V. Aquilanti, S. Cavalli, D. De Fazio, Interacting resonances in the F+H_2 reaction revisited: Complex terms, Riemann surfaces, and angular distributions, J. Chem. Phys. 126 (2007) 084305.
[111] W.H. Miller, Recent advances in quantum mechanical reaction scattering theory, Annu. Rev. Phys. Chem. 41 (1990) 245.
[112] F.J. Aoiz, L. Banares, V.J. Herrero, The H+H_2 reactive system. Progress in the study of the dynamics of the simplest reaction, Int. Rev. Phys. Chem. 24 (2005) 119.
[113] L. Schnieder, K. Seekamp-Rahn, J. Borkowski, E. Wrede, K.H. Welge, F.J. Aoiz, L. Banares, M.J.D'Mello, V.J. Herrero, V. Saez Rabanos, R.E. Wyatt, Experimental studies and theoretical predictions for the H+D_2→HD+D reaction, Science 269 (1995) 207.
[114] T.N. Kitsopoulos, M.A. Buntine, D.P. Baldwin, R.N. Zare, D.W. Chandler, Reaction product imaging: The H+D_2 reaction, Science 260 (1993) 1605.
[115] C.A. Mead, D.G. Truhlar, On the determination of Born-Oppenheimer nuclear motion wave function including complications due to conical intersections and identical nuclei, J. Chem. Phys. 70 (1979) 2284.
[116] A. Kuppermann, Y-S.M. Wu, The geometrical phase shows up in chemical reactions, Chem. Phys. Lett. 205 (1993) 577.
[117] S.D. Chao, R.T. Skodje, Search for resonance signatures in H+D_2 scattering, Chem. Phys. Lett. 336 (2001) 364.
[118] S.C. Althorpe, F. Fernandez-Alonso, B.D. Bean, J.D. Ayers, A.E. Pomerantz, R.N. Zare, E. Wrede, Observation and interpretation of a time-delayed mechanism in the hydrogen exchange reaction, Nature 416 (2002) 6876.
[119] A.I. Boothroyd, W.J. Keogh, P.G. Martin, M.R. Peterson, A refined H_3 potential energy surface, J. Chem. Phys. 104 (1996) 7139.
[120] M.L. Dubernet, J.M. Hutson, Atom-molecule van der Waals complexes containing open-shell atoms. 2. The bound states of Cl-HCl, J. Phys. Chem. 98 (1994) 5844.
[121] T. Takayangi, The effect of van der Waals resonances on reactive cross sections for the F+HD reaction, Chem. Phys. Lett. 433 (2006) 15.
[122] E. Wurzberg, P.L. Houston, The temperature dependence of hydrogen abstraction reactions: F+HCl, F+HBr, F+DBr, and F+HI, J. Chem. Phys. 72 (1980) 5915.
[123] A M. Zolot, D.J. Nesbitt, Quantum state resolved scattering dynamics of F+HCl→ HF(v,j)+Cl, J. Chem. Phys. 127 (2007) 114319.
[124] R. Sayos, J. Hernando, J. Hijazo, M. Gonzalez, An analytical potential energy surface of the HFCL(2A′) system based on ab initio calculations. Variational transition state theory study of the H+ClF→F+HCl,Cl+HF, and F+HCl→Cl+HF reactions and their isotope variants, Phys. Chem. Chem. Phys. 1 (1999) 947.
[125] B.Y. Tang, B.H. Yang, K.L. Han, R.Q. Zhang, J.Z.H. Zhang, Time-dependent wave packet studies of the F+HCl and F+DCl reactions, J. Chem. Phys. 113 (2000) 10105.
[126] M.P. Deskevich, M.Y. Hayes, K. Takahashi, R.T. Skodje, D.J. Nesbitt, Multireference configuration interaction calculations for the F(^{2}P)+HCl→HF+Cl(^{2}P) reaction: A correlation scaled ground state (1^2A′) potential energy surface, J. Chem. Phys. 124 (2006) 224303.
[127] M.Y. Hayes, M.P. Deskevich, D.J. Nesbitt, K. Takahashi, R.T. Skodje, A simple picture for the rotational enhancement of the rate for the F+HCl→HF+Cl reaction: A dynamical study using a new ab initio potential energy surface, J. Phys. Chem. A 110 (2006) 436.
[128] [128] K. Takahashi, M.Y. Hayes, R.T. Skodje, in press.
[129] J.M. Hutson, The intermolecular potential of Ar-HCl: Determination from high-resolution spectroscopy, J. Chem. Phys. 89 (1988) 4550.
[130] R.J. Leroy, G.C. Corey, J.M. Hutson, Predissociation of weak-anisotropy van der Waals molecules—Theory, approximations, and practical predictions, Faraday Discus. 73 (1982) 339.

CHAPTER 4

Quasi-Bound States of Electronic and Positronic Few-Body Systems: Analysis of Multichannel Scattering Information

Isao Shimamura[a]

Contents

[a] Atomic Physics Laboratory, RIKEN, Wako, Saitama 351-0198, Japan
E-mail address: shimamur@ribf.riken.jp

Advances in Quantum Chemistry, Volume 63
ISSN 0065-3276, DOI: 10.1016/B978-0-12-397009-1.00004-7

Abstract We discuss three aspects of the analysis of the quasi-bound-state (QBS) or resonance-state effects on multichannel continuum wavefunctions for few-body atomic systems. Section 1 is devoted to a brief introductory account of the basic concept necessary for understanding the later sections. General properties of the scattering matrix S and a related time-delay matrix Q are discussed in Section 2. Both isolated and overlapping resonances are treated, starting from single-channel problems and extending the theory for multichannel cases. Useful relations are derived in detail on the basis of linear algebra. The concept of the resonance channel and nonresonance channel spaces, separated from each other, is introduced via the Q-matrix diagonalization. Outstanding examples of resonance analysis by the inspection of the eigenvalues of the Q matrix are presented. They include the extraction

of resonances from a monotonically decreasing phase shift due to a strong background, the detection of a weak resonance, seemingly a nearly constant background behind a strong resonance, and the decomposition of several overlapping resonances into the individual components, some of which are difficult to identify by the conventional methods.

Section 3 examines effective potentials for understanding QBSs. First, the information obtainable from the asymptotic long-range potentials is summarized. This includes the analysis of infinite series of QBSs supported by an attractive Coulomb or dipole potential, the latter appearing in charged-particle collisions with hydrogen-like atoms. The infinite series of dipole-supported QBSs is terminated to only a few resonances, sometimes to one or two, by correcting for relativistic and quantum electrodynamic effects. The dipole potential can also cause the background phase shift to diverge as the energy tends to a channel threshold from above, complicating a resonance structure.

The hyperspherical coordinate approach is then briefly discussed. Accurate numerical calculations for three-body systems are possible by solving coupled-channel equations in terms of these coordinates. The resultant resonance structures can be visually and qualitatively interpreted by inspecting the adiabatic potentials with the hyperradius adopted as the adiabatic parameter. Sometimes the adiabatic correction or diabatic connection, or both are necessary for proper resonance analysis. By combining with the knowledge of the long-range potentials, resonances can often be ascribed to particular adiabatic or diabatic hyperspherical potentials out of an intertwined set of potential curves. In particular, when two or more adiabatic potentials exhibit strongly avoided crossings, some resonances appear as if they were associated with no hyperspherical potentials, even though a careful diabatic interpretation can clearly explain them. A shift in hyperspherical potentials with a continuous change in some parameter(s) in the system can result in a sudden change from a bound state to QBS or from a Feshbach to shape resonance without any essential change in the main part of the wavefunction.

Section 4 analyzes the energy dependence of the cross sections near the threshold for the formation of a QBS. The Wigner threshold law breaks down close to the threshold since the threshold itself has an uncertainty due to the finite lifetime of the QBS. The modifications, due to Baz', for a blurred threshold are explained. Positron–atom collisions are discussed as a prototype, where a bound electron–positron pair (positronium, Ps) can be formed. It is a QBS since it annihilates eventually. Pair annihilation, or positron absorption, can also occur during the collision. The conventional theory leads to a divergent positron absorption cross section at the Ps formation threshold E_{th}, and to a Ps formation cross section starting from zero and rapidly increasing above E_{th}. Both of these processes have a common final channel of pair annihilation and should be treated collectively. This is possible by phenomenologically modeling pair annihilation as particle loss due to an imaginary potential in the Schrödinger equation. This approach proves the continuous and smooth transition from positron absorption to Ps formation across E_{th}, following the Baz' threshold law. Thus, the two processes are indistinguishable in the energy region of this transition.

1. INTRODUCTION

1.1. Quasi-bound states

A quasi-bound state (QBS) in the time-independent picture is a kind of continuum state having properties similar to but not exactly the same as true bound states. The magnitude of a bound-state wavefunction decreases rapidly as the distance r from the center increases to large values, so that the wavefunction is normalizable. Wavefunctions for QBSs also decrease rapidly as r grows, but only until some distances, beyond which there remains a tail part oscillating for ever with some small amplitude. Mathematically, they are unnormalizable continuum wavefunctions. Nevertheless, they reveal physical properties much like bound states. For example, they manifest themselves as nearly line spectra in photoabsorption, though broader in general than bound-state line spectra measured with high resolution, and though asymmetric as a function of the photon energy, unlike bound-state spectra. The width of a QBS line represents uncertainty Γ in the energy E_r of this state.

The large magnitude of the inner part of a QBS wavefunction in comparison with its asymptotic part implies occupation of the inner region of the configuration space for a long time in the time-dependent picture, i.e., a long lifetime τ of this state. In terms of a collision process, mutually colliding pair of particles with a total energy of $\sim E_r$ may form a QBS as an intermediate complex for a certain lifetime τ, after which it again disintegrates into two particles and the collision process is over. Thus, this lifetime is the time delay in the relative motion in the collision. The uncertainty principle requires the relation $\tau\Gamma \simeq \hbar$ between the lifetime τ and the energy uncertainty Γ of a QBS.

The effects of an intermediate QBS on the collision may be guessed by analogy with a Rydberg series of bound states of particular symmetry supported by a Coulomb potential. The number of nodes of the radial wavefunction of a Rydberg state increases one by one as the principal quantum number increases one by one. If an additional short-range potential introduces a new bound-state level (called an intruder or an interloper) somewhere in the energy spectrum of the Rydberg series, every Rydberg-state level lying above this new energy level will have a wavefunction with one more node than it used to have in the absence of the short-range potential. Replacing the Rydberg states by continuum states and the interloper by a QBS of energy E_r with an uncertainty Γ, one may expect a continuum state with an energy above E_r to have one more node than a continuum state below E_r. In other words, the phase shift $\delta_l(E)$ of a partial-wave continuum wavefunction suddenly increases by about π radians in a region of energy E centered at E_r and of a width of the order of Γ, thus introducing a sharp structure of width $\sim\Gamma$ in the cross section around $E \simeq E_r$ (Sections 2.1.1 and 2.1.2). This structure, being sharper for a longer lifetime $\tau \simeq \hbar/\Gamma$, can be of a variety of shapes depending on the background phase shift δ_b, from which $\delta_l(E)$ rises abruptly by $\sim\pi$.

The cause for this variety will be easily understood visually in Section 2.1.1 based on Figure 4.2.

Electron–atom or electron–molecule collision processes are defined precisely by specifying the initial and final quantum states of the target atom or molecule. For an interacting pair of particles A + B in general, the specification of the quantum states of both particles A and B defines a "channel," so that a two-body collision process is defined by specifying the channels before and after the collision, e.g., $A_n+B_m \rightarrow A_{n'}+B_{m'}$. The total system AB may emit a photon, resulting in a channel $(AB)_i+h\nu$. Such a channel is the starting point of photodissociation $h\nu+(AB)_i \rightarrow A_{n'}+B_{m'}$ or of photoionization $h\nu+A_n \rightarrow A^+_{n'}+e^-$. A channel may be impossible to occur for large distances between A and B if the energy of the total system AB is insufficient for disintegrating into A + B in the specified quantum states. Such a channel is referred to as "closed" at this energy. A channel allowed to occur in the asymptotic region of the A − B distance is referred to as "open." If a constituent particle or particles are exchanged between the collision partners, as in a reactive collision A + BC → AB + C, the way the total system ABC dissociates into fragments, e.g., A + BC or AB + C, is called an "arrangement channel."

This article deals with QBSs in nonrelativistic quantum mechanics. Suppose that a QBS Ψ satisfies the time-independent Schrödinger equation with a Hamiltonian H. One may extract a normalizable wavefunction Φ out of Ψ such that $\Phi \simeq \Psi$ in the large-amplitude region, by writing

$$H\Psi = (H_{\mathrm{Q}} + H')\Psi = E\Psi, \tag{1}$$

$$H_{\mathrm{Q}}\Phi = E_{\mathrm{Q}}\Phi, \tag{2}$$

where Φ is to be found in a specified functional space. Either Ψ or Φ, depending on the context, is referred to as a QBS, a decaying state, or a resonance state of H, although Φ is a bound-state eigenfunction of H_{Q} (the subscript indicating "quasi-bound") and not of H itself. A QBS Ψ occurs only in a particular region of energy E of width of order $\Gamma \simeq \hbar/\tau$.

The decomposition of H into H_{Q} and H' (and hence, the definition of Φ) is not unique, but may be chosen conveniently for theoretical formulation, for computational purposes, or for physical interpretation. If H_{Q} is properly chosen, H' affects only slightly the energy values at which a QBS occurs. However, H' introduces an infinitely oscillating part of the wavefunction by changing Φ into Ψ.

1.2. Decomposition of the Hamiltonian for electronic systems

An electron–atom or electron–molecule collision system consists of particles that never annihilate and that interact each other only via Coulomb forces.

Then, the whole Hamiltonian is expressible as

$$H = T + V = -\sum_i \frac{\hbar^2}{2m_i}\nabla_i^2 + \sum_{i>j} V_{ij}^{\mathrm{C}}, \tag{3}$$

where i and j refer to the constituent particles, m_i is the mass of particle i, V_{ij}^{C} is the Coulomb potential between particles i and j, and $i > j$ indicates the sum over all pairs of particles.

A theoretically attractive choice of H_{Q} would be to confine all electrons within the closed channels to prevent them from going out as far as to the asymptotic region. For the hydrogen negative ion H^-, for example, this is possible by projecting out all the hydrogenic states $\psi_{nlm}(\mathbf{r}_i)$ in the open channels by the projection operator $Q_i = 1 - \sum |\psi_{nlm}(\mathbf{r}_i) >< \psi_{nlm}(\mathbf{r}_i)|$, so that

$$H_{\mathrm{Q}} = QHQ, \quad Q = Q_1Q_2 = Q_2Q_1, \tag{4}$$

and the eigenvalue problem (2) is cast into a form

$$QHQ\Phi = E_{\mathrm{Q}}Q\Phi. \tag{5}$$

Here, eigenstates of H_{Q} are to be found in the closed-channel space, hence $Q\Phi$ on the right-hand side. The eigenfunctions $Q\Phi$ of Eq. (5) with Eq. (4), which are bound states, turn into QBSs due to the coupling with open channels introduced by the perturbation H'. The eigenfunctions $Q\Phi$ often appear to be affected only little by the perturbation H' in the region of configuration space that mainly determines E_{Q}. Thus, E_{Q} is found in many examples to be a good approximation to the resonance energy calculated accurately by using the whole Hamiltonian H [1–3].

If one constructs a Hamiltonian matrix in terms of some normalizable basis functions and diagonalizes it, one obtains eigenfunctions and eigenenergies of the Hamiltonian projected onto the functional space spanned by these basis functions. The eigenenergies stable against the change in the basis set are known to be most likely good approximations to resonance energies. The wavefunctions defined by the corresponding eigenvectors can be interpreted as Φ in Eq. (2). This method of finding QBSs is known as the stabilization method [4–7]. Here, one may define a projection operator $Q = |\Phi >< \Phi|$ with a normalized Φ. Then, Eq. (2) takes a form of Eq. (5).

The formal theory of resonances due to Feshbach begins with the decomposition of the Hamiltonian in terms of a projection operator Q [8]. He defines Q as the projection onto the closed-channel space, just like the example of H^- discussed around Eqs. (4) and (5). Then, QBSs described well by the eigenfunctions $Q\Phi$ of Eq. (5) with his Q may be called "Feshbach resonances." A simplified picture would be that eigenstates $Q\Phi$ are supported by some attractive effective potential approaching asymptotically the threshold energy of a closed channel. If this is the case, then the energies E_{Q} of

such eigenstates must lie below this threshold energy. Based on this view, resonances lying below the threshold energy of some asymptotic channel are customarily referred to as Feshbach resonances. Feshbach resonances sometimes form an infinite series converging to the threshold if *QHQ* has an asymptotic attractive Coulomb (Section 3.1.1) or dipole (Section 3.1.2) potential.

Resonances unassociated with eigenstates of Feshbach's *QHQ* are often associated with the shape of some effective potential in an open channel, normally a combination of short-range attractive and long-range repulsive potentials, forming a barrier, within which a large part of the wavefunction is kept. These resonances are called "shape resonances" or "potential resonances." They occur at energies above and usually close to the threshold of that open channel.

Channels are well defined only in the asymptotic region. Nevertheless, they may be extended somehow into the region of short distances between the collision partners. For electron–atom collisions, for example, the wavefunction for the total system may be expanded in terms of the complete set of atomic wavefunctions, and each term may be understood to define a channel since this definition is consistent with the channels in the asymptotic region. However, this set of channels may arbitrarily be transformed linearly into a different set of channels in the short-distance region. In terms of resonances, therefore, the threshold for an open channel has real significance only for resonance wavefunctions extending to the asymptotic region. Classification into Feshbach and shape resonances merely according to the resonance position being below or above a channel threshold is physically meaningful only for those loosely quasi-bound states and not for tightly quasi-bound states. Indeed, there are examples of resonances continuously changing their energy positions across a channel threshold (i.e., changing from Feshbach to shape resonances or vice versa) without much change in their physical character, as the value of some parameter (particle masses, for example) in the scattering process continuously changes; see Section 3.2.4.

In actual resonance calculations, explicit decomposition of the Hamiltonian is not always needed. The whole Schrödinger equation (1) is often solved somehow without explicit use of H_{Q} or H'. General methods for analyzing results from such a treatment are the main subject of this article. A comprehensive review of computational methods or computational results is outside of its scope.

1.3. Positronic bound states as quasi-bound states

Positron is the antiparticle of electron and is another kind of fermion having the same mass m_e and spin $s = 1/2$ as electron and the charge $+e$ opposite to the electron's. A physical system containing a positron e^+ and electrons e^- can change the number of its constituent particles due to the electron–positron pair annihilation, which occurs when they occupy a common position. The simplest example is positronium Ps, a hydrogen-like bound

system e^+e^-. Positronium is a kind of QBS since it decays in a finite lifetime τ, emitting γ rays [9–11].

Pair annihilation can occur also during the collision of a positron with an atom or a molecule. This is called the direct mechanism of collisional pair annihilation. If positronium is formed in collision, annihilation also occurs in it, which is referred to as the indirect mechanism.

A negative imaginary potential in the time-independent Schrödinger equation absorbs the particle flux, thus violating the law of conservation of flux, which is satisfied for real potentials [12, 13]. Then, the quantum electrodynamical phenomenon of pair annihilation can be represented by particle loss due to an effective absorption potential $H' = -iV_{\text{abs}}$ since the exact mechanism of positron loss is totally irrelevant to the study of the atomic processes in consideration [9, 10, 14–16]. The only important aspect of pair annihilation for the present purpose is the correct description of the loss rate. The absorption potential H' is proportional to the delta function $\delta(\mathbf{r})$ of the e^+–e^- distance vector $\mathbf{r}$ (Section 4.2).

The reduced mass of positronium is half the electron mass m_e. Then, long before annihilation, the relative e^+–e^- motion in positronium is described by the hydrogenic wavefunction with its size doubled and with a binding energy of $6.8\,\text{eV}/n^2$, i.e., half the hydrogen value, n being the principal quantum number. The correction on this energy of the positronium Ps(ns) in an s state, having a nonzero value of the wavefunction $\psi(ns)$ at the coalescence point, is

$$E_n^{(1)} = <\psi(ns)|H'|\psi(ns)> \equiv -i\Gamma_n/2 \tag{6}$$

("$\equiv$" indicating "define Γ_n by this") in the first order in the perturbation potential H' [9, 10]. This is an accurate approximation since H' is very weak compared with the Coulomb potential; see Section 4.2.

For a time-independent Hamiltonian, the wavefunction satisfying the time-dependent Schrödinger equation contains a multiplicative factor $\exp(-iEt/\hbar)$. For positronium this time-dependent factor leads to a probability density proportional to

$$\begin{aligned} |\exp(-iEt/\hbar)|^2 &\simeq |\exp(-iE_n^{(1)}t/\hbar)|^2 \\ &= \exp(-\Gamma_n t/\hbar) \\ &\equiv \exp(-t/\tau_n). \end{aligned} \tag{7}$$

The time constant τ_n of this exponential decay is equal to $\hbar/\Gamma_n$, so that Γ_n as defined by Eq. (6) is known from the uncertainty principle to be the uncertainty in the energy $-6.8\,\text{eV}/n^2$. In a similar way, an imaginary part $-i\Gamma/2$ of the energy of a physical system indicates an exponential decay of this system with a time constant $\tau = \hbar/\Gamma$.

The rate of positron absorption in positron–atom collisions, proportional to the flux loss due to $-iV_{\text{abs}}$, should be obtainable by solving the

Schrödinger equation

$$[H - E]\,\Psi = [H_Q - iV_{\rm abs} - E]\,\Psi = 0. \tag{8}$$

Here, H_Q is the Coulomb-interaction Hamiltonian similar to Eq. (3), and E is a real-valued energy of the whole system, i.e., the sum of the collision energy and the energy of the target state before collision. If the target atom contains more than one electron, the absorption potential $-iV_{\rm abs}$ is to be summed over all the target electrons since the incident positron can annihilate with any of the electrons.

The absorption rate can be calculated by treating $-iV_{\rm abs}$ as a small perturbation and by adopting the Coulomb Schrödinger equation

$$[H_Q - E]\Phi = 0 \tag{9}$$

as the unperturbed equation. This has long been accepted as the standard, well-established method of calculating the annihilation rate [11, 17]. This approximation is also supported by the extremely small probability of pair annihilation during the collision, or by the much shorter collision time than the lifetime of a positronium under most experimental conditions.

Close to the threshold for the formation of positronium, however, the effects of $-iV_{\rm abs}$ are significant since it introduces ambiguity Γ_n into the energy of positronium, and hence, into the threshold energy. Thus, the threshold effects are described incorrectly by the unperturbed wavefunction Φ. Indeed, the absorption cross section diverges unphysically toward the threshold according to the standard perturbation theory [15, 16, 18, 19]; see Section 4.3.3 for further details.

Most positron collision processes can be treated with high precision by considering only the Coulomb interactions with no absorption potentials taken into account. Then, the same kind of QBSs as explained in Section 1.2 for electronic systems are possible in positron collisions too.

1.4. Non-Hermitian Hamiltonians

The absorption potential is imaginary, and hence, the Hamiltonian H including it is non-Hermitian. For this reason, the energy eigenvalues of positronium have an imaginary part $-i\Gamma_n/2$ representing the uncertainty in the observed value of energy. For describing positron scattering processes, however, the Schrödinger equation with the non-Hermitian Hamiltonian H should be solved with a real-valued energy E, as was noted below Eq. (8).

On the other hand, we sometimes discuss the Schrödinger equation without an absorption potential, for example, the Coulomb few-body Schrödinger equation with the Hamiltonian (3), assuming the energy to take complex values. This is analytic continuation of the quantal problem into fake, complex energies. This way, we depart from what actually occurs in nature for real energies. By regarding the nature as a special

case of something much more general, however, we try to attain deeper understanding of nature, in particular, of QBSs. Indeed, a singularity in the quantity $S_l(E) = \exp[2i\delta_l(E)]$, found at an energy of $E_r - i\Gamma/2$, can be shown to indicate the existence of a QBS at energy E_r with a lifetime of $\tau = \hbar/\Gamma$, resulting in a sharp structure in the cross section near E_r [12, 20, 21], as will be described in the next section. There, a partial-wave radial wavefunction will be expressed as a linear combination of incoming and outgoing waves, the latter having a coefficient $S_l(E)$. Therefore, there is no incoming wave at a pole of $S_l(E)$. In other words, the positions $E = E_r - i\Gamma/2$ of QBS poles of $S_l(E)$ are eigenvalues of the Hamiltonian H with the asymptotically outgoing boundary condition [12, 22].

Various different methods of finding these complex eigenvalues $E_r - i\Gamma/2$ have been proposed. A successful method is to replace the relative distance r_{ij} between each pair of particles i and j in the system by a complex variable $r_{ij}e^{i\theta}$ in the Coulomb few-body Hamiltonian (3), so that the Hamiltonian H is transformed into a complex operator, or a non-Hermitian operator $H(\theta)$ [23, 24]. The complex eigenvalues of a matrix of $H(\theta)$, constructed in terms of square-integrable basis functions $\{u_s\}$ with variable parameters, are found to be stable against the change in the size of the basis set, in the nonlinear parameters in $\{u_s\}$, and, in particular, the angle θ of rotation in the complex-coordinate plane, if these eigenvalues correspond to poles $E_r - i\Gamma/2$ of $S_l(E)$ for $H(\theta = 0)$ in the complex-energy plane. This method is referred to as the complex-coordinate rotation (CCR) method, complex-rotation method, or complex-scaling method [25, 26]. It has proved powerful as a means to compute simultaneously the resonance positions and widths in few-body atomic systems using only normalizable basis functions, which are much easier to treat than continuum wavefunctions. Such computations of the resonance parameters E_r and Γ, however, need to be complemented by some other theoretical methods for the purpose of elucidating how the resonances affect the observable cross sections for various initial and final channels. This article will present no further discussion of the complex-rotation method, but some results of computations using it will be cited later.

A technique for direct computations of the eigenvalues $E_r - i\Gamma/2$ of $H(\theta = 0)$ with the outgoing-wave boundary condition is reviewed in detail in a chapter in Part I of this two-volume special issue of Advances in Quantum Chemistry on Unstable States in the Continuous Spectra [27]. Determination of the wavefunction Φ of Eq. (2) with a real eigenvalue E_Q using a judiciously chosen real, square-integrable basis set, followed by diagonalization of a complex Hamiltonian matrix for the whole $H_Q + H'$ constructed in terms of basis functions of complex-rotated coordinates, is shown to be quite useful.

In fact, even the usual Hamiltonian H with a real potential and the usual boundary conditions is not always Hermitian; the relation

$$(\phi, H\psi) = (H\phi, \psi) \tag{10}$$

is guaranteed only if one or both of the functions ϕ and ψ are normalizable. A funny consequence of careless use of Eq. (10) would be a "proof" that

no scattering can occur in any potential. Based on the Schrödinger equation $H\Psi = (T + V)\Psi = E\Psi$ for scattering by a potential V and that for free motion $T\Phi = E\Phi$, one may use the well-known fact that the scattering amplitude f is proportional to $(\Phi, V\Psi)$ and may show that

$$f \propto (\Phi, [H - T]\Psi) = (\Phi, [E - T]\Psi) = ([E - T]\Phi, \Psi) = (0, \Psi) = 0. \qquad (11)$$

Here, the Hermitian property of $E - T$ has been assumed in shifting its position, because of which the scattering amplitude has been "proved" to be zero irrespective of the potential V and of the energy E.

2. RESONANCE ANALYSIS: INFORMATION FROM ASYMPTOTIC WAVEFUNCTIONS

All the information on the measurable scattering quantities is concentrated into the asymptotic part of the continuum wavefunction, regardless of the dynamics of the physical system described by the inner-region part of the wavefunction. Significant effects of the inner-region physics should be reflected on the asymptotic quantities. This section is concerned with such effects of QBSs, or resonance effects, manifesting themselves in these asymptotic quantities.

2.1. Single-channel scattering

We begin our discussion with the simple case of a spinless particle of mass m and kinetic energy $E = \hbar^2 k^2/2m$ in a spherical, time-independent potential $V(r)$, so that the Schrödinger equation can be decomposed into uncoupled partial waves l. For a particular l, the scattering matrix or the S matrix is defined as $S(k) = \exp[2i\delta(k)]$ in terms of the phase shift $\delta(k)$. Here and in the following, the subscript l on the S matrix and the phase shift is suppressed. The asymptotic form of the time-dependent radial wavefunction is expressible as

$$\begin{aligned} u(r, t; k) &\longrightarrow e^{-iEt/\hbar} \sin[kr - l\pi/2 + \delta(k)] \\ &\propto \quad e^{-iEt/\hbar}[e^{-i(kr - l\pi/2)} - S(k)e^{+i(kr - l\pi/2)}]. \end{aligned} \qquad (12)$$

For a real potential, the space part of the radial wavefunction for a real energy may be chosen to be real and the phase shift is real. Therefore, the absolute value of the S matrix is unity. This guarantees the flux conservation since, then, the incoming wave and the outgoing wave in Eq. (12) have fluxes of the same magnitude in opposite directions.

2.1.1. Resonance S matrix, phase shift, and the cross section

We consider the analytic continuation of the $S(k)$ matrix into the complex k plane. Then, the phase shift is complex in general and the absolute value of

$S(k)$ can be of any positive value or zero. If $S(k)$ has a pole at some complex k, the incoming-wave term is negligible there compared with the outgoing-wave term. If a pole lies at $k = \pm i\kappa$ with a positive κ, Eq. (12) behaves as $e^{\mp\kappa r}e^{-iEt/\hbar}$, and the potential supports a bound state (if $k = i\kappa$) or what is called a virtual state (if $k = -i\kappa$) of energy $E = -\hbar^2\kappa^2/2m$.

If a pole lies at $k = k_1 - ik_2$ with $k_1 > k_2 > 0$, i.e., at $E = E_r - i\Gamma/2$ with $E_r = (\hbar^2/2m)(k_1^2 - k_2^2) > 0$ and $\Gamma = 2(\hbar^2/m)k_1k_2$, the wavefunction has an asymptotic form $e^{k_2r-\Gamma t/2\hbar}e^{i(k_1r-E_rt/\hbar)}$. The asymptotic probability density is proportional to $e^{2k_2r}e^{-\Gamma t/\hbar}$, decaying with a time constant $\tau = \hbar/\Gamma$, just like Eq. (7). This is typical of QBSs mentioned so far. This state, however, is not really physically acceptable since it has an unphysical complex energy and grows exponentially as r increases, just like virtual states. On the other hand, this S-matrix pole affects $S(E)$ at physical, real energies and induces resonance processes, as will be seen below, if this pole lies close to the real axis of energy E or wave number k. For this reason it is called a resonance pole and the unphysical complex-energy state a resonance state. Recall that, in Section 1.1, resonance states are explained to refer either to Ψ in Eq. (1) or to Φ in Eq. (2), depending on the context. Now, here is a third meaning of the same word. They are closely related to each other, of course.

The general form of $S(E)$ satisfying the condition that $|S(E)| = 1$ for real E and having a pole, assumed as a simple pole, at $E = E_r - i\Gamma/2 \equiv \mathcal{E}$ is expressible as

$$S(E) = e^{i\delta_b}\frac{E-\mathcal{E}^*}{E-\mathcal{E}}e^{i\delta_b} = e^{i\delta_b}\left(1-\frac{i\Gamma}{E-\mathcal{E}}\right)e^{i\delta_b} \equiv S_{\mathrm{BW}}(E) \tag{13}$$

with any slowly varying or background phase $\delta_b(E)$, assumed to be real at real E. The asterisk on $\mathcal{E}$ indicates its complex conjugate. Equation (13) is Breit–Wigner's one-level or single-pole formula for the single-channel S matrix [28].

By writing $E - \mathcal{E} = (E - E_r) + i\Gamma/2 = Ae^{-i\delta_r}$ for real E and noting that $\tan\delta_r = -(\Gamma/2)/(E - E_r)$, one may show that

$$S_{\mathrm{BW}}(E) = e^{2i\delta_r}e^{2i\delta_b} = \exp\left[2i\left(-\arctan\frac{\Gamma/2}{E-E_r}+\delta_b\right)\right] \equiv e^{2i\delta_{\mathrm{BW}}}, \tag{14}$$

$$\delta_{\mathrm{BW}}(E) = \delta_r(E) + \delta_b(E) = -\arctan\frac{\Gamma/2}{E-E_r} + \delta_b(E) \tag{15}$$

modulo π (meaning, plus any multiple of π), and that

$$\cot[\delta_b(E) - \delta_{\mathrm{BW}}(E)] = -\cot\delta_r(E) = \frac{E-E_r}{\Gamma/2} \equiv \varepsilon. \tag{16}$$

The reduced energy ε defined by Eq.(16) proves to be useful later. A quantity

$$q(E) = -\cot\delta_b(E) \tag{17}$$

is also defined, where δ_r in ε is replaced by δ_b.

Equations (15) and (16) are Breit–Wigner's one-level formula for the phase shift. If the pole lies close to the real E axis, i.e., if Γ is very small, the part δ_r of the phase shift increases very rapidly with E by $\pi/2$ within the energy region of width Γ and centered at E_r. It increases by nearly π within several times Γ. This is a resonance phenomenon.

The partial-wave integral cross section $\sigma_l(E)$ is calculable as

$$\begin{aligned} E\sigma_l(E) \propto \sin^2\delta_{\mathrm{BW}}(E) &= \sin^2(\delta_r+\delta_b) \\ &= \frac{(\sin\delta_r\cos\delta_b+\cos\delta_r\sin\delta_b)^2}{(\sin^2\delta_r+\cos^2\delta_r)(\sin^2\delta_b+\cos^2\delta_b)} \\ &= \frac{(q+\varepsilon)^2}{(1+q^2)(1+\varepsilon^2)} = \frac{(1+\varepsilon/q)^2}{(1+q^{-2})(1+\varepsilon^2)}, \end{aligned} \tag{18}$$

where two forms are shown, one convenient for small values of q and the other for large values of q (small values of δ_b). This is essentially what is often referred to as Fano profile [29], except that Eq. (18) is normalized to the maximum value. The curves in the original paper by Fano [29] are normalized to the off-resonance ($\varepsilon \to \pm\infty$) cross section $(1+q^2)^{-1}$, so that for near-symmetric profiles, i.e., for small background ($\delta_b \simeq 0, q \gg 1$), the peaks would be too high for inclusion in the figure. The present Figure 4.1 shows the profile (18) for some constant values of δ_b, or q. These values determine the shape of the profile, and hence, q is referred to as the shape parameter. In actual cases, the energy dependence of the background δ_b, and hence q, within the energy region of the resonance can change the profile significantly. This can happen for very broad resonances.

The original derivation of the Fano profile in Ref. [29] is more general. It applies to any transition matrix for a final state with a QBS Φ interacting with a background continuum. Resonance photoionization cross sections, for example, is describable by Eq. (18) with some background augmented. Fano [29] also generalizes his derivation for either more than one QBS or more than one continuum, but not for both simultaneously, which is the most difficult case and will be discussed in Section 2.3 of this article.

The variety of the resonance profiles of Figure 4.1 for different values of δ_b is readily understood from Figure 4.2, which shows the essential factor $\sin^2\delta(E)$ in the partial-wave cross section $\sigma_l(E)$. As $\delta(E)$ increases from δ_b to $\delta_b+\pi$, the quantity $\sin^2\delta(E)$ ranges over a period and comes back to the initial value. Different choices of the starting point δ_b of a period cut out different parts of Figure 4.2 of width π radians. Thus, for $\delta_b = 0$, $\sin^2\delta(E)$ starts from zero, takes a maximum value of one at $\delta(E_r) = \pi/2$, and finishes with zero, showing a symmetric peak as a function not only of δ but also of E since the derivative $\mathrm{d}\delta(E)/\mathrm{d}E$ is symmetric with respect to the resonance center E_r. For $\delta_b = \pi/2$, $\sin^2\delta(E)$ starts from one, takes a minimum value of zero at $\delta(E_r) = \pi$, and comes back again to one, showing a symmetric dip. For $\delta_b = \pi/4$, the curve starts from $1/2$ and changes through 1, $1/2$, 0, and again $1/2$, showing an asymmetric profile with a peak on the left and a dip

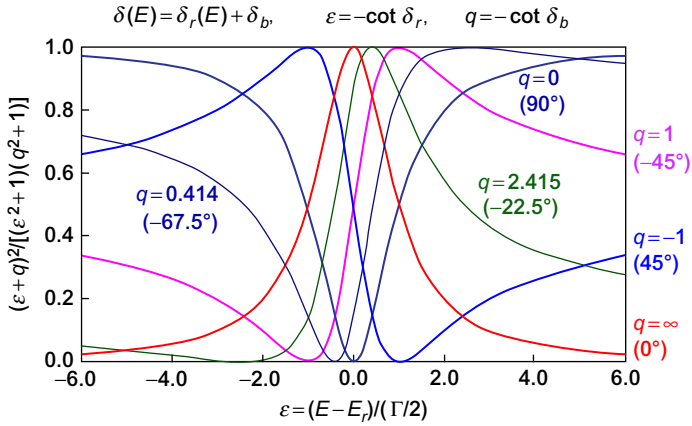

Figure 4.1 Fano profile of resonance cross sections normalized by the maximum cross section. The shape parameter $q = -\cot\delta_b$ is assumed to be a constant independent of energy E. In actual processes, its dependence on E can alter the profile significantly. The background phase shift δ_b is indicated in the parentheses below each value of q.

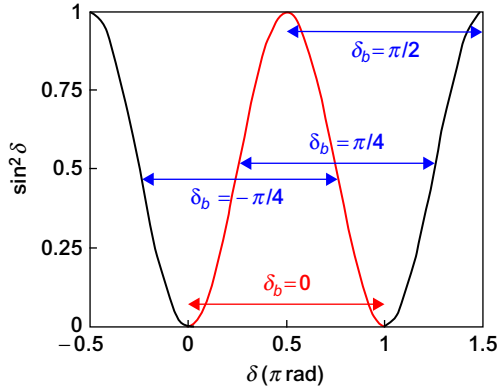

Figure 4.2 Visual explanation of the effect of the constant background phase shift δ_b on the resonance profile as a function of the phase shift $\delta(E)$ when it increases from δ_b to $\delta_b + \pi$. The partial-wave cross section $\sigma_l(E)$ proportional to $\sin^2\delta(E)$ shows a symmetric peak for $\delta_b = 0$ and a symmetric dip for $\delta_b = \pi/2$ since $d\delta(E)/dE$ is symmetric with respect to E_r, and an asymmetric profile with a peak and a dip for $\delta_b = \pm\pi/4$. See text.

on the right. For $\delta_b = -\pi/4$, a dip lies on the left and a peak on the right. Note that $d\delta(E)/dE$ is quite large near E_r, so that the $\sin^2\delta$ profile is squeezed into a narrower energy profile near the resonance center E_r than far from E_r; compare Figure 4.1 with Figure 4.2.

2.1.2. Time delay and the density of states

It is of interest to note from Eq. (16) that $\mathrm{d}\delta_r/\mathrm{d}\varepsilon = (1+\varepsilon^2)^{-1}$. In the limit of no background, Eq. (18) takes a form

$$\lim_{q\to\infty} E\sigma_l(E) \propto \frac{1}{\pi}\frac{\mathrm{d}\delta_r}{\mathrm{d}E} = \frac{L(E)}{h} \equiv \rho_r(E), \tag{19}$$

where

$$L(E) = \frac{\hbar\Gamma}{(E-E_r)^2 + (\Gamma/2)^2}. \tag{20}$$

The Lorentzian profile (20) is going to appear often later in the resonance theory. It is a symmetric peak with a maximum at $E = E_r$. The full width at half the maximum (FWHM) of this peak is Γ, and hence, the FWHM of the symmetric peak in Figure 4.1 is Γ if transformed into a function of the energy E. Therefore, the cross-section structure, i.e., the resonance structure, is narrower for smaller Γ. A feature of the Lorentzian profile (20) to be noted is that the width parameter Γ also determines its peak height $4\hbar/\Gamma$. This fact will be taken advantage of in the resonance analysis procedure, as will be explained in Section 2.2.5.

Equation (19) may be interpreted as the increase in the density of states in the energy-level spectrum introduced by a QBS as compared with the case of no interaction; hence, the notation $\rho_r(E)$. A simple way of understanding this is to evaluate the spacing $\Delta E = E_{n+1} - E_n$ between two adjacent energy levels determined by box-normalization at a large distance $r = a$ when there is a nonzero scattering phase shift $\delta(E)$. Let Δk be the corresponding difference $k_{n+1} - k_n$ in the wave number and $\Delta\delta$ be the corresponding increase $\delta(E_{n+1}) - \delta(E_n)$ in the phase shift. Since $k_n a + \delta(E_n)$ increases by π as n increases by 1, the density of states is $[\{(\Delta k)a + \Delta\delta\}/\pi]/\Delta E$, of which the contribution $\rho(E)$ by scattering is $(\Delta\delta/\pi)/\Delta E \to (\mathrm{d}\delta/\mathrm{d}E)/\pi$ as $a \to \infty$. If the background phase shift δ_b is a constant independent of E, we recover $\rho_r(E)$ of Eq. (19). Note that $\rho_r(E)$ is normalized so that its integral over the whole energy region is unity. In this sense, it may be regarded as the probability density of a resonance state.

Now we consider a wave packet

$$\psi(r,t) = \int_{\Delta k} c(k)u(r,t;k)\mathrm{d}k \tag{21}$$

formed by superposing the radial wavefunction $u(r,t;k)$ of Eq. (12) with the coefficient $c(k)$ spread over a narrow region Δk of k. In the asymptotic region of r, the integrand in Eq. (21) oscillates rapidly with the change in k, and the integral vanishes except where the phase in $u(r,t;k)$ takes a stationary value as a function of k.

For the incoming wave, this stationary phase condition is $\mathrm{d}(-kr - Et/\hbar)/\mathrm{d}k \simeq 0$, from which we know the motion of the wave packet

$$r = -\frac{\mathrm{d}E}{\mathrm{d}(\hbar k)}t = -\frac{\hbar k}{m}t, \tag{22}$$

the inward motion with a constant group velocity $\hbar k/m$ at negative time, arriving in the potential region at $t \simeq 0$.

For the outgoing wave, we have $\mathrm{d}(2\delta + kr - Et/\hbar)/\mathrm{d}k \simeq 0$, and hence,

$$r = \frac{\mathrm{d}E}{\mathrm{d}(\hbar k)}t - 2\frac{\mathrm{d}\delta}{\mathrm{d}k} = \frac{\hbar k}{m}\left[t - 2\hbar\frac{\mathrm{d}\delta}{\mathrm{d}E}\right], \tag{23}$$

the outward motion with the same constant group velocity as the incoming wave packet, but with the delay in time [30–32]

$$\Delta t = 2\hbar\frac{\mathrm{d}\delta(E)}{\mathrm{d}E} = h\rho(E). \tag{24}$$

In the absence of any interaction, the outgoing wave packet comes out to the asymptotic region without delay. When scattering occurs, the wave packet spends some time in the potential region before coming out from there if Δt is positive. If a resonance occurs, the time delay is calculable from Eqs. (15) and (19) as

$$\Delta t_{\mathrm{BW}}(E) = 2\hbar\frac{\mathrm{d}\delta_r}{\mathrm{d}E} + 2\hbar\frac{\mathrm{d}\delta_b}{\mathrm{d}E} = h\rho_r(E) + 2\hbar\frac{\mathrm{d}\delta_b}{\mathrm{d}E} = L(E) + 2\hbar\frac{\mathrm{d}\delta_b}{\mathrm{d}E}. \tag{25}$$

The resonance phase shift δ_r produces much time delay of Lorentzian shape if Γ is small. The peak value of the time delay at $E = E_r$ is $4\hbar/\Gamma = 4\tau$ if the background term is neglected. The Lorentzian time delay averaged over the probability density $\rho(E)$ is $h\int\rho_r^2(E)\mathrm{d}E = 2\tau$, of which τ is spent for the formation of the QBS and the other τ for its decay.

In a resonance phenomenon in two-body collisions A+B, time delay occurs in the relative A − B motion. The particles A and B stay near each other for much longer time than in the absence of any interactions between them, or form a temporary complex or a QBS with a lifetime $\tau = \hbar/\Gamma$.

Sometimes in the literature, a resonance refers to the passage of the phase shift across $\pi/2$, but that does not necessarily mean steep slope of $\delta(E)$, a large time delay, or formation of a QBS. On the other hand, a large time delay is not necessarily associated with the formation of a QBS. For example, Wigner's threshold law for a short-range potential states that the s-wave phase shift $\delta_0(E)$ is proportional to $E^{1/2}$ at low energies E [33]. This leads to the time delay $\Delta t \propto E^{-1/2}$, which becomes extremely large at very low E (and is positive if the interaction is attractive), in spite of its irrelevance to any QBS [34]. Note

that the time for free passage over a specified region is also proportional to $E^{-1/2}$. Thus, the time delay proportional to $E^{-1/2}$, if positive, increases the passage time by some multiplicative factor independent of E at low E. Dalitz and Moorhouse consider another interesting case of the time delay Δt of a Gaussian function of the energy E [34]. This peaked function, apparently similar to a Lorentzian function, corresponds to an S matrix having no singularity in a finite complex-E plane.

Finally, attention is drawn to the possibility that the effect of a resonance due to an S-matrix pole is canceled by the strong background with the result that the net time delay becomes negative, as will be illustrated in Section 2.2.6.

2.1.3. Overlapping resonances

If several poles of the S matrix lie at $E = E_\nu - i\Gamma_\nu/2 \equiv \mathcal{E}_\nu$ ($\nu = 1, \ldots, N$) close to each other and to the real E or k axis, an appropriate form of the S matrix would be

$$S(E) = e^{i\delta_b} \prod_\nu \frac{E - \mathcal{E}_\nu^*}{E - \mathcal{E}_\nu} e^{i\delta_b} = e^{i\delta_b} \prod_\nu \left(1 - \frac{i\Gamma_\nu}{E - \mathcal{E}_\nu}\right) e^{i\delta_b} \tag{26}$$

as a generalization of the single-pole Breit–Wigner formula (13). Following the procedure for the single-pole case, we write $E - \mathcal{E}_\nu = (E - E_\nu) + i\Gamma_\nu/2 = A_\nu e^{-i\delta_\nu}$ for real E. Then, it follows that $\exp(2i\delta) = \exp(2i\delta_b + \sum_\nu 2i\delta_\nu)$ and that [35]

$$\delta(E) = \sum_\nu \delta_\nu(E) + \delta_b(E) = -\sum_\nu \arctan \frac{\Gamma_\nu/2}{E - E_\nu} + \delta_b(E). \tag{27}$$

Resonance poles lying within the widths of each other are called overlapping resonances. When they occur, the rapid rise of the phase shift due to one pole begins before the rise due to an adjacent pole finishes. In this sense, the effects of overlapping resonances on the phase shift and, in particular, on the cross section are difficult to separate, in general. Nonetheless, the overlapping Lorentzian profiles in the time-delay spectrum

$$\Delta t(E) = \sum_\nu 2\hbar \frac{\mathrm{d}\delta_\nu}{\mathrm{d}E} + 2\hbar \frac{\mathrm{d}\delta_b}{\mathrm{d}E} = \sum_\nu L_\nu(E) + 2\hbar \frac{\mathrm{d}\delta_b}{\mathrm{d}E} \tag{28}$$

with

$$L_\nu(E) = \frac{\hbar\Gamma_\nu}{(E - E_\nu)^2 + (\Gamma_\nu/2)^2} \tag{29}$$

should be easily recognizable and the resonance parameters E_ν and Γ_ν easily obtainable by a least-squares fit to accurately calculated time delay $\Delta t(E)$, or equivalently, the phase-shift derivative.

2.2. Multichannel scattering: Isolated resonances

Let T as a superscript on a matrix indicate the transposed matrix and the dagger the Hermitian conjugate, and hence, $A^\dagger = (A^T)^* = (A^*)^T$. Also, let I denote the unit matrix of the same order as the other matrices in the same equation.

For multichannel scattering where there are two or more open channels, the S matrix is a true matrix with elements S_{ij} and the cross section for the transition from channel i to channel j is proportional to $|\delta_{ij} - S_{ij}|^2$. The symmetry of collision processes with respect to the time reversal leads to the symmetric property of the S matrix, $S^T = S$, which, in turn, leads to the principle of detailed balance between mutually reverse processes. The conservation of the flux of probability density for a real potential and a real energy requires that $SS^\dagger = S^\dagger S = I$, i.e., S is unitary. For a complex energy or for a complex potential, in general, the flux is not conserved and S is non-unitary.

In the following, N_o denotes the order of the S matrix, i.e., the number of open channels of a particular symmetry under consideration.

2.2.1. S matrix for an isolated resonance

A QBS Φ formed in some way or other may decay into any channel i of the same symmetry as Φ at a rate $\Gamma_i/\hbar$ that may differ depending on the channel. The element S_{ij} $(i, j = 1, 2, \ldots, N_o)$ must include both Γ_i and Γ_j on an equal footing because of the time-reversal symmetry. The lifetime τ of state Φ is the inverse of the rate $\Gamma/\hbar$ of decay into all channels, i.e., the sum of all $\Gamma_i/\hbar$, the total width Γ being $\sum_i \Gamma_i$.

We define a normalized column vector $\mathbf{g}$ and a projection matrix P by

$$\begin{aligned} \mathbf{g}^T &= \Gamma^{-1/2}\left(\Gamma_1^{1/2}, \Gamma_2^{1/2}, \ldots, \Gamma_{N_o}^{1/2}\right), \\ P = \mathbf{g}\mathbf{g}^T = \mathbf{g}\mathbf{g}^\dagger, &\quad P_{ij} = (\Gamma_i\Gamma_j)^{1/2}/\Gamma, \qquad \mathrm{Tr}\, P = \sum_i P_{ii} = 1, \end{aligned} \tag{30}$$

where Tr indicates a trace, or the sum of the diagonal elements. The vector $\mathbf{g}$ and the matrix P satisfy the relations

$$\begin{aligned} \mathbf{g}^T\mathbf{g} = \mathbf{g}^\dagger\mathbf{g} = 1, \\ P^\dagger = P, \quad P^2 = (\mathbf{g}\mathbf{g}^T)(\mathbf{g}\mathbf{g}^T) = \mathbf{g}\mathbf{g}^T = P. \end{aligned} \tag{31}$$

We note that $P\mathbf{g} = \mathbf{g}\mathbf{g}^T\mathbf{g} = \mathbf{g}$, so that $\mathbf{g}$ is an eigenvector of P with an eigenvalue 1. The real symmetric matrix P is of rank 1 since all its rows (or columns) are linearly dependent. Hence, the other eigenvalues of P are all zero. This indeed satisfies the general relation that the sum of all the eigenvalues of a matrix is equal to its trace. Thus, P is diagonalized by an orthogonal matrix O_P as

$$O_P P = \Pi O_P, \quad \Pi_{11} = 1, \quad \Pi_{ij} = 0 \quad \text{otherwise.} \tag{32}$$

We begin with the simple case where the background scattering matrix S_b is diagonal with diagonal elements $(S_b)_{ii} = e^{2i\phi_i}$, ϕ_i being the background phase shifts. This excludes the possibility of any inelastic processes occurring in background scattering. For describing an isolated QBS, all the S-matrix elements must have the same single simple pole on the complex E plane, at $E = E_r - i\Gamma/2 = \mathcal{E}$, following Section 2.1.1. A symmetric S matrix satisfying this condition, being unitary at real E, and including Γ_i and Γ_j on a par would be [21, 36]

$$S_{ij} = e^{i\phi_i}\left(\delta_{ij} - \frac{i\Gamma_i^{1/2}\Gamma_j^{1/2}}{E-\mathcal{E}}\right)e^{i\phi_j}, \tag{33}$$

which is a matrix generalization of Eq. (13). This form is often referred to as the Breit–Wigner one-level formula for the multichannel S matrix.

However, the assumption of no inelastic scattering off resonance is too restrictive and often unrealistic. Hence, we consider a more general form in the following, which we call the Breit–Wigner S matrix in this article, namely [8, 35, 37],

$$\begin{aligned} S(E) = BS_rB^T = S_b - \frac{i\Gamma}{E-\mathcal{E}}BPB^T \equiv S_{\mathrm{BW}}(E), \\ S_r(E) = I - \frac{i\Gamma}{E-\mathcal{E}}P \end{aligned} \tag{34}$$

with a slowly varying background scattering matrix $S_b(E)$, written as the product

$$S_b(E) = BB^T \tag{35}$$

in terms of a unitary matrix $B(E)$; $BB^\dagger = B^\dagger B = I$. Note that $S_bS_b^\dagger = BB^T(B^T)^\dagger B^\dagger = I$, and similarly, $S_b^\dagger S_b = I$, and therefore S_b is naturally a unitary matrix. Also, $S_b^T = (BB^T)^T = BB^T = S_b$, i.e., symmetric. It is also easy to show that S_r is symmetric and unitary at real E. The $N_\mathrm{o} \times N_\mathrm{o}$ resonance S matrix (34) contains only N_o width parameters $\{\Gamma_i\}$ and an additional position parameter E_r except for the background information.

2.2.2. S-matrix eigenchannels and eigenphases

A simple parameterization of the S matrix in the form (33) or (34) might appear impractical when many channels, and hence many fitting parameters $\{\Gamma_i\}$ and E_r, are involved. However, the diagonalization of the S matrix greatly simplifies such parametrization and also provides a clear physical idea.

This diagonalization is achieved by a transformation

$$OS = \Lambda O, \quad \Lambda_{\alpha\alpha'} = \delta_{\alpha\alpha'}\exp[2i(\delta)_\alpha] \tag{36}$$

by some real, orthogonal matrix O since S is symmetric. Furthermore, the unitarity of S leads to the relation that $I = OS^{\dagger}SO^{T} = (OS^{\dagger}O^{T})(OSO^{T}) = \Lambda^{\dagger}\Lambda$, from which it follows that the square of the absolute value of each diagonal element $\Lambda_{\alpha\alpha}$ of Λ is unity. That is why $\Lambda_{\alpha\alpha}$ has been written as $\exp[2i(\delta)_{\alpha}]$ in Eq. (36). The phase $(\delta)_{\alpha}$ is called an eigenphase, and the new set of channels α that the matrix O linearly transforms the original physical channels into are called eigenchannels; the Greek index is used to distinguish the eigenchannel space from the physical channel space.

If scattering starts from one of the eigenchannels, the only possible final channel is exactly the same one. There are no transitions to other eigenchannels. In general, all the other eigenchannels are coupled to this one during the collision, but they are closed and forbidden asymptotically, though not due to any energy condition. After this linear transformation, the eigenphases $(\delta)_{\alpha}$ determine all the apparently single-channel scattering processes. Their simple sum, $\delta(E) = \sum_{\alpha}(\delta)_{\alpha}$, is referred to as the eigenphase sum. The same notation as the phase shift in single-channel scattering should not cause much confusion.

The background S matrix (35) is also diagonalized by an orthogonal matrix O_b:

$$O_b S_b = O_b B B^T = \Lambda_b O_b, \quad (\Lambda_b)_{\beta\beta'} = \delta_{\beta\beta'} \exp[2i(\delta_b)_{\beta}]. \tag{37}$$

The background eigenphase sum is defined as $\delta_b(E) = \sum_{\beta}(\delta_b)_{\beta}$. The diagonalization (37) may be achieved by choosing O_b to be

$$O_b = \Lambda_b^{1/2} B^{\dagger}, \tag{38}$$

and hence, $O_b B = \Lambda_b^{1/2} = (\Lambda_b^{1/2})^T = (O_b B)^T$. Therefore, it follows that

$$B^T B = B^T (O_b^T O_b) B = (O_b B)^T (O_b B) = \Lambda_b. \tag{39}$$

Now, we note that the determinants of matrices have a property that $\det(AB) = \det(BA) = (\det A)(\det B)$, and hence, the determinant of a matrix remains intact by a unitary transformation of this matrix. Using this fact, one may show that the eigenphase sum and the background eigenphase sum may be related in a simple way to the determinants of the S and S_b matrices as

$$\det S(E) = \det(OSO^T) = \det \Lambda = \prod_{\alpha} \exp[2i(\delta)_{\alpha}] = \exp[2i\delta(E)], \tag{40}$$

$$\det S_b(E) = \det(O_b S_b O_b^T) = \det \Lambda_b = \exp[2i\delta_b(E)]. \tag{41}$$

To study the properties of the eigenphase sum in resonance scattering, we further note that $\det(I + cP) = 1 + c$, where c is any constant. This

can be shown easily since all the elements of the diagonalized matrix $O_P(I+cP)O_P^T = I+c\Pi$ are unity except for one diagonal element equal to $1+c$, according to Eq. (32). Using Eqs. (40), (34), (39), and (41) in this order, we derive, by letting $\delta_{\rm BW}(E)$ denote the eigenphase sum for $S_{\rm BW}(E)$,

$$\begin{aligned}\exp[2i\delta_{\rm BW}(E)] &= \det S_{\rm BW}(E) = \det(B^\dagger S_{\rm BW} B) = \det(S_r \Lambda_b) \\ &= \left(1 - \frac{i\Gamma}{E-\mathcal{E}}\right) \exp[2i\delta_b(E)],\end{aligned} \tag{42}$$

as was derived by Weidenmüller [38]; see also Ref. [39]. This result has the same appearance as Eq. (13) for single-channel scattering. A remarkable fact is that the pole of $\det S_{\rm BW}(E)$ is simple in spite of the fact that all S-matrix elements have a simple pole. This shows that the representation (34) of the resonance S matrix is indeed appropriate.

The same procedure as the derivation of Eq. (15) from Eq. (13) immediately yields the result that

$$\delta_{\rm BW}(E) = \delta_r(E) + \delta_b(E) = -\arctan\frac{\Gamma/2}{E-E_r} + \delta_b(E), \tag{43}$$

or that

$$E - E_r = (\Gamma/2)\cot[\delta_b(E) - \delta_{\rm BW}(E)], \tag{44}$$

which has the same form as Eq. (15) or Eq. (16), but now the phase shift $\delta_{\rm BW}(E)$ and the background phase shift $\delta_b(E)$ have been changed into the eigenphase sums. With a small number of fitting parameters, Eqs. (43) and (44) appear to be convenient for resonance fitting.

Historically, the initial general anticipation was that, for an isolated resonance, only one eigenphase should exhibit a resonance behavior and that all the others represent the background [40, 41]. This would mean, however, that the resonance eigenphase increases rapidly by π across the other, nearly constant eigenphases, contradicting the noncrossing rule for the eigenvalues. In fact, the same pole structure of all S-matrix elements forces every eigenphase to behave like an incomplete resonance. Figure 4.3 shows eigenphases for ^1S electron scattering by the hydrogen atom below the $n=3$ excitation threshold, calculated by Burke et al. by solving close-coupling equations [42–44]; this figure is also reproduced in Ref. [45].

The trend of Figure 4.3 is explained by the relation

$$E - E_r = \sum_\beta (\Gamma_\beta/2)\cot[(\delta_b)_\beta - (\delta)_\alpha] \tag{45}$$

derived by Macek [45]; note the resemblance to Eq. (44). This equation has N_o solutions for $(\delta)_\alpha$, one corresponding to each background eigenphase, thus

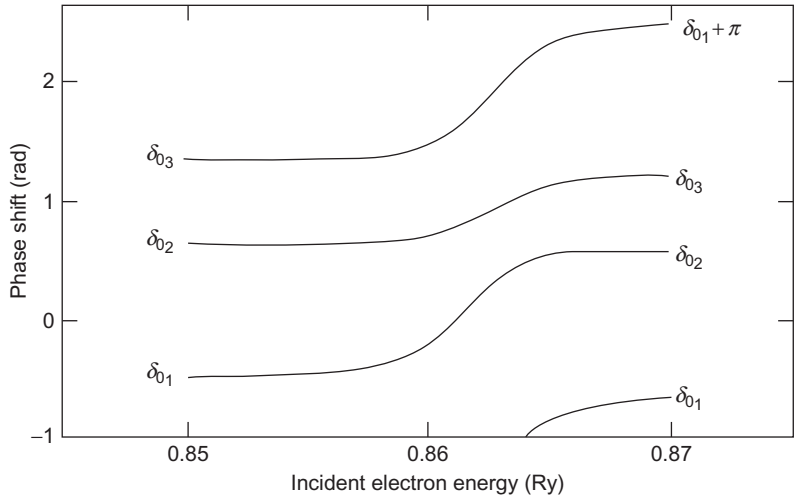

Figure 4.3 *S*-matrix eigenphases for e^--H(^1S) scattering below the H($n=3$) excitation threshold. Figure from Ref. [43] (see also Ref. [44]).

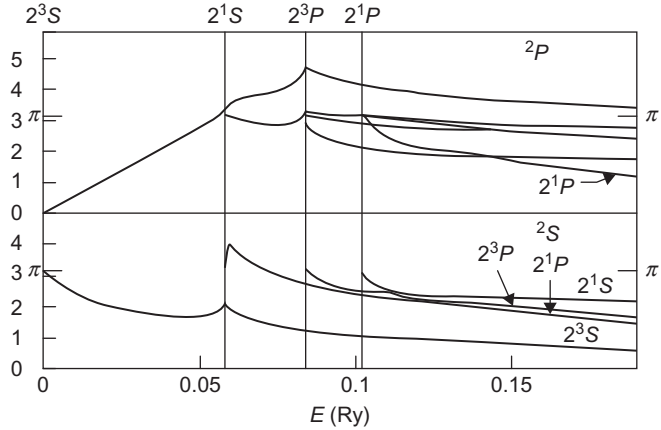

Figure 4.4 *S*-matrix eigenphases for e^--He (^2S, ^2P) scattering near the He($n=2$) excitation thresholds. The energy is measured from the He (2^3S) threshold. Taken from Ref. [43].

determining the energy dependence of all the eigenphases. They increase rapidly with energy E across the center E_r of the resonance. This equation seems to have been used rarely since a much simpler and useful relation (43) or (44) is satisfied by a single quantity, the eigenphase sum [38, 39].

Figure 4.4 shows another example, also from close-coupling calculations by Burke et al. [43], for ^2S and ^2P electron scattering by the helium atom near

the $n = 2$ thresholds. The very complex structure of this figure makes it difficult to extract resonance information. This is considered to be mainly because of the threshold behavior, together with the effects of the long-range potentials. The background changes appreciably with energy and is intertwined intricately with resonances. However, the second ^2S eigenphase sharply rises immediately after its start at the He (2^1S) threshold, which suggests the existence of a resonance. The eigenphase sum should be useful for analyzing it, but another concept turns out to be more useful, in fact.

2.2.3. Time-delay matrix Q: Relation to the eigenphase sum

The eigenphase sum $\delta(E)$ is also seen to appear in the trace

$$\mathrm{Tr}\left(-i\hbar\frac{\mathrm{d}\Lambda}{\mathrm{d}E}\Lambda^\dagger\right) = 2\hbar\frac{\mathrm{d}\delta}{\mathrm{d}E}, \tag{46}$$

as is seen from the explicit expressions for the diagonal matrix elements $\Lambda_{\alpha\alpha}$ in Eq. (36). The right-hand side resembles the time delay (24) in single-channel scattering and is indeed large in a resonance region according to Eq. (43). Also, a straightforward calculation shows that S_r of Eq. (34) satisfies

$$-i\hbar\frac{\mathrm{d}S_r}{\mathrm{d}E} = L(E)PS_r, \quad -i\hbar\frac{\mathrm{d}S_r}{\mathrm{d}E}S_r^\dagger = L(E)P. \tag{47}$$

Both of these facts suggest the relevance of the quantity $-i\hbar(\mathrm{d}S/\mathrm{d}E)S^\dagger$ to resonance scattering.

An important perspective of multichannel resonance scattering may be gained from the lifetime matrix $Q(E)$, introduced by Smith [46] as a generalization of the time delay Δt of Eq. (24) in single-channel scattering. It is now more often called the time-delay matrix or the delay-time matrix. After extending Δt for matrix elements $Q_{ij}(E)$ for multichannel scattering, he proved that

$$Q(E) = i\hbar S\frac{\mathrm{d}S^\dagger}{\mathrm{d}E} = -i\hbar\frac{\mathrm{d}S}{\mathrm{d}E}S^\dagger = Q^\dagger(E). \tag{48}$$

One may regard this relation between Q and S as a definition of $Q(E)$ for the purpose of the following discussion. For single-channel scattering, the substitution of the expression $S = e^{2i\delta}$ here immediately recovers the time delay Δt of Eq. (24), which is the additional time spent by the projectile in the collision compared with a passage in the absence of any interaction with the target [30–32]. For multichannel scattering, the diagonal elements Q_{ii} are real and have the physical meaning of the average time delay, over all possible exit channels, starting from the initial channel i. Eisenbud [30]

also generalized the single-channel time delay Δt for multichannel scattering. The relation between the result of Eisenbud and Smith's Q matrix has been discussed in detail recently [47].

As a preliminary for deriving a useful expression, we note that the trace of a matrix is invariant under unitary transformation and that $\mathrm{Tr}(AB) = \mathrm{Tr}(BA)$. For any unitary matrix U, it follows that $0 = (UU^\dagger)' = U'U^\dagger + UU^{\dagger\prime}$ and that $\mathrm{Tr}(U'U^\dagger + U^{\dagger\prime}U) = 0$, the prime indicating the energy derivative. Therefore, we have

$$\begin{aligned} & -i\hbar\,\mathrm{Tr}\left[(USU^\dagger)'(USU^\dagger)^\dagger\right] \\ &= -i\hbar\,\mathrm{Tr}\left[(US'U^\dagger + U'SU^\dagger + USU^{\dagger\prime})(US^\dagger U^\dagger)\right] \\ &= -i\hbar\,\mathrm{Tr}\left[S'S^\dagger + U'U^\dagger + U^{\dagger\prime}U\right] \\ &= -i\hbar\,\mathrm{Tr}\left[S'S^\dagger\right] = \mathrm{Tr}\,Q. \end{aligned} \tag{49}$$

A choice of U as O of Eq. (36) leads to $USU^\dagger = \Lambda$. Then, Eq. (46) used in Eq. (49) shows that

$$\mathrm{Tr}\,Q(E) = 2\hbar\frac{\mathrm{d}\delta(E)}{\mathrm{d}E} \tag{50}$$

with the eigenphase sum $\delta(E)$ [34]. This is an extension of the theorem (24) for multichannel scattering and is a general result holding true for both resonance and nonresonance scattering. This trace can be proved to be equal to the density of states $\rho(E)$ times the Planck constant h, as an extension of Eq. (24) [48].

Substitution of Eq. (43) into Eq. (50) yields

$$\mathrm{Tr}\,Q_{\mathrm{BW}}(E) = 2\hbar\frac{\mathrm{d}\delta_r}{\mathrm{d}E} + 2\hbar\frac{\mathrm{d}\delta_b}{\mathrm{d}E} = L(E) + 2\hbar\frac{\mathrm{d}\delta_b}{\mathrm{d}E}, \tag{51}$$

which has the same form in appearance as Eq. (25).

Another, more direct derivation of this result without use of the expression (43) for the resonance eigenphase sum would be of interest. Because $B^\dagger S_{\mathrm{BW}} B = S_r\Lambda_b$ due to Eqs. (34) and (39), the choice $U = B^\dagger$ in Eq. (49) leads to the expression

$$\mathrm{Tr}\,Q_{\mathrm{BW}} = -i\hbar\,\mathrm{Tr}\left[(S_r\Lambda_b)'\Lambda_b^\dagger S_r^\dagger\right] = -i\hbar\,\mathrm{Tr}\left[S_r'S_r^\dagger + \Lambda_b'\Lambda_b^\dagger\right] \tag{52}$$

since S_r is unitary. The term $-i\hbar\mathrm{Tr}(S_r'S_r^\dagger)$ is known to be $L(E)$ from Eqs. (47) and (30). The other term $-i\hbar\mathrm{Tr}(\Lambda_b'\Lambda_b^\dagger)$ is similar to Eq. (46) and is easily calculated to be $2\hbar\mathrm{d}\delta_b/\mathrm{d}E$. Thus, Eq. (52) reproduces Eq. (51). Its integration recovers Eq. (43), which is its second derivation.

2.2.4. Q-matrix eigenchannels and resonance eigenchannel space

The time-delay matrix $Q(E)$ can be diagonalized by a unitary transformation

$$U_Q Q = \Lambda_Q U_Q, \quad (\Lambda_Q)_{\gamma\gamma'} = \delta_{\gamma\gamma'} q_\gamma. \tag{53}$$

The eigenvalues q_γ are real since $Q(E)$ is Hermitian, as seen from Eq. (48). The set of original physical channels are linearly transformed into a new set of channels by the unitary matrix U_Q. We refer to these new channels as Q-matrix eigenchannels, or Q-eigenchannels, for short. In the rest of Section 2, the eigenvalues q_γ and the corresponding Q-eigenchannels will turn out to be quite useful in resonance analysis.

Substitution of the Breit–Wigner S matrix (34) into Eq. (48) for the Q matrix and the assumption of an energy-independent B, i.e., an energy-independent background S_b yield the expression

$$Q_{\mathrm{BW}}(E) = -i\hbar(BS_r'B^T)(BS_rB^T)^\dagger = -i\hbar BS_r'S_r^\dagger B^\dagger = L(E)BPB^\dagger \tag{54}$$

according to Eq. (47). Since B is unitary and since the eigenvalues of a matrix are unchanged by its unitary transformation, the largest and the only nonzero eigenvalue $q_{\max}$ of $Q_{\mathrm{BW}}(E)$ is $L(E)$ and all of the other eigenvalues are zero [43, 49]. This is clearly consistent with the trace (51). Another way of understanding it is to confirm that $Q_{\mathrm{BW}}(E)$ is positive definite since

$$\mathbf{u}^\dagger Q_{\mathrm{BW}}(E)\mathbf{u} = L(E)\mathbf{u}^\dagger B\mathbf{g}\mathbf{g}^\dagger B^\dagger\mathbf{u} = L(E)(\mathbf{u}^\dagger B\mathbf{g})(\mathbf{u}^\dagger B\mathbf{g})^\dagger \geq 0 \tag{55}$$

for any vector $\mathbf{u}$. Thus, all eigenvalues are positive or zero and one of them is equal to their sum, so that all the others are zero.

It is also clear from Eq. (54) that

$$Q_{\mathrm{BW}}(E)(B\mathbf{g}) = L(E)B\mathbf{g}\mathbf{g}^\dagger B^\dagger B\mathbf{g} = L(E)(B\mathbf{g}), \tag{56}$$

i.e., the energy-independent vector $B\mathbf{g}$ is the eigenvector for the eigenvalue $L(E)$ [43, 49]. This eigenvector depends on the background S_b, unlike the eigenvalue $L(E)$. The other eigenvectors of $Q_{\mathrm{BW}}(E)$ are orthogonal to $B\mathbf{g}$ and can be made independent of E since any unitary transformation of the $N_o - 1$ degenerate eigenvectors into a new set of linearly independent vectors is allowed.

We have seen that, if the background S_b is independent of energy, then

1. we can extract E_r and Γ from the trace or the only nonzero eigenvalue $L(E)$ of Q,
2. we can also extract all partial widths $\{\Gamma_i\}$, or the (energy-independent) branching ratios $\{\Gamma_i/\Gamma\}$, from the corresponding eigenvector multiplied

by $B^{-1} = B^{\dagger}$ from left since $g_i \propto \Gamma_i^{1/2}$ according to Eq. (30) and $\sum_i \Gamma_i = \Gamma$, and

3. all eigenvectors can be chosen to be independent of E.

Note that, if S_b depends on the energy E, the eigenvector corresponding to the largest Q-matrix eigenvalue $q_{\max}$ depends on E and does not directly give the resonance branching ratios $\{\Gamma_i/\Gamma\}$; however, see Ref. [50].

The result of this sub-subsection indicates a salient feature of the Q-eigenchannels; for an isolated resonance with an energy-independent background, the whole channel space is separated clearly into a single-element resonance Q-eigenchannel space and $(N_o - 1)$-element nonresonance Q-eigenchannel space. Unlike the S-matrix eigenchannels, all Q-matrix eigenchannels are completely nonresonant, except for one. This resonance Q-eigenchannel alone represents the dynamics of the resonance process in terms of the Lorentzian-shape eigenvalue $L(E)$, having a strong dependence on the energy E, whereas the resonance Q-eigenchannel itself is independent of E. This concept of resonance Q-eigenchannel space will be generalized for overlapping resonances later in Sections 2.3.3 and 2.3.4.

Figure 4.5 shows the eigenvalues of the Q matrix for electron scattering by helium, using the same S matrix as diagonalized in Figure 4.4 [43]. In spite of the complicated structure of the S-matrix eigenphases due to the threshold effects, the resonance Q-eigenvalue stands out conspicuously as a sharp peak

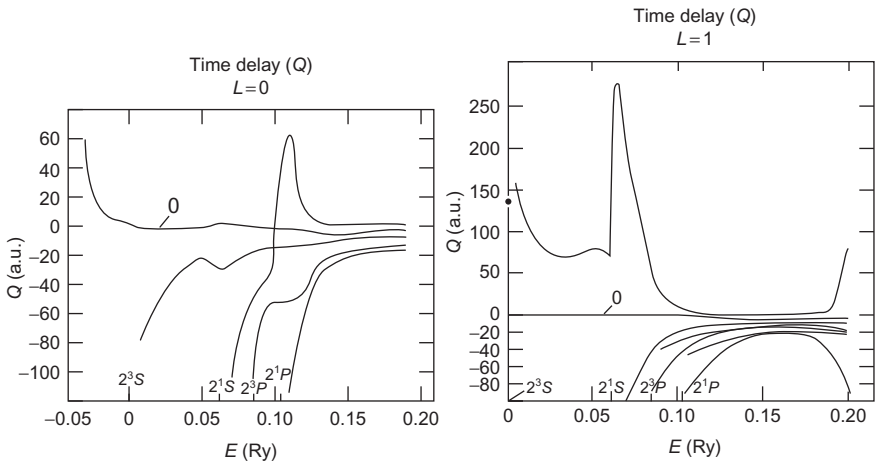

Figure 4.5 Eigenvalues of the time-delay matrix $Q(E)$ for e^--He ^2S (left) and ^2P (right) scattering near the He($n = 2$) excitation thresholds; based on the same S-matrix data as were used in more complicated Figure 4.4. The energy is measured from the He (2^3S) threshold. Symbol "0" indicates the eigenvalue corresponding to elastic scattering from the ground state. Figure from Ref. [43].

from each set of curves, while the other eigenvalues are smooth and negative except for the elastic eigenvalue.

2.2.5. Analysis of isolated resonances with weak background

The asymptotic wavefunctions obtained from multichannel scattering calculations provide the S matrix, the eigenphases and eigenphase sum, and the cross sections. In principle, any of these quantities may be chosen for fitting the resonance formula to determine accurate values of the resonance parameters E_r and Γ.

In the field of photoionization, the Fano formula for the cross section has often been used for resonance fitting. Note, however, that the same resonance can sometimes stand out sharply from the background, but can also fail to manifest themselves clearly in the photoionization cross section, depending upon the initial bound state of the dipole transition [51]. Thus, the cross-section inspection might miss some resonances. The asymptotic quantities of the final continuum-state wavefunction, if available, should be much more convenient in general for the purpose of resonance search and analysis.

The cross sections for scattering are often affected significantly by the background, as is seen clearly in Figure 4.1 of the Fano profile. On the other hand, the background, if independent of energy, simply raises or lowers the overall eigenphase sum $\delta(E)$ in the resonance region, and thus, $\delta(E)$ is much easier for analysis of narrow, isolated resonances than the cross sections.

The constant background disappears if the energy derivative of $\delta(E)$ is taken. This would even simplify the resonance analysis and would stress the structures due to resonances. Thus, $\mathrm{d}\delta(E)/\mathrm{d}E$ or the trace of the $Q(E)$ matrix should be more advantageous for the resonance search and fitting based on the Breit–Wigner formula (51). The center of the fitted Lorentzian profile $L(E)$ is obviously the resonance position E_r, whereas the parameter Γ determines both the FWHM and the peak height of the profile, the former being Γ and the latter $4\hbar/\Gamma$; see Eq. (20) and the remarks below it. One may exploit this fact for the reliability check of the resonance fit by confirming the consistency between the width and the height of the peak. A careful analysis would be possible by the least-squares fit with a background eigenphase sum $\delta_b(E)$ quadratic in E, for example, or its contribution to $\mathrm{Tr}\, Q(E)$ linear in E, if the resonance is fairly broad.

In actual computations, the numerical differentiation can introduce a large error and should be avoided. A simple solution to this would be to fit spline functions, or a piecewise polynomial and overall smooth function of E, to the numerically calculated eigenphase sum $\delta(E)$, and then to differentiate the spline functions analytically [52, 53]. In the R-matrix method [44], the analytic E dependence of the R matrix and associated matrices can be taken advantage of in the direct differentiation of these quantities. This technique was found to be useful for automatic and fast analysis of the results of R-matrix method calculations [54–56].

It should be born in mind that our discussion now centers on extracting the resonance position E_r and the total width Γ from the much richer scattering information that the S and Q matrices contain. Multichannel continuum wavefunctions are usually calculated for more general purposes of obtaining the scattering amplitudes and the cross sections for various state-to-state processes and of unraveling the dynamics of the whole continuum system including both resonance and nonresonance mechanisms and the intricate interference between them.

For a nearly constant background S_b the study of the trace of the Q matrix and that of its eigenvalues are almost equivalent. In actual physical problems, however, the energy dependence of $S_b(E)$ is not necessarily negligible, and more than one appreciable Q-matrix eigenvalue may exist. Then, an inspection of the eigenvalues $\{q_\gamma(E)\}$, containing more information than $\mathrm{Tr}\, Q(E)$, should be desirable in general. This is the next subject of our discussion.

2.2.6. Negative time delay: Resonances buried in the background

We take up an example of the Coulomb three-body system $e^+e^-e^-$ (the positronium negative ion Ps^-), or equivalently, its charge-conjugate system $e^+e^-e^+$ (Ps^+) with the same interactions. This system has only one bound state but many QBSs formed, for example, in resonance electron scattering by the positronium. Some of these resonances are narrow but others are fairly broad. Analysis of narrow, isolated resonances is simple in general; it is usually easy to extract the resonance parameters E_r and Γ by examining the cross sections, the eigenphase sum, the eigenphase-sum derivative or $\mathrm{Tr}\, Q(E)$, or the Q-eigenvalues, any of which without problems. On the other hand, broad resonances, especially those lying close to a threshold, can often be tricky and one may have to choose an analysis method carefully.

Figure 4.6 presents selected results of the calculations by solving close-coupling equations for $Ps^-(^1S^e, {}^3P^o, {}^1D^e)$ in terms of the hyperspherical coordinates near the $Ps(n = 3)$ threshold [53]; see Section 3.2.2 for hyperspherical close-coupling (HSCC) equations. The eigenphase sum $\delta(E)$ for $^1S^e$ scattering in Figure 4.6a shows a typical resonance behavior, though it increases only by less than $\pi/2$ due to the rapidly decreasing background eigenphase sum. The trace of the Q matrix (broken curve), proportional to $\mathrm{d}\delta(E)/\mathrm{d}E$, has a typical Lorentzian profile, which is nearly a mere vertical shift of the largest eigenvalue $q_{\max}(E)$. Another eigenvalue is negative, nearly constant but fairly large, and all of the others are almost zero and indistinguishable from the horizontal axis.

On the other hand, the curves for $^3P^o$ scattering in Figure 4.6b deserve close examination. The eigenphase sum decreases monotonically in this figure, suggesting no resonances occurring in this energy region. Nevertheless, its energy derivative, or $\mathrm{Tr}\, Q(E)$, exhibits a weak peak of negative value. Indeed, it is due to the largest eigenvalue $q_{\max}(E)$, having a Lorentzian profile and

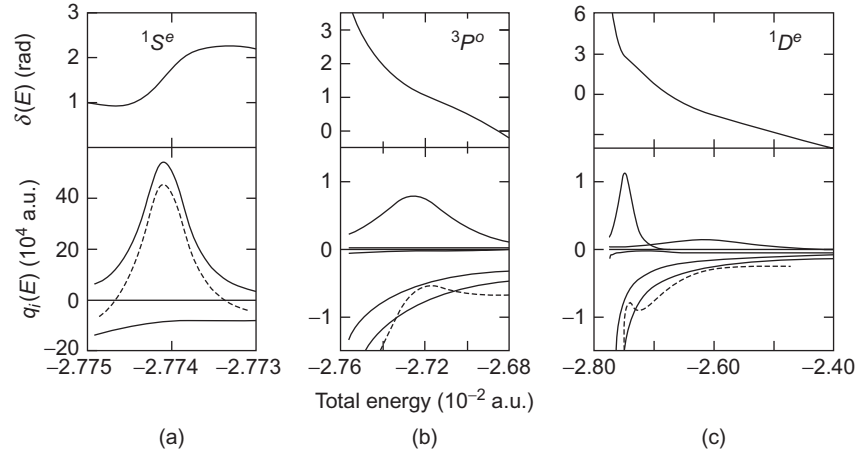

Figure 4.6 The eigenphase sum $\delta(E)$ and the trace (− − −) and the eigenvalues $\{q_i(E)\}$ (——) of the time-delay matrix $Q(E)$ as functions of the total energy E for positronium negative ion Ps^- above the $Ps(n=3)$ threshold (at $E=-0.02778$ a.u.). (a) $^1S^e$. (b) $^3P^o$. (c) $^1D^e$. The number N_o of open channels is 6 for (a), 9 for (b), and 10 for (c). Some eigenvalues are too small to be distinguished from the $q_i = 0$ line. For $^3P^o$ and $^1D^e$, the eigenphase sum decreases monotonically, indicating a negative time delay and no resonance, in spite of the actual existence of a resonance or resonances revealed by the eigenvalue(s) $q_i(E)$. Figure from Ref. [53].

clearly indicating the existence of a QBS. The two negative and large eigenvalues wash away the time delay due to $q_{\max}(E)$, and the overall effect is the time "advance." Without the Q-eigenvalue analysis, this resonance could have been missed. In fact, a careful inspection of $\delta(E)$ reveals a kink, corresponding to the resonance peak in $d\delta(E)/dE$.

The trend of Figure 4.6c for $^1D^e$ scattering is similar. Here, however, a second, extremely broad Lorentzian peak emerges in $q_{\max}(E)$, which is hardly discernible in the trace. This broad peak and the narrower peak appear to cross each other at first sight, but they avoid crossing due to the noncrossing rule for the Q-matrix eigenvalues. Such an avoided crossing will be discussed later in Section 2.3 in detail.

A completely different approach of directly calculating the positions of S-matrix poles in the complex energy plane, by the technique of CCR (see Section 1.4), also finds out these resonances with the positions E_r and the widths Γ in good agreement with the Q-eigenvalue results, corroborating the reliability of both approaches [57, 58]. Specifically, the Q-eigenvalue results for the $^3P^o$ resonance of Figure 4.6b are $(E_r, \Gamma) = (-2.7249 \times 10^{-2}, 4.8 \times 10^{-4})$ in atomic units [53], and the CCR results are $(-2.725 \times 10^{-2}, 4.60 \times 10^{-4})$ a.u. [57]. For the two $^1D^e$ resonances of Figure 4.6c, the Q-eigenvalue results are $(-2.7480 \times 10^{-2}, 3.1 \times 10^{-4})$ a.u. and $(-2.617 \times 10^{-2}, 2.1 \times 10^{-3})$

a.u. [53], whereas the CCR method gives $(-2.7400 \times 10^{-2}, 3.2 \times 10^{-4})$ a.u. and $(-2.618 \times 10^{-2}, 2.04 \times 10^{-3})$ a.u. [57, 58].

The strong background that overcomes a resonance and makes the time delay negative even in the energy region of the resonance is due to the long-range dipole potential (behaving asymptotically as $\propto r^{-2}$) between the electron and the positronium in an excited state [53, 59, 60], as will be discussed in Section 3.1.3. In such a case, the fitting formula should take into account the divergence of $\delta_b(E)$ as E approaches a threshold $E_{\rm th}$ from above, by an additional term in $\mathrm{Tr}\, Q(E)$ proportional to $(E - E_{\rm th})^{-1}$.

2.3. Multichannel scattering: Overlapping resonances

A number of closely lying resonances in multichannel scattering is a difficult problem to treat theoretically. Even the representation of the S matrix is very complex for these overlapping resonances as compared with the Breit–Wigner one-level formula. Various alternative proposals are found in the literature, as is reviewed by Belozerova and Henner [61]. This is mainly due to the formidable task of constructing an explicitly unitary and symmetric S matrix having more than one pole when analytically continued into the complex k plane. Thus, possible practical forms of the S matrix for overlapping resonances may be explicitly symmetric and implicitly unitary, or explicitly unitary and implicitly symmetric.

2.3.1. Difficulty in the representation of the S matrix

An explicitly symmetric representation of the S matrix for N overlapping resonances, satisfying the time reversal symmetry, may be (e.g., Ref. [62])

$$S = S_b - \sum_{\nu=1}^{N} \frac{i\Gamma_\nu}{E - \mathcal{E}_\nu} (B\mathbf{v}_\nu)(B\mathbf{v}_\nu)^T = B\left(I - \sum_{\nu=1}^{N} \frac{i\Gamma_\nu}{E - \mathcal{E}_\nu} \mathbf{v}_\nu \mathbf{v}_\nu^T\right) B^T \qquad (57)$$

with $\mathcal{E}_\nu = E_\nu - i\Gamma_\nu/2$. For N isolated resonances, this form is consistent with the theory of Section 2.2.1 if $\mathbf{v}_\nu$ is chosen as $\mathbf{g}$ of Eq. (30) for each resonance. When the resonances overlap each other, the vectors $\mathbf{v}_\nu$ are *complex* in general and no longer expressible in terms of partial widths, unlike $\mathbf{g}$ in Eq. (30). Also, $\mathbf{v}_\nu^\dagger \mathbf{v}_\nu \neq 1$ in general.

The form (57) is not necessarily unitary. The unitarity at real E is achieved by forcing the N complex vectors $\mathbf{v}_\nu$ to satisfy appropriate constraints. For this purpose, the number of parameters would be insufficient if the vectors $\mathbf{v}_\nu$ were real. McVoy [35] works out expressions for the parameters satisfying the unitarity constraints for double resonances, $N = 2$. For $N \geq 3$, however, the expressions are too cumbersome to present explicitly.

Abandoning the explicit symmetry, Simonius [63] proposed a representation of the S matrix for N overlapping resonances that is explicitly unitary at

real E; it has a form

$$S(E) = B\mathscr{P}_N B^T \equiv S_{\text{Sim}}(E) \tag{58}$$

with the product

$$\mathscr{P}_n = \prod_{\nu=1}^{n} S_\nu = S_1 S_2 \cdots S_n \quad \text{for } n \geq 1, \quad \mathscr{P}_0 = I \tag{59}$$

in terms of unitary matrices S_ν, which are defined by

$$S_\nu(E) = I - \frac{i\Gamma_\nu}{E - \mathcal{E}_\nu} P_\nu = I - \frac{i\Gamma_\nu}{E - \mathcal{E}_\nu} \mathbf{g}_\nu \mathbf{g}_\nu^\dagger \tag{60}$$

similarly to S_r in Eq. (34). The definition of $\mathscr{P}_0$ in Eq. (59) is unnecessary here, but will be used later. The complex vectors $\mathbf{g}_\nu$, satisfying $\mathbf{g}_\nu^\dagger \mathbf{g}_\nu = 1$ for the unitarity of S_ν, should be interpreted as characterizing the mixing of the channels. Equation (58) is a natural extension of the single-channel overlapping-resonance formula (26) for multichannel resonances. For N isolated resonances, Eq. (58) is consistent with the theory of Section 2.2.1 if $\mathbf{g}_\nu$ is chosen as $\mathbf{g}$ of Eq. (30) for each resonance.

The projection matrices P_ν satisfy the relations

$$P_\nu = \mathbf{g}_\nu \mathbf{g}_\nu^\dagger = P_\nu^2 = P_\nu^\dagger, \quad \operatorname{Tr} P_\nu = 1, \quad P_\nu \mathbf{g}_\nu = \mathbf{g}_\nu. \tag{61}$$

In general, there is no commutation of the P_ν nor of the S_ν matrices:

$$[P_\nu, P_{\nu'}] \neq 0, \quad [S_\nu, S_{\nu'}] \neq 0 \quad \text{for } \nu \neq \nu'. \tag{62}$$

Therefore, a fixed order of the factors in $\mathscr{P}_N$ is implied as indicated by Eq. (59). The symmetry of $S_{\text{Sim}}(E)$ of Eq. (58) should be and is assumed to be enforced by an appropriate choice of vectors $\{\mathbf{g}_\nu\}$. In practice, this is difficult to express explicitly. However, determination of $\{\mathbf{g}_\nu\}$ by parameter fitting is impractical, anyway. The S matrix (58) is often very useful when $\mathbf{g}_\nu$ need not be specified explicitly, as will be seen in the following, since it is quite a general representation that is unitary at real E and has poles at the right positions in the complex E plane.

The derivation of the eigenphase sum for the Simonius S matrix, $S_{\text{Sim}}(E)$, is straightforward by generalizing the procedure for an isolated resonance shown in Section 2.2.2. Compared with the Breit–Wigner S matrix, $S_{\text{BW}}(E)$, the matrix S_r in Eq. (34) is now replaced by $\mathscr{P}_N$, or the product of matrices S_ν, each having the same apparent form as S_r but with different resonance parameters and a different projection matrix. Since the determinant of the

product $\prod_\nu S_\nu$ is equal to the product of the determinants of respective S_ν, Eq. (42) for $\det S_{\rm BW}(E)$ is now changed into the form

$$\det S_{\rm Sim}(E) = \exp[2i\delta_b(E)] \prod_{\nu=1}^{N} \left(1 - \frac{i\Gamma_\nu}{E - \mathcal{E}_\nu}\right). \tag{63}$$

This has the same appearance as Eq. (26) for the S matrix for overlapping resonances in single-channel scattering. Since Eq. (63) is equal to $\exp(2i\delta)$ according to Eq. (40), the same argument that led to Eq. (27) applies to the eigenphase sum $\delta_{\rm Sim}(E)$ for the Simonius S matrix with a result that

$$\delta_{\rm Sim}(E) = -\sum_{\nu=1}^{N} \arctan \frac{\Gamma_\nu/2}{E - E_\nu} + \delta_b(E), \tag{64}$$

having exactly the same form as Eq. (27). It is independent of the order of S_ν appearing in $S_{\rm Sim}$ of Eq. (58) in spite of the order-dependent definition of $S_{\rm Sim}$. This is one of the reasonable results supporting the proposal of the form of $S_{\rm Sim}(E)$.

2.3.2. Time-delay matrix Q and its trace

The relation (50) between the time-delay matrix Q and the eigenphase sum δ is quite general and applies to the Simonius Q matrix, too. Thus, it follows from Eq. (64) that

$$\mathrm{Tr}\, Q_{\rm Sim}(E) = 2\hbar \frac{\mathrm{d}\delta_{\rm Sim}(E)}{\mathrm{d}E} = \sum_{\nu=1}^{N} L_\nu(E) + 2\hbar \frac{\mathrm{d}\delta_b}{\mathrm{d}E} \tag{65}$$

with the same form as Eq. (28). The Lorentzian profiles $L_\nu(E)$ have the same form as Eq. (29).

A direct proof of Eq. (65) without using the explicit form (64) of $\delta_{\rm Sim}(E)$ would be instructive. This aim is achieved by following the procedure of deriving Eq. (51) for $\mathrm{Tr}\, Q_{\rm BW}(E)$ via Eq. (52). Since $S_{\rm Sim}$ is just $S_{\rm BW}$ with its S_r replaced by $\mathscr{P}_N$, it follows from Eq. (52) that

$$\mathrm{Tr}\, Q_{\rm Sim} = -i\hbar\, \mathrm{Tr}\,(\mathscr{P}'_N \mathscr{P}_N^\dagger) - i\hbar\, \mathrm{Tr}\,(\Lambda'_b \Lambda_b^\dagger), \tag{66}$$

$\mathscr{P}_N$ being unitary just as S_r. A straightforward calculation shows that $-i\hbar S'_\nu(E) = L_\nu P_\nu S_\nu$ in the same way as Eq. (47), and hence, due to the unitarity of S_ν, that

$$\begin{aligned} -i\hbar \mathscr{P}'_N \mathscr{P}_N^\dagger &= -i\hbar \sum_{\nu=1}^{N} S_1 S_2 \cdots S_{\nu-1} S'_\nu S_{\nu+1} \cdots S_N S_N^\dagger \cdots S_1^\dagger \\ &= \sum_{\nu=1}^{N} L_\nu \mathscr{P}_{\nu-1} P_\nu (\mathscr{P}_{\nu-1})^\dagger. \end{aligned} \tag{67}$$

Noting that $\mathrm{Tr}\, P_\nu = 1$ according to Eq. (61) and that L_ν is not a matrix but a multiplicative factor, we find that the first term in Eq. (66) is reduced to $\sum L_\nu$, which is independent of the order of S_ν in the definition of S_{Sim}. The second term was already shown, below Eq. (52), to be equal to $2\hbar \mathrm{d}\delta_b/\mathrm{d}E$. Thus, Eq. (66) recovers the trace formula (65).

The explicit form of $Q_{\mathrm{Sim}}(E)$ is calculable by substituting $S_{\mathrm{Sim}}(E)$ into Eq. (48) for the Q matrix and by using the unitarity of B and S_ν and Eq. (67) as

$$\begin{aligned} Q_{\mathrm{Sim}}(E) &= -i\hbar \left[B\mathscr{P}'_N B^T + B'\mathscr{P}_N B^T + B\mathscr{P}_N (B^T)' \right] (B^T)^\dagger \mathscr{P}_N^\dagger B^\dagger \\ &= \sum_{\nu=1}^{N} Q_\nu(E) + Q_b(E), \end{aligned} \tag{68}$$

where

$$Q_\nu(E) = L_\nu (B\mathscr{P}_{\nu-1}) P_\nu (B\mathscr{P}_{\nu-1})^\dagger = L_\nu (B\mathscr{P}_{\nu-1}\mathbf{g}_\nu)(B\mathscr{P}_{\nu-1}\mathbf{g}_\nu)^\dagger \tag{69}$$

and

$$Q_b(E) = -i\hbar [B'B^\dagger + S_{\mathrm{Sim}}(B'B^\dagger)^T S_{\mathrm{Sim}}^\dagger]. \tag{70}$$

This general expression for $Q_{\mathrm{Sim}}(E)$ looks cumbersome unless $B(E)$, and hence, the background S matrix $S_b(E)$ is independent of E [64]. On the other hand, its trace has been shown to take a simple form (65). The trace is independent of the order of the resonances S_ν, which it should be, but Q_{Sim} itself is unfortunately not, since $\mathscr{P}_{\nu-1}$ in Q_ν is not.

2.3.3. Avoided double resonance and resonance eigenchannel space

Two overlapping resonances with an energy-independent background S_b is the simplest case of Eq. (68), reducing to

$$Q_{\mathrm{Sim}}(E) = B[L_1(E)P_1 + L_2(E)S_1 P_2 S_1^\dagger]B^\dagger. \tag{71}$$

Its unitary transform

$$\mathcal{Q}_{\mathrm{ut}} = S_1^\dagger B^\dagger Q_{\mathrm{Sim}} B S_1 = L_1 P_1 + L_2 P_2, \tag{72}$$

where the commutativity of P_ν and S_ν has been used, has the same eigenvalues and the trace as Q_{Sim}; $\mathrm{Tr}\, Q_{\mathrm{Sim}} = \mathrm{Tr}\, \mathcal{Q}_{\mathrm{ut}} = L_1 + L_2$ in agreement with Eq. (65).

We consider the eigenvectors of $\mathcal{Q}_{\mathrm{ut}}$ in the form of a linear combination of the vectors $\mathbf{g}_1$ and $\mathbf{g}_2$ [65]. This approach is a generalization of the theory for

isolated resonances discussed in Section 2.2.4. The eigenvalue equation for $\mathcal{Q}_{\rm ut}$ may be written as

$$0 = (\mathcal{Q}_{\rm ut} - q)\mathbf{x} = (L_1\mathbf{g}_1\mathbf{g}_1^\dagger + L_2\mathbf{g}_2\mathbf{g}_2^\dagger - q)(c_1\mathbf{g}_1 + c_2\mathbf{g}_2). \tag{73}$$

Multiplication by $\mathbf{g}_1^\dagger$ and by $\mathbf{g}_2^\dagger$ from left results in the coupled equations

$$\begin{pmatrix} L_1 - q & \rho_{12}L_2 \\ \rho_{12}^* L_1 & L_2 - q \end{pmatrix} \begin{pmatrix} c_1 + \rho_{12}c_2 \\ \rho_{12}^* c_1 + c_2 \end{pmatrix} = 0 \tag{74}$$

for the coefficients c_1 and c_2, where $\rho_{12} = \mathbf{g}_1^\dagger\mathbf{g}_2$. The nontrivial solutions require that the determinant of the matrix on the left-hand side be zero, so that two eigenvalues of $Q_{\rm Sim}$ are found to be [65]

$$q_\gamma = q_\pm = \frac{L_1 + L_2}{2} \pm \frac{[(L_1 - L_2)^2 + 4\beta L_1 L_2]^{1/2}}{2}, \quad 0 \le \beta = |\rho_{12}|^2 \le 1. \tag{75}$$

This represents a typical avoided-crossing formula. The corresponding mixing ratios $r_\pm = c_2/c_1$ are obtainable from the equation

$$q_\pm = (1 + \rho_{12}r_\pm)L_1 = (1 + \rho_{12}^* r_\pm^{-1})L_2. \tag{76}$$

Equation (75) contains only five parameters, namely, the resonance parameters E_1, Γ_1, E_2, and Γ_2 and the overlap parameter β. Details of the vectors $\mathbf{g}_i$ or the mixing ratios $r_\pm$ are irrelevant to the Q-matrix eigenvalues for the case of two overlapping resonances with an energy-independent background.

The sum of these two eigenvalues $q_+ + q_- = L_1 + L_2$ is equal to the trace. Also, $\mathcal{Q}_{\rm ut}$ is positive definite. Therefore, all eigenvalues other than $q_\pm$ must be zero. The eigenvectors of $Q_{\rm Sim}$ corresponding to these zero eigenvalues are orthogonal to both $BS_1\mathbf{g}_1$ and $BS_1\mathbf{g}_2$. This is a generalization of the result for isolated resonances, namely, for double resonance with a constant background, the whole channel space is separated clearly into a two-element resonance Q-eigenchannel space and $(N_{\rm o} - 2)$-element nonresonance Q-eigenchannel space. All the Q-matrix eigenchannels are completely nonresonant, except for the two. These two resonance Q-eigenchannels alone represent the resonance process in terms of the Lorentzian eigenvalues $L_1(E)$ and $L_2(E)$ avoided from each other near the crossing point.

The strength of the resonance–resonance interaction, or of avoidance between $L_1(E)$ and $L_2(E)$ to form $q_\pm$, is determined by two kinds of overlap: (1) that between the two Lorentzian profiles $L_1(E)$ and $L_2(E)$ and (2) the parameter $\beta = |\mathbf{g}_1^\dagger\mathbf{g}_2|^2$. The product $L_1(E)L_2(E)$ in the formula (75) for the nonzero eigenvalues is almost zero for any E if the two resonances are well separated. Then, one of the two eigenvalues $q_\pm$ will be nearly equal to $L_1(E)$

and the other to $L_2(E)$. When $L_1(E)$ and $L_2(E)$ overlap each other significantly, the two limiting cases of Eq. (75) are

$$\begin{aligned} &\beta \to 0: \quad q_\pm \to L_i(E), \quad i = 1,2 \\ &\beta \to 1: \quad q_+ \to L_1(E) + L_2(E), \quad q_- \to 0. \end{aligned} \tag{77}$$

As an example, we take up the positronium negative ion Ps^- again, calculated by solving HSCC equations [65]; see Section 3.2.2. Shown in Figure 4.7 are the two extremes of overlapping resonances, namely, (a) those of symmetry $^1P^o$ lying just below the threshold $E = -0.02778$ a.u. for the channel $e^- + Ps(n=3)$, illustrating the case of strong interaction, $\beta \simeq 1$, and (b) those of symmetry $^1D^e$ just above this threshold, illustrating weak interaction, $\beta \simeq 0$. The solid curves in Figures 4.7a and 4.7b represent the two largest eigenvalues of the Q matrix obtained from the HSCC calculations. The broken curves are the results of fitting of Eq. (75) and the dotted curve was obtained by fitting with the background contribution augmented; see Ref. [65] for the details of fitting. For Figure 4.7a, the fitting to the largest calculated Q eigenvalue is perfect and the broken curve is indistinguishable from the solid curve. The error in the fitting of the second largest

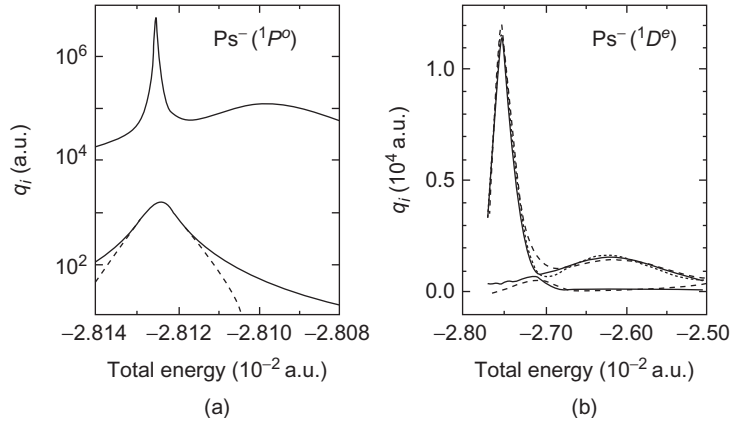

Figure 4.7 Eigenvalues $q_i(E)$ of the time-delay matrix $Q(E)$ for the positronium negative ion Ps^- as functions of the total energy E in the region of an overlapping double resonance. The small eigenvalues irrelevant to the avoided crossing are excluded. Solid curves: hyperspherical close-coupling calculations. Broken curves: fitting of Eq. (75). (a) Strong avoidance case with $\beta = 0.95$ in the symmetry $^1P^o$. The upper broken curve is indistinguishable from the solid curve. (b) Weak avoidance case with $\beta = 0.10$ in the symmetry $^1D^e$; the dotted curve reproducing the upper solid curve better than the broken curve is the result of fitting with a weak background added to Eq. (75). The solid curves are the same as a part of Figure 4.6c. Figure from Ref. [65].

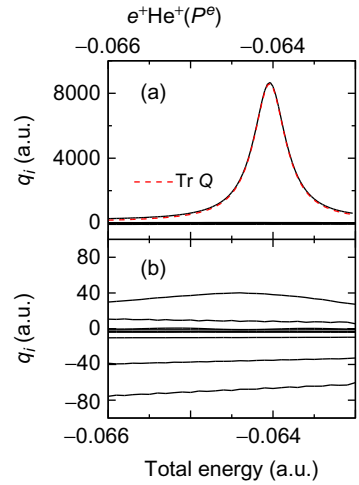

Figure 4.8 The eigenvalues $\{q_i(E)\}$ of the time-delay matrix $Q(E)$ for $e^+He^+(P^e)$ as functions of the total energy E below the threshold $E_{th} = -0.0625$ a.u. of $He^{2+} + Ps(n = 2)$; results of hyperspherical close-coupling calculations [66]. (a) The whole view, where only the largest eigenvalue $q_{max}(E)$ is distinguishable from zero, and is indistinguishable from the trace of $Q(E)$. (b) An enlargement, where $q_{max}(E)$ lies far outside of the figure. The second largest eigenvalue, visible only in (b), represents a broad resonance with a width Γ of 0.014 a.u. and a central position E_r of -0.0640 a.u. within $\Gamma/10$ of the threshold E_{th}. Taken from Ref. [66].

eigenvalue is also small, considering the logarithmic scale. The largest eigenvalue in Figure 4.7b contains a weak background, with which the fitting is quite good. Thus, the description of avoided Lorentzian profiles has proved to be justified for these double-resonance Q-eigenvalues from the HSCC calculations.

A noteworthy case of overlapping resonances is found in Figure 4.8 for the three-body system $e^+He^+(P^e)$ [66]. At first sight, the upper figure including all the $Q(E)$-matrix eigenvalues and their sum, Tr $Q(E)$, appears as if it were a typical isolated resonance with almost no background effect discernible. The largest eigenvalue $q_{max}(E)$ almost coincides with Tr $Q(E)$. A Lorentzian profile fits to it quite accurately. By careful examination of the second largest eigenvalue by enlarging the scale as in the lower figure, a much weaker and broader but typical Lorentzian emerges. This is a clear indication of the importance and power of detailed analysis of the Q-matrix eigenvalues. The broader resonance would have been missed by the inspection of only the eigenphase sum or the trace of the time-delay matrix.

A resonance fit finds the position and the width of the narrower resonance to be $E_r = -0.06404$ a.u. and $\Gamma = 4.7 \times 10^{-4}$ a.u. and those of the broader one to be $E_r = -0.0640$ a.u. (1.5×10^{-3} a.u. below the threshold

$E_{\rm th}(2) = -0.0625$ a.u. for the channel $He^{2+} + Ps(n=2)$) and $\Gamma = 1.4\times10^{-2}$ a.u. These values are corroborated by CCR calculations (see Section 1.4), yielding $(E_r, \Gamma) = (-0.06405, 4.75\times10^{-4})$ a.u. for the narrower resonance and $(E_r, \Gamma) = (-0.0643, 1.8\times10^{-2})$ a.u. for the broader resonance [67]. The centers of the two resonances almost coincide with each other, but the broader resonance extends over an energy region (across the threshold $E_{\rm th}(2)$) one order of magnitude broader than the energy difference between its resonance center and $E_{\rm th}(2)$. The mechanism that produces this pair of resonances will be discussed toward the end of Section 3.2.5. A similar pair of narrow and broad resonances is found also for the D^o symmetry around $E_{\rm th}(2)$ [66].

2.3.4. Diabatic decomposition of several overlapping resonances

There seems no simple unitary transform of the time-delay matrix $Q_{\rm Sim}$, such as Eq. (72), if more than two resonances overlap each other. Instead, we may take advantage of the rank 1 of the projection matrix P_ν of Eq. (61) in Q_ν of Eq. (69). Thus, for the eigenvalue equation

$$Q_\nu(E) B\mathscr{P}_{\nu-1}\mathbf{g}_\nu = L_\nu(E) B\mathscr{P}_{\nu-1}\mathbf{g}_\nu \tag{78}$$

following from Eq. (69) for each Q_ν in $Q_{\rm Sim}$ of Eq. (68), the only nonzero eigenvalue of $Q_\nu(E)$ is $L_\nu(E)$ and the corresponding eigenvector is $B\mathscr{P}_{\nu-1}\mathbf{g}_\nu$. It follows that $Q_\nu\mathbf{u} = 0$ for any vector $\mathbf{u}$ orthogonal to $B\mathscr{P}_{\nu-1}\mathbf{g}_\nu$. This immediately leads to a theorem that $Q_{\rm Sim}\mathbf{u} = 0$ for any vector $\mathbf{u}$ orthogonal to all the eigenvectors $B\mathscr{P}_{\nu-1}\mathbf{g}_\nu$ of $Q_\nu(E)$ for $\nu = 1, 2, \ldots, N$, provided that S_b be independent of E [68].

The matrix $Q_{\rm Sim}(E)$ projected onto the vector space spanned by $\{B\mathscr{P}_{\nu-1}\mathbf{g}_\nu\}_{\nu=1}^N$, when diagonalized, provides all the N nonzero eigenvalues of $Q_{\rm Sim}(E)$. Since the overlapping resonances interact with each other in the sense that the vectors $B\mathscr{P}_{\nu-1}\mathbf{g}_\nu$ for $\nu = 1, 2, \ldots, N$ are nonorthogonal to each other in general, the resultant N eigenvalues are the Lorentzians $L_\nu(E)$ avoiding each other around their crossing points, thus satisfying the noncrossing rule of the eigenvalues. The sum of these eigenvalues, however, is a simple sum of the Lorentzians, as was already shown in Eq. (65).

For double resonances, the vector space corresponding to the resonance eigenchannel space is spanned by $B\mathbf{g}_1$ and $BS_1\mathbf{g}_2$. This might appear to contradict the result of Section 2.3.3, namely, that the eigenvectors for the two nonzero Q-eigenvalues are linear combinations of $BS_1\mathbf{g}_1$ and $BS_1\mathbf{g}_2$. In fact, this apparent contradiction is resolved by the fact that $S_\nu\mathbf{g}_\nu$ is proportional to $\mathbf{g}_\nu$, as is evident from Eq. (60).

To rephrase, the vector space spanned by $\{B\mathscr{P}_{\nu-1}\mathbf{g}_\nu\}_{\nu=1}^N$ defines the N-element resonance Q-eigenchannel space, which alone describes the resonance processes, if the background S matrix is independent of E. The vector space complement to it defines the $(N_o - N)$-element nonresonance Q-eigenchannel space, which is totally unassociated with the resonance

states or the resonance processes asymptotically, although it may be coupled with the resonance states in the inner region of the configuration space. Only N eigenvalues of $Q_{\rm Sim}(E)$ are nonzero, and they form a set of Lorentzian profiles $\{L_v(E)\}_{v=1}^{N}$ avoiding each other at their crossing points, either strongly or weakly, depending on the interactions between the resonances [68].

In the last two paragraphs, the number N of overlapping resonances has been assumed implicitly not to exceed the number N_o of open channels. If $N > N_o$, as in overlapping resonances in single-channel scattering discussed in Section 2.1.3, then the N_o eigenvalues of the Q matrix represent as many as N Lorentzians. Hence, the sum of more than one Lorentzian appears in one or more eigenvalues, which decreases the number of avoided crossings. In this case, as in the case of $N = N_o$, there exists no nonresonance Q-eigenchannel space and the resonances can decay into any Q-eigenchannel.

Figure 4.9 provides a whole view of the Q-matrix eigenvalues $\{q_i(E)\}$ and Tr $Q(E)$, calculated for He($^1P^o$) using the HSCC equations, in an energy region between the thresholds of $He^+(n=4) = -0.125$ a.u. and $He^+(n=5) = -0.08$ a.u. [69]. Some Lorentzian peaks stand out distinctly and no complicated analysis appears to be necessary for them. On the other hand, many

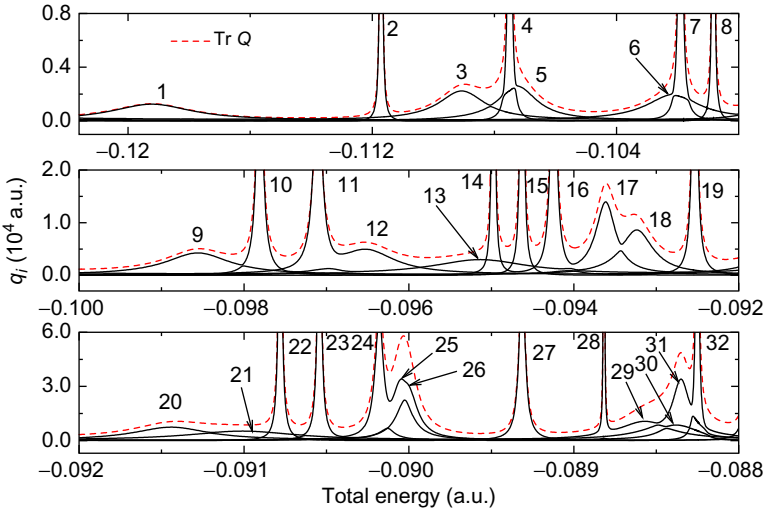

Figure 4.9 The eigenvalues $\{q_i(E)\}$ (black solid curves) of the time-delay matrix $Q(E)$ for He($^1P^o$) and their sum, Tr $Q(E)$ (red broken curves), obtained from hyperspherical close-coupling calculations and plotted against the total energy E. The resonance peaks are numbered from the lower to higher energy positions. Most eigenvalues are too small to be distinguishable from the base line $q_i(E) = 0$. Figure from Ref. [69].

cases of typical overlapping resonances including weak ones are also found. The many, seemingly crossing curves in fact avoid crossing on a closer view of accurate curves. The cross sections corresponding to these overlapping resonances should be too complicated for fruitful resonance analysis.

Figure 4.10 pays particular attention to two narrow energy regions in Figure 4.9 as examples. Rapid increase in the eigenphase sum $\delta(E)$ is noticeable at two places in Figure 4.10a, suggesting two resonances. Another resonance emerges in $\mathrm{Tr}\,Q(E)$ in Figure 4.10b, showing that the derivative $\mathrm{d}\delta/\mathrm{d}E$ is a better probe of resonances than $\delta(E)$ itself. An even more sensitive probe turns out to be the eigenvalues $\{q_i(E)\}$ in Figure 4.10b. Quite obvious avoided crossings with weak avoidance or weak resonance interactions are observed, which, if "diabatically" connected, reveal as many as five Lorentzian profiles in this energy region. At least two of them (resonances

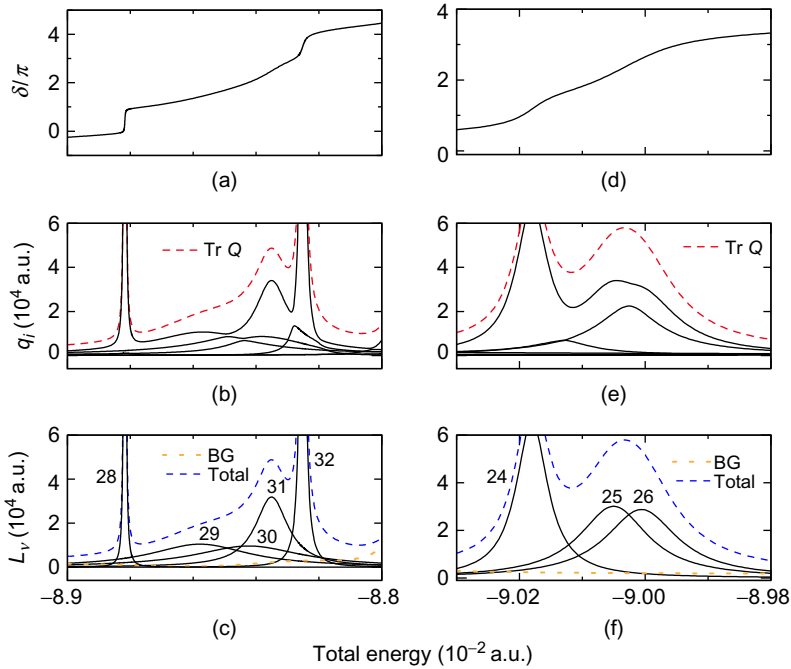

Figure 4.10 Detailed analysis of two sets of overlapping resonances in He($^1P^o$) shown in Figure 4.9. Left: Resonances 28–32. Right: Resonances 24–26. (a), (d) Calculated eigenphase sum $\delta(E)$ in units of π radians. (b), (e) The eigenvalues $\{q_i(E)\}$ (black solid curves) of the calculated $Q(E)$ matrix and their sum, $\mathrm{Tr}\,Q(E)$ ($= 2\hbar\mathrm{d}\delta/\mathrm{d}E$) (red broken curve). (c), (f) The Lorentzians $L_\nu(E)$ representing the decomposed resonances (black solid curves), the background (BG: orange dotted curve), and their sum (Total: blue broken curve), obtained by fitting Eq. (65) to the calculated $\mathrm{Tr}\,Q(E)$ of (b), (e). Figure from Ref. [69].

29 and 30) would have been missed without recourse to the Q-eigenvalues. The detailed resonance structure in $\{q_i(E)\}$ having been uncovered, Eq. (65) with five Lorentzians and a background of polynomial in E of a low degree is then fitted to the calculated $\mathrm{Tr}\,Q(E)$ (red broken curve) of Figure 4.10b. This fitting is extremely accurate with no appreciable deviation of the fitted blue broken curve in Figure 4.10c from the red broken curve in Figure 4.10b. Figure 4.10c includes all the five Lorentzian profiles obtained in this way, which are effectively the diabatization of $\{q_i(E)\}$.

Another case distinct from this is found in the range $-0.0903 < E < -0.0898$ a.u. The eigenphase sum $\delta(E)$ in Figure 4.10d increases nearly by 3π in this energy range, suggesting the occurrence of three resonances. However, an appreciable slope change in $\delta(E)$ occurs only twice, which is indeed supported by $\mathrm{Tr}\,Q(E)$ in Figure 4.10e having only two peaks. In fact, the largest eigenvalue in Figure 4.10e has a weak kink just below $E = -9.00 \times 10^{-2}$ a.u. This kink, together with the broad peak in the next largest eigenvalue, represents a strongly avoided crossing between two resonances. Including another marked peak at lower energies, three resonances are detected. Thus, a three-Lorentzian fit of $\mathrm{Tr}\,Q(E)$ is appropriate. This leads to Figure 4.10f of diabatically decomposed resonances similar to Figure 4.10c. Indeed, the strong interactions between resonances 25 and 26 are seen to generate the avoided crossing in $\{q_i(E)\}$ of Figure 4.10e around $E = -9.00 \times 10^{-2}$ a.u. The avoided crossings between resonance 24 and the strongly interacting resonances 25/26 complicate the eigenvalue profiles.

To conclude, the careful inspection of the Q-matrix eigenvalues reveals otherwise hidden resonances, determines the number of Lorentzian profiles $L_\nu(E)$ to be included in the formula (65) to be fitted to calculated $\mathrm{Tr}\,Q(E)$, and suggests approximate values of the parameters E_ν and Γ_ν for each $L_\nu(E)$. This fitting procedure breaks a group of overlapping resonances down into separate diabatic components and provides a transparent understanding of how they are superimposed into the whole group of resonances that brings about very complex cross-section shapes.

3. RESONANCE ANALYSIS: INFORMATION FROM CHANNEL POTENTIALS

Obviously, much information on the resonance dynamics should normally be gained by close examination of the structure of the wavefunction in the internal region of the configuration space. However, it is often possible also to infer either the dominant roles or the secondary roles of the interaction potentials in resonance processes without going into details of the wavefunction. The inspection of the potentials can often lead to transparent visual understanding of the essential dynamics.

The interaction potential is unambiguously specified in potential scattering problems. In multichannel scattering involving N_p particles, the interaction potentials may be different depending on the physical picture the theory is based on. Let the coordinate variables of the constituent particles of the system be denoted collectively by $\mathbf{R} = (\mathbf{r}_1, \mathbf{r}_2, \ldots, \mathbf{r}_{N_p})$. In many theoretical formulations, the wavefunction $\Psi(\mathbf{R})$ of the whole system (separated from the spin wavefunction, under the assumption of spin-independent interactions) is expanded in terms of some complete set of basis functions $\{\psi_n(\hat{\mathbf{R}})\}$ as $\sum_n F_n(R)\psi_n(\hat{\mathbf{R}})$. It is substituted into the Schrödinger equation, and coupled-channel equations for the unknown functions $\{F_n(R)\}$ are derived. Here, R is a scalar variable defined by combining $\mathbf{r}_1, \mathbf{r}_2, \ldots, \mathbf{r}_{N_p}$ in some way or other, and plays the role of the reaction coordinate. All the other coordinates are collectively represented by $\hat{\mathbf{R}}$, though not necessarily angular coordinates only. The interaction potential in the coupled-channel equations in this representation takes the form of a matrix, whose elements, $V_{nn'}$, are not necessarily simple multiplicative operators depending only on R. If they are, however, or if they may be approximated as such, and if a few channels only are important or if the off-diagonal potentials are weak, then we can often obtain significant information about the resonance dynamics from the potential matrix without detailed knowledge of the relevant wavefunction.

Section 3.1 discusses the cases where only the channels having a common asymptotic energy determine the dominant dynamics at large distances R. There, a natural choice of R should be the ordinary distance between the two fragments the whole system asymptotically separates into. Another choice of R, appropriate for studying the dynamics in the whole region $0 \leq R$ and especially powerful for three-body problems, is discussed in Section 3.2.

Separation of the effects due to the long-range and short-range interactions greatly advances the understanding of the dynamics prevailing in continuum processes. Particularly useful general theoretical frameworks to this effect have been the R-matrix theory [44, 70] and the multichannel quantum defect theory (MQDT) [71, 72]. They have been applied successfully to a wide variety of atomic and molecular systems, and the relevant material is too rich to be covered in this article.

3.1. Long-range potentials

3.1.1. Infinite series of Feshbach resonances due to the Coulomb tail

If the collision system can separate asymptotically into a pair of charged particles of opposite signs, the attractive Coulomb tail of the interaction between them supports an infinite number of bound Rydberg states in each closed channel (with a threshold energy E_{th}). Its coupling with open channels, if any, normally turns these bound states into an infinite series of quasi-bound

Rydberg states, which are Feshbach resonance states. Their complex energies $\mathcal{E}_n$, for a fixed angular momentum and labeled by the principal quantum number n, satisfy the Rydberg formula with a complex quantum defect $\mu_n + i\gamma_n$,

$$\begin{aligned}\mathcal{E}_n &= E_{r,n} - i\Gamma_n/2 \\ &= E_{\rm th} - (n - [\mu_n + i\gamma_n])^{-2} \\ &\simeq E_{\rm th} - (n-\mu_n)^{-2} + 2i\gamma_n(n-\mu_n)^{-3} \ \text{ for } \ \gamma_n^2 \ll (n-\mu_n)^2, \end{aligned} \tag{79}$$

in Rydberg units appropriate for the pair of charged particles in consideration, here assumed to have a unit charge [71, 73–75].

When two or more series of quasi-bound Rydberg states interact, or couple each other, the resonance positions may be analyzed on the basis of the MQDT [71, 72]. For treating the complex energies of the QBSs belonging to these coupled series, a multichannel complex quantum defect theory needs to be developed. Overlapping resonances occur frequently when this series coupling occurs. Examples of such overlapping resonances are found in Figure 4.9.

Photoionization of neutral atoms and molecules and electron–ion collisions, for example, are rich in infinite Rydberg series of Feshbach resonances. On the other hand, only a finite number of Feshbach (and possibly shape) resonances occur in electron-neutral collisions and photodetachment of an electron attached to a neutral species, with an exception of the following cases.

3.1.2. Series of Feshbach resonances due to the dipole potential

Another type of interactions that can support an infinite number of bound states has an attractive dipole potential $\hbar^2\alpha/(2\mu R^2)$ asymptotically. Here, α is some constant, R is the distance between the centers of mass of the two subsystems which the whole system separates into, and μ is their reduced mass. Such an interaction occurs between a charged particle and a hydrogen-like atom in an excited state [59, 60].

Consider a structureless charged particle interacting with a neutral hydrogen-like atom in $2s$ or $2p$ state. For a total orbital angular momentum $L \geq 1$, there are three degenerate channels with the angular momentum of the relative motion L, $L \pm 1$; for $L = 0$, there are only two. The dipole term, behaving like $\propto R^{-2}$, in the multipole expansion of the interaction potential couples the $2s$ channel with the $2p$ channels, differing by one unit of angular momentum. Together with the diagonal centrifugal potential, the asymptotic potential is described by a three-by-three matrix times R^{-2}. This matrix can be diagonalized by a unitary transformation of the three degenerate channels, and thus, the coupled equations are changed into three decoupled equations

with potentials behaving as $\hbar^2\alpha_i/(2\mu R^2)$ $(i = 1, 2, 3)$. This is the linear Stark effect due to the first-order perturbation on the degenerate sublevels by the electric field of the charged particle.

The coefficient α_i may be positive, negative, or vanishing. Any dipole potential with a coefficient α less than $-1/4$ (overcritical dipole) is known to support an infinite number of bound states converging to the asymptotic energy, or the threshold energy $E_{\rm th}$, of those degenerate channels [12]. These bound states turn into an infinite series of Feshbach resonances, called "dipole resonances," via coupling with open channels [60]. The resonance parameters for the higher members, labeled by an integer ν, of an infinite series are expressible as [60]

$$\begin{aligned} E_{r,\nu} &= E_{\rm th} - \varepsilon_\nu, \quad \varepsilon_\nu = \varepsilon_0 \exp(-\zeta\nu), \\ \Gamma_\nu &= \Gamma_0 \exp(-\zeta\nu), \\ \zeta &= 4\pi\,(-1-4\alpha)^{-1/2}, \end{aligned} \tag{80}$$

where ζ is common to both the resonance positions and widths for each series. In other words, the ratio of adjacent ε_ν and Γ_ν are the same; $\varepsilon_{\nu+1}/\varepsilon_\nu = \Gamma_{\nu'+1}/\Gamma_{\nu'} = e^{-\zeta}$. Equation (80) can be inaccurate for the lower members. The constants ε_0 and Γ_0 depend on the whole interaction including the short-range potentials, and their determination requires a full scattering calculation.

Simple analytic formulas for α for the decoupled $2s$–$2p$ channels are derivable for any value of L and for any combination of the masses of the point charge, m_0, and of the two particles, m_1 and m_2, constituting the hydrogen-like atom [76]:

$$\begin{aligned} \alpha_1 &= (L-1)L - x, \\ \alpha_2 &= L(L+1), \\ \alpha_3 &= (L+1)(L+2) + x, \\ x &= [(2L+1)^2 + \beta^2]^{1/2} - (2L+1), \end{aligned} \tag{81}$$

where

$$\beta = \frac{6\mu_{0,12}}{\mu_{12}}, \quad \mu_{12} = \frac{m_1 m_2}{m_1 + m_2}, \quad \mu_{0,12} = \frac{m_0(m_1+m_2)}{m_0 + m_1 + m_2}. \tag{82}$$

Here, all the three particles are assumed to have a unit charge. The value of β is 6 for H^- with an infinitely heavy nucleus and is 8 for Ps^-. With the values of α from these analytic formulas, and hence ζ, Eq. (80) played an essential role in the analysis of the Feshbach series of resonances in muonic

three-body systems [76]. Incidentally, channel 2 represented by α_2 is inactive asymptotically and is uncoupled with other channels even before the dipole diagonalization. Its usual centrifugal potential remains intact by the unitary transformation.

The dipole interaction couples higher sublevel channels too, for which the order of the coefficient matrix on R^{-2} is larger than for the $2s$–$2p$ channel coupling. Numerical values of α and/or ζ (or $e^{-\zeta}$) for the decoupled higher sublevel channels are tabulated for some three-body systems [44, 53, 66, 77–79].

Known values of ζ render Eq. (80), plotted semilogarithmically, quite useful in grouping resonances into series, in clarifying which decoupled channels they belong to, i.e., by which potential they are mainly supported, and in extending the series to obtain the resonance positions and widths of still uncalculated higher members, often more accurately than even elaborate scattering calculations.

In fact, the relativistic effects and the radiative corrections split the nonrelativistically degenerate hydrogenic sublevels. At distances R where the dipole potential is comparable to or weaker than the splitting ΔE between the nearly degenerate levels, i.e., at large R where ΔE is no more negligible, the attractive long-range potential decays more rapidly than R^{-2} and terminates the dipole resonance series at some finite number $\nu_{\max}^{(d)}$ [60]. In spite of the spectroscopically very fine splittings, this series termination effect is remarkable.

Assume that the probability density of a QBS is highest near the outer turning point $R_{\rm tp}$ determined by the long-range potential $V_{\rm asym}(R)$. One may estimate $\nu_{\max}^{(d)}$ based on the rough criterion that a dipole resonance vanishes if its binding energy ($\simeq |V_{\rm asym}(R_{\rm tp})|$) is less than the splitting ΔE since this would mean contradictorily that this "dipole resonance" must be supported by $V_{\rm asym}(R)$ of shorter range than the dipole potential [78]. According to this criterion, the mainly fine-structure splitting of $\sim$41 μeV between the higher-lying $2p_{3/2}$ and the lower-lying $2s_{1/2}$ levels of the hydrogen atom ($2p_{1/2}$ lying slightly below $2s_{1/2}$) terminates the ${}^1S^e$ dipole series at $\nu_{\max}^{(d)} = 4$, the ${}^3S^e$ series at 3, the ${}^1P^o$ series at 2, the ${}^3P^o$ series at 3, and there is only one dipole resonance of symmetry ${}^1D^e$ [79]. The situation for the series below the $n = 3$ levels of the H atom is similar; $\nu_{\max}^{(d)}$ values of 2 to 7 are reported for S, P, D, F, and G series [78, 79].

For more accurate estimation, complex-rotation calculations [80] and coupled-channel calculations [81, 82] with the correct relativistic and radiative splitting ΔE taken into account reveal that, for H^- Feshbach series below the H($n = 2$) threshold, the number $\nu_{\max}$ of resonances for the ${}^1S^e$ series is 4 (and the same for the system e^+H) [81], $\nu_{\max} = 3$ for the ${}^1P^o$ series [80, 82], and $\nu_{\max} = 4$ for the ${}^3P^o$ series [82]. The relativistic effects also mix different LS states. This affects the resonance positions only slightly, but the components

other than the main one increases as the resonance level approaches the series limit [80, 82]. For example, the fourth resonance of main symmetry $^3P^o$ contains 17% of $^1P^o$ component, changing this QBS into an optically allowed state [82].

The Lamb shift splits the $2s_{1/2}$ and $2p_{1/2}$ levels of the muonic hydrogen μp and its isotopes μd and μt ($p, d, t =$ proton, deuteron, triton) by as much as $\sim$0.2 eV. For the resonance series of the muonic molecule $dt\mu$ with total angular momentum $L = 0$ and 1 converging to the energy of $t\mu(n = 2)$, $\nu_{\max}$ is estimated to be as large as 10 due to the mass effect. For the $dd\mu$ series with $L = 0$ and 1 converging to $d\mu(n = 2)$, $\nu_{\max} = 5$ for the ungerade series (in the homonuclear molecular picture of this three-body system) and $\nu_{\max} = 9$ to 10 for the gerade series [76].

The lesson we learn from these considerations is the need to understand that elaborate nonrelativistic calculations of dipole-supported resonances lying within ΔE of the corresponding nonrelativistic threshold E_{th} are mere model calculations that result in what are quite far from the actual physical system.

The dipole potential is known to occur even in the asymptotic absence of a charged particle. Thus, a series of dipole-supported bound states and QBSs are possible for systems of three neutral particles. This phenomenon, called the Efimov effect, will be discussed briefly in the last paragraph of Section 3.2.2.

3.1.3. Near-threshold background due to the dipole potential

The asymptotic overcritical dipole potential also affects the threshold behavior of the phase shift [60, 72, 83, 84]. Thus, the eigenphase sum includes a term $\delta_b^{\text{dip}}(E)$ that diverges logarithmically toward the threshold E_{th} for these sublevels, $\delta_b^{\text{dip}}(E)$ satisfying a formula

$$\tan \delta_b^{\text{dip}}(E) = -\coth(\zeta/16) \tan\{(\zeta/16\pi) \ln(E - E_{\text{th}}) + \chi\} \tag{83}$$

with an almost constant χ for $E \simeq E_{\text{th}}$. This formula is awkward in actual applications to a fitting procedure. Since it reduces to a simple relation $\delta_b^{\text{dip}}(E) \simeq -(\zeta/16\pi) \ln(E - E_{\text{th}}) - \chi$ for large $|\alpha|$, an expression

$$\delta_b(E) = -c_{-1} \ln(E - E_{\text{th}}) + c_0 + c_1 E + c_2 E^2, \tag{84}$$

or even without the last term, was proposed and found to be convenient and useful for practical purposes of resonance fitting just above a threshold that produces an overcritical dipole potential [53]. A term inversely proportional to $E - E_{\text{th}}$ was used empirically in Ref. [85]. Compared to this form, Eq. (84) indeed gave a numerically better fit [53]. As the energy departs farther and farther from E_{th}, the logarithmic term becomes more and more slowly

varying with the energy, thus making a simpler form $\delta_b(E) = c_0 + c_1E + c_2E^2$ accurate enough.

In terms of the time-delay matrix Q, Eq. (84) implies a convenient fitting formula

$$\mathrm{Tr}\, Q(E) = \frac{\hbar\Gamma}{(E - E_r)^2 + (\Gamma/2)^2} - \frac{C_{-1}}{E - E_{\mathrm{th}}} + C_1 + 2C_2E \quad (C_i = 2\hbar c_i) \tag{85}$$

just above a threshold E_{th} associated with an overcritical dipole potential. The term inversely proportional to $E - E_{\mathrm{th}}$ in $\mathrm{Tr}\, Q(E)$ can sometimes even dominate over the Lorentzian term. The strong background overcoming a resonance, illustrated in Section 2.2.6, is due to this term.

3.2. Hyperspherical picture

3.2.1. Hyperspherical coordinates

The natural choice of the reaction coordinate R, mentioned just before Section 3.1, for describing the channels with the asymptotic arrangement A + B is the distance between the centers of mass of A and B. This defines the conceptually simplest set of close-coupling equations. However, the corresponding potential matrix elements $V_{nn'}(R)$ are difficult to interpret since many channels are coupled to each other strongly in general. Thus, no single potential is expected to predict the physics of the processes under consideration.

An alternative would be the hyperspherical coordinate system, introduced into the study of the ground-state helium by Gronwall [86], developed for nuclear reactions by Delves [87, 88], adopted in molecular reactive collisions by Smith [89], and initiated applications to two-electron excited QBSs by Macek [90]. The hyperradius ρ and one of the hyperangles, the radial hyperangle α, are defined by

$$\rho^2 = r_1^2 + r_2^2, \quad \tan\alpha = r_2/r_1 \tag{86}$$

in terms of the radial coordinates of the two electrons [72, 90–92]. Note that α is confined within the region $0 \le \alpha \le \pi/2$ since both r_1 and r_2 are positive or zero. Mathematically, Eq. (86) is a mere transformation of the rectangular coordinates (r_1, r_2) into the polar coordinates (ρ, α). Physically speaking, however, the polar coordinates introduce a new concept, compared with the independent electron coordinates, for describing efficiently the strong electron–electron correlation in QBSs by treating the two electrons collectively and on equal footing. The hyperradius ρ describes the size of the whole system, whereas the radial hyperangle α describes the correlation between r_1

and r_2, called the radial correlation. The angular coordinates $(\hat{\mathbf{r}}_1, \hat{\mathbf{r}}_2)$ and the angle α constitute the five-dimensional hyperangle Ω. The four-dimensional space $(\hat{\mathbf{r}}_1, \hat{\mathbf{r}}_2)$ may be represented by some other choice of angular coordinates, one of which may be the angle θ_{12} between the vectors $\mathbf{r}_1$ and $\mathbf{r}_2$, describing the angular correlation between the two electrons. The whole system of coordinates $\mathbf{R} = (\rho, \Omega)$ is referred to as the hyperspherical coordinate system for two-electron atoms. Note that there is only one radial coordinate extending to infinity, unlike the independent-electron coordinates, and all the others are angular coordinates ranging over a finite coordinate space; the limit $R \to \infty$ occurs for either $r_1 \to \infty$ or $r_2 \to \infty$, or both. This fact is quite convenient conceptually, for theoretical argument, and also for practical calculations.

A general three-body system ABC has three possible asymptotic arrangement channels A + BC, B + CA, and C + AB (except for the three-body breakup) if all the three pairs AB, BC, and CA have a bound state or states. The corresponding sets of Jacobi coordinates are (see Figure 4.11) the distance vector $\mathbf{r}_{BC}$ from C to B and that to A from the center of mass of BC, $\mathbf{R}_{A\text{-}BC}$, and similar sets $(\mathbf{r}_{CA}, \mathbf{R}_{B\text{-}CA})$ and $(\mathbf{r}_{AB}, \mathbf{R}_{C\text{-}AB})$. The reduced masses appropriate for the motion in $\mathbf{r}_{BC}$ and in $\mathbf{R}_{A\text{-}BC}$ are denoted by μ_{BC} and $\mu_{A\text{-}BC}$, and so on. The convenient choice of Jacobi coordinates changes from the initial to the final channel in rearrangement collisions, and hence, the treatment of the whole process inevitably contains more than one set of Jacobi coordinates. This not only complicates the theoretical development but also leads to a set of coupled *integro*-differential equations involving nonlocal potentials, rather than coupled differential equations, making practical calculations much harder. The hyperspherical coordinates can cure this difficulty.

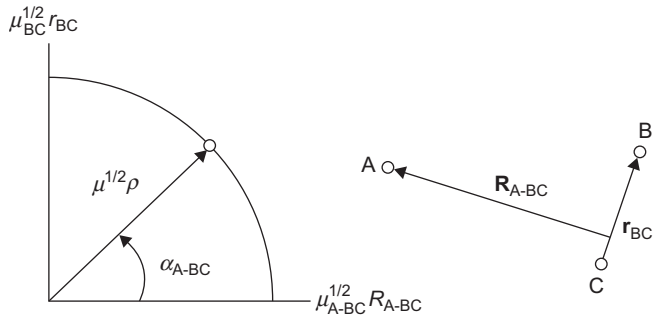

Figure 4.11 One of the three sets of Jacobi coordinates and the corresponding hyperspherical coordinates. For two-electron atoms with an infinitely heavy nucleus C, $\mathbf{r}_{BC} = \mathbf{r}_2$, $\mathbf{R}_{A\text{-}BC} = \mathbf{r}_1$, and $\mu_{BC} = \mu_{A\text{-}BC} = m_e$, which is usually chosen for μ in Eq. (87).

The hyperradius ρ is defined in terms of the Jacobi coordinates as (Figure 4.11)

$$\begin{aligned}\mu\rho^2 &= \mu_{\mathrm{BC}} r_{\mathrm{BC}}^2 + \mu_{\mathrm{A\text{-}BC}} R_{\mathrm{A\text{-}BC}}^2 \\ &= \mu_{\mathrm{CA}} r_{\mathrm{CA}}^2 + \mu_{\mathrm{B\text{-}CA}} R_{\mathrm{B\text{-}CA}}^2 \\ &= \mu_{\mathrm{AB}} r_{\mathrm{AB}}^2 + \mu_{\mathrm{C\text{-}AB}} R_{\mathrm{C\text{-}AB}}^2 \end{aligned} \tag{87}$$

with an arbitrary normalizing mass μ, which merely scales ρ. The three different definitions turn out to give exactly the same ρ [93, 94]. This is an outstanding feature of this hyperradius, indicating its suitability as a reaction coordinate for describing the whole reaction process involving all the arrangement channels by a single, common variable. It also follows that the coupled equations to be derived have no integral operators, or no nonlocal potentials. Unfortunately, the radial hyperangles (Figure 4.11)

$$\tan\alpha_{\mathrm{A\text{-}BC}} = \frac{\mu_{\mathrm{BC}}^{1/2} r_{\mathrm{BC}}}{\mu_{\mathrm{A\text{-}BC}}^{1/2} R_{\mathrm{A\text{-}BC}}}, \quad \text{etc.,} \tag{88}$$

and the sets of the other four hyperangles $(\hat{\mathbf{r}}_{\mathrm{BC}}, \hat{\mathbf{R}}_{\mathrm{A\text{-}BC}})$, etc., differ depending on the choice of the Jacobi coordinates, although the whole sets of five hyperangles $\Omega_{\mathrm{A\text{-}BC}} = (\alpha_{\mathrm{A\text{-}BC}}, \hat{\mathbf{r}}_{\mathrm{BC}}, \hat{\mathbf{R}}_{\mathrm{A\text{-}BC}})$, etc., span a common five-dimensional angular space independent of the choice of the Jacobi coordinates. For simplicity of notation, the subscripts indicating a particular set of Jacobi coordinates will be henceforth replaced by the shorthand "c," for example, $\mathbf{r}_c$, $\mathbf{R}_c$, α_c, and Ω_c.

Equation (87) is simplified for two-electron atoms; assuming particle C to be an infinitely heavy nucleus, we have $\mathbf{r}_{\mathrm{BC}} = \mathbf{r}_2$, $\mathbf{R}_{\mathrm{A\text{-}BC}} = \mathbf{r}_1$, $\mu_{\mathrm{BC}} = \mu_{\mathrm{A\text{-}BC}} = m_e$, m_e being the electron mass. For the positronium ion Ps^-, the choice of the positron to be particle C results in the quantities $\mathbf{r}_{\mathrm{BC}} = \mathbf{r}_2$, $\mathbf{R}_{\mathrm{A\text{-}BC}} = \mathbf{r}_1 - \mathbf{r}_2/2$, $\mu_{\mathrm{BC}} = m_e/2$, and $\mu_{\mathrm{A\text{-}BC}} = (2/3)m_e$. Usually, the normalizing mass μ is conveniently chosen to be m_e for these systems. This choice recovers Eq. (86) for two-electron atoms.

3.2.2. Coupled-channel equations

By the transformation of the independent-particle coordinates into the hyperspherical coordinates the Hamiltonian for the three-body system changes into the form

$$H = -\frac{\hbar^2}{2\mu}\left(\frac{\mathrm{d}^2}{\mathrm{d}\rho^2} + \frac{5}{\rho}\frac{\mathrm{d}}{\mathrm{d}\rho}\right) + H_{\mathrm{ad}}(\Omega_c;\rho), \tag{89}$$

separated into the dynamical term and the adiabatic term

$$H_{\mathrm{ad}}(\Omega_c;\rho) = \frac{\hbar^2 \boldsymbol{\Lambda}^2(\Omega_c)}{2\mu\rho^2} + V^{\mathrm{C}}(\Omega_c;\rho). \tag{90}$$

Here, V^{C} is the sum of all the two-body interactions and $\mathbf{\Lambda}(\Omega_{\mathrm{c}})$ is the angular momentum operator suitable for the five-dimensional angular space. The latter is referred to as the grand angular momentum operator. It introduces the centrifugal potential for the motion in ρ. It takes an explicit form

$$\begin{aligned}\mathbf{\Lambda}^2(\Omega_{\mathrm{c}}) &= -\frac{1}{S_{\mathrm{c}}C_{\mathrm{c}}}\frac{\partial}{\partial\alpha_{\mathrm{c}}}\left(S_{\mathrm{c}}C_{\mathrm{c}}\frac{\partial}{\partial\alpha_{\mathrm{c}}}\right)+\frac{\mathbf{l}^2_{\mathbf{r}_{\mathrm{c}}}}{S_{\mathrm{c}}}+\frac{\mathbf{l}^2_{\mathbf{R}_{\mathrm{c}}}}{C_{\mathrm{c}}}\\ &= -\frac{\partial^2}{\partial\alpha_{\mathrm{c}}^2}-4\cot(2\alpha_{\mathrm{c}})\frac{\partial}{\partial\alpha_{\mathrm{c}}}+\frac{\mathbf{l}^2_{\mathbf{r}_{\mathrm{c}}}}{S_{\mathrm{c}}}+\frac{\mathbf{l}^2_{\mathbf{R}_{\mathrm{c}}}}{C_{\mathrm{c}}}\end{aligned} \tag{91}$$

with

$$S_{\mathrm{c}}=\sin^2\alpha_{\mathrm{c}},\quad C_{\mathrm{c}}=\cos^2\alpha_{\mathrm{c}}, \tag{92}$$

where $\mathbf{l}_{\mathbf{r}_{\mathrm{c}}}$ and $\mathbf{l}_{\mathbf{R}_{\mathrm{c}}}$ are the usual angular momentum operators for the motion in $\mathbf{r}_{\mathrm{c}}$ and in $\mathbf{R}_{\mathrm{c}}$, respectively. They exert the centrifugal force on the motion in r_{c} and that in R_{c} separately, and in turn, on the motion in ρ through Eq. (87). The differential operators in α_{c} directly exerts the centrifugal force in ρ by the angular motion in α_{c} in the plane of Figure 4.11. This centrifugal force resists, in particular, the simultaneous approach of r_{c} and R_{c} to short distances, or the simultaneous approach of the two electrons to the nucleus in two-electron atoms.

Equation (91) is in fact identical for all choices of the set "c" of Jacobi coordinates [93, 94]. The adiabatic Hamiltonian $H_{\mathrm{ad}}(\Omega_{\mathrm{c}};\rho)$ of Eq. (90) contains ρ as a parameter, rather than a variable, and its eigenvalue equation

$$H_{\mathrm{ad}}(\Omega_{\mathrm{c}};\rho)\Phi_n(\Omega_{\mathrm{c}};\rho)=\mathcal{V}_n(\rho)\Phi_n(\Omega_{\mathrm{c}};\rho) \tag{93}$$

defines the adiabatic hyperangular functions and the corresponding potentials. The expansion

$$\Psi(\rho,\Omega_{\mathrm{c}})=\sum_n \rho^{-5/2}\mathcal{F}_n(\rho)\Phi_n(\Omega_{\mathrm{c}};\rho) \tag{94}$$

of the whole three-body wavefunction $\Psi(\rho,\Omega_{\mathrm{c}})$ in terms of the adiabatic functions $\{\Phi_n(\Omega_{\mathrm{c}};\rho)\}$ and its insertion into the Schrödinger equation leads to second-order differential equations for $\{\mathcal{F}_n(\rho)\}$,

$$\left(-\frac{\hbar^2}{2\mu}\frac{\mathrm{d}^2}{\mathrm{d}\rho^2}+\mathcal{V}_n(\rho)+\frac{\frac{3}{2}\left(\frac{3}{2}+1\right)\hbar^2}{2\mu\rho^2}-E\right)\mathcal{F}_n(\rho)-\frac{\hbar^2}{2\mu}\sum_{n'}\mathcal{W}_{nn'}(\rho)\mathcal{F}_{n'}(\rho)=0, \tag{95}$$

where the nonadiabatic coupling operators

$$\mathcal{W}_{nn'}(\rho) = 2\left(\Phi_n \left| \frac{\mathrm{d}}{\mathrm{d}\rho} \right| \Phi_{n'}\right)_{\Omega_c} \frac{\mathrm{d}}{\mathrm{d}\rho} + \left(\Phi_n \left| \frac{\mathrm{d}^2}{\mathrm{d}\rho^2} \right| \Phi_{n'}\right)_{\Omega_c} \tag{96}$$

stem from the differential operators in Eq. (89). These coupled equations are referred to as the hyperspherical coupled-channel or close-coupling (HSCC) equations.

The direct numerical solution of the HSCC equations (95) would be impractical because of the sharply peaked nonadiabatic coupling potentials near any of the many avoided crossings. This difficulty is often circumvented by the diabatic-by-sector technique to solve, effectively, the coupled equations (95) [95, 96]. By this technique, the region of ρ up to some large value is divided into many sectors, labeled by i. The adiabatic functions $\{\Phi_n(\Omega_c; \rho)\}$ at some fixed point $\rho = \rho_i$ in each sector are employed throughout the sector as the diabatic basis functions $\{\phi_n^{(i)}(\Omega_c)\}$ for expansion. The expansion then takes a form $\Psi^{(i)}(\rho, \Omega_c) = \sum_n \rho^{-5/2} F_n^{(i)}(\rho)\phi_n^{(i)}(\Omega_c)$, and the coupled equations in each sector i are

$$\left(-\frac{\hbar^2}{2\mu}\frac{\mathrm{d}^2}{\mathrm{d}\rho^2} - E\right) F_n^{(i)}(\rho) + \sum_{n'} V_{nn'}^{(i)}(\rho) F_{n'}^{(i)}(\rho) = 0 \tag{97}$$

with the coupling potential matrix

$$V_{nn'}^{(i)}(\rho) = \int \mathrm{d}\Omega_c [\phi_n^{(i)}(\Omega_c)]^* H_{\mathrm{ad}}(\Omega_c; \rho)\phi_{n'}^{(i)}(\Omega_c). \tag{98}$$

This coupling potential is smooth everywhere, which allows numerical calculations with high precision. There is no nonadiabatic coupling since the basis functions $\{\phi_n^{(i)}(\Omega_c)\}$ are independent of ρ in each sector. The solution $\Psi^{(i)}(\rho, \Omega_c)$ is connected smoothly, in principle, from sector to sector by a unitary frame transformation from the ith set of channels to the $(i+1)$st set [97–99]. The coordinate system is transformed from the hyperspherical to the Jacobi coordinates at some large ρ, beyond which the conventional close-coupling equations are employed for determining the asymptotic form of the wavefunction appropriate for the scattering boundary condition [100].

A recent numerical development is the introduction of the slow or smooth variable discretization (SVD) technique [101–103]. In the diabatic-by-sector method, the basis functions to expand the total wavefunction are fixed within each sector. In the SVD method, the hyperangular basis functions are constructed using the discrete variable representation (DVR) [104]. The requirement is only that the total wavefunction be smooth in the adiabatic parameter ρ. By expanding the hyperradial wavefunctions using DVR basis functions, a new set of hyperangular basis functions are determined and they

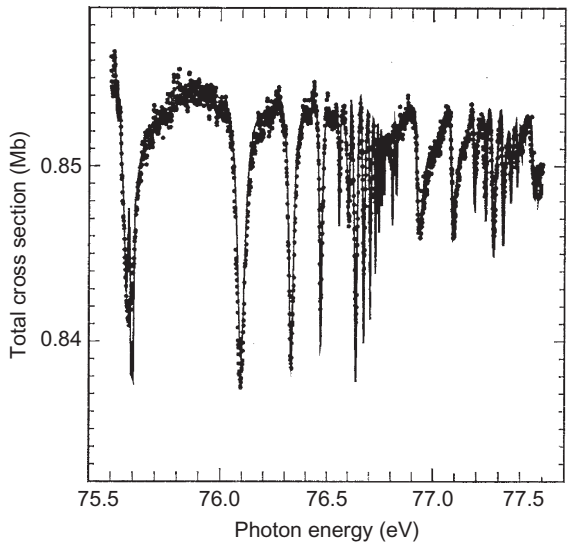

Figure 4.12 Photoionization spectrum of He(1^1S) between the thresholds for $He^+(n=4)$ and $He^+(n=6)$. Dots: Experiment [126]. Curve: Hyperspherical close-coupling calculations convoluted with an experimental energy resolution of 6 meV and the background linear in photon energy subtracted. This background is caused mostly by the decay of the electron current in the storage ring. Figure from Ref. [51].

are used together to propagate the total wavefunction from one end of the sector to the other. This technique was found to be quite efficient.

The HSCC equations have been solved for various Coulomb three-body processes, such as photoionization and photodetachment of two-electron systems and positronium negative ions [51, 105–111], electron or positron collisions [52, 112–115], ion–atom collisions [116–119], and muon-involving collision systems [103, 114, 120–125]. Figures 4.6, 4.7, 4.8, 4.9, and 4.10 are all due to HSCC calculations. Figure 4.12 illustrates the good agreement between the results of HSCC calculations [51] and the high-resolution photoionization experiment on helium [126]. See Ref. [127] for further detailed account of the comparison between the theory and experiment on QBSs of helium up to the threshold of $He^+(n=9)$.

It should be added that the hyperspherical coordinate method has been extended in further different directions, such as reactive and nonreactive molecular interactions [128–133], three- and four-electron systems [134–137], three-boson systems [94, 138–143], and extension for four-body and even larger systems [144–150]. In this regard, a remark on the so-called Efimov effects [151–153] is due here.

When the constituent two-body interactions in a three-body system produce an s-wave scattering length a of much larger magnitude $|a|$ than

the characteristic range r_0 of the two-body interactions, an attractive long-range effective three-body interaction emerges irrespective of the detailed forms of the two-body interactions. This effective interaction takes a form of a dipole potential at hyperradii between r_0 and $|a|$ and can support a number of weakly bound three-body states [151, 152] as well as QBSs (Section 3.1.2), which may affect, for example, three-body recombination processes in trapped ultracold gases, and hence, Bose–Einstein condensates [94, 138–143]. The hyperspherical-coordinate approach has been essential in most of these theoretical developments for unraveling this intriguing Efimov effects. The three-body Efimov resonance effects have indeed been observed in recent experiments [154, 155]. This is currently quite an active research field requiring detailed reviews [94, 143, 150].

3.2.3. Adiabatic potentials and adiabatic corrections

The results of HSCC calculations have proved much more rapid convergence with the number of coupled channels than the conventional close-coupling equations in terms of the independent-particle coordinates or the Jacobi coordinates based on them. This is considered to be because of the particle–particle correlations considerably taken into account already in the choice of the hyperspherical coordinate system. The results suggest an approximate adiabaticity with respect to the hyperradius ρ, even when the mass ratios might appear to violate the conditions for the adiabaticity, for example, for Ps^- with three equal masses. Then, it makes sense to study an adiabatic approximation with ρ adopted as the adiabatic parameter.

By neglecting the off-diagonal coupling potentials in the coupled equations [Eq. (95)], we obtain a single-channel approximation

$$\left(-\frac{\hbar^2}{2\mu}\frac{\mathrm{d}^2}{\mathrm{d}\rho^2} + U_n(\rho) - E\right)\mathcal{F}_n(\rho) = 0 \tag{99}$$

with

$$U_n(\rho) = \mathcal{V}_n(\rho) + \frac{(15/4)\hbar^2}{2\mu\rho^2} - \frac{\hbar^2}{2\mu}\left(\Phi_n \left| \frac{\mathrm{d}^2}{\mathrm{d}\rho^2} \right| \Phi_n\right)_{\Omega_c} \tag{100}$$

since $\left(\Phi_n \left| \mathrm{d}/\mathrm{d}\rho \right| \Phi_n\right)_{\Omega_c} = 0$. This is similar to the adiabatic approximation used for separating the electronic and nuclear motions of diatomic molecules. A further approximation

$$U_n(\rho) \simeq \mathcal{V}_n(\rho) + \frac{(15/4)\hbar^2}{2\mu\rho^2} \tag{101}$$

of neglecting the so-called adiabatic correction term, or the last term on the right-hand side of Eq. (100), is also often discussed. This is similar to

the Born–Oppenheimer approximation for diatomic molecules. In the literature of hyperspherical coordinate methods, both $U_n(\rho)$ with and without the adiabatic correction term are referred to as the adiabatic hyperspherical potentials, or simply, the hyperspherical potentials.

Let us recollect the linear Stark effect discussed in Section 3.1.2. The asymptotic interaction between a charged particle A and an excited neutral hydrogenic system BC has a decoupled dipole form $\hbar^2\alpha_i/(2\mu_{\text{A-BC}}R^2_{\text{A-BC}})$ for each channel i after unitary transformation to diagonalize the potential matrix; here and in the following, no confusion of α_i with the radial hyperangle should occur. The already diagonal hyperspherical potentials $U_n(\rho)$ of Eq. (101), without the adiabatic correction term, represent all the interaction potentials in the three-body system ABC exactly, and the coupling matrix elements $\mathcal{W}_{nn'}(\rho)$ in coupled equations (95) are due only to the nonadiabatic operators. Also, the distance $\mu^{1/2}_{\text{A-BC}}R_{\text{A-BC}}$ is equal to $\mu^{1/2}\rho$ to the lowest order for $R_{\text{A-BC}} \gg r_{\text{BC}}$, according to Eq. (87). Therefore, the adiabatic hyperspherical potentials $U_n(\rho)$ of Eq. (101) have an asymptotic form $\hbar^2\alpha_n/(2\mu\rho^2)$ with exactly the same α values as the dipole potential in the Jacobi coordinates. Then, the argument developed in Sections 3.1.2 and 3.1.3 applies equally well to the asymptotic hyperspherical potentials.

The virtue of the hyperspherical potentials $U_n(\rho)$ is that they often provide correct qualitative information on the essential physics prevailing in strongly correlated three-body systems not only in the asymptotic region of ρ but also over the whole region, although the adiabatic picture is numerically much less precise in general than the usual adiabatic potentials for low-lying molecular electronic states. The early work by Macek [90] already reveals the usefulness of the hyperspherical potentials on the physical grounds discussed there in detail. The predictions by the hyperspherical potentials have been mostly corroborated by HSCC calculations, and the latter have been interpreted clearly by the former, especially for resonance processes.

Examples of the helium potentials $U_n(\rho)$ of Eq. (101) from Ref. [90] are found in Figure 4.13; note the difference in the notation between this article and Ref. [90]. In this figure, only the hyperangular states decomposing into the channels $e^- + \text{He}^+(n=2)$ are shown. There are two curves for the S^e states and three for the P^o states, all of which possess an attractive Coulomb tail. All of these potentials support Rydberg series of bound states, which turn into Feshbach resonance states owing to the coupling with the open channel $e^- + \text{He}^+(1s)$. Its adiabatic potential curve lies much lower than the energy region of the figure. The lowest member of the Rydberg series supported by each potential is indicated by a horizontal line. All adiabatic potentials rise as $\propto \rho^{-2}$ at short hyperradii because of the centrifugal potential due to the grand angular momentum. Their short-range and long-range behaviors differ from those of typical diatomic adiabatic potentials as functions of the internuclear distance R, the latter being $\propto R^{-1}$ at short distances and

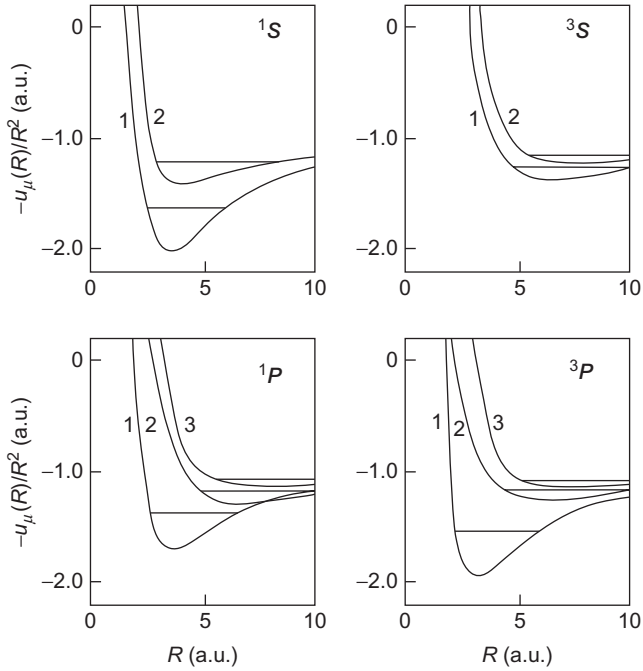

Figure 4.13 Adiabatic hyperspherical potentials, Eq. (101), in a.u. without the adiabatic correction term for He of symmetries $^{1,3}S^e$ and $^{1,3}P^o$ converging to the asymptotic limit $e^- + \mathrm{He}^+(n=2)$, plotted against the hyperradius R in a.u. Each potential supports an infinite number of Rydberg states of Feshbach resonance, of which the lowest level is indicated by a horizontal line. Figure from Ref. [90]. Note the difference in notation.

decaying much faster than the Coulomb potential as the molecule dissociates into two neutral atoms.

One of the great advantages of the hyperspherical potentials is that they can be classified in terms of the so-called correlation quantum numbers, a new set of approximate quantum numbers suitable for specifying strongly correlated dynamics. In terms of two-electron atoms, the quantum number T may be understood to represent the projection of the total orbital angular momentum $\mathbf{L}$ onto the interelectronic axis. It satisfies the relation $T \leq L$, provided that T is a fairly good quantum number [72, 77, 92]. The quantum number K is approximately equal to the expectation value of $-r_< \cos\theta_{12}$, where $r_<$ is the radial coordinate of the inner electron [72, 77, 92]. Both T and K represent the angular correlations. The radial correlation is described by A, which takes a value 0 or ± 1 and is usually specified by a superscript 0 or $\pm$ [72, 92, 156]. $A = 1$ if the wavefunction of the radial hyperangle α is nearly symmetric around $\alpha \simeq \pi/4$, i.e., around $r_1 \simeq r_2$, and $A = -1$ if nearly

antisymmetric. In other words, $A = -1$ if the wavefunction has a node near $\alpha = \pi/4$, and $A = 1$ if it has an antinodal structure. Otherwise, $A = 0$.

The profound implication of and the insight given by this classification scheme is fully described in the literature [72, 92, 93]. This article avoids too brief a summary of this knowledge and concentrates on the other aspects of the theory.

3.2.4. Feshbach versus shape resonances in the hyperspherical picture

We examine Figure 4.14, left figure, for adiabatic hyperspherical potentials (full curves: without the adiabatic correction term) for $H^-(^1P^o)$ converging to the asymptotic limit $e^- + H(n = 2)$. An avoided crossing between the two lowest curves is clearly observed. In fact, the corresponding $He(^1P^o)$ potentials in Figure 4.13 also have an avoided crossing, which appears as if it were a real crossing in the small figure. In these weak-avoidance cases, the resonances are better described by diabatically connected potentials than by the adiabatic potentials. Indeed, the physical characters, including the correlation quantum numbers, of each hyperangular state of H^- shown in Figure 4.14 changes smoothly with ρ along the diabatic potential, as shown by Lin [157, 158], although the exact definition of his "diabatic" potential is unclear.

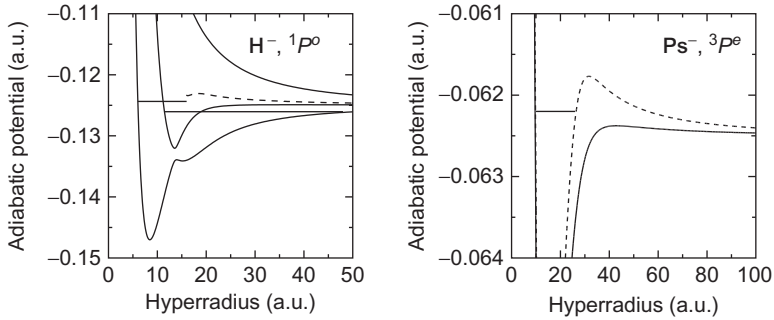

Figure 4.14 The effect of the adiabatic correction. Left: Hyperspherical potentials, Eq. (101), without the adiabatic correction term (full curves) for $H^-(^1P^o)$ converging to the asymptotic limit $e^- + H(n = 2)$. The lowest asymptotic potential supports an infinite series of dipole Feshbach resonances, of which only the lowest level is indicated by the longer horizontal line. The asymptotically second lowest potential supports a shape resonance (indicated by the shorter horizontal line) confined within the potential barrier, which is high enough if the adiabatic correction is introduced (broken curve). Diabatically connected potentials (not shown) describe the resonances better than the adiabatic potentials. Right: The hyperspherical potential with (broken curve) and without (full curve) the adiabatic correction term for $Ps^-(^3P^e)$ converging to the asymptotic limit $e^- + Ps(n = 2)$. The adiabatic correction introduces a high potential barrier, creating a shape resonance indicated by a straight line. Calculations and figures: courtesy A. Igarashi.

According to Eq. (81) with $\beta = 6$, the three α values for $H^-(^1P^o)$ in Figure 4.14 are -3.708, 2.000, and 9.708. Thus, the asymptotically lowest hyperspherical potential supports an infinite series of Feshbach resonances in the nonrelativistic approximation, although only three lowest members remain as resonances after corrections for the relativistic and radiative effects [80, 82], as was mentioned in Section 3.1.2. Only the lowest member is indicated in the figure by a horizontal line. This resonance is supported by the diabatic potential with $A = -1$ connecting from the lowest curve for large ρ to the middle curve for small ρ.

The second lowest asymptotic potential is inactive and the dipole potential is actually a mere centrifugal potential. As a diabatic potential with $A = +1$, however, it is strongly attractive at small ρ. Inside the high enough potential barrier introduced by the adiabatic correction term (see broken curve) at large ρ, this attractive potential supports a QBS (indicated by the shorter horizontal line) lying at an energy above the asymptotic limit $e^- + H(n = 2)$. This is a typical shape resonance in the hyperspherical picture. In this way, the hyperspherical potentials provide a transparent visual understanding of the shape versus Feshbach resonances [157, 158]. In fact, the adiabatic correction term is strongly peaked at the ρ values near the avoided crossing, although the region of this peak is excluded from the broken curve in Figure 4.14 (courtesy A. Igarashi). This suggests that unambiguous understanding of this shape resonance is gained by taking account of the channel coupling.

This shape resonance observed clearly in photodetachment spectra of H^- [159, 160] used to be called the $2s2p$ shape resonance, although it lies above the limit energy of $2s\infty p$. The orbital of the outer electron in H^- is quite different from Rydberg orbitals. Therefore, a careless analogy with the Rydberg states in helium can easily lead to misunderstanding.

Hyperspherical potentials are useful in studying similar three-body systems by changing the charges or the masses of the constituent particles. Thus, Chen and Lin compared hyperspherical potentials for systems consisting of two identical singly charged particles (with a mass m) and a third particle (with a mass M) having an opposite unit charge, for various values of the mass ratio $\lambda = m/M$ [156]. For example, in the second bound state of H^- (i.e., $\lambda \to 0$), namely, $H^-(2p^2\,{}^3P^e)$, the outer electron is weakly bound to $H(n = 2)$ (by only 9.7 meV) and is parity forbidden to escape into the energywise open channel $e^-(l = 1) + H(1s)$. The closed channel $e^-(l = 1) + H(2s)$ is also parity forbidden. Hence, there is only one hyperspherical potential approaching the threshold $H(n = 2)$, and no dipole coupling occurs. The hyperspherical potential supporting the state $H^-(2p^2\,{}^3P^e)$ has too weak a potential barrier to support a shape resonance. However, for $\lambda = 1$, i.e., for Ps^- the corresponding hyperspherical potential, if the adiabatic correction term is added, has a significant potential barrier, as is found in the right figure of Figure 4.14; see the broken curve. Thus, the level $Ps^-(2p^2\,{}^3P^e)$ is pushed up compared with

the excited bound state of H^-, and lies above the energy of $Ps(n=2)$, turning into a shape resonance in agreement with the calculations in, e.g., Refs. [161, 162]. Detailed calculations prove that this $^3P^e$ state is unbound and is a shape resonance for $0.3 < \lambda < 17.0$ [163].

A similar phenomenon is found also near higher thresholds. The shape resonances of $Ps^-(^1S^e, {}^1D^e)$, shown in Figure 4.6 to lie just above the threshold $E_{th}(n=3)$ of $Ps(n=3)$, are lowered across this threshold as λ decreases, and they turn into Feshbach resonances for $H^-(^1S^e, {}^1D^e)$ [53]. Such change of shape resonances in Ps^- into Feshbach resonances in H^- is found also at higher thresholds $E_{th}(n=4,5,6)$ [164]. A continuous change in λ is considered to change the large-amplitude part of the QBS wavefunction slowly and smoothly as the resonance position shifts across a threshold, i.e., as the shape resonance suddenly turns into a Feshbach resonance. The criterion for classifying resonances into these two categories is an asymptotic threshold energy, which is almost irrelevant to the main part of the QBS wavefunction. Thus, this classification is physically not too essential, unless the main part of the wavefunction is supported by the long-range tail of the interaction potential.

The hyperspherical potentials in Figures 4.13 and 4.14 look simple. Resonances appear to be easily attributable to an adiabatic or a diabatic potential. In comparison to these potentials, Figure 4.15 for the higher-lying adiabatic potentials of $He(^1P^o)$ is quite complex because of a large number of curves presenting many avoided crossings. There are $2n-1$ potentials converging to each asymptotic limit $e^- + He^+(n)$. Every one of these potentials supports an infinite Rydberg series of Feshbach resonances. Therefore, many

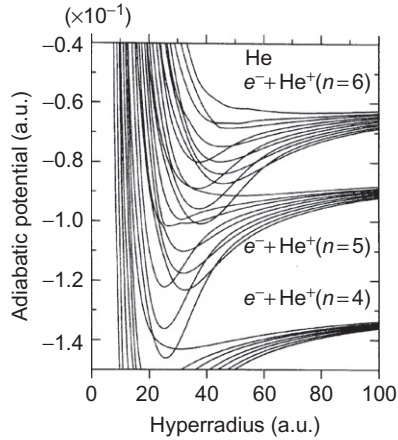

Figure 4.15 Hyperspherical potentials without the adiabatic correction term for $He(^1P^o)$ converging to the asymptotic limits $e^- + He^+(n=4,5,6)$. Each potential supports an infinite Rydberg series of Feshbach resonances. Some of them exhibit typical cases of inter-series overlapping resonances illustrated in Figures 4.9 and 4.10. Figure from Ref. [69].

overlapping resonances are readily expected from this figure. Indeed, the results already shown in Figures 4.9 and 4.10 are due to these potentials.

3.2.5. Diabatic potentials in rearrangement collisions

The three-body systems discussed so far contain two identical particles. Another system of interest, e^+He^+, contains three different particles and can decay into two different arrangement channels

$$\mathrm{Ps}(n) + \mathrm{He}^{2+} \longleftarrow e^+\mathrm{He}^+ \longrightarrow e^+ + \mathrm{He}^+(n'), \tag{102}$$

giving the possibility of rearrangement collisions. The hyperspherical potentials of symmetries $e^+\mathrm{He}^+(P^e, D^o)$ converging to the thresholds $\mathrm{Ps}(n=2,3)$ and $\mathrm{He}^+(n'=5-8)$ are shown in Figure 4.16 as full curves [66]. The arrangement $e^+ + \mathrm{He}^+$ has a repulsive Coulomb interaction asymptotically, whereas the asymptotic potentials behave as $\sim\pm\rho^{-2}$ for the arrangement $\mathrm{Ps} + \mathrm{He}^{2+}$.

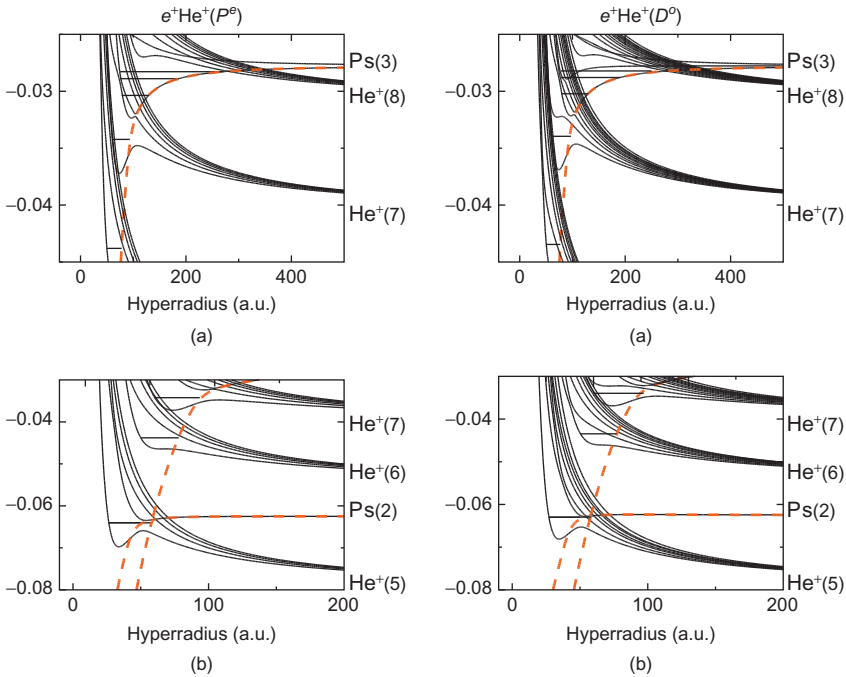

Figure 4.16 Hyperspherical potentials without the adiabatic correction term (full curves) for systems of unnatural parity $e^+\mathrm{He}^+(P^e)$ (left) and $e^+\mathrm{He}^+(D^o)$ (right) converging to the asymptotic limits $e^+ + \mathrm{He}^+(n=5-8)$ and $\mathrm{He}^{2+} + \mathrm{Ps}(n=2,3)$. The diabatic broken curves are for the $\mathrm{He}^{2+} + \mathrm{Ps}$ configurations only; see text. The vertical positions of the symbols $\mathrm{He}^+(n)$ and $\mathrm{Ps}(n)$ on the right roughly indicate the asymptotic threshold energies. The calculated resonance levels are shown by horizontal bars, some of which are unexpected from the adiabatic potentials. Adapted from Ref. [66].

This difference in the slope of curves introduces many avoided crossings between potentials representing different asymptotic arrangements. These avoided crossings are of a kind absent in He, H^-, or Ps^-.

The symmetries P^e and D^o of the particular examples in Figure 4.16 are of unnatural parity $\pi = (-1)^{L+1}$. For this class of parity, a positron–electron pair of vanishing angular momentum is forbidden. This makes the pair annihilation rate in this three-body system extremely low since the expectation value of the delta function of the positron–electron distance vanishes. Also, the only channel approaching $Ps(n=2) + He^{2+}$, namely, the $Ps(2p)$ channel, is asymptotically repulsive and no dipole Feshbach resonance series exists below this threshold. Below the $Ps(n=3)$ threshold, however, the dipole coupling between the $Ps(3p)$ and $Ps(3d)$ channels produces an infinite series of Feshbach resonances described by Eq. (80). The parameter ζ in Eq. (80) is found by diagonalization of these two asymptotic channels to be 0.7633 for P^e and 0.7862 for D^o. This may be confirmed by detailed HSCC calculations, followed by the analysis of the time-delay matrix eigenvalues, yielding accurate resonance parameters [66].

The obtained resonance levels are shown in Figure 4.16 by horizontal bars. We first pay attention to the three resonances lying just below the threshold $Ps(n=3)$, for each symmetry. The positions $E_{r,\nu} = E_{\text{th}} - \varepsilon_\nu$ and widths Γ_ν ($\nu = 1, 2, 3$) of these resonances are plotted semilogarithmically in Figure 4.17.

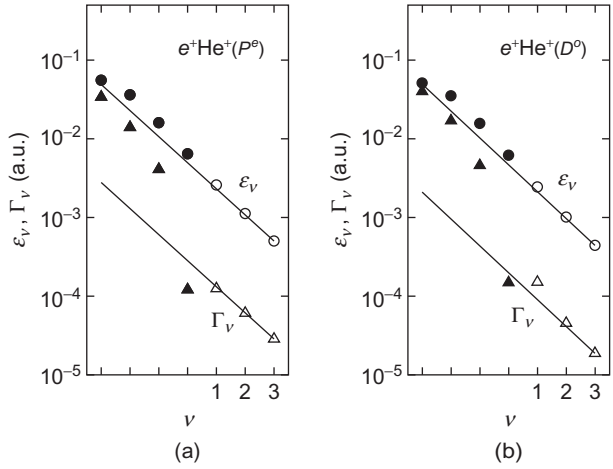

Figure 4.17 Semilogarithmic plot of the positions $E_{r,\nu} = E_{\text{th}} - \varepsilon_\nu$ and widths Γ_ν of (a) the three $e^+He^+(P^e)$ and (b) the three $e^+He^+(D^o)$ resonances lying below the $Ps(n = 3)$ threshold $E_{\text{th}} = -0.027778$ and above the lower thresholds (open circles and triangles). The straight lines have known slopes of 0.763 (for P^e) and 0.786 (for D^o). Their vertical positions are adjusted to reproduce the two highest members of the resonance series. Some lower-lying resonances are also included (solid circles and triangles) and discussed in the text. Figure from Ref. [66].

Straight lines are drawn with the slopes ζ known from the channel diagonalization. The vertical positions of these lines are chosen to reproduce the members $\nu = 2, 3$ well. The HSCC resonances are seen to satisfy Eq. (80) quite well with the known ζ common to both $E_{r,\nu}$ and Γ_ν. This proves clearly that, for both P^e and D^o symmetries, the three resonances belong to a common infinite series of dipole resonances converging to the threshold Ps($n = 3$). Indeed, Figure 4.16 suggests that the lowest of the potentials with an asymptotic limit Ps($n = 3$) + He^{2+} (henceforth denoted by $U_{\rm dip}(\rho)$), showing a minimum, supports these resonances. The width Γ_1 for $e^+He^+(D^o)$ is a little off the straight line, presumably due to the effects of the avoided crossing of $U_{\rm dip}(\rho)$ with lower potentials.

Frequently, more than one series of dipole resonances converges to a common series limit. Then, the resonance energies might appear quite irregular. Nevertheless, the resonances can be often classified unambiguously into different series by referring to the value of ζ for each series and by using a semilogarithmic plot similar to Figure 4.17, unless the coupling between series complicates the energy spectrum too much. Such a procedure is applied successfully in Ref. [66] to the double series in $e^+H(P^e)$ and in $e^+H(D^o)$, converging to the energy of H($n = 5$).

The next resonance in Figure 4.16 to discuss in detail lies right in the middle of the three-potential avoided crossing. The $e^+He^+(P^e)$ resonance at -0.03423 a.u. in Figure 4.16, left upper figure, is located just in between the minimum of an upper potential and the maximum of the next highest potential. No adiabatic potential is seen to support this resonance. Therefore, it must be supported by a diabatically connected potential, i.e., by an extension of the attractive part of $U_{\rm dip}(\rho)$ further down. If so, this resonance may be regarded as another member of the infinite series of dipole resonances already discussed above. This interpretation is corroborated by indicating the energy position and width of this resonance in Figure 4.17, left figure, by a solid circle and a solid triangle to the left of ε_1 and Γ_1. Indeed, the resonance energy lies close to the straight line, suggesting its membership of the same series. The width is off the straight line, which is understandable since the width is very sensitive to the coupling with other channels, in general.

A similar resonance occurs for $e^+He^+(D^o)$ at -0.03396 a.u. in Figure 4.16, right upper figure, which is also plotted in Figure 4.17, right figure, by a solid circle and a solid triangle to the left of ε_1 and Γ_1. Both the energy position and the width are seen to suggest that this resonance belongs to the same series as $(\varepsilon_\nu, \Gamma_\nu)$ $(\nu = 1, 2, 3)$.

A means to extrapolate the attractive part of $U_{\rm dip}(\rho)$ is to remove from the adiabatic potentials the contributions from the arrangement $e^+ + He^+$. This may be effected by constructing the basis functions for the adiabatic hyperangular states in Eq. (93) in terms only of the Jacobi coordinates for the arrangement Ps + He^{2+}. The two lowest potential curves (henceforth denoted by $V_2(\rho)$ and $V_3(\rho)$) obtained in this way are included in Figure 4.16 as red broken curves. The curve approaching Ps($n = 3$), i.e., $V_3(\rho)$, can be

regarded as supporting all the four resonances discussed so far for both symmetries.

Furthermore, even three more lower-lying resonances at -0.0438 a.u., -0.0640 a.u., and -0.0833 a.u. (outside of the energy region of Figure 4.16) for P^e and -0.04346 a.u., -0.063 a.u., and -0.0790 a.u. (outside of Figure 4.16) for D^o, all lying far from the already discussed four resonances, also appear to be supported by the same diabatic potential $V_3(\rho)$ and to belong to the same Feshbach series. These energy values, included in Figure 4.17, indeed exhibit near linearity, although the widths are far from the straight line because of the much stronger effects of coupling with other channels on the widths than on the resonance energies.

One of the $e^+\mathrm{He}^+(P^e)$ resonances lies at -0.0640 a.u., near the crossing point of the two diabatic broken curves in Figure 4.16, left figure. In fact, this is one of the two overlapping resonances discussed in relation to Figure 4.8. A very broad ($\Gamma = 1.4\times10^{-2}$ a.u.) low-lying member of the dipole series supported by $V_3(\rho)$ happens to be centered near a narrow ($\Gamma = 4.7\times10^{-4}$ a.u.) independent Feshbach resonance supported by $V_2(\rho)$. Similar pair of broad and narrow overlapping resonances supported by $V_3(\rho)$ and $V_2(\rho)$ occurs also for $e^+\mathrm{He}^+(D^o)$; see Figure 4.16, right figure.

All in all, adiabatic and diabatic hyperspherical potentials have proved to be quite useful in detailed interpretation of the resonance information obtained by the time-delay analysis of the scattering parameters calculated accurately from the HSCC equations.

4. THRESHOLD BEHAVIOR OF THE FORMATION OF A QUASI-BOUND STATE

Pair annihilation of a positron e^+ and an electron e^- by γ-ray emission was briefly explained in Section 1.3. There, the hydrogen-like system e^+e^-, or positronium Ps, was described quantum mechanically as a QBS having a finite lifetime τ because of an absorption potential $-iV_{\mathrm{abs}}$. This potential also causes positron flux loss, or positron absorption, in collisions with atoms.

The energy of a QBS has an ambiguity. This introduces an ambiguity in the threshold energy for the formation of a QBS, for example, positronium. Then, the cross section for the formation of positronium near the threshold is considered to violate the threshold law normally ascribed to Wigner [33]. This section discusses an alternative threshold law due to Baz' [165], which appears to be seldom cited in the literature. This is a general theory applicable to any kind of QBSs. It will be shown here to be able to describe both positronium formation and positron absorption collectively by a single threshold formula. For its numerical corroboration, accurate calculations are carried out by properly incorporating an imaginary absorption potential into the Schrödinger equation. This also solves the unphysical divergence difficulty of the conventional treatment of positron absorption.

4.1. Threshold law with an ambiguous threshold energy

Consider an endothermic reaction $A + B \to C + D$, or an excitation process if C and D are the same as A and B, with a threshold energy $E_{th} > 0$. Suppose that the interaction between C and D is of short range. Let the lowest possible angular momentum of the relative C-D motion be L. Then, the dominant term in the reaction or excitation cross section $\sigma(E)$ at energies E near and above the threshold E_{th} is

$$\sigma(E) = c_L(E - E_{th})^{L+1/2} \tag{103}$$

with c_L a constant depending on the process. Combined with the principle of detailed balance [12], this formula also expresses a threshold behavior $\propto (E - E_{th})^{L-1/2}$ for the reverse exothermic or deexcitation process. Equation (103) is often referred to as the Wigner threshold law. In fact, it had been widely known before the publication of Wigner [33] concerning the general theory of the effects of long-range potentials on the threshold laws; see footnote 1 of Ref. [33]. The cross section for a channel that is open even below the threshold E_{th} of another channel can exhibit a cusp shape, either peak or dip, at this threshold E_{th}. This was pointed out by Wigner [33] and was discussed in detail by Baz' [166]; see also Ref. [12]. Reference [167] reviews various threshold laws.

Our interest in this section is in the case where the particle D is formed in a QBS and decays subsequently into $D_a + D_b$, for example, in a finite lifetime τ. Then, the threshold energy E_{th} has an uncertainty $\Gamma = \hbar/\tau$. The threshold law (103) must be "blurred" in some sense and is considered to break down for $E - E_{th}$ comparable to or lower than Γ.

Baz' [165] treats the wavefunction for the particle D as a resonance state in the continuum $D_a + D_b$ and derives a cross-section formula

$$\sigma_L(E) \simeq C_L \mathrm{Re}[\{\Gamma(\varepsilon + i)\}^{L+1/2}] + C'_L \tag{104}$$

for the new channel C + D with a relative angular momentum L, at energies close to and both above and below the threshold energy E_{th} for the opening of this channel. Here, the reduced energy $\varepsilon = (E - E_{th})/(\Gamma/2)$ has essentially the same significance as the definition in Eq. (16) with respect to a resonance position. Both C_L and C'_L may be regarded as constants independent of E in a small region of E around the threshold. In fact, the particle D need not disintegrate into two fragments after its lifetime. The threshold law (104) remains valid for any kind of decay mode of D.

For $L = 0$, Eq. (104) reduces to

$$\begin{aligned} \sigma_0(E) &\simeq C_0(\Gamma/2)^{1/2}\{(\varepsilon^2 + 1)^{1/2} + \varepsilon\}^{1/2} + C'_0 \\ &= C_0(\Gamma/2)^{1/2}\{(\varepsilon^2 + 1)^{1/2} - \varepsilon\}^{-1/2} + C'_0. \end{aligned} \tag{105}$$

The physical meaning of this energy dependence will become clear later in the consideration around Eq. (125). Far from the threshold, Eq. (105) takes a form

$$\begin{aligned} \sigma_0(E) &\simeq C_0(\Gamma\varepsilon)^{1/2} \quad \text{for } \varepsilon \gg 1, \\ \sigma_0(E) &\simeq C_0(\Gamma/|\varepsilon|)^{1/2}/2 \quad \text{for } \varepsilon \ll -1 \end{aligned} \tag{106}$$

to the extent that the constant C_0' is negligible. The first of these equations reproduces the Wigner threshold law (103) for $L=0$. The knowledge of the large cross section for $\varepsilon \gg 1$ above threshold immediately provides the small cross section for $\varepsilon \ll -1$ below threshold, which may be too small to measure. The same can be said for Eq. (104) for a general L.

Far above the threshold, the uncertainty Γ in the threshold energy is negligible, and the imaginary part in the square brackets in Eq. (104) is practically absent. Thus, the Baz' threshold law reduces to the Wigner law for $\varepsilon \gg 1$ also for a general L. If the threshold energy has no ambiguity, Eq. (104) vanishes for $E < E_{\text{th}}$, as it should, since the quantity inside the square brackets is pure imaginary, then.

Baz' [165] also derives a formula for elastic scattering at wave number k and energy E near E_{th}. For the s wave, the S matrix takes a form

$$S_0(E) \simeq e^{2i\eta_0}\,[1 - C_0(k^2/2\pi)\{\Gamma(\varepsilon + i)\}^{1/2}], \tag{107}$$

where η_0 may be regarded as a constant in the energy region of the applicability of this formula. For $\Gamma \to 0$, i.e., in the limit of a stable-state formation threshold, the quantity in the braces tends to $\Gamma\varepsilon = 2(E - E_{\text{th}})$, and Eq. (107) reduces to the usual elastic scattering formula near the threshold of opening of a new channel [12, 166]. When a cusp appears in the elastic cross section at $E = E_{\text{th}}$ for $\Gamma = 0$, the introduction of nonzero Γ rounds off or smooths out the sharp cusp to some extent, more so for larger Γ [165].

4.2. Absorption potential for pair annihilation

The phenomenon of pair annihilation depends on the spin state of the e^+–e^- pair. Two γ-ray photons are emitted in opposite directions if it is a singlet pair ($S=0$), and three γ rays are emitted in directions on a common plane if it is triplet ($S=1$). The absorption potential appropriate for the singlet and the triplet annihilation in the absence of any other particles is [9, 10]

$$\begin{aligned} {}^{1,3}H' &= -i({}^{1,3}V_{\text{abs}}) \\ &= -i(\hbar c r_0^2)({}^{1,3}C)\,\alpha^S \delta(\mathbf{r}) \\ &= -i(e^2/a_B)({}^{1,3}C)\,\alpha^{S+3}\delta(\mathbf{r}) \end{aligned} \tag{108}$$

in the lowest-order approximation, if the relative electron–positron motion, i.e., the motion in the e^+–e^- distance vector $\mathbf{r}$, is much slower than the light velocity c in vacuum. Here,

$$ {}^1C = 2\pi \quad \text{and} \quad {}^3C = 8(\pi^2 - 9)/9, \tag{109} $$

α ($=7.297\times10^{-3}$) is the fine-structure constant, a_B is the Bohr radius, and r_0 ($=e^2/m_ec^2=2.818\times10^{-13}$ cm) is the classical electron radius. The factor α^{S+3} in the last equality shows that ${}^{1,3}H'$ is much weaker than the Coulomb potentials. The 3-γ annihilation is slower than the 2-γ annihilation by a factor

$$ \begin{aligned} \beta_{31} &\equiv \alpha \left(\frac{{}^3C}{{}^1C} \right) = \frac{4\alpha(\pi^2 - 9)}{9\pi} \\ &= 0.898 \times 10^{-3} = (1.114 \times 10^3)^{-1}. \end{aligned} \tag{110} $$

The first-order correction on the nonrelativistic energy $-6.8\,\text{eV}/n^2$ of the positronium Ps($ns\,{}^{1,3}S$) in an s state with a wavefunction $\psi(ns\,{}^{1,3}S)$ is [9, 10]

$$ E^{(1)} = (\psi(ns\,{}^{1,3}S)|{}^{1,3}H'|\psi(ns\,{}^{1,3}S)) \equiv -i\Gamma(ns\,{}^{1,3}S)/2. \tag{111} $$

The values of Γ for positronium defined by Eq. (111) are calculated to be

$$ \begin{aligned} \Gamma(ns\,{}^1S) &= cr_0^2/2n^3 = 5.29 \times 10^{-6} n^{-3}\,\text{eV}, \\ \Gamma(ns\,{}^3S) &= \beta_{31}\Gamma(ns\,{}^1S) = 4.75 \times 10^{-9} n^{-3}\,\text{eV}, \end{aligned} \tag{112} $$

from which the lifetimes $\tau = \hbar/\Gamma$ follow as

$$ \begin{aligned} \tau(ns\,{}^1S) &= 1.245 \times 10^{-10} n^3\,\text{s}, \\ \tau(ns\,{}^3S) &= 1.39 \times 10^{-7} n^3\,\text{s}. \end{aligned} \tag{113} $$

The uncertainties (112) for $n=1$ may be compared with the hyperfine splitting 0.841 meV between the para-positronium Ps($1s\,{}^1S$) and ortho-positronium Ps($1s\,{}^3S$) in the ground state [168, 169], which will be referred to in the next subsection.

4.3. Collisional positron absorption

4.3.1. Positron–atom collision processes

Recent progress in the study of positron scattering and positron annihilation processes is reviewed in Refs. [11, 170–172]. Experimentally, the positron sources from radioisotopes and from electron accelerators are quite weak and have a broad spectrum of energies as compared with electron sources, making precise measurements of positron collision processes extremely difficult. Such measurements, however, have become possible recently due to the

developments in efficient positron accumulators to trap and cool positron plasmas, which are used, in turn, to create beams with as narrow energy spreads as ∼20 meV[170, 172].

Possible final channels in positron collisions with atoms A are

$$\begin{aligned} e^+ + \mathrm{A} &\to \mathrm{A} + e^+, \ \ \mathrm{A}^+ + e^- + e^+ \quad \text{(direct process)}, \\ &\to \mathrm{A}^+ + \mathrm{Ps}(nl) \to \mathrm{A}^+ + n'h\nu \quad \text{(Ps formation)}, \\ &\to \mathrm{A}^+ + n'h\nu \quad \text{(pair annihilation)}. \end{aligned} \tag{114}$$

Measured direct processes include elastic scattering, electronic and, for the molecular target, vibrational excitation, and ionization, as well as the total cross section. Some cross sections are measured differentially in the scattering angle or in the kinetic energy of the emitted electrons. Doubly and even triply differential ionization cross sections are reported.

The positronium formation process is allowed if the energy of the incident positron exceeds the ionization potential of atom A less the binding energy $6.8n^{-2}$ eV of Ps(nl) with a slight uncertainty Γ in the threshold energy. For some systems, it is exothermic and positronium can be formed for any incident positron energy. The Ps formation eventually ends up with a channel that is indistinguishable from a pair annihilation channel [15, 16, 173, 174]. These two kinds of processes lead to the same final channel either directly or indirectly via an intermediate resonance state, Ps. The direct annihilation has a much lower rate than the Ps formation. Thus, by neglecting the former, the Ps formation cross section is determined by measuring the rate of positron loss in collision.

Annihilation at positron energies below the threshold for Ps formation, which used to be measured for a variety of high-density gases, can now be measured by introducing low-pressure gas in the presence of a cloud of trapped positrons, thus avoiding the density-dependent effects. It has become possible even to use a positron beam to determine the annihilation cross section as a function of the positron energy.

4.3.2. Indistinguishable positronium formation and positron absorption

Theoretically, the direct and indirect routes to the same final pair annihilation channel interfere with each other in general. Conventionally, however, they have been distinguished as completely different processes, one as a rearrangement collision due only to the Coulomb Hamiltonian, and the other as pair annihilation during the collision. This is based on the observation of two extremely different time scales; the lifetime $10^{-10}n^3$ s or longer of Ps(ns) and the time less than 10^{-16} s of the passage of a positron with a kinetic energy of 1 eV or higher for a distance of 1 a.u. A positronium is quite stable during the collision and begins to annihilate long after the collision is over.

On the other hand, Ps formation is a good theoretical atomic physics example of the processes that Baz' considered, although the original objective of

the Baz' threshold law was applications to nuclear reactions. The theory does not depend on the particular type of decay mechanism. Annihilation is certainly one of the decay modes covered by this theory. Thus, the second and third processes in Eq. (114), namely, Ps formation and pair annihilation, or positron absorption, should be described collectively by the threshold-law formula (104).

Then, according to the statement below Eq. (106), the absorption cross section below the Ps formation threshold $E_{\rm th}$ and within the energy range of applicability of the Baz' law is derivable from the knowledge of the Ps formation cross section above $E_{\rm th}$, in spite of the fact that these two cross sections are conventionally obtained completely independently. The absorption cross section below $E_{\rm th}$ must smoothly connect to the Ps formation cross section above $E_{\rm th}$ according to a *single known formula* (104).

Nevertheless, the conventional absorption cross section is known to diverge as the collision energy approaches $E_{\rm th}$ from below [18, 19]. On the other hand, the conventional Ps formation cross section starts from zero at $E_{\rm th}$ and grows rapidly as the positron energy increases. These unphysical results stem from the complete neglect of the uncertainty in the threshold energy $E_{\rm th}$. They should be remedied by a proper account of the width of the Ps energy due to the absorption potential in the Schrödinger equation. Furthermore, the sharp dip cusp in the elastic positron–hydrogen scattering at $E_{\rm th}$ found in Ref. [175] would have been rounded off if the uncertainty in the Ps energy were properly taken into account, although this change should be too slight to be discernible in the relevant figure in Ref. [175].

These theoretical expectations will be confirmed by accurate calculations in the following. Naturally, it turns out that most of the interesting effects of the uncertainty Γ in the threshold energy are observable only in the energy region of the transition from positron absorption to Ps formation, i.e., in an extremely narrow region of the order of several Γ, which is inaccessible by experiment. This is to be easily expected also from the much longer Ps lifetime than the typical collision time. Nonetheless, these actually unmeasurable effects on the collisional pair annihilation are theoretically accessible and play the role of a good prototype of more general processes exhibiting a typical threshold behavior for the formation of a QBS of any level width Γ. Careful examination of accurately calculable examples would be valuable for the purpose of generalizing the physical understanding for cases of larger Γ. Finally, it should be noted that the Baz' formula (104) is applicable in a much broader energy region than the transition region and that the known relation between the cross sections for positron absorption below the threshold and Ps formation above the threshold is valuable.

4.3.3. Physical interpretation of the divergent and smooth threshold laws

A proper quantum mechanical means to allow for the uncertainty in the Ps formation threshold in a positron scattering problem is to introduce the

absorption potential $-i({}^{1,3}V_{\rm abs})$ of Section 4.2 into the Schrödinger equation. For simplicity of description, we will discuss singlet or triplet positron scattering by the hydrogen atom H(1s) at energies below the threshold for excitation of H($n=2$). The positron flux loss due to $-i({}^{1,3}V_{\rm abs})$, which is the incident positron velocity v times the absorption cross section ${}^{1,3}\sigma_{\rm abs}$, is calculable by [13]

$$v({}^{1,3}\sigma_{\rm abs}) = (2/\hbar)({}^{1,3}\Psi|{}^{1,3}V_{\rm abs}|{}^{1,3}\Psi) \tag{115}$$

if the wavefunction ${}^{1,3}\Psi$ of the total system is normalized to the unit flux of incident wave and satisfies the wave equation

$$[{}^{1,3}H - E\,]\,{}^{1,3}\Psi = [H_{\rm C} - i({}^{1,3}V_{\rm abs}) - E\,]\,{}^{1,3}\Psi = 0. \tag{116}$$

Here, $H_{\rm C}$ is the Coulomb-three-body Hamiltonian like Eq. (3), and E is a real-valued energy of the whole system, i.e., the sum of the collision energy and the energy of the target state before collision. For spin-unpolarized positron and atomic beams, the total annihilation cross section is calculated by the statistically weighted average

$$\sigma_{\rm abs}^{\rm tot} = ({}^{1}\sigma_{\rm abs} + 3\,{}^{3}\sigma_{\rm abs})/4. \tag{117}$$

The absorption potential $-i({}^{1,3}V_{\rm abs})$ is quite weak compared with the Coulomb potential, as is noted below Eq. (109). Therefore, ${}^{1,3}\Psi$ in Eq. (115) can normally be replaced by the solution Φ of the spin-independent Coulomb Schrödinger equation

$$[H_{\rm C} - E\,]\Phi = 0 \tag{118}$$

for the same real-valued energy E, so that we have

$${}^{1,3}\sigma_{\rm abs} \simeq {}^{1,3}\sigma_{\rm abs}^{(0)} \equiv \frac{2}{v\hbar}(\Phi|{}^{1,3}V_{\rm abs}|\Phi) = \frac{2}{v\hbar}\left(\frac{e^2}{a_B}\right)({}^{1,3}C)\,\alpha^{S+3}(\Phi|\delta(\mathbf{r})|\Phi), \tag{119}$$

except in the very vicinity of a Ps formation threshold (in accordance with the argument in Section 4.1). This is the well-established method of calculating the annihilation rate [11, 17], as applied to positron collisions with hydrogen atoms, $e^+ + {\rm H}$.

The absorption cross section ${}^{1,3}\sigma_{\rm abs}$ of Eq. (115) contains both Ps formation and direct collisional absorption. The uncertainty in the threshold energy is negligible for $|\varepsilon| \gg 1$, which means that the absorption potential is negligible there. Therefore, ${}^{1,3}\sigma_{\rm abs}$ for $\varepsilon \ll -1$ is safely approximated by the conventional absorption cross section ${}^{1,3}\sigma_{\rm abs}^{(0)}$ of Eq. (119). Furthermore,

${}^{1,3}\sigma_{\rm abs}$ for $\varepsilon \gg 1$ is practically the same as the conventional Ps formation cross section $\sigma_{\rm Ps}^{(0)}$ from the Coulomb three-body treatment. There is no difference between the singlet and triplet collisions in the Coulomb three-body treatment, so that we have

$$ {}^1\sigma_{\rm abs}(E) = {}^3\sigma_{\rm abs}(E) = \sigma_{\rm Ps}^{(0)}(E) \quad \text{for } \varepsilon \gg 1. \tag{120} $$

It also follows from Eq. (119) that

$$ {}^3\sigma_{\rm abs}(E) = {}^3\sigma_{\rm abs}^{(0)}(E) = \beta_{31}\,{}^1\sigma_{\rm abs}^{(0)}(E) = \beta_{31}\,{}^1\sigma_{\rm abs}(E) \quad \text{for } \varepsilon \ll -1 \tag{121} $$

with a constant β_{31} ($\simeq 10^{-3}$) of Eq. (110).

Furthermore, comparison of Eq. (120) with Eq. (106) for the S wave shows that the constant C_0 in the latter equation is nearly the same for both singlet and triplet scattering. Then, it follows from Eq. (105) that

$$ {}^3\sigma_{\rm abs}({}^3\varepsilon)/{}^1\sigma_{\rm abs}({}^1\varepsilon) = ({}^3\Gamma/{}^1\Gamma)^{1/2} = \beta_{31}^{1/2} \tag{122} $$

for $L = 0$ in the energy region of validity of the Baz' threshold law. Here, the singlet–triplet comparison is made for functions of the reduced energy ε, which is different for the singlet and triplet scattering by definition (hence, ${}^3\varepsilon$ and ${}^1\varepsilon$). In this way, there exist various simple relations between the singlet and triplet cross sections derived for different energy regions.

The asymptotic outgoing wavefunction for a Ps formation channel, Ps + p, is

$$ \psi_{\rm Ps}(\mathbf{r}) f(\hat{\mathbf{R}}, \varepsilon) \exp(iKR)/R, \tag{123} $$

where $\psi_{\rm Ps}(\mathbf{r})$ is the wavefunction of the positronium, $f(\hat{\mathbf{R}}, \varepsilon)$ is the amplitude of this channel, $\mathbf{R}$ is the Ps-p distance vector, and K is the wave number of the motion in R. This wave number is complex in general because of the imaginary potential, and will be denoted by $K_{\rm re} + iK_{\rm im}$. The behavior of the absorption cross section for $E \simeq E_{\rm th}$ may be examined by inserting Eq. (123) into the wavefunction in Eq. (115) or in Eq. (119), other contributions to this cross section being slowly varying close to $E_{\rm th}$. Then, the integral of Eq. (115) or Eq. (119) is expressible as

$$ \Gamma F(\varepsilon) \int^{\infty} {\rm d}R \exp(-2K_{\rm im}R) = \Gamma F(\varepsilon)/(2K_{\rm im}) + G(\varepsilon), \tag{124} $$

where the term $G(\varepsilon)$, arising from small values of R, is slowly varying with ε. The factor Γ results from the expectation value of $\delta(\mathbf{r})$ with respect to the positronium wavefunction $\psi_{\rm Ps}(\mathbf{r})$; see Eq. (111). Thus, it arises even for

Eq. (119), which was derived with the assumption of no uncertainty in the threshold energy. The quantity $F(\varepsilon)$ is proportional to the integral of $|f(\hat{\mathbf{R}}, \varepsilon)|^2$ over the angle $\hat{\mathbf{R}}$, which behaves as $\propto |\varepsilon|^L$ for $\varepsilon \simeq 0$ according to the Wigner law.

First, consider the Coulomb three-body wavefunction Φ, i.e., the case of no uncertainty in the threshold energy $E_{\rm th}$. If $\varepsilon < 0$, i.e., $E < E_{\rm th}$, the wave number K is pure imaginary $iK_{\rm im}$ and $K_{\rm im} \propto |\varepsilon|^{1/2}$. As $|\varepsilon| \to 0$, the factor $F(\varepsilon)/K_{\rm im}$ in Eq. (124) behaves as $\propto |\varepsilon|^{L-1/2}$. It decreases toward zero for $L \geq 1$, but diverges as $|\varepsilon|^{-1/2}$ for $L = 0$. This unphysical result is a clear indication of the breakdown of the first-order perturbation approximation (119).

The reason for this divergence can be understood as follows. The integral (124) represents the cumulative intra-positronium annihilation as positronium leaves away from the proton until the channel wavefunction decays as $\exp(-K_{\rm im}R)/R$. The extremely slow decay of this wavefunction near $\varepsilon = 0$, together with the nearly constant $F(\varepsilon)$ as $|\varepsilon| \to 0$, causes the S-wave divergence.

The introduction of the absorption potential into the Schrödinger equation produces an imaginary part $-i\Gamma/2$ in the energy of the positronium, and in turn, also in the relative kinetic energy between the departing pair Ps and p in the positronium channel since the total energy E is unchanged and is real; the kinetic energy $E - E_{\rm th}$ is changed into $E - (E_{\rm th} - i\Gamma/2) = (\Gamma/2)(\varepsilon + i)$, which appears in the Baz' formula (104). The wave number K is complex even for $\varepsilon > 0$. This turns the positronium channel into a closed channel even for $\varepsilon > 0$ since the channel wavefunction behaves as $\exp(-K_{\rm im}R)\exp(iK_{\rm re}R)/R$. It follows for both $\varepsilon > 0$ and $\varepsilon < 0$ that

$$\begin{aligned} K_{\rm re} &= \Gamma^{1/2}[(\varepsilon^2+1)^{1/2} + \varepsilon]^{1/2}, \\ K_{\rm im} &= \Gamma^{1/2}[(\varepsilon^2+1)^{1/2} - \varepsilon]^{1/2} \end{aligned} \tag{125}$$

and that $K_{\rm re}K_{\rm im} = \Gamma$. The integral (124) combined with Eq. (125) reproduces the Baz' formula (105), which is now seen to be proportional to $K_{\rm im}^{-1}$. This argument deals with both energy regions $E < E_{\rm th}$ and $E > E_{\rm th}$ collectively without any distinction. The smooth continuity of the "absorption" cross section below $E_{\rm th}$ to the "Ps formation" cross section above $E_{\rm th}$ is guaranteed, and these two kinds of process are indeed indistinguishable near $E = E_{\rm th}$.

It is known from Eq. (125) that the exponent $2K_{\rm im}$ in the integral (124) decreases from $2(2\Gamma|\varepsilon|)^{1/2}$ for $\varepsilon \ll -1$ to $2\Gamma^{1/2}$ for $\varepsilon = 0$, and further to $(2\Gamma/\varepsilon)^{1/2}$ for $\varepsilon \gg 1$. The decrease becomes rapid for $|\varepsilon| \ll 1$. This shows that the annihilation in the Ps channel occurs only at short distances R if $E \ll E_{\rm th}$. As E approaches $E_{\rm th}$, the annihilation region suddenly extends to large distances R. As E departs further from $E_{\rm th}$, the annihilation region extends even further.

4.3.4. Annihilation calculations with an absorption potential

The exact energy region of the applicability of a threshold law is normally unknown from the theory. To study the validity of the *S*-wave threshold formula (105), the behavior of the higher partial waves, and the smoothing effects on the cusp structure in the elastic cross section, a rigorous treatment of the Schrödinger equation (116) is indispensable. For this purpose, the HSCC equations involving an imaginary potential were solved for positron–hydrogen collisions in Refs. [15, 16] at energies close to the "threshold" for the formation of para-Ps($1s\,^1S$) and that for ortho-Ps($1s\,^3S$) in the ground state. The two thresholds are separated from each other by a hyperfine splitting of 0.841 meV, which is artificially introduced into the Schrödinger equation.

The *S*-wave contributions to ${}^{1,3}\sigma_{\rm abs}$ are plotted as full curves in Figure 4.18 versus the reduced energy ε, which is actually defined with different parameters $E_{\rm th}$ and Γ depending on the spin. In the energy region across the threshold for Ps(1*s*), covered in Figure 4.18, the circles representing the Baz' threshold law (105) are seen to be quite accurate. Also, the simple relation (122) is observed quite well. The absorption cross sections ${}^{1,3}\sigma_{\rm abs}^{(0)}$ (broken curves) calculated in the conventional manner (119) digress from the full curves close to the threshold and diverge. The Ps formation cross sections $\sigma_{\rm Ps}^{(0)}$ (dotted curves) calculated from the Coulomb three-body Hamiltonian start to grow from the threshold according to the Wigner threshold law (103) or (106) and approach the full curves as well as the Baz' formula.

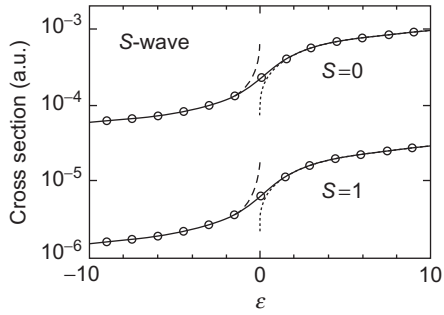

Figure 4.18 The near-threshold *S*-wave singlet ($S=0$) and triplet ($S=1$) absorption cross sections in $e^+ + \mathrm{H}(1s)$ scattering, plotted versus reduced energy $\varepsilon = (E - E_{\rm th})/(\Gamma/2)$. The threshold energy $E_{\rm th}$ and the width Γ differ depending on the spin *S*. Full curves: cross section ${}^{1,3}\sigma_{\rm abs}$ of Eq. (115) from hyperspherical close-coupling calculations including the absorption potential $-i({}^{1,3}V_{\rm abs})$. Dotted curves for $\varepsilon > 0$: positronium formation cross section calculated without $-i({}^{1,3}V_{\rm abs})$. Broken curves for $\varepsilon < 0$: absorption cross section ${}^{1,3}\sigma_{\rm abs}^{(0)}$ of Eq. (119) calculated without $-i({}^{1,3}V_{\rm abs})$ (first-order perturbation approximation). Circles: Baz' threshold formula fitted to the full curves. Figure from Ref. [16].

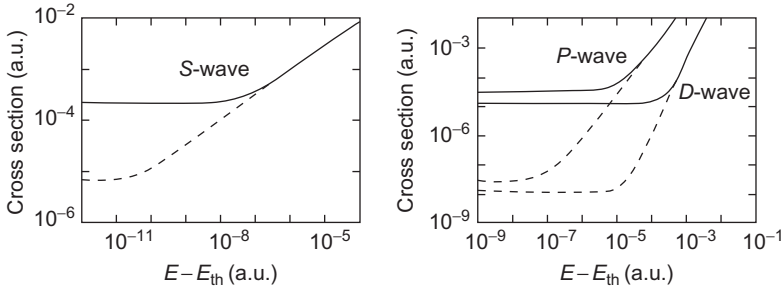

Figure 4.19 The partial-wave singlet (full curves) and triplet (broken curves) absorption cross sections in $e^+ + \mathrm{H}(1s)$ collisions, plotted versus the incident positron energy measured from the threshold energy for positronium formation. Results of hyperspherical close-coupling calculations including the absorption potential $-iV_{\mathrm{abs}}$ in the Hamiltonian. Note that the thresholds E_{th} for the full and broken curves are different by 0.841 meV, the hyperfine splitting. Figure from Ref. [16].

The three lowest partial-wave cross sections for singlet (full curves) and triplet (broken curves) annihilation are shown in Figure 4.19 in a broader energy range than Figure 4.18 above the thresholds. The singlet and triplet thresholds are adjusted to lie at the same position in Figure 4.19. As is evident from the data in Figure 4.18 at $\varepsilon = 0$, the ratio ${}^3\sigma_{\mathrm{abs}}(E = {}^3E_{\mathrm{th}})/{}^1\sigma_{\mathrm{abs}}(E = {}^1E_{\mathrm{th}})$ of the S-wave cross sections is $\beta_{31}^{1/2}$, and the ratio ${}^3\sigma_{\mathrm{abs}}(E)/{}^1\sigma_{\mathrm{abs}}(E)$ approaches 1.0 as the energy E increases; see Eqs. (122) and (120). Each higher partial-wave cross section starts from a constant value near $\varepsilon = 0$ that depends on S and L but satisfies Eq. (121) valid for $\varepsilon \ll -1$, namely, ${}^3\sigma_{\mathrm{abs}}/{}^1\sigma_{\mathrm{abs}} = \beta_{31}$. This is because these cross sections remain almost constant down to the region $\varepsilon \ll -1$. As E increases, the P- and D-wave cross sections in Figure 4.19 (as well as the F- and G-wave cross sections found in Ref. [15]) gradually approach the Wigner-type form (103) independent of the spin S due to the relation (120).

A procedure in this time-independent approach that corresponds to following the time evolution of the collision system would be to study the annihilation function ${}^{1,3}P(\rho)$ defined in terms of the hyperspherical coordinates by

$$ {}^{1,3}\sigma(E) = \int {}^{1,3}P(\rho)\mathrm{d}\rho = \frac{2}{v\hbar}\int \rho^5 \mathrm{d}\rho \, ({}^{1,3}\Psi|{}^{1,3}V_{\mathrm{abs}}|{}^{1,3}\Psi)_\Omega. \tag{126} $$

The annihilation function ${}^{1,3}P(\rho)$ may be decomposed into three contributions, namely, that from the direct-collision channels in ${}^{1,3}\Psi$, that from the Ps-formation channels, and the cross terms (or the interference terms) between the two kinds of channels. This decomposition is arbitrary to some

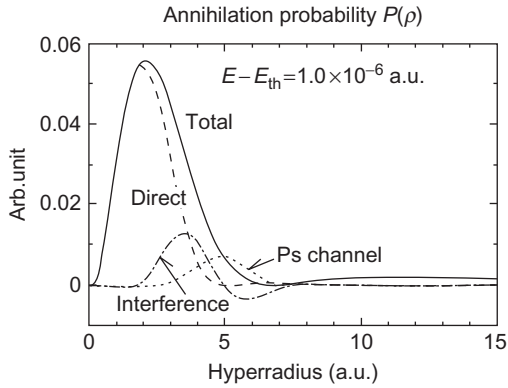

Figure 4.20 The ^{1}S-wave annihilation function $P(\rho)$ defined by Eq. (126), ρ being the hyperradius, for $e^+ + H(1s)$ scattering at an energy of 10^{-6} a.u. above the positronium formation threshold. The total $P(\rho)$ is decomposed into the contributions from the direct channels $e^+ + H$, the positronium formation channels $p + Ps$, and the interference between them. Results of hyperspherical close-coupling calculations including the absorption potential $-iV_{abs}$ in the Hamiltonian. Figure from Ref. [16].

extent since the channels are well defined only in the asymptotic regions of the configuration space. Nevertheless, it would be of interest to decompose $^{1,3}P(\rho)$ based on the definition of channels in terms of the hyperspherical coordinates to gain some idea of the interference effects.

Figure 4.20 shows an example of such a decomposition, calculated at E slightly above the threshold E_{th}. At this energy, the direct annihilation has a large peak at small values of ρ, and after it decreases, annihilation via Ps formation begins to contribute and keeps contributing up to very large ρ. Significant interference is clearly seen at intermediate values of ρ. Its absolute magnitude depends on the energy E and on the particular definition of the channels. However, Figure 4.20 illustrates at least the inseparability of the two different mechanisms of positron absorption at energies E close to E_{th}.

Finally, the cusp structure in the elastic cross section at the threshold energy for Ps(1s) production is examined. This structure was pointed out by Humberston et al. [175] reporting an elaborate variational calculation for the Coulomb three-body problem of $e^+ + H(1s)$ scattering. Another calculation based on the HSCC equations for the Hamiltonian including the absorption potential, carried out by Igarashi (unpublished), yields the results shown in Figure 4.21. The left figure is quite similar to the corresponding one in Ref. [175], clearly exhibiting a dip cusp. A closer view of a very narrow energy range around the threshold (right figure) reveals that the cross section is quite smooth across the threshold. This is due to the effects of the uncertainty in the threshold energy introduced by the absorption potential.

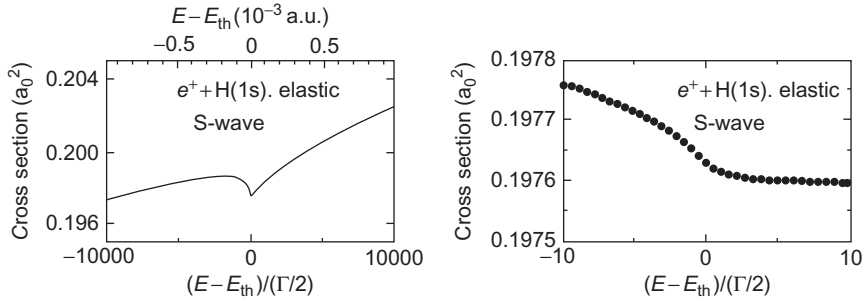

Figure 4.21 The ^{1}S-wave elastic cross section for $e^+ + H(1s)$ scattering near the positronium formation threshold E_{th}, plotted versus reduced energy $(E - E_{th})/(\Gamma/2)$. Results of hyperspherical close-coupling (HSCC) calculations including the absorption potential $-iV_{abs}$ in the Hamiltonian to account for the pair annihilation. Left: global view including the cusp structure. Right: an enlargement of the threshold vicinity with a smooth energy dependence. Calculations and figures: courtesy to A. Igarashi.

5. CONCLUSION

Converged numerical calculations are possible on many few-body continuum processes. They are particularly suitable for testing various methods of resonance analysis and for attaining deeper understanding of the QBS dynamics. Out of a wide variety of resonance analysis techniques found in the literature, only a few have been discussed in this article. A comprehensive review of computational methods for numerical values of resonance parameters has not been attempted in this article.

Eigenvalues of the time-delay matrix, calculable from the S matrix, are a powerful tool for analyzing complicated resonances, such as a few overlapping resonances and resonances obscured by another much stronger resonance or by a strong background. Illustrative applications have been presented. The eigenvectors of the time-delay matrix provide the concept of completely separate resonance channel space and nonresonance channel space. Only the former is associated with resonances, and the latter is irrelevant to any resonances.

Hyperspherical coordinates provide another powerful tool for precise three-body calculations, on one hand, and for visual understanding of QBS dynamics in terms of hyperspherical potentials playing a role similar to molecular adiabatic potentials. Adiabatic hyperspherical potentials exhibit many avoided crossings, which often must be cast into diabatic potentials to extract essential physics.

Decay of a QBS can be described by a flux loss into channels that are not treated explicitly. This is possible by introducing an imaginary, absorption potential. Theoretical formulations are independent of the decay

mechanisms. Electron–positron pair annihilation has been discussed in detail as an example. Positronium, regarded as a QBS, illustrates phenomena associated with ambiguous threshold energy for a new channel. The Wigner threshold law for the cross sections needs modification for ambiguous threshold.

ACKNOWLEDGMENTS

The author would like to thank Professor A. Igarashi, Miyazaki University, for long-standing collaborations and discussion concerning the work related to this article. Thanks are due to him also for his preparation of some of the figures presented in this article based on his own calculations.

REFERENCES

[1] A.K. Bhatia, A. Temkin, J.F. Perkins, Hylleraas variational calculation of auto-ionization states, Phys. Rev. 153 (1967) 177.
[2] J.C.Y. Chen, M. Rotenberg, Effect of a long-range potential on compound states in the (e, H) system, Phys. Rev. 166 (1968) 7.
[3] A.K. Bhatia, A. Temkin, P auto-ionization states of He and H^-, Phys. Rev. 182 (1969) 15.
[4] H.S. Taylor, J.K. Williams, Proposed theory of calculating the energy of negative-ion resonant elastic scattering states and of the pre-ionization states of electronic spectroscopy, J. Chem. Phys. 42 (1965) 4063.
[5] A.U. Hazi, H.S. Taylor, Stabilization method of calculating resonance energies: Model problem, Phys. Rev. A 1 (1970) 1109.
[6] M.F. Fels, A.U. Hazi, Calculation of energies and widths of resonances in inelastic scattering: Stabilization method, Phys. Rev. A 5 (1972) 1236.
[7] H.S. Taylor, Models, interpretations, and calculations concerning resonant electron scattering processes in atoms and molecules, Adv. Chem. Phys. 18 (1970) 91.
[8] H. Feshbach, A unified theory of nuclear reactions. II, Ann. Phys. (N.Y.) 19 (1962) 287.
[9] J.J. Sakurai, Advanced Quantum Mechanics, Addison-Wesley, Boston, 1967.
[10] V.B. Berestetskii, E.M. Lifshitz, L.P. Pitaevskii, Quantum Electrodynamics, Pergamon, Oxford, 1982.
[11] M. Charlton, J.W. Humberston, Positron Physics, Cambridge University Press, Cambridge, United Kingdom, 2001.
[12] L.D. Landau, E.M. Lifshitz, Quantum Mechanics, third ed., Pergamon, Oxford, 1977.
[13] L.I. Schiff, Quantum Mechanics, third ed., McGraw-Hill, New York, 1968.
[14] I.A. Ivanov, J. Mitroy, Optical model theory for positron annihilation during scattering, J. Phys. B: At. Mol. Opt. Phys. 33 (2000) L831.
[15] A. Igarashi, M. Kimura, I. Shimamura, A unified treatment of positron annihilation and positronium formation, Phys. Rev. Lett. 89 (2002) 123201.
[16] A. Igarashi, M. Kimura, I. Shimamura, N. Toshima, Inseparable positron annihilation and positronium formation in positron-atom collisions: Description in terms of an absorption potential, Phys. Rev. A 68 (2003) 042716.
[17] P.A. Fraser, Positrons and positronium in gases, Adv. At. Mol. Phys. 4 (1968) 63.
[18] P. Van Reeth, J.W. Humberston, The energy dependence of the annihilation rate in positron-atom scattering, J. Phys. B: At. Mol. Opt. Phys. 31 (1998) L231.

[19] G.G. Ryzhikh, J. Mitroy, *T*-matrix theory of positron annihilation on hydrogen, J. Phys. B: At. Mol. Opt. Phys. 33 (2000) 2229.
[20] N.F. Mott, H.S.W. Massey, The Theory of Atomic Collisions, Oxford University Press, Oxford, 1965.
[21] J.M. Blatt, V.F. Weisskopf, Theoretical Nuclear Physics, Springer, New York, 1979.
[22] A.J.F. Siegert, On the derivation of the dispersion formula for nuclear reactions, Phys. Rev. 56 (1939) 750.
[23] E. Balslev, J.M. Combes, Spectral properties of many-body Schrödinger operators with dilatation analytic interactions, Commun. Math. Phys. 22 (1971) 280.
[24] B. Simon, Quadratic form techniques and the Balslev-Combes theorem, Commun. Math. Phys. 27 (1972) 1.
[25] Y.K. Ho, The method of complex coordinate rotation and its applications to atomic collision processes, Phys. Rep. 99 (1983) 1.
[26] N. Moiseyev, Quantum theory of resonances: Calculating energies, widths and cross-sections by complex scaling, Phys. Rep. 302 (1998) 211.
[27] C.A. Nicolaides, Theory and state-specific methods for the analysis and computation of field-free and field-induced unstable states in atoms and molecules, Adv. Quant. Chem. 60 (2010) 163.
[28] G. Breit, E. Wigner, Capture of slow neutrons, Phys. Rev. 49 (1936) 519.
[29] U. Fano, Effects of configuration interaction on intensities and phase shifts, Phys. Rev. 124 (1961) 1866.
[30] L. Eisenbud, Dissertation, Princeton University, June 1948 (unpublished).
[31] D. Bohm, Quantum Mechanics, Prentice-Hall, New York, 1951, Chap. 11.
[32] E.P. Wigner, Lower limit for the energy derivative of the scattering phase shift, Phys. Rev. 98 (1955) 145.
[33] E.P. Wigner, On the behavior of cross sections near thresholds, Phys. Rev. 73 (1948) 1002.
[34] R.H. Dalitz, R.G. Moorhouse, What is resonance? Proc. R. Soc. London A 318 (1970) 279.
[35] K.W. McVoy, Overlapping resonances and *S*-matrix unitarity, Ann. Phys. (N.Y.) 54 (1969) 552.
[36] W. Brenig, R. Haag, Allgemeine Quantentheorie der Stoßprozesse, Fortschr. Phys. 7 (1959) 183.
[37] C.J. Goebel, K.W. McVoy, Eigenphases and the generalized Breit-Wigner approximation, Phys. Rev. 164 (1967) 1932.
[38] H.A. Weidenmüller, Resonances and eigenphases of the *S*-matrix, Phys. Lett. B 24 (1967) 441.
[39] A.U. Hazi, Behavior of the eigenphase sum near a resonance, Phys. Rev. A 19 (1979) 920.
[40] R.H. Dalitz, Strange-particle resonant states, Ann. Rev. Nucl. Sci. 13 (1963) 339.
[41] R.H. Dalitz, R.G. Moorhouse, The P_{11} pion-nucleon phase shift – a resonant state at 1400 MeV? Phys. Lett. 14 (1965) 159.
[42] P.G. Burke, S. Ormonde, W. Whitaker, Low-energy electron scattering by atomic hydrogen: I. The close-coupling approximation, Proc. Phys. Soc. (London) 92 (1967) 319.
[43] P.G. Burke, J.W. Cooper, S. Ormonde, Low-energy scattering of electrons by helium, Phys. Rev. 183 (1969) 245.
[44] P.G. Burke, R-Matrix Theory of Atomic Collisions: Application to Atomic, Molecular and Optical Processes, Springer, Heidelberg, 2011.
[45] J. Macek, Behavior of eigenphases near a resonance, Phys. Rev. A 2 (1970) 1101.
[46] F.T. Smith, Lifetime matrix in collision theory, Phys. Rev. 118 (1960) 349; Erratum, *ibid*. 119 (1960) 2098.
[47] H. Haberzettl, R. Workman, Time delay in a multichannel formalism, Phys. Rev. C 76 (2007) 058201.
[48] J.L. Kinsey, The density of states for interacting systems with inelastic transitions and its relation to the collision lifetime, Chem. Phys. Lett. 8 (1971) 349.

[49] L. Celenza, W. Tobocman, Calculation of the lifetime of a metastable system, Phys. Rev. 174 (1968) 1115.
[50] D.T. Stibbe, J. Tennyson, Time-delay matrix analysis of resonances in electron scattering: e^--H_2 and H_2^+, J. Phys. B: At. Mol. Opt. Phys. 29 (1996) 4267.
[51] J.-Z. Tang, I. Shimamura, Mechanism of the enhancement of some high-lying resonance series in the photoionization spectra of excited helium, Phys. Rev. A 50 (1994) 1321.
[52] A. Igarashi, I. Shimamura, Stable complex-rotation eigenvalues that correspond to no full resonances in scattering: Examples in positron scattering by the helium ion, Phys. Rev. A 70 (2004) 012706.
[53] A. Igarashi, I. Shimamura, Time-delay matrix analysis of resonances: Application to the positronium negative ion, J. Phys. B: At. Mol. Opt. Phys. 37 (2004) 4221.
[54] L. Quigley, K. Berrington, The *QB* method: Analysing resonances using *R*-matrix theory. Applications to C^+, He and Li, J. Phys. B: At. Mol. Opt. Phys. 29 (1996) 4529.
[55] C.P. Ballance, B.M. McLaughlin, O. Nagy, K.A. Berrington, P.G. Burke, The $2p\sigma_u\ ^{1,3}\Sigma_g^+$ interloper resonances in $e^-N_2^+$ collisions, J. Phys. B: At. Mol. Opt. Phys. 31 (1998) L305.
[56] C.P. Ballance, K.A. Berrington, B.M. McLaughlin, Detection and analysis of interloping molecular resonances, Phys. Rev. A 60 (1999) R4217.
[57] Y.K. Ho, A.K. Bhatia, *P*-wave shape resonances in positronium ions, Phys. Rev. A 47 (1993) 1497.
[58] A.K. Bhatia, Y.K. Ho, Complex-coordinate calculations of doubly excited $^{1,3}D^e$ resonant states of Ps^-, Phys. Rev. A 48 (1993) 264.
[59] M.J. Seaton, Strong coupling in optically allowed atomic transitions produced by electron impact, Proc. Phys. Soc. (London) 77 (1961) 174.
[60] M. Gailitis, R. Damburg, The influence of close coupling on the threshold behaviour of cross sections of electron-hydrogen scattering, Proc. Phys. Soc. (London) 82 (1963) 192.
[61] T.S. Belozerova, V.K. Henner, Overlapping resonances in multichannel reactions, Phys. Part. Nucl. 29 (1998) 63.
[62] J. Humblet, L. Rosenfeld, Theory of nuclear reactions I. Resonant states and collision matrix, Nucl. Phys. 26 (1961) 529.
[63] M. Simonius, Overlapping resonances and unitarity of the scattering matrix, Nucl. Phys. A 218 (1974) 53.
[64] V.L. Lyuboshitz, On collision duration in the presence of strong overlapping resonance levels, Phys. Lett. B 72 (1977) 41.
[65] I. Shimamura, J.F. McCann, A. Igarashi, Eigenvalues of the time-delay matrix in overlapping resonances, J. Phys. B: At. Mol. Opt. Phys. 39 (2006) 1847.
[66] I. Shimamura, H. Wakimoto, A. Igarashi, Resonance states of unnatural parity in positronic atoms, Phys. Rev. A 80 (2009) 032708.
[67] Y.K. Ho, Z.-C. Yan, Unnatural parity resonant states in the e^+-He^+ system, J. Phys. B: At. Mol. Opt. Phys. 42 (2009) 044006.
[68] I. Shimamura, Complete separation of resonance and nonresonance channel spaces, J. Phys. B: At. Mol. Opt. Phys. 44 (2011) 201002.
[69] K. Aiba, A. Igarashi, I. Shimamura, Time-delay matrix analysis of several overlapping resonances: Applications to the helium atom and the positronium negative ion, J. Phys. B: At. Mol. Opt. Phys. 40 (2007) F9.
[70] A.M. Lane, R.G. Thomas, R-matrix theory of nuclear reactions, Rev. Mod. Phys. 30 (1958) 257.
[71] M.J. Seaton, Quantum defect theory, Rep. Prog. Phys. 46 (1983) 167.
[72] U. Fano, A.R.P. Rau, Atomic Collisions and Spectra, Academic Press, Orlando, 1986.
[73] M.J. Seaton, Quantum defect theory VII. Analysis of resonance structures, J. Phys. B: At. Mol. Phys. 2 (1969) 5.
[74] D. Norcross, M.J. Seaton, Quantum defect theory. IX. Complex quantum defects for the e-Be^+ system, J. Phys. B: At. Mol. Phys. 3 (1970) 579.

[75] I. Shimamura, C.J. Noble, P.G. Burke, Complex quantum defects of superexcited Rydberg states of H_2, Phys. Rev. A 41 (1990) 3545.
[76] I. Shimamura, Series of resonance states of muonic molecules, Phys. Rev. A 40 (1989) 4863.
[77] D.R. Herrick, Resonance-channel quantum numbers in electron-hydrogen and proton-hydrogen scattering from group theory of the long-range dipole interaction, Phys. Rev. A 12 (1975) 413.
[78] M. Gailitis, On the series of double-excited states for the H^- ion below the $N = 3$ threshold, J. Phys. B: At. Mol. Phys. 13 (1980) L479.
[79] A. Pathak, A.E. Kingston, K.A. Berrington, Resonances in H^- associated with the $n = 2, 3$ and 4 hydrogenic thresholds, J. Phys. B: At. Mol. Opt. Phys. 21 (1988) 2939.
[80] E. Lindroth, A. Bürgers, N. Brandefelt, Relativistic effects on the H^- resonances converging to the $H(n = 2)$ threshold, Phys. Rev. A 57 (1998) R685.
[81] T. Purr, H. Friedrich, A.T. Stelbovics, Truncated dipole series in the electron-hydrogen and positron-hydrogen systems, Phys. Rev. A 57 (1998) 308.
[82] T. Purr, H. Friedrich, Mixing of *LS* configurations in terminating dipole series of H^-, Phys. Rev. A 57 (1998) 4279.
[83] C. Greene, U. Fano, G. Strinati, General form of the quantum-defect theory, Phys. Rev. A 19 (1979) 1485.
[84] C.W. Clark, Eigenphase sum in electron scattering by polar molecules, Phys. Rev. A 30 (1984) 750.
[85] J. Callaway, The ^1P shape resonance in electron-hydrogen scattering, Phys. Lett. A 81 (1981) 495.
[86] T.H. Gronwall, The helium wave equation, Phys. Rev. 51 (1937) 655.
[87] L.M. Delves, Tertiary and general-order collisions, Nucl. Phys. 9 (1959) 391.
[88] L.M. Delves, Tertiary and general-order collisions (II), Nucl. Phys. 20 (1960) 275.
[89] F.T. Smith, Generalized angular momentum in many-body collisions, Phys. Rev. 120 (1960) 1058.
[90] J.H. Macek, Properties of autoionizing states of He, J. Phys. B: At. Mol. Phys. 1 (1968) 831.
[91] U. Fano, Correlations of two excited electrons, Rep. Prog. Phys. 46 (1983) 97.
[92] C.D. Lin, Doubly excited states, including new classification schemes, Adv. At. Mol. Phys. 22 (1986) 77.
[93] C.D. Lin, Hyperspherical coordinate approach to atomic and other Coulombic three-body systems, Phys. Rep. 257 (1995) 1.
[94] E. Nielsen, D.V. Fedorov, A.S. Jensen, E. Garrido, The three-body problem with short-range interactions, Phys. Rep. 347 (2001) 373.
[95] J.C. Light, R.B. Walker, An *R* matrix approach to the solution of coupled equations for atom-molecule reactive scattering, J. Chem. Phys. 65 (1976) 4272.
[96] J.M. Launay, M. Le Dourneuf, Hyperspherical description of collinear reactive scattering, J. Phys. B: At. Mol. Phys. 15 (1982) L455.
[97] J.-z. Tang, S. Watanabe, M. Matsuzawa, General computational method for two-electron systems, Phys. Rev. A 46 (1992) 2437.
[98] B. Zhou, C.D. Lin, J.-Z. Tang, S. Watanabe, M. Matsuzawa, A hyperspherical close-coupling calculation of photoionization from the He atom, Li^+ and C^{4+} ions. I. Below the $N = 2$ threshold, J. Phys. B: At. Mol. Opt. Phys. 26 (1993) 2555.
[99] A. Igarashi, N. Toshima, Hyperspherical coupled-channel study of positronium formation, Phys. Rev. A 50 (1994) 232.
[100] B.L. Christensen-Dalsgaard, Combined hyperspherical and close-coupling description of two-electron wave functions: Application to *e*-H elastic-scattering phase shifts, Phys. Rev. A 29 (1984) 2242.
[101] O.I. Tolstikhin, S. Watanabe, M. Matsuzawa, 'Slow' variable discretization: a novel approach for Hamiltonians allowing adiabatic separation of variables, J. Phys. B: At. Mol. Opt. Phys. 29 (1996) L389.

[102] M. Hesse, A.T. Le, C.D. Lin, Protonium formation in the $\bar{p}$-H collision at low energies by a diabatic approach, Phys. Rev. A 69 (2004) 052712.
[103] A.T. Le, C.D. Lin, Muon transfer from muonic hydrogen to atomic oxygen and nitrogen, Phys. Rev. A 71 (2005) 022507.
[104] J.C. Light, I.P. Hamilton, J.V. Lill, Generalized discrete variable approximation in quantum mechanics, J. Chem. Phys. 82 (1985) 1400.
[105] J.-Z. Tang, Y. Wakabayashi, M. Matsuzawa, S. Watanabe, I. Shimamura, Critical study of photodetachment of H^- at energies up to the $n = 4$ threshold, Phys. Rev. A 49 (1994) 1021.
[106] J.-Z. Tang, I. Shimamura, High-lying doubly excited resonances in the photodetachment of H^-, Phys. Rev. A 51 (1995) R1738.
[107] J.-Z. Tang, C.D. Lin, B. Zhou, I. Shimamura, Resonances in photodetachment of $H^-(2p^2\,{}^3P^e)$, Phys. Rev. A 51 (1995) 4694.
[108] A. Menzel, S.P. Frigo, S.B. Whitfield, C.D. Caldwell, M.O. Krause, J.-Z. Tang, I. Shimamura, Decay paths of interfering two-electron excitations in helium, Phys. Rev. Lett. 75 (1995) 1479.
[109] J.-Z. Tang, I. Shimamura, Double photoionization of helium at low photon energies, Phys. Rev. A 52 (1995) R3413.
[110] J.-Z. Tang, I. Shimamura, Differential cross sections for photoionization of He, J. Electron Spectrosc. Related Phenomena 79 (1996) 259.
[111] A. Igarashi, I. Shimamura, N. Toshima, Photodetachment cross sections of the positronium negative ion, New J. Phys. 2 (2000) 17.
[112] D. Kato, S. Watanabe, Ab initio study of interelectronic correlations in electron-impact ionization of hydrogen, Phys. Rev. A 56 (1997) 3687.
[113] A. Igarashi, I. Shimamura, *S*-wave resonances in positron scattering by He^+, Phys. Rev. A 56 (1997) 4733.
[114] A. Igarashi, I. Shimamura, N. Toshima, Hyperspherical close-coupling study of hyperfine transitions in low-energy $p + p\mu$ and $e^{\pm} + \mathrm{Ps}$ scattering, Phys. Rev. A 58 (1998) 1166.
[115] A.-T. Le, M.W.J. Bromley, C.D. Lin, Positronium formation in positron-Li and positron-Na collisions at low energies, Phys. Rev. A 71 (2005) 032713.
[116] C.-N. Liu, A.-T. Le, T. Morishita, B.D. Esry, C.D. Lin, Hyperspherical close-coupling calculations for charge-transfer cross sections in $He^{2+} + H(1s)$ collisions at low energies, Phys. Rev. A 67 (2003) 052705.
[117] A.-T. Le, C.D. Lin, L.F. Errea, L. Mendez, A. Riera, B. Pons, Comparison of hyperspherical versus common-reaction-coordinate close-coupling methods for ion-atom collisions at low energies, Phys. Rev. A 69 (2004) 062703.
[118] T.-G. Lee, M. Hesse, A.-T. Le, C.D. Lin, Charge transfer in slow collisions of O^{8+} and Ar^{8+} ions with H(1*s*) below 2 keV/amu, Phys. Rev. A 70 (2004) 012702.
[119] P. Barragan, A.-T. Le, C.D. Lin, Hyperspherical close-coupling calculations for electron-capture cross sections in low-energy $Ne^{10+} + H(1s)$ collisions, Phys. Rev. A 74 (2006) 012720.
[120] A. Igarashi, N. Toshima, T. Shirai, Muon transfer and elastic scattering in $t + d\mu$ collisions at low energies Phys. Rev. A 50 (1994) 4951.
[121] A. Igarashi, M.P. Faifman, I. Shimamura, Nonadiabatically coupled hyperspherical equations applied to the collisional spin flip of muonic hydrogen, Hyperfine Interac. 138 (2001) 77.
[122] A. Dupays, B. Lepetit, J.A. Beswick, C. Rizzo, D. Bakalov, Nonzero total-angular-momentum three-body dynamics using hyperspherical elliptic coordinates: Application to muon transfer from muonic hydrogen to atomic oxygen and neon, Phys. Rev. A 69 (2004) 062501.
[123] A. Dupays, Isotopic effects in the muon transfer from $p\mu$ and $d\mu$ to heavier atoms, Phys. Rev. Lett. 93 (2004) 043401.

[124] A. Igarashi, N. Toshima, Three-body muon-transfer collisions from hydrogen isotope to He^{2+} and Li^{3+} ions, Eur. Phys. J. D 40 (2006) 175.
[125] A. Igarashi, N. Toshima, Application of hyperspherical close-coupling method to antiproton collisions with muonic hydrogen, Eur. Phys. J. D 46 (2008) 425.
[126] M. Domke, C. Xue, A. Puschmann, T. Mandel, E. Hudson, D.A. Shirley, et al., Extensive double-excitation states in atomic helium, Phys. Rev. Lett. 66 (1991) 1306.
[127] M. Domke, K. Schulz, G. Remmers, G. Kaindl, D. Wintgen, High-resolution study of $^1P^o$ double-excitation states in helium, Phys. Rev. A 53 (1996) 1424.
[128] A. Ohsaki, H. Nakamura, Hyperspherical coordinate approach to atom-diatom chemical reactions in the sudden and adiabatic approximations, Phys. Rep. 187 (1990) 1.
[129] V. Aquilanti, S. Cavalli, The quantum-mechanical Hamiltonian for tetraatomic systems in symmetric hyperspherical coordinates, J. Chem. Soc., Faraday Trans. 93 (1997) 801.
[130] M. Ragni, A.C.P. Bitencourt, V. Aquilanti, Hyperspherical and related types of coordinates for the dynamical treatment of three-body systems, Prog. Theor. Chem. Phys. 16 (2007) Part I, 123.
[131] P.R.P. Barreto, A.F. Albernaz, F. Palazzetti, A. Lombardi, G. Grossi, V. Aquilanti, Hyperspherical representation of potential energy surfaces: intermolecular interactions in tetra-atomic and penta-atomic systems, Phys. Scr. 84 (2011) 028111.
[132] A. Kuppermann, Reactive scattering with row-orthonormal hyperspherical coordinates. 3. Hamiltonian and transformation properties for pentaatomic systems, J. Phys. Chem. A 113 (2009) 4518.
[133] D. Wang, A. Kuppermann, Analytical derivation of row-orthonormal hyperspherical harmonics for triatomic systems, J. Phys. Chem. A 113 (2009) 15384.
[134] T. Morishita, C.D. Lin, Hyperspherical analysis of doubly and triply excited states of Li, Phys. Rev. A 57 (1998) 4268.
[135] T. Morishita, C.D. Lin, Comprehensive analysis of electron correlations in three-electron atoms, Phys. Rev. A 59 (1999) 1835.
[136] T. Morishita, C.D. Lin, Radial and angular correlations and the classification of intershell $2l2l'3l''$ triply excited states of atoms, Phys. Rev. A 67 (2003) 022511.
[137] T. Morishita, C.D. Lin, Hyperspherical analysis of radial correlations in four-electron atoms, Phys. Rev. A 71 (2005) 012504.
[138] E. Nielsen, J.H. Macek, Low-energy recombination of identical bosons by three-body collisions, Phys. Rev. Lett. 83 (1999) 1566.
[139] B.D. Esry, C.H. Greene, J.P. Burke Jr., Recombination of three atoms in the ultracold limit, Phys. Rev. Lett. 83 (1999) 1751.
[140] J.P. D'Incao, B.D. Esry, Manifestations of the Efimov effect for three identical bosons, Phys. Rev. A 72 (2005) 032710.
[141] N.P. Mehta, S.T. Rittenhouse, J.P. D'Incao, C.H. Greene, Efimov states embedded in the three-body continuum, Phys. Rev. A 78 (2008) 020701.
[142] Y. Wang, J.P. D'Incao, C.H. Greene, Efimov effect for three interacting bosonic dipoles, Phys. Rev. Lett. 106 (2011) 233201.
[143] E. Braaten, H.-W. Hammer, Universality in few-body systems with large scattering length, Phys. Rep. 428 (2006) 259.
[144] J.L. Bohn, B.D. Esry, C.H. Greene, Effective potentials for dilute Bose-Einstein condensates, Phys. Rev. A 58 (1998) 584.
[145] D. Kushibe, M. Mutou, T. Morishita, S. Watanabe, M. Matsuzawa, Aspects of hyperspherical adiabaticity in an atomic-gas Bose-Einstein condensate, Phys. Rev. A 70 (2004) 063617.
[146] S.T. Rittenhouse, M.J. Cavagnero, J. von Stecher, C.H. Greene, Hyperspherical description of the degenerate Fermi gas: *s*-wave interactions, Phys. Rev. A 74 (2006) 053624.

[147] S.T. Rittenhouse, C.H. Greene, The degenerate Fermi gas with density-dependent interactions in the large-N limit under the K-harmonic approximation, J. Phys. B: At. Mol. Opt. Phys. 41 (2008) 205302.
[148] Y. Wang, B.D. Esry, Efimov trimer formation via ultracold four-body recombination, Phys. Rev. Lett 102 (2009) 133201.
[149] J.P. D'Incao, J. von Stecher, C.H. Greene, Universal four-boson states in ultracold molecular gases: Resonant effects in dimer-dimer collisions, Phys. Rev. Lett. 103 (2009) 033004.
[150] S.T. Rittenhouse, J. von Stecher, J.P. D'Incao, N.P. Mehta, C.H. Greene, The hyperspherical four-fermion problem, J. Phys. B: At. Mol. Opt. Phys. 44 (2011) 172001.
[151] V. Efimov, Energy levels arising from resonant two-body forces in a three-body system, Phys. Lett. B 33 (1970) 563.
[152] V. Efimov, Weakly-bound states of three resonantly-interacting particles, Sov. J. Nucl. Phys. 12 (1971) 589 [Yad. Fiz. **12** (1970) 1080].
[153] V. Efimov, Low-energy properties of three resonantly-interacting particles, Sov. J. Nucl. Phys. 29 (1979) 546 [Yad. Fiz. **29** (1979) 1058].
[154] T. Kraemer, M. Mark, P. Waldburger, J.G. Danzl, C. Chin, B. Engeser, et al., Evidence for Efimov quantum states in an ultracold gas of caesium atoms, Nature 440 (2006) 315.
[155] M. Berninger, A. Zenesini, B. Huang, W. Harm, H.-C. Nagerl, F. Ferlaino, et al., Universality of the three-body parameter for Efimov states in ultracold cesium, Phys. Rev. Lett. 107 (2011) 120401.
[156] Z. Chen, C.D. Lin, Classification of Coulombic three-body systems in hyperspherical coordinates, Phys. Rev. A 42 (1990) 18.
[157] C.D. Lin, Feshbach and shape resonances in the e-H ^1P system, Phys. Rev. Lett. 35 (1975) 1150.
[158] C.D. Lin, Properties of resonance states in H^-, Phys. Rev. A 14 (1976) 30.
[159] H.C. Bryant, B.D. Dieterle, J. Donahue, H. Sharifian, H. Tootoonchi, D.M. Wolfe, et al., Observation of resonances near 11 eV in the photodetachment cross section of the H^- ion, Phys. Rev. Lett. 38 (1977) 228.
[160] M. Halka, H.C. Bryant, C. Johnstone, B. Marchini, W. Miller, A.H. Mohagheghi, et al., Branching ratio of the $H^-(n = 2)$ shape resonance, Phys. Rev. A 46 (1992) 6942.
[161] J. Botero, C.H. Greene, Resonant photodetachment of the positronium negative ion, Phys. Rev. Lett. 56 (1986) 1366.
[162] J. Botero, Adiabatic study of the positronium negative ion, Phys. Rev. A 35 (1987) 36.
[163] A.K. Bhatia, R.J. Drachman, Three-body Coulomb bound states, Phys. Rev. A 35 (1987) 4051.
[164] Y.K. Ho, A.K. Bhatia, $^{1,3}P^o$ resonance states in positronium ions, Phys. Rev. A 44 (1991) 2890.
[165] A.I. Baz', Energy dependence of cross sections near the "threshold" for unstable particle production, Sov. Phys. JETP 13 (1961) 1058.
[166] A.I. Baz', The energy dependence of a scattering cross section near the threshold of a reaction, Sov. Phys. JETP 6 (1958) 709.
[167] H.R. Sadeghpour, J.L. Bohn, M.J. Cavagnero, B.D. Esry, I.I. Fabrikant, J.H. Macek, A.R.P. Rau, Collisions near threshold in atomic and molecular physics, J. Phys. B: At. Mol. Opt. Phys. 33 (2000) R93.
[168] G.S. Adkins, R.N. Fell, P.M. Mitrikov, Calculation of the positronium hyperfine interval, Phys. Rev. Lett. 79 (1997) 3383.
[169] A.H. Hoang, P. Labelle, S.M. Zebarjad, Single photon annihilation contributions to the positronium hyperfine splitting to order $m_e\alpha^6$, Phys. Rev. Lett. 79 (1997) 3387.
[170] C.M. Surko, G.F. Gribakin, S.J. Buckman, Low-energy positron interactions with atoms and molecules, J. Phys. B: At. Mol. Opt. Phys. 38 (2005) R57.
[171] G. Laricchia, S. Armitage, Á. Kövér, D.J. Murtagh, Ionizing collisions by positrons and positronium impact on the inert atoms, Adv. At. Mol. Opt. Phys. 56 (2008) 1.

[172] G.F. Gribakin, J.A. Young, C.M. Surko, Positron-molecule interactions: Resonant attachment, annihilation, and bound states, Rev. Mod. Phys. 82 (2010) 2557.
[173] G.F. Gribakin, J. Ludlow, Enhancement of positron-atom annihilation near the positronium formation threshold, Phys. Rev. Lett. 88 (2002) 163202.
[174] J. Ludlow, G.F. Gribakin, Effect of a finite-energy spread of the positron beam on the threshold behavior of the positron annihilation cross section, Phys. Rev. A 66 (2002) 064704.
[175] J.W. Humberston, P. Van Reeth, M.S.T. Watts, W.E. Meyerhof, Positron-hydrogen scattering in the vicinity of the positronium formation threshold, J. Phys. B: At. Mol. Opt. Phys. 30 (1997) 2477.

CHAPTER 5

Atomic Resonance States and Their Role in Charge-Changing Processes

Eva Lindroth[a] and **Luca Argenti**[b]

Contents

Abstract Resonant states play a governing role in many charge-changing processes in atoms; the photoionization of atoms in gas phase and the corresponding time-reversed process of dielectronic recombinations being the two most prominent and well-known examples. This is so thanks to their strongly localized character, which leads to large transition matrix elements and to the unusually long timescale at which their dynamics unfolds, if compared to

[a] Department of Physics, Stockholm University, AlbaNova University Center, 106 91 Stockholm, Sweden
[b] Dept. Química, Módulo 13, Universidad Autónoma de Madrid, 28049 Madrid, Spain
E-mail address: lindroth@physto.se

Advances in Quantum Chemistry, Volume 63
ISSN 0065-3276, DOI: 10.1016/B978-0-12-397009-1.00005-9

free-electron wave packets. Many resonances correspond also to highly correlated electronic states. Hence, on the one hand, high-resolution extreme ultraviolet (XUV) and soft x-ray photoelectron spectroscopy, which give access to electronic resonances, provide unique insight into the effects of electronic correlation in the energy domain; on the other hand, new laser techniques able to produce light pulses of sub-femtosecond duration give a complementary, much needed, view of electronic correlation resolved in time. Here, we discuss resonances in atoms and atomic ions in all these respects. First, we survey how resonances can be accurately localized and characterized with complex scaling, standard scattering techniques and, for heavy ions, with relativistic many-body theory. The need for high precision is particularly stringent in the latter case since resonances located just above the ionization threshold, and thus whose parameters are most affected by numerical uncertainties, are often the most important for recombination. Second, we examine how the spectral properties of resonances translate in the time domain and how the course of the ionization process can be steered with external ultra-short driving laser pulses.

1. INTRODUCTION

Resonances can be described as states that are mainly localized but with a coupling to the ionization continuum, and they are of special interest to describe fragmentation processes induced when atomic system interact with electromagnetic fields or with impinging particles. The coupling may, for example, be due to electron–electron interaction (Auger effect) or due to static or time-dependent external fields (field ionization). The large spatial overlap between resonance states and bound states can result in substantial transfer of population from the latter to the former when the system absorbs energy. Due to the coupling to the continuum, the net result is an efficient path to ionization, often manifested in strong peaks in ionization spectra.

Despite being called a *state*, a resonance does not show up as an eigenstate of an Hermitian Hamiltonian. However, as it represents a particle state that is localized in space for some time and that delocalizes with a small but finite rate, a resonance is reminiscent of a stationary state, but with a decaying norm. Indeed, it can be shown that we can represent resonance states as eigenstates of a non-Hermitian Hamiltonian, whose complex eigenvalues lie in the lower half of the complex plane.

Sigert [1] defined resonance states as corresponding to solutions of the Schrödinger equation with asymptotically purely outgoing behavior. For a very simple, but illustrative, example on how the requirement of purely outgoing waves yields solutions of the Schrödinger equation with complex energies, which in addition can be identified with poles of the scattering amplitude, see Ref. [2]. A rigorous discussion can be found in Ref. [3]. A truly widespread theoretical approach to find such outgoing solutions is that of complex scaling (also called complex rotation) [3–9]. A more

recent discussion on some aspects of the method can be found, for example, in Ref. [10]. In complex scaling, the radial coordinate is scaled by a complex phase factor. As a consequence, the Hamiltonian becomes non-Hermitian; easily implemented boundary conditions will allow for outgoing, not for incoming, waves. With such an Hamiltonian we do find resonances as eigenstates. Their eigenvalues are complex: energy positions and half widths are obtained as their real and imaginary parts, respectively. The latter gives directly the transition rate from the localized part of a resonance state to the continuum. For states that decay through Auger emission, the method, in its traditional form of *uniform scaling*, has been combined with a number of calculation schemes such as Hylleraas wavefunctions [8, 11–13], configuration interaction [14], many-body perturbation theory (MBPT) [15–18], parametric coordinates [19, 20], or hyperspherical harmonics [21]. Most studies have focused on the determination of resonance parameters, but the method has also been employed to calculate resonances in the photoabsorption cross section [22–25] as well as electron–ion recombination cross sections, both in a nonrelativistic and in a relativistic framework [26–36]. Also states that couple to the continuum due to the interaction with a static electric field have been successfully treated with complex rotation [37–40].

Complex rotation can be usefully applied also to the case of the interaction of an atom with a time-dependent perturbation. With the Floquet formalism by Shirley [41], it was shown that, for a time-periodic field, the *dressed* states of the combined atom–field system can be characterized non-perturbatively by the eigenstates of a *time-independent*, infinite-dimensional matrix. The combination of the Floquet approach with complex rotation, proposed by Chu, Reinhardt, and coworkers [37, 42, 43], permits to account for the field-induced coupling to the continuum in an efficient way. As in the time-independent case, this results in complex eigenvalues (this time to the Floquet Hamiltonian matrix) and again the imaginary parts give the transition rate to the continuum. This combination has since then been successfully used to examine various strong field phenomena; a review can be found in Ref. [44].

An alternative to *uniform* complex scaling (used in the studies mentioned so far) is *exterior* complex scaling [45, 46], where the scaling of the coordinates starts at some finite distance from the origin. This approach has been used extensively on electron scattering problems in the absence of resonances, for example, in Refs. [47–50], for a review see Ref. [51], as well as to obtain resonance parameters in connection with electronic autoionization [52, 53].

A key feature of *exterior* complex scaling, especially important for scattering problems, is that the unaltered inner region allows extraction of physical quantities from the amplitude of the wavefunction or from the outgoing flux, in the same manner as if it had been the eigenstate of an Hermitian Hamiltonian. The unaltered inner region is also an important property of *complex absorbing potentials*, i.e., artificial potentials introduced in the asymptotic region to prevent unphysical reflections caused by the use of finite basis

sets or grids. The aim is again to allow for outgoing waves only. As with complex scaling, the Hamiltonian becomes non-Hermitian, and again resonances can be found as eigenstates with complex eigenvalues. An early example of a calculation of resonance parameters in this way can be found in Ref. [54]. The relation between complex absorbing potentials and exterior complex scaling has been studied by several authors, see, for example, Refs. [55–58]. It can be shown that in the limit of vanishing reflection from the artificial potential the methods should produce the same resonance parameters [55], and Moiseyev [57] has discussed how an (exterior) complex scaled Hamiltonian, under certain constraints, can be recast in the form of an Hamiltonian with an absorbing potential. A variety of absorbing potentials have been used in the literature [59]. The most common and simple approach consists in adding to the Hamiltonian an imaginary monomial term of the form $-iV_0(r-r_0)^n\theta(r-r_0)$, but more elaborate complex potentials can be used to minimize the reflection.

The last decade has seen a rapid development of the ability to produce laser pulses of increasingly shorter time duration. Through techniques such as high harmonic generation and new machines such as free-electron lasers, atomic and molecular systems can be studied at the femto- and attosecond timescales. Fast processes such as ionization and charge transfer can thus to an increasing extent be monitored in real time, thereby promising new insights in these fundamental processes, as well as new possibilities to steer and control them. The possibility to follow the population and depopulation of metastable states is here especially intriguing: resonances are often intermediate steps in those processes that require high electronic excitation and are thus natural targets for altering the path of a reaction. For a review of the many interesting aspects of rapidly growing field opened by subfemtosecond pulses, see, for example, Ref. [60]. Although uniform complex scaling has been used in connection with short light pulses [61–63], exterior complex scaling, and, to an even larger extent, absorbing boundaries have been much more utilized. In the following, we present calculations done with both methods.

This review is organized as follows. In Section 2, we discuss the concept of resonance and how a resonance can be characterized, with particular reference to the method of complex rotation. In Section 3, we discuss the crucial role of autoionizing states to predict and understand electron–ion recombination. In this context, complex scaling has been a very important tool, especially in its relativistic formulation. Section 4 discusses in more detail the method of complex rotation applied to the solution of the Dirac equation. Finally, in Section 5, we turn to the investigation of resonance states in the time domain. In particular, we illustrate simulations of realistic XUV-pump IR-probe experiments, which allow to show how autoionization occurs through collision-like events even in the lowest lying resonances and which give the possibility to control the branching ratios of multichannel

above-the-threshold ionization. The method developed for these studies is outlined in Section 5.1.

2. RESONANCE CHARACTERIZATION

As anticipated in the introduction, a resonance does not show up as an eigenstate of an Hermitian Hamiltonian. However, as it represents a particle state that is localized in space for some time and delocalizes at a small rate, it is natural to think of it as a stationary state with a decaying norm. How do we obtain a description that fits this physical picture? In order to lay the ground for the answer offered to this question by the method of complex scaling, let us first briefly summarize how resonances are characterized in the frame of classical scattering theory, i.e., the theory of the continuous spectrum of Hamiltonian operator in quantum mechanics. Formally, resonances are defined as single-rank poles of the scattering matrix $\mathbf{S}(E)$ [Eq. (70)] [64, 65] in the lower half part of the complex energy plane [66–69]. This means that, close to an isolated resonance, the scattering matrix can be parametrized in the following way

$$\mathbf{S}(E) = \mathbf{S}_{\mathrm{bg}}(E)^{1/2}\left(\mathbf{1} - i\Gamma\frac{\mathbf{u}\mathbf{u}^{\dagger}}{E - E_0 + i\Gamma/2}\right)\mathbf{S}_{\mathrm{bg}}^{1/2}(E), \quad \mathbf{u}^{\dagger}\mathbf{u} = 1, \tag{1}$$

where $\mathbf{S}_{\mathrm{bg}}(E)$ is a slowly varying background factor. The middle factor has a pole at $z = E_0 - i\Gamma/2$, where E_0 and Γ are the resonance energy and width, respectively. The square modules of the components of the vector $\Gamma\mathbf{u}^{\dagger}\mathbf{S}_{\mathrm{bg}}^{1/2}(E)$ give the partial widths of the resonance, i.e., the probability that the resonance decays in a given channel.

In order to determine the resonance energy and total width alone, it is sufficient to look for the poles of the determinant of $\mathbf{S}(E)$

$$\det\mathbf{S}(E) = e^{2i\varphi_{\mathrm{t}}(E)}, \quad \varphi_{\mathrm{t}}(E) = \sum_{\alpha}^{\mathrm{open}}\varphi_{\alpha}(E), \tag{2}$$

where $\varphi_{\alpha}(E)$ are the eigenphases of $\mathbf{S}(E)$ and $\varphi_{\mathrm{t}}(E)$ is the total phase shift. Indeed, due to the minimal rank assumption on the poles of $\mathbf{S}(E)$, its determinant clearly has the same poles as the matrix itself. Since the scattering matrix is unitary, its determinant $\det\mathbf{S}(E)$ is a unimodular function on the real axis, therefore, it can be parametrized in the vicinity of an isolated pole with a Breit–Wigner phase factor [70]:

$$e^{2i\phi(E;E_r,\Gamma_r)} = \frac{E - E_r - i\Gamma_r/2}{E - E_r + i\Gamma_r/2}, \quad \phi(E;E_r,\Gamma_r) = \arctan\left[2(E - E_r)/\Gamma_r\right] + \frac{\pi}{2}, \tag{3}$$

where E_r and Γ_r are, respectively, the energy and the width of the rth resonance (to be more precise, both E_r and Γ_r are smooth functions of the energy, which can be continued analytically in the complex energy plane. The complex resonance energies are given by the solutions to the equation $z - [E_r(z) - i\Gamma_r(z)/2]$ in the lower half of the complex plane). From Eq. (3), we see that in correspondence to each resonance the total phase shift increases by π. This means that the derivative of φ_t/π can be interpreted as a density of states

$$\rho(E) = \frac{1}{\pi}\frac{d\varphi_t(E)}{dE}. \tag{4}$$

The density of states so defined can be shown to be connected to the time delay that an electron experiences when scattering off the parent ion. The connection between time delay and energy derivative of the phase shift in the single channel case was first discussed by Eisenbud and Wigner [71, 72], and later generalized and extended, with the concept of "dwell time," to the multichannel case by Smith [73]. Smith introduced a time-delay matrix $\mathbf{Q}$, defined as

$$\mathbf{Q} = i\hbar\,\mathbf{S}\mathrm{d}\mathbf{S}^{\dagger}/\mathrm{d}E, \tag{5}$$

whose diagonal elements Q_{ii} represent the average, over the final channels, of the retardation experienced by an electron that impinges on the parent ion in the channel i. It is easy to demonstrate that the trace of $\mathbf{Q}$ corresponds to the density of states times the Plank's constant,

$$\mathrm{tr}\,\mathbf{Q} = 2\hbar\frac{\mathrm{d}\varphi_t(E)}{\mathrm{d}E} = h\rho(E). \tag{6}$$

In the case of a single-channel, this relation reduces to the well-known expression for the Eisenbud–Wigner–Smith time delay

$$\tau = 2\hbar\frac{d\varphi_t(E)}{dE}. \tag{7}$$

Conversely, a coherent superposition of continuum states with a population closely reproducing an isolated peak in the density of states, which corresponds to a resonance, can be built in such a way to give rise to a localized state. From this localized state, there will be an outward probability density flux, i.e., it will have a finite lifetime. In the limit of a resonance position far from any ionization threshold and a narrow energy width, the decay rate will be exponential with the rate constant $\Gamma/\hbar$. The decay is to all the available open channels, in proportion to their partial widths.

For energy intervals comprising N_{res} resonances and which are not too large, $\det \mathbf{S}(E)$ can be approximated with a product of N_{res} Breit–Wigner phase factors times a smooth background phase factor:

$$\det \mathbf{S}(E) = \exp\left[2i\sum_{r=1}^{N_{\text{res}}} \phi(E; E_r, \Gamma_r) + 2i\phi_{\text{bg}}(E)\right].$$

Therefore, if the total phase shift is known as a function of the energy, the positions of the resonances can be determined by fitting it with a linear combination of arctangent functions plus a smooth polynomial background. See, for example, Ref. [74] and references therein.

In Figure 5.1, we illustrate this fitting procedure for the case of an isolated multiplet of $^1P^o$ doubly excited states in helium, below the $N = 5$ single ionization threshold. The total phase shift used for this example has been determined by solving the multichannel e–He^+ scattering problem with the K-matrix B-spline method [75], which is briefly outlined in Section 5.1. The multiplet comprises nine resonances, classified here with the Stark approximate quantum numbers $[N_1N_2m]^A$ (for a review of the several different approximate classification schemes for the doubly excited states of helium, see Ref. [76] and references therein). The total phase shift divided by π, around an isolated doubly excited states multiplet in helium manifold is reported as a function of energy together with its derivative (scaled to fit in the plot). The fitting function (nine resonance terms plus a polynomial background of fourth degree) is superposed to the phase shift as a

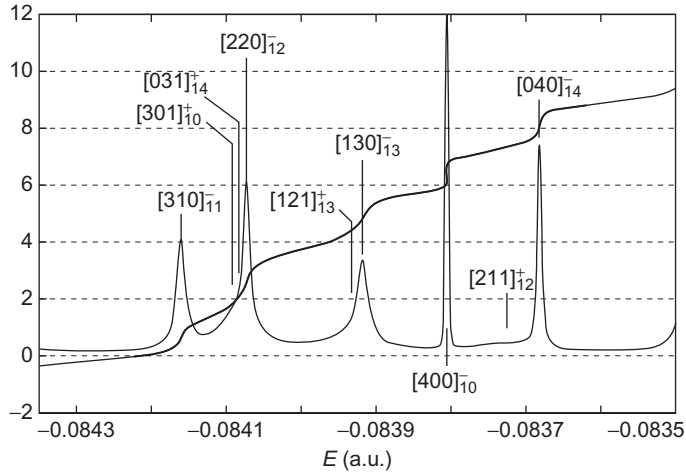

Figure 5.1 Total phase shift and state density for an isolated multiplet in the $^1P^o$ helium below $N = 5$ ionization threshold.

Table 5.1 Parameters of a selected group of $^1P^o$ helium resonances below $N = 5$ ionization threshold, corresponding to the peaks shown in Figure 5.1

$[N_1N_2m]^A$	E (au)	$\Gamma/2$ (a.u.)
$[031]^+_{14}$	−0.084 080	6.79[−5]
	−0.084 092	6.29[−5][a]
$[121]^+_{13}$	−0.083 935	4.19[−5]
	−0.083 966	5.68[−5][a]
$[211]^+_{12}$	−0.083 729	5.76[−5]
	−0.083 737	5.97[−5][a]
$[301]^+_{10}$	−0.084 087	2.38[−5]
	−0.084 103	2.48[−5][a]
$[040]^-_{14}$	−0.083 682	2.76[−6]
	−0.083 678	2.87[−6][a]
$[130]^-_{13}$	−0.083 918	7.79[−6]
	−0.083 919	7.60[−6][a]
$[220]^-_{12}$	−0.084 073	4.76[−6]
	−0.084 079	5.84[−6][a]
$[310]^-_{11}$	−0.084 160	6.37[−6]
	−0.084 169	5.77[−6][a]
$[400]^-_{10}$	−0.083 805	3.77[−7]
	−0.083 820	3.21[−7][a]

[a]Rost *et al*. (1997) [76].

thicker line. The resonance parameters obtained through the fitting are listed in Table 5.1 alongside those computed by Rost *et al*. with the method of complex scaling [76].

2.1. The method of complex rotation

We saw above that the increased density of states associated with a pole in the scattering matrix is proportional to the time delay experienced by an electron that scatters off the parent ion. This means that it can be interpreted as the lifetime of the transient state the particle forms around the ion. The lifetime is associated with a spread in energy, i.e., an energy width. As discussed in the introduction, if we want to describe the transient state, not as a density of states, but as a state with a single energy, it is natural that this energy should be complex. A negative imaginary part gives directly a decaying norm, which in turn signals that there is a dissipation. Hence, if the state is to be an eigenstate of an Hamiltonian, then this Hamiltonian cannot possibly be Hermitian. Conceptually, the simplest way to construct a non-Hermitian Hamiltonian whose complex eigenenergies correspond to

the positions of the resonances of the system, would be to impose purely outgoings waves, cf. Refs. [1, 3], through perfectly absorbing boundaries. Such boundary conditions are not trivial to construct though. Complex rotation [3, 5–7, 9] provides a more elegant solution, which over the years has proven easy to implement and reliable to use. As discussed in the introduction, numerous implementations exist in the literature. The simple scaling of the radial variable generates a non-Hermitian Hamiltonian with well-known analytical properties. Namely, such a rotated Hamiltonian will, in addition to bound states with real energies, have eigenstates above the ionization limit with complex energies independent of the actual rotation angle (provided it is large enough). This property can be shown for the so-called dilatation analytic potentials, including the important case of the many-particle Coulomb interaction, see, for example, the discussions in Refs. [9, 77, 78]. The complex energies are associated with resonances: the real part gives the energy position and the imaginary part the half width, $\Gamma/2$, so that the norm of such a state will decay with a decay constant $\Gamma/\hbar$. That the complex scaling technique, which originally was introduced [6] for scattering problems, could be used to calculate the width of atomic autoionizing state, was first clarified by Simon [7, 79]. Finally, in addition to the bound and resonance states, a third class of eigenstates of the complex rotated Hamiltonian exists; those belonging to the continuum. Their energies are rotation angle dependant and complex and will be discussed more below.

Although the most obvious benefit offered by the method of complex scaling is the straightforward calculation of resonance parameters, the method has also other advantages. When it is used to calculate other atomic processes that involve the coupling to the continuum, for example, photoabsorption, convergence with respect to the number of basis states is achieved with surprisingly few states. The reason behind this is the properties of the so-called pseudo-continuum states, produced upon discretization of the complex rotated Hamiltonian. Such a pseudo-continuum state can represent outgoing electron flux in a much broader energy range than is possible with a unscaled Hamiltonian [62]. We illustrate this in Figure 5.2. Here, the hydrogen atom is exposed to a light pulse, and the probability that the atom remains in the ground state is displayed as a function of time. The black solid line shows the result using uniform complex scaling with only 30 basis functions (expressed in B-splines) per angular symmetry (ℓ). Without complex rotation many more basis states have to be used. Eventually, with 100 basis functions, we see that it seems as the result is converging toward the complex scaling result. The properties of the complex rotated pseudo-continuum will be discussed more below.

Complex rotation of the Hamiltonian, $H \to H^\theta$, is usually performed by a direct transformation of the radial variable: either uniformly,

$$r \to re^{i\theta}, \tag{8}$$

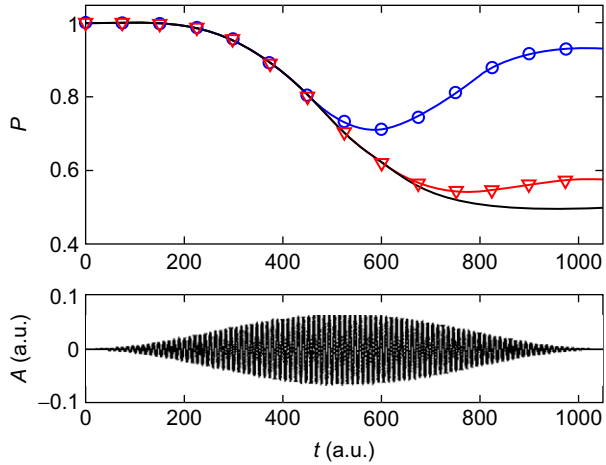

Figure 5.2 Hydrogen exposed to an electromagnetic field pulse with peak intensity $5.0 \cdot 10^{13}$ W/cm^2 and carrier frequency $\omega = 0.6$ a.u. ≈ 16 eV/$\hbar$. Upper panel: Population of the ground state computed *without* complex rotation (line with circles and line with triangles, respectively, 50 and 100 atomic states for each angular symmetry) and *with* complex rotation (black solid line, 20° and 30 states). The energy width associated with each rotated pseudo-continuum state explains the improved description. Lower panel: The vector potential describing the pulse.

or just outside some radius R_0 (exterior complex scaling), for example, in the form

$$r \to R_0 + (r - R_0)\, e^{i\theta}, \text{ for } r > R_0. \tag{9}$$

With the scaling in Eq. (8), the one-particle hydrogen-like Schrödinger equation without external fields transforms as

$$H = \frac{\mathbf{p}^2}{2\,m} - \frac{Ze^2}{4\pi\,\varepsilon_0 r} \to H^\theta = \frac{\mathbf{p}^2}{2\,m} e^{-2i\theta} - \frac{Ze^2}{4\pi\,\varepsilon_0 r} e^{-i\theta}, \tag{10}$$

while the sharp exterior scaling in Eq. (9) gives the Hamiltonian

$$H^\theta = \begin{cases} \frac{\mathbf{p}^2}{2\,m} - \frac{Ze^2}{4\pi\,\varepsilon_0 r} & \text{for } r < R_0, \\ \frac{\mathbf{p}^2}{2\,m} e^{-2i\theta} - \frac{Ze^2}{4\pi\,\varepsilon_0 r} e^{-i\theta} & \text{for } r > R_0. \end{cases} \tag{11}$$

The fact that the transformation in Eq. (9) has a cusp at $r = R_0$ and the implications for the Hamiltonian in Eq. (11), and its eigenstates have been discussed in Refs. [51, 58, 80].

At first sight, one might think that complex scaling is just a variable transformation. Since one does not expect a variable transformation to change

the description of the physics, one might wonder how useful it could be. In reality, however, we impose also some reasonable boundary conditions on the wavefunctions, and hereby we do affect which physical situation we describe. A solution to the unrotated Hamiltonian in (10) that lies in the continuum, that is, with a positive energy and a sinusoidal wavefunction at infinity, will after rotation grow exponentially as $r \to \infty$. Conversely, if one insists in seeking the solution to the secular problem in the space of square integrable functions, we will necessarily find nonreal eigenvalues. Indeed, the eigenvalues of the continuum of the rotated Hamiltonian, Eq. (10), are generally complex. The fact that this complexity arises due to the boundary conditions has been discussed in a pedagogically way by Reinhardt [9], and can be seen as follows. For large r, the continuum solution to the Schrödinger equation for hydrogen-like systems, the (regular) Coulomb function, is proportional to

$$\sim \sin\left(kr + \frac{Z}{ka_0}\ln\left(2kr\right) - \frac{\ell\pi}{2} + \sigma_\ell\right), \tag{12}$$

where a_0 is the Bohr radius and σ_ℓ is the Coulomb phase shift. Now, for uniform complex scaling $r \to r\exp\left(i\theta\right)$, and Eq. (12) transforms to

$$\sim \sin\left(kre^{i\theta} + \frac{Z}{ka_0}\ln\left(2kre^{i\theta}\right) - \frac{\ell\pi}{2} + \sigma_\ell\right). \tag{13}$$

The requirement that all eigenvectors, both the proper and the generalized ones, remain finite as $r \to \infty$

$$\limsup_{r\to\infty} |\Psi(r)| < \infty, \tag{14}$$

leads to the conclusion that k must also be rotated into the complex plane to compensate for the rotation of r. Since Eq. (12) approaches $\sin\left(kr\right)$ when $r \to \infty$ this amounts to the transformation $k \to k\exp\left(-i\theta\right)$, leading to

$$E_k \to E_k e^{-2i\theta}. \tag{15}$$

In practical implementations of complex scaling, the Hamiltonian is regularly discretized in finite space, for example, in a box of radius R. This yields a discrete pseudo-continuum with energies that fulfill $\mid E_k \mid e^{-2i\theta}$ for $Z = 0$ and approaches it with increasing k and R for $Z \neq 0$. If exterior complex scaling is made in such a finite box, Eq. (15) is adjusted to

$$E_k \to E_k e^{-2i\theta'},\ \tan\theta' = (1 - R_0/R)\tan\theta, \tag{16}$$

where R_0 is the scaling radius in Eq. (9). Equation (15) is recovered in the limit when $R \to \infty$. In conclusion, it is a combination of complex rotation and *boundary conditions* that results in complex energies for the pseudo-continuum. Although well known, see, for example, Ref. [81], this is not always pointed out in the literature on complex rotation.

It is illustrative to consider how a real calculation is done in some detail. In practice, a finite set of $L^2(\mathbb{R})$ functions, able to adequately describe the desired solutions, will span the domain to which the rotated Hamiltonian is eventually restricted. It is through the specification of these functions that the boundary conditions are enforced. With several widespread numerical basis functions, like, for example, B-splines [82] and finite-element discrete-variable-representation functions [83], this typically means that the functions themselves are restricted to a finite radial box and that they are capable of reproducing only a limited number of nodes. These approaches have the advantage of keeping the dimension of the space small, thus reducing computational costs. However, the use of any other suitable finite set of $L^2(\mathbb{R})$ functions will lead to equivalent results. Approximate eigenstates of the Hamiltonian can now be found by diagonalization of its matrix representation on the finite space. As a consequence of these restrictions, instead of a whole branching cut, we recover of course just a finite number of positive energy solutions, the so-called *pseudo-continuum*. Notice that one of the restrictions applied to the basis functions, i.e., that to a box of finite radius R, is equivalent to the addition of a potential $V(r) \to \infty$ for $r \geq R$, to the Hamiltonian. The original Hamiltonian and that of which we have a matrix representation will then only have those eigenstates in common, which are still adequately described within the restricted space. At first sight, it might seem as a severe limitation that the pseudo-continuum is so unphysical; in fact, it can thereby be an even better tool for the expansion of the physical continuum states. Before giving evidence of this claim, however, we need to discuss a more fundamental question, that is, how the inner product between functions of the complex scaled radius is to be defined.

2.1.1. Non-Hermitian Hamiltonians and the inner product

The correct form of the inner product is often just mentioned in passing when complex rotation is discussed, and then usually only for a rotation of an originally real matrix representation of the Hamiltonian. A clearer understanding can be obtained by going back to matrix algebra where the form of the inner product is a direct consequence of the symmetry of the matrix.

A general diagonalizable $n \times n$ matrix has n right (column) eigenvectors, $\mathbf{R}_i$, corresponding to n eigenvalues, λ_i. It also has n left (row) eigenvectors, $\mathbf{L}_i$, corresponding to the same n eigenvalues. Left and right eigenvectors associated with different eigenvalues are orthogonal to each other, i.e., $\mathbf{L}_i \cdot \mathbf{R}_j = 0$ if $\lambda_i \neq \lambda_j$. As is well known, the left eigenvector of a symmetric matrix (real or complex) is identical to the transpose of the corresponding right eigenvector,

while for a Hermitian matrix it also has to be complex conjugated. Below we derive a general relation between right and left eigenvectors to any matrix representing an *initially* Hermitian operator that has been complex rotated. The matrix representation of an unrotated Hermitian operator is a Hermitian matrix $\mathbf{B}$;

$$\mathbf{B} = \mathbf{B}_{\mathrm{Re}} + i\mathbf{B}_{\mathrm{Im}}, \tag{17}$$

where $\mathbf{B}_{\mathrm{Re}}$ and $\mathbf{B}_{\mathrm{Im}}$ are real and imaginary matrices. Since $\mathbf{B}$ is Hermitian, $\mathbf{B}_{\mathrm{Re}}$ is symmetric and $\mathbf{B}_{\mathrm{Im}}$ is antisymmetric, i.e.,

$$\mathbf{B}^{\mathrm{T}} = \mathbf{B}_{\mathrm{Re}} - i\mathbf{B}_{\mathrm{Im}}. \tag{18}$$

The matrix elements in both $\mathbf{B}_{\mathrm{Re}}$ and $\mathbf{B}_{\mathrm{Im}}$ will, for both uniform and exterior complex scaling, be built from terms which, when the matrix representation of the rotated operator is constructed, are multiplied with complex constants. This will make the matrices $\mathbf{B}_{\mathrm{Re}}$ and $\mathbf{B}_{\mathrm{Im}}$ complex, but they will still be symmetric and antisymmetric, respectively, with respect to transposition, i.e.,

$$\left(\mathbf{B}^{\theta}\right)^{\mathrm{T}} = \mathbf{B}^{\theta}_{\mathrm{Re}} - i\mathbf{B}^{\theta}_{\mathrm{Im}}. \tag{19}$$

We now return to the question of how a left eigenvector to a matrix relates to the corresponding right eigenvector. According to the definition, a left eigenvector to a matrix $\mathbf{B}$ is a row vector, $\mathbf{L}$, that fulfills

$$\mathbf{L}\mathbf{B} = \lambda\mathbf{L}. \tag{20}$$

When the transpose is taken of both the left- and the right-hand side of Eq. (20), it reads

$$\begin{aligned} (\mathbf{L}\mathbf{B})^{\mathrm{T}} &= \lambda\mathbf{L}^{\mathrm{T}} \\ &\Longleftrightarrow \\ \mathbf{B}^{\mathrm{T}}\mathbf{L}^{\mathrm{T}} &= \lambda\mathbf{L}^{\mathrm{T}}. \end{aligned} \tag{21}$$

Before proceeding, we note that if $\mathbf{B}$ is symmetric, $\mathbf{B}^{\mathrm{T}} = \mathbf{B}$, Eq. (21) is identical to the corresponding right eigenvalue equation and thus $\mathbf{L}^{\mathrm{T}} = \mathbf{R}$. If we further take the complex conjugate of Eq. (21), we get

$$\begin{aligned} \mathbf{B}^{\mathrm{T}*}\mathbf{L}^{\mathrm{T}*} &= \lambda^{*}\mathbf{L}^{\mathrm{T}*} \\ &\Longleftrightarrow \\ \mathbf{B}^{\dagger}\mathbf{L}^{\dagger} &= \lambda^{*}\mathbf{L}^{\dagger}. \end{aligned} \tag{22}$$

We see that if $\mathbf{B}$ is Hermitian, i.e., $\mathbf{B}^{\dagger} = \mathbf{B}$, λ is real and Eq. (22) is identical to the corresponding right eigenvalue equation, and consequently $\mathbf{L}^{\dagger} = \mathbf{R}$. For

the matrix in Eq. (19), which has the symmetry of the matrix representation of the rotated Hermitian Hamiltonian, we have

$$\left(\mathbf{B}^{\theta}\right)^{\dagger} = \left(\mathbf{B}^{\theta}_{\mathrm{Re}}\right)^{*} + i\left(\mathbf{B}^{\theta}_{\mathrm{Im}}\right)^{*}. \tag{23}$$

Since all the complexity in the matrices $\mathbf{B}_{\mathrm{Re}}$ and $\mathbf{B}_{\mathrm{Im}}$ comes from the complex constants introduced through complex rotation, complex conjugation simply means that $\exp(i\theta) \to \exp(-i\theta)$, which identically gives the matrix representation of the operator rotated with $-\theta$, i.e.,

$$\left(\mathbf{B}^{\theta}\right)^{\dagger} = \mathbf{B}^{-\theta}_{\mathrm{Re}} + i\mathbf{B}^{-\theta}_{\mathrm{Im}} = \mathbf{B}^{-\theta}. \tag{24}$$

From Eq. (22) it now follows that

$$\begin{aligned} \left(\mathbf{B}^{\theta}\right)^{\dagger}\mathbf{L}^{\dagger} &= \lambda^{*}\mathbf{L}^{\dagger}, \\ \mathbf{B}^{-\theta}\mathbf{L}^{\dagger} &= \lambda^{*}\mathbf{L}^{\dagger}, \end{aligned} \tag{25}$$

and we can conclude that the left eigenvectors of the matrix after rotation with θ are the complex conjugated transpose of the right eigenvectors to the matrix after rotation with $-\theta$,

$$\mathbf{L}^{\theta} = \left(\mathbf{R}^{-\theta}\right)^{\dagger}, \tag{26}$$

where the eigenvalue associated with $\mathbf{R}^{-\theta}$ is λ^{*} if that associated with $\mathbf{L}^{\theta}$ is λ. Equation (26) is valid for left eigenvectors of all matrices, symmetric or not, produced by complex rotation of an initially Hermitian matrix. The ordinary Hermitian relation is found as a special case when $\theta = 0$. Likewise, the complexity of the eigenvectors of a complex symmetric matrix, obtained when an originally real matrix is complex rotated, originates from the complex rotation only, and thus $\mathbf{R}^{-\theta} = \mathbf{R}^{*}$. Then, Eq. (26) gives the familiar result that the left eigenvectors are just the transpose of the right ones. For the general case, for example, when the interaction with an external field is treated in velocity gauge no easy recipe exists to find the left eigenfunctions and one has to restore to Eq. (26).

2.1.2. Continuum representation

We can now return to the question of the representation of an outgoing wave with a complex rotated pseudo-continuum. An interesting example is the outgoing component of a resonance state, for example, a doubly excited state in a two-electron system, for example, with the Hamiltonian

$$H_{12} = \sum_{i=1,2}\left(-\frac{\hbar^2}{2m}\nabla_i^2 - \frac{e^2}{4\pi\varepsilon_0}\frac{Z}{r_i}\right) + \frac{e^2}{4\pi\varepsilon_0}\frac{1}{r_{12}}. \tag{27}$$

For transparency, we now use exterior complex scaling [Eq. (9)]. With $Z = 2$ the lowest resonance of ^1S-symmetry is known to be ~ -0.78 a.u., see, for example, Ref. [15]. The bound part is dominated by $2s^2$ and the outgoing component is $1s\,\varepsilon s$. Projection of the resonance wavefunction onto $1s$ should then, for large enough r, gives an outgoing Coulomb wave

$$\phi^k_{\ell=0}(r) = -iA\left\{G_\ell(\eta, kr) + iF_\ell(\eta, kr)\right\}e^{i(\delta)}, \quad \eta = -\frac{e^2}{4\pi\varepsilon_0}\frac{Zm}{\hbar^2 k}, \tag{28}$$

composed of regular (F) and irregular (G) Coulomb functions and which asymptotically approaches,

$$\phi^k_{\ell=0}(r) \sim Ae^{i\left(kr-\eta ln(2kr)-\frac{\ell\pi}{2}+\sigma_\ell\right)}e^{i\delta}, \tag{29}$$

where σ_ℓ is the Coulomb phase and δ is an additional resonance phase shift. The resonance wavefunction has a complex eigenenergy, resulting in a complex k

$$k_i = \frac{\sqrt{2m(E-E_i)}}{\hbar} = \frac{\sqrt{2m}}{\hbar}\sqrt{|E-E_i|}e^{-i\gamma_i/2}, \quad \gamma_i = \arctan\frac{\Gamma/2}{E_r - E_i}, \tag{30}$$

where E_i is the energy of the remaining ion. We note in passing that the imaginary part is negative and will cause e^{ikr} to grow exponentially with r. A constraint on the complex rotation of the radial coordinate r is thus that it has to be large enough to compensate this growth in order for the resonance wavefunction to be normalizable. For uniform complex scaling, this gives the familiar condition $\theta > \gamma_i/2$. For exterior complex scaling, the same condition holds for θ' in Eq. (16), and thus a larger angle is needed for finite values of R_0/R. The projection of the resonance wavefunction onto $1s$ is shown in Figure 5.3. The dashed line shows the extracted component of the numerical resonance wavefunction, while the thin line shows the comparison with the analytic Coulomb function in Eq. (28), generated with the routine provided in Ref. [84], and then scaled and phase shifted to fit. Only the imaginary parts of the complex wavefunctions are plotted for clarity. The agreement is nearly perfect in the unscaled region $r < R_0$, here $R_0 = 20$ Bohr radii. A small difference is found only close to the nucleus, basically inside the $1s$-electron probability density, as can be seen in Figure 5.4. This difference reflects the effect on the resonance wavefunction from the non-Columbic potential. Outside R_0 the extracted component of the numerical resonance wavefunction is rapidly decaying due to the exponential suppression of e^{ikr} from the imaginary part of r.

It is evident that the pseudo-continuum states are able to give a good representation of the outgoing wave. In fact, this representation is even superior with complex rotation, as indicated in Figure 5.2. The reason for this

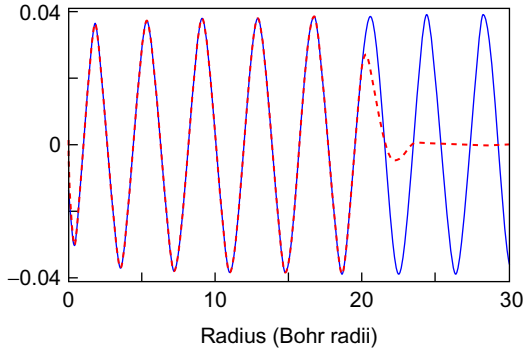

Figure 5.3 Thick dashed line: A wavefunction, associated with the $(2s^2)^1S$ resonance in helium, projected onto He^+ $(1s)$. The obtained function describes the outgoing wave (here only the imaginary part of the wavefunctions is plotted). The radial coordinate is complex rotated for $r > 20$ Bohr radii. Thin solid line: Coulomb function with complex k. Phase shifted and scaled to fit.

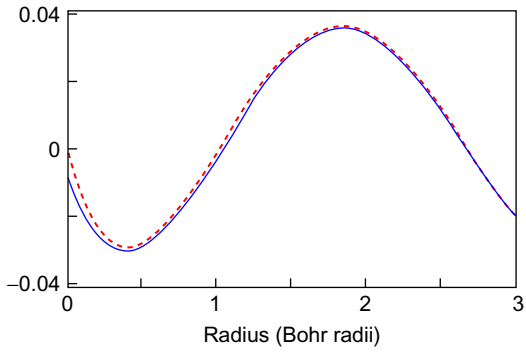

Figure 5.4 The same functions as displayed in Figure 5.3, but for the innermost region.

is that the energy interval represented by a certain pseudo-continuum state increases in the complex rotated case, and this interval increases further with scaling angle. This phenomenon is illustrated in the case of uniform complex scaling in Figure 5.5, which shows the projections of a particular box normalized complex rotated eigenstate, $\Phi^{\theta}_{n,\ell,m}(\mathbf{r})$, onto rotated continuum functions for the hydrogen atom, $\psi^{\rm out}_{k,\ell,m}(\mathbf{r}e^{i\theta})$, where the radial part is given by Eq. (28). More specifically, the figure shows

$$F^{\theta}_{n,\ell,m}(k) \equiv \int_0^R \left(\Phi^{-\theta}_{n,\ell,m}(\mathbf{r})\right)^* \psi^{\rm out}_{k,\ell,m}(\mathbf{r}e^{i\theta}) e^{3i\theta} \mathrm{d}V, \tag{31}$$

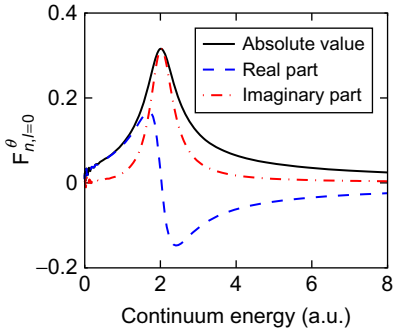

Figure 5.5 The figure shows the projection of a box normalized pseudo-continuum state onto rotated analytical continuum states with outgoing, plane wave asymptotic behavior, i.e., $F^{\theta}_{n,\ell,m}$ in Eq. (31). The *x*-axis shows the energy of the analytical continuum states. The half width of the distribution increases with increasing θ. More specifically, the width of $|F^{\theta}_{n,\ell,m}|^2$ coincides quite well with twice the absolute value of the imaginary part of the energy of the box normalized pseudo-continuum state, $\mathrm{Im}(E_n)$. This particular case corresponds to the $\ell = 0$ channel with the scaling angle $\theta = 5^\circ$ and a box state with $\mathrm{Re}(E_n) = 2.0$ a.u.

where the factor $e^{3i\theta}$ is just due to the choice of normalization [62]. The left function, $(\Phi^{-\theta}_{n,\ell,m}(\mathbf{r}))^*$, coincides with $\Phi^{\theta}_{n,\ell,m}$ since all complexity arises from the complex scaling in this case. The eigenenergy corresponding to the box normalized state in Figure 5.5 is complex, whereas the eigenenergies of the $\psi^{\mathrm{out}}_{k,\ell,m}$-states are real. For the illustration in Figure 5.5, a "box energy" E^{θ}_n with a real part of 2.0 a.u. is chosen, the angular quantum number ℓ is zero and the scaling angle θ is 5°. The figure clearly shows a broad distribution in the projection $F^{\theta}_{n,\ell=0}$ centered around the real part of E^{θ}_n. The width of the distribution is dictated by the scaling angle θ.

If we, in the $\ell = 0$ channel, neglect the Coulomb potential, both the outgoing wave and the pseudo-continuum states have very simple analytical forms; the reduced wavefunctions are $r\exp(i\theta)\psi^{\mathrm{out}}_{k,\ell=0} = \sqrt{2/\pi}\ \exp(ikr\exp(i\theta))$ and $r\exp(i\theta)\Phi^{\theta}_{n,\ell,m}(\mathbf{r}) = \sqrt{2/R}\ \sin(k_n r)$ with $k_n = n\pi/R$. The latter wavefunction is thus unaffected by the complex scaling, although the energy E^{θ}_n is, as in the Coulomb case, complex: $E^{\theta}_n = (\hbar k_n)^2\ \exp(-2i\theta)/2\,m$, cf. the relation in Eq. (15). In this context, the projections $F^{\theta}_{n,\ell}$ may be found analytically:

$$\left|F^{\theta}_{n,\ell=0}\right|^2 = \frac{2\hbar^2}{\pi m R}\ \frac{|E^{\theta}_n|}{|E^{\theta}_n|^2 + \varepsilon_k^2 - 2|E^{\theta}_n|\,\varepsilon_k\cos(2\theta)}, \tag{32}$$

with $\varepsilon_k \equiv (\hbar k)^2/2\,m$. Although the neglect of the Coulomb potential is a rather crude approximation, the simple function of Eq. (32) exhibits most of the relevant features of the one that includes the Coulomb potential. For fixed

"box energy" E_n^θ, the function has its maximum value for

$$\varepsilon_k = |E_n^\theta| \cos(2\theta) = \mathrm{Re}(E_n^\theta), \tag{33}$$

and the half width is

$$\frac{\Delta\varepsilon_k}{2} = |E_n^\theta| \sin(2\theta) = \mathrm{Im}(E_n^\theta). \tag{34}$$

Numerical inspection shows that the identification of the maximum of $|F_{n,\ell}^\theta|^2$ with the real part of E_n^θ, as well as that of the half width of $|F_{n,\ell}^\theta|^2$ with the imaginary part of E_n^θ, remains very reasonable estimates also when the Coulomb potential is included. This analysis explains the much improved basis set convergence with complex scaling discussed in connection with Figure 5.2.

3. RESONANCES IN ELECTRON–ION RECOMBINATION

As an example of a process where resonances are truly important, we will now discuss electron–ion recombination. The interest in this process is due to several practical applications and to very fundamental questions. It appears as an important process in astrophysical plasmas [85], the chemistry of interstellar clouds [86], modeling of supernova reminiscence, and earth atmosphere, and in fusion plasma [87]. Recombination can cause significant energy losses from plasma as being a source for radiation. This radiation has, on the other hand, proven to be a valuable tool for plasma diagnostics. In fact, the resonant process dielectronic recombination (DR) (see below) was postulated to explain discrepancies in the ionization balance of the solar corona [88, 89]. Much of the energy transport and reactions in these plasma and media occur as electrons collide with atomic and molecular ions. In such collisions, the ions can be excited or further ionized, or the electrons can recombine leading to emission of photons, excitation of ions, or dissociation of molecules. Electron–ion recombination occurring in fusion or astrophysical plasma provides also a tool for their spectroscopic investigations. On the fundamental level, studies of electron–ion impact phenomena can be very useful for developing our understanding of the structure and decay modes in many electron systems. During the last decade, recombination studies obtained a decisive role also in fundamental atomic spectroscopy [16, 27–35, 90–95]. This is due to the possibilities given by coolers in storage rings and by electron-beam ion traps (EBITs), which allow measurements of electron-impact ionization and recombination with unprecedented resolution and luminosity. They can serve, for example, as testing grounds for highly accurate calculations of energy levels in few electron ions.

The most fundamental process in the interaction of free electrons with ions is radiative recombination (RR). Here, a photon is directly emitted with the capture of an electron into the quantum state n of the ion $A^{(q-1)}$, cf. process (35). This process can happen for any collision energy, i.e., it is *nonresonant*. In DR, process (36), on the other hand, a free electron is captured simultaneously with the excitation of a bound electron in the ion. Due to energy conservation, the binding of the captured electron plus its kinetic energy must equal the excitation energy of the bound electron, the process can thus only happen when the incoming electron is on *resonance*. The resulting resonance (or doubly excited) state (n', n'') will generally have a very large probability to autoionize and loose the electron again, but it may emit a photon and end up in a state (n''') below the ionization threshold. This last step completes DR. RR and DR are the dominating processes for electron–ion recombination in dilute plasma. Additional processes have though to be considered for dense and cold plasma (three-body recombination) and for molecules (dissociative recombination). Schematically, we write RR and DR as

$$A^{q+} + e^- \longrightarrow A^{(q-1)+}(n) + \hbar\omega, \tag{35}$$

$$+ e^- \longrightarrow A^{(q-1)+}(n', n'') \longrightarrow A^{(q-1)+}(n''') + \hbar\omega, (q < Z) \tag{36}$$

and note that these processes are the time-inverse of photoionization. In Eqs. (35) and (36), Z is the nuclear charge and q is the charge state. Both processes can be described as photorecombination and can in principle provide two different pathways between the same initial and final states (that is when $n = n'''$), thus there is a possibility of interference which would lead to asymmetric line profiles [96] in the recombination spectra. In contrast to the situation for photoionization, however, such an interference is seldom seen in experiments. There are several reasons for this. First, overlapping resonance profiles often mask the underlying asymmetry. Overlapping resonances are much less seen in photoionization due to the high selectivity for the dominating dipole transitions. Here, resonances of all angular and spin symmetries will contribute rather equally. Second, process (35) populates mainly the ground state, while process (36) predominantly populates excited states. Thus, the dominating contributions are really to different final states and do not contribute to any asymmetry. Measurements that sum over all final states that contribute to recombination, as storage ring experiments, will then hardly see any asymmetry. In EBITs, however, both the recombined ion and the photon in Eqs. (35) and (36) are detected. Then, the recombination to a single final state can be isolated, and Fano profiles have indeed been reported [97, 98]. These studies were also made on highly charged ions, resulting in an increased yield of the RR process and thereby also in an increased asymmetry.

It is worth noting that the cross section for recombination scales as the inverse of the collisional energy, and thus goes to infinity when the electron energy goes to zero, which is another way of saying that the probability for recombination then goes to unity. The rate coefficients, i.e., the cross section times the electron velocity is, however, always finite. Still it is primarily the lowest energy region that can be dominated by recombination through process (35). The left panel of Figure 5.6 shows a storage ring measurement [99, 100] (shaded area) of sodium-like silicon recombining into magnesium-like silicon. The peak at zero relative energy is due to RR. The remaining spectrum is, however, completely dominated by the resonant process of DR. The rate coefficient maps out the resonances of the ion , which is clearly seen when the experimental data are shown together with the level scheme of the doubly excited states as it is done in Figure 5.6. The energy region displayed is just up to 1.4 eV above the Si^{2+} ionization threshold, and the recombination is due to 28 resonances, mostly of $3p4\ell$-type. For systems with a more complicated shell structure, the density of resonances can be much higher. So high in fact that individual resonances cannot be distinguished and are only seen as an increased recombination level. One of the most prominent example of this phenomena is the system of Au^{25+} [101]. For such cases, the predictive power of theory is still very small. Evidently, methods that have been developed for an accurate description of every resonance might not be the best way forward. One possibility would be to use statistical methods as has been advocated by Gribakin *et al*. [102–104].

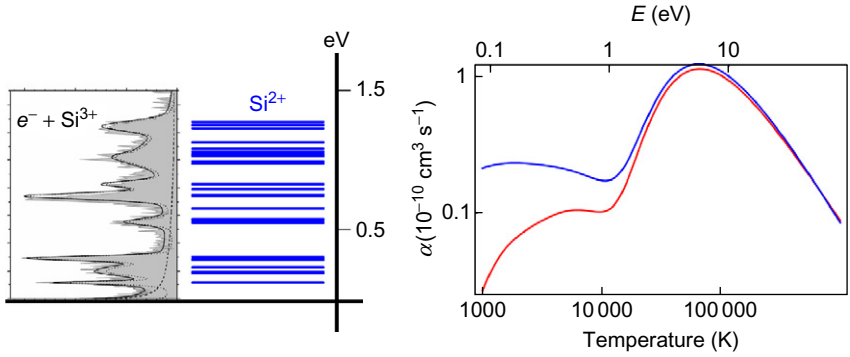

Figure 5.6 The left panel shows storage ring results [100] in the form of rate coefficients (shaded area) for Si^{3+} recombining into Si^{2+}. The thick line is the calculated cross section [100] folded with the electron beam temperature. The energies of the resonant states (doubly excited states) in Si^{2+} are shown in the form of a level scheme. It is obvious that the rate coefficients map out the energy level scheme. The right panel shows the rate coefficients as a function of temperature. The upper black line shows the storage ring results folded with a Maxwellian energy distribution, see [99], while the lower grey curve shows a theoretical prediction [107].

In storage rings, cold electrons collide with cold ions and the recombination can be studied as a function of the tunable relative energy, see Refs. [105, 106] for recent reviews. For plasma physics applications, it is more common to show the rate coefficient as a function of temperature. In a plasma, it is the finite energy distribution, given by the temperature, that can tune the electrons into resonance with the doubly excited states of the recombined ion. Rate coefficients displayed in this way are shown in the right panel of Figure 5.6. Here, the black (upper) line shows the storage ring results from the left panel (although for a wider energy range) folded with a Maxwellian energy distribution, see [99] for details, while the grey (lower) curve shows a calculated prediction [107]. In Ref. [107], data for 22 sodium-like ions between Mg^{+} and Xe^{43+} were presented as a part of a larger effort to provide recombination data for all astrophysically relevant ions. Calculated data, obtained with the so-called AUTOSTRUCTURE code, was then converted to a simple formula with fitting coefficients. We can see that the agreement is good for high temperatures. In this region, the recombination rate is given by a large number of resonances where the exact position of each is not very crucial. For low temperatures (and thus mainly low collision energies), the situation is very different. Details in the treatment of the system-like many-body effects, relativistic effects, etc. are able to shift resonances below, closer to, or further away from threshold, thereby dramatically changing the recombination rate prediction. This energy region is accordingly not at all as well represented with the data from the codes developed to efficiently address a large number of resonances and here we see a large discrepancy in Figure 5.6. Now, sodium- and magnesium-like ions have in fact a rather simple electronic structure and hence it is possible to perform full many-body calculations for these systems. Such a calculation is of course more tedious and can in practice only be carried out for selected cases and selected energy ranges. The solid black line in the left picture of Figure 5.6 shows results from such a more dedicated effort with relativistic MBPT (RMBPT) [100]. It is clear that it agrees well and on an absolute scale with the experiment. Figure 5.7 shows more details from the calculation. For such low-charged systems as Si^{2+} and Si^{3+}, it is the electron correlation that provides the largest obstacle for the calculation, and from Figure 5.7, it is evident that precise determination of many resonance positions is necessary for good agreement with experiment. However, relativistic effects are not at all unimportant for light systems. One obvious example can be the broad peak around 0.2 eV in Figure 5.7. The three calculated peaks, slightly shifted compared to each other, are the three fine-structure components of a resonance of ^{3}F-symmetry. A more important relativistic effect is though that several resonances are only coupled to the continuum due to spin–orbit coupling, i.e., without relativistic effects they would neither autoionize nor contribute to recombination. One example of this is the narrow peak at ∼0.1 eV. It has odd parity and is of ^{1}D-symmetry, but in the decay channel $3s\varepsilon\ell_j$ an odd ℓ

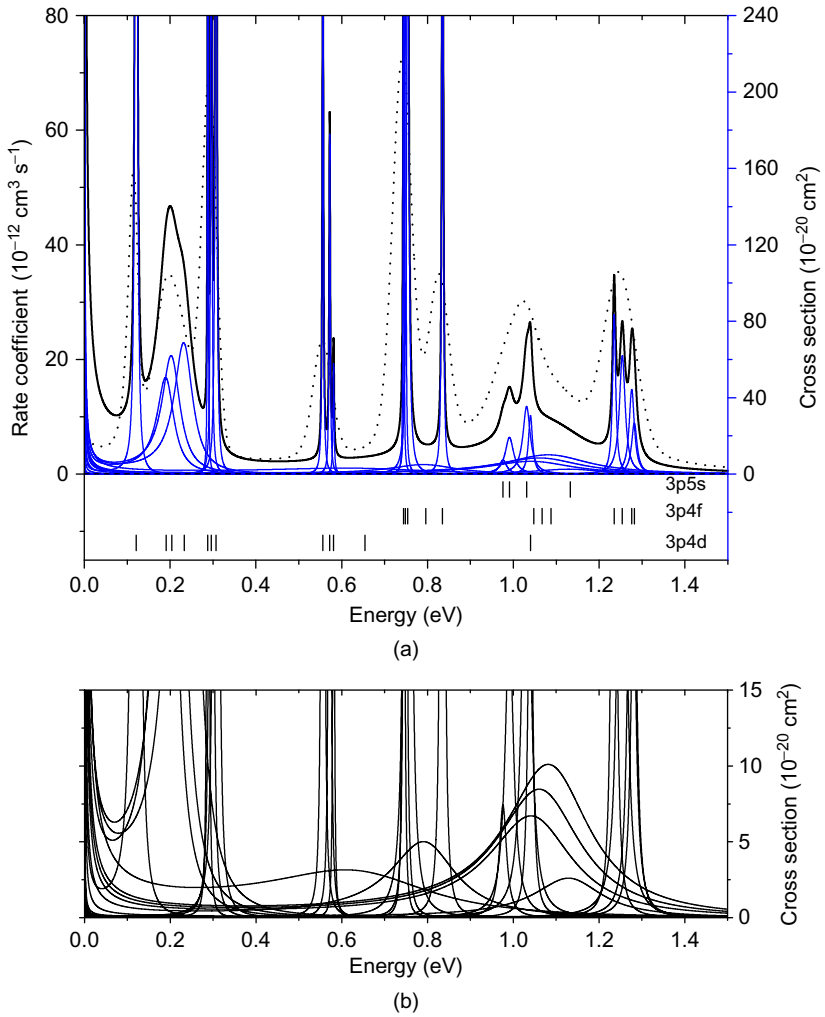

Figure 5.7 (a) Individual cross sections of the low-energy DR resonances, obtained by the RMBPT calculation, are shown by thin solid lines with the corresponding electron configurations indicated by vertical bars. The thick solid line (black) shows the total DR cross section (sum of all individual DR resonances). Dots show the rate coefficients obtained from the convolution of the total DR cross section with the velocity distribution of the electrons from the experiment. (b) A zoomed view of the individual DR cross sections, to emphasize the wide resonances.

cannot couple to total $L = 2$, and this would prohibit Auger decay, as well as dielectronic capture, in a nonrelativistic description. Still the contribution to the recombination rate is important, and this is due to the fact that recombination depends on the probability to form the resonance state times

the probability that is stabilize, i.e., to

$$A_a^{\mathrm{c}} \frac{\sum_i A_r^i}{\sum_k A_r^k + \sum_j A_a^j}, \tag{37}$$

where A_a^{c} denote the dielectronic capture rate (equal to the Auger rate), A_r a radiative rate, and the sum over i runs over all photon transitions leading to a state below the ionization thresholds, while those over k and j over all possible transitions from the state through either radiative or Auger decay. For resonances lying closely above the ionization threshold autoionization is usually a very strong process with a probability roughly scaling as $1/\varepsilon_e$, the energy of the ejected electron. It dominates thus over radiative transitions with many orders of magnitude, and just over the first ionization threshold, Eq. (37) will then approximately equal $\sum_i A_r^i$. Even if autoionization has to occur through an LS-forbidden channel, its rate is often larger, or of the same order as, the radiative rate, and thus the recombination rate is not much affected. This is the reason why nonrelativistically forbidden transitions can have a large influence.

3.1. Precision studies through resonances in electron–ion recombination

Finally, we would like to mention the development of DR studies into a new spectroscopical tool. An early example where such resonances were used to accurately determine an excitation energy in a highly charged ion was the $4p_{1/2}$–$4s$ splitting in copper-like lead [29] which was determined with an accuracy of ∼1 meV, corresponding to a precision of 8×10^{-6}. During later years, it has been possible to study hyperfine structure and isotope shifts through DR resonances [95, 108, 109]. In Ref. [95], the $2s_{1/2}$–$2p_{3/2}$ transition energy in lithium-like scandium was determined with an accuracy of 4.6 ppm. Hereby, the evaluation of radiative contributions such as self-energy and vacuum polarization in a many electron environment can be put to a stringent test as discussed in Ref. [95]. We will discuss the method with this system as the example.

The method is based on the nearly complete cancellation between the target excitation energy and the binding energy of the attached electron for certain low-energy resonances. For a lithium-like system, a resonance can be formed in the following way;

$$e^- + A^{q+}\left(1s^2 2s_{1/2}\right) \longrightarrow A^{(q-1)+}\left(1s^2 2p_j n\ell_{j'}\right), \tag{38}$$

where $E(1s^2 2p_j n\ell_{j'}) > E(1s^2 2s_{1/2})$. For a highly charged system, the state $n\ell_{j'}$ will be a Rydberg state; for lithium-like Sc^{18+}, the lowest resonances are

found for $n = 10$ and for Kr^{33+} for $n = 15$. The resonance will be found at energies

$$\varepsilon = E\left(1s^2 2p_j\right) - E\left(1s^2 2s\right) - \Delta E, \tag{39}$$

where ΔE is the binding energy of the outer Rydberg electron. This binding energy can be accurately determined by calculations since it is dominated by the Dirac energy and only small corrections are given by many-body effects. With $Z = 18$, the Dirac hydrogen-like binding energy is 44.114 29 eV for $10d_{3/2}$ and 44.101 57 eV for $10d_{5/2}$. This value is thus obtained under the assumption that the core screens exactly three units of charge. If we include the interaction with the inner $1s^2$ core through the Dirac–Fock potential we obtain instead 44.213 87 and 44.200 09 eV, respectively, and adding also the Breit interaction and true correlation effects from the $1s^2$ core we get a further, but slight, change to 44.214 58 and 44.200 93 eV. It remains now to add the interaction with the $2p$-electron. This interaction is term dependent and we see in Table 5.2 the results for the three lowest resonances $(2p_{3/2}10d_{3/2})_{J=2}$, $(2p_{3/2}10d_{3/2})_{J=3}$, and $(2p_{3/2}10d_{5/2})_{J=4}$. The first line, labeled first-order Coulomb interaction, gives the results after diagonalization of the Hamiltonian matrix of all $2p_j 10\ell_{j'}$ configurations, coupled to one specific J. In particular, this means that $(2p_{3/2}10d_{3/2})_J$ and $(2p_{3/2}10d_{5/2})_J$ are allowed to mix. We see in

Table 5.2 Binding energies for the lowest lying $Sc^{17+}(1s^2 2p_{3/2}10d_j)_J$ resonances relative $Sc^{18+}(1s^2 2p_{3/2})$ (results in eV)

	$J = 2$	$J = 3$	$J = 4$
Orbital energies (see text) + Coulomb interaction first order	44.27255	44.23494	44.27570
Breit interaction first order	−0.00063	0.00002	0.00013
Mass polarization first order	0.00002	0.00001	0.00005
Coulomb interaction second order	0.00288	0.00574	0.00383
Breit–Coulomb second order	0.00000	0.00002	0.00000
Higher-order Coulomb correlation	0.00008	0.00001	−0.00011
Core polarization of $2p_{3/2}10d_j$ interaction	−0.00011	−0.00004	−0.00044
Total	44.27480 (11)	44.24071 (9)	44.27916 (11)
Experimental [95]	0.03465 (10)	0.06861 (10)	0.03036 (10)
Extracted energy splitting in Si^{18+} $1s^2 2p_{3/2}$–$1s^2 2s_{1/2}$	44.30945 (15)	44.30932 (15)	44.30952 (15)

Table 5.2 that the results for the three terms are now changed by up to 70 meV compared to the situation before adding the detailed interaction with the $2p$ electron. After inspection of the other entries in Table 5.2, we can conclude that only two types of contributions, namely from the core Dirac–Fock potential discussed above and from the first-order Coulomb matrix element, are in the 10 meV range. These effects are well defined and can be unambiguously calculated. At the next level, contributions of a few meV are coming from true electron correlation, while additional interactions and higher-order effects give even smaller contributions. It is the smallness of all these contributions that gives the high accuracy with which the binding energy can be calculated for a Rydberg electron. The errors given for the calculated values in Table 5.2 represent neglected contributions from high partial-wave angular momenta ($\ell = 12$–∞) contributions to the second-order correlation energy as well as uncalculated higher-order correlation, conservatively estimated from the calculated all-order ladder diagram (sixth line in Table 5.2). Now these calculated Rydberg electron binding energies can be combined with the measured resonance positions [95] to extract the target excitation energy. Since we have results for three resonances, it can be done in three different ways. The results are shown in Table 5.2. The three resonances provide slightly different results for the $2p_{3/2}$–$2s_{1/2}$ energy splitting, but the differences are within the estimated error bars confirming the expected accuracy of the method.

4. COMPLEX ROTATION AND THE DIRAC EQUATION

There is a large number of nonrelativistic studies with complex rotation in the literature. Although much less is done with the Dirac equation, calculations on resonant electron–ion recombination (cf. Section 3) and on unstable core-hole states in heavy elements [110, 111], as well on Stark Shift [39] have been shown to give reliable results. In the case of electron–ion recombination, the relativistic effects are much larger than one would naively assume. In most systems, there are states above the ionization limit that cannot autoionize in LS-coupling, of symmetry reasons. Neither can they then contribute to recombination. In many cases, some admixture of an other spin or angular momentum symmetry, generated by spin–orbit coupling, would open the path to autoionization. Although it may seem contra intuitive, this non relativistically forbidden decay mode can be the most probable decay path the state takes after being formed in an electron–ion collision, even for rather lighticons ions. This can be understood from the fact that when autoionization is nonrelativistically allowed it often dominates over radiative decay with orders of magnitude and thus even a tiny admixture of a component that can decay by autoionization, can suffice to make this path important. In connection with a process such as DR, these states can then contribute significantly. Important nonrelativistically forbidden resonances have been found

in the recombination spectra of most Li-like ions and in some cases, as for recombination of C^{3+} [27], they are dominating.

We start from the Dirac one-particle Hamiltonian for an electron bound to a point nucleus

$$h = c\alpha \cdot \mathbf{p} + (\beta - 1)\, mc^2 - \frac{e^2}{4\pi\varepsilon_0}\frac{Z}{r} = \begin{pmatrix} -\frac{e^2}{4\pi\varepsilon_0}\frac{Z}{r} & c\sigma \cdot \mathbf{p} \\ c\sigma \cdot \mathbf{p} & -\frac{e^2}{4\pi\varepsilon_0}\frac{Z}{r} + 2\,mc^2 \end{pmatrix}. \quad (40)$$

The scaling of the radial coordinate with a complex constant, $e^{i\theta}$, as in Eq. (8) gives then the scaled Hamiltonian

$$h = \begin{pmatrix} -\frac{e^2}{4\pi\varepsilon_0}\frac{Z}{re^{i\theta}} & c\sigma \cdot \mathbf{p}\, e^{-i\theta} \\ c\sigma \cdot \mathbf{p}\, e^{-i\theta} & -\frac{e^2}{4\pi\varepsilon_0}\frac{Z}{re^{i\theta}} + 2\,mc^2 \end{pmatrix}. \quad (41)$$

Following the discussion in Section 2.1, we will use a matrix representation of the Dirac Hamiltonian. One possibility is to discretize Eq. (40) on a lattice in a spherical box as described in Ref. [112], yielding an eigenvalue problem that can be solved using standard matrix techniques. With complex rotation, the real symmetric matrix in Ref. [112] will instead be complex symmetric. In Section 2.1, we discussed that the pseudo-continuum solutions, found as eigenstates to the matrix representation of the Schrödinger equation, have complex energies that approximately scale as $E_k \to E_k e^{-2i\theta}$, see Eqs. (13)–(15). In the relativistic case, we will find the same behavior for low-energy pseudo-continuum states. This is illustrated in Figure 5.8 where the solid line shows the expected rotation of 2θ and the dots the calculated $s_{1/2}$-spectrum energies for one electron in the potential from a helium nucleus, showing clearly this trend above zero energy. The dots falling on the x-axis are eigenvalues to the bound states well represented in the box. For energy states with a kinetic energy much larger than mc^2, the diagonal terms in Eq. (41) will be

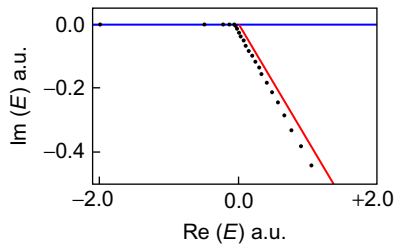

Figure 5.8 Energy eigenvalues (dots) of the discretized and complex rotated one-particle Dirac Hamiltonian with s-symmetry. Bound states that are well represented in the box and on the grid are lying on the x-axis. The low-energy pseudo-continuum states are rotated with an angle of approximately 2θ (where θ is the complex rotation angle) down from the real axis, as indicated with the straight solid line.

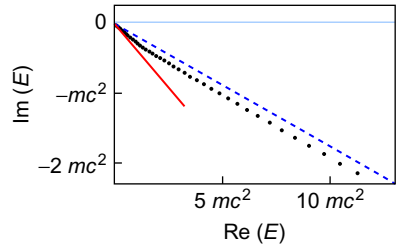

Figure 5.9 Energy eigenvalues (dots) to the discretized and complex rotated one-particle Dirac Hamiltonian with *s*-symmetry. The high-energy pseudo-continuum states are rotated with an angle θ (indicated with the dashed line) down from the real axis, where θ is the complex rotation angle. For low energies, the line of dots bends and approaches the solid line, which indicates the expected rotation of 2θ in the nonrelativistic domain.

small and the equation will tend toward uncoupled first-order differential equations leading to $\mathrm{Re}\,(E)\,/\mathrm{Im}\,(E) = -\tan\theta$. This is illustrated in Figure 5.9 where the calculated points tend to the dashed line for high energies. The different behavior for low-energy states close to zero energy is seen as a bending when the calculated points approach the dashed line.

An important point to consider when the Dirac equation, Eq. (40), is considered is that it has also eigenstates with energies below $-2\,mc^2$. This negative energy continuum should be considered as filled in vacuum and is only available for electrons if an electron–positron pair has been previously created. The situation is similar to that when there is a more or less inert core inside the active electrons. The Pauli principle then prevents transitions into the core states if not a hole has been previously created. Two choices are then possible: either one is satisfied with the inert core approximation or one keeps track of the creation and refilling of core-holes, with the help of second quantization. To create a real electron–positron pair, at least $2\,mc^2$ of energy is needed. Although virtual pairs do still contribute to all bound state energies, the large energy difference between positive and negative energy solutions makes the virtual pair contribution very small, of the order $\alpha^3 Z^3$ a.u., and thus this is a rather insignificant effect for all but the heaviest atoms. The contribution has been calculated for the helium ground state in Ref. [113] and is there found to be below 10^{-7} a.u. For doubly excited states, the contribution should be even smaller and virtual creation of electron–positron pairs can usually be safely neglected, i.e., the vacuum can be treated as an inert core. The negative energy continuum states should then not be allowed to mix into the wavefunction, which formally means that the two-electron operators in the two-particle Hamiltonian should be surrounded by projection operators [114]

$$H = \sum_{i=1}^{2} h_i + \mathcal{V}_{12} = \sum_{i=1}^{2} h_i + \Lambda_1^+ \Lambda_2^+ V_{12} \Lambda_1^+ \Lambda_2^+. \tag{42}$$

When working on a positive energy solution, the operators Λ^+ give unity, but on a negative energy solution, they give zero. The eigenstates to a matrix representation of Eq. (40) can conveniently be used to express the $\Lambda^\pm$ operators. The electron–electron interaction operator, V_{12}, is dominated by the Coulomb interaction, which when complex rotation is used is written

$$\frac{e^2}{4\pi\varepsilon_0}\frac{1}{r_{12}}e^{-i\theta}. \tag{43}$$

In addition, V_{12} should include corrections due to the finite speed of the electromagnetic interaction, as well as magnetic contributions present due to the electron spin. An approximate way to account for these effects, correct to order α^2 a.u., is provided by the Breit operator [115]

$$-\frac{e^2}{4\pi\varepsilon_0}\frac{1}{2}\left(\frac{\boldsymbol{\alpha}_1\cdot\boldsymbol{\alpha}_2}{r_{12}}+\frac{(\boldsymbol{\alpha}_1\cdot\mathbf{r_{12}})\,(\boldsymbol{\alpha}_2\cdot\mathbf{r_{12}})}{r_{12}^3}\right)e^{-i\theta}, \tag{44}$$

here with the complex scaling added. The use of Eqs. (43) and (44) implies that we work in the so-called Coulomb gauge. Other choices are possible, but it has been shown that Coulomb gauge is the most practical choice for modestly charged systems [116, 117]. Since Eq. (44) works on both the spin and the orbital part of the wavefunction it may, as the usual spin–orbit interaction, cause departure from LS-coupling. A third two-particle operator arises from nuclear recoil. Nonrelativistically, it has the well-known form

$$\frac{\mathbf{p}_1\cdot\mathbf{p}_2}{M}e^{-i2\theta}, \tag{45}$$

again with the proper complex scaling constant and is readily derived from the relation between nuclear and electronic momenta in the center of mass system: $\mathbf{p}^N=-\sum_i\mathbf{p}_i^e$. The full relativistic form can be found in Refs. [118, 119].

4.1. Perturbation expansion from an extended model space

MBPT starts with the partition of the Hamiltonian into $H=H_0+V$. The basic idea is to use the known eigenstates of H_0 as the starting point to find the eigenstates of H. The most advanced solutions to this problem, such as the coupled-cluster method, are iterative: well-defined classes of contributions are iterated until convergence, meaning that the perturbation is treated to *all orders*. Iterative MBPT methods have many advantages. First, they are economical and still capable of high accuracy. Only a few selected states are treated and the size of a calculation scales thus modestly with the basis set used to carry out the perturbation expansion. Radial basis sets that are complete in some discretized space can be used [112, 120, 121], and the basis

set dependence can be more or less eliminated. Second, MBPT approaches are applicable on true many-electron atoms. This is in contrast to methods that indeed are capable of higher accuracy; with perimetric coordinates, the partial wave expansion of the electron–electron interaction is avoided and extremely precise results can be obtained, see, for example, Ref. [20]. Methods of this type are however hardly extendable beyond pure three-body systems. They are also hard to extend to relativistic calculations. For example, the implementation of projection operators, Eq. (42), would be far from straight forward, while it is trivial for an MBPT expansion based on finite basis sets [112, 120, 121].

The drawback with perturbative approaches is of course that there is no guarantee that they will converge. There is a vast literature on coupled cluster methods in general and their convergence properties in particular, see, for example, Refs. [122–125]. A first concern is the presence of degenerate or quasi-degenerate solutions to H_0. In relativistic calculations, these are encountered even more often than nonrelativistically. For example, a state dominated by the $2s2p$ configuration would relativistically generally be a mixture of the $2s2p_{1/2}$ and $2s2p_{3/2}$ configurations, close in energy and often with rather equal weights. The proximity of these configurations is of course even more pronounced for light systems and for low enough nuclear charges it will eventually be impossible to start a perturbation expansion from one of the configurations, see, for example, the discussion in Ref. [126]. The remedy in this situation is to start the perturbation expansion from a mixture of the close configurations through the use of an extended model space, also called a multireference scheme.

A multireference scheme [124], applicable also on (quasi) degenerate states, divides the full space into the *model space* (P space) and the complimentary space (Q space). The interaction within P is treated exactly (through direct diagonalization of the Hamiltonian), while that between P and Q is handled through the perturbation expansion. With an ideal choice of P, the interaction between P and Q should be weak, usually due to a large energy gap. When the perturbation expansion is carried out to all orders, it should now, provided the model space is well chosen, converge fast. In relativistic calculations, it is natural to form the model space from all the fine-structure components of the configuration of interest. For example, for a $2p^2$ configuration, the model space will include the $2p_{1/2}^2$, $2p_{3/2}^2$, and $2p_{1/2}2p_{3/2}$ configurations. It is also possible, and sometimes advantageous, to include the whole $n\ell_j n'\ell'_{j'}$ manifold, i.e., in this case also the $2s_{1/2}^2$ configuration. With this approach, a large number of open shell atoms and ions can be treated successfully. More information about the application of this method to relativistic calculations can be found in Refs. [30, 126].

Unfortunately, there are still systems where problems are encountered, and the main reason is that it is not possible to find a suitable model space, i.e., one with the properties mentioned above. Relativistic and nonrelativistic

systems do not really differ in this respect, instead it is the calculation of resonance states that is especially plagued by the so-called *intruder states*; states emerging from Q space that couple strongly with one or several P states and prevent convergence. An obvious solution would be to change the partition into P and Q so that the intruder is absorbed in P, but in many cases this only leads to the appearance of new intruders. This happens when an ionization threshold happens to lie in the middle of a manifold or when manifolds are overlapping. An example of the former is the two $\left(4s4p_j\right)_{J=1}$ states in Ni^{16+} [33]. The two configurations with $j = 1/2$ and $j = 3/2$ are quasi-degenerate, couple strongly and should both be in the model space. The lower energy state, which dominantly has triplet character, is however bound and mixes strongly with the Rydberg series, which prevents convergence. This affects then also the other $J = 1$ state, dominantly of singlet character, since both states are spanned by the same model space. It would for many applications be interesting with a method that allowed calculation of, in this example, the higher lying singlet state without an explicit representation of the triplet state. One possibility is to introduce a *intermediate* space [127], which is placed between P and Q and acts as a buffer. Several promising studies have been done with such an approach [128–133], and at least one attempt has been made to use this idea on resonance states [18].

In spite of the intruder state problem, there is a range a systems where (relativistic) MBPT can produce reliable and accurate results for energies and width of resonance states. A few examples are given below.

4.2. Some examples

4.2.1. Helium and helium-like ions

The doubly excited states of helium have been the subject of a large number of studies, some of these extremely accurate [19, 20], but very few have considered relativistic corrections. The reason might be that the interest in very accurate methods is motivated mainly by highly excited regions with a dense spectrum of resonances, where relativistic effects play little role. Still the potentially interesting question of the stability of the most narrow resonances can only be answered, if relativistic effects are considered. A group of such very narrow resonances is found among the lowest helium doubly excited states; $2p^2\,{}^3P_J$ states cannot autoionize nonrelativistically since they are below all ${}^3P^e$ continua. Auger decay is however still possible due to spin–orbit coupling. For example, the $J = 2$ state may mix slightly with $2p^2\,{}^1D_2$ with a leading mixing coefficient scaling as $\alpha^2 Z^4/\Delta E$, where ΔE is the energy difference to $2p^2\,{}^1D_2$. The autoionization rate will then scale as the square of this times the rate of the $2p^2\,{}^1D_2$ state itself. Since the nonrelativistic rate to a first approximation is independent of nuclear charge and the energy splitting between two states belonging to the same configuration scales as

Z, we expect a rate $\sim\alpha^4Z^6$. For the $J = 1$ state, there is no state within the configuration to mix with and we expect a slower increase with Z; $\sim \alpha^4Z^4$.

To find the eigenstates of the many-body Hamiltonian in Eq. (42), the electron–electron interaction is written as a multipole expansion, and partial waves up to $\ell = 10$ is included in the wavefunctions, this expansion is further extrapolated. In practice, we have here separated out the nonrelativistic part [15] and followed the relativistic corrections separately. The perturbation expansion is made first with Coulomb interaction only and then with both Coulomb and Breit interactions. These results are given separately in Tables 5.3–5.5, first relativistic corrections without the Breit contributions, and then the Breit contributions by themselves. The resonance energies should in principle be independent of the rotation angle. Due to numerical imperfections, this is not completely true. To test the dependence on the rotation angle, we have made three separate calculations rotated 10°, 15°, and 20°, which are in all other respects identical. The real part of the energies differ at most with a few units in the ninth figure. For the resonances with LS-allowed autoionization rates, these rates are stable to five or six digits. Numerical uncertainties arise also from discretization of the grid. Such uncertainties are well under control for energy positions and allowed autoionization widths. Some of the forbidden autoionization rates are however extremely narrow and requires stability with up to 12 figures. To handle this situation, we have chosen to perform calculations for a few different values of the fine-structure constant, α. The widths grow fast with it, $\sim\alpha^4$, and for larger values, the numerical stability is much better. We then scale the results to the recommended value $\alpha = 1/137.035\,999\,11$. The result for $J = 0$ can be trusted to within one unit in the given figure in Table 5.5. For $J = 1$, the result should

Table 5.3 The total binding energy (E) and autoionization half width ($\Gamma/2$) for the helium doubly excited states of odd parity below $He^+(n = 2)$

	$2s2p\ ^1P_1$	$2s2p\ ^3P_0$	$2s2p\ ^3P_1$	$2s2p\ ^3P_2$
Energy				
Nonrelativistic [15]	−0.693135	−0.760492	−0.760492	−0.760492
Mass polarization	0.0000021	−0.0000004	−0.0000004	−0.0000004
Relativistic corrections	−0.0000279	−0.0000452	−0.0000395	−0.0000280
Breit corrections	0.0000002	0.0000019	0.0000004	0.0000004
Total	−0.693161	−0.760536	−0.760532	−0.760520
$\Gamma/2$ autoionization	0.000686	0.000150	0.000150	0.000150

The results are given in atomic units. To convert to eV use 1 a.u. $= 27.211\,384\,5\,M/(M + m_e)$eV $= 27.207\,653$ eV.

Table 5.4 The total binding energy and autoionization half width ($\Gamma/2$) for the helium doubly excited even parity states below He^+ ($n = 2$), where autoionization is nonrelativistically allowed

	$2s^2\ {}^1S_0$	$2p^2\ {}^1S_0$	$2p^2\ {}^1D_2$
Energy			
Nonrelativistic [15]	−0.777868	−0.621926	−0.701946
Mass polarization	−0.0000004	0.0000101	0.0000008
Relativistic corrections	−0.0000420	−0.0000231	−0.0000195
Breit corrections	0.0000002	0.0000008	−0.0000007
Total	−0.777910	−0.621938	−0.701965
$\Gamma/2$ autoionization	0.002271	0.000108	0.001181

The results are given in atomic units, see Table 5.3.

be correct to within 10%, while the much larger rate for $J = 2$ can be trusted to around 1%. It is the relatively strong mixing with the nearby rather broad $\left(2p^2\right)^1 D_2$ state, which yields the much broader width of that fine-structure component.

The leading contribution to the widths in Table 5.5 is due to spin–orbit mixing in the field of the nucleus, but also the electronic field contribute although with a weaker Z-scaling. The contributions from the Breit interaction to the energy is very small for a light system as helium, but the spin–spin and spin–orbit interactions included in this way are of the same formal order as the spin–orbit interaction from the Coulomb part of the electronic interaction. The Breit interaction is in fact also of relatively large importance for the decay rate of the most long-lived states.

There were some studies of relativistic corrections to the doubly excited states of helium already in the eighties. Chung and Davis [134] used nonrelativistic wavefunctions and calculated the effects of the relativistic correction operators. Their result for the relativistic and mass polarization corrections to the energy position of the $2s2p^1P$ state yielded $-0.26 \cdot 10^{-4}$ a.u., which agrees to within all given figures with the present calculation. Aspromallis *et al*. [135] used the Breit–Pauli Hamiltonian and calculated among other things the fine-structure splittings in $2p^3P$ to: 8.490×10^{-6}, 5.792×10^{-6}, and 1.43×10^{-5} a.u., for the ${}^3P_2 - {}^3P_1$, ${}^3P_1 - {}^3P_0$, and ${}^3P_2 - {}^3P_0$ splittings, respectively, which agree to within 2% with the results in Table 5.5.

The forbidden autoionization rates increase strongly with nuclear charge. As discussed above, we expect the width of $(2p^2)^3P_{J=0}$ and $(2p^2)^3P_{J=2}$ to scale as Z^6 since they can mix with states formed from the same configuration that can autoionize nonrelativistically, while the width of $(2p^2)^3P_{J=1}$ is expected to grow as Z^4. This is illustrated in Figure 5.10, which also shows that for $Z = 20$ the difference between forbidden and allowed transitions has vanished.

Table 5.5 The total binding energy (E) and autoionization half width ($\Gamma/2$) for the helium doubly excited states of even parity, and where autoionization is nonrelativistically forbidden, below $He^+(n = 2)$

	$2p^2\ {}^3P_0$		$2p^2\ {}^3P_1$		$2p^2\ {}^3P_2$	
	E [a.u.]	$\Gamma/2$ $[10^{-9}$ a.u.$]$	E [a.u.]	$\Gamma/2$ $[10^{-9}$ a.u.$]$	E [a.u.]	$\Gamma/2$ $[10^{-9}$ a.u.$]$
Nonrelativistic [15]	−0.710500	0.000	−0.710500	0.000	−0.710500	0.000
Mass polarization	0.0000064	0.000	0.0000064	0.000	0.0000064	0.000
Relativistic corrections	−0.0000292	0.003	−0.0000238	0.002	−0.0000131	0.933
Breit corrections	0.0000013	0.003	0.0000017	0.033	−0.0000007	0.216
Total	−0.710522	0.006	−0.710516	0.035	−0.710507	1.149

The results are given in atomic units, see Table 5.3.

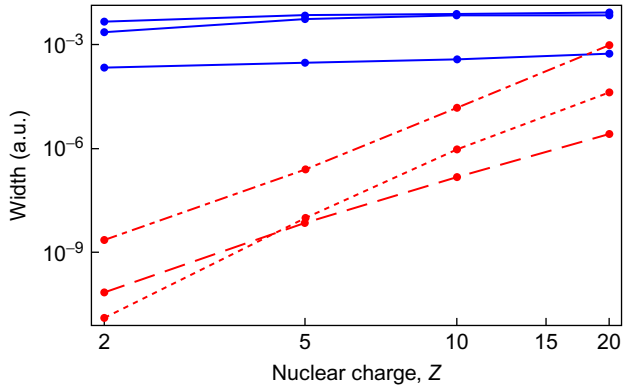

Figure 5.10 The variation of the autoionization width of the helium $n_1 = n_2 = 2$ resonances of even parity as a function of nuclear charge, Z. The three dashed lines show the widths for the $2p^2\,{}^3P_J$ resonances that cannot autoionize nonrelativistically, short dashed line ($J = 0$), long dashed line ($J = 1$), and long-short dashed line ($J = 2$). The three solid lines show the width of the three resonances for which autoionization is nonrelativistically allowed for comparison. A logarithmic scale is used to highlight the Z-dependence.

4.2.2. Beryllium-like ions

The nonrelativistically forbidden autoionization rates in Table 5.5 are still rather slow. One reason for this is that the ionization has to be to the $n = 1$ state of He^+, which is rather far away in energy. For Be-like systems the situation is very different. For the neutral system, even the state Be($1s^2 2p^2\,{}^1S_0$) is a resonance, lying only 0.00456 ± 0.00002 a.u. [136] above the ionization limit, $Be^+(1s^2 2s\,{}^1S_0)$. For Be-like ions, we will find that the lowest $1s^2 2pn\ell$ resonance appears for higher and higher n. For Be-like carbon, n has to be equal to 4 or more [27, 36], for nitrogen equal to 5 [28], for fluorine equal to 6 [30], and for sodium equal to 7 [34]. For heavier elements, the $1s^2 2p_{1/2} n\ell$ and $1s^2 2p_{3/2} n\ell$ form separate series; for example, in Be-like krypton, the first resonances in the former series are for $n = 11$, but in the latter series the resonances begin at $n = 15$ [31]. In many cases, the ionization threshold falls in the middle of a manifold making some states bound, while others are placed in the continuum. The threshold can even fall within a fine-structure multiplet; in Be-like fluorine, the two lowest energy resonances are dominantly of $2p6p\,{}^3P$ symmetry, while the third component ($J = 0$) is bound. Although the former two can only autoionize through spin–orbit coupling, they are broad, the lowest ($J = 1$) state ~25 meV and the $J = 2$ state ~0.1 meV.

For a process like electron–ion recombination, the presence of resonances closely above the ionization threshold has a large impact on the recombination rate. A number of storage ring measurements, which can map out the resonances in great detail, have clearly shown that one cannot dismiss such resonances just because they would not be able to ionize in LS-coupling.

Table 5.6 Calculated energies and widths for the lowest energy resonances in C^{2+}

Term	Level J	Energy (eV)	Width (meV)
$2p4d\ ^3D$	1	0.176	0.09
	2	0.177	0.18
	3	0.180	0.08
$2p4f\ ^1F$	3	0.236	0.10
$2p4f\ ^3F$	2	0.240	0.001
	3	0.242	0.25
	4	0.243	0.33

The energies are given relative the $C^{3+}(1s^22s)$ threshold.

It is interesting to look at a light ion in this respect. In Be-like carbon, all the resonances listed in Table 5.6 would not autoionize in a nonrelativistic framework, still they dominate the recombination spectrum [27].

5. RESONANCES IN THE TIME DOMAIN

The rearrangement of atoms in molecules in the course of a chemical reaction takes place on the same timescale as the molecular vibrations, 10–1000 fs. Here, a prominent example of recent progress is the detailed and quantitative understanding of each step in the *dissociation* of the simplest molecules (H_2, D_2, H_2^+, D_2^+), see, for example, Refs. [137–141] and references therein. The more recently opened attosecond regime is relevant to investigate the time development of electronic wave packets in both atoms and molecules. With the novel ultra-short *pump and probe* technique made possible by high-harmonic generation in connection with sophisticated phase-stabilization and gating techniques, a sub-femtosecond XUV (*pump*) pulse initiates a process in the atomic target, usually involving high-lying electronic states, and a second *probe* pulse takes "snapshots" of its evolution. As mentioned in the introduction, such pump-probe schemes bear the ultimate promise of filming atomic events. A very interesting target for such studies is core-hole creation and decay. The appearance of a core-hole triggers electron dynamics on a range of different timescales, leading to electron rearrangement and further ionization. Especially when the hole decay is coupled to the environment (atoms adsorbed on surfaces or embedded in larger molecules), time-resolved studies may give a handle on physics that cannot be studied in the frequency domain. A pioneering experiment was made when Drescher *et al*. used a *pump–probe* setup to follow the decay of an inner-shell vacancy in

krypton in the time domain [142]. Later studies have also demonstrated control over energy and energy spread of the Auger electron through the delay between two pulses [143]. In more complicated systems, several processes, on different timescales compete. One example can be the lifetime of a 4*d* hole in xenon adsorbed on a surface [144]. Potentially, such a measurement could be sensitive to solid-states effects, i.e., to the coupling between the electron dynamics induced in the surface due to the creation of the core-hole and the decay of the core-hole itself. Likewise, studies of photoelectrons emitted from a tungsten surface irradiated by an XUV [145] pulse that measured a ∼100 as time delay between photoelectrons emitted from localized core states and delocalized conduction-band states promise possibilities to investigate the timescale of a variety of processes; charge transfer and screening, image charge screening and decay, electron scattering, etc. The interpretation of such experiments is, however, far from trivial. This is underlined by recent atomic studies, where a ∼20 as delay between the emission of electrons from the 2*p* orbitals of neon atoms after exposure to a sub-100 as light pulse, with respect to those released from the 2*s* orbital, has been measured [146]. Even in such a relatively simple system, the quantitative understanding is still under development [147, 148]. This is underlined by subsequent measurements on argon [149].

It is clear that a core-hole represents a very interesting example of an unstable state in the continuum. It is, however, also rather complicated [150]. A simpler system with similar characteristics is a doubly excited state in few-body systems, as helium. Here, it is possible [151–153] to simulate the whole sequence of events that take place when the interaction with a short light pulse first creates a wave packet in the continuum, including doubly excited states, and the metastable components subsequently decay on a timescale that is comparable to the characteristic time evolution of the electronic wave packet itself. On the experimental side, techniques for such studies are emerging. Mauritsson *et al*. [154] studied recently the time evolution of a *bound* wave packet in He, created by an ultra-short (350 as) pulse and monitored by an IR probe pulse, and Gilbertson *et al*. [155] demonstrated that they could monitor and control helium autoionization. Below, we describe how a simulation of a possible pump-probe experiment, targeting resonance states in helium, can be made.

5.1. Analysis of time-dependent wave packets in terms of scattering states – why and how

The pump-probe spectroscopic time-resolved study of autoionization processes in atoms and molecules uses an ultra-short (100–500 as) XUV pulses for the pump stage in conjunction with an intense (10^{12}–10^{14} W/cm^2), few-cycle IR pulse as probe. Traditional time-independent approaches are inadequate to interpret these kind of experiments. This is so because, on the

one hand, due to the time-energy uncertainty relation, the spectrum of a sub-femtosecond XUV pump pulse spans an energy interval that is several electronvolts wide; as a result, many dynamical ionization regimes, multiply excited autoionizing states, multichannel single ionization states and, possibly, multiple ionization states as well, are activated at the same time. On the other hand, the intense IR pulse causes multiphoton or even nonperturbative transitions (e.g., tunneling and over-the-barrier ionization) from the coherent superposition of the diverse ionization states created by the XUV, and its duration is often too short to be well approximated with a stationary nonperturbative approach, like the Floquet method.

The most effective way to reproduce the outcomes of the experiments carried out with the new light sources is, rather, the direct integration of the time-dependent Schrödinger equation. Such an approach, however, also poses problems on its own right. A typical photofragmentation experiment results in the multicoincidence detection, resolved in energy and angles [156, 157], of the photofragments, which emerge from the interaction of the target with the ionizing radiation. Therefore, the central question in time-dependent theoretical approaches is: How do we extract this kind of information from the time-dependent wave packet obtained in a simulation?

This question has a considerable relevance not only for the comparison with experiment but also from a purely theoretical perspective. If we want to acquire insight into the mechanism of the ionization reaction while it unfolds, we need to devise meaningful ways of inspecting the wavefunction also before the interaction with the external laser field is over. The unique ability of theoretical simulation to constantly monitor the wave packet is arguably helpful to devise efficient control protocols of the course of the fragmentation process itself.

As far as the purely experimental aspect of the question is concerned, the answer is well known: the scattering states of the radiationless Hamiltonian provide the complete, time-invariant characterization of the unbound time-dependent wave packet we look for. At large distances, the interaction between the two charged fragments that emerge from the ionization (in this chapter, we will not be concerned with multiple ionization) is reduced to the Coulomb potential. Therefore, a continuum (generalized) eigenstate of the full Hamiltonian, corresponding to a certain energy E, can be further labeled with the quantum numbers of a complete set of observables commuting with the asymptotic Hamiltonian H_0, i.e., the quantum numbers of the parent ion, and those characterizing the motion of an electron in a Coulomb field,

$$H_0\varphi_{\alpha E} = E\varphi_{\alpha E}, \quad \langle\varphi_{\alpha E}|\varphi_{\beta E'}\rangle = \delta_{\alpha\beta}\delta(E - E'), \tag{46}$$

where α indicates the set of such additional quantum numbers. The correspondence between the eigenstates of the full and of the asymptotic Hamiltonian can be accomplished in two alternative ways, which result in

scattering states fulfilling either incoming ($\psi^-_{\alpha E}$) or outgoing ($\psi^+_{\alpha E}$) boundary conditions,

$$H\psi^{\pm}_{\alpha E} = E\psi^{\pm}_{\alpha E}, \quad \langle \psi^{\pm}_{\alpha E} | \psi^{\pm}_{\beta E'} \rangle = \delta_{\alpha\beta}\delta(E - E'). \tag{47}$$

The states $\psi^{\pm}_{\alpha E}$ correspond to wave packet controlled in the far past and in the far future, respectively. Let us see what this means. In the absence of external time-dependent fields, the scattering component of the time-dependent wave function $\psi(t)$ can be expanded in terms of either of the two sets of scattering states; for example, those with incoming boundary conditions

$$\Psi(t) = \sum_{\alpha} \iint d\epsilon \; \psi^-_{\alpha\epsilon} \, e^{-i\epsilon t} \, c_\alpha(\epsilon), \tag{48}$$

where $c_\alpha(E) = \langle \psi^-_{\alpha E} | \Psi(0) \rangle$. The scattering states with incoming boundary conditions are "controlled" in the far future in the sense that $e^{iH_0 t}\Psi(t)$ converges in norm to a superposition of eigenstates $\varphi_{\alpha\epsilon}$ of the *unperturbed* Hamiltonian H_0, with the same expansion coefficients as in Eq. (48) [65]

$$\text{as } t \to \infty \quad e^{iH_0 t}\Psi(t) \Rightarrow \sum_{\alpha} \iint d\epsilon \; \varphi_{\alpha\epsilon} \, c_\alpha(\epsilon). \tag{49}$$

As a consequence, the probability $P_\alpha(E)$ of measuring the asymptotically good quantum numbers (E, α) at the end of the propagation is given by the square module of the coefficients $c_\alpha(E)$

$$P_\alpha(E) = |c_\alpha(E)|^2, \tag{50}$$

and can be computed in two alternative ways: either by projecting, *at any time* after the external field is over, the time-dependent wavefunction on the scattering states of the full Hamiltonian; or, by projecting, *at infinite time* the time-dependent wavefunction on the eigenstates of the asymptotic Hamiltonian

$$P_\alpha(E) = \begin{cases} \left| \langle \psi^-_{\alpha E} | \Psi(t) \rangle \right|^2 \quad \forall\, t, & (a) \\ \lim_{t\to\infty} \left| \langle \varphi_{\alpha E} | \Psi(t) \rangle \right|^2 . & (b) \end{cases} \tag{51}$$

The convenience of using scattering states is striking. The outcome of an experiment can be evaluated as soon as the external time-dependent field is over (method *a*), without having to wait until the ionizing wave packet reaches the asymptotic region (method *b*). We will later argue that scattering states are also good candidates for the second aspect of our initial

question, i.e., on how the wavefunction could be inspected during the time propagation.

All the methods that require the wavefunction to reach the asymptotic region (approach *b*) face the same problem. The propagation of the fully correlated wavefunction for long times and at large distances is computationally expensive. This limitation can become particularly severe since continuum wave packets can take an *arbitrarily long* time to reach a relatively small radius. This is the case, for example, of the states lying just above an ionization threshold; then the wave packet comprises components with vanishingly small kinetic energy. If several channels with different thresholds are simultaneously open, then slow and fast photoelectrons are present at the same time. In this case, in order for the slowest part of the wavefunction to reach the asymptotic region, the propagation box must be large enough to accommodate also the fastest components and, as a result, the computational cost of the simulation easily swells beyond manageable proportions.

A second example, perhaps the most relevant in the present context, where approach (*b*) is a dead-end, is provided by resonant states in general, and by Rydberg series of doubly excited states, a commonplace of atomic photoionization spectra, in particular. First, the convergence of the resonant profiles in those channels, where the excited resonances decay, takes a time proportional to the lifetime of the longest-lived resonance, which is excited in the simulation. Second, doubly excited states have, in general, nonvanishing scalar products with all the eigenstates of the unperturbed Hamiltonian, but these scalar products are particularly large with some of those channel functions of H_0 in which the doubly excited states eventually do *not* decay.

Despite all the caveats associated to method (*b*), method (*a*) has at times been deemed impractical [158] due to the alleged overcomplexity associated to the calculation of the correlated ionization wavefunctions of the radiationless Hamiltonian. To be sure, computing the continuum eigenstates of a multi-electron system is by no means a trivial task. As a matter of fact, however, this task has been already accomplished successfully in the course of the last four decades or so [159–172]. Today, we have several accurate methods at our disposal capable of computing multi-electron single-ionization scattering states, see, for example, Refs. [75, 173–184] and references therein. In the following, we briefly survey one of them, the B-spline K-matrix method [75], and we illustrate the convenience of following the approach (*a*) by applying the scattering states obtained with it to the analysis of the XUV-pump IR-probe investigation of doubly excited states in helium [153]. Reliable accurate methods to disentangle the double escape channels have also recently emerged [51, 177, 178, 181, 182, 185–190].

5.1.1. Calculation of the single-ionization scattering states of helium

The L^2 K-matrix method [191, 192] is a technique to carry out configuration interaction in the continuum, on the line of the pioneering paper by

Fano [96]. The K-matrix method has been successfully applied to a number of problems in atomic physics [167, 193], particularly in conjunction with B-splines [75, 194–200]. B-splines are a convenient tool to represent accurately in finite boxes the radial component of continuum atomic orbitals [82], their major feature being a property known as effective completeness [201].

The B-spline K-matrix method follows the close-coupling prescription: a complete set of stationary eigenfunctions of the Hamiltonian $\psi^{\mathcal{P}}_{\alpha E}$ in the continuum is approximated with a linear combination of partial wave channels (PWCs) $\phi_{\alpha E}$ plus a localized (or pseudostate) channel (LC):

$$\psi^{\mathcal{P}}_{\alpha E} = \phi_{\alpha E} + \sum_{\gamma} \int\!\!\!\!\!\!\diagup d\epsilon\, \phi_{\gamma\epsilon} \frac{\mathcal{P}}{E-\epsilon} \mathbf{K}_{\gamma\epsilon,\alpha E}, \tag{52}$$

where the index α runs over the open channels at energy E, while the index γ runs over all available channels (open and closed) including the LC.

A PWC function is defined as an $(N-1)$-electron bound parent state (atom or ion) Φ_{I_α} with well-defined spin, parity, angular momentum and energy $I_\alpha \equiv (S_\alpha, \Pi_\alpha, L_\alpha, E_\alpha)$, coupled first to the spin-angular part of a single-particle state for the Nth electron, with definite orbital angular momentum ℓ_α, to form a state with definite parity Π, spin S, angular momentum L, and their projections Σ and M (for brevity, we indicate these global quantum numbers with the collective index Γ)

$$\Phi^{\Gamma}_{\alpha} = \sum_{\substack{\sigma_\alpha \sigma \\ m_\alpha m}} C^{S\Sigma}_{S_\alpha \sigma_\alpha \frac{1}{2}\sigma} C^{LM}_{L_\alpha m_\alpha \ell_\alpha m} \Phi^{\sigma_\alpha m_\alpha}_{I_\alpha}(\mathbf{x}_1, \ldots, \mathbf{x}_{N-1})\ {}^2\chi_\sigma(\zeta_N) Y_{\ell_\alpha m}(\hat{r}_N), \tag{53}$$

where $\mathbf{x}_i = (\vec{r}_i, \zeta_i)$ indicate the space-spin coordinates of the ith electron, and second to a radial orbital for the Nth electron, with asymptotic energy $E - E_\alpha$, to form an antisymmetric N electron function

$$\phi^{\Gamma}_{\alpha E} = f\mathcal{A}\ \Phi^{\Gamma}_{\alpha}(\mathbf{x}_1, \ldots, \mathbf{x}_{N-1}; \hat{r}_N, \zeta_N) \varphi^{\Gamma}_{\alpha E}(r_N), \tag{54}$$

where $\mathcal{A}$ is the antisymmetrizer for N particles and f is a normalization constant. It is understood that all the expressions that follow refer to the same global symmetry Γ; hence, from now on, we will avoid to indicate this symbol, unless necessary. The orbital $\varphi_{\alpha E}$ is defined, up to a constant factor, by requiring that the Hamiltonian is diagonal within each (α) subspace,

$$\langle \phi_{\alpha E} | \mathcal{H} | \phi_{\alpha E'} \rangle = E\ \delta(E - E'), \quad E > E_\alpha, \tag{55}$$

$$\langle \phi_{\alpha E_i} | \mathcal{H} | \phi_{\alpha E_j} \rangle = E_i\ \delta_{ij}, \quad E_i, E_j < E_\alpha. \tag{56}$$

The normalization of $\varphi_{\alpha\epsilon}$ and the factor f are fixed, for states whose energy E_i lies below the threshold E_α, by the two requirements

$$\langle \phi_{\alpha E_i} | \phi_{\alpha E_i} \rangle = 1, \quad \langle \varphi_{\alpha E_i} | \varphi_{\alpha E_i} \rangle = 1. \tag{57}$$

For energies lying above the threshold, the radial orbital fulfills the asymptotic behavior

$$\varphi_{\alpha E} \sim \sqrt{\frac{2k_\alpha}{\pi}}\,\Phi_\alpha \frac{\sin\theta_\alpha(r)}{k_\alpha r}, \quad \theta_\alpha(r) = k_\alpha r + \frac{Z}{k_\alpha}\ln 2k_\alpha r - \ell_\alpha \pi/2 + \sigma_{\ell_\alpha} + \delta_\alpha, \quad (58)$$

where $k_\alpha = \sqrt{2(E - E_\alpha)}$, Z is the charge of the parent ion, $\sigma_{\ell_\alpha}(k_\alpha)$ is the Coulomb phase shift, and $\delta_\alpha(k_\alpha)$ is an additional phase shift characteristic of the channel; finally, the factor f is determined by imposing the normalization

$$\langle \phi_{\alpha E} | \phi_{\alpha E'} \rangle = \delta(E - E'). \quad (59)$$

In the energy region comprised between two excitation thresholds of the parent ion, a first good approximation to the scattering states is obtained by including, in the close-coupling expansion, only those channels whose spectrum superpose with the energy interval. These comprise all the open channels and those few closed channels whose Rydberg states give rise to Feshback resonances in that energy region.

However, to obtain results with good accuracy, it is also necessary to include a pseudostate (or localized) channel, which accounts for those closed channels that have not been included, as well as for the multiple ionization channels, since the set of single-ionization PWCs alone would be incomplete. The localized channel may comprise a large number of normalized many-electron functions χ_i built from localized orbitals

$$\chi_i = \sum_j \Big[\bigwedge_k \varphi_{k_j} \Big]_{\mathbf{LS}} c_j^i, \quad \langle \chi_i | \chi_j \rangle = \delta_{ij}, \quad (60)$$

and which separately diagonalize the Hamiltonian

$$\langle \chi_i | H | \chi_j \rangle = \delta_{ij} E_i. \quad (61)$$

To avoid numerical instabilities due to the inevitable redundancies between the LC and the PWCs, it is generally good practice to enforce as an additional requirement the quasi-orthogonality of the localized functions to the PWCs

$$\forall \alpha, \quad \langle \chi_i | P_\alpha | \chi_j \rangle = 0, \quad P_\alpha = \sum\!\!\!\!\!\!\int \mathrm{d}E\, |\phi_{\alpha E}\rangle\langle\phi_{\alpha E}|. \quad (62)$$

When the PWCs are orthogonal among themselves (an assumption which is in fact not necessary and that thus far was not made) and to the localized channel, as is the case for the present treatment of the helium atom, the close-coupling *ansatz* [Eq. (52)] is equivalent to the Lippmann–Schwinger equation with the principal-value Green function [65]

$$\psi_{\alpha E}^{\mathcal{P}} = \phi_{\alpha E} + G_o^{\mathcal{P}}(E) V \psi_{\alpha E}^{\mathcal{P}}, \quad (63)$$

with $V \equiv H - H_0$ and

$$H_0 = \sum_\alpha \sum\!\!\!\!\!\!\int \mathrm{d}E \; |\phi_{\alpha E}\rangle E \langle \phi_{\alpha E}|, \tag{64}$$

where the sum over the channels includes also the localized one. The *off-shell* reaction matrix K is then given by

$$K_{\gamma\epsilon,\alpha E} \equiv \langle \phi_{\alpha\epsilon} | V | \psi^{\mathcal{P}}_{\alpha E} \rangle. \tag{65}$$

Equation (52) may be solved for the off-shell reaction K-matrix functions by requiring $\psi^{\mathcal{P}}_{\alpha E}$ to be an eigenfunction of the complete projected Hamiltonian with eigenvalue E:

$$\langle \phi_{\beta E'} | \, E - \mathcal{H} \, | \psi^{\mathcal{P}}_{\alpha E} \rangle = 0 \quad \forall \, \beta, E'.$$

This leads to a system of integral equations for the of-shell reaction matrix $\mathbf{K}$:

$$\mathbf{K}_{\beta E',\alpha E} - \sum_\gamma \sum\!\!\!\!\!\!\int \mathrm{d}\epsilon \; \mathbf{V}_{\beta E',\gamma\epsilon}(E) \frac{\mathcal{P}}{E-\epsilon} \mathbf{K}_{\gamma\epsilon,\alpha E} = \mathbf{V}_{\beta E',\alpha E}(E), \tag{66}$$

where the effective potential $\mathbf{V}(E)$ is defined as a linear combination of the Hamiltonian matrix $\mathbf{H}$ and the overlap matrix $\mathbf{S}$

$$\mathbf{V}_{\alpha\epsilon,\beta\epsilon'}(E) = \langle \phi_{\alpha\epsilon} | \, \mathcal{H} - E \, | \phi_{\beta\epsilon'} \rangle (1 - \delta_{\alpha\beta}) = \left[\mathbf{H}_{\alpha\epsilon,\beta\epsilon'} - E \, \mathbf{S}_{\alpha\epsilon,\beta\epsilon'} \right] (1 - \delta_{\alpha\beta}).$$

The system of integral equations [Eq. (66)] is eventually discretized and solved with numerical linear algebra procedures. At each energy, the system (66) must be solved for each of the open channels. A complete set of linearly independent degenerate real (i.e., stationary) continuum solutions $\psi^{\mathcal{P}}_{\alpha E}$ is thus obtained. The stationary scattering states $\psi^{\mathcal{P}}_{\alpha E}$ are not orthogonal; it can be shown that their superposition is given by

$$\langle \psi^{\mathcal{P}}_{\alpha E} | \psi^{\mathcal{P}}_{\beta E'} \rangle = \delta(E - E') (\delta_{\alpha\beta} + \pi^2 \left[\mathbf{K}^2(E) \right]_{\alpha\beta}). \tag{67}$$

where $\mathbf{K}_{\alpha,\beta}(E) \equiv \mathbf{K}_{\alpha E,\beta E}$ is the on-shell reactance matrix (Sect. 7.2.3 in Ref.[65]).

The scattering states $\psi^{\pm}_{\alpha}$ fulfilling outgoing (incoming) boundary conditions, i.e., which correspond to wave packets controlled in the past (future), are given by

$$\psi^{\pm}_{\alpha E} = \sum_\beta \psi^{\mathcal{P}}_{\beta E} \left[\frac{1}{\mathbf{1} \pm i\pi \mathbf{K}(E)} e^{\pm i \mathbf{\Delta}} \right]_{\beta\alpha}, \quad \mathbf{\Delta}_{\alpha\beta} = \delta_{\alpha\beta} \left(\sigma_{\ell_\alpha} + \delta_\alpha - \ell_\alpha \pi/2 \right)$$

they are orthonormal

$$\langle \psi^{\pm}_{\alpha E} | \psi^{\pm}_{\beta E'} \rangle = \delta_{\alpha\beta}\delta(E - E'), \tag{68}$$

and for large values of one of the N electron radial variables, say r_N, the scattering functions $\psi^{\pm}_{\alpha E\ell}$ is such that its only incoming (outgoing) component is

$$\left[\psi^{\pm}_{\alpha E\ell}\right]_{\text{in/out}} \sim \mp\sqrt{\frac{2k}{\pi}}\,\Phi_\alpha\,\frac{e^{\pm i(kr_N + \frac{1}{k}\ln 2kr_N)}}{2i\,kr_N}. \tag{69}$$

The on-shell unitary scattering matrix $\mathbf{S}(E)$, defined as

$$\langle \psi^{-}_{\alpha E} | \psi^{+}_{\beta E'} \rangle = \delta(E - E')\mathbf{S}_{\alpha\beta}(E), \tag{70}$$

has the following expression in terms of the on-shell reaction matrix $\mathbf{K}$

$$\mathbf{S} = e^{i\boldsymbol{\Delta}}\,\frac{\mathbf{1} - i\pi\mathbf{K}}{\mathbf{1} + i\pi\mathbf{K}}\,e^{i\boldsymbol{\Delta}}. \tag{71}$$

Note that if the PWCs are decoupled ($\mathbf{K} = \mathbf{0}$), the scattering matrix becomes $\mathbf{S}(E) = \exp(2i\boldsymbol{\Delta})$.

To conclude, the scattering states with incoming boundary conditions, which correspond, in the far future, to Coulomb plane waves, are a linear combination of the $\psi^{\Gamma(-)}_{\alpha E}$ states

$$\psi^{-}_{\alpha;E\hat{\Omega}\sigma} = \sum_{\Gamma\ell m} C^{LM}_{L_\alpha M_\alpha,\ell m} C^{S\Sigma}_{S_\alpha\Sigma_\alpha,\frac{1}{2}\sigma} Y^*_{\ell m}(\hat{\Omega})\psi^{\Gamma(-)}_{\alpha\ell E}, \tag{72}$$

with the normalization

$$\left\langle \psi^{-}_{\alpha;E\hat{\Omega}\sigma} | \psi^{-}_{\beta;E'\hat{\Omega}'\sigma'} \right\rangle = \delta_{\alpha\beta}\delta_{\sigma\sigma'}\delta(E - E')\delta(\cos\theta - \cos\theta')\delta(\phi - \phi'). \tag{73}$$

5.1.2. Projection of the time-dependent wavefunction on the scattering states

The channel-resolved photoelectron distribution of the time-dependent wavefunction $\psi(t)$ at the end of the external pulses is obtained by taking the square module of the projection of $\psi(t)$ with the scattering functions $\psi^{\Gamma(-)}_{\alpha E}$.

$$\frac{\mathrm{d}P^{\Gamma}_{\alpha E}}{\mathrm{d}E} = \left|\langle \psi^{\Gamma(-)}_{\alpha E} | \psi(t)\rangle\right|^2. \tag{74}$$

In order to extract the photoelectron distribution differential in the angle, the projection must be taken instead with the $\psi^{-}_{\alpha;E\hat{\Omega}\sigma}$. Taking into account the

azimuthal symmetry of the system, which is the case when the initial state is totally symmetric and the external field is linearly polarized, the channel-resolved photoelectron density as a function of both the energy and the ejection angle with respect to the radiation polarization is given by

$$\frac{\mathrm{d}P_\alpha}{\mathrm{d}E\,\mathrm{d}\cos\theta} = \sum_{\Sigma_\alpha M_\alpha \sigma} \int_0^{2\pi} \mathrm{d}\phi \left| \langle \psi^-_{\alpha;E\hat{\Omega}\sigma} | \psi(t) \rangle \right|^2 . \tag{75}$$

With few passages, it can be shown that this expression reduces to

$$\frac{\mathrm{d}P_\alpha}{\mathrm{d}E\,\mathrm{d}\cos\theta} = \sum_j \frac{2j+1}{2} P_j(\cos\theta) \sum_{LL'\ell\ell'} \Pi_{L\ell} (-1)^{L+L_\alpha+\ell+j} \times$$
$$\times\, C^{\ell' 0}_{\ell 0, j 0}\, C^{L' 0}_{L 0, j 0} \begin{Bmatrix} L & j & L' \\ \ell' & L_\alpha & \ell \end{Bmatrix} \langle \psi(t) | \psi^{\Gamma(-)}_{\alpha\ell E} \rangle \langle \psi^{\Gamma'(-)}_{\alpha\ell' E} | \psi(t) \rangle ,$$

where it is understood that the total spin, the spin projection, as well as the projection of the angular momentum are the same for both Γ and Γ'.

5.2. Simulation of a He resonance population and decay

We illustrate the use of multichannel single-ionization scattering states for the interpretation of time-resolved experiments in the case of the attosecond-XUV-pump IR-probe attosecond interferometric spectroscopy of the doubly excited states of helium.

The simulation is so conceived. Starting from the ground state of the helium atom, a short XUV pump pulse with an energy peaked around 65 eV creates a coherent superposition of $^1P^o$ continuum states across the $N = 2$ ionization threshold. In particular, it excites a coherent autoionizing wave packet of doubly excited states below the threshold, and a whole interval of unstructured continuous states, above the threshold, in the $2s$ and $2p$ channels. After a time delay of the order of few femtoseconds, a short, relatively intense IR pulse causes the above-the-threshold ionization of the residual population of the doubly excited states in the $N = 2$ channels. In the $N = 2$ channel, the interplay between the unstructured amplitude, from the ground state, created by the XUV pulse, and the ATI amplitudes from the whole group of doubly excited states, created by the IR pulse, gives rise to interference fringes in the channel-resolved fully differential photoelectron angular distributions, which, if collected as a function of the time delay between the two pulses, encode the electronic dynamics of the doubly excited wave packet.

This example incorporates several of those features that greatly benefit from a scattering-based analysis, namely: the population of several doubly excited states with short as well as long lifetimes and a fully differential multichannel signal for extremely slow electrons.

5.2.1. Time propagation

For the simulation, the time-dependent Schrödinger equation is integrated numerically with an exponential propagator

$$\psi(t + \mathrm{d}t) = \exp\left[-iH(t + \mathrm{d}t/2)\mathrm{d}t\right]\psi(t), \tag{76}$$

where $H(t)$ is the atomic Hamiltonian in velocity gauge. The wavefunction ψ is expanded in a multichannel close-coupling B-spline basis with total angular momentum up to $L = 6$, and the right-hand side of Eq. (76) is evaluated with the Arnoldi algorithm. This second-order propagation scheme explicitly enforces unitarity and is thus very stable.

5.2.2. Close-coupling scheme

Each subspace with definite angular momentum L comprises the $1s\phi_L$, $2s\phi_L$, $2p\phi_{L+1}$, and $2p\phi_{L-1}$ (for $L > 0$) close-coupling channels, where the notation $nl\phi_{l'}$ indicates that one electron is frozen in the nl He^+ orbital, while the other electron has the orbital angular momentum l'. In the S symmetry, the basis includes also the Hartree–Fock $1s^2_{HF}$ configuration for a better representation of the ground state. The radial part of the atomic orbitals is expanded in a B-spline basis of order 10, with an asymptotic spacing between consecutive nodes of 0.5 Bohr radii, up to a given maximum radius R. To compute the yield of the excited ions, a box with $R \sim 400$ Bohr radii was found to be sufficient, while for the partial differential photoelectron angular distributions a larger box, $R \sim 800$ Bohr radii, was used.

5.2.3. Absorbing boundaries

Due to the limits that are inherent to any numerical treatment, it is necessary to study the atom in a restricted region of space. However, when equations with propagating solutions are involved, like in the present case, serious mathematical difficulties arise as a consequence. If the finite volume is simply truncated with a hard wall unphysical reflections result. There are several methods to deal with this complication. The most straightforward remedy is to use some kind of absorbing potential, i.e., a potential that absorbs the outgoing wave packet at some distance from the region of interest and thereby prevents reflection at the box boundary. However, such potentials give rise to reflections in their own rights. The construction of a potential that really absorbs everything instead (a so-called *perfect absorber*), is a nontrivial task [59]. In our studies, we have used an approach where the potential is different for each channel and where it has a real component that accelerates the particles toward the boundary region and thereby minimizes the reflection [202]. A bonus of this approach is that the absorption in each channel can be followed in time, i.e., each decay mode can be monitored. In formal terms, the channel-specific absorbing potential V included in the

Hamiltonian is

$$V = c \sum_{\alpha} V_{\alpha}, \quad V_{\alpha} = P_{\alpha}(r - R_0)^2\, \theta(r - R_0) P_{\alpha}, \tag{77}$$

where the sum runs over all channels, P_α is the projector onto the close-coupling channel α, and c is a complex coefficient chosen as $c = -(1 + 5i)10^{-4}$. R_0, the radius beyond which the potential is active, is set to ∼100 Bohr radii from the box boundary. The absorbing potential V allows one to record the annihilation rate in each channel and thus to reconstruct the yields of all the parent ions.

5.2.4. Analysis through projection of scattering states

As detailed in Section 5.1.2, the photoelectron distribution in a channel, identified by a parent ion $\alpha = 1s,\ 2s,\ 2p$ is obtained by projecting the propagating wavefunction $\Psi(t)$ onto the helium scattering states, which satisfy incoming boundary conditions

$$P_\alpha(E, \hat{\Omega}) = \sum_{m\sigma\sigma'} \left| \langle \psi^{-}_{\alpha,m,\sigma;E,\hat{\Omega},\sigma'} | \Psi(t) \rangle \right|^2 . \tag{78}$$

In Eq. (78), E and $\hat{\Omega}$ denote the photoelectron energy and propagation direction, respectively; the sum runs over the projection m of the angular momentum of the electron in the parent ion, its spin σ, and the spin of the photoelectron σ'. The scattering states are computed with the procedure detailed in Section 5.1.1.

5.2.5. Simulation results

The time-dependent external field in the simulation comprises two laser pulses, an XUV pump pulse followed by an intense IR probe pulse, both with a Gaussian envelope. In order to consider a realistic case, we use parameters not too far from those used in experiments, compare with Ref. [154], but the XUV pulse is in our simulation centered around the first doubly excited states with $^1P^o$ symmetry (∼60 eV). The XUV-pump pulse is 385 ats long (full width at half maximum of the intensity), with the energy peaked at 60.69 eV, and an intensity of $2 \cdot 10^{13}$ W/cm^2; the probe is a Ti:sapphire 800 nm (1.55 eV) pulse, 3.77 fs long (fwhm), with an intensity of 10^{12} W/cm^2.

The XUV pulse populates a coherent superposition, $|\psi_P\rangle$, of $^1P^o$ doubly excited states below the $N = 2$ threshold, mainly those belonging to the principal sp^+_n series [96]:

$$|\psi_P\rangle \sim \sum_n |sp^+_n\rangle\, c_n\, e^{-iZ_n t}, \tag{79}$$

where $Z_n = E_n - i\Gamma_n/2$ is the complex energy of the sp^+_n resonance, with position E_n and width Γ_n. The localized part of each term in this series is

approximately represented by a symmetric linear combination of sp configurations, $sp_n^+ \propto 2snp + 2pns$ [96]. As a consequence, the localized part of $|\Psi_P\rangle$ is characterized by a symmetric breathing of p and s orbitals coupled to the $2s$ and $2p$ parent ions, respectively: With the present pulse parameters, the two lowest doubly excited states in the sp^+ series, sp_2^+ and sp_3^+, which with the described close-coupling scheme, lie ~5.04 and ~1.69 eV below the $N = 2$ threshold, with lifetimes of ~17.6 and ~80 fs, respectively, are by far the most populated ones. For several tens of femtoseconds, these two states dominate the dynamics of the metastable electron wave packet.

In Figure 5.11d, we show the electron density up to 700 Bohr radii at $t = 14.51$ fs after the pump pulse. It consists of distinct wave fronts spreading out with virtually constant speed; in other words, the metastable wave packet decays by ejecting electrons in isolated bursts. This peculiar behavior

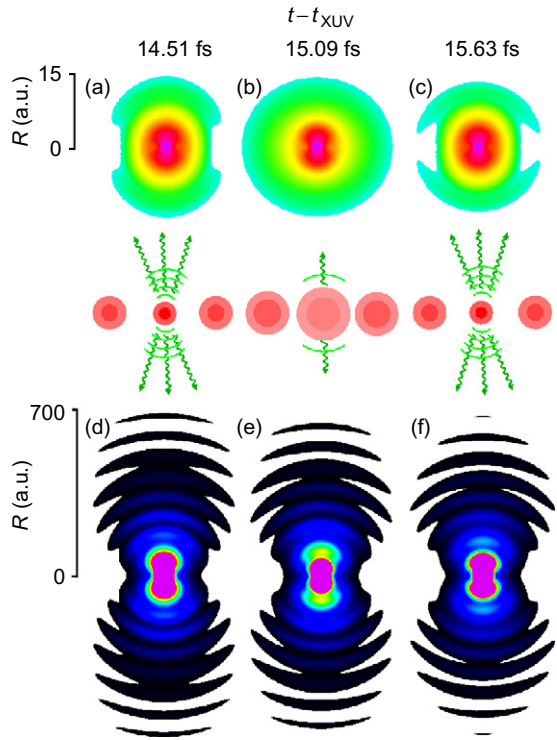

Figure 5.11 Charge density after the XUV-pump pulse, at small (top row) and large (bottom row) radii. At each breathing cycle, the metastable wave packet, formed by a coherent superposition of doubly excited states, ejects a burst of electrons. The peak of the free electron density originating close to the nucleus results in a wave front, which propagates outward at almost constant speed, up to very large distances.

can be understood in terms of interference between the long-range part of the wavefunctions describing the two decaying sp_2^+ and sp_3^+ states. To investigate this, we traced the position of 15 consecutive wave fronts in the time interval from 10 to 30 fs after the pump pulse, and extrapolated their evolution backward in time to the moments at which they were created in the vicinity of the nucleus. The average time interval between consecutive wave fronts turns out to be ∼1.2 fs, very close to the beating period between the sp_2^+ and the sp_3^+ resonances, 1.24 fs. Individual intervals vary slightly around this average value, with a frequency corresponding to the energy difference between the sp_3^+ and the sp_4^+ resonances.

Interestingly, enough a rather mechanistic interpretation is possible here. The Auger decay of doubly excited states is known to be triggered by electronic correlation; one of the electrons transfers part of its excitation energy to the other, which in turn is ejected into the continuum. Pisharody and Jones provided a spectacular and extreme example of this mechanism [203]; they showed that the decay of some autoionizing states of helium, where both electrons are highly excited, takes place through a single violent electron–electron collision. A similar picture applies also when only one of the two electrons is highly excited [204]. In this case, the autoionization is found to take place at the encounter of the external electron satellite with the excited core. In the present case, though, neither of the two electrons is highly excited. In fact, the metastable wave packet has the smallest excitation possible, it lacks a clear semiclassical analogue, and the two electrons are constantly in close interaction.

The panels in the first and last columns in Figure 5.11 correspond to two selected consecutive times at which a wave front originates close to the nucleus, 14.51 and 15.63 fs, while the central column corresponds to a time halfway between these two. In the upper row of Figure 5.11, we show the electron density within 15 Bohr radii from the nucleus; its breathing motion is evident: At $t = 14.51$ fs (a) the central part of the wave packet is at the peak of its contraction. At $t = 15.09$ fs (b) it reaches its maximal expansion. Finally, at $t = 15.63$ fs (c), it is contracted again. Thus, the relation between the breathing of the electron density at small radii and the ejection of isolated electron density bursts is more subtle than the obvious correspondence between their periodicities. Indeed, the instants at which the wave fronts are born in the vicinity of the nucleus correspond closely to the stages of maximum contraction of the localized part of the metastable wave packet. This evidence supports the idea that the collisional description of the autoionization dynamics of the doubly excited state of helium holds down to the least excited ones.

So far we have considered the absorption of an XUV pump pulse with attosecond extension. The next step in the simulation is to apply a probe pulse. During the time between the pump and the probe, the system undergoes two different kinds of temporal evolution. One is the semiperiodic

breathing of the localized part of the wavefunction due to the superposition of many metastable states with different energies. The other is the decay of the doubly excited states by autoionization into the $1s\varphi_p$ channel. Through the selection of a particular time delay between the two pulses, we probe this evolution at different stages. We consider next probing with a 10^{12} W/cm^2 IR pulse (800 nm or 1.55 eV). Although there is a lot of interest in possible experiments with short wavelength XUV probe pulses, most experiments use Ti:sapphire IR pulses similar to what we have considered.

At the intensity 10^{12} W/cm^2, the IR probe pulse has little effect on the component of the wavefunction still in the $1s^2$ ground state, but it has a profound effect on the ionization of the doubly excited states. In addition to the decay by electron emission (Auger), they can now also decay through photoionization into the $He^+(n = 2)$ channels (predominately). They can further be photoexcited to nearby resonances of different symmetries from which subsequent Auger decay can take place, albeit with a different rate than from the original $^1P^o$ states. To illustrate the result from such a calculation, Figure 5.12 shows the angular resolved photoelectron spectrum for a specific time delay between the two pulses. It shows the situation at a given time after the second pulse, long enough that the photoelectrons from the first (XUV) pulse have been absorbed by the boundaries, cf. Eq. (77). The $He^+(1s)$, $He^+(2s)$, and $He^+(2p)$ channels are shown separately. The elastic $He^+(1s)$ channel is also shown in more detail to highlight the large number of doubly excited states of a variety of symmetries that are populated.

Figure 5.13 shows the angular resolved spectrum in the $He^+(2p)$ channel, i.e., the right upper panel in Figure 5.12, in more detail. First, Figure 5.13a shows the spectrum after the (XUV) pump pulse but before the IR-pulse, then Figure 5.13b–d shows it after the IR-pulse for three different time delays. The fringes (which are also visible in Figure 5.12) come from the interference between the continuum created by the XUV-pulse and that created by the IR-pulse. The probe pulse ionizes the atom from the doubly excited state generating a short series of peaks above the $N = 2$ threshold, which interfere with the XUV direct-ionization amplitude. Such fringes have already been observed in helium close to the $N = 1$ threshold [154]. In the lapse between the two pulses, the direct-ionization amplitude accumulates a phase, which, to a first approximation, is linear in both energy and time delay:

$$\varphi_{direct}(E, t) = \varphi_{direct}(E, t_0) + E(t - t_0) \tag{80}$$

[in Eq. (80) we are neglecting the Coulomb–Volkov phase; see Ref. [205] for more details]. As a consequence, prominent interference fringes, with a characteristic energy spacing $\Delta E \sim 2\pi/(t - t_0)$, emerge. For a time delay of around 16 fs, we thus expect an energy spacing of ~0.01 a.u. between two consecutive maxima. The sp_2^+ and sp_3^+ $^1P^o$ resonances are separated from the

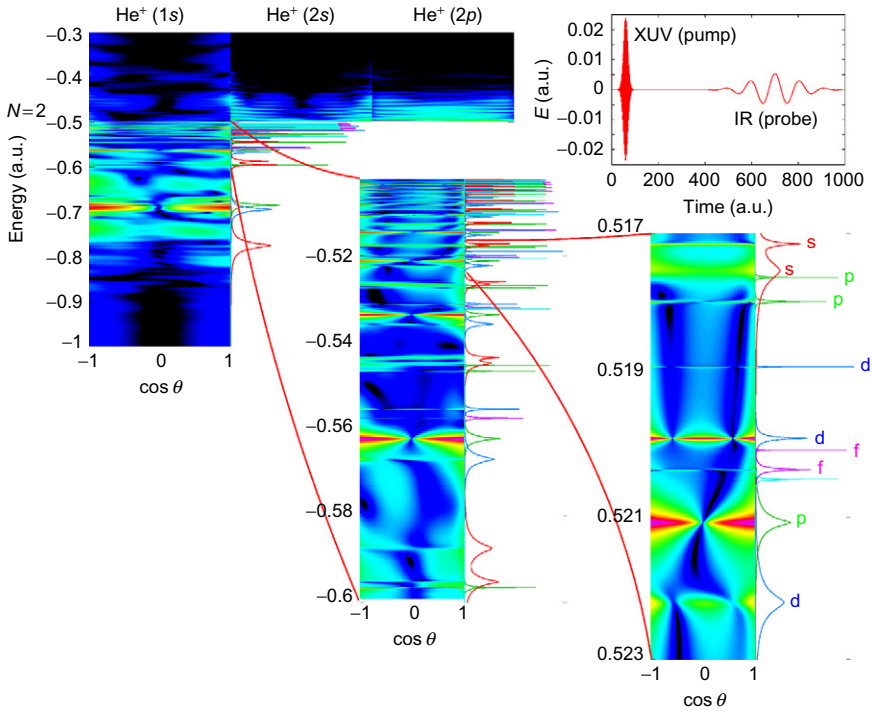

Figure 5.12 Double differential photoelectron spectrum (logarithmic scale) of the helium atom after exposure to two short pulses (see text and the inset, where one atomic unit of time is $\approx 24.19 \cdot 10^{-18}$ s). The three upper columns show different ionization channels: where the parent ion H^+ is left in 1*s*, 2*s*, or 2*p*. The *x*-axis shows the cosine of the photoelectron ejection angle with respect to the (linear) polarization of the laser light, and the *y*-axis shows the total energy in atomic units (1 a.u. $\approx$ 27.21 eV). The two magnifications show in more detail the region below the second ionization threshold, which is crowded with doubly excited states (autoionizing resonances). The first (XUV) pulse populates only states with $^1P^o$ symmetry. From these, the second (IR) pulse populates, through multiphoton transitions, all the nearby resonances. The subsequent Auger decay of these states results in the depicted photoelectron spectrum where the angular distribution reveals the angular momentum of the outgoing electron. The nodal structure of the resonant peaks, clearly visible in the most detailed picture, follows the assignment of the resonances, which are reported schematically on the side.

$N = 2$ ionization threshold by roughly the energy of three and one IR photons, respectively. Since the absorption of an odd number of photons by a $^1P^o$ state results in an even parity state, the 2*p* multiphoton ionization amplitude, created by the IR pulse, should have odd parity right above the threshold and change to even parity for photoelectron energies around 1.4 eV (corresponding to absorption of four IR photons from the sp_2^+ resonance and two from

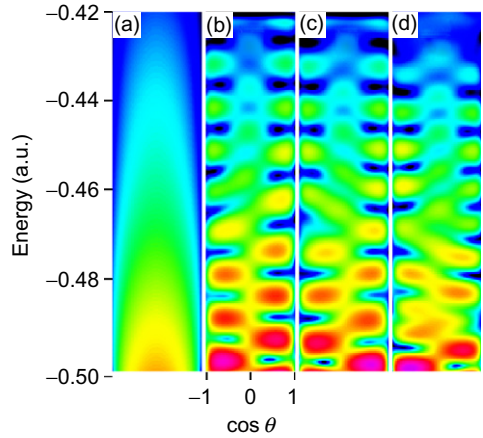

Figure 5.13 Helium photoelectron angular distribution in the $He^+(2p)$ channel (logarithmic scale). *x*-Axis: cosine of the electron ejection angle relative the laser polarization, *y*-axis: total energy (1 a.u. $\sim$ 27 eV). (a) After the XUV-pulse after the IR-pulse for three different time delays, separated from each other by half the IR-pulse period, 15.53 fs (b), 16.87 fs(c), and 18.21 (d). The fringes in (b)–(d) arise due to the interference between the (XUV-pulse) direct ionization from the ground state and the (IR-pulse) ionization from the doubly excited populated by the XUV-pulse.

the sp_3^+). Indeed, the interference pattern between multiphoton and direct ionization amplitudes (Figure 5.13b) is asymmetric with respect to $\cos\theta$ close to the threshold, and symmetric above $E = -0.45$ a.u. At each increase of the time delay by half an IR cycle, the relative phase between direct and indirect multiphoton amplitudes changes by π close to the threshold, while it remains the same one-photon energy above. This can be seen by comparing Figure 5.13b with Figure 5.13c, which indeed are approximately mirror images of each other, while Figure 5.13d again is similar to Figure 5.13b.

In Figure 5.14, we have plotted the total yield of the 2*s* and 2*p* excited states of the He^+ parent ion as a function of the time delay between the two pulses. Each point here represents thus a whole panel in Figure 5.13, integrated over angles and energies. Both ion yields are modulated by an approximately sinusoidal oscillation with the same period and with a quite substantial amplitude. The frequency of the oscillation is readily recognized as that of the *beating* between the two lowest $^1P^o$ resonances belonging to the most strongly populated resonances series, cf. Figure 5.11. When fitted with the function

$$A \cdot \sin(\omega t + \phi) + c_0 + c_1 t + c_2 t^2,$$

the two curves in Figure 5.14 give the same $\omega = 0.121(3)$ a.u., i.e., the energy difference between the two lowest sp^+ resonances, $\Delta E = 0.123$ a.u. What the

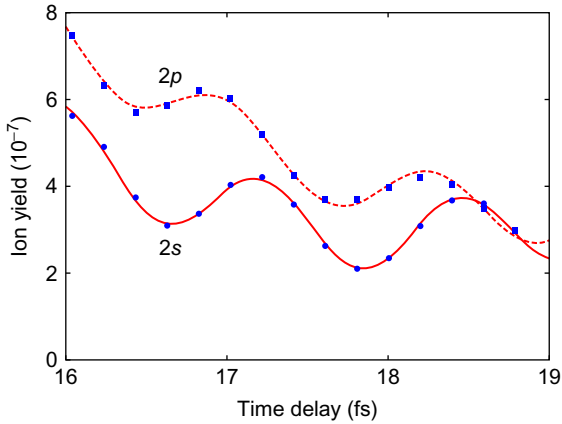

Figure 5.14 The helium ionization yield for the ion being left in the $He^+(2s)$ and $He^+(2p)$ excited states as a function of the time delay between the initial XUV *pump* pulse and the IR *probe* pulse. The oscillations are due to *breathing* between different doubly excited states (resonances).

plot shows is the enhanced or reduced ionization of the atom during its *breathing* in space, accomplished due to the superposition of different resonances. Interestingly enough, the two oscillations are out of phase by as much as 60°, indicating that the transition to the two channels sample different stages of the electronic breathing. Moreover, the population of the sp_2^+ resonance immediately after the pump pulse is larger than that of the sp_3^+ resonance. Since the sp_2^+ lifetime is the shortest, there is a moment at which the decay rates of the two resonances become comparable. At this point, the beating between the two resonances is maximal. This feature suggests the possibility to control the branching ratio of the two ionization-excitation channels and, in turn, to alter the course of reactions where metastable electronic states play a dominant role.

5.2.6. Perspectives

In principle, with the scattering wavefunctions at one's disposal, it is possible to segment a complex superposition of single-ionization states in to portions belonging to different symmetries, channels, and spectral domains. Indeed, if we indicate with $\left\{\mathcal{W}^{\Gamma}_{\alpha j}\right\}_{j=1,N^{\Gamma}_{\alpha}}$ a partition of unity of the (Γ,α) spectrum

$$\sum_{j=1}^{N^{\Gamma}_{\alpha}} \mathcal{W}^{\Gamma}_{\alpha j}(E) = 1, \tag{81}$$

we can write the resolution of the identity as

$$\hat{1} = \sum_{\Gamma\alpha j} \oint\!\!\!\!\!\!\int \mathrm{d}\epsilon \mathcal{W}^{\Gamma}_{\alpha j}(\epsilon) |\psi^{\Gamma(\pm)}_{\alpha\epsilon}\rangle\langle\psi^{\Gamma(\pm)}_{\alpha\epsilon}|. \tag{82}$$

The propagating wavefunction at a given time t_0 after a pump pulse can, in turn, be expressed as

$$|\psi(t_0)\rangle = \sum_{\Gamma\alpha j} |\psi^{\Gamma}_{\alpha j}(t_0)\rangle, \tag{83}$$

$$|\psi^{\Gamma}_{\alpha j}(t_0)\rangle = \oint\!\!\!\!\!\!\int \mathrm{d}\epsilon \mathcal{W}^{\Gamma}_{\alpha j}(\epsilon) |\psi^{\Gamma(\pm)}_{\alpha\epsilon}\rangle\langle\psi^{\Gamma(\pm)}_{\alpha\epsilon}|\psi(t_0)\rangle. \tag{84}$$

Given this partition (or any partition, for what that matters), thanks to the linearity of the Schrödinger equation, it is then possible to follow the effect of a pump pulse on each and every segment *separately*

$$|\psi(t)\rangle = \sum_{\Gamma\alpha j} |\psi_{(\Gamma\alpha j;t_0)}(t)\rangle, \tag{85}$$

$$|\psi_{(\Gamma\alpha j;t_0)}(t)\rangle = \mathcal{T} \exp\left[-i \int_{t_0}^{t} \mathcal{H}(\tau) d\tau\right] |\psi^{\Gamma}_{\alpha j}(t_0)\rangle, \tag{86}$$

thus providing useful insight into the interferometric spectroscopy of the ionizing states created by the pump stage:

$$\frac{dP^{\Gamma}_{\alpha,E}}{dE} = \sum_{\Gamma'\beta i} \sum_{\Gamma''\gamma j} \langle\psi^{\Gamma(-)}_{\alpha E}|\psi_{(\Gamma''\gamma j;t_0)}(t)\rangle\langle\psi_{(\Gamma'\beta i;t_0)}(t)|\psi^{\Gamma(-)}_{\alpha E}\rangle. \tag{87}$$

Stated otherwise, in this way, it is possible to disentangle from the energy and angle-resolved interferometric pattern in photoelectron distributions recorded experimentally, the contribution of those amplitudes that correspond to a definite intermediate step along the path that leads to the ionization.

ACKNOWLEDGMENTS

Financial support from the Swedish Research Council (VR), the Göran Gustafsson Foundation, and from the European COST Action CM0702 is gratefully acknowledged.

REFERENCES

[1] A.J.F. Siegert, On the derivation of the dispersion formula for nuclear reactions, Phys. Rev. 56 (8) (1939) 750.

[2] E. Lindroth, L. Argenti, J Bengtsson, F Ferro, M. Genkin, S. Selstø, The structure behind it all. J. Phys. Conf. Ser. 194 (1) (2009) 012001.

[3] B.R. Junker, Recent computational developments in the use of complex scaling in resonance phenomena, Adv. At. Mol. Phys. 18 (1982) 208.

[4] A.M. DyKhne, A.V. Chaplik, Normalization of the wave functions of quasistationary states, JETP 13 (1961) 1002.

[5] J. Aguilar, J.M. Combes, A class of analytic perturbations for one-body Schrödinger Hamiltonians, Commun. Math. Phys. 22 (1971) 269.

[6] E. Balslev, J.M. Combes, Spectral properties of many-body Schrödinger operators with dilatation-analytic interactions, Commun. Math. Phys. 22 (1971) 280.

[7] B. Simon, Resonances in n-body quantum systems with dilatation analytic potentials and the foundations of time-dependent perturbation theory, Ann. Math. 97 (2) (1973) 247.

[8] G.D. Doolen, J. Nuttal, R.W. Stagat, Electron-hydrogen resonance calculation by the coordinate-rotation method, Phys. Rev. A 10 (5) (1974) 1612.

[9] W.P. Reinhardt, Complex coordinates in the theory of atomic and molecular structure and dynamics, Annu. Rev. Phys. Chem. 33 (1982) 223.

[10] C.A. Nicolaides, Theory and state-specific methods for the analysis and computation of field-free and field-induced unstable states in atoms and molecules, in: C.A. Nicolaides, E. Brändas (Eds.), Unstable States in the Continuous Spectra, Part I: Analysis, Concepts, Methods, and Results, Vol. 60 of Advances in Quantum Chemistry, Academic Press, 2010, p. 163–267.

[11] Y.K. Ho, Autoionisation states of H^- below the N=3 hydrogenic threshold, J. Phys. B At. Mol. Opt. Phys. 10 (1977) L373.

[12] Y.K. Ho, Autoionization states of helium isoelectronic sequence below the n=3 hydrogenic thresholds, J. Phys. B At. Mol. Opt. Phys. 12 (1979) 387.

[13] Y.K. Ho, Doubly excited $^3P^o$ states of He below the N=2 and N=3 He^+ thresholds, Phys. Rev. A 48 (1993) 3598.

[14] K.T. Chung, B.F. Davis, Saddle-point complex-rotation method for resonances, Phys. Rev. A 26 (1982) 3278.

[15] E. Lindroth, Calculation of doubly excited states of helium with a finite discrete spectrum, Phys. Rev. A 49 (1994) 4473.

[16] D.R. DeWitt, E. Lindroth, R. Schuch, H. Gao, T. Quinteros, W. Zong, Spectroscopy of highly doubly excited states of helium through dielectronic recombination, J. Phys. B 28 (1995) L147.

[17] E. Lindroth, A.-M. Mårtensson-Pendrill, The $(2p^2)\ ^1S$ state of beryllium, Phys. Rev. A 53 (1996) 3151.

[18] D. Nikolic, E. Lindroth, Intermediate Hamiltonian to avoid intruder state problems for doubly excited states, J. Phys. B 37 (2004) L285.

[19] D. Wintgen, D. Delande, Double photoexcitation of ^1P states in helium, J. Phys. B 26 (1993) L399.

[20] A. Bürgers, D. Wintgen, J.-M. Rost, Highly doubly excited S states of the helium atom, J. Phys. B 28 (1995) 3163.

[21] S. Berkovic, R. Krivec, V. Mandelzweig, L. Stotland, Hyperspherical approach to the calculation of few-body atomic resonances, Phys. Rev. A 55 (1997) 988.

[22] T.N. Rescigno, V. McKoy, Rigorous method for computing photoabsorption cross sections from a basis-set expansion, Phys. Rev. A 12 (2) (1975) 522.

[23] E. Lindroth, Photodetachment of H^- and Li^-, Phys. Rev. A 52 (1995) 2737.

[24] E. Lindroth, A. Bürgers, N. Brandefelt, Relativistic effects on the H^- resonances converging to the $H(n = 2)$ threshold, Phys. Rev. A 57 (2) (1998) R685.
[25] J.L. Sanz-Vicario, E. Lindroth, N. Brandefelt, Photodetachment of negative helium ions below and above the 1s ionization threshold: A complex scaled configuration-interaction approach, Phys. Rev. A 66 (2002) 052713.
[26] W. Zong, R. Schuch, E. Lindroth, H. Gao, D.R. DeWitt, S. Asp, et al., Accurate determination of dielectronic recombination resonances with lithium-like argon, Phys. Rev. A 56 (1997) 386.
[27] S. Mannervik, D. DeWitt, L. Engström, J. Lidberg, E. Lindroth, R. Schuch, et al., Strong relativistic effects and natural line widths observed in dielectronic recombination of lithium-like carbon, Phys. Rev. Lett 81 (1998) 313.
[28] P. Glans, E. Lindroth, N.R. Badnell, N. Eklöw, W. Zong, E. Justiniano, et al., Dielectronic recombination of N^{4+}, Phys. Rev. A 64 (2001) 043609.
[29] E. Lindroth, H. Danared, P. Glans, Z. Pešić, M. Tokman, G. Vikor, et al., QED effects in Cu-like Pb recombination resonances near threshold, Phys. Rev. Lett. 86 (2001) 5027.
[30] M. Tokman, N. Eklöw, P. Glans, E. Lindroth, R. Schuch, G. Gwinner, et al., Dielectronic recombination resonances in F^{6+}, Phys. Rev. A 66 (2002) 012703.
[31] S. Madzunkov, E. Lindroth, N. Eklöw, M. Tokman, A. Paál, R. Schuch, QED effects in lithiumlike krypton, Phys. Rev. A 65 (2002) 032505.
[32] T. Mohamed, D. Nikolić, E. Lindroth, S. Madzunkov, M. Fogle, M. Tokman, et al., Dielectronic recombination of lithiumlike beryllium: A theoretical and experimental investigation, Phys. Rev. A 66 (2) (2002) 022719.
[33] M. Fogle, N. Eklöw, E. Lindroth, T. Mohamed, R. Schuch, M. Tokman, Spectroscopic study of Mg-like Ni by dielectronic recombination of stored ions, J. Phys. B 36 (2003) 2563.
[34] D. Nikolic, E. Lindroth, S. Kieslich, S. Schippers, C. Brandau, W. Shi, et al., Dielectronic recombination resonances in Na^{8+}, Phys. Rev. A 70 (2004) 062723.
[35] S. Kieslich, S. Schippers, W. Shi, A. Müller, G. Gwinner, M. Schnell, et al., Determination of the 2s-2p excitation energy of lithiumlike scandium using dielectronic recombination, Phys. Rev. A 70 (2004) 042714.
[36] A. Derevianko, V.A. Dzuba, M.G. Kozlov, Relativistic many-body calculation of low-energy dielectronic resonances in Be-like carbon, Phys. Rev. A 82 (2) (2010) 022720.
[37] A. Maquet, S.-I. Chu, W.P. Reinhardt, Stark ionization in dc and ac fields: An L^2 complex-coordinate approach, Phys. Rev. A 27 (6) (1983) 2946.
[38] A. Scrinzi, Ionization of multielectron atoms by strong static electric fields, Phys. Rev. A 61 (4) (2000) 041402.
[39] I.A. Ivanov, Y.K. Ho, Complex rotation method for the Dirac Hamiltonian, Phys. Rev. A 69 (2004) 023407.
[40] A. Mihelič, M. Žitnik, *Ab Initio* calculation of photoionization and inelastic photon scattering spectra of He below the $N = 2$ threshold in a dc electric field, Phys. Rev. Lett. 98 (2007) 243002.
[41] J.H. Shirley, Solution of the Schrödinger equation with a Hamiltonian periodic in time, Phys. Rev. 138 (4B) (1965) B979.
[42] S.-I. Chu, WP. Reinhardt, Intense field multiphoton ionization via complex dressed states: Application to the H atom, Phys. Rev. Lett. 39 (19) (1977) 1195.
[43] C.R. Holt, M.G. Raymer, W.P. Reinhardt, Time dependences of two-, three-, and four-photon ionization of atomic hydrogen in the ground 1^2S and metastable 2^2S states, Phys. Rev. A 27 (6) (1983) 2971.
[44] S.-I. Chu, D.A. Telnov, Beyond the Floquet theorem; generalized Floquet formalisms and quasienergy methods for atomic and molecular multiphoton processes in intense laser fields, Phys. Rep. 390 (2004) 1.
[45] C.A. Nicolaides, D.R. Beck, The variational calculation of energies and widths of resonances, Phys. Lett. 65A (1978) 11.

[46] B. Simon, The definition of molecular resonance curves by the method of exterior complex scaling, Phys. Lett. 71A (1979) 211.
[47] C.W. McCurdy, T.N. Rescigno, D. Byrum, Approach to electron-impact ionization that avoids the three-body Coulomb asymptotic form, Phys. Rev. A 56 (3) (1997) 1958.
[48] T.N. Rescigno, M. Baertschy, D. Byrum, C.W. McCurdy, Making complex scaling work for long-range potentials, Phys. Rev. A 55 (6) (1997) 4253.
[49] D.A. Horner, F. Morales, T.N. Rescigno, F. Martín, C.W. McCurdy, Two-photon double ionization of helium above and below the threshold for sequential ionization, Phys. Rev. A 76 (3) (2007) 030701.
[50] T.N. Rescigno, W. Vanrose, D.A. Horner, F. Martın, C.W. McCurdy, First principles study of double photoionization of H_2 using exterior complex scaling, J. Electron Spectros. Relat. Phenom. 161 (2007) 85.
[51] C.W. McCurdy, M. Baertschy, T.N. Rescigno, Solving the three-body Coulomb breakup problem using exterior complex scaling, J. Phys. B At. Mol. Opt. Phys. 37 (2004) R137.
[52] N. Elander, E. Yarevsky, Exterior complex scaling method applied to doubly excited states of helium, Phys. Rev. A. 57 (1998) 3119.
[53] F. Morales, C.W. McCurdy, F. Martín, Validity of the isolated resonance picture for H_2 autoionizing states, Phys. Rev. A 73(1) (2006) 014702.
[54] G. Jolicard, J. Humbert, Study of the one-channel resonance states. Method without a stabilization procedure in the framework of the optical potential model, Chem. Physics, 118 (3) (1987) 397.
[55] U.V. Riss, H.-D. Meyer, Reflection-free complex absorbing potentials, J. Phys. B At. Mol. Opt. Phys. 28(8) (1995) 1475.
[56] U.V. Riss, H.-D. Meyer, The transformative complex absorbing potential method: A bridge between complex absorbing potentials and smooth exterior scaling, J. Phys. B At. Mol. Opt. Phys. 31 (10) (1998) 2279.
[57] N. Moiseyev, Derivations of universal exact complex absorption potentials by the generalized complex coordinate method, J. Phys. B At. Mol. Opt. Phys. 31 (7) (1998) 1431.
[58] A. Scrinzi, Infinite-range exterior complex scaling as a perfect absorber in time-dependent problems, Phys. Rev. A 81 (5) (2010) 053845.
[59] J.G. Muga, J.P. Palao, B. Navarro, I.L. Egusquiza, Complex absorbing potentials, Phys. Rep. 395 (6) (2004) 357.
[60] T. Mercouris, Y. Komninos, C.A. Nicolaides, The state-specific expansion approach to the solution of the polyelectronic time-dependent Schrödinger equation for atoms and molecules in unstable states. in: C.A. Nicolaides, E. Brändas (Eds.), Unstable States in the Continuous Spectra, Part I: Analysis, Concepts, Methods, and Results, Vol. 60 of Advances in Quantum Chemistry, Academic Press, 2010, pp. 333–405.
[61] A. Scrinzi, B. Piraux, Two-electron atoms in short intense laser pulses, Phys. Rev. A 58 (2) (1998) 1310.
[62] J Bengtsson, E. Lindroth, S. Selstø, Solution of the time-dependent Schrödinger equation using uniform complex scaling, Phys. Rev. A 78 (3) (2008) 032502.
[63] S. Selstø, E. Lindroth, J. Bengtsson, Solution of the Dirac equation for hydrogenlike systems exposed to intense electromagnetic pulses, Phys. Rev. A 79 (4) (2009) 043418.
[64] J.R. Taylor, Scattering Theory, John Wiley & Sons Inc., New York, 1972.
[65] R.G. Newton, Scattering Theory of Waves and Particles, Dover Publications Inc., Mineola, NY, 2002.
[66] G.Breit, E. Wigner, Capture of slow neutrons, Phys. Rev. 49 (1936) 519.
[67] E.P. Wigner, Resonance reactions and anomalous scattering, Phys. Rev. 70 (1946) 15.
[68] H. Feshbach, Unified theory of nuclear reactions, Ann. Phys. 5 (1958) 357.
[69] H. Feshbach, A unified theory of nuclear reactions. ii. Ann. Phys. 19 (1962) 287.

[70] A.U. Hazi, Behavior of the eigenphase sum near a resonance, Phys. Rev. A 19 (1979) 920.
[71] L. Eisenbud, The Formal Properties of Nuclear Collisions, Ph.D. Thesis (unpublished), Princeton University, June 1948.
[72] E.P. Wigner, Lower limit for the energy derivative of the scattering phase shift, Phys. Rev. 98 (1955) 145.
[73] F.T. Smith, Lifetime matrix in collision theory, Phys. Rev. 118 (1) (1960) 349.
[74] H. Friedrich, Theoretical Atomic Physics, second ed., Springer Verlag, Heidelberg, 1998.
[75] L. Argenti, R. Moccia, K-matrix method with B-splines : σ_n, β_n and resonances in He photoionization below $N = 4$, J. Phys. B At. Mol. Opt. Phys. 39 (2006) 2773.
[76] J.M. Rost, K. Schulz, M. Domke, G. Kaindl, Resonance parameters of photo doubly excited helium, J. Phys. B At. Mol. Opt. Phys. 30 (1997) 4663.
[77] B. Simon, Resonances and complex scaling: A rigorous overview, Int. J. Quantum Chem. 14 (4) (1978) 529.
[78] R. Yaris, J. Bendler, R.A. Lovett, C.M. Bender, P.A. Fedders, Resonance calculations for arbitrary potentials, Phys. Rev. A 18 (5) (1978) 1816.
[79] B. Simon, Convergence of time dependent perturbation theory for autoionizing states of atoms, Phys. Lett. A 36 (1976) 23.
[80] A. Scrinzi, N. Elander, A finite element implementation of exterior complex scaling for the accurate determination of resonance energies, 98 (5) (1993) 3866.
[81] Y.K. Ho, The method of complex coordinate rotation and its applications to atomic collision processes, Phys. Rep. 99 (1983) 1.
[82] H. Bachau, E. Cormier, P. Decleva, J.E. Hansen, F. Martín, Applications of B-splines in atomic and molecular physics, Rep. Prog. Phys. 64 (2001) 1815.
[83] T.N. Rescigno, C.W. McCurdy, Numerical grid methods for quantum-mechanical scattering problems, Phys. Rev. A 62 (3) (2000) 032706.
[84] J. Thompson, A.R. Barnett, COULCC: A continued-fraction algorithm for Coulomb functions of complex order with complex arguments, Comput. Phys. Comm. 36 (1985) 363.
[85] J. Dubau, S. Volonte, Dielectronic recombination and its applications in astronomy, Rep. Prog. Phys. 43 (1980) 199.
[86] D.E. Osterbrock, Astrophys. of Gaseous Nebulae and Active Galactic Nuclei, Univ. Science Books, Mill Valley, CA, 1989.
[87] Y. Hahn, Electron-ion recombination processes in plasmas, in: R. Janev (Ed.), Atomic and Molecular Processes in Fusion Edge Plasmas, Plenum Publications Corp., New York, 1995, p. 91.
[88] A. Burgess, Dilectronic recombination and the temperature of the solar corona, Astrophys. J. 139 (1964) 776.
[89] A. Burgess, A general formula for the estimation of dielectronic recombination coefficients in low-density plasmas, Astrophys. J. 141 (1965) 1588.
[90] W. Spies, A. Müller, J. Linkemann, A. Franck, M. Wagner, C. Kozhuharov, et al., Dielectronic and radiative recombination of lithiumlike gold, Phys. Rev. Lett. 69 (1992) 2768.
[91] G. Kilgus, D. Habs, D. Schwalm, A. Wolf, R. Schuch, N.R. Badnell, Dielectronic recombination from the ground state of heliumlike carbon ions, Phys. Rev. 47 (1993) 4859.
[92] D.R. DeWitt, R. Schuch, T. Quinteros, H. Gao, W. Zong, H. Danared, et al., Absolute dielectronic recombination cross sections of hydrogenlike helium, Phys. Rev. A 50 (1994) 1257.
[93] H.T. Schmidt, P. Forck, M. Grieser, D. Habs, J. Kenntner, G. Miersch, et al., High-precision measurement of the magnetic-dipole decay rate of metastable heliumlike carbon ions in a storage ring, Phys. Rev. Lett. 72 (1994) 1616.
[94] S. Mannervik, S. Asp, L. Broström, D.R. DeWitt, J. Lidberg, R. Schuch, et al., Spectroscopic study of lithiumlike carbon by dielectronic recombination of a stored ion beam, Phys. Rev. A 55 (1997) 1810.

[95] M. Lestinsky, E. Lindroth, D.A. Orlov, E.W. Schmidt, S. Schippers, S. Böhm, et al., Screened radiative corrections from hyperfine-split dielectronic resonances in lithiumlike scandium, Phys. Rev. Lett. 100 (3) (2008) 033001.
[96] U. Fano, Effects of configuration interaction on intensities and phase shifts, Phys. Rev. 124 (1961) 1866.
[97] A.J. González Martínez, J.R. Crespo López-Urrutia, J. Braun, G. Brenner, H. Bruhns, A. Lapierre, et al., State-selective quantum interference observed in the recombination of highly charged $Hg^{75+\cdots 78+}$ mercury ions in an electron beam ion trap, Phys. Rev. Lett. 94 (20) (2005) 203201.
[98] N. Nakamura, A.P. Kavanagh, H. Watanabe, H.A. Sakaue, Y. Li, D. Kato, et al., Asymmetric profiles observed in the recombination of Bi^{79+}: A benchmark for relativistic theories involving interference, Phys. Rev. A 80 (1) (2009) 014503.
[99] I. Orban, P. Glans, Z. Altun, E. Lindroth, A. Källberg, R. Schuch, Determination of the recombination rate coefficients for Na-like Si forming Mg-like Si, A&A 459 (1) (2006) 291.
[100] I. Orban, E. Lindroth, P. Glans, R. Schuch, Spectroscopic study of doubly excited states in Mg-like Si using dielectronic recombination, J. Phys. B 40 (2007) 1063.
[101] A. Hoffknecht, O. Uwira, A. Frank, J. Haselbauer, W. Spies, N. Angert, et al., Recombination of Au^{25+} with free electron at very low energies, J. Phys. B 31 (1998) 2415.
[102] G.F. Gribakin, A.A. Gribakina, V.V. Flambaum, Quantum chaos in multicharged ions and statistical approach to the calculation of electron-ion resonant radiative recombination, Aust. J. Phys. 52 (1999) 443.
[103] V.V. Flambaum, A.A. Gribakina, G.F. Gribakin, C. Harabati, Electron recombination with multicharged ions via chaotic many-electron states, Phys. Rev. A 66 (3) (2002) 012713.
[104] G.F. Gribakin, S. Sahoo, Mixing of dielectronic and multiply-excited states in electron-ion recombination: A study of Au^{24+}, J. Phys. B 36 (2003) 3349.
[105] R. Schuch, S. Böhm, Atomic physics with ions stored in the round, J. Phys. Conf. Ser. 88 (2007) 012002.
[106] A. Müller, Resonance phenomena in electron-ion and photon-ion collisions, J. Phys. Conf. Ser. 194 (1) (2009) 012002.
[107] Z. Altun, A. Yumak, N.R. Badnell, S.D. Loch, M.S. Pindzola, Dielectronic recombination data for dynamic finite-density plasmas, *A&A* 447 (3) (2006) 1165.
[108] R. Schuch, E. Lindroth, S. Madzunkov, M. Fogle, T. Mohamed, P. Indelicato, Dielectronic resonance method for measuring isotope shifts, Phys. Rev. Lett. 95(18) (2005) 183003.
[109] C. Brandau, C. Kozhuharov, Z. Harman, A. Muller, S. Schippers, Y.S. Kozhedub, et al., Isotope shift in the dielectronic recombination of three-electron $^{A}Nd^{57+}$, Phys. Rev. Lett. 100 (7) (2008) 073201.
[110] P. Indelicato, S. Boucard, E. Lindroth, Relativistic and many-body effects in K, L, and M shell ionization energy for elements with $10 \leq Z \leq 100$ and the determination of the 1s Lamb shift for heavy elements, Eur. Phys. J. D 3 (1998) 29.
[111] R.D. Deslattes, E.G. Kessler, P. Indelicato, L. de Billy, E. Lindroth, J. Anton, X-ray transition energies: New approach to a comprehensive evaluation, Rev. Mod. Phys. 75 (2003) 35.
[112] S. Salomonson, P. Öster, Relativistic all-order pair functions from a discretized single-particle dirac Hamiltonian, Phys. Rev. A 40 (1989) 5548.
[113] I. Lindgren, H. Persson, Sten Salomonson, L. Labzowsky, Full QED calculations of two-photon exchange for heliumlike systems: Analysis in the Coulomb and Feynman gauges, Phys. Rev. A 51 (2) (1995):1167.
[114] J. Sucher, Foundations of the relativistic theory of many-electron atoms, Phys. Rev. A 22 (1980) 348.
[115] G. Breit, Dirac's equation and the spin–spin interactions of two electrons, Phys. Rev. 39 (1932) 616.

[116] E. Lindroth, A.-M. Mårtensson-Pendrill, Further analysis of the complete Breit interaction, Phys. Rev. A 39 (1989) 3794.
[117] I. Lindgren, Gauge dependence of interelectronic potentials, J. Phys. B At. Mol. Opt. Phys. 23 (1990) 1085.
[118] C.W.P. Palmer, Reformulation of the theory of the mass shift, J. Phys. B At. Mol. Phys. 20 (22) (1987) 5987.
[119] V. M. Shabaev, A.N. Artemyev, Relativistic nuclear recoil corrections to the energy levels of multicharged ions, J. Phys. B At. Mol. Opt. Phys. 27 (7) (1994) 1307.
[120] W.R. Johnson, S.A. Blundell, J. Sapirstein, Finite basis sets for the Dirac equation constructed from B splines, Phys. Rev. A 37 (1988) 307.
[121] S. Salomonson, P. Öster, Solution of the pair equation using a finite discrete spectrum, Phys. Rev. A 40 (1989) 5559.
[122] T.H. Schucan, H.A. Weidenmüller, Perturbation theory for the effective interaction in nuclei, Ann. Phys. 76 (2) (1973) 483.
[123] T.H. Schucan, H.A. Weidenmüller, The effective interaction in nuclei and its perturbation expansion: An algebraic approach, Ann. Phys. 73 (1) (1972) 108.
[124] I. Lindgren, The Rayleigh-Schrödinger perturbation and the linked-diagram theorem for a multi configurational model space, J. Phys. B At. Mol. Opt. Phys. 7 (1974) 2441.
[125] R.J. Bartlett, M. Musiał, Coupled-cluster theory in quantum chemistry, Rev. Mod. Phys. 79 (1) (2007) 291.
[126] A.-M. Mårtensson-Pendrill, I. Lindgren, E. Lindroth, S. Salomonson, D.S. Staudte, Convergence of relativistic perturbation theory for the 1s2p states in low-Z heliumlike systems, Phys. Rev. A 51 (1995) 3630.
[127] J.P. Malrieu, Ph. Durand, J.P. Daudey, Intermediate Hamiltonians as a new class of effective Hamiltonians, J. Phys. A 18 (1985) 809.
[128] A. Landau, E. Eliav, U. Kaldor, Intermediate Hamiltonian Fock-space coupled-cluster method, Chem. Phys. Lett. 313 (1999) 399.
[129] A. Landau, E. Eliav, Y. Ishikawa, U. Kaldor, Intermediate Hamiltonian Fock-space coupled-cluster method; excitations energies of barium and radium, J. Chem. Phys. 113 (2000) 9905.
[130] A. Landau, E. Eliav, Y. Ishikawa, U. Kaldor, Intermediate Hamiltonian Fock-space coupled-cluster methods; excitations energies of xenon and radon, J. Chem. Phys. 115 (2001) 6862.
[131] A. Landau, E. Eliav, Y. Ishikawa, U. Kaldor, Mixed-sector intermediate Hamiltonian Fock-space coupled cluster approach, J. Chem. Phys. 121(14) (2004) 6634.
[132] E. Eliav, M.J. Vilkas, Y. Ishikawa, U. Kaldor, Extrapolated intermediate Hamiltonian coupled-cluster approach: Theory and pilot application to electron affinities of alkali atoms, J. Chem. Phys. 122 (22) (2005) 224113.
[133] E. Eliav, A. Borschevsky, K.R. Shamasundar, S. Pal, U. Kaldor, Intermediate Hamiltonian Hilbert space coupled cluster method: Theory and pilot application, Int. J. Quantum Chem. 109 (13) (2009) 2909.
[134] K.T. Chung, B.F. Davis, Helium $2s2p\,^1$P with relativistic corrections, Phys. Rev. A 31 (1985) 1187.
[135] G. Aspromallis, Y. Komninos, C.A. Nicolaides, Electron correlation and relativistic effects on the energies and widths of doubly excited states of he, J. Phys. B At. Mol. Phys. 17 (6) (1984) L151.
[136] C.W. Clark, J.D. Fasset, T.B. Lucatorto, L.J. Moore, Observation of autoionizing states of beryllium by resonance-ionization mass spectrometry, J. Opt. Soc. Am. B 2 (1985) 891.
[137] J.H. Posthumus, The dynamics of small molecules in intense laser fields, Rep. Prog. Phys. 67 (5) (2004) 623.
[138] Ch. Siedschlag, A.J. Verhoef, J.I. Khan, M. Schultze, Th. Uphues, Y. Ni, et al., Control of electron localization in molecular dissociation, Science 312 (2006) 246.

[139] Th. Ergler, B. Feuerstein, A. Rudenko, K. Zrost, C.D. Schröter, R. Moshammer, et al., Quantum-phase resolved mapping of ground-state vibrational D_2 wave packets via selective depletion in intense laser pulses, Phys. Rev. Lett. 97 (2006) 103004.
[140] F. He, A. Becker, U. Thumm, Strong-field modulated diffraction effects in the correlated electron-nuclear motion in dissociating H_2^+, Phys. Rev. Lett. 101 (21) (2008) 213002.
[141] M. Kremer, B. Fischer, B. Feuerstein, V.L.B. de Jesus, V. Sharma, C. Hofrichter, et al., Electron localization in molecular fragmentation of H_2 by carrier-envelope phase stabilized laser pulses, Phys. Rev. Lett. 103 (21) (2009) 213003.
[142] M. Drescher, M. Hentschel, R. Kienbergerand, M. Uiberacker, V. Yakovlev, A. Scrinzi, et al., Time-resolved atomic inner-shell spectroscopy, Nature 419 (2002) 803.
[143] H. Wang, M. Chini, S. Chen, C.-H. Zhang, F. He, Y. Cheng, et al., Attosecond time-resolved autoionization of argon, Phys. Rev. Lett. 105 (14) (2010) 143002.
[144] L. Miaja-Avila, G. Saathoff, S. Mathias, J. Yin, C. La-o-vorakiat, M. Bauer, et al., Direct measurement of core-level relaxation dynamics on a surface-adsorbate system, Phys. Rev. Lett. 101 (4) (2008) 046101.
[145] A.L. Cavalieri, N. Müller, Th. Uphues, V.S. Yakovlev, A. Baltuška, B. Horvath, et al., Attosecond spectroscopy in condensed matter, Nature 449 (2007) 1029.
[146] M. Schultze, M. Fiess, N. Karpowicz, J. Gagnon, M. Korbman, M. Hofstetter, et al., Delay in photoemission, Science 328 (2010) 1658.
[147] A.S. Kheifets, I.A. Ivanov, Delay in atomic photoionization, Phys. Rev. Lett. 105 (23) (2010) 233002.
[148] S. Nagele, R. Pazourek, J. Feist, K. Doblhoff-Dier, C. Lemell, K. Tőkési, et al., Time-resolved photoemission by attosecond streaking: Extraction of time information, J. Phys. B At. Mol. Opt. Phys. 44 (8) (2011) 081001.
[149] K. Klünder, J.M. Dahlström, M. Gisselbrecht, T. Fordell, M. Swoboda, D. Guénot, et al., Probing single-photon ionization on the attosecond time scale, Phys. Rev. Lett. 106 (14) 143002.
[150] Th. Mercouris, Y. Komninos, C.A. Nicolaides, Time-resolved hyperfast processes of strongly correlated electrons during the coherent excitation and decay of multiply excited and inner-hole excited states, Phys. Rev. A 76 (3) (2007) 033417.
[151] Th. Mercouris, Y. Komninos, C.A. Nicolaides, Theory and computation of the attosecond dynamics of pairs of electrons excited by high-frequency short light pulses, Phys. Rev. A 69 (2004) 032502.
[152] Th. Mercouris, Y. Komninos, C.A. Nicolaides, Time-dependent formation of the profile of the he $2s2p\,^1p^o$ state excited by a short laser pulse, Phys. Rev. A 75 (1) (2007) 013407.
[153] L. Argenti, E. Lindroth, Ionization branching ratio control with a resonance attosecond clock, Phys. Rev. Lett. 105 (2010) 053002.
[154] J. Mauritsson, T. Remetter, M. Swoboda, K. Klünder, A. L'Huillier, K.J. Schafer, et al., Attosecond electron spectroscopy using a novel interferometric pump-probe technique, Phys. Rev. Lett. 105 (2010) 053001.
[155] S. Gilbertson, M. Chini, X. Feng, S. Khan, Y. Wu, Z. Chang, Monitoring and controlling the electron dynamics in helium with isolated attosecond pulses, Phys. Rev. Lett. 105 (26) (2010) 263003.
[156] J. Ullrich, R. Moshammer, A. Dorn, R. Dörner, L.Ph.H. Schmidt, H. Schmidt-Böcking, Recoil-ion and electron momentum spectroscopy: Reaction-microscopes, Rep. Prog. Phys. 66 (2003) 1463.
[157] R. Dörner, V. Mergel, O. Jagutzki, L. Spielberger, J. Ullrich, R. Moshammer, et al., Cold target recoil ion momentum spectroscopy: A 'momentum microscope' to view atomic collision dynamics, Phys. Rep. 330 (2000) 95.
[158] L.B. Madsen, L.A.A. Nikolopoulos, T.K. Kjeldsen, J. Fernández, Extracting continuum information from $\Psi(t)$ in time-dependent wave-packet calculations, Phys. Rev. A 76 (2007) 063407.

[159] J.T. Broad, W.P. Reinhardt, One- and two-electron photoejection from H^-: A multichannel $J-$matrix calculation, Phys. Rev. A 14 (1976) 2159.
[160] J.T. Broad, W.P. Reinhardt, J-matrix method: Multichannel scattering and photoionization, J. Phys. B At. Mol. Opt. Phys. 9 (1976) 1491.
[161] B.H. Bransden, A.T. Stelbovics, An L^2 approach to the solution of coupled-channel scattering equations, J. Phys. B At. Mol. Opt. Phys. 17 (1984) 1877.
[162] H. A. Slim, A.T. Stelbovics, The L^2 method and finite-basis expansions in coupled channels, J. Phys. B: At. Mol. Opt. Phys. 22 (1989) 475.
[163] M.L. Du, A. Dalgarno, Artificial-channel method for multichannel-decay-resonance energies and widths, Phys. Rev. A 43 (1991) 3474.
[164] D.H. Madison, J. Callaway, Accuracy of pseudostates for the electron-hydrogen scattering problem, J. Phys. B At. Mol. Opt. Phys. 20 (1987) 4197.
[165] I. Bray, D.A. Konovalov, I.E. McCarthy, Convergence of an L^2 approach in the coupled-channel optical-potential method for $e-$H scattering, Phys. Rev. A 43 (1991) 1301.
[166] R. Moccia, P. Spizzo, Lithium anion photodetachment up to the 3s threshold: A K-matrix L^2 basis calculation, J. Phys. B: At. Mol. Opt. Phys. 23 (1990) 3557.
[167] R. Moccia, P. Spizzo, Helium photoionization between the $N = 2$ and $N = 3$ thresholds including angular distribution and resonance properties: A k-matrix L^2 basis-set calculation, Phys. Rev. A 43 (1991) 2199.
[168] I. Sánchez, F. Martín, L^2 calculation of multichannel photoionization parameters in the neighborhood of the $3s3p\ ^1P^o$ resonance of he, Phys. Rev. A 44 (1992) 13(R).
[169] P.G. Burke, A. Hibbert, W.D. Robb, Electron scattering by complex atoms, J. Phys. B At. Mol. Phys. 4 (1971) 153.
[170] P.G. Burke, W.D. Robb, The R-matrix theory of atomic processes, Adv. At. Mol. Phys. 11 (1975) 143.
[171] R.K. Nesbet, Variational Methods in Electron-Atom Scattering Theory, Plenum, New York, 1980.
[172] T. Brage, C.F. Fischer, G. Miecznikt, Non-variational, spline-Galerkin calculations of resonance positions and widths, and photodetachment and photo-ionization cross sections for H^- and He, J. Phys. B At. Mol. Opt. Phys. 25 (1992) 5289.
[173] P.G. Burke, K.A. Berrington, Atomic and Molecular Processes: An R-matrix Approach, Institute of Physics, Bristol, 1993.
[174] P.G. Burke, C.J Noble, V. M. Burke, R-matrix theory of atomic, molecular and optical processes, Adv. At. Mol. Opt. Phys. 54 (2006) 237.
[175] P.G. Burke, R-Matrix Theory of Atomic Collisions: Application to Atomic, Molecular and optical Processes, Springer-Verlag Gmbh & Co. Kg, Berlin/Heidelberg, 2011.
[176] A.D. Alhaidari, E.J. Heller, H.A. Yamani, M.S. Abdelmonem (Eds.), The J-Matrix method, Developments and Applications, Springer, Dordrecht, Germany, 2008.
[177] A.S. Kheifets, I. Bray, Photoionization with excitation and double photoionization of the helium isoelectronic sequence, Phys. Rev. A 58 (1998) 4501.
[178] P.J. Marchalant, K. Bartschat, R-matrix with pseudostates calculation for single and double ionization of helium by photon impact, Phys. Rev. A 56 (1997) 1697–1700.
[179] M. Venuti, P. Decleva, Convergent multichannel continuum states by a general configuration interaction expansion in a B-spline basis: Application to H^- photodetachment, J. Phys. B At. Mol. Opt. Phys. 30 (1997) 4839.
[180] W. Vanroose, J. Broeckhove, F. Arickx, Modified J-matrix method for scattering, Phys. Rev. Lett. 88 (2001) 010404.
[181] A. Palacios, C.W. McCurdy, T.N. Rescigno, Extracting amplitudes for single and double ionization from a time-dependent wave packet, Phys. Rev. A 76 (4) (2007) 043420.
[182] A. Palacios, T.N. Rescigno, C.W. McCurdy, Cross sections for short-pulse single and double ionization of helium, Phys. Rev. A 77 (2008) 032716.

[183] D.A. Horner, C.W. McCurdy, T.N. Rescigno, Electron-helium scattering in the S-wave model using exterior complex scaling, Phys. Rev. A 71 (2005) 012701.
[184] L.A.A. Nikolopoulos, P. Lambropoulos, Multichannel theory of two-photon single and double ionization of helium, J. Phys. B At. Mol. Opt. Phys. 34 (2001) 545.
[185] A.K. Kazansky, P. Selles, L. Malegat, Hyperspherical time-dependent method with semiclassical outgoing waves for double photoionization of helium, Phys. Rev. A 68 (2003) 052701.
[186] L. Malegat, P. Selles, A.K. Kazansky, Absolute differential cross sections for photo double ionization of helium from the ab initio hyperspherical R-matrix method with semiclassical outgoing waves, Phys. Rev. Lett. 85 (2000) 4450.
[187] T.N. Rescigno, M. Baertschy, W.A. Isaacs, C.W. McCurdy, Collisional breakup in a quantum system of three charged particles, Science 286 (1999) 2474.
[188] C.W. McCurdy, F. Martín, Implementation of exterior complex scaling in B-splines to solve atomic and molecular collision problems, J. Phys. B At. Mol. Opt. Phys. 37 (2004) 917.
[189] L. Malegat, H. Bachau, A. Hamido, B. Piraux, Analysing a two-electron wavepacket by semiclassically propagating its Fourier components in space, J. Phys. B At. Mol. Opt. Phys. 43 (2010) 245601.
[190] E. Foumouo, P. Antoine, H. Bachau, B. Piraux, Attosecond timescale analysis of the dynamics of two-photon double ionization of helium, New J. Phys. 10 (2008) 025017.
[191] I. Cacelli, V. Carravetta, R. Moccia, Molecular photoionization cross sections and asymmetry parameters by L^2 basis functions calculations: H_2O, J. Chem. Phys. 85 (1986) 7038.
[192] I. Cacelli, V. Carravetta, A. Rizzo, R. Moccia, The calculation of photoionisation cross sections of simple polyatomic molecules by L^2 methods, Phys. Rep. 205 (1991) 283.
[193] S. Mengali, R. Moccia, Non-empirical core polarization effects on the optical properties of Mg(I): I. discrete and continuum energy spectrum up to the third ionization threshold, J. Phys. B At. Mol. Opt. Phys. 29 (1996) 1597.
[194] T.K. Fang, T.N. Chang, *B*-spline-based multichannel *K*-matrix method for atomic photo ionization, Phys. Rev. A 61 (2000) 062704.
[195] Y. Jiang, J. Yan, J. Li, J. Sun, L. Wan, Photoionization of helium between the $N = 2$ and $N = 5$ thresholds of He^+: Partial differential cross sections, Phys. Rev. A 61 (2000) 032721.
[196] L. Argenti, R. Moccia, ^3S, $^3P^{o,e}$, $^3D^{e,o}$ resonance series in helium, J. Phys. B: At. Mol. Opt. Phys. 40 (2007) 3655.
[197] L. Argenti, R. Moccia, He photoionization: β_N and σ_N below $N = 5$ and 6 thresholds, Th. Chem. Acc. 118 (3) (2007) 485.
[198] L. Argenti, Rydberg and autoionizing triplet states in Helium up to the $N = 5$ threshold, At. Data Nucl. Data Tables 94 (2008) 903.
[199] L. Argenti, R. Moccia, Helium 2 ^3S photoionization up to the $N = 5$ threshold, J. Phys. B At. Mol. Opt. Phys. 41 (3) (2008) 035002.
[200] L. Argenti, R. Moccia, Nondipole effects in helium photoionization, J. Phys. B At. Mol. Opt. Phys. 43 (2010) 235006.
[201] L. Argenti, R. Colle, On the B-splines effective completeness, Comp. Phys. Commun. 180 (9) (2009) 1442.
[202] J.-Y. Ge, J.Z.H. Zhang. Channel-dependent complex absorbing potential for multi-channel scattering, Chem. Phys. Lett. 292 (1-2) (1998) 51.
[203] S.N. Pisharody, R.R. Jones, Probing two-electron dynamics of an atom, Science 303 (5659) (2004) 813.
[204] J.B.M. Warntjes, C. Wesdorp, F. Robicheaux, L.D. Noordam, Stepwise electron emission from autoionizing magnesium stark states, Phys. Rev. Lett. 83 (3) (1999) 512.
[205] N. Choi, T. Jiang, T. Morishita, M.-H. Lee, C.D. Lin, Theory of probing attosecond electron wave packets via two-path interference of angle-resolved photoelectrons, Phys. Rev. A 82 (2010) 013409.

CHAPTER 6

Electronic Decay in Multiply Charged Polyatomic Systems

Vitali Averbukh[a] and **Přemysl Kolorenč**[b]

Contents

Abstract Inner-shell ionization of atoms, molecules, and clusters often leads to creation of highly excited ionic states that are embedded into double (or even multiple) ionization continua and decay by electron emission. The most common electronic decay process triggered by core ionization is known as Auger effect. The dynamics of the Auger decay is usually assumed to be exponential, and the process is characterized by a decay rate. The advent of the high-intensity x-ray free-electron lasers and their envisaged applications in

[a] Department of Physics, Imperial College London, Prince Consort Road, SW7 2AZ London, UK
E-mail address: v.averbukh@imperial.ac.uk
[b] Institute of Theoretical Physics, Faculty of Mathematics and Physics, Charles University in Prague, V Holešovičkách 2, 180 00 Prague, Czech Republic
E-mail address: kolorenc@mbox.troja.mff.cuni.cz

Advances in Quantum Chemistry, Volume 63
ISSN 0065-3276, DOI: 10.1016/B978-0-12-397009-1.00006-0

molecular imaging have made it necessary to consider Auger-type processes in polyatomic systems under conditions of multiple ionization, both in the core and in the valence shells. Here, we review our recent theoretical work on the theory of electronic decay in multiply charged molecules and clusters. Particular attention is given to the effects of the spectator vacancies on the Auger decay rates, trapping of the Auger electron in a multiply charged system, and collective decay of two vacancies.

1. INTRODUCTION

In 1925, Pierre Auger discovered a "compound photoelectric effect" [1] that constituted emission of secondary electrons with kinetic energies independent of the energy of the ionizing photon. This phenomenon, now known as Auger effect [2], is a consequence of the electron-electron interaction in an atom (or a molecule) bearing an inner-shell vacancy. If the energy of the inner-shell-ionized state is higher than the double ionization potential, one of the outer-shell electrons can recombine into the vacant inner-shell orbital (see Figure 6.1) giving another outer-shell electron (Auger electron) enough energy to be ionized. Auger effect is, thus, a basic manifestation of electronic correlation in matter. Since the kinetic energies of the Auger electrons are related to the quantized energies of the singly and the doubly ionized states, they can serve as a fingerprint of a given atom. A small shift of the atomic Auger energies due to the chemical environment (chemical shift) can provide further information on the studied species. This makes Auger electron spectroscopy [2] particularly useful for surface analysis [3].

The first theory of Auger effect was given by G. Wentzel (1927) in his seminal work on nonradiative quantum jumps [4]. Wentzel used hydrogenic bound-state functions and the asymptotic forms of the free electron

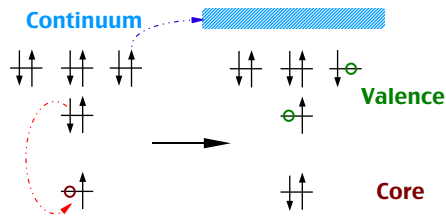

Figure 6.1 Schematic representation of one of the channels of the $1s^{-1}$ Ne^{+} Auger decay: one of the valence electrons ($2s$) is filling the core vacancy while another one ($2p$) is ejected into continuum. The same final state results also from the $2p \rightarrow 1s$ recombination and $2s$ ionization (not shown here). The former ("direct") and the latter ("exchange") contributions interfere due to electron indistinguishability.

waves to predict the order of magnitude of an electronic decay rate in a two-electron system. Adapted to a single Auger decay channel leading to a singlet final state of the dication (see Figure 6.1), Wentzel's expression reads

$$\Gamma = \pi \left| \left\langle \varphi_{\mathrm{val}}(\vec{r}_1)\varphi'_{\mathrm{val}}(\vec{r}_2) \left| \frac{1}{r_{12}} \right| \varphi_{\mathrm{core}}(\vec{r}_1)\varphi_{\varepsilon}(\vec{r}_2) \right\rangle + \left\langle \varphi_{\mathrm{val}}(\vec{r}_1)\varphi'_{\mathrm{val}}(\vec{r}_2) \left| \frac{1}{r_{12}} \right| \varphi_{\mathrm{core}}(\vec{r}_2)\varphi_{\varepsilon}(\vec{r}_1) \right\rangle \right|^2 , \quad (1)$$

It embodies the idea that one of the electrons participating in the Auger transition "jumps" from a valence orbital, φ_{val}, to the core orbital, φ_{core}, while the second electron is ejected from another valence orbital, φ'_{val}, to the continuum with the kinetic energy ε (cf. Figure 6.1). Electron indistinguishability leads to two interfering pathways for such a jump, often called "direct" and "exchange." Despite the strong approximations used in Wentzel's original theory (e.g., use of very approximate electronic orbitals), it does predict the order of magnitude of the Auger rate almost well (1 fs^{-1}, to be compared with 0.1–0.5 fs^{-1} for the *K*-shell Auger of second row elements [5]).

Auger decay can be triggered by photoionization of a core electron using x-ray radiation. Recently, new-generation x-ray sources – x-ray free electron lasers (XFELs) – have become available at a number of facilities around the world [6]. These sources are characterized by uncommonly high intensities (up to $\sim 10^{18}$ $\mathrm{W/cm^2}$) and, prospectively, also by very short pulse durations (down to ~1 fs) [6]. This unique characteristics of XFEL radiation led researchers to propose that it can be suitable for imaging of macromolecules in gas phase by single-molecule x-ray diffraction [7]. Significant experimental progress with nanometer-resolution XFEL imaging has been achieved recently [8]. Feasibility of extending this fascinating idea to atomic-resolution measurements depends on the extent of the radiation damage caused by the XFEL radiation. Thus, theoretical simulations of the radiation damage could be very helpful in choosing the optimal pulse characteristics for the envisaged atomic-resolution imaging.

State-of-the-art molecular mechanics simulations of macromolecule–XFEL interaction [7] rely on the classical description of atomic and electronic motion, in combination with quantum-mechanical rates for the electronic processes induced by the high-intensity x-rays. The latter include photoionization, predominantly of inner-shell electrons, and Auger processes following the creation of the corresponding inner-shell vacancies. In the high-intensity regime necessary for obtaining the diffraction picture of a single molecule with atomic resolution, the target species become multiply ionized well within the XFEL pulse duration [7, 9, 10]. It could be expected, therefore, that many of the electronic processes leading to the radiation

damage are modified by the presence of multiple positive charges. Concentrating specifically on the Auger decay, the core hole lifetimes could be affected by additional positive charges residing both on the atom bearing the core vacancy and on the neighboring atoms. Several important aspects make electronic decay in such multiply ionized systems different from the ones in free atoms. First, the rate of the exponential decay in the field of a positive charge (or charges) does not have to match the one in the singly core-ionized molecule. Furthermore, multiple ionization can lead to Auger electrons trapping, changing Auger dynamics qualitatively from exponential to oscillatory one. Finally, a collective decay of two vacancies becomes possible. Here, we review our recent progress in ab initio studies of Auger dynamics under conditions of multiple ionization. The general theoretical framework is given in Section 2. Applications of the ab initio theory to Auger decay in the presence of single or multiple spectator charges are given in Section 3. Several directions for future studies are outlined in Section 4.

2. FANO-ADC THEORY OF ELECTRONIC DECAY WIDTHS

Dynamics of the electronic decay in isolated atomic and small molecular systems ionized by low-intensity (e.g., synchrotron) radiation is understood fairly well [2, 11]. At high enough energies of the ionizing photon, the inner-shell ionization event and the decay of the resulting vacancy state can be treated separately, with the latter being described as a nonradiative transition. The concept of sudden ionization and the validity of the two-step description of the Auger transition are discussed, for example, in Refs. [12, 13]. The nonradiative electronic decay process can be treated within a number of theoretical formalisms, including, for example, that of non-Hermitian quantum mechanics [14, 15]. In Auger physics, we are typically dealing with long-lived resonances for which the Fano theory [16, 17] provides a particularly useful theoretical framework. Within this formalism, the nonradiative transition occurs due to coupling between the artificially constructed bound-like state, Φ, describing the inner-shell-ionized system with the energy above the double ionization threshold and the continuum states of the same energy, $\chi_{\beta,\epsilon_\beta}$ describing the doubly ionized system in its βth state with the energy E_β and the emitted Auger electron with kinetic energy ϵ_β. In Fano approach, the continuum states $\chi_{\beta,\epsilon_\beta}$ are constructed in such a way that, to a good approximation, they are not coupled by the full Hamiltonian $\hat{H}$:

$$\langle \chi_{\beta',\epsilon'} | \hat{H} | \chi_{\beta,\epsilon} \rangle \approx (E_\beta + \epsilon)\, \delta_{\beta',\beta}\, \delta(E_{\beta'} + \epsilon' - E_\beta - \epsilon)\,. \tag{2}$$

It can be shown [16, 17] that the bound-like state Φ, once prepared, will decay approximately exponentially in time,

$$|\langle\Phi|\Psi(t)\rangle|^2 = e^{-\Gamma t/\hbar}, \quad \Psi(t=0) = \Phi\,, \tag{3}$$

where $\Psi(t)$ is the full wavefunction of the system and the decay rate, $\Gamma/\hbar$, is given through

$$\Gamma = \sum_{\beta=1}^{N_c} \Gamma_\beta = 2\pi \sum_{\beta=1}^{N_c} \left|\langle\Phi|\hat{H} - E_r|\chi_{\beta,\epsilon_\beta}\rangle\right|^2, \tag{4}$$

where N_c is the number of the bound states of the doubly ionized system being energetically lower than the inner-shell-ionized state Φ, or in other words, the number of the open decay channels and E_r is the energy of the decaying state.

For the result (4) to be applicable to the computation of the electronic decay rates, one has to provide sensible approximations for the multi-electron bound (Φ) and continuum ($\chi_{\beta,\epsilon_\beta}$) wavefunctions. In the simplest case of single inner-shell ionization, these are wave functions of a singly ionized N-electron system, that is, $(N-1)$-electron states. Such states can be conveniently constructed using the technique of single-ionization algebraic diagrammatic construction (ADC) [18]. The ADC methodology has been originally developed within the Green's function formalism [19]. Here, however, we would like to briefly review the single-ionization ADC from a different standpoint, using the intermediate state representation (ISR) as proposed by Schirmer [20].

Consider the Hartree–Fock (HF) ground state of the N-electron neutral cluster, Φ_0^N. One can form a complete orthonormal set of the $(N-1)$-electron basis functions, $\Phi_J^{(N-1)}$, applying the so-called physical excitation operators, $\{\hat{C}_J\}$, to the HF ground state:

$$\Phi_J^{(N-1)} = \hat{C}_J \Phi_0^N, \tag{5}$$
$$\{\hat{C}_J\} \equiv \{c_i;\, c_a^\dagger c_i c_j, i<j;\, c_a^\dagger c_b^\dagger c_i c_j c_k, a<b, i<j<k;\, \ldots\}\,,$$

where c_i and $c_a^\dagger$ are annihilation and creation operators, respectively, the subscripts $i, j, k, \ldots$ relate to the occupied spin-orbitals and the subscripts $a, b, c, \ldots$ relate to the unoccupied spin-orbitals. The basis set (5) is used in the familiar configuration interaction (CI) expansion of the wavefunction. This expansion, once truncated after some specific excitation class [J], possesses such important drawbacks as slow convergence and lack of size consistency.

The ADC method overcomes these drawbacks by using a more complicated basis for the expansion of the $(N-1)$-electron wavefunctions. The idea is to apply the physical excitation operators, $\{\hat{C}_J\}$, to the perturbation-theoretically corrected, or "correlated", ground state of the neutral system,

$$\begin{aligned} \Psi_J^0 &= \hat{C}_J \Psi_0^N, \\ \Psi_0^N &= \Phi_0^N + \Psi_0^{(1)} + \Psi_0^{(2)} + \Psi_0^{(3)} + \cdots, \end{aligned} \tag{6}$$

where $\Psi_0^{(n)}$ is the nth-order correction to the HF ground state obtained by the standard many-body perturbation theory (see, e.g., Ref. [21]). Unfortunately, the resulting correlated excited states (CESs), Ψ_J^0, are not orthonormal. ADC takes care of this problem by orthonormalizing them in two steps to obtain the so-called intermediate states, $\tilde{\Psi}_J$. First, Gram–Schmidt orthogonalization *between the excitation classes* is performed to obtain the "precursor" states, $\Psi_J^\#$:

$$\Psi_J^\# = \Psi_J^0 - \sum_{\substack{K \\ [K]<[J]}} \left\langle \tilde{\Psi}_K | \Psi_J^0 \right\rangle \tilde{\Psi}_K , \tag{7}$$

that is, the functions belonging to the higher [e.g., two-hole, one-particle (2h1p) or $[J]=2$] excitation class are made orthogonal to those of all the lower [in this case, only one-hole (1h) or $[K]=1$] excitation classes. Second, the precursor states are orthonormalized symmetrically *inside each excitation class*:

$$\tilde{\Psi}_J = \sum_{\substack{J' \\ [J']=[J]}} \left(\underline{\underline{\rho}}^{\#-\frac{1}{2}} \right)_{J',J} \tilde{\Psi}_{J'} , \qquad \left(\underline{\underline{\rho}}^{\#} \right)_{J',J} = \langle \Psi_{J'}^\# | \Psi_J^\# \rangle, \tag{8}$$

where $\left(\underline{\underline{\rho}}^{\#} \right)_{J',J}$ is the overlap matrix of the precursor states belonging to the same excitation class. The above two-step procedure can be applied iteratively, noting that the CESs of the lowest (1h) excitation class are by definition also the precursor states. Any state of the $(N-1)$-electron system can be represented using the orthonormal basis of the intermediate states:

$$\Psi_q^{(N-1)} = \sum_i \sum_{[J]=i} Y_{q,J} \tilde{\Psi}_J . \tag{9}$$

The expansion coefficients, Y_J, are obtained by the diagonalization of the Hamiltonian matrix constructed in the basis of the intermediate states. It is a crucial feature of the ADC approach that the Hamiltonian matrix elements of the type $\langle \tilde{\Psi}_J | H | \tilde{\Psi}_J \rangle$ can be expressed analytically via the orbital energies and the electron repulsion integrals if one performs the orthonormalization

procedure of Eqs. (7) and (8) approximately and consistently with the order of the many-body perturbation theory, which is used for the construction of the correlated ground state [see Eq. (6)]. Moreover, it can be shown [20] that the truncation of the expansion (9) after the excitation class $[J] = m$ introduces an error of the order of $2m$, which should be compared to $m + 1$ for the slower-converging CI expansion. The accuracy of the expansion in excitation classes (9) should be, of course, consistent with that of the perturbation theoretical series for the correlated ground state (6). Thus, the order, n, at which the perturbation theoretical expansion (6) is truncated is the single parameter defining the level of the ADC approximation. For this reason, ADC schemes of various quality are usually denoted as ADC(n), $n = 2, 3, 4, \ldots$ in full analogy with the well-known MP2, MP3, MP4, ... perturbation-theoretical techniques for the ground state of the neutral system. The ADC(2) scheme for singly ionized states describes the many-electron wavefunctions in the basis of 1h and 2h1p intermediate states treating the coupling between the 1h states and between 1h states and 2h1p states in the second and in the first order, respectively. ADC(2) approximation neglects the coupling between the different 2h1p basis functions. The extended ADC(2) scheme [ADC(2)x] takes into account the coupling between the 2h1p states in the first order (i.e., on CI level). The third-order ADC(3) scheme, while still confined to the basis of 1h and 2h1p intermediate states, treats the coupling between the 1h states and between 1h states and 2h1p states in the third and in the second order, respectively. A detailed description of the single-ionization ADC(2) and ADC(3) schemes, including the expressions for the Hamiltonian matrix elements can be found in Ref. [22]. The proof of the size consistency of the ADC(n) schemes has been given in Refs. [20]. The main limitation of the existing ADC(n) schemes is that they are applicable to ionized and/or excited states of closed-shell systems only.

Let us show how the ADC(n) schemes can be used for the ab initio calculations of the decay rates within Fano formalism. To this end, we need to show that both bound (Φ) and continuum ($\chi_{\beta,\epsilon_\beta}$) $(N-1)$-electron states [see Eq. (4)] can be approximated by the expansion in the basis of the intermediate states (9). In order to describe a perfectly bound state, the wavefunction Φ must not contain any component corresponding to the possible final states of the decay. These components are to be found among the $m = 2$ (2h1p) and the higher excitation classes. Indeed, the final state of the Auger decay is characterized by two vacancies ("holes") and a single electron in the continuum ("particle") (here we neglect the effect of satellites and double Auger decay [2]). In a simple approximation, the 2h1p configurations corresponding to the open decay channels originate from the $(N-2)$-electron 2h configurations, which are lower in energy than the decaying state:

$$E_{i,j}^{(N-2)} = \langle \Phi_{i,j}^{(N-2)} | H | \Phi_{i,j}^{(N-2)} \rangle < E_\Phi, \quad \Phi_{i,j}^{(N-2)} = c_i c_j \Phi_0^N . \tag{10}$$

Consequently, in order to obtain the ADC(n) approximation for Φ, one can limit the physical excitation operators used in the construction of the CESs to those which satisfy the appropriate energy criterion:

$$\begin{aligned}\Psi_J^0 &= \hat{C}_J \Psi_0^N, \\ \{\hat{C}_J\} &\equiv \Big\{ c_i;\ c_a^\dagger c_i c_j, i<j, E_{i,j}^{(N-2)} > E_\Phi; \\ &\qquad c_a^\dagger c_b^\dagger c_i c_j c_k, a<b, i<j<k, E_{i,j,k}^{(N-3)} > E_\Phi; \ldots \Big\}.\end{aligned} \tag{11}$$

Similarly, the continuum-like functions, $\chi_{\beta,\epsilon_\beta}$, describing the possible final states of the electronic decay, are naturally found among the ADC(n) eigenstates of the 2h1p character

$$\chi_{\beta,\epsilon} \sim \Psi_q^{\mathrm{2h1p}} = \sum_i \sum_{[J]=i} Y_{q,J} \tilde{\Psi}_J, \quad 1 - \sum_{[J]=2} |Y_{q,J}|^2 \ll 1 \tag{12}$$

that correspond to the open decay channels. Upon the completion of the selection process, one can construct and diagonalize the initial state and the final state Hamiltonians on the basis of the restricted sets of the intermediate states using the standard methods. The ADC(n) state approximating the Φ component can be identified, for example, as the one possessing the maximal overlap with the cluster orbital representing the initial vacancy. Since no configurations corresponding to the open decay channels were used in the ADC-ISR expansion for the bound-like component, Φ, it will be one of the lowest-energy eigenvectors of the ADC Hamiltonian. Therefore, a highly efficient Davidson diagonalization technique [23] can be used to diagonalize the matrix.

Despite the ability of ADC(n) to produce 2h1p-like wavefunctions in the continuum region of the spectrum, there still exists a major difficulty in associating these ADC(n) eigenstates with the approximate continuum states of Fano theory. The difficulty stems from the fact that the ADC(n) calculations, and ab initio quantum chemical calculations in general, are routinely performed using the $\mathcal{L}^2$ bases, usually the Gaussian ones. As a result, the $\mathcal{L}^2$ and not the scattering boundary conditions are imposed and the Ψ_q^{2h1p} functions are not properly normalized,

$$\langle \Psi_q^{\mathrm{2h1p}} | \Psi_{q'}^{\mathrm{2h1p}} \rangle = \delta_{q,q'} \tag{13}$$

[cf. Eq. (2)]. Moreover, the corresponding eigenenergies, E_q^{2h1p}, are discrete and are not expected to fulfill the energy conservation relation for the non-radiative decay, $E_q^{\mathrm{2h1p}} = E_\Phi$, except by coincidence. An efficient way to deal with the above complications is provided by the computational approach

developed by Langhoff and Hazi and known as Stieltjes-Chebyshev moment theory or Stieltjes imaging [24]. This approach rests in the fact that although decay width (4) cannot be calculated using the discretized continuum functions directly, the spectral moments of Eq. (4) calculated using the pseudospectrum are good approximations to the spectral moments constructed using the true continuum [24]:

$$\sum_{\beta} \int E^k \left| \langle \Phi | H - E_r | \chi_{\beta,\epsilon_\beta} \rangle \right|^2 dE \approx \sum_{q} \left(E_q^{2h1p} \right)^k \left| \langle \Phi | H - E_r | \Psi_q^{2h1p} \rangle \right|^2 . \qquad (14)$$

Using the techniques of moment theory, one can recover the correct value of the decay width (4) from the pseudospectrum through a series of consecutive approximations of increasing order, n_S [24]. Stieltjes imaging has been first applied to the calculation of Auger decay widths by Carravetta and Ågren [25]. A particularly efficient realization of the Stieltjes imaging procedure has been described in detail in Ref. [26]. Standard formulation of the moment theory requires full diagonalization of the final state Hamiltonian matrix, which poses a formidable challenge for polyatomic systems. This computational bottleneck was realized already early on [27], and a number of suggestions as to how it can be overcome exist in the literature [28]. More recently, it has been suggested to use block-Lanczos pseudospectrum, rather than full spectrum, as the input for the Stieltjes imaging procedure [29]. It has been shown that the Lanczos-Stieltjes technique can be used for efficient computation of both intra- and interatomic decay widths [30].

The Fano-ADC technique outlined above can be generalized to the case of multiply ionized systems. Full description of the effect of the additional vacancies requires, of course, an ab initio approach that explicitly takes into account multiple ionization. In the case of a single additional charge, the ADC scheme for doubly ionized states would be appropriate. Such a scheme was developed by Schirmer and Barth [31]. The extended second-order ADC technique for double ionization [31] treats explicitly the two-hole (2h) and the three-hole one-particle (3h1p) excitation classes up to the second and first orders, respectively. Fano-ADC(2)x for decay widths of doubly ionized states embedded into triple ionization continua has been developed in Ref. [32].

3. APPLICATIONS OF FANO-ADC THEORY TO AUGER DECAY IN THE MULTIPLY IONIZED SYSTEMS

Let us describe several recent applications of the Fano-ADC theory to Auger decay in multiply ionized systems. We shall start with the simplest problem of this kind – effect of a single neighboring charge on the rate of atomic Auger decay. Then, we shall explore the effect of a spectator vacancy residing

on the core-ionized atom undergoing an Auger transition. Finally, we shall investigate the effect of Auger electron trapping in a multiply ionized cluster.

3.1. Auger decay in the field of a positive charge

Suppose an Auger transition occurs in the field of a stationary point charge being at distance R from the core-ionized atom, R being in the order of 1 Å or bigger. In such a case, Wentzel's formula (1) suggests that the Auger rate can be influenced by the charge through the distortions of the electronic orbitals participating in the transition. The tightly bound core orbital, φ_{core}, is not likely to be affected, since its binding energy is typically at least two orders of magnitude higher than interaction energy of the core electron with a unit charge at 1 Å distance. Typical kinetic energy of an Auger electron is also much higher than its interaction energy with the point charge. A visible effect of the charge on the Auger rate (1) can come, nevertheless, through distortion of the valence orbitals, φ_{val} and φ'_{val}, especially if the latter are easily polarizable. Indeed, binding energies of atomic valence orbitals ranging from ∼3.9 to ∼24.6 eV are of the same order of magnitude as the electron–proton attraction at the distance of 1 Å (∼14.4 eV).

Let us look closer at the possible effect of the point charge on the Auger rate bearing in mind the importance of the valence orbital distortion. To this end, we shall further simplify Wentzel's expression (1) by neglecting the "exchange" and representing the "direct" Auger transition matrix element as a repulsion energy between two charge clouds:

$$V_{\text{Auger}} = \int \mathrm{d}^3 r_1 \int \mathrm{d}^3 r_2 \, \varphi_{\text{val}}(\vec{r}_1)\varphi_{\text{core}}(\vec{r}_1) \, \frac{1}{r_{12}} \, \varphi'_{\text{val}}(\vec{r}_2)\varphi_{\varepsilon}(\vec{r}_2) \tag{15}$$

and using multipole expansion [33]:

$$V_{\text{Auger}} = \sum_{l,m} \left\langle \varphi_{\text{val}}(\vec{r}_1) \left| r_1^l Y_{lm}(1) \right| \varphi_{\text{core}}(\vec{r}_1) \right\rangle \left\langle \varphi'_{\text{val}}(\vec{r}_2) | Y_{lm}(2)/r_2^{l+1} | \varphi_{\varepsilon}(\vec{r}_2) \right\rangle , \tag{16}$$

where Y_{lm} are spherical harmonics as defined in Ref. [33]. Effectively, multipole expansion breaks the two-electron transition into the recombination and the ionization parts. The lowest nonzero angular momentum contribution to the expansion (16) defines the multiplicity of the given Auger transition.

Following Bloch [34], one can perform a crude analysis of Eq. (16) assuming that the recombination matrix element scales as r_{core}^l, where r_{core} is the spatial extension of the core orbital, while the ionization matrix element scales as $1/r_{\text{val}}^{l+1}$, where r_{val} is the spatial extension of the valence orbital. Since $r_{\text{core}} \ll r_{\text{val}}$, we obtain

$$V_{\text{Auger}} \sim r_{\text{core}}^l / r_{\text{val}}^{l+1} . \tag{17}$$

Practically, this scaling means that in order to increase the Auger rate, one has to lower the multiplicity of the transition, l, and/or to contract the valence orbital. Both these effects can be achieved through valence orbital distortion by the point charge. Indeed, at atom–proton distances larger than r_{val} one can expect orbital distortion to result in the symmetry lowering that naturally leads to the change in Auger transition multiplicity. At shorter distances, a proton penetrating the valence electron cloud would lead to an effective r_{val} smaller than that in a free system. In what follows, we shall explore these effects quantitatively using Fano-ADC theory of the Auger decay widths.

Let us first consider a simple Auger process with only a single decay channel [$N_c = 1$, see Eq. (4)]. Although not characteristic of K-shell Auger, such processes take place upon $(n-1)p$ ionization of alkaline earth atoms, for example, in $(2p^{-1})$ Mg^+, where the only nonradiative decay pathway involves the two $3s$ electrons: $(2p^{-1})$ $Mg^+ \rightarrow (3s^{-2})$ $Mg^{2+} + e^-$. Assume that $(2p^{-1})$ Mg^+ Auger decay occurs in the field of a stationary positive charge, say, of a proton fixed at the distance R from the Mg^+ ion. Then, following the arguments given above, we should expect the decay width, Γ, to vary as a function of R due to distortion of the valence $3s$ orbital. In Figure 6.2 we present the results of our Fano-ADC(2)x calculations for the $\Gamma(R)$ in the $(2p^{-1})$ Mg^+–H^+ system [35] that indeed reveals such a variation.

At large Mg–proton separations, the Fano-ADC(2)x width converges to about 0.16 meV, in a good agreement with the theoretical value of Walters and Bhalla for the isolated Mg atom (0.145 meV) [36]. Our results show that at the distances below 4 Å, the decay width grows very strongly with decreasing Mg^+–H^+ distance. Practically, the same result is obtained when removing the Gaussian basis from the proton, that is, the possible transfer of Mg electron density to the neighboring charge does not play a key role in the effect (see Figure 6.2). Moreover, the predicted increase of the decay width is not an artifact of the Gaussian basis set itself that, of course, also changes with R – this is verified by repeating the Fano-ADC(2)x calculation in full Gaussian basis, but with zero charge on the "proton," finally, the clear indication that the predicted effect is due to the distortion of the valence orbital comes from another set of ab initio calculations, in which, we "freeze" the Gaussian orbital coefficients in the Mg $3s$ orbital of Mg–H^+ at their values at the largest considered distance of $R = 6.5$ Å. The results presented in Figure 6.2 show that the strong effect of the Auger width increase practically vanishes if the $3s$ orbital is frozen [35].

Further insight into the strong variation of the Auger decay width as a function of the Mg–proton distance is gained by the qualitative analysis in the spirit of Eqs. (16) and (17). Indeed, at $R \rightarrow \infty$ $(2p^{-1})$ Mg^+ Auger transition is of dipole–dipole type [$l = 1$, see Eq. (16)]. As the Mg–proton distance decreases, the Mg $3s$ orbital is distorted such that it attains a nonzero p_z component, reducing the multiplicity of the Auger transition to $l = 0$ and leading to the increase in the Auger width. This effect of the valence orbital distortion

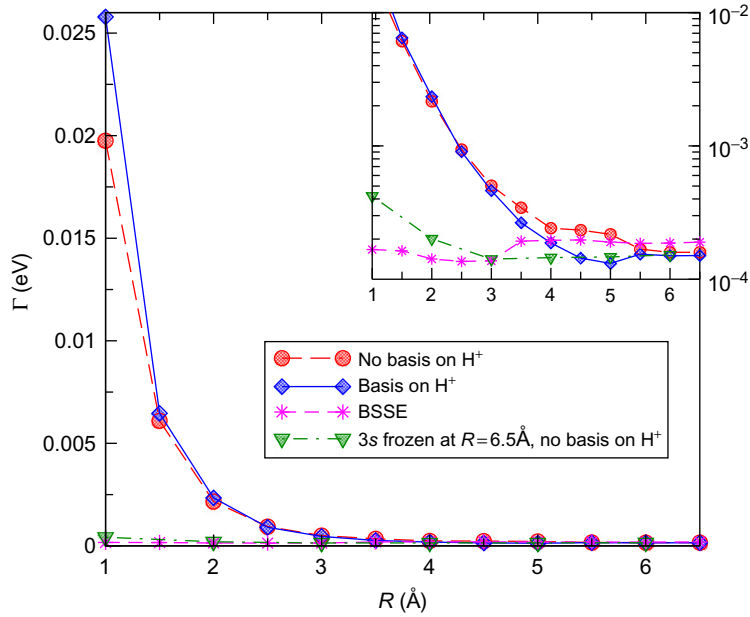

Figure 6.2 Auger decay width of $(2p_z^{-1})$ Mg^+–H^+ as a function of the Mg–proton distance, R. z is Mg–proton axis. Diamonds and solid line: Fano-ADC(2)x calculation with atomic orbital basis centered both on Mg and on the proton; circles and long-dashed line: Fano-ADC(2)x calculation with atomic orbital basis centered only on Mg; stars and short-dashed line: Fano-ADC(2)x calculation for $(2p_z^{-1})$ Mg^+ alone, with atomic orbital basis centered both on Mg and at the distance R along the z-axis, showing the so-called basis set superposition error (BSSE); triangles and dashed-dotted line: Fano-ADC(2)x calculation with atomic orbital basis centered on Mg only, with the 3s orbital of Mg being frozen at its shape at $R = 6.5$Å. The inset shows the low-Γ part of the plot on logarithmic scale. See Ref. [35] for the details of the computation.

at $R > 2.5$ Å is readily seen in the data presented in Figure 6.3 [panels (a) and (b)]. As the proton approaches the Mg^+ ion further, it penetrates the valence electron orbital and eventually leads to its contraction, see Figure 6.3, panel (c). Thus, also at $R > 2.5$ Å, although the distortion of the 3s orbital along the Mg–proton axis decreases, the orbital contraction effect [quantified by decrease of $r_{\rm val}$ – see Eq. (17)] leads to further increase of the Auger rate.

The above analysis suggests that the spectacular effect of the neighboring charge on the single-channel Mg 2p Auger decay has to do with the polarizable Mg 3s orbital that is involved both in the recombination and in the ionization parts of the two-electron transition. Let us consider now a more general situation, in which a polarizable orbital is involved only in the ejection of the Auger electron. An example of such a transition is readily provided by 2s-ionized Mg. Indeed, 2s ionization leads to the process in which

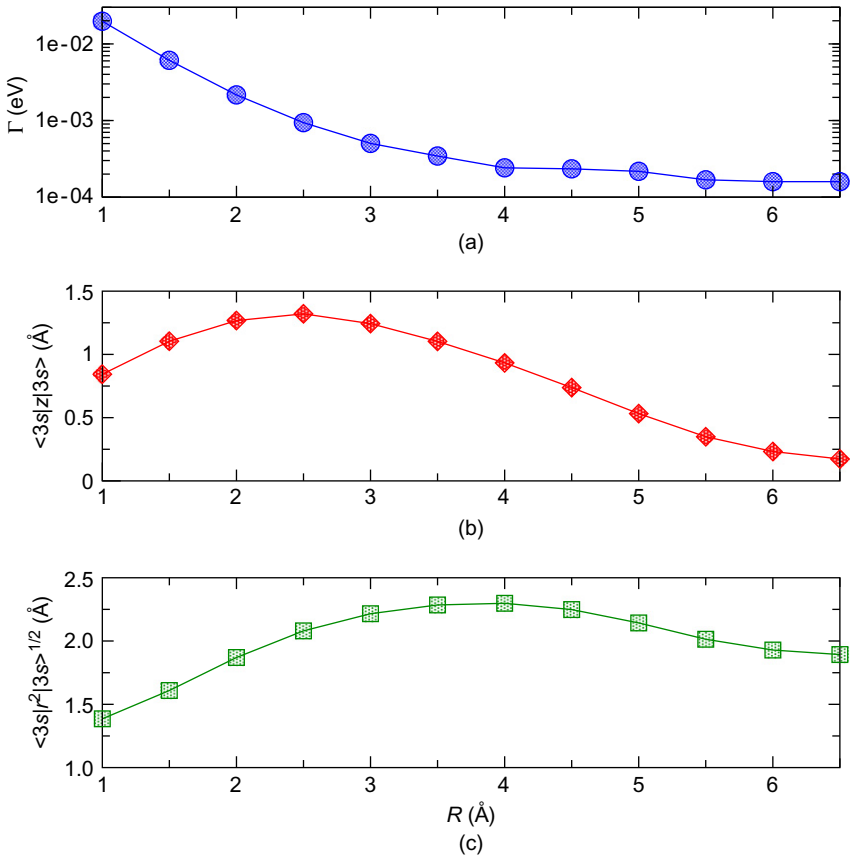

Figure 6.3 (a) Fano-ADC(2)x result for the Auger decay width of $(2p_z^{-1})$ Mg^+–H^+ as a function of the Mg–proton distance, *R* (logarithmic scale); (b) *z* expectation value of the Mg 3*s* orbital as a function of the Mg–proton distance, *R*, showing the extent of the orbital distortion along the Mg–proton axis; (c) mean radius of the Mg 3*s* orbital as a function of the Mg–proton distance, *R*, showing the spatial extent. See Ref. [35] for the details of the computation.

one of the 2*p* electrons fills the vacancy while a 3*s* electron is ejected into continuum: $(2s^{-1})$ $Mg^+ \rightarrow (2p^{-1}3s^{-1})$ $Mg^{2+} + e^-$. This decay is characterized by the recombination transition occurring within a single $(n = 2)$ electronic shell and as such belongs to the class of Coster-Kronig (CK) decay processes [2]. The efficient recombination part of the transition and the relatively low kinetic energies of the CK electrons contribute to the typically large widths of the CK decay. In the particular case of $(2s^{-1})$ Mg^+, the CK transition is by far the leading decay channel with the competing $(2s^{-1})$ $Mg^+ \rightarrow (3s^{-2})$ $Mg^{2+} + e^-$ Auger decay being much weaker.

Figure 6.4 shows the results of the Fano-ADC(2)x calculation of the $(2s^{-1})$ Mg^+ decay width in the Mg^+–H^+ system as a function of the Mg–proton distance. The decay is completely dominated by the CK process, accounting for 95–99% of the total electronic decay width. At large R, the Fano-ADC(2)x result assuming no electron density on the proton is in excellent agreement with the R-matrix prediction for bare $(2s^{-1})$ Mg^+ [37]. We observe a well-pronounced dependence of the CK on the Mg–proton distance that is drastically reduced by artificially "freezing" the 3s orbital at its large-R shape. The magnitude of the neighboring charge effect is smaller than in the case of the $(2p^{-1})$ Mg^+ decay, apparently because the distorted valence orbital is only involved in the ionization part of the two-electron transition. Noteworthy is a clearly distinguishable effect that the electronic density on the proton has on the decay. Allowing part of the electronic density to reside on the proton diminishes the electronic density on the core ionization site and as a result leads to the reduction of the CK decay width (see Figure 6.4).

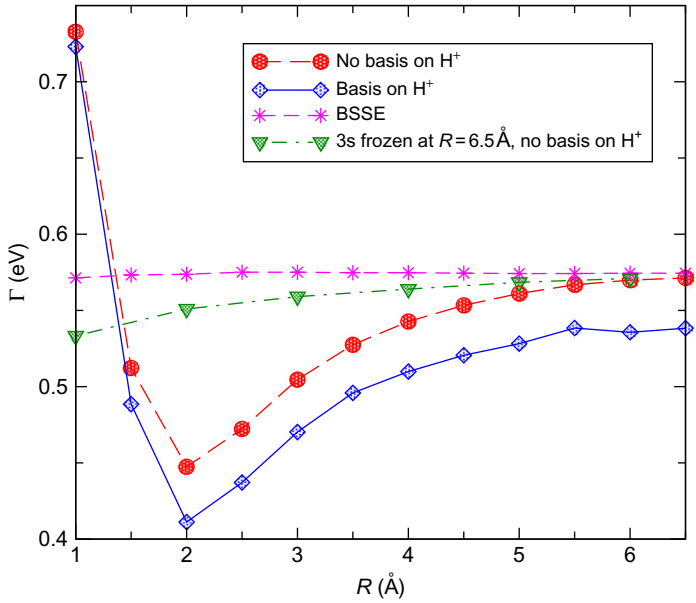

Figure 6.4 Decay width of $(2s^{-1})$ Mg^+–H^+ as a function of the Mg–proton distance, R. Diamonds and solid line: Fano-ADC(2)x calculation with atomic orbital basis centered both on Mg and on the proton; circles and long-dashed line: Fano-ADC(2)x calculation with atomic orbital basis centered only on Mg; stars and short-dashed line: BSSE (see Figure 6.2); triangles and dashed-dotted line: Fano-ADC(2)x calculation with atomic orbital basis centered on Mg only, with the 3s orbital of Mg being frozen at its shape at $R = 6.5$Å. See Ref. [35] for the details of the computation.

Assuming that the neighboring charge was formed long before an instantaneous Mg core ionization, the physical decay width is produced by the Fano-ADC calculation with basis set on the proton. If, on the other hand, Mg and a neighboring site ionization occur closely in time on the scale of the CK lifetime, the dynamics of the neighboring hole should be taken into account. Such a hole dynamics induced by electron correlation can take place at fixed nuclear geometries on the timescales comparable to the ones of CK or Auger decay [38] and is expected to be strongly influenced by the nuclear motion, at least on a bit longer timescales. Consideration of this effect should be a subject of future studies.

In summary, ab initio results for a number of Auger-type transitions show a pronounced dependence of the Auger width on the atom–proton distance. The origin of this dependence can be traced to the distortion of the outer valence atomic orbital by the field of the proton. A simple qualitative physical picture can be used to explain the Auger rate dependence in terms of the change of multiplicity of Auger transitions and the valence orbital contraction as a result of the interaction with the positive charge. The magnitude of the predicted neighboring charge effect differs substantially between different Auger-type transitions, but is found to be the strongest at the atom–proton distances of about 1–2 Å, that is, at the distances of the order of chemical bond length. At the distances of 3–4 Å, typical of the bond lengths in van der Waals clusters, the neighboring charge effect is much less pronounced.

3.2. *K*-shell Auger lifetime variation in doubly ionized Ne and first-row hydrides

Auger decay lifetimes can be affected not only by the additional positive charges residing on neighboring atoms but also by the multiple ionization of the atom bearing the core vacancy. Here, we shall explore the effect of the double ionization of a single atom on the Auger lifetimes. Since the Auger transitions of interest for the radiation damage in single-molecule x-ray diffraction are mainly induced by *K*-shell ionization of C, N, and O atoms, we specifically target doubly (*KK*- and *KL*-) ionized states of CH_4, NH_3, and H_2O as model systems, comparing them with the corresponding transition in the isoelectronic Ne atom.

Let us first consider Auger processes in doubly ionized Ne as a simple prototype system. Auger-active states of Ne^{2+} can be classified as stemming from $1s^{-2}$, $1s^{-1}2s^{-1}$ and $1s^{-1}2p^{-1}$ configurations. The first one of those, that is, the "hollow atom," has recently been observed in the XFEL studies [39]. Looking at the spectator–core–hole *KK–KLL* Auger decay process in the hollow Ne, one immediately notices that it has twice the number of the decay pathways relative to the normal *K–LL* Auger transition. In the simplest approximation, one would expect, thus, the *KK–KLL* decay rate to be just

twice the *K–LL* one. Further, one notices that a couple of a bit more subtle effects can push the hollow Ne decay rate into opposite directions. First, double *K*-shell ionization leads to contraction of the valence orbitals in the initial state of the process, making the Auger matrix elements larger. Second, the kinetic energy of the *KK–KLL* Auger electrons is a bit higher than that of the *K–LL* (by about 70 eV [40]) ones which could have just the opposite effect. Looking at the theoretical values for the *KK–KLL* widths available in the literature, namely 707 meV (C.P. Bhalla *et al.*, 1973 [41]), 804 meV (M.H. Chen, 1991 [42]), and 623 meV (Pelicon *et al.*, 2001 [43]), one finds that all of them exceed the normal Auger width in Ne (240 meV [5]) by more than twice, suggesting that the effect of the valence orbital contraction is the dominant one. The Voigt fit analysis of a 3 eV wide *KK–KLL* feature in the experimental spectrum [40] supports this conclusion.

In the very recent work [44], the Auger decay widths were calculated using the Fano-ADC method outlined in Section 2. Our Fano-ADC computation for the hollow Ne produces the decay width of 506 meV, which is lower than the available literature values and extremely close to twice the normal Auger width. In fact, it has been found that all the *KK–KLL* decay channels attain about twice as larger partial widths than their *K–LL* counterparts [44]. Noteworthy, our Fano-ADC result for the normal Auger width 251 meV agrees rather well with the recommended literature value [5], and our partial width analysis for the *K–LL* transition is in good correspondence with the available experimental and theoretical results [45] (see Table 6.1). Nevertheless, the discrepancy between our result and the literature values (by themselves having a spread of more than 20%, see Table 6.2) could well result from the underestimation of the very strong relaxation effects in the hollow atom states by the second-order ADC scheme employed in our calculation. We believe that further work on the decay lifetimes of the hollow Ne is needed.

Auger dynamics of a hollow Ne atom presents a particular interest because a three-electron *KK–LLL* process can contribute to the decay of the core vacancies. Such a process, in which two valence electrons recombine into the core orbital to produce an extra-energetic free electron, has been first observed in doubly *L*-shell-ionized Ar atoms [52] and later in Kr and Xe [53]. The corresponding partial decay width in *LL*-ionized Ar was estimated to be in the range of 0.01–1 meV. To our knowledge, there are so far no theoretical or experimental data available for such a three-electron Auger transition in hollow Ne. Our Fano-ADC calculation for the Ne *KK–LLL* process gives the partial decay width of about 0.05 meV, well within the range of the estimated *LL–MMM* Ar values. Assuming that our calculation underestimates the valence orbital contraction effect, this figure presents a lower bound for the three-electron process width. Although clearly negligible relative to the total hollow Ne decay width, the *KK–LLL* process can well be observable, as in the case of heavier rare gas atoms, since it produces highly energetic

Table 6.1 Comparison of the branching ratios of the *K–LL* Auger transition in singly core-ionized Ne

Ne^+ Transition		Present	Kelly [46]	Yarzhemsky [45]	Nicolaides1 [47]	Nicolaides2 [48]	Howat1 [49]	Howat2 [49]	Exp. [50, 51]
	^3P	0.0	0.0	0.0	–	–	–	–	–
$K–L_{2,3}L_{2,3}$	^1D	50.5	61.2	58.2	67.1	66.9	57.3	61.2	60.9
	^1S	9.5	9.6	10.2	5.7	4.7	9.0	9.2	9.5
$K–L_1L_{2,3}$	^3P	10.6	6.1	9.3	3.5	3.8	9.6	7.8	6.3
	^1P	19.5	17.0	16.8	18.4	19.5	18.5	16.7	17.2
$K–L_1L_1$	^1S	9.9	6.1	5.5	5.3	5.1	5.7	5.0	6.1
Total width (meV)		**251**	**219**	**242**	**227**	**230**	**288**	**244**	**220 ± 30**

Branching ratios are given in %, the total widths are in meV. Howat1 and Howat2 results correspond to the Hartree–Fock and transition state basis sets of Ref. [49] respectively. The experimental values for *K–LL* transition are taken from Albiez *et al.* [50] (branching ratios) and from Avaldi *et al.* [51] (total width).

Table 6.2 Comparison of the branching ratios of the *KK–KLL* Auger transitions in doubly core-ionized Ne

Ne^{2+} Transition		Present	Pelicon [43]	Chen [42]	Bhalla [41]
	^2P	0.0	0.3	0.4	
$KK - KL_{2,3}L_{2,3}$	^2D	59.0	49.2	44.0	66.2
	^2S	8.1	9.2	12.6	
$KK - KL_1L_{2,3}$	$^2P^{(-)}$	6.9	1.1	0.7	
	$^2P^{(+)}$	22.6	33.0	31.6	25.0
$KK - KL_1L_1$	^2S	3.4	7.0	10.7	7.9
Total width (meV)		**506**	**623**	**805**	**707**

Branching ratios are given in %, the total widths are in meV.

electrons well outside the energy region of the two-electron transitions. Interestingly, an analogous "collective" interatomic three-electron process can turn out to be the main decay channel in doubly inner-valence-ionized clusters (see Section 3.4 and Ref. [48]).

Going from hollow Ne to core-valence-ionized Ne, one should consider two types of configurations, namely $1s^{-1}2s^{-1}$ and $1s^{-1}2p^{-1}$ ones, which lead to both singlet and triplet states and turn out to have distinctly different patterns of lifetime variation with the spin multiplicity. The results of our Fano-ADC calculations of Auger widths for core-valence-ionized Ne are given in Table 6.3. Looking at the results of these ab initio calculations, one readily notices that while spin multiplicity plays no role for the Auger widths of the $KL_{2,3}$ states, the widths of the KL_1 states depend crucially on whether the two holes form a singlet or a triplet. Indeed, the corresponding ^1S state decays about 1.6 times faster than the triplet state. The origin of this trend becomes apparent if one looks at the partial widths of the KL_1 states (see Table 6.3). In the decay of the singlet initial state, the recombination from 2*s* orbital to 1*s* one is operative and $2s^{-1}\,2p^{-2}$ and $2s^{-2}\,2p^{-1}$ electronic configurations of the Ne^{3+} final states are about evenly populated. In the case of the triplet decaying state, however, the single electron in the 2*s* orbital has the same spin as the one in the 1*s* orbital and, therefore, cannot fill the 1*s* vacancy. The $Ne^{3+}(2s^{-2}\,2p^{-1}\,^2P)$ channel is still accessible but only via higher-order processes comprising three-electron transitions. This leads to a radical drop in efficiency by nearly 90%. This effect fully explains the difference between the total Auger rates for the singlet ^1S and triplet ^3S initial states. Comparing this situation to the decay of the $KL_{2,3}$ states, one notices that the partial decay widths for the $Ne^{3+}(2s^{-1}\,2p^{-1})$ channels remain more or less unchanged when going from singlet to triplet initial states, up to some redistribution of intensity between different terms of the $2s^{-1}2p^{-2}$ final configuration. In total, the

Table 6.3 Fano-ADC total and partial Auger decay widths (in meV) for doubly ionized Ne atom

Final state	$1s^{-1}\,2s^{-1}$ ^1S	$1s^{-1}\,2s^{-1}$ ^3S	$1s^{-1}\,2p^{-1}$ ^1P	$1s^{-1}\,2p^{-1}$ ^3P
$2p^{-3}\,{}^4S$	–	0	–	0 (0)
$2p^{-3}\,{}^2D$	0	0	78 (75)	77 (76)
$2p^{-3}\,{}^2P$	1	0	31 (37)	33 (37)
$2s^{-1}\,2p^{-2}\,{}^4P$	–	0	–	12 (11)
$2s^{-1}\,2p^{-2}\,{}^2D$	127	135	7 (0)	23 (28)
$2s^{-1}\,2p^{-2}\,{}^2S$	16	15	4 (0)	6 (6)
$2s^{-1}\,2p^{-2}\,{}^2P$	0	0	53 (52)	26 (23)
$2s^{-2}\,2p^{-1}\,{}^2P$	123	16	24 (23)	25 (23)
Total width	**267**	**166**	**197** (187)	**202** (204)

Electronic configurations and terms of the decaying states are specified in the first row. The literature values in parentheses are taken from Ref. [55]. See Ref. [44] for the details of the Fano-ADC computation.

Table 6.4 Comparison of the Fano-ADC results with the available theoretical and experimental values for the *K–LL* Auger decay widths in CH_4, NH_3, and H_2O molecules

	Present	Theory			Experiment			
CH_4	85	[56] 75	[57] 96	[58] 96	[59] 107 ± 10	[60] 120 ± 10	[61] 83 ± 10	[62] 94 ± 1
NH_3	123	[63] 106						
H_2O	148	[25] 150			[64] 160 ± 5			

The decay widths are in meV, citations are given in square brackets. Experimental value for ammonia is lacking because of the vibrational broadening in the Auger electron spectrum of ammonia [65]. See Ref. [44] for the details of the Fano-ADC computation.

decay widths of both singlet and triplet $1s^{-1}2p^{-1}$ states are about 80% of the Ne $K-LL$ Auger rate, which is close to what is expected on the basis of the simple counting of the available Auger decay pathways.

Let us now consider the effect of a spectator vacancy on the Auger rate of the C, N, and O core hole in CH_4, NH_3, and H_2O molecules, respectively. These molecules are isoelectronic with Ne; however, the degeneracy of the outer valence orbitals is preserved only in the tetrahedral CH_4. The Fano-ADC Auger widths of the singly core-ionized molecules [44] are presented in Table 6.4 alongside the available literature data. The calculated total Auger

widths for the Auger-active main electronic states of the doubly ionized molecules are given in Table 6.5. The results for the molecular Auger decay widths reveal the trends analogous to the one observed in Ne atom. In particular, it has been found that inner-valence spectator vacancies in methane, ammonia, and water play the same important role as it does in neon: the singlet- to-triplet ratio of the decay widths ranges from 1.6 (NH_3, H_2O) to 1.8 (CH_4). As in the case of Ne atom, this very pronounced difference is due to the fact that the transitions involving inner-valence-core recombination are, at least in the first order of perturbation theory, forbidden in the decay of the triplet states. In the case of outer-valence spectator hole, the effect of the spin multiplicity on the Auger rate is small, beyond the accuracy of our computational method. Furthermore, we find that the Fano-ADC decay widths of the hollow ($1s^{-2}$) molecules is approximately twice larger than the corresponding normal Auger widths, in accordance with the doubling of the available decay pathways. Assuming that our calculation for hollow molecules suffer from underestimation of the relaxation in the initial state in the same way

Table 6.5 Fano-ADC total Auger decay widths (in meV) for different electronic states of doubly ionized CH_4, H_2O, and NH_3 molecules

Decaying state	Γ (meV)	Decaying state	Γ (meV)
Ne ($\Gamma_{1s^{-1}} = 251$ meV)		CH_4 ($\Gamma_{1a_1^{-1}} = 85$ meV)	
$1s^{-1}\,2p^{-1}\,{}^1P$	197	$1a_1^{-1}\,1t_2^{-1}\,{}^1T_2$	68
$1s^{-1}\,2p^{-1}\,{}^3P$	202	$1a_1^{-1}\,1t_2^{-1}\,{}^3T_2$	69
$1s^{-1}\,2s^{-1}\,{}^1S$	267	$1a_1^{-1}\,2a_1^{-1}\,{}^1A_1$	90
$1s^{-1}\,2s^{-1}\,{}^3S$	166	$1a_1^{-1}\,2a_1^{-1}\,{}^3A_1$	49
$1s^{-2}\,{}^1S$	506	$1a_1^{-2}\,{}^1A_1$	167
NH_3 ($\Gamma_{1a_1^{-1}} = 123$ meV)		H_2O ($\Gamma_{1a_1^{-1}} = 148$ meV)	
$1a_1^{-1}\,3a_1^{-1}\,{}^1A_1$	92	$1a_1^{-1}\,1b_1^{-1}\,{}^1B_1$	110
$1a_1^{-1}\,3a_1^{-1}\,{}^3A_1$	94	$1a_1^{-1}\,1b_1^{-1}\,{}^3B_1$	116
$1a_1^{-1}\,1e^{-1}\,{}^1E$	100	$1a_1^{-1}\,3a_1^{-1}\,{}^1A_1$	121
$1a_1^{-1}\,1e^{-1}\,{}^3E$	105	$1a_1^{-1}\,3a_1^{-1}\,{}^3A_1$	118
		$1a_1^{-1}\,1b_2^{-1}\,{}^1B_2$	122
		$1a_1^{-1}\,1b_2^{-1}\,{}^3B_2$	126
$1a_1^{-1}\,2a_1^{-1}\,{}^1A_1$	126	$1a_1^{-1}\,2a_1^{-1}\,{}^1A_1$	157
$1a_1^{-1}\,2a_1^{-1}\,{}^3A_1$	81	$1a_1^{-1}\,2a_1^{-1}\,{}^3A_1$	99
$1a_1^{-2}\,{}^1A_1$	230	$1a_1^{-2}\,{}^1A_1$	311

The Fano-ADC Auger decay widths of the single core vacancies are given for each molecule in parentheses. To facilitate the comparison, the Fano-ADC results for Ne atom are also given. See Ref. [44] for the details of the Fano-ADC computation.

as our results for hollow Ne, the true decay rates of the *KK*–*KLL* widths of the first-row hydrides could be about 20% higher than our theoretical predictions.

In summary, the spin state of the two holes has a major effect on the rate of the Auger decay of one-site doubly ionized states. Although singlet core-inner-valence-ionized states decay about as fast as the singly core-ionized ones, their triplet counterparts decay by up to a factor of 1.8 slower. This trend appears to be completely general and is easily explained by spin selection rules. Interestingly, the singlet–triplet factor is largest for methane, which leads one to believe that sp^3 hybridized carbon Auger decay in general can proceed significantly slower in the presence of an inner-valence hole. Depending on how probable the inner-valence ionization is for the given experimental conditions, this effect can have significant implications on the timescale of the Auger dynamics in multiply ionized biomolecules.

3.3. Suppression of exponential Auger decay in multiply charged systems

Up to now, we have considered the effect of an additional positive charge on the rate of the exponential Auger decay of a core vacancy. Interestingly, the Auger dynamics can change qualitatively in a highly ionized system. Under conditions of multiple ionization, the kinetic energy of the Auger electron may not suffice for leaving the system and the electron will be trapped by the field of the positive charges surrounding the inner-shell-ionized atom [66]. On a more formal level, the final states of the decay, $\chi_{\beta,\epsilon}$, around the resonance energy, E_r, will no longer form a continuum, but will rather turn into closely spaced bound states. An electron occupying one of such states will be delocalized across the whole system, yet, will not be able to leave it. With discrete final states, however, one cannot expect the familiar notion of the exponential decay to remain valid and the very basics of our understanding of electronic decay dynamics should be reconsidered. Indeed, a trapped (e.g., Auger) electron can participate in an "inverse Auger" process, that is, it can fill one of the vacancies created by the Auger transition, giving a core electron enough energy to be promoted to another vacancy of the Auger final state. Therefore, the survival probability of the core hole state [see Eq. (3)] can exhibit oscillatory rather than exponential character. This situation is formally similar to the one encountered in the nonradiative decay of excited electronic molecular states due to vibronic coupling. The reason is that the final states of this type of nonradiative decay in molecules can be bound vibrational states of a lower-energy electronic state, that is, not a continuum. For the idealized Bixon–Jortner model assuming uniform energy spacing between the adjacent final states, ε, and uniform initial–final states coupling [67], one can show that the exponential decay persists for times of the order of $\hbar/\varepsilon$. Of course, such a model could be hardly applicable to the

complicated many-electron states involved in the electronic decay. The essential open question is therefore: Can electronic decay processes in a highly charged environment be characterized, even approximately, by exponential dynamics?

In Ref. [68], the character of the electronic decay dynamics in a multiply charged system was investigated by constructing a simple but realistic model based on the L_1–$L_{2,3}M$ CK decay in Ar (see Ref. [69] and references therein). Due to the relatively low energy of the recombination transition within a single shell, CK processes are characterized by the emission of relatively slow electrons with kinetic energies of the order of several tens of electron volt. This circumstance makes CK decay processes in general and the Ar L_1–$L_{2,3}M$ decay in particular very well suited for the study of the effect of Auger electron trapping by neighboring charges. Indeed, consider an Ar cluster, for example, Ar_{13}, interacting with an intense XFEL radiation. Neutral Ar_{13} in its ground state has an icosahedral (I_h) equilibrium geometry with the central Ar surrounded by 12 symmetry-equivalent peripheral Ar atoms [70]. Simulations of Ar_{13}–XFEL interaction [10] show that one could easily reach a situation where all the Ar atoms in the cluster are singly ionized well before the cluster geometry suffers a significant distortion. Imagine, for simplicity, that the central atom of Ar_{13} is ionized in its 2*s* subshell while the 12 surrounding Ar atoms bear either 2*p* or outer-shell vacancies. Such a distribution of vacancies among the electronic shells is not implausible given that the photoionization cross sections of the outer shell and 2*p* electrons of Ar are higher than that of the 2*s* electron [71]. With the lifetime of about 0.3 fs [69], CK decay of the 2*s* vacancy is more than an order of magnitude faster than Auger decay of $(2p^{-1})$ Ar^+ [69, 72]. The timescale for the second ionization of one of the Ar atoms in the case of a long ($\sim$100 fs) XFEL pulse is controlled by the pulse intensity and can be in the range between 10 and 100 fs [10]. For these reasons, we assume the vacancy states of the 12 Ar atoms surrounding the 2*s*-ionized one to be stationary on the time scale of the CK process. If, nevertheless, the Auger decay or a second photoionization event occurs, it would effectively increase the positive charge of the cluster and lead to a stronger trapping of the would-be CK electron.

The kinetic energies of the CK electrons generated by the L_1–$L_{2,3}M$ decay in isolated $(2s^{-1})$ Ar^+ vary between about 29 and 47 eV [69]. In a multiply ionized Ar_{13} cluster, the energies of the corresponding final doubly ionized states of the central Ar will be elevated (relative to an isolated Ar) by the energy of the interaction of the additional central charge with the 12 peripheral ones. In the simple point-charge approximation, this energy elevation is given by $\Delta E = 12/R_{\mathrm{eq}}$, where R_{eq} is the equilibrium central–peripheral atom distance in the neutral Ar_{13}. With $R_{\mathrm{eq}} = 6.96$ a.u. [70], ΔE turns out to be just enough to put all the $(2p^{-1}3l^{-1})$ $Ar^{2+}(Ar^+)_{12}$ states of the cluster above the energy of the initial 2*s* vacancy. Hence, as long as the ionized cluster does

not expand, the CK electron that left the central Ar will always be bound to the cluster as a whole. In what follows, we would like to study the implication of the CK electron trapping in $(2s^{-1})$ $Ar^+(Ar^+)_{12}$ on the dynamics of the electronic decay process modeling the peripheral Ar ions by point charges (protons).

In Ref. [68], the initial and the final states of the CK decay in $2s^{-1}$ $Ar^+(H^+)_{12}$ were calculated according to the Fano-ADC scheme (11,12):

$$\Phi = a_{2s}\tilde{\Psi}_{2s} + \sum_{jka} b^a_{jk}\tilde{\Psi}^a_{jk}\,, \tag{18}$$

$$\chi_n = \sum_{j'k'a'} c^{a'(n)}_{j'k'}\tilde{\Psi}^{a'}_{j'k'}\,,$$

where the possible pairs of the j,k indices are restricted to the doubly ionized configurations with energies higher than that of Ψ_{2s}, while the possible pairs of the j',k' indices are restricted to doubly ionized configurations with energies lower than that of Ψ_{2s}, that is, to the open channels of the CK transition in an isolated Ar. With the initial and final states of the nonradiative transition specified, we obtain the evolution of the initial state by propagating it in time under the Fano type Hamiltonian, $\hat{H}$, built in the basis of $\{\Phi, \chi_n\}$:

$$\Psi(t) = e^{-i\hat{H}t/\hbar}\Phi,\ \ \hat{H} = |\Phi\rangle E_\Phi\langle\Phi| + \sum_n |\chi_n\rangle E_n\langle\chi_n| + (|\Phi\rangle\gamma_n\langle\chi_n| + \text{c.c.})\,, \tag{19}$$

where the initial–final coupling matrix elements are given by $\gamma_n = \langle\Phi|\hat{H}|\chi_n\rangle$.

The survival probability of the $2s$ vacancy state of the central Ar atom in the model Ar_{13} cluster obtained using Eqs. (3) and (19) (see Figure 6.5) shows a roughly exponential dynamics on the short time scale. During the initial 0.7 fs, the population of the $2s$ vacancy state exhibits oscillations superimposed over exponential decay with the mean rate being very close to the one of the L_1–$L_{2,3}M$ transition in an isolated Ar. A striking change of behavior occurs, however, at $t > 0.7$ fs, where even the approximately exponential decay pattern is suppressed completely by an oscillatory one. During this phase of the time evolution, the $2s$ vacancy population rises roughly from 1% to 10% in a clear manifestation of a partial "inverse Auger" transition and then falls back. At later times, the calculated survival probability keeps oscillating within a similar range. Our assumption that surrounding vacancies are stationary limits, however, the validity of the present calculation to times smaller than the Ar $L_{2,3}$–MM Auger life time of $t = 3.7$ fs. Another insight into the mechanism of the exponential decay suppression comes from the examination of the properties of the many-electron wavefunction, $\Psi(t)$, for example, of $\langle\Psi(t)|r^2|\Psi(t)\rangle$ (see Figure 6.1b). In Figure 6.5,

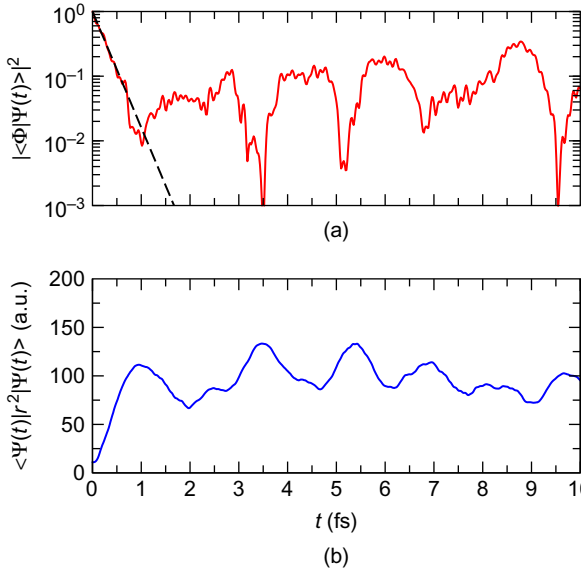

Figure 6.5 (a) Solid line: survival probability of the 2*s* vacancy in $Ar^+(H^+)_{12}$ plotted on the logarithmic scale. Dashed line: same for the exponential decay of the 2*s* vacancy in an isolated Ar^+. (b) Time dependence of the r^2 expectation value measuring the spatial extension of the $Ar^+(H^+)_{12}$ electronic wavefunction. See Ref. [68] for the details of the computation.

one can easily notice that the plots of the spatial extent of $\Psi(t)$ and of the survival probability of the 2*s* vacancy state behave as mirror images of each other with the minima of the former corresponding to the maxima of the latter. This suggests the following simple physical picture of the predicted Auger oscillations. The Auger electron wave packet emitted by the central ion is reflected back by the charged cluster potential, leading to peaks of $\langle r^2\rangle(t)$ (Figure 6.5). Propagating back toward the central atom, the Auger electron partly recombines in an inverse Auger transition leading to the partial revivals of $|\langle\Phi|\Psi(t)\rangle|^2$ (Figure 6.5).

In summary, the dynamics of the electronic decay of inner-shell vacancies in a charged environment, such as created by interaction of a cluster with a high intensity FEL radiation, can be qualitatively different from the one induced by a low-intensity source. If the emitted electrons are slow enough to be trapped by the neighboring charges, the familiar exponential decay will be suppressed by quantum beats between the initial state and the quasi-continuum of discrete final states. Physically, the predicted oscillations correspond to creation of the initial vacancy due to the reflections of the emitted electron by the charged cluster potential and the subsequent inverse Auger transition.

3.4. Collective interatomic decay of multiple vacancies in clusters

In the above example, we have considered a situation where the presence of additional positive charges leads to suppression of electronic decay through channel closing. It would be tempting to ask whether the reverse physical situation is possible, that is, whether multiple ionization can lead to channel opening resulting in a decay process that occurs exclusively in a multiply inner-shell-ionized system. In fact, an example of such a process, that is, *KK–LLL* decay has been already mentioned in connection with double-core ionization (see Section 3.2). There, however, a collective decay of two core holes is completely overwhelmed by the much more probable normal Auger decay. A recent theoretical work [54] shows that an analogous interatomic collective process can be the dominant decay pathway in doubly ionized clusters.

Interatomic Coulombic decay (ICD) is an electronic decay process that is particularly important for those inner-shell or inner-subshell vacancies that are not energetic enough to give rise to Auger decay. Typical examples include inner-valence-ionized states of rare gas atoms. In isolated systems, such vacancy states are bound to decay radiatively on the nanosecond timescale. A rather different scenario is realized whenever such a low-energy inner-shell-ionized species is let to interact with an environment, for example, in a cluster. In such a case, the existence of the doubly ionized states with positive charges residing on two different cluster units leads to an interatomic (or intermolecular) decay process in which the recombination part of the two-electron transition takes part on one unit, whereas the ionization occurs on another one. ICD [73–75] is mediated by electronic correlation between two atoms (or molecules). In clusters of various sizes and compositions, ICD occurs on the timescale from hundreds of femtoseconds [18] down to several femtoseconds [76–79].

Consider now an inner-shell vacancy state that is not energetic enough to decay by either Auger or ICD mechanisms. Such are, for example, ns^{-1} states of Ar^+, Kr^+, and Xe^+, either isolated or in an environment of other rare gas atoms. Consider further two such vacancy states, say, in a Kr cluster or, a bit more generally, in a mixed Kr/X cluster, where X is another atom or molecule. Neither of the vacancies can decay by electron emission because the energy provided by the $4p \rightarrow 4s$ recombination is not sufficient for $4p$ ionization of either Kr^+ (as needed for Auger decay) or a neutral Kr (as needed for ICD). However, if two 4*s*-ionized kryptons recombine simultaneously, the released energy would be enough to ionize X:

$$(4s^{-1}, 4s^{-1})(Kr^+)_2X \rightarrow 2\,(4p^{-1})Kr^+ + X^+ + e^- . \qquad (20)$$

A schematic representation of such a collective decay process, or collective ICD (CICD), is given in Figure 6.6. Simple energy considerations imply that,

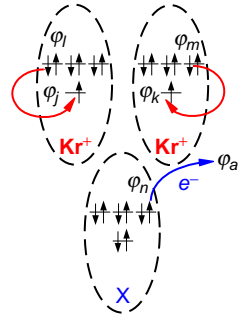

Figure 6.6 Schematic representation of collective interatomic decay of two inner-shell vacancies, see Eq. (20).

in general, the collective decay occurs without facing a competition from the ICD if $1.5 < (E_{\rm iv} - E_{\rm c})/E_{\rm ion} < 2$, where $E_{\rm iv}$ is the inner valence ionization energy of the given species, $E_{\rm c}$ is the energy of Coulombic repulsion between two singly ionized atoms or molecules (typically 3–4 eV at the equilibrium distances of neutral van der Waals clusters) and $E_{\rm ion}$ is the single ionization energy.

Some qualitative understanding of the CICD can be gained by means of Wentzel-type theory that treats the initial and final states of the decay as single Slater determinants taking electronic repulsion responsible for the transitions as a perturbation. The collective decay of two inner-shell vacancies (see Figure 6.6) is a three-electron transition mediated by two-electron interaction. Thus, the process is forbidden in the first-order perturbation theory, and its rate cannot be calculated by the first-order expressions, such as (1). Going to the second-order perturbation theory, the expression for the collective decay width can be written as

$$\Gamma = 2\pi \left| \sum_i \frac{\langle f|\hat{V}|i\rangle\langle i|\hat{V}|0\rangle}{E_0 - E_i} \right|^2 \delta(E_f - E_0), \quad \hat{V} = \sum_{p<q} \frac{e^2}{r_{pq}}. \tag{21}$$

Here, $|0\rangle$ is the initial doubly inner-shell-ionized [(N-2)-electron two-hole (2h)] state that can be derived from the N-electron HF ground state of the neutral system, $|\Phi_0^{\rm HF}\rangle$, by the application of the annihilation operators, $|0\rangle = \hat{c}_j\hat{c}_k|\Phi_0^{\rm HF}\rangle$, $|f\rangle$ is a final state of the three-hole-one-particle (3h1p) type, $|f\rangle = \hat{c}_a^\dagger\hat{c}_l\hat{c}_m\hat{c}_n|\Phi_0^{\rm HF}\rangle$, and $|i\rangle$'s are the intermediate states. The δ-function of the final–initial energy difference in Eq. (21) reflects the conservation of energy in the course of the nonradiative transition.

Equation (21) suggests that the CICD rate is formed by a superposition of interfering decay pathways, each of which is defined by an intermediate state, $|i\rangle$. Further analysis shows that such states can be either of 2h or of 3h1p type. Consider, for example, $|i\rangle = \hat{c}_l\hat{c}_m|\Phi_0^{\rm HF}\rangle$, where $\hat{c}_{l,m}$ correspond to the

Kr outer-shell vacancies present in the final state, $|f\rangle$. Physically, this means that the three-electron transition consists of virtual two-electron recombination on krypton cations followed by ionization of X (see Figure 6.6). The corresponding recombination matrix element entering Eq. (21) is

$$\begin{aligned}\langle i|V|0\rangle &= \langle \Phi_0^{\mathrm{HF}} \hat{c}_m^\dagger \hat{c}_l^\dagger |\hat{V}| \hat{c}_j \hat{c}_k \Phi_0^{\mathrm{HF}}\rangle \\ &= \langle \varphi_l(\vec{r}_1)\varphi_m(\vec{r}_2)|1/r_{12}|\varphi_k(\vec{r}_1)\varphi_j(\vec{r}_2)\rangle - \langle \varphi_l(\vec{r}_1)\varphi_m(\vec{r}_2)|1/r_{12}|\varphi_j(\vec{r}_1)\varphi_k(\vec{r}_2)\rangle,\end{aligned} \tag{22}$$

where the electron repulsion matrix elements involve the outer-shell ($\varphi_{l,m}$) and the inner shell ($\varphi_{j,k}$) of the Kr's. Assuming that $\varphi_{j,l}$ are localized on the left Kr while $\varphi_{k,m}$ belong to the right Kr (see Figure 6.6), we can obtain the dependence on the recombination matrix element on the interatomic distance, $R_{\mathrm{Kr-Kr}}$, in the limit of large Kr–Kr separation:

$$\begin{aligned}\langle i|V|0\rangle &\approx -\langle \varphi_l(\vec{r}_1)\varphi_m(\vec{r}_2)|1/r_{12}|\varphi_j(\vec{r}_1)\varphi_k(\vec{r}_2)\rangle \\ &\approx -\frac{1}{R_{\mathrm{Kr-Kr}}^3}\langle \varphi_l(\vec{r}_1)|e\vec{r}_1|\varphi_j(\vec{r}_1)\rangle \cdot \langle \varphi_m(\vec{r}_1)|e\vec{r}_2|\varphi_k(\vec{r}_1)\rangle,\end{aligned} \tag{23}$$

where we have neglected the exchange contribution that decreases exponentially with $R_{\mathrm{Kr-Kr}}$ and approximated the direct integral by the leading (dipole–dipole) term of the multipole expansion. The last expression suggests an appealing physical interpretation of the collective decay at large internuclear distances as a two-virtual-photon transition with the two dipole matrix elements in Eq. (23) being regarded as two virtual photons that are "emitted" by the Kr^+'s and "absorbed" by X. Within this simple picture, the CICD is analogous to multi-photon transition while Auger decay and ICD are analogous to a single-photon transition.

Proceeding with the large-R analysis of the ionization matrix element, $\langle f|\hat{V}|i\rangle$, we find that at large Kr_2–X separations it decreases as $1/R_{\mathrm{Kr_2-X}}^2$. As a result, the contribution of the two-electron recombination – ionization pathway to the decay width depends on the cluster geometry as $1/R_{\mathrm{Kr-Kr}}^6 R_{\mathrm{Kr_2-X}}^4$. Since the decomposition of the $(Kr^+)_2X$ cluster along the Kr^+–Kr^+ coordinate automatically means elongation of the Kr_2–X distance as well, the power law exponents are effectively summed, resulting in the $1/R_{\mathrm{Kr-Kr}}^{10}$ dependence. A detailed analysis shows that this type of power law is characteristic of all the possible decay pathways.

Quantitative results for the collective interatomic decay in $(4s^{-1}, 4s^{-1})$ $(Kr^+)_2Ar$ have been obtained in Ref. [54] using Fano-ADC theory. The results for Γ as a function of the Kr–Kr distance (at $R_{\mathrm{Kr_2-Ar}}^{\mathrm{eq}} = 3.3$Å [54]) are shown in Figure 6.7a. At the equilibrium Kr–Kr distance ($R_{\mathrm{Kr_2}}^{\mathrm{eq}} = 4.0$Å [54]), the collective decay width reaches 1.9 meV for triplet and 2.0 meV for singlet doubly ionized states, which corresponds to lifetimes around 300 fs. The predicted lifetime is *five orders of magnitude* shorter than the one of the

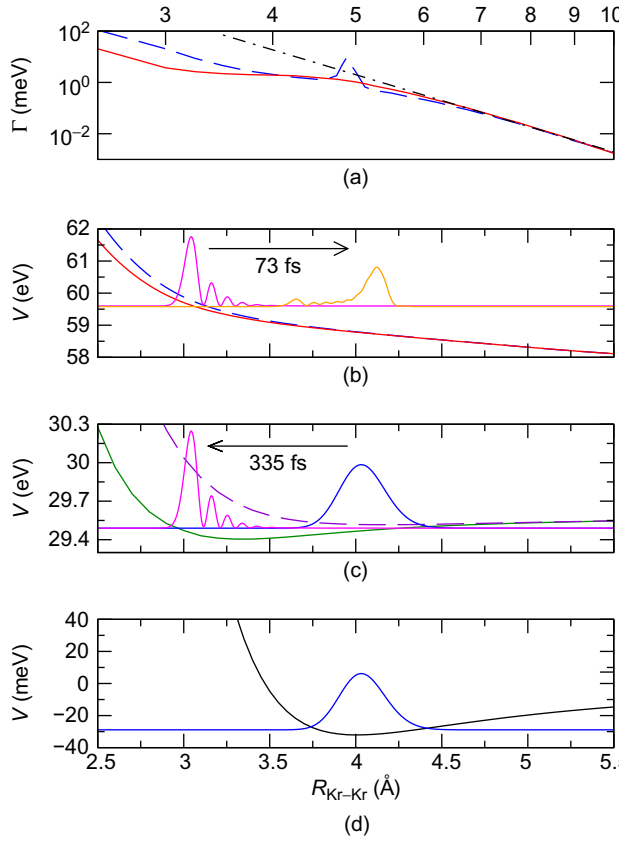

Figure 6.7 (a) Collective decay widths of $(4s^{-1}, 4s^{-1})$ $(Kr^+)_2Ar$ as functions of R_{Kr-Kr} at $R^{eq}_{Kr_2-Ar} = 3.3$Å. Solid line: triplet, dashed line: singlet, dashed-dotted line: $1/R^{10}$ fit (please, note the doubly logarithmic scale). (b) PESs of $(4s^{-1}, 4s^{-1})$ $(Kr^+)_2Ar$ states, cut at $R^{eq}_{Kr_2-Ar} = 3.3$Å. Solid line: triplet state, dashed line: singlet state. Shown also is the vibrational wave packet promoted from the $(4s\sigma_u^{-1})$ state of $(Kr_2)^+Ar$ [see panel (c)] at the moment of closest approach of the two kryptons, $t_{min} = 335$ fs, and 73 fs later. Direction of motion of the wave packet is shown by an arrow. (c) PESs of $(4s\sigma_{g,u}^{-1})$ $(Kr_2)^+Ar$ states, cut at $R^{eq}_{Kr_2-Ar} = 3.3$Å. Solid line: ungerade state, dashed line: gerade state. Shown also is the vibrational wave packet promoted from the ground state [see panel (d)] at $t = 0$ (right) and at t_{min} (left). Direction of motion of the wave packet is shown by an arrow. (d) PES of the neutral $(Kr_2)Ar$, cut at $R^{eq}_{Kr_2-Ar} = 3.3$Å. Shown also is the vibrational ground state.

radiative decay [54], which means that the process is not suppressed by photon emission. At Kr–Kr separation above 6 Å, the collective decay width shows the predicted $1/R^{10}$ behavior (see Figure 6.7a).

The CICD rate as a function of the Kr–Kr distance was used in the nuclear wave packet simulation of the process within the Born–Oppenheimer picture

[54]. The relevant cuts of the Kr_2Ar potential energy surfaces (PESs) at the symmetric geometry with R_{Kr_2-Ar} frozen at its equilibrium value are shown in Figure 6.7. It is assumed that in the beginning the cluster is in its ground vibrational state. At some later time, 4*s* photoionization occurs on the Kr atoms due to the interaction with the high-intensity FEL beam. The double photoionization can occur either directly by a "vertical," that is instantaneous transition to the $(4s^{-1}, 4s^{-1})$ $(Kr^+)_2Ar$ PES or in two stages, bringing the cluster first onto a $(Kr_2)^+Ar$ PES and only later (by another vertical transition) to a doubly ionized PES (see Figure 6.7). The important difference between the one-step and the two-step processes is that the former creates a vibrational wave packet centered around the equilibrium distance of the neutral ($R_{Kr-Kr} = 4.0$Å), while in the latter process the wave packet created on the singly ionized PES can evolve before being promoted to the repulsive decaying state. If at the first stage of the sequential process the $(4s)\,\sigma_u$ orbital of Kr_2 is ionized, the resulting vibrational motion can explore the region of much smaller Kr–Kr distances than in the case of the one-step double ionization. Thus, two-step ionization process, in particular the one proceeding via $(4s)\sigma_u$ ionization, leads the system to the region of much higher collective decay widths than the one-step double ionization and is expected to give a higher yield of the electronic decay. Nuclear dynamics simulations have shown that the CICD yields in the case of one-step double photoionization are 31% and 38% (for triplet and singlet doubly ionized states, respectively), whereas for the two-step ionization into the singlet state, the electronic decay yield reaches 65% [54]. Thus, the nuclear dynamics simulations show that the CICD process can compete successfully with the disintegration of the doubly ionized cluster.

4. OUTLOOK

The results presented in this overview point at the significant impact of the charged environment on the Auger-type processes in polyatomic systems. The specific effects of the additional charges on the decay of inner-shell-ionized species range from strong modulation of the exponential decay rate to transition to nonexponential dynamics (in the case of channel closing) or, on the contrary, onset of exponential electronic (nonradiative) decay (in the case of channel opening). The initial work presented here is nothing but a first step toward systematic exploration of this new inner-shell physics. Let us outline a few directions that we think will be most relevant for the future ab initio studies.

On the methodology side, it would be important to generalize the Fano-ADC theory of Section 2 to the case of triple ionization using the second-order ADC scheme of Ref. [80]. Moreover, the problem of different level of treatment of adjacent excitation classes within the existing ADC

schemes deserves some attention. Indeed, normal Auger dynamics can be formally regarded as a transition between 1h and 2h1p states, which are described by us at the moment up to second and first orders, respectively. A balanced description would mean a more accurate (second-order) treatment of 2h1p's. This would require formulation of a new type of ADC schemes in which the adjacent excitation classes are treated up to the same order. Finally, the Fano-type computational approach presented here is by no means limited to the ADC ab initio methodology. An immediate idea would thus be to construct the analogous schemes based on the equation of motion coupled cluster (EOMCC) methods [81]. This could be particularly relevant for treatment of inner-shell ionization of open-shell systems, for which the EOMCC methods have been developed [82].

As far as physical applications go, Auger-type processes in multiply ionized "building blocks" of biomolecules are the immediate target of the theory with the aim to provide an accurate input for the molecular dynamics simulations of the radiation damage. Besides the *K–LL* Auger in C, N, and O atoms in charged environment, the effect of inner-shell ionization of heavier atoms, such as S, on the radiation damage would be very interesting to explore. The higher-order physical processes involving more than a single participator vacancy, such as collective decay, are extremely interesting from the physical point of view, and their role in molecular inner-shell physics is yet to be understood. Moreover, the effect of charged environment on the ICD rates is yet to be investigated. Finally, it is important to take into account the effect of the ionizing field itself, going beyond sudden ionization paradigm and exploring the processes that are forbidden without the presence of the external field, such as laser-enabled Auger decay [83].

ACKNOWLEDGMENTS

P. K. acknowledges the financial support from the Czech Science Foundation (grant GAČR 202/09/0786) and from the Institutional research plan MSM0021620860. V. A. thanks J.-M. Rost and U. Saalmann for fruitful collaboration on some of the subjects covered in this review. V. A. acknowledges the financial support of the Max Planck Institute for the Physics of Complex Systems (Dresden, Germany) and of the EPSRC (UK) through the Career Acceleration Fellowship (award PHQL_P21289).

REFERENCES

[1] P. Auger, Sur l'effet photoélectrique composé, J. de Phys. 6 (1925) 205.
[2] W. Mehlhorn, Auger-electron spectrometry of core levels of atoms, in: B. Crasemann (Ed.), Atomic Inner-Shell Physics, Plenum, New York, 1985.
[3] N.H. Turner, J.A. Schreifels, Surface analysis: X-ray photoelectron spectroscopy and Auger electron spectroscopy, Anal. Chem. 72 (2000) 99.
[4] G. Wentzel, Über strahlunglose quantensprünge, Zeits. f. Physik 43 (1927) 524.

[5] J.L. Campbell, T. Papp, Widths of the atomic K - N7 levels, At. Data Nucl. Data Tables 77 (2001) 1.
[6] J. Feldhaus, J. Arthur, J.B. Hastings, X-ray free-electron lasers, J. Phys. B 38 (2005) S799; Y. Ding, A. Brachmann, F.-J. Decker, D. Dowell, P. Emma, J. Frisch, S. Gilevich, G. Hays, Ph. Hering, Z. Huang, R. Iverson, H. Loos, A. Miahnahri, H.-D. Nuhn, D. Ratner, J. Turner, J. Welch, W. White, J. Wu, Measurements and simulations of ultralow emittance and ultrashort electron beams in the linac coherent light source, Phys. Rev. Lett. 102 (2009) 254801; T. Tanaka, T. Shintake, (Eds.), *SPring-8 Compact SASE Source Conceptual Design Report*, RIKEN (2005); M. Altarelli et al., (Eds.), *Technical Design Report*, DESY-2006-097 (2007).
[7] R. Neutze, R. Wouts, D. van der Spoel, E. Weckert, J. Hajdu, Potential for biomolecular imaging with femtosecond X-ray pulses, Nature 406 (2000) 752; R. Neutze, G. Huldt, J. Hajdu, D. van der Spoel, Potential impact of an X-ray free electron laser on structural biology, Rad. Phys. Chem. 71 (2004) 905.
[8] H.N. Chapman et al., Femtosecond X-ray protein nanocrystallography, Nature 470 (2011) 73; M.M. Seibert et al., Single mimivirus particles intercepted and imaged with an X-ray laser, Nature 470 (2011) 78.
[9] H.M. Quiney, K.A. Nugent, Biomolecular imaging and electronic damage using X-ray free-electron lasers, Nat. Phys. 7 (2011) 142.
[10] U. Saalmann, J.M. Rost, Ionization of clusters in strong X-ray laser pulses, Phys. Rev. Lett. 89 (2002) 143401.
[11] H. Ågren, A. Cesar, C.-M. Liegener, Theory of molecular Auger spectra, Adv. Quant. Chem. 23 (1992) 1.
[12] B.T. Pickup, On the theory of fast photoionization processes, Chem. Phys. 19 (1977) 193.
[13] O. Gunarsson, K. Schönhammer, Dynamical theory of Auger processes, Phys. Rev. B 22 (1980) 3710.
[14] N. Moiseyev, Non-Hermitian Quantum Mechanics, Cambridge University Press, Cambridge, UK, 2011.
[15] R. Santra, L.S. Cederbaum, Non-Hermitian electronic theory and applications to clusters, Phys. Rep. 368 (2002) 1.
[16] U. Fano, Effects of configuration interaction on intensities and phase shifts, Phys. Rev. 124 (1961) 1866.
[17] T. Åberg, G. Howat, Theory of Auger effect, in: W. Mehlhorn (Ed.), Corpuscles and Radiation in Matter, Handbuch der Physik, Vol. 31, Springer, Berlin, 1982.
[18] V. Averbukh, L.S. Cederbaum, Ab initio calculation of interatomic decay rates by a combination of the Fano ansatz, Green's-function methods, and the Stieltjes imaging technique, J. Chem. Phys. 123 (2005) 204107.
[19] J. Schirmer, L.S. Cederbaum, O. Walter, New approach to the one-particle Green's function for finite Fermi systems, Phys. Rev. A 28 (1983) 1237; L.S. Cederbaum, Greens functions and propagators for chemistry, in: P.v.R. Schleyer, P.R. Schreiner, N.A. Allinger, T. Clark, J. Gasteiger, P. Kollman, H.F. Schaefer III (Eds.), Encyclopedia of Computational Chemistry, Wiley, New York, 1998.
[20] J. Schirmer, Closed-form intermediate representations of many-body propagators and resolvent matrices, Phys. Rev. A 43 (1991) 4647; F. Mertins, J. Schirmer, Algebraic propagator approaches and intermediate-state representations. I. The biorthogonal and unitary coupled-cluster methods, Phys. Rev. A 53 (1996) 2140; A.B. Trofimov, J. Schirmer, Molecular ionization energies and ground- and ionic-state properties using a non-Dyson electron propagator approach, J. Chem. Phys. 123 (2005) 144115.
[21] A. Szabo, A.S. Ostlund, Modern Quantum Chemistry: Introduction to Advanced Electronic Structure Theory, Dover, New York, 1996.
[22] J. Schirmer, A.B. Trofimov, G. Stelter, A non-Dyson third-order approximation scheme for the electron propagator, J. Chem. Phys. 109 (1998) 4734.
[23] E. Davidson, The iterative calculation of a few of the lowest eigenvalues and corresponding eigenvectors of large real-symmetric matrices, J. Comp. Phys. 17 (1975) 87.

[24] P.W. Langhoff, Stieltjes-Tchebycheff moment-theory approach to molecular photoionization studies, in: T. Rescigno, V. McKoy, B. Schneider (Eds.), Electron-Molecule and Photon-Molecule Collisions, Plenum, New York, 1979; A.U. Hazi, Stieltjes-moment-theory technique for calculating resonance widths, in: T. Rescigno, V. McKoy, B. Schneider (Eds.), Electron-Molecule and Photon-Molecule Collisions, Plenum, New York, 1979.
[25] V. Carravetta, H. Ågren, Stieltjes imaging method for molecular Auger transition rates: Application to the Auger spectrum of water, Phys. Rev. A 35 (1987) 1022.
[26] F. Müller-Plathe, G.H.F. Diercksen, Molecular photoionization cross sections by moment theory. An introduction, in: S. Canuto, J. D'Albuquerque e Castro, F.J. Paixão (Eds.), Electronic Structure of Atoms, Molecules and Solids, World Scientific, Singapore, 1990; F. Müller-Plathe, G.H.F. Diercksen, Perturbative-polarization-propagator study of the photoionization cross section of the water molecule, Phys. Rev. A 40 (1989) 696.
[27] R.K. Nesbet, Stieltjes imaging method for computation of oscillator-strength distributions for complex atoms, Phys. Rev. A 14 (1976) 1065.
[28] V.V. Ivanov, A.V. Luzanov, Semiempirical and ab initio calculations of the full configuration interaction using iterated Krylovs spaces, J. Struct. Chem. 38 (1997) 10; H. Ågren, V. Carravetta, H.J.Aa. Jensen, P. Jørgensen, J. Olsen, Multiconfiguration linear-response approaches to the calculation of absolute photoionization cross sections: HF, H_2O, and Ne, Phys. Rev. A 47 (1993) 3810; V. Carravetta, Y. Luo, H. Ågren, Accurate photoionization cross sections of diatomic molecules by multi-configuration linear response theory, Chem. Phys. 174 (1993) 141.
[29] K. Gokhberg, V. Vysotskiy, L.S. Cederbaum, L. Storchi, F. Tarantelli, V. Averbukh, Molecular photoionization cross sections by Stieltjes-Chebyshev moment theory applied to Lanczos pseudospectra, J. Chem. Phys. 130 (2009) 064104.
[30] S. Kopelke, K. Gokhberg, L.S. Cederbaum, F. Tarantelli, V. Averbukh, Autoionization widths by Stieltjes imaging applied to Lanczos pseudospectra, J. Chem. Phys. 134 (2011) 024106; S. Kopelke, K. Gokhberg, V. Averbukh, F. Tarantelli, L.S. Cederbaum, Ab initio interatomic decay widths of excited states by applying Stieltjes imaging to Lanczos pseudospectra, J. Chem. Phys. 134 (2011) 094107.
[31] J. Schirmer, A. Barth, Higher-order approximations for the particle-particle propagator, Z. Phys. A 317 (1984) 267.
[32] P. Kolorenč, V. Averbukh, K. Gokhberg, L.S. Cederbaum, Ab initio calculation of interatomic decay rates of excited doubly ionized states in clusters, J. Chem. Phys. 129 (2008) 244102.
[33] P. M. Morse, H. Feshbach, Methods of Theoretical Physics, McGraw-Hill, New York, 1953.
[34] F. Bloch, Double electron transitions in X-ray spectra, Phys. Rev. 48 (1935) 187.
[35] V. Averbukh, U. Saalmann, J.-M. Rost, Auger decay in the field of a positive charge, submitted to Phys. Rev. A.
[36] D.L. Walters, C.P. Bhalla, Nonrelativistic Auger rates, X-ray rates, and fluorescence yields for the 2p shell, Phys. Rev. A 4 (1971) 2164.
[37] A.G. Kochur, D. Petrini, E.P. da Silva, 2s-photoionisation of atomic magnesium: Shake processes and Coster-Kronig radiationless decay, A&A 365 (2001) 248.
[38] J. Breidbach, L.S. Cederbaum, Migration of holes: Formalism, mechanisms, and illustrative applications, J. Chem. Phys. 118 (2003) 3983; A.I. Kuleff, J. Breidbach, L.S. Cederbaum, Multielectron wave-packet propagation: General theory and application, J. Chem. Phys. 123 (2005) 044111.
[39] L. Young et al., Femtosecond electronic response of atoms to ultra-intense X-rays, Nature 466 (2010) 56; J. Wark, Atomic physics: X-ray laser peels and cores atoms, Nature 466 (2010) 35.
[40] S.H. Southworth, E.P. Kanter, B. Krässig, L. Young, G.B. Armen, J.C. Levin, D.L. Ederer, M.H. Chen, Double K-shell photoionization of neon, Phys. Rev. A 67 (2003) 062712.
[41] C.P. Bhalla, N.O. Folland, M.A. Hein, Theoretical K-shell Auger rates, transition energies, and fluorescence yields for multiply ionized neon, Phys. Rev. A 8 (1973) 649.

[42] M.H. Chen, Auger transition rates and fluorescence yields for the double-K-hole state, Phys. Rev. A 44 (1991) 239.
[43] P. Pelicon, I. Čadež, M. Žitnik, Ž. Šmit, S. Dolenc, A. Mühleisen, R.I. Hall, Formation of the hollow $1s^0\ ^1S$ state of Ne^{2+} by electron impact: Observation by means of an Auger hypersatellite, Phys. Rev. A 62 (2000) 022704.
[44] P. Kolorenč, V. Averbukh, J. Chem. Phys. 135 (2011) 134314.
[45] V.G. Yarzhemsky, A. Sgamellotti, Auger rates of second-row atoms calculated by many-body perturbation theory, J. Elec. Spec. Rel. Phen. 125 (2002) 13.
[46] H.P. Kelly, K Auger rates calculated for Ne^+, Phys. Rev. A 11 (1975) 556.
[47] C.A. Nicolaides, Th. Mercouris, Y. Komninos, Many-electron theory of autoionizing states using complex coordinates: The position and the partial and total widths of the Ne^+ 1*s* hole state, Int. J. Quantum Chem. 26 (1984) 1017.
[48] C. A. Nicolaides, Th. Mercouris, Partial widths and interchannel coupling in autoionizing states in terms of complex eigenvalues and complex coordinates, Phys. Rev A 32 (1985) 3247.
[49] G. Howat, T. Åberg, O. Goscinski, Relaxation and final-state channel mixing in the Auger effect, J. Phys. B 11 (1978) 1575.
[50] A. Albiez, M. Thoma, W. Weber, W. Mehlhorn, KL2,3 ionization in neon by electron impact in the range 1.550 keV: Cross sections and alignment, Z. Phys. D 16 (1990) 97.
[51] L. Avaldi, G. Dawber, R. Camilloni, G.C. King, M. Roper, M.R.F. Siggel, G. Stefani, M. Zitnik, A. Lisini, P. Decleva, Measurement of Ne 1*s* and 1*snl* satellite photoelectron spectra near threshold, Phys. Rev. A 51 (1995) 5025.
[52] V.V. Afrosimov, Yu.S. Gordeev, A.N. Zinov'ev, D.Kh. Rasulov, A.P. Shergin, Observation of new types of Auger transitions in atoms with two internal vacancies, JETP Lett. 21 (1975) 249.
[53] I. Lee, R. Wehlitz, U. Becker, M. Ya. Amusia, Evidence for a new class of many-electron Auger transitions in atoms, J. Phys. B 26 (1993) L41.
[54] V. Averbukh, P. Kolorenč, Collective interatomic decay of multiple vacancies in clusters, Phys. Rev. Lett. 103 (2009) 183001.
[55] N.M. Kabachnik, J. Tulkki, H. Aksela, S. Ricz, Coherence and correlation in the anisotropy of Ne KL-LLL satellite Auger decay, Phys. Rev. A 49, 4653 (1994).
[56] E. Hartmann, X-ray fluorescence yields for light emitter atoms: Carbon, J. Phys. B 21 (1988) 1173.
[57] M. Coville, T.D. Thomas, Molecular effects on inner-shell lifetimes: Possible test of the one-center model of Auger decay, Phys. Rev. A 43 (1991) 6053.
[58] F.P. Larkins, Influence of core hole screening on molecular Auger rates and inner-shell lifetimes, J. Electron Spectrosc. Relat. Phenom. 67 (1994) 159.
[59] L. Asplund, U. Gelius, S. Hedman, K. Helenelund, K. Siegbahn, P.E.M. Siegbahn, Vibrational structure and lifetime broadening in core-ionised methane, J. Phys. B 18 (1985) 1569.
[60] P.A. Heimann, L.J. Medhurst, M.R.F. Siggel, D.A. Shirley, C.T. Chen, Y. Ma, F. Sette, Zero electron kinetic energy photoemission of CH_4 and CD_4 at the carbon K ionization threshold, Chem. Phys. Lett. 183 (1991) 234.
[61] H.M. Köppe, B.S. Itchkawitz, A.L.D. Kilcoyne, J. Feldhaus, B. Kempgens, A. Kivimäki, M. Neeb, A.M. Bradshaw, High-resolution C 1*s* photoelectron spectra of methane, Phys. Rev. A 53 (1996) 4120.
[62] T.X. Carroll, N. Berrah, J. Bozek, J. Hahne, E. Kukk, L.J. Sæthre, T.D. Thomas, Carbon 1*s* photoelectron spectrum of methane: Vibrational excitation and core-hole lifetime, Phys. Rev. A 59 (1999) 3386.
[63] F.P. Larkins, L.C. Tulea, E.Z. Chelkowska, Auger electron spectra of molecules: The first row hydrides, Aust. J. Phys 43 (1990) 625.
[64] R. Sankari, M. Ehara, H. Nakatsuji, Y. Senba, K. Hosokawa, H. Yoshida, A. De Fanis, Y. Tamenori, S. Aksela, K. Ueda, Vibrationally resolved O 1*s* photoelectron spectrum of water, Chem. Phys. Lett. 380 (2003) 647.

[65] R.W. Shaw Jr., J.S. Chen, T.D. Thomas, Auger spectrum of ammonia, J. Elec. Spec. Rel. Phen. 11 (1977) 91; J.M. White, R.R. Rye, J.E. Houston, Experimental Auger electron spectrum of ammonia, Chem. Phys. Lett. 46 (1977) 146; R. Camilloni, G. Stefani, A. Giardini-Guidoni, The measured Auger electron spectrum of ammonia vapour, Chem. Phys. Lett. 50 (1977) 213.
[66] C. Gnodtke, U. Saalmann, J.M. Rost, Ionization and charge migration through strong internal fields in clusters exposed to intense x-ray pulses, Phys. Rev. A 79 (2009) 041201(R).
[67] M. Bixon, J. Jortner, Intramolecular radiationless transitions, J. Chem. Phys. 48 (1967) 715.
[68] V. Averbukh, U. Saalmann, J.M. Rost, Suppression of exponential electronic decay in a charged environment, Phys. Rev. Lett. 104 (2010) 233002.
[69] T. Kylli, J. Karvonen, H. Aksela, A. Kivimäki, S. Aksela, R. Camilloni, L. Avaldi, M. Coreno, M. de Simone, R. Richter, K.C. Prince, S. Stranges, L_1–$L_{2,3}M$ Coster-Kronig transitions in argon, Phys. Rev. A 59 (1999) 4071.
[70] D.J. Wales et al., The Cambridge Cluster Database, 2007, http://www-wales.ch.cam.ac.uk/CCD.html. A. Cuccoli, A. Macchi, V. Tognetti, R. Vaia, Monte Carlo computations of the quantum kinetic energy of rare-gas solids, Phys. Rev. B 47 (1993) 14923.
[71] D.A. Verner, D.G. Yakolev, I.M. Band, M.B. Trzhaskovskaya, Subshell photoionization cross sections and ionization energies of atoms and ions from He to Zn, At. Data Nucl. Data Tabl. 55 (1993) 233.
[72] J.C. Fuggle, S.F. Alvarado, Core-level lifetimes as determined by x-ray photoelectron spectroscopy measurements, Phys. Rev. A 22 (1980) 1615.
[73] L.S. Cederbaum, J. Zobeley, F. Tarantelli, Giant intermolecular decay and fragmentation of clusters, Phys. Rev. Lett. 79 (1997) 4778.
[74] S. Marburger, O. Kugeler, U. Hergenhahn, T. Möller, Experimental evidence for interatomic Coulombic decay in Ne clusters, Phys. Rev. Lett. 90 (2003) 203401.
[75] T. Jahnke, A. Czasch, M.S. Schöffler, S. Schössler, A. Knapp, M. Käsz, J. Titze, C. Wimmer, K. Kreidi, R.E. Grisenti, A. Staudte, O. Jagutzki, U. Hergenhahn, H. Schmidt-Böcking, R. Dörner, Experimental observation of interatomic Coulombic decay in neon dimers, Phys. Rev. Lett. 93 (2004) 163401.
[76] G. Öhrwall, M. Tchaplyguine, M. Lundwall, R. Feifel, H. Bergersen, T. Rander, A. Lindblad, J. Schulz, S. Peredkov, S. Barth, S. Marburger, U. Hergenhahn, S. Svensson, O. Björneholm, Femtosecond interatomic Coulombic decay in free neon clusters: Large lifetime differences between surface and bulk, Phys. Rev. Lett. 93 (2004) 173401.
[77] R. Santra, J. Zobeley, L.S. Cederbaum, Electronic decay of valence holes in clusters and condensed matter, Phys. Rev. B 64 (2001) 245104.
[78] N. Vaval, L.S. Cederbaum, Ab initio lifetimes in the interatomic Coulombic decay of neon clusters computed with propagators, J. Chem. Phys. 126 (2007) 164110.
[79] V. Averbukh, L.S. Cederbaum, Interatomic electronic decay in endohedral fullerenes, Phys. Rev. Lett. 96 (2006) 053401.
[80] A. Tarantelli, L.S. Cederbaum, Approximation scheme for the three-particle propagator, Phys. Rev. A 46 (1992) 81.
[81] J. Geersten, M. Rittby, R.J. Bartlett, The equation-of-motion coupled-cluster method: Excitation energies of Be and CO, Chem. Phys. Lett. 164 (1989) 57; D.C. Comeau, R.J. Bartlett, The equation-of-motion coupled-cluster method. Applications to open- and closed-shell reference states, Chem. Phys. Lett. 207 (1993) 414.
[82] M. Włoch, J.R. Gour, K. Kowalski, P. Piecuch, Extension of renormalized coupled-cluster methods including triple excitations to excited electronic states of open-shell molecules, J. Chem. Phys. 122 (2005) 214107.
[83] P. Ranitovic, X.M. Tong, C.W. Hogle, X. Zhou, Y. Liu, N. Toshima, M.M. Murnane, H.C. Kapteyn, Laser-enabled Auger decay in rare-gas atoms, Phys. Rev. Lett. 106 (2011) 053002; X.M. Tong1, P. Ranitovic, C.W. Hogle, M.M. Murnane, H.C. Kapteyn, N. Toshima, Theory and experiment on laser-enabled inner-valence Auger decay of rare-gas atoms, Phys. Rev. A 84 (2011) 013405.

INDEX

Note: The letters '*f*' and '*t*' following locators denote figures and tables respectively.